Kevin O'Donnell
Volkmar Dierolf *Editors*

TOPICS IN APPLIED PHYSICS 124

Rare-Earth Doped III-Nitrides for Optoelectronic and Spintronic Applications

Springer

Topics in Applied Physics
Volume 124

Available online at
SpringerLink.com

Topics in Applied Physics is part of the SpringerLink service. For all customers with standing orders for Topics in Applied Physics we offer the full text in electronic form via SpringerLink free of charge. Please contact your librarian who can receive a password for free access to the full articles by registration at:

springerlink.com → Orders

If you do not have a standing order you can nevertheless browse through the table of contents of the volumes and the abstracts of each article at:

springerlink.com → Browse Publications

For other titles published in this series, go to
www.springer.com/series/560

Topics in Applied Physics

Topics in Applied Physics is a well-established series of review books, each of which presents a comprehensive survey of a selected topic within the broad area of applied physics. Edited and written by leading research scientists in the field concerned, each volume contains review contributions covering the various aspects of the topic. Together these provide an overview of the state of the art in the respective field, extending from an introduction to the subject right up to the frontiers of contemporary research.

Topics in Applied Physics is addressed to all scientists at universities and in industry who wish to obtain an overview and to keep abreast of advances in applied physics. The series also provides easy but comprehensive access to the fields for newcomers starting research.

Contributions are specially commissioned. The Managing Editors are open to any suggestions for topics coming from the community of applied physicists no matter what the field and encourage prospective editors to approach them with ideas.

Kevin O'Donnell • Volkmar Dierolf
Editors

Rare Earth Doped III-Nitrides for Optoelectronic and Spintronic Applications

Springer

Editors
Professor Kevin O'Donnell
Department of Physics
University of Strathclyde
John Anderson Building
107 Rottenrow East
Glasgow, G4 0NG
Scotland, UK

Professor Volkmar Dierolf
Physics Department
Lehigh University
16 Memorial Drive East
Bethlehem, PA 18015
USA

Published by Springer,
P.O. Box 17, 3300 AA Dordrecht, The Netherlands
In association with
Canopus Academic Publishing Limited,
15 Nelson Parade, Bedminster, Bristol, BS3 4HY, UK

www.springer.com and www.canopusbooks.com

ISSN 0303-4216
ISBN 978-90-481-2876-1 e-ISBN 978-90-481-2877-8
Springer Dordrecht Heidelberg London New York

Library of Congress Control Number: 2010924738

© Canopus Academic Publishing Limited 2010
No part of this work may be reproduced, stored in a retrieval system, or transmitted in any form or by any means, electronic, mechanical, photocopying, microfilming, recording or otherwise, without written permission from the Publisher, with the exception of any material supplied specifically for the purpose of being entered and executed on a computer system, for exclusive use by the purchaser of the work.

Cover design: eStudio Calamar S.L.

Printed on acid-free paper

Springer is part of Springer Science+Business Media (www.springer.com)

Preface

It has been noted several times previously that the Rare Earths (RE), a sequence of elements with atomic numbers in the range from 58 (Ce) to 71 (Lu), are neither earths nor particularly rare. They are metals, whose ores are often found together with oxides of the "alkaline earths" (Ca, Mg), staples of the building industry, while Cerium, for example, is the 25th most abundant element in the Earth's crust. However, the chemical similarity of all REs to each other and to Lanthanum, reflected in their alternative descriptor, Lanthanoids, made extraction of the separate elements difficult until technical advances in the 1960s kick-started the modern era of RE science.

The most widespread commercial use of RE metals at present is in the production of super-strong permanent magnets, containing Neodymium: check your refrigerator door for an example. RE ferromagnetism arises from the angular momentum of electrons in partially filled 4*f* atomic shells. In chemical compounds of RE with non-metals, the 4*f* shell is surrounded by filled 5*s* and 5*p* orbitals, while bonding involves the outerlying $5d^1$ and $6s^2$ electrons, resulting (usually) in a RE^{3+} ion that is chemically similar to La^{3+}. (RE may also be found in a divalent charge state, with an 'extra' electron in the 5*d* shell.) Hence the sequence of trivalent ions from Ce^{3+} to Yb^{3+} is characterised by a 4*f* shell occupation that rises from 1 to 13 electrons. Another widespread use of Neodymium, which will be familiar to readers of this book if not to the public at large, is in the Nd:YAG laser, widely used both at its fundamental wavelength of 1064 nm in the infra-red and when frequency-doubled into the visible. The invention of this laser in 1964 followed the realisation that intra-4*f* shell optical transitions, forbidden by selection rules in the free RE ion, become allowed when odd-parity crystal fields "mix in" higher-lying orbitals[1]. Subsequently, the energy levels of all RE^{3+} ions, introduced as dopants into $LaCl_3$, were explored using optical absorption and emission spectroscopies and summarised in the famous Dieke diagram[2]. Since the

[1] G. S. Ofelt, J. Chem. Phys. 37, 511 (1962); B. R. Judd, Phys. Rev. 127, 750 (1962).
[2] G. H. Dieke, *Spectra and Energy Levels of Rare Earth Ions in Crystals* (Interscience Publishers, New York, 1968).

4*f* electron wavefunctions are shielded from the RE's surroundings, the energy levels of the resulting multi-electron states are discrete and well-defined. Optical transitions between these levels produce characteristically sharp spectral features.

The doping of III-nitride semiconductors with RE ions is the subject of this book. Chapter 1 provides the theoretical background and points out particular difficulties associated with describing the interaction between the optically active electrons and the band structure of the host material. This turns out to be a recurring theme throughout the book. Chapter 2 describes doping by ion implantation. The impact of fast ions causes lattice damage and the effects of annealing this damage are treated in detail. Chapter 3 continues with the topic of ion beams in their role of determining the lattice location of implanted ions. Chapters 4 and 5 describe the development of III-N RE electroluminescent devices. Chapter 6 introduces the topic of RE-doped III-N quantum dots. Chapter 7 describes the spectral characterisation of, mainly, Eu-doped III-N hosts, including AlGaN and AlInN, and introduces the topic of 'site multiplicity'. Chapter 8 explores site multiplicity for a number of different ions in different hosts and offers a useful comparison of samples doped by different methods. The excitation model for RE ions in solids is outlined in Chapter 9 and Chapter 10 returns to the theme of ferromagnetism of RE, presenting a systematic study of the growth and magnetic properties of Gd-doped GaN. This is followed by a short summing-up chapter with a view to our future prospects.

Glasgow — Kevin O'Donnell

Bethlehem, PA — Volkmar Dierolf

April 2010

Contents

1 Theoretical Modelling of Rare Earth Dopants in GaN 1
R. Jones and B. Hourahine
1.1 Introduction 1
1.2 Theoretical Modelling 2
1.2.1 Quantum Mechanical Methods 3
1.2.2 4f Electrons 5
1.2.3 The RE Pseudopotential 6
1.2.4 Basis Functions 7
1.2.5 Semi-Empirical Modelling 7
1.2.6 Semi-Empirical LDA+U 8
1.2.7 Clusters and Supercells 10
1.2.8 Kohn-Sham and Occupancy Levels 11
1.2.9 Formation Energies, Vibrational Modes, Energy Levels 11
1.3 Er, Eu and Tm in GaN 13
1.3.1 Treatment of f-Electrons – Substitutional Er_{Ga} 15
1.4 Deep Level Transient Spectroscopy 16
1.5 Excitation and Emission in GaN:Eu 17
1.6 RE Defects in AlN 18
1.7 Conclusions 20
References 21

2 RE Implantation and Annealing of III-Nitrides 25
Katharina Lorenz, Eduardo Alves, Florence Gloux, Pierre Ruterana
2.1 Introduction 26
2.2 Implantation Damage in GaN 27
2.2.1 Implantation Geometry Dependence 27
2.2.2 Fluence Dependence 29
2.2.3 Implantation Temperature Dependence 35

2.3 Annealing and Optical Activation of RE Ions 37
2.3.1 Optical Activation by High Temperature Annealing 38
2.3.2 Influence of Annealing Atmosphere 39
2.3.3 Annealing of AlN-Capped Samples 42
2.3.4 Annealing at Ultrahigh Pressure 46
2.4 RE Doping of AlN and AlN-Containing Ternary Alloys 48
2.5 Summary 52
References 52

3 Lattice Location of RE Impurities in III-Nitrides 55
André Vantomme, Bart De Vries, Ulrich Wahl
3.1 Introduction 56
3.2 Lattice Sites in Wurtzite Crystals 57
3.3 Experimental Lattice Site Determination 59
3.3.1 Ion Beam Channelling 60
3.3.2 Emission Channelling 61
3.3.3 X-Ray Absorption Fine Structure (XAFS) 65
3.3.4 Hyperfine Interactions 66
3.4 Lattice Site in Wurtzite Crystals 66
3.4.1 Lattice Location of High-Fluence GaN:RE Implants by RBS/C 66
3.4.2 Lattice Location of Low-Fluence GaN:RE by EC 71
3.5 RE Lattice Site Dependence on Experimental Parameters 79
3.5.1 Dependence on the Fluence 79
3.5.2 Dependence on the Implantation Geometry 83
3.5.3 Dependence on the Implantation Temperature 86
3.5.4 Co-Implantation of RE and O or Other Impurity 86
3.6 The Effect of Sample Mosaicity on Determining the Lattice Sites: AlN vs. GaN 90
3.7 Conclusions 94
Acknowledgements 95
References 96

4 Electroluminescent Devices Using RE-Doped III-Nitrides 99
Akihiro Wakahara
4.1 Introduction 99
4.2 General Treatment of EL devices 101
4.3 III-N:RE EL Devices 102
4.4 Light Emitting Diode with RE-doped GaN Active Layer 109
4.5 Summary 111
References 112

5 Er-Doped GaN and $In_xGa_{1-x}N$ for Optical Communications 115
R. Dahal, J. Y. Lin, H. X. Jiang and J.M. Zavada
5.1 Introduction 116
5.2 Er Doping of GaN and InGaN by Ion Implantation 117
5.3 *In Situ* Er Doping of GaN by MBE and HVPE 129
5.4 MOCVD Growth of Er-Doped III-Nitrides 136
5.4.1 Er-Doped GaN 138
5.4.2 Er-Doped InGaN 142
5.5 Current-Injected 1.54 μm LEDs Based on GaN:Er 150
5.6 Er-Doped Nitride Amplifier (EDNA) Development 152
5.7 Summary 155
Acknowledgements 155
References 156

6 Rare-Earth-Doped GaN Quantum Dots 159
B. Daudin
6.1 Introduction 159
6.2 Growth of GaN QDs 161
6.2.1 Undoped Dots 161
6.2.2 Rare-Earth-Doped Dots 163
6.3 Optical Properties 168
6.3.1 Eu-Doped GaN QDs Embedded in AlN 168
6.3.2 Eu-Doped InGaN QDs Embedded in GaN 171
6.3.3 Tm-Doped Dots 172
6.3.4 Tb-Doped GaN QDs 175
6.3.5 Photoluminescence Dynamics of RE-Doped GaN QDs 177
6.4 Electroluminescence of Rare Earth-Doped GaN QDs 183
6.5 Conclusion 185
Acknowlegements 186
References 186

7 Visible Luminescent RE-doped GaN, AlGaN and AlInN 189
Robert Martin
7.1 Introduction to Luminescence of RE-Doped GaN 189
7.2 Preparation of Samples 192
7.3 Cathodoluminescence and X-Ray Microanalysis 192
7.4 Annealing Temperature Dependence of RE Luminescence 197
7.5 Site Multiplicity in GaN:Eu Revealed by Photoluminescence Spectroscopy 200
7.6 Luminescence of Eu Ions in AlGaN across the Entire Alloy Composition Range 205
7.7 Luminescence of RE Ions in AlInN Hosts 213
7.8 Conclusion 216
Acknowledgements 217
References 217

8 Combined Excitation Emission Spectroscopy (CEES) of RE Ions in Gallium Nitride 221
Volkmar Dierolf
8.1 Introduction 221
8.1.1 RE Ions in GaN: General Considerations 222
8.1.2 CEES Experimental Setup 223
8.2 Application of CEES to Erbium in GaN 226
8.2.1 Introduction 226
8.2.2 Direct Excitation of 1.5 μm Emission 226
8.2.3 Two-Step Excitation of 980 nm and 820 nm Emission 231
8.2.4 Three-Step Excitation of 670 nm and 550 nm Emission 236
8.2.5 Direct Excitation of 670 nm and 550 nm Emission 237
8.2.6 Comparison of in situ Doped MBE and MOCVD Grown GaN:Er Samples 239
8.2.7 Above Bandgap Excitation of 1.5 μm Emission 241
8.2.8 Summary of CEES Spectroscopy of GaN:Er 242
8.3 Application of CEES to Neodymium in GaN 242
8.3.1 Introduction and Experimental Background 242
8.3.2 Assignment of Excitation and Emission Peaks 243
8.3.3 Electron-Phonon Coupling 246
8.3.4 Inhomogeneous Broadening: Spectral and Spatial Aspects 246
8.3.5 Summary of CEES of GaN:Nd 249
8.4 Application of CEES to Europium in GaN and AlGaN 250
8.4.1 Introduction 250
8.4.2 Energetic Fingerprints of Different Sites 251
8.4.3 Electron Phonon Coupling 255
8.4.4 Effect of Growth Conditions 257
8.4.5 Excitation under Non-Resonant Conditions 260
8.4.6 Summary 265
8.5 Conclusion 266
Acknowledgements 266
References 267

9 Excitation Mechanisms of RE Ions in Semiconductors 269
Alain Braud
9.1 Introduction 270
9.2 Excitation Mechanisms 271
9.2.1 Excitation Paths Involving Electron-Hole Pairs 271
9.2.2 Excitation Paths Involving Change of RE Ion Charge 274
9.2.3 Excitation Paths Involving Donor-Acceptor Pairs 278
9.2.4 Energy Transfer Processes 280
9.3 RE Excitation Processes in GaN 282
9.3.1 RE Excitation Schemes 282

9.3.2 Isolated RE Ions Versus RE Ions Coupled to Carrier Traps 283
9.3.3 Effective Excitation Cross-Section 288
9.3.4 RE-Related Carrier Trap 294
9.4 Conclusion 303
Acknowledgements 305
References 305

10 High-Temperature Ferromagnetism in the Super-Dilute Magnetic Semiconductor GaN:Gd 309
O. Brandt, S. Dhar, L. Pérez, V. Sapega
10.1 Introduction 310
10.2 Experimental 311
10.2.1 Sample Growth and Structural Characterization 311
10.2.2 Assessment of Electrical and Magnetic Properties 312
10.2.3 Assessment of Optical Properties 313
10.3 Basic Structural and Magnetic Properties 314
10.3.1 Gd Incorporation in GaN 314
10.3.2 Magnetic Characteristics 318
10.4 Phenomenological Model 323
10.5 Optical Properties 326
10.6 Magnetic Phases and Anisotropy 331
10.6.1 Magnetic Phases 332
10.6.2 Magnetic Anisotropy 334
10.6.3 Discussion 336
10.7 Recent Studies in the Literature 338
10.8 Conclusions 339
Acknowledgements 340
References 340

11 Summary and Prospects for Future Work 343
References 345

12 Index 347

List of Contributors

Eduardo Alves
Instituto Tecnológico e Nuclear
Estrada Nacional 10
2686-953 Sacavém
Portugal

O. Brandt
Paul-Drude-Institut für Festkorperelektronik
Hausvogteiplatz 5-7
10117 Berlin
Germany

Alain Braud
Centre de Recherche sur les Ions, les Matériaux et la Photonique (CIMAP)
UMR 6252 CNRS-CEA-ENSICAEN
Université de Caen
14050 Caen
France

R. Dahal
Department of Electrical & Computer Engineering
Texas Tech University
Lubbock
TX 79409
United States

Subhabrata Dhar
Department of Physics
Indian Institute of Technology Bombay
Powai
Mumbai 400076
India

B. Daudin
CEA-CNRS group “Nanophysique et Semiconducteurs”
Institut Néel/CNRS-Univ. J. Fourier and CEA Grenoble
INAC, SP2M
17 rue des Martyrs
38 054 Grenoble
France

Volkmar Dierolf
Physics Department
Lehigh University
16 Memorial Drive East
Bethlehem
PA 18015
United States

Bart De Vries
Instituut voor Kern- en Stralingsfysica and INPAC
Celestijnenlaan 200 D
K.U.Leuven
B-3001
Leuven
Belgium

Florence Gloux
CIMAP, UMR 6252
CNRS-ENSICAEN-CEA-UCBN
14050 Caen Cedex
France

B. Houraine
SUPA Dept of Physics
University of Strathclyde
Glasgow G4 0NG
United Kingdom

H. X. Jiang
Department of Electrical & Computer Engineering
Texas Tech University
Lubbock
TX 79409
United States

R. Jones
Department of Physics
The University of Exeter
Exeter, EX4 4QL
United Kingdom

J. Y. Lin
Department of Electrical & Computer Engineering
Texas Tech University
Lubbock
TX 79409
United States

Katherina Lorenz
Instituto Tecnológico e Nuclear
Estrada Nacional 10
2686-953 Sacavém
Portugal

Robert Martin
SUPA Dept of Physics
University of Strathclyde
Glasgow G4 0NG
United Kingdom

Lucas Pérez
Departmento de Física de Materiales
Universidad Complutense
28040 Madrid
Spain

Pierre Ruterana
CIMAP, UMR 6252
CNRS-ENSICAEN-CEA-UCBN
14050 Caen Cedex
France

Victor Sapega
Ioffe Physico-Technical Institute
Russian Academy of Sciences
194021 St. Petersburg
Russia

André Vantomme
Instituut voor Kern- en Stralingsfysica and INPAC
Celestijnenlaan 200 D
K.U.Leuven
B-3001
Leuven
Belgium

Ulrich Wahl
Instituto Tecnológico e Nuclear
Estrada Nacional 10
2686-953 Sacavém
Portugal

Akahiro Wakahara
Toyohashi University of Technology
Dept Electrical and Electronic Engineering
1-1 Hibarigaoka
Tempaku
Toyohashi
Aichi 441-8580
Japan

J. M. Zavada
Department of Electrical & Computer Engineering
North Carolina State University
Raleigh
NC 27695
United States

Chapter 1
Theoretical Modelling of Rare Earth Dopants in GaN

R. Jones and B. Hourahine

Abstract We review theoretical investigations into the structure and electrical activity of rare earth (RE) dopants in III-V semiconductors especially GaN. Substitutional rare earth dopants in GaN are found to be electrically inactive and require another defect to enable them to act as strong exciton traps. In contrast AlN is distinctive as it possesses a deep donor level. The electronic structure of complexes of the RE with other defects is discussed along with implications for efficient room temperature luminescence.

1.1 Introduction

Rare Earth (RE) doped semiconductors exhibit sharp intra-*f* luminescence lines that in wide-band materials such as GaN and SiC, or in Si nanocrystals, persist to room temperature. This has naturally led to increased interest in the dopants in these materials. Moreover, red, green and blue emissions from RE-doped GaN, either doped during growth [1, 2] or afterwards by ion implantation [3, 4] have been reported.

As far as we are aware, all confirmed optical transitions in doped semiconductors we discuss are due to the trivalent oxidation state RE^{3+}. Thus irrespective of doping and material, the *f*-shell of Er for example contains the fixed number of 11 electrons. The localized nature of the *f*-shell ensures that the influence of the

R. Jones
Department of Physics, The University of Exeter, Exeter, EX4 4QL, United Kingdom
R.Jones@ex.ac.uk

B. Hourahine
SUPA Dept of Physics, University of Strathclyde, Glasgow G4 0NG, United Kingdom
benjamin.hourahine@strath.ac.uk

crystal field of the host on the RE is slight, confined to splitting the degenerate multiplet states of the RE and relaxing the selection rules for dipole-allowed transitions. However, it is by no means obvious that the RE defect does not seriously perturb the electronic structure of the host. The size of the RE ion, number of valence electrons and electronegativity may be different from those of the replaced atom and it might be expected that the RE would induce one or more gap levels either occupied by valence electrons or the *f*-shell. This is even more the case in group-IV semiconductors where the RE has a different valence from the host [5]. However, we have found that RE impurities, substituting for Ga in the III-V semiconductors GaAs and GaN, do not introduce any gap levels and hence are unable to bind excitons [6, 7]. This is similar to the substitutional N defect in GaAs where the isovalent impurity is unable to bind an exciton and does not possess a gap level. N in GaP does on the other hand possess a gap acceptor level and is able to bind an exciton. In GaAs, N has a level resonant with the conduction band which in high concentrations affects the absorption spectrum but is invisible in photoluminescence [8]. Clusters of nitrogen atoms, however, at neighbouring As sites form gap levels extending to $Ec - 80$ meV [8]. It is an interesting question whether pairs of RE impurities on neighbouring Ga lattice sites in GaN give gap levels. However, such pairs may not be efficient exciton traps as non-radiative decay through Auger excitation may limit their optical activity (concentration quenching). It seems more likely that RE related traps require the pairing of the RE impurity with an intrinsic defect. This immediately explains why large doping concentrations of the RE (~1%) are necessary for strong emission [9] and high resolution photoluminescence (PL) and photoluminescent excitation spectroscopy (PLE) in GaN reveal [10] the presence of many RE centres of low symmetry, usually described as 'multiple sites'. In GaN the RE-V_N defect is suggested to be a dominant trap [7, 11] .

The situation may be quite different for RE dopants in AlN. We have found that Er, Tm and Eu dopants in hexagonal AlN, with a gap of 6.12 eV, introduce a deep donor level around 0.5 eV above the valence band [12]. This surprising result may be due to the large band gap revealing more levels or the greater ionicity of the material.

We review below results that have been obtained on RE dopants in GaN and AlN using density functional techniques.

1.2 Theoretical Modelling

There are various ways in which defects in materials and especially covalently bonded semiconductors like GaN can be modelled. Quantum mechanical methods like density functional theory (DFT) that attempt to solve the many-body Schrödinger equation with minimal approximation can be distinguished from more approximate methods. Current computational power limits routine application of DFT methods to ~ 500 group-IV atom clusters or supercells. More ap-

proximate atomistic methods, such as tight binding schemes, can deal with systems around an order of magnitude larger. To extend this especially to problems involving diffusion and atomic motion, molecular dynamics, Monte Carlo and continuum methods can be used. These normally require some atomistic potential or functional form giving the binding and migration energies of defects. One limitation is then the accuracy of data input to the modelling.

1.2.1 Quantum Mechanical Methods

The energy of an assembly of atoms is obtained from the many-body Schrödinger equation involving both ions and electrons. This is impossible to solve exactly and progress can only be made if a set of approximations are made.

The first approximation is due to Born and Oppenheimer [13] who argued that since the nuclear mass is so much larger than that of the electrons, we can treat the nuclear motion classically and reduce the Schrödinger equation to one involving only the electrons moving in a potential of fixed nuclei at sites denoted by **R**. The solution of this equation is the *structural energy* $E(\mathbf{R})$. To determine dynamical quantities like vibrational modes and diffusion barriers, we then need to solve the classical problem of the nuclei moving in the force field $-\nabla_{\mathrm{R}} E(\mathbf{R})$.The equilibrium structure (and other stationary points, such as saddle points in a chemical reaction) is given by $|\nabla_{\mathrm{R}} E(\mathbf{R})| = 0$, however, multiple local equilibria usually exist in real systems.

We next consider the Schrödinger equation of the electrons. This equation still cannot be solved exactly because of the interaction between each electron pair, i and j, described by a Coulomb potential,

$$\sum_{i,j(\neq i)} V(\mathbf{r}_i - \mathbf{r}_j) \ .$$

If this term were to be neglected, then the Schrödinger equation is separable and the exact wave-function can be written down as a sum of product orbitals $\Pi_i \phi_i(\mathbf{r}_i)$, where $\phi_i(\mathbf{r})$ are the eigenfunctions of a Hamiltonian for independent electrons. Of course, we must require that the total fermionic wavefunction be antisymmetric and this can be achieved by a suitable sum over permutations of the single-particle orbitals. For example, in the case of the H_2 molecule, the two electrons are described by a wavefunction of the form

$$\frac{1}{\sqrt{2}}\left(\phi_1(\mathbf{r}_1)\phi_2(\mathbf{r}_2) - \phi_1(\mathbf{r}_2)\phi_2(\mathbf{r}_1)\right) .$$

Here $\phi_\lambda(\mathbf{r})$ is a spin-orbital. This general type of wavefunction is called a Slater determinant [14] and is specified by a particular electronic configuration, i.e., a listing of the single particle spin-orbitals λ occupied by N electrons, which

are then understood to have the correct antisymmetry guaranteed by the form of the determinant.

The neglect of the electron-electron interaction term is too extreme to allow useful results and various attempts have been made to take this interaction into account. The two principle schemes are Hartree-Fock (HF) and density functional theory (DFT). Both of these replace the potential acting on electron *i*, i.e.,

$$\sum_{i,j(\neq i)} V(\mathbf{r}_i - \mathbf{r}_j) ,$$

by an average over the positions of the other electrons. Thus this potential becomes $V_{\text{eff}}(\mathbf{r}_i)$. Clearly the Schrödinger equation is then separable and we can write the wavefunction as a Slater determinant. In these theories, the effective potential is composed of two terms: the Hartree potential $V_{\text{H}}(\mathbf{r})$ and the exchange-correlation potential $V_{\text{XC}}(\mathbf{r})$. The former is the electrostatic potential due to the density of charge $en(\mathbf{r})$ at the point r where

$$n(\mathbf{r}) = \sum_{\lambda} f_{\lambda} \mid \phi_{\lambda}(\mathbf{r}) \mid^2,$$

where f_{λ} is the occupancy of the orbital λ. The exchange-correlation potential differs in the two theories.

In HF, the exchange part of this potential arises directly from the antisymmetry of the determinantal wavefunction, leading to a complicated integral equation that depends on the orbital $\phi_{\lambda}(\mathbf{r})$ and the other occupied orbitals. The correlation part of the potential is more problematic, as it cannot be expanded with the simple single determinental wavefunction of HF, but can be included via approaches such as *configuration interaction* between different determinants or via perturbation theory [15]. In DFT, the exchange-correlation is rigorously determined only by the electron density [16, 17]. This is an important result but the precise dependence on the density is not known except for the particular case of the homogeneous electron gas. In this case, the Schrödinger equation has been evaluated by a mixture of perturbation theory and numerical simulations and the dependence of the energy on n determined. In this way V_{XC} is known accurately. Now for inhomogeneous problems, *e.g.* molecules and solids, we assume that V_{XC} at a point r is given by the homogeneous electron gas value involving the density $n(\mathbf{r})$ at the same point r. This is called the local density functional approximation (LDA). To illustrate this, for large electron densities, V_{XC} is proportional to $n^{1/3}$ and thus in local density functional theory $V_{\text{XC}}(\mathbf{r})$ is also proportional to $n^{1/3}(\mathbf{r})$. It is possible to go beyond local density functional theory using, for example, a gradient corrected formalism (GGA) or hybrid functionals containing contributions from the Hartree-Fock potential [18] but the agreement of the extended treatments with experiment, at least for problems in condensed matter physics, is not uniformly better than that provided by the simpler local density theory.

Further approximations are often made. The electrons of say Ga are divided into a set of core electrons, *e.g.* $1s^2 2s^2 2p^6 3s^2 3p^6$ as well as the three valence

electrons $4s^2 4p^1$ and the $3d^{10}$ electrons. Only the latter 13 are included in the calculation thorough a specially constructed *pseudopotential* which leads to the same atomic valence energy levels but has no core states. The *pseudowavefunctions* of the valence energy levels are exactly the same as those of the atom outside a small core radius so that the bonding properties of the *pseudoatom* are close to those of the true atom. However, the obtained Ga-N bond length is too short unless the 3*d* electrons are included. The effects of these 3*d* electrons are often included via the non-linear core correction (NLCC) [19].

1.2.2 4f Electrons

Theorists have had to face the problem that the usual approaches for the simulation of large electronic systems (LDA or GGA) cannot satisfactorily describe compounds with strong electron-electron interactions due to the failure of the mean field approach, the assumption that all electrons experience an average potential. LDA is in fact a one-electron method with an orbitally independent potential, and applying it to a system containing transition metals (TM) or rare earths (RE) with partially filled *d*- or *f*-shells gives results consistent with a metallic electronic structure and itinerant *d*- or *f*-electrons, which is certainly incorrect for most RE compounds and several examples of TM systems (NiO being the classic example). Other choices for the exchange correlation such as GGA, which are still mean-field corrections for the non-interacting system, again suffer from the same pathology. A proper treatment of the strongly correlated 4*f* electrons of the lanthanides requires contributions beyond a classical mean-field approach and computational methods which are able to address this correlation problem, such as the GW approximation [20] or LDA extensions including orbital dependent potential like self interaction correction (SIC) [21, 22], are computationally demanding.

In the strongly correlated systems the *d*- or *f*-electrons are often strongly localized and there is a noticeable energy difference between occupied and unoccupied states with strong *d* or *f* character, which are called *lower* and *upper* Hubbard bands, in analogy with the Hubbard Hamiltonian approach. There have been a number of attempts to go beyond the LDA to make it able to account for strong electron-electron correlation in such systems. The full SIC approach [21] can reproduce the localized nature of *d* and *f* electrons in TM and RE compounds as well as the total energy of these systems but is not intended to reproduce the one-electron energies of conventional band-structure. Additionally SIC is known to over-correct many properties [23]. As discussed in Sect. 1.2.6 there have also been several recent attempts to approximate the effects of the SIC method with (semi-)local corrections, such as the LDA+*U* approach. This is conceptually similar to the Hubbard Hamiltonian description: the non-local and energy dependent self energy is approximated by a frequency independent but non-local screened Coulomb potential.

As illustrated in Sect. 1.3.1 we find that in general, as was suggested over ten years ago by Pethukov et al. [24], including the strongly localized RE 4*f* electrons in the pseudopotential core is a satisfactory approximation when *f*-electrons are not directly involved in the chemical bonding and the ionization energy of the 4*f* states is large in comparison with the band-gap. In particular, structural properties like lattice constants or bulk moduli are quite unaffected by the details of the method used to treat the 4*f* orbitals.

1.2.3 The RE Pseudopotential

The accurate description of elements such as Er provides several challenges to traditional pseudopotenials for LDA density functional theory calculations. Firstly, the electronic configuration of Er requires that the valence shell contains both 5*s* and 6*s* electrons. Most of the commonly used semi-nonlocal forms for the pseudopotential (involving only θ and ϕ projection), for example those introduced by Hamman, Schlüter and Chiang [25], and by Troullier and Martins [26], allow only for a fit to a single orbital with a given angular momentum. It is therefore not possible to use these schemes to account simultaneously for both the 5*s* and 6*s* electrons. A completely separable pseudopotential must be used. We chose the dual-space separable pseudopotentials developed by Hartwigsen, Goedecker and Hutter [27]. These pseudopotentials are fitted to the energies and charge densities of all-electron calculations for a large number of occupied and unoccupied levels, including the occupied 5*s* and 6*s* orbitals in the case of Erbium.

A pseudopotential for Er has previously been published [27] which included this extended norm-conservation. This is a semi-core pseudopotential, in which several of the higher-lying core levels are included in the valence shell. For Er this results in 22 valence electrons per atom including the incomplete 4*f* shell. However, the *f*-electrons are highly correlated and cannot be described accurately by the LDA. Consequently, the Er potential available in the literature does not in fact perform very well in the description of Er systems.

More accurate pseudopotentials have been generated in which the 4*f* electrons are included in the core. Although the energy of the 4*f* orbitals is comparable to that of the outer valence orbitals, it is in fact the case that the *f*-electrons do not play a major role in the bonding of RE compounds, as we discuss below. The effect of the 4*f* electrons can therefore be accounted for within the core, provided that we take account of the non-linear core corrections (NLCC) to the exchange-correlation energy [19]. With the 4*f* electrons included in the core there is a significant core charge density in the region where the valence charge is localized, and the NLCC is necessary to correctly describe the exchange-correlation energy as the valence charge density varies from its atomic form. A partial NLCC scheme is sometimes used in which the all-electron core charge is cut off at very small radii by matching the full charge to a smooth function, and a fit of the resulting charge density to a sum of Gaussians used to compute the exchange-correlation

energy and potential for the total charge density. In practice, the form of the pseudopotential, and the fitting procedure employed, are as proposed in [27] while the LDA exchange-correlation functional used is the Padé parameterization described previously [28].

For the case of Er, the close energy spacing of the 4*f*, 6*s*, 5*d* and 6*p* orbitals results in a large number of possible electron configurations with similar total energies. To select the most appropriate configuration in which to place the atom for all-electron calculations, the environment of the atom must be considered. Since we are most interested in Er in its 3+ oxidation state, we consider the 4*f* shell to have an occupation of 11, and one less than its ground state configuration as an isolated atom. There are then three electrons to be placed between the outermost (6*s*, 5*d* and 6*p*) orbitals. Pseudopotentials were generated for the $5d^1 6s^1 6p^1$, $5d^0 6s^2 6p^1$ and $5d^1 6s^2 6p^0$ configurations. Tests of these three different pseudopotentials in condensed matter environments confirmed that the exact choice of electron occupation numbers in these outer shells did not affect the predicted physical properties for Er. The pseudopotential used for the calculations presented below was that fitted to the all-electron levels of the $5d^1 6s^1 6p^1$ configuration.

1.2.4 Basis Functions

In order to solve the DFT equations for solid state problems, the wavefunctions are represented by basis functions: often plane waves, but localized ones such as Gaussian orbitals have become increasingly popular. The disadvantage with plane waves lies on the large number of functions (typically about 100 per atom) required to converge the properties of interest, compared to about 20 basis functions per atom for localized sets. However, programming and efficiently computing the matrix elements of the Hamiltonian between localized basis sets are now the important issues. Well known codes using plane waves are vasp [29, 30] and abinit [31], while siesta [32] and aimpro [33, 34] use localized basis functions.

1.2.5 Semi-Empirical Modelling

It is possible to approximate the Kohn-Sham DFT equations to give a family of semi-empirical methods with much lower computational costs. These methods can be viewed as a form of tight-binding. The Density Functional based Tight binding method (DFTB) [35] is an approximate second-order expansion of the Kohn-Sham Density-Functional Theory (DFT) with respect to fluctuations in the charge density. This gives a transparent and parameter-free technique where all terms can be readily pre-calculated using DFT. Besides the usual “band structure” and short-range repulsive terms of tight-binding, the final approximate Kohn-Sham func-

tional includes a Coulomb interaction between charge fluctuations. At large distances this accounts for long-range electrostatic forces while it approximately includes the exchange-correlation at short range. This method has been applied with some success to solid state [36], molecular or biological systems [37]. Materials like silicon [38], SiC [39], diamond [40], boron and boron nitride [41] and III-V semiconductors like GaN [42] and GaAs [43] have been successfully studied within the DFTB approach. The spin-polarized, charge self consistent, DFTB approach has been extensively discussed elsewhere [44, 45, 46].

The study of strongly correlated systems (like RE or transition metal containing compounds) requires somewhat different techniques to the usual methods for the simulation of solid state systems, because of the nature of these atoms. RE ions for example have atomic numbers between 57 and 70, hence relativistic effects become important. Additionally, many properties of transition metal or lanthanide elements depend on the strongly correlated behavior of their *d*- or *f*-electrons. To study such cases requires a more sophisticated theory than simple mean-field methods. To address all of this additional complexity in treating lanthanides, the DFTB method has been substantially extended to treat strongly correlated systems, by adpting LDA+*U* [47, 48] and pseudo-SIC-like [49, 50] approaches. We would like to remark that (to our knowledge) DFTB contains the first TB implementation of LDA+*U* and SIC-like methods.

1.2.6 Semi-Empirical LDA+U

As discussed by Anisimov et al. [51], it is natural to separate electrons into localized *d*- or *f*-electrons and delocalized *s*-and *p*-electrons. While for the latter an orbitally independent one-electron potential (as in LDA) will suffice, a Hartree-Fock like interaction better describes the local interactions of the strongly localized *d*- or *f*-electrons. This is proportional to

$$\frac{1}{2}\sum\nolimits_{i,j(\neq i)} n_i n_j \,,$$

where n_i are the occupancies of the localized shells. If we assume that the Coulomb energy of the electron-electron interaction, as a function of the total number of electrons

$$N = \sum_i n_i$$

is well represented by LDA (even if it gives wrong single-particle energies), then LDA already contains part of this energy. This must be subtracted from the total energy and replaced with a Hubbard model-like term. As a result we get the functional [52, 53]:

$$E = E_{LDA} - \frac{1}{2}UN(N-1) + \frac{U}{2}\sum_{i,j(\neq i)}^{\text{site}} n_i n_j = E_{LDA} + \Delta E_{LDA+U}$$

where U is the on-site electron-electron repulsion. Strictly speaking, the process of subtracting the double-counting of the electron-electron interaction of strongly correlated electrons from the LDA total energy and substituting it with a Hubbard Hamiltonian-like term is not unambiguous. The electron-electron interactions have already been taken into account in a amean field way with LDA, while the Hubbard Hamiltonian also incorporates a large part of the total Coulomb energy of the system. One can try to identify those parts of the DFT total energy corresponding to the interactions included with the Hubbard Hamiltonian in order to subtract them. This is not trivial, because while the Kohn-Sham Hamiltonian is written in terms of the total density, the Hubbard Hamiltonian is written in terms of orbital occupation numbers, and a direct link is not straightforward. Secondly, even if it were possible to exactly remove the on-site Coulombic contribution in the LDA and Hartree contributions, it would be undesirable, as the spatial variation of the Coulomb and exchange-correlation potential is important and better described in DFT than in the Hubbard approach. It is instead better to try and identify a mean-field part of the Hubbard Hamiltonian and subtract that, leaving only a correction to the LDA solution.

Unfortunately this subtraction is not uniquely defined. In the "around mean field" (AMF) limit the LDA+U correction to the electronic potential averaged over all occupied states in a given shell is zero (the name refers to this being one possible way to define a mean field theory). For strongly correlated systems (or in the presence of a crystal/ligand field) the limit of uniform occupancy is not correct and the AFM functional leads to rather unrealistic results for strongly localized electrons. This has led to the suggestion of another correction which produces the correct behavior in the fully localized limit (FLL) where the eigenvalues of the local occupation matrix are either 0 or 1, i.e. electrons are either fully present or absent at the site. Most of the modern LDA+U calculations rely on one of these two functionals, although in real materials the occupation numbers should lie between these two limits, hence neither AMF nor FLL are strictly speaking correct for real systems: one should therefore use an interpolation between the two limits [54]. However AMF and FLL will bracket the correct LDA+U double counting term.

While it has previously been suggested that for *empirical* tight-binding the effects of on-site correlation can be mimicked by an empirical adjustment of symmetry-resolved on-site energies [55], this is problematic for low symmetry *d*-electron systems and for *f*-manifolds. In the RE ions of interest here, the so-called fully localized limit should be achieved (i.e., the orbital occupations of states localized within the 4*f* manifold should be either be 0 or 1 [53, 52]).

In the simplest rotationally invariant form of LDA+U [56] the correction to the LDA potential is of the form

$$\Delta V^{\sigma}_{\mathrm{m}\nu} = -(U-J)_l \left(n^{\sigma}_{\mu\nu} - DC[n^{\sigma}_{\mu\nu}] \right),$$

where n^{σ} is the local spin occupation matrix within a given atomic manifold (labelled by μ and ν), and (U–J) is the screened and spherically averaged electron-electron interaction. $DC[n]$ is the double counting term appropriate for the two limiting cases FLL and AMF [47, 57].

Full self-interaction corrected (SIC) LDA is relatively computationally expensive, hence several cheaper approximations have appeared. It is possible to demonstrate [47] that LDA+U without the double-counting correction is equivalent to an approximation to the full SIC based on the method proposed by Vogl [49] and its recent refinements [50, 58], which is referred to as pseudo-SIC (or pSIC). This correction includes only contributions near to atoms, so cannot address problems such as the derivative discontinuity in Kohn-Sham DFT. The connection to LDA+U allows us to obtain energy expressions which are variationally connected to the potential [47, 59], as well as deriving atomic forces [60], while giving a unique recipe for the (U–J) terms from the LDA functional.

1.2.7 Clusters and Supercells

The structural energy $E(\mathbf{R})$ is of fundamental importance and can be found for a molecule, a cluster of atoms, or indeed for a periodically repeated cell, often called a supercell. The latter is made up of several unit cells of the bulk, but each supercell contains only one defect. Periodic boundary conditions imply that low order electric multipoles must vanish within the cell to ensure energy convergence. For example, when a defect is charged, a uniform compensating background charge has to be added to ensure that the cell is neutral. However, if no higher order corrections are considered, the self-consistent electron density n is such that the electric dipole and quadrupole within the cell vanish [61]. A problem with the supercell approach related to the study of defects is the so called defect-image interaction. The interaction between a defect and its periodically repeated copies may lead to spurious results. This is especially true when dealing with vacancy-related defects which produce long range strain fields, or shallow centers with long range electronic states. Another problem, particularly in modelling defects in GaN, InN and AlN, arises from the treatment of exchange and correlation for which local density functional theory, in the supercell formalism, leads to band gaps much smaller than the experimental values. This causes severe problems in the treatment of charged defects and will be discussed further below.

On the other hand, the difficulty for clusters is that their surfaces must be saturated, e.g., by hydrogen [33], otherwise the gap levels associated with surface dangling bonds could interfere with those of a defect.

For supercell calculations, one also needs to integrate quantities such as the band structure over the Brillouin zone (BZ). This can be done in several ways but

a method introduced by Monkhorst and Pack [62] is one of the most common. A uniform mesh of points is generated to lie within the BZ, and *folded* according to the symmetry operations of the zone. The integrand is then sampled on the irreducible points k_i, normally referred as *special k*-points, which have a representativity w_i that depend on their site symmetry. This scheme has been particularly successful due to its robustness and ease of implementation. Convergence tests are also straightforward by simply generating higher density *k*-point sets.

1.2.8 Kohn-Sham and Occupancy Levels

The structural energy $E(\mathbf{R})$ can be written in terms of energy-levels $\mathcal{E}_\lambda$ associated with each spin-orbital $\phi_\lambda(\mathbf{r})$ by

$$E(\mathbf{R}) = \sum_\lambda f_\lambda \mathcal{E}_\lambda - \frac{1}{2} E_H + \int d\mathbf{r}\{\varepsilon_{XC} - \mu_{XC}\} n(\mathbf{r}) + E_{ion} .$$

Here f_λ is the occupancy of level λ, E_H is the Hartree energy or the electrostatic energy of the electron density $n(\mathbf{r})$ and ε_{XC} and μ_{XC} are the exchange correlation energy and potential densities, respectively, which depend only on $n(\mathbf{r})$. The last term is the electrostatic energy of all the ions. The first term is the band structure energy which in the simplest case dominates the total energy.

Consider now a situation in which an electron is removed from level σ by an ionization process. In the simplest case when the band structure energy dominates, the ionization energy is simply the change in the band structure energy, i.e., it is just $-\mathcal{E}_\sigma$. Similarly, optical absorption from state σ to μ, results in an energy change $\mathcal{E}_\mu - \mathcal{E}_\sigma$. These results impart a temptingly simple interpretation of the Kohn-Sham energy levels $\mathcal{E}_\lambda$. However, since the charge density changes whenever ionization or optical absorption takes place, the change in energy is not simply the band structure term and the change in all the terms must be considered.

In the special case of the highest occupied Kohn-Sham level however, its enery corresponding to the electron chemical potential of the system (Janak's theorem [63]). This allows the energy of the highest occupied state to be correctly interpreted as the 1st ionization energy of the system.

1.2.9 Formation Energies, Vibrational Modes, Energy Levels

The formation energy F of a defect [64] is defined in terms of the structural energy of a cell containing n_i atoms of species i by

$$F = E(\mathbf{R}) - \sum_i n_i \mu_i \ .$$

Here μ_i is the chemical potential of species i. The chemical potential is determined by the energy per atom from a reservoir in equilibrium with the defective crystal. For instance, for oxygen defects in GaN, the chemical potential of oxygen is usually determined by the energy of an O atom in O_2 (but may instead be limited by the possibility of native oxide formation).

The formation energy controls the equilibrium concentration of defects which in the dilute approximation is given by $gN\exp(-F/kT)$ where N is the density of atomic sites and g is the orientational and spin degeneracy of the defect. Strictly speaking, even at 0 K where entropic terms vanish, the formation energy should include a PV term appropriate for an enthalpy, a zero-point motion sum

$$\frac{1}{2}\sum_i \hbar\omega_i$$

over all available vibrational frequencies ω_i, and a term $-qE_F$ for defects which are charged with q electrons. Here E_F is the Fermi-level. However, for low defect concentrations usually found in solids, and when ultra-light impurities such as hydrogen or muonium are not involved, we have to consider the last term only.

Localized vibrational modes and their frequencies are quantities which can be accurately predicted by *ab-initio* methods. These can be directly compared with infra-red absorption, Raman scattering or photoluminescence data. Most often, two main approximations are made, namely (i) the adiabatic (or Born-Oppenheimer) approximation, discussed previously, where the nuclei are regarded as point-like masses surrounded by electrons that adiabatically follow their vibrational movement, and (ii), the harmonic approximation, according to which, the structural energy $E(\mathbf{R})$ of the defective system is expanded to second order of the atomic displacements [65]. Hence, from the second derivatives of the energy with respect to atomic coordinates,

$$\Phi_{ij} = \partial^2 E/\partial \mathbf{r}_i \partial \mathbf{r}_j$$

we obtain a dynamical matrix

$$D_{ij} = \Phi_{ij}/\sqrt{m_i m_j}$$

(where m_i is the mass of the atom i), whose eigenvalues and eigenvectors give the squared frequencies ω^2 and the corresponding normal coordinates [33].

We define a donor as a defect which is positively charged when ionized, while an acceptor is a defect which is negatively charged when ionized. The donor level relative to E_v is the energy required to excite a electron from the top of the valence band to the positively charged defect. Alternatively, it is the energy necessary to excite a hole from the positively charged defect to the top of the valence band. On the other hand, an acceptor level relative to E_c is the energy required to excite an electron, trapped on a negatively charged defect, to the

bottom of the conduction band. In terms of total energies the donor level with respect to the valence band is the difference in energies between the final and initial states or $E(\mathbf{R}^0) - E(\mathbf{R}^+) - E_v$ while the acceptor level with respect to the conduction band is $E_c - E(\mathbf{R}^-) + E(\mathbf{R}^0)$. Here $\mathbf{R}^0$, $\mathbf{R}^\pm$ are the stable structures of the defect in each charge state. These electrical levels are thermodynamic quantities. The energy with respect to the Fermi level tells us the charge state taken by a defect. In this sense they should not be confused with one-electron energies or the Kohn-Sham levels ε_λ discussed above.

There is no standard procedure for the calculation of the energy levels of defects. One common way [64] is to model the defect in a supercell, and to evaluate the formation energy *F(q)* of the defect with *q* electrons *q* =…,–1,0,+1,…,

$$F(q) = E(\mathbf{R}^q) - \sum_i n_i \mu_i - qE_F,$$

where E_F is the Fermi level position with respect to E_v. However, problems arise in evaluating these energies accurately. For example the calculation of E_v is not straightforward as the highest occupied crystalline state shifts when the defect is introduced in the supercell. Moreover, and as mentioned above, total energies within the supercell approximation are affected by multiple interactions due to the three-dimensional replication of defects. This is more grave when charged states are involved in the calculations. Several correction procedures have been proposed, the most popular by Makov and Payne, which accounts for the energy of an array of point-like charges [66]. For instance, to correct the formation energy from the dominant monopole interaction between charged defects one has to add $\alpha_M q^2/L\varepsilon$ to *F(q)*. Here α_M is the Madelung constant associated with a supercell of characteristic length *L*, and ε is the permittivity of the host crystal. Given that ε = 8.9 in GaN [67], and considering a standard characteristic supercell size L ~ 11–17 Å, we end with corrections of the order of 0.1 eV for first ionized states, and ~ 0.4 eV for second ionized states. The latter is unacceptably large compared to a 3.4 eV gap and care [68] is therefore needed when applying such corrections.

An alternative procedure [69, 70] is to compare the calculated level positions with those of a standard defect whose donor or acceptor levels are known. We shall discuss this in more detail below.

1.3 Er, Eu and Tm in GaN

Emission channelling techniques and Rutherford backscattering (RBS) experiments provide evidence that some RE dopants, e.g., Pr [71], occupy Ga substitutional sites, while others, such as Eu [72, 73], appear to occupy a site displaced from the substitutional one. Er inhabits a number of sites [74]. The general multiplicity of RE sites is supported by PL and photoluminescent excitation (PLE) studies [10, 75, 76]. The majority species (99%) is excited by resonant 4*f*-pumping

but not by above-gap excitation and this is consistent with the view that the substitutional species cannot bind an exciton at room temperature. The minority centre responsible for the above gap luminescence possesses a broad absorption band within ~ 0.4 eV of the band edges, probably related to a carrier trap. For Eu doped GaN, initial PLE studies [76] reveal a broad peak around 0.37 eV of the band edges and in a similar region to a band seen by Fourier transform infra-red spectroscopy [77], with a later study [75] monitoring the $^5D_0 \rightarrow ^7F_2$ demonstrating distinct differences in emission excited via either the broad sub-gap feature or above gap excitation.

Density functional calculations have shown [7] that isolated Eu, Er and Tm defects which substitute for Ga, are less stable than a RE-N rock salt precipitate by 1.2 – 1.5 eV per RE atom. These high energies show that the dissolved fraction of the RE in *equilibrium* with a cubic precipitate, at 1000 °C, is much less than 1 at%. The cubic phases are however metallic and consequently their formation would degrade the optical properties of the material. In practice, higher dissolved fractions will arise if the RE is bound to a native defect or impurity. The RE-N bonds have calculated lengths around 2.2 – 2.1 Å and within about 3% to the lengths found in EXAFS [78]. However, in the case of Eu, some studies [73, 72] have found that Eu is displaced from its lattice site, possibly indicating a complex with another defect. The identity of the complexes is however not known at present.

The electronic band structures in the region of the fundamental gap of RE-doped GaN are strikingly similar to those of GaN, indicating that substitutional defects are electrically and optically inert. This is consistent with carrier measurements before and after implantation with the RE [79]. These experiments clearly show that substitutional RE cannot be an electron trap and by inference cannot be an exciton trap. This result points to the role played by RE complexes in serving as exciton traps. A number of complexes involving the RE have been investigated theoretically, including RE bound to N or Ga vacancies, Ga interstitials, oxygen impurities. The RE-VN complex is found to possess the greatest binding energy, ~ 1.0 to 0.7 eV, sufficiently large that most nitrogen vacancies would remain bound to the RE at typical annealing temperatures of 1000 °C. The electronic structure of the complex shows a half-filled level about 0.2 eV below E_c for all three REs. This has to be contrasted with the isolated V_N defect which has an occupied level in the conduction band [80, 81, 82] and is auto-ionized. The 0.2 eV may be related to the broad band found by PLE and IR-studies of Eu doped material discussed above [76, 77].

The formation energy of V_N is however large, (~1–4 eV [80]) and we have to suppose that the defects are introduced by implantation or during low temperature growth. The RE increases the vacancy concentration by lowering its formation energy, by around 1 eV in the case of Eu-V_N. The concentration of such vacancies is expected to be enhanced in *p*-type GaN as well as material grown under less N rich conditions, as apparently observed [10, 83].

1.3.1 Treatment of f-Electrons – Substitutional Er_{Ga}

To demonstrate the validity of using pseudopotentials to represent the 4*f* semicore states of the lanthanides, we now discuss the Er substitutional RE_{Ga} in hexagonal (wurtzite) GaN in some detail, stressing the differences between the LDA and LDA+U approaches. RE_{Ga} substitutionals are the simplest stable lanthanide defects in GaN [57, 59, 84, 85, 86, 87, 88]. From experimental studies we know that Er ions in GaN, prefer the Ga position [89], occur in the 3+ valence state [90] and possess C_{3v} symmetry [91] with relatively short distances to the surrounding N-ligands [92].

Table 1.1. Bond lengths **Å** and local strain around the C_{3v} Er_{Ga} substitutional in hexagonal GaN. For the definition of the entries in the table see the text. The local strain is defined as the ratio between the Er-N_1 bonds and the Ga-N_1 bonds in the bulk. For further details see the individual references.

	Er-N_1	Er-N_2	Er-Ga_1	Er-Ga_2	Strain
LDA [84]	2.13	2.16	3.22	3.26	
Exp. [78]	2.17	2.17	3.26	3.26	
DFTB [57]	2.15	2.17	3.32	3.35	11.6%
DFTB+*U* FLL [57]	2.18	2.20	3.28	3.38	13.1%
DFTB+*U* AMF [57]	2.17	2.19	3.29	3.37	12.6%
pSIC DFTB [57]	2.17	2.18	3.29	3.36	12.6%

The local structure of the defects is insensitive to whether the Ga-3*d* orbitals are treated as valence or core. The results here use a parameterization where the Ga-3*d* states are not included in the valence, but these do not differ substantially from results obtained by including them [57]. Supercells containing 256 atoms and a 4×4×4 Monkhorst-Pack *k*-point sampling were used to calculate the results reported here. The substitutional Er_{Ga} in the lowest energy configuration is found to have C_{3v} symmetry as expected. The Er ion is surrounded by four N atoms, one (identified by the label Er-N_1 in the Table 1.1) being slightly more distant from the Er ion than the other three (Er-N_2 in the Table 1.1). According to the C_{3v} symmetry the Er second neighbors can be similarly divided in two groups (called Er-Ga_1 and Er-Ga_2 in Table 1.1).

We find that, after geometry optimization, substitutional Er sits on-site: the calculated bond lengths to neighbours are reported in Table 1.1 together with experimental and the results of LDA treatments. The calculated values are in good agreement with the experimental measurements and the lattice distortion has values very close to previous pseudopotential LDA results [84]. Different orbital-dependent calculation schemes do not significantly influence the system geometry. Apart from the relatively small compressive stress in the neighborhood of the defect (Er is bigger than Ga with covalent (3+ ionic) radii of 1.57 (1.03) and 1.26 (0.62) Å respectively) no other effects on the host geometry are observed. The

compressive stress, estimated by comparing Er-N bonds with Ga-N bonds in the bulk, is reported in the last column of Table 1.1.

The very simple LDA-like formulation of the DFTB approach provides Er-N bond lengths already in good agreement with experimental data. The LDA+*U* like and pSIC implementations lead only to small changes. In other words, relaxing the structure with or without the contributions of the orbital-dependent potential does not substantially change the predicted geometry of the system and influences only slightly the bond lengths: bond lengths calculated with and without the orbital dependent potentials differ at most by 0.03 Å (See Table 1.1).

When we apply the +*U* potential to the partially filled erbium *f*-shell, the occupied part of the atomic manifold is pushed downwards into the valence band and the empty states are pushed upwards into the conduction band, leaving the original band gap completely empty. A detailed discussion of the interpretation of this clear gap can be found in Ref. [93] and references therein. The DOS changes are consistent with what is observed for the band structure: the *f*-related peak in the band gap is removed, leaving the GaN band gap clear. This vindicates the pseudopotential approach, and agrees with the resulting clear gap [84], i.e., simple RE substitutionals do not induce localized states in the band gap. We have compared the results with LDA+*U* results from the Wien2K code [59, 94], which also demonstrate the same clear band gap.

In this situation a simple LDA-like approach treating the *f*-electrons as core like electrons produces the same results as a more sophisticated approach with non-meanfield description of the *f*-electrons. So far we have neglected in our discussion effects of spin-orbit coupling, however we have also carried out provisional calculations in the case of Er [59, 46] in addition to the LDA+*U*-like treatment for DFTB. Using spin-DFTB and a 4*f* spin orbit constant of 2234 cm^{-1}, with the Er magnetic moment in the *a* plane [95], we find that the 7-fold degenerate atomic level splits into 4 filled and 3 empty non-degenerate levels which remain in the gap spanning a range of ~ 700 meV. Applying the FLL-LDA+*U* approach and the same constant for the spin-orbit splitting ejects these states from the gap, demonstrating that in this case correlation has a larger effect than spin-orbit coupling.

1.4 Deep Level Transient Spectroscopy

There have been some recent reports using deep level transient spectroscopy (DLTS). Song et al. [79]. carried out DLTS, Hall and CV measurements on implanted GaN:Er and GaN:Pr and annealed to 1000 °C The samples remained n-type with $n_0 \sim 2\times10^{17}$ cm^{-3}. Since the implanted RE concentration greatly exceeded this, Er and Pr must be defects without deep electron traps as expected. The Hall mobility was about ~50% of the undoped material (450 cm^2/ Vs) indicating residual implantation damage.

DLTS studies of the undoped material showed the presence of a deep trap at E_c –0.27 eV with concentration ~ 3×10^{14} cm^{-3}. In implanted and annealed mate-

rial, the $E_c - 0.27$ eV trap is still detected but its density has slightly increased. V_N is however a donor and presumably there are deeper acceptor defects. The dominant levels in Er doped material are $E_c - 0.188$ and $E_c - 0.6$ eV with concentrations $\sim 5.2\times10^{16}$ cm^{-3}. The same levels are found in Pr doped material. The suggestion was made that the $E_c - 0.188$ eV is due to an RE-V_{Ga} pair, although this would be a donor level. The $E_c - 0.6$ eV level was tentatively attributed to N_{Ga}, which is also a donor defect. Thus there remain about 10^{17} cm^{-3} acceptors unaccounted for. It may be these have levels in the lower part of the band gap.

Other deep level transient spectroscopic studies (DLTS) have involved Er in implanted GaN and have reported levels at $E_c - 0.3$,0.188,0.6 and at $E_c - 0.4$ eV [96]. The identity of the defects is not at present known.

1.5 Excitation and Emission in GaN:Eu

Eu^{3+} has a configuration $4f^6$ and a ground state of $^7F_0$. Several transitions due to Eu in GaN are identified. For example, $^5D_0 \rightarrow {}^7F_2$ at ~ 622 nm, $^5D_0 \rightarrow {}^7F_3$ at ~ 664 nm and $^5D_0 \rightarrow {}^7F_1$ at ~ 602 nm [75]. Recently, there has been a detailed study of the excitation mechanism of Eu in GaN [97], concentrating on the two dominant intra-*f* transitions due to Eu: $^5D_0 \rightarrow {}^7F_2$ and $^5D_0 \rightarrow {}^7F_3$ at 1.992 and 1.864 eV respectively whose radiative decay times are in the ratio of about 10:1. The PL intensities drop by factors of 5 and about 4 from 86 K to room temperature showing an increasing importance of non-radiative processes. The rise time of luminescence is about 10 μs for both lines and independent of T while the decay time is approximately 200 μs and is composed of two components: a fast and slow one. The fast one is due to additional non-radiative transitions which depend on T but whose origin is unclear. The intra-*f* luminescence mechanism involves firstly an excitation of the GaN host. Since the lifetimes of free-excitons and neutral donor bound excitons is about 1 and 10 ns, there must be a very efficient mechanism for exciton capture in defect related states in proximity with the RE. This is then followed by resonant Auger excitation of the $^5D_0$ state. The two processes have not been separated but the RE excitation takes a surprisingly long time $\tau_{HE} \sim 0.4$ μs which is independent of T. Radiative decay to $^7F_2$ from $^5D_0$ takes place in a time τ_{decay} or 166μs at low temperatures, but above 200 K it rapidly decreases being activated with energy 16 meV. This is attributed to a transfer to a state 16 meV above $^5D_0$. This state could be another RE multiplet, from which non-radiative deexcitation occurs or a state made up of defect related orbitals, for example V_N.

1.6 RE Defects in AlN

Several optical transitions of RE ions have been reported in AlN. The 1.54μm transition due to Er^{3+} has been closely studied [98, 99]. PLE studies show a broad band with excitation energies above about 2 eV and superimposed sharp spikes. This indicates at least two classes of Er^{3+} center. The broad band is attributed to optically excited Er related defects possessing gap levels and the spikes to direct intra-*f* excitation [98]. PL studies of AlN:Tm reveal intense 465 and 478 nm blue lines when excited above 4.3 and 4 eV respectively, possibly relating to two different defects [100]. RE doping of AlN and AlGaN alloys seems to result in more efficient and temperature stable luminescence than GaN [99, 98]. Moreover, the PL intensity of $Al_\chi Ga_{1-\chi}N$:Tb [101] and the CL intensity of $Al_\chi Ga_{1-\chi}N$:Eu [102] increase dramatically with χ up to 15%. Lattice location studies demonstrate that implanted Er [103], Yb and Tm [104] primarily lie at substitutional Al sites although more recent RBS data [105] suggests some displacement away from the Al site.

Density functional calculations of RE and other defects in AlN have been carried out in Ref. [11]. Use of DFT is more difficult in this material as there is a large difference between the calculated 4.2 eV and observed 6.1 eV band gap. To get around this problem, the electrical levels are obtained user a marker method (see Sect. 1.2.6) where transition energies are compared with those of Si_{Al} which has donor and acceptor levels [106] found experimentally at $E_v + 6.06$ eV and $E_c - 0.32$ eV. This donor level is close to a PL line attributed to a Si bound exciton at 6.024 eV [107]. If there are large lattice relaxations in one of more charge states of the defect, then optical transitions may not be directly related to the donor or acceptor levels. For example, the energy for a vertical Frank-Condon transition, taking an electron from the top of the valence band and adding to the neutral defect, is the acceptor level referenced to the valence band, together with the relaxation energy $E^-[\mathbf{R}^0] - E^-[\mathbf{R}^-]$ (see Fig. 1.1). The relaxation energy may be considerable and leads to a broad PL spectrum typically seen in large band gap semiconductors. RE defects are an exception, as the internal excitation with the 4*f* shell will not lead to any appreciable structural change.

Er, Tm and Eu dopants readily substitute for Al in agreement with site-location studies [103, 104]. With respect to solid RE-nitride, the formation energies of the substitutional Er, Eu and Tm defects lie between 1.6 and 2.2 eV. These positive energies reveal that the isolated defects are less stable than a corresponding RE-nitride precipitate. In contrast with GaN the RE defects in AlN possess donor levels around $E_v + 0.5$ eV.

Oxygen is found to have high solubility with O_N being the most common defect which acts as a substitutional donor with a level at $E_v + 5.85$ eV. An acceptor level is also evaluated 0.75 eV below that of Si at $E_c - 1.06$ eV. Like Si_{Al}, O_N is a DX-center in agreement with previous work [108, 109]. The optical (Frank-Condon) ionization energy for O_N^- is found to be 2.25 eV and close to a 2.8-2.9 eV optical absorption peak reported in AlN:O [110]. The low formation energy for O_{Al} in

AlN suggests that high concentrations can be expected and larger oxygen aggregates are readily formed. Other defects investigated also have deep levels. V_N^+ has donor and acceptor levels lying around $E_v + 4.64$ and $E_c - 1.36$ eV respectively showing that V_N is a positive *U*-defect [111].

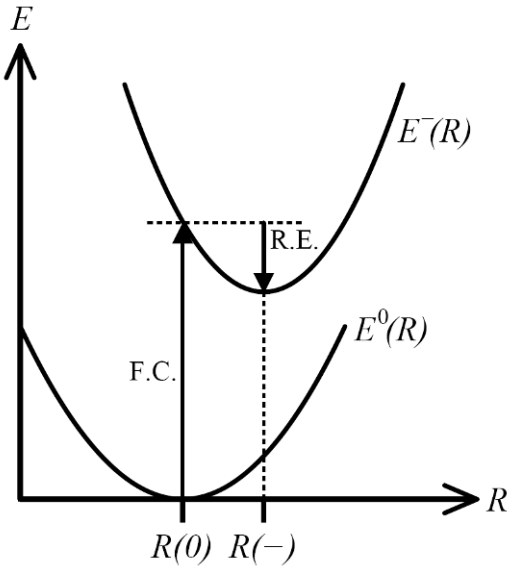

Fig. 1.1. Schematics of the energy configurations describing the capture of an electron by a neutral defect resulting in a vertical optical transition. The Frank-Condon absorption energy F.C. is $E^-[\mathbf{R}^0] - E^0[\mathbf{R}^0] - E_v$. This energy is numerically the sum of the acceptor level of the defect referenced to the valence band. $E^-[\mathrm{R}^-] - E^0[\mathbf{R}^0] - E_v$, together with the relaxation energy R.E. which is $E^-[\mathbf{R}^0] - E^-[\mathbf{R}^-]$.

RE_{Al}-O_N complexes have also been considered. The formation energies of these are negative. This implies that the oxygen atom is more stable bound to a RE dopant than in the oxygen molecule. The defects possess a donor level around $E_v + 5.7$ eV and an acceptor level about $E_c - 0.8$ eV, and are thus negative-*U* centers. In contrast, the formation energies of RE-V_N defects are very large (>5.2 eV) and the equilibrium concentration of this defect is negligible. Such defects may be created, however, during ion implantation. They possess deep single donor and acceptor levels around $E_v + 4.4$ eV and $E_c + 1.5$ eV respectively.

In summary, the density functional calculations of Er, Eu and Tm dopants in hexagonal AlN show that the RE substitute for Al atoms but, in contrast to isolated RE dopants in GaN, introduce deep donor levels ($E_v + 0.5$ eV) which may be involved in the luminescence mechanism especially during electro- and cathdoluminescence. They could for example account for the enhanced CL intensity observed in $Al_\chi Ga_{1-\chi}N$:Eu for $\chi > 0.15$ [102].

1.7 Conclusions

The calculations have provided details of the structure and electrical properties of RE defects in semiconductors. RE impurities have low solubilities and prefer to form precipitates in many semiconductors. RE-nitride precipitates are metallic and would degrade the optical properties of the material. In GaN, isolated RE impurities are electrically inert. In AlN the substitutional defects appear to possess gap levels. These levels are occupied by valence electrons and not those of the *f*-shell. There is no evidence that the RE defect exists in a divalent form, for example Er^{2+}. The lack of any electrical level in the gap suggests that the substitutional defect is not responsible for the main optical activity leading to room temperature emission.

RE dopants readily form stable defects with oxygen and these are known to be important optical centres in GaAs [6, 12]. They may also be important in AlN. The RE-Oxygen defects reduce precipitation and possess gap levels which could be involved in photoemission. In GaN, the density functional calculations show that the RE impurity binds strongly to nitrogen vacancies and possesses levels around $E_c - 0.2$ eV which could serve as exciton traps. RE-Oxygen defects in GaN also possess shallow donor levels but are less stable than the complex with a nitrogen vacancy. The low concentration of active defects however, has so far prevented a complete understanding of their properties.

References

1. A. J. Steckl, J. Heikenfeld, D.S. Lee, M. Garter, Mater. Sci. Eng. B **81** (2001) 97.
2. Y. Q. Wang, A. J. Steckl, Appl. Phys. Lett. **82** (2003) 502.
3. H. J. Lozykowski, M. Jadwisienczak, J. Han, I. G. Brown, Appl. Phys. Lett. **77** (2000) 767.
4. A. Vantomme, S.M. Hogg, M.F. Wu, B. Pipeleers, M. Swart, S. Goodman, D. Auret, K. Iakoubovskii, G.J. Adriaenseens, K. Jacobs, I. Moerman, Nucl. Instrum. Methods B **175** (2001) 148.
5. D. Prezzi, T. A. G. Eberlein, J.-S. Filhol, R. Jones, M. J. Shaw, P. R. Briddon, and S. Öberg, Phys. Rev. B **69**, 193202 (2004).
6. J. Coutinho, R. Jones, M. J. Shaw, P. R. Briddon, and S. Öberg, Appl. Phys. Lett. **84**, 1683 (2004).
7. J.-S. Filhol, R. Jones, M. J. Shaw, and P. R. Briddon, Appl. Phys. Lett. **84**, 2841 (2004).
8. P. R. C. Kent, A. Zunger, Appl. Phys. Lett. **79**, 2339 (2001).
9. D. S. Lee, J. Heikenfeld, A. J. Steckl, U. Hommerich, J. T. Seo, A. Braud, and J. Zavada, Appl. Phys. Lett. **79**, 719 (2001).
10. S. Kim, S. J. Rhee, X. Li, J. J. Coleman, S. G. Bishop, and P. B. Klein, Appl. Phys. Lett. **76**, 2403 (2000)
11. S. Petit, R. Jones, M. J. Shaw and P. R. Briddon, B. Hourahine and T. Frauenheim, Phys. Rev. B **72** 073205 (2005)
12. D. Prezzi, T. A. G. Eberlein, R. Jones, J. S. Filhol, J. Coutinho, M. J. Shaw, P. R. Briddon, Phys. Rev. B **71** (2005) 245203.
13. M. Born and K. Huang, *Dynamical Theory of Crystal Lattices*, (Oxford University Press, London, 1954).
14. J. C. Slater, *Quantum Theory of Atomic Structure*, Vol. 2, (McGraw Hill, New York, 1960).
15. A. Szabo and N. S. Ostlund Modern Quantum Chemistry: Introduction to Advanced Electronic Structure Theory (Dover Publications Inc., 2000).
16. P. Hohenberg and W. Kohn, Phys. Rev. **136**, B864 (1964).
17. W. Kohn and L. J. Sham, Phys. Rev. **140**, A1133 (1965).
18. R. G. Parr and W. Yang *Density-Functional Theory of Atoms and Molecules* (Oxford University Press, USA 1995).
19. S. G. Louie, S. Froyen, and M. L. Cohen, Phys. Rev. B **60**, 14132 (1999); D. Porezag, M. R. Pederson, and A. Y. Liu, Phys. Stat. Sol. (b) **217**, 219 (2000).
20. F. Aryasetiawan, O. Gunnarson, Rep. Prog. Phys. **61**, 237 (1998).
21. J. P. Perdew and A. Zunger, Phys. Rev. B **23**, 5048 (1981).
22. A. Svane and O. Gunnarson, Phys. Rev. Lett. **65**, 1148 (1990).
23. O. A. Vydrov, G. E. Scuseria, J. P. Perdew, A. Ruzsinszky and G. I. Csonka, J. Chem. Phys. **124**, 094108 (2006).
24. A. G. Petukhov, W. R. L. Lambrecht and B. Segall, Phys. Rev. B **53**, 4324 (1996).
25. D. R. Hamann, M. Schlüter, and C. Chiang, Phys. Rev. Lett. bf 43, 1494 (1979); G. B. Bachelet, D. R. Hamann and M. Schlüter, Phys. Rev. B **26**, 4199 (1982).
26. N. Troullier, and J. l. Martins, Phys. Rev. B **43** 1993 (1991).
27. C. Hartwigsen, S. Goedecker, J. Hutter, Phys. Rev. B **58**, 3641 (1998).
28. S. Goedecker, M. Teter, and J. Hutter, Phys. Rev. B, **54** (3), 1703 (1996).

29. J. P. Perdew, J. A. Chevary, S. H. Vosko, K. A. Jackson, M. R. Pederson, D. J. Singh, and C. Fiolhais, Phys. Rev. B **46**, 6671 (1992).
30. G. Kresse and J. Furthmuller, Phys. Rev. B **54**, 11169 (1996).
31. X. Gonze, J.-M. Beuken, R. Caracas, F. Detraux, M. Fuchs, G.-M. Rignanese, L. Sindic, M. Verstraete, G. Zerah, F. Jollet, M. Torrent, A. Roy, M. Mikami, Ph. Ghosez, J.-Y. Raty, D. C. Allan, Comp. Mat. Sci. **25**, 478 (2002).
32. J. M. Soler, E. Artacho, J. D. Gale, A. Garca, J. Junquera, P. Ordejón and D. Sánchez-Portal, J. Phys.: Condens. Matter **14**, 2745 (2002).
33. R. Jones and P. R. Briddon, Chapt. 6 in *Identification of Defects in Semiconductors*, edited by M. Stavola, Vol. 51A in the series Semiconductors and Semimetals (Academic Press, Boston, 1998), p. 287.
34. P. R. Briddon and R. Jones, Phys. Stat. Sol. (b) **217**, 131 (2000).
35. B. Aradi, B. Hourahine and T. Frauenheim, J. Phys. Chem. A, **111**, 5678 (2007).
36. M. Haugk, J. Elstner, Th. Frauenheim, T. E. M. Staab, C. D. Latham, R. Jones, H. S. Leipner, T. Heine, G. Seifert and M. Sternberg, Phys. Stat. Sol B **217**, 473 (2000).
37. M. Elstner, Th. Frauenheim, E. Kaxiras, G. Seifert, S. Suhai, Phys. Stat. Sol B **217**, 375 (2000).
38. A. Sieck, Structure and physical properties of Si clusters and of vacancy clusters in bulk Si, Ph.D Thesis, Paderborn (2001).
39. E. Rauls, Annealing mechanisms of point defects in SiC. Ph.D Thesis, Paderborn (2003).
40. D. Porezag, Th. Frauenheim, Th. Köhler, G. Seifert and R. Kaschner, Phys. Rev. B **51**, 12947 (1995).
41. J. Widany, Th. Frauenheim, Th. Köhler, M. Sternberg, D. Porezag, G. Jungnickel and G. Seifert, Phys. Rev. B **53**, 4443 (1996).
42. J. Elsner, R. Jones, M. I. Heggie, K. Sitch, M. Haugk, Th. Frauenheim, S. Oberg and P. R. Briddon, Phys. Rev. B **58**, 12571 (1993).
43. J. Elsner, M. Haugk, J. Jungnickel and Th. Frauenheim, J. Mater. Chem. **6**, 1649 (1996).
44. T. Frauenheim, G. Seifert, M. Elstner, T. Niehaus, C. Kohler, M. Amkreutz, M. Sternberg, Z. Hajnal, A. Di Carlo, S. Suhai, J. Phys. Cond. Matter **14**, 3015 (2002).
45. C. Köhler, G. Seifert and Th. Frauenheim, Chem. Phys. **309**, 23 (2005).
46. C. Köhler, T. Frauenheim, B. Hourahine, G. Seifert and M. Sternberg. J. Phys. Chem. A, **111** (2007), 5622.
47. B. Hourahine, S. Sanna, B. Aradi, C. Köhler, T. Niehaus and T. Frauenheim, J. Phys. Chem. A **111** (2007), 5671.
48. A. I. Liechtenstein, V. I. Anisimov, J. Zaanen, Phys. Rev. B **52**, R5467 (1995).
49. D. Vogl, P. Krüger and J. Pollmann, Phys. Rev. B **58**, 3865 (1998). *ibid* **55**, 12836 (1997).
50. A. Filippetti and N. A. Spaldin, Phys. Rev. B **67**, 125109 (2003).
51. V. I. Anisimov, F. Aryasetiawan and A. I. Lichtenstein, J. Phys. Cond. Matt. **9**, 767 (1997).
52. M. T. Czyżyk and G. A. Sawatzky, Phys. Rev. B **49**, 14211 (1994).
53. V. I. Anisimov, I. V. Solovyev, M. A. Korotin, M. T. Czyżyk, and G. A. Sawatzky, Phys. Rev. B **48**, 16929 (1993).
54. A. G. Pethukov, I. I. Mazin, L. Chioncel and A. I. Lichtenstein, Phys. Rev. B **67**, 153106 (2003).
55. D. A. Papaconstantopoulos and C. S. Hellberg, Phys. Rev. Lett. **89**, 029701 (2002).
56. S. L. Dudarev, G. A. Botton, S. Y. Savrasov, C. J. Humphreys, A. P. Sutton, Phys. Rev. B **57**, 1505 (1998).
57. S. Sanna, B. Hourahine, T. Gallauner and T. Frauenheim, J. Phys. Chem. A, **111** (2007), 5665.

58. C. D. Pemmaraju, T. Archer, D. Sanchez-Portal and S. Sanvito, Phys. Rev. B **75**, 045101 (2007).
59. S. Sanna, B. Hourahine, Ü. Gerstmann and T. Frauenheim, Phys. Rev. B **76** (2007), 155128.
60. M. J. Han, T. Ozaki and J. Yu, Phys. Rev. B **73**, 045110 (2006).
61. L. Kleinman, Phys. Rev. B **24**, 7412 (1981).
62. H. J. Monkhorst, and J. D. Pack, Phys. Rev. B **13**, 5188 (1976).
63. J. F. Janak, Phys. Rev. B **18**, 7165 (1978).
64. J. E. Northrup and S. B. Zhang, Phys. Rev. B **47**, 6791 (1993).
65. A. M. Stoneham, *Defects in Solids*, (Oxford University Press, London, 1975).
66. G. Makov and M. C. Payne, Phys. Rev. B **51**, 4014 (1995).
67. V. Bougrov, M. E. Levinshtein, S. L. Rumyantsev, A. Zubrilov, Chapter 1 in Properties of Advanced Semiconductor Materials GaN, AlN, InN, BN, SiC, SiGe. Ed. M. E. Levinshtein, S. L. Rumyantsev and M. S. Shur, John Wiley & Sons, Inc., New York, 2001.
68. N. D. M. Hine, K. Frensch, W. M. C. Foulkes, and M. W. Finnis, Phys. Rev. B **79** 024112 (2009).
69. A. Resende, R. Jones, S. Öberg and P. R. Briddon, Phys. Rev. Lett. **82**, 2111 (1999).
70. J. Coutinho and V. J. B. Torres, R. Jones, P. R. Briddon, Phys. Rev. B **67** 035205 (2003).
71. U. Wahl, A. Vantomme, G. Langouche, J. P. Araujo, L. Peralta, J. G. Correia and the ISOLDE Collaboration, J. Appl. Phys. **88**, 1319 (2000)
72. T. Monteiro, C. Boemare, M. J. Soares, R. A. Sa Ferreira, L. D. Carlos, K. Lorenz, R. Vianden, E. Alves, Physica B **308**, 22 (2001)
73. H. Bang, S. Morishima, Z. Li, K. Akimoto, M. Nomura, and E. Yagi, J. Cryst. Growth **237** 1027 (2002).
74. T. Monteiro, J. Soares, M. R. Correia, and E. Alves, J. Appl. Phys. **89**, 6183 (2001)
75. K. Wang, R. W. Martin, K. P. O'Donnell, V. Katchkanov, E. Nogales, K. Lorenz, E. Alves, S. Ruffenach, and O. Briot, Appl. Phys. Lett. **87**, 112107 (2005)
76. E. E. Nyein, U. Hömmerich, J. Heikenfeld, D. S. Lee, A. J. Steckl, and J. M. Zavada, Appl. Phys. Lett. **82**, 1655 (2003)
77. Z. Li, H. Bang, G. Piao, J. Sawahata, K. Akimoto, J. Cryst. Growth **240** 382 (2002)
78. P. H. Citrin, P. A. Northrup, R. Birkhahn and A. J. Steckl, Appl. Phys. Lett. **76** 2865 (2000).
79. S. F. Song, W. D. Chen, C. Zhang, L. Bian, C. C. Hsu, L. W. Lu. Y. H. Zhang, and J. Zhu, Appl. Phys. Lett. **86** 152111 (2005).
80. J. Neugebauer, and C. G. Van de Walle, Phys. Rev. B **50** 8067 (1994)
81. T. Mattila, and R. M. Nieminen, Phys. Rev. B **55** 9571 (1997)
82. C. D. Latham, R. Jones, S. Öberg, R. M. Nieminen, and P. R. Briddon, Phys. Rev. B **68**, 205209 (2003).
83. M. Pan, and A. J. Steckl, Appl. Phys. Lett. **83**, 9 (2003).
84. J.-S. Filhol, R. Jones, M. J. Shaw, P. R. Briddon, Appl. Phys. Lett. **84**, 2841 (2004).
85. P. Dorembos and E. van der Kolk, Appl. Phys. Lett. **89**, 061122 (2006).
86. A. Svane, N. E. Christensen, L. Petit, Z. Szotek, W. M. Temmerman, Phys. Rev. B **74**, 165204 (2006).
87. S. Sanna, B. Hourahine, T. Frauenheim and Ü. Gerstmann, Phys. Status Solidi C, **5** (2008), 2358.
88. B. Hourahine, S. Sanna, B. Aradi, C. Köhler and T. Frauenheim, Physica B **376** (2006), 512.
89. U. Wahl, E. Alves, K. Lorenz, J. G. Correia, T. Monteiro, B. de Vries, A. Vantomme and R. Vianden, Mat. Sci. Eng. **N105**, 132 (2003).

90. J. T. Torvik, R. J. Feuerstein, J. I. Pankove C. H. Qiu and F. Namavar, Appl. Phys. Lett. **69**, 2098 (1996).
91. V. Glukhanyuk, H. Przybylińska, A. Kozanecki and W. Lantsch, Phys. Stat. Sol. a **201**, 195 (2004).
92. V. Katchkanov, J. F. W. Mosselmans, K. P. O'Donnel, E. Nogales, S. Hernandez, R. W. Martin, A. J. Stekl and D. S. Lee Optical Materials **28**, 785 (2006).
93. K. P. O'Donnell, B. Hourahine, Eur. Phys. J. Appl. Phys. **36**, 91 (2006).
94. WIEN2k, P. Blaha, K. Schwarz, G. Madsen, D. Kavasnicka and J. Luitz, Inst. f. Materials Chemistry, TU Vienna.
95. M. Kotzian, N. Rösch, M. C. Zerner, Theor. Chim. Acta **81**, 201 (1992).
96. T. Wojtowicz, V. Matias, P. Marie, M. Mamos, B. Pipeleers, P. Ruterana, and A. Vantomme, Mater. Sci. Eng. B **105** 122 (2003).
97. Chang-Won Lee, H. O. Everitt, D. S. Lee and A. J. Steckl, J. M. Zavada, J. Appl. Phys. **95**, 7717 (2004)
98. X. Wu, U. Hömmerich, J. D. MacKenzie, C. R. Abernathy, S. J. Pearton, R. G.Wilson, R. N. Schwartz, and J. M. Zavada, J. Luminescence, 72, 284, (1997).
99. F. Lu, R. Carius, A. Alam, M. Heuken, A. Rizzi and C. Buchal, Thin Solid Films **425**, 171 (2003).
100. U. Hömmerich, E. E. Nyein, D. S. Lee, A. J. Steckl, J. M. Zavada,Appl. Phys. Lett. **83**,4556 (2003).
101. Y. Nakanishi, A. Wakahara, H. Okada, A. Yoshida, T. Ohshima, and H. Itoh, Phys. Stat. Sol. b **240**, 372 (2003).
102. Y. Nakanishi, A. Wakahara, H. Okada, A. Yoshida, T. Ohshima, T. Itoh, H. ang Shibata, and M. Tanaka, Phys. Stat. Sol. c **1** 2623 (2003).
103. F. Lu, A. Rizzi, and R. Carius, Chin. Phys. Lett. **19**, 1844 (2002).
104. U. Vetter, J. Zenneck, and H. Hofsäss, Appl. Phys. Lett. **83**, 2145 (2003).
105. M. Peres, A. Cruz, M. J. Soares, A. J. Neves, T. Monteiro, K. Lorenz, E. Alves, Superlattices and Microstructures **40** 537 (2006).
106. R. Zeisel, M. W. Bayerl, S. T. B. Goennenwein, R. Dimitrov, O. Ambacher, M. S. Brandt, and M. Stutzmann, Phys. Rev. B **61**, R16283 (2000).
107. K. B. Nam, M. L. Nakarmi, J. Li, J. Y. Lin, and H. X. Jiang, Appl. Phys. Lett. **83**, 2787 (2003).
108. C. H. Park and D. J. Chadi, Phys. Rev. B **55**, 12995 (1997).
109. C. G. Van de Walle, Phys. Rev. B **57**, R2033 (1998).
110. G. A. Slack, L. J. Schowalter, D. Morelli, and J. A. Freitas Jr, J. Cryst. Growth **246**, (2002).
111. F. Bernardini, and V. Fiorentini, J. Applied Phys. **85**, 2001 (1999).

Chapter 2
RE Implantation and Annealing of III-Nitrides

Katharina Lorenz, Eduardo Alves, Florence Gloux, Pierre Ruterana

Abstract Ion implantation is a convenient method to introduce Rare Earth (RE) ions into a host matrix in a controlled manner with a reproducible profile; it also allows lateral patterning for selective area doping. However, a major drawback of the technique is the lattice damage inevitably caused by energetic heavy ions as they penetrate a crystalline host. The crystalline quality is usually recovered, at least partially, by post-implant thermal annealing of samples at high temperatures; recovery of implantation damage in GaN correlates with the activation of electrical, optical or magnetic dopants. In this chapter we first review the structural aspects of ion implantation damage in GaN; we then focus on the damage accumulation during implantation and on the optical activation of RE ions. The influence of the major implantation parameters, fluence, energy, temperature, and geometry, on structural and optical properties of RE-implanted GaN is discussed. Post-implant annealing of GaN at high temperatures requires special measures to protect the surface from nitrogen loss during the treatment. The efficacy of different annealing procedures, including AlN-capping and applying ultra-high nitrogen pressures, are critically assessed. Finally, investigations of RE implantation of the less-studied binary AlN and AlN-containing alloys, AlGaN and AlInN, are briefly reviewed.

Katharina Lorenz, Eduardo Alves
Instituto Tecnológico e Nuclear, Estrada Nacional 10, 2686-953 Sacavém, Portugal
e-mail: lorenz@itn.pt, ealves@itn.pt

Florence Gloux, Pierre Ruterana
CIMAP, UMR 6252, CNRS-ENSICAEN-CEA-UCBN, 14050 Caen Cedex, France
e-mail: pierre.ruterana@ensicaen.fr

2.1 Introduction

A convenient method to introduce Rare Earth (RE) ions into a host matrix is by ion implantation. Ion implantation is a key technology in semiconductor industry. It allows introduction of dopants in a controlled manner with reproducible profiles, it is not restricted by solubility limits and has the facility of lateral patterning for selective area doping. However, in the case of semiconductors with high melting points but relatively low dissociation temperatures like GaN, the lack of an efficient procedure to remove implantation damage still hampers the use of ion implantation in industry. Nevertheless, ion implantation has proved to be a valuable technique to introduce RE ions into GaN and other III-nitrides for research purposes; efficient optical activation has been demonstrated for a number of RE^{3+} ions with light emission in the infra red, visible and ultraviolet spectral regions.

First reports of sharp RE visible emission lines from Dy, Er, Eu, Ho, Pr, Sm and Tm-implanted GaN include references [1, 2, 3, 4].

A nominally undoped GaN template is bombarded with RE ions accelerated to energies of typically a few hundred keV, resulting in doped layer thicknesses of ~ 100 nm. In this way, typical problems that occur during in-situ doping by MBE growth can be avoided, such as the accumulation of RE at the surface or even phase segregation. In general, the MOCVD GaN templates used for ion implantation are of better crystalline quality than in-situ doped MBE GaN:RE. Furthermore, since ion implantation is a ballistic process, chemical properties play a minor role in damage production and annealing processes are similar for the different RE ions. It is not necessary to optimize implantation parameters for each RE ion separately.

The main drawback of the ion implantation technique comes from correlated damage to the crystal lattice since every energetic ion will displace a large number of host atoms in a collision cascade. Although a fraction of the vacancies and interstitials created can recombine during the implantation (dynamic annealing), point defects will start to aggregate, above a certain ion fluence, and extended defects, defect clusters or stacking faults, can form; the crystalline lattice will eventually become amorphous. For a detailed discussion of the processes occurring during ion implantation refer to textbooks like [5].

The loss of crystalline quality after ion implantation is usually addressed by thermally annealing implants at high temperatures. Several groups have correlated the recovery of implantation damage in GaN with the activation of electrical, optical or magnetic dopants by annealing. In this chapter we will briefly review the structural aspects of ion implantation damage in GaN and subsequently focus our attention on the damage accumulation during implantation of RE ions and their optical activation.

2.2 Implantation Damage in GaN

Tan et al. [6] performed the first investigations of damage accumulation in GaN during ion implantation and found evidence of substantial dynamic annealing during implantation, resulting in very high thresholds for amorphization – orders of magnitude higher than in GaAs, for example. In the following years several groups studied the accumulation of implantation damage in GaN; reviews can be found in [7, 8, 9]. Wendler et al. [10] performed an extensive Rutherford Backscattering/Channelling (RBS/C) study of implantation damage build-up in GaN at 15 K using different ions and a wide range of fluence. They identified three stages of damage formation up to amorphization, separated by fluence regions in which the damage level saturates. This damage accumulation behaviour shows that strong dynamic annealing occurs in GaN even at low temperature. Similar behaviour was reported for implantation at room temperature (RT) [11]; in this case, amorphization was observed to take place layer by layer starting at the surface.

In the following sub-sections the main parameters that influence the build-up of implantation damage in GaN will be discussed for the case of RE implantation. RBS/C assesses implantation damage and RE profiles while Transmission Electron Microscopy (TEM) reveals the microscopic nature of the introduced defects; in combination, these techniques comprehensively investigate the structural properties of RE-implanted GaN.

Fig. 2.1 shows random and aligned RBS/C spectra after implantation of 300 keV Eu ions into GaN along the surface normal to a fluence of 3×10^{15} at/cm^2 at room temperature; the aligned spectrum of a virgin sample is shown for comparison. The spectra reveal a damage profile typical of medium energy heavy ion implantation. There are two damage peaks, one at the surface and a second in the bulk, close to the end of range of the implanted ions (marked with S and B, respectively, in Fig. 2.1). Close to the surface, the aligned and random spectra have almost the same yield: channelling is suppressed, indicating the presence of a layer of amorphous or polycrystalline material.

2.2.1 Implantation Geometry Dependence

The sample in Fig. 2.1 was implanted with the beam directed along the *c*-axis. In ion implantation experiments samples are often tilted off-axis by typically 7–10º in order to *prevent* channelling of the ions and to attain a more well-defined implantation profile. However, it was shown by Vantomme et al. [12] that RE implantation damage in GaN can be reduced substantially by using the channelling geometry. The reduction of lattice damage is due to a decrease in the number of primary knock-on atoms when the ions are channelled along a low index crystallographic direction and the increased depth of the defected layer.

Fig. 2.2 [13] shows RBS/C spectra for samples implanted with 80 keV Er ions to a fluence of 2.5×10^{14} at/cm^2 using tilt angles of 0º, 6º and 10º. For random implantation the two damage peaks at the surface and bulk are visible. The bulk damage especially is strongly reduced when the tilt angle is decreased and for perfect alignment only the surface damage peak is visible but also smaller than for random implantation.

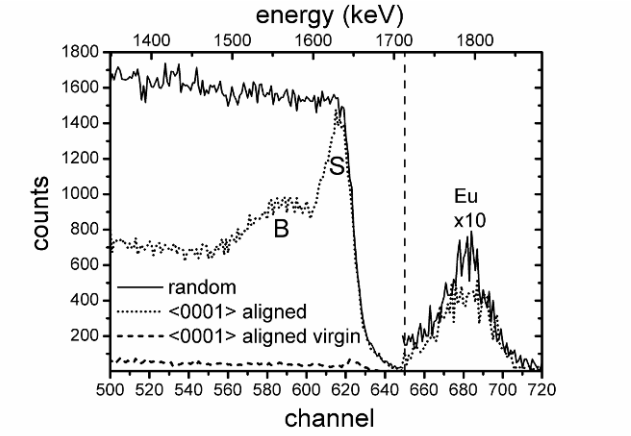

Fig. 2.1. RBS/C random and <0001> aligned spectra after implantation with 3×10^{15} Eu/cm^2 into GaN at room temperature. Two damage regions are visible, one at the surface S and one in the bulk B near the end of range of the implanted ions. An aligned spectrum of a virgin sample is shown for comparison.

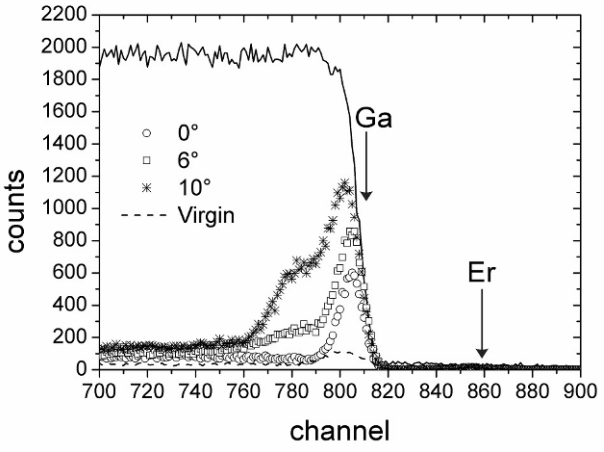

Fig. 2.2. RBS/C spectra of GaN implanted with 2.5×10^{14} Er/cm^2 at three different tilt angles: 0º, 6º and 10º. [13]

Defect production in crystals can also be investigated using high resolution X-ray diffraction (XRD): Liu et al. [14] measured an expansion of the GaN lattice after ion implantation. The introduction of strain by RE implantation shows a distinct difference for channelled and random implantation (Fig. 2.3, [13]). In the 2θ-ω scan the 0002 reflection from the implanted region is visible as a shoulder at the low angle side of the reflection for unimplanted GaN. The position of this secondary peak in the XRD scan is seen to shift to lower angles with increasing implantation angle as a larger number of introduced defects cause an increase of the c-lattice parameter. At the same time the intensity of the peak is reduced for higher implantation angles because the crystal quality deteriorates. Pipeleers et al. studied in detail both channelled and random implantation at two energies (80 and 170 keV Er ions) for fluences up to 1×10^{15} at/cm^2 [15]. The damage build-up curve is similar for both implantation geometries, with low defect accumulation at first followed by a super-linear increase. In the second regime the reduction of damage build-up for channelled implantation is most pronounced meaning that higher implantation fluences can be used until a certain damage level is reached. In a third regime the surface damage peak becomes very prominent and the differences between channelled and random implantation become small because the ions de-channel very quickly in the highly damaged surface layer.

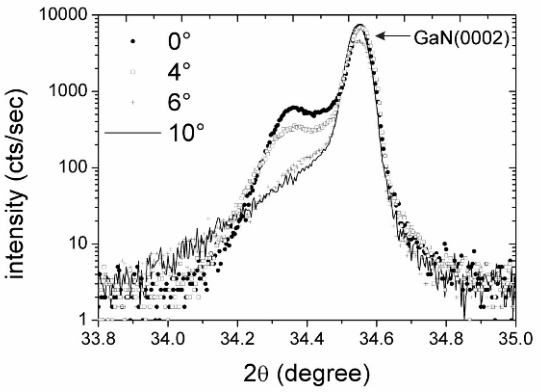

Fig. 2.3. High-resolution X-ray 2θ–θ diffraction of the GaN 0002 reflection from samples implanted with 2.5×10^{14} Er/cm^2 at angles of 0º, 4º, 6º and 10º. [13]

2.2.2 Fluence Dependence

Among all the factors that determine the damage accumulation during implantation, ion fluence is probably the most critical. In the case of RE doping, relatively high fluences are necessary since light emission depends strongly on the number of RE ions that can be introduced, with the optimum doping level thought to be

close to 1%. However, irrecoverable damage may be introduced at sufficiently high fluences.

The atomic displacements along the *c*-axis within the implanted areas can be investigated using transmission electron microscopy (TEM), by imaging the samples in 0002 weak beam conditions. The observed contrast may be related to clusters of interstitials or vacancies.

A series of GaN samples was implanted in channelling geometry with 300 keV Eu to fluences in the range 6×10^{13} at/cm^2 to 9.6×10^{15} at/cm^2 at room temperature (some samples implanted with Tm or Er are also included in the structural analysis). As shown in Fig. 2.4a for 2×10^{15} Er/cm^2 implantation, the area with point defect clusters runs from the sample surface towards the bulk down to 220 nm. Besides point defect clusters, stacking faults and dislocation loops are the most common defects formed by ion implantation in GaN [16]. When a threshold fluence of $2\text{-}3\times10^{15}$at/cm^2 is reached for the investigated ions (300 keV Er, Eu, Tm), a completely disordered layer is formed starting at the surface. In cross sectional TEM bright field micrographs, the surface layer has a typical contrast as seen in Fig. 2.4b for the highest fluence (9.6×10^{15} at/cm^2). A highly magnified micrograph of such an area (Fig. 2.5) shows that this layer is not in fact amorphous, but consists of a large number of nano-crystals (NC) with random orientations. The bright spots correspond to voids (black arrow) which are almost uniformly distributed throughout the surface layer. The average diameter of the voids is 2-3 nm, but some are as large as 5 nm. Lattice fringes can be seen throughout the whole layer, but each series extends only a few nanometers, indicating that the whole area is composed of disoriented NC. The exact mechanism of the formation of this nanocrystalline surface layer (NCSL) and the critical parameter that leads to nanocrystallinity in some cases and amorphization in others remain to be established. Fig. 2.6 shows the thickness of the NCSL as a function of ion fluence [17]: beyond a threshold ($2\text{-}3\times10^{15}$ at/cm^2 for 300 keV implantation) the NCSL thickness increases strongly with fluence and then saturates.

The damage profiles and RE doping profiles extracted from the RBS/C spectra are overlaid on TEM images in Fig. 2.4. The damage profile was determined from the RBS/C spectra using the DICADA code [18], to calculate the de-channelling rate with depth, assuming a random displacement of atoms. However, the fact that the determined damage level does not return to zero in the *un*implanted region of the sample proves that this assumption is not fully justified; the increased dechannelling in ion-implanted GaN is probably due to the large number of extended defects which are often found in compounds with efficient dynamic annealing [19]. Indeed, as will be shown in Sect. 2.2.2.1, a large number of stacking faults are present in these samples.

A correspondence of the surface RBS/C peak with the nanocrystalline layer and of the bulk damage region with the Eu profile is revealed in Fig. 2.4. For the highest fluences a strong surface erosion is evidenced by RBS/C [20] which is accompanied by a segregation of the implanted RE ions at the sample surface and a second Eu peak is observed (Fig. 2.4 (b)).

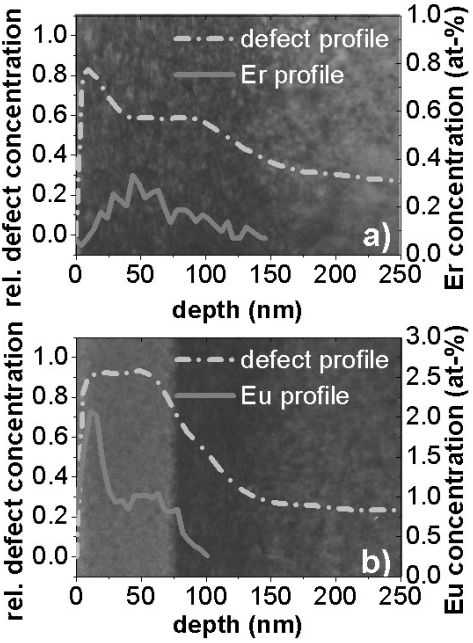

Fig. 2.4. Weak beam TEM images of GaN implanted with 300 keV Er or Eu ions at room temperature to a fluence of (a) 2×10^{15} Er/cm^2 and (b) 9.6×10^{15} Eu/cm^2. Overlaid to the images are the defect concentration profiles and RE depth profiles derived from the RBS/C spectra.

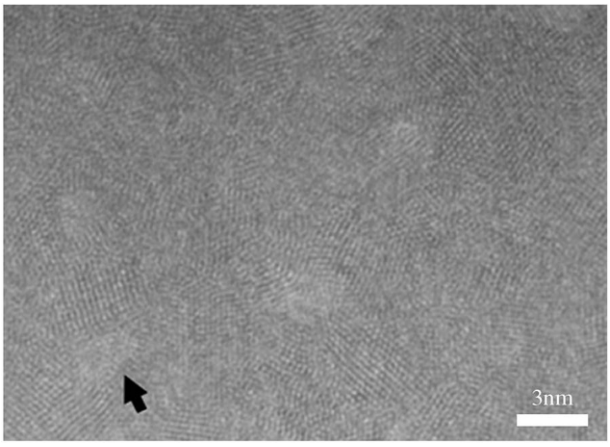

Fig. 2.5. High resolution TEM image showing the nanocrystalline nature of the surface layer: misoriented nanocrystallites and voids (black arrow).

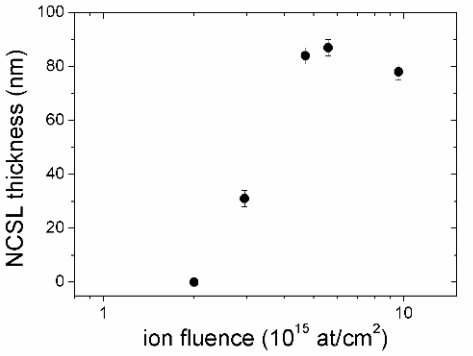

Fig. 2.6. Thickness of the nanocrystalline surface layer for 300 keV RE implants at room temperature into GaN as measured by TEM.

It should be noted that the onset of the NCSL depends not only on the implantation fluence but also on the implantation energy and temperature. For 150 keV implantation NCSL was observed for fluences as low as 3×10^{14} at/cm^2 [15]. Moreover, the nanocrystallization can be completely suppressed by implantation at high temperature as will be shown in Sect. 2.2.3.

The damage build-up curve in Fig. 2.7 shows the relative Ga defect concentration at the maximum of the surface and bulk defect peaks as a function of the implantation fluence. The curves have a sigmoidal shape and four regimes can be distinguished: in the low fluence regime I strong dynamic annealing keeps the damage accumulation rate low. For medium fluences (regime II) implantation damage increases steeply. In regime III the damage in the bulk of the samples saturates while the damage at the surface increases further and only saturates for fluences above 2×10^{15} at/cm^2 [21]. Each of these regimes can be associated with the predominance of different defects as discussed in the next section.

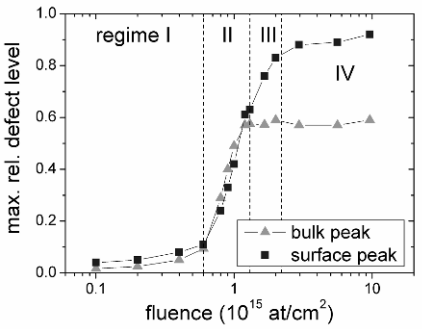

Fig. 2.7. The relative defect concentration in the Ga-sublattice as a function of the fluence measured at the maxima of the surface and bulk defect peaks for 300 keV RT implanted GaN.

2.2.2.1 Microscopic Picture of Implantation Damage

In this sub-section the microscopic nature of implantation damage is discussed. 0002 weak-beam TEM imaging (Fig. 2.4a) maps displacements along the *c*-axis caused by point defect clusters in a sample implanted with 300 keV Er ions to 2×10^{15} at/cm^2. The displacement of atoms is not limited to the **c** direction; the damage also takes place in the basal planes. A weak-beam micrograph for the same fluence but recorded using $g=10\bar{1}0$ is shown in Fig. 2.8. The corresponding displacements are clearly visible in the form of bright horizontal non-continuous features; the highest density of the damage in the basal planes extends down to 150 nm (white arrows).

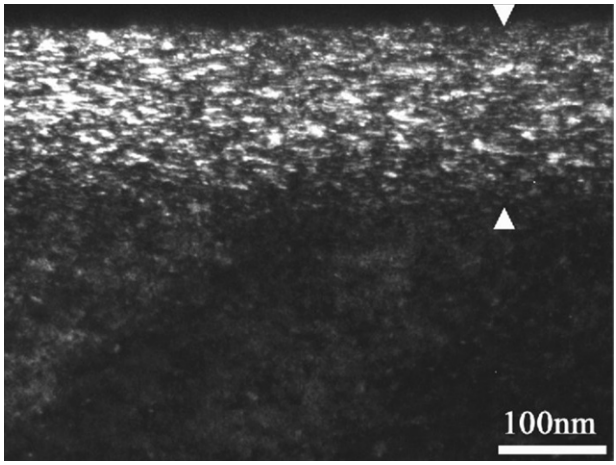

Fig. 2.8. A $10\bar{1}0$ weak beam image of a GaN layer implanted with Eu to a fluence of 2×10^{15} at/cm^2; visible damage in the basal plane extends between the two arrows.

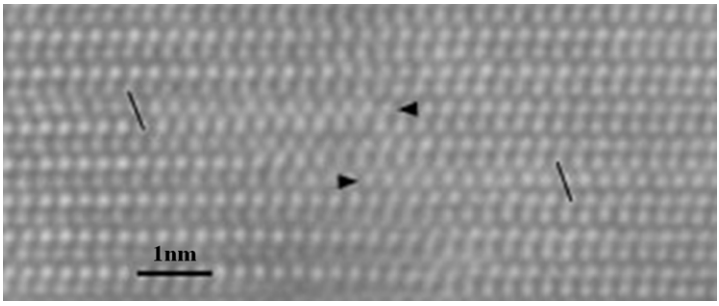

Fig. 2.9. A high resolution micrograph of the same Eu-implanted layer shown in Fig. 2.8 recorded along the $[1\bar{1}20]$ zone axis. The inclined segments indicate the position of the I1 basal stacking fault; the prismatic section extends between the two arrows.

In high resolution TEM (HRTEM) observations along the $[1\bar{1}20]$ zone axis (Fig. 2.9), the implanted areas exhibit a typical microstructure which is connected to the horizontal features of Fig. 2.8 [17]. These defects are mostly small basal stacking faults of I_1= 1/6 $[20\bar{2}3]$ type and their length in the basal plane can be quite small, about 7 nm. They easily fold out of the basal planes, giving rise to prismatic stacking faults (PSF). These layers do not exhibit only the I_1 faults; I_2 and E types (see [22] for details) are also present but in much lower density.

When folding from the basal to the prismatic planes, we have mainly observed the Drum configuration (D = ½ $[10\bar{1}1]$) [23]. As can be seen in Fig. 2.9, the same basal stacking fault has undergone a climb process by folding in the prismatic plane; the process took place through a change of the displacement vector from 1/6$[20\bar{2}3]$ to ½ $[10\bar{1}1]$ and back. In this instance, the resulting prismatic stacking fault is very short, extending only to 1.5**c**. One point that may be underlined is the low concentration of I_2 stacking faults, which may be connected to their intrinsic nature, which is a pure displacement in the basal plane, as opposed to the highest concentration of I_1 faults which have a component along the **c** axis.

Comparing TEM results with the RBS/C damage build-up (Fig. 2.7), it is possible to associate each damage regime with a predominant defect type. In regime I implantation damage consists mainly of point defect clusters and a few stacking faults. In regime II a strong increase of the stacking fault density is observed. The stacking fault density in the bulk saturates in regimes III and IV in good agreement with the RBS/C results showing a saturation of the bulk damage level for high fluences.

While TEM shows that nanocrystallization occurs only when a threshold fluence is exceeded, RBS/C spectra reveal a surface damage peak at lower fluences, showing that two different damage regions exist. This primary surface damage probably acts as a nucleation site for the formation of the NCSL. The formation of NCSL during implantation has important consequences because it has been shown that this layer does not regrow during thermal annealing, but sublimates at temperatures required to activate the implanted dopants [20].

The origin of the highly damaged (NC/amorphous) surface layer is so far not clearly understood and different theories are discussed in the literature (see for example [24]). One model assumes that the sample surface acts as a sink for diffusing defects. This theory is supported by the fact that for implantation at 15 K, when no or little diffusion is expected, the surface peak is much less pronounced than for room temperature implantation [10]. Another possibility is that sputtering (possibly an enhanced sputtering of nitrogen) introduces surface damage which then propagates deeper into the sample or acts as trap for further defects. This theory is backed by the observation that implanting through a thin AlN capping layer pushes the threshold for the formation of the NCSL to higher fluences (Sect. 2.3).

2.2.3 Implantation Temperature Dependence

It was mentioned before that GaN exhibits strong dynamic annealing during ion implantation, even at very low temperatures. The implantation temperature effect has been investigated for Eu and Tm implantation of GaN and improved structural and optical properties were found [21, 25, 26]: for 300 keV Eu ion implantation at 500 ºC, at fluences up to 7.3×10^{15} at/cm^2, no surface damage peak appears in RBS/C spectra; TEM analysis confirms an absence of NCSL in these samples.

Fig. 2.10 shows the TEM weak-beam image and the Eu- and defect profiles for a sample implanted with 3×10^{15} at/cm^2. The Eu and damage profiles extend deeper into the sample than for room temperature implantation because ions implanted along the *c*-axis are steered along the atomic rows. For room temperature implantation this channelling effect is decreased by the formation of the NCSL, which de-channels the ions. Fig. 2.11 shows the concentration of Ga-defects for RT and 500 ºC implantation as a function of the fluence, as extracted from RBS/C spectra using the DICADA code and integrated over the whole implanted region. It is clear that implantation at 500 ºC significantly decreases the damage concentration in the medium fluence regime. TEM for these fluences also shows a decrease of the number of stacking faults for implantation at high temperature [27].

Implanted RE ions occupy, on average, substitutional or near-substitutional Ga-sites of the wurtzite GaN structure, as will be discussed in detail in Chap. 3. For low fluences (< 10^{15} at/cm^2) the substitutional fraction directly after implantation is close to 100% [28]. It is possible to estimate the fraction (f_S) located along the *c*-axis from the random and <0001> aligned RBS/C data. (Note that we are not sensitive to displacements *along* the <0001> direction when measuring only this axis). f_s is given by:

$$f_r = \frac{(1-\chi_{\min}^{RE})}{(1-\chi_{\min}^{Ga})} \tag{1}$$

with $\chi_{\min}^{RE}$ and $\chi_{\min}^{Ga}$ the minimum yield (integrated backscattering yield of the aligned spectrum divided by that of the random spectrum, in a window comprising the implanted region) for the RE and Ga atoms, respectively.

The substitutional fraction is shown in Fig. 2.12a as a function of the implantation fluence for two implantation temperatures; the fraction decreases with fluence for both temperatures but at a slower rate for 500 ºC implantation. Surprisingly, if the substitutional fraction is plotted as a function of the bulk damage level (Fig. 2.12b) the curves for both implantation temperatures overlap, indicating similarity of the rates of damage build-up and RE incorporation. The substitutional fraction decreases linearly with the bulk damage level until the latter saturates and f_S then decreases steeply.

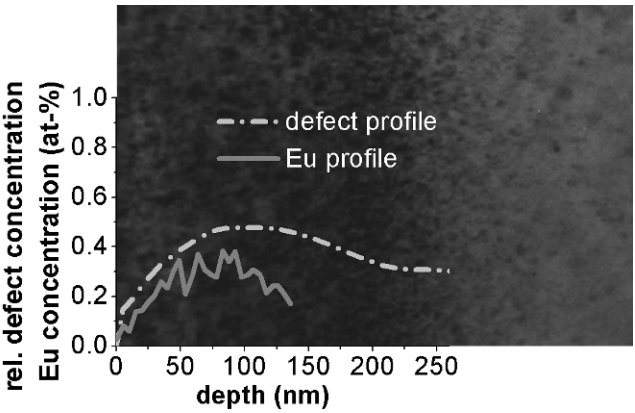

Fig. 2.10. Weak beam TEM image of GaN implanted with 300 keV Eu ions at 500 ºC to a fluence of 7.6×10^{15} Eu/cm^2. Overlaid to the image are the defect concentration profiles and Eu depth profiles derived from the RBS/C spectra.

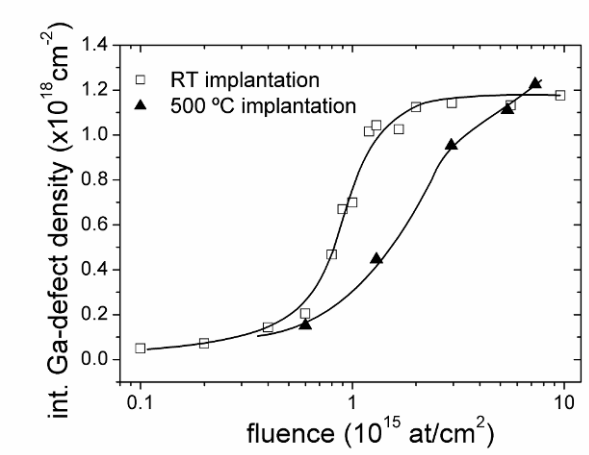

Fig. 2.11. Integrated Ga-defect density as a function of the fluence extracted from RBS/C random and <0001> aligned spectra for 300 keV Eu implantation into GaN at room temperature and 500 ºC. In the intermediate fluence regime, implantation at elevated temperature reduces the incorporated lattice damage significantly.

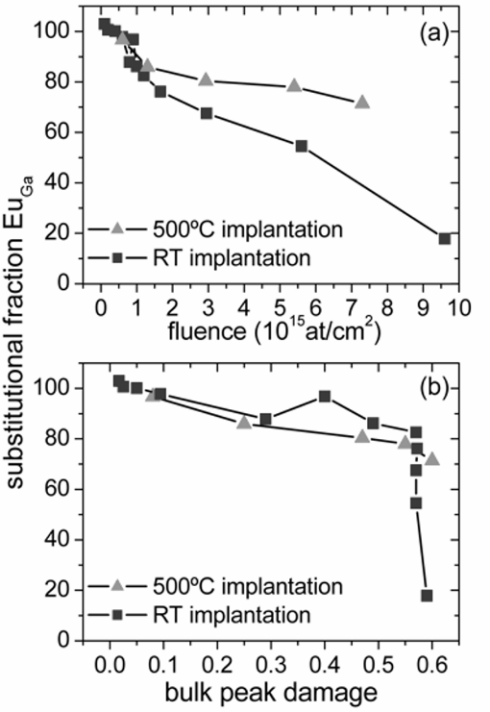

Fig. 2.12. RBS/C results of GaN implanted with 300 keV Eu ions at room temperature and at 500 ºC. (a) Fraction f_S of Eu ions in substitutional Ga-sites as a function of the fluence, (b) Substitutional Eu fraction f_S as a function of the bulk peak damage.

2.3 Annealing and Optical Activation of RE Ions

Post-implant high temperature annealing is necessary in order to remove implantation damage and also to optically activate RE ions. An empirical rule states that efficient removal of implantation damage should take place by annealing at two thirds of a material's melting temperature (in Kelvin). Therefore, annealing of GaN should be performed at temperatures near 1600 ºC. However, at ~ 800 ºC nitrogen already starts to diffuse out of the sample and higher annealing temperatures require an increase of the partial nitrogen pressure to suppress the surface dissociation [29]. Several approaches to a solution of this problem have been reported in the literature including the use of a proximity cap (i.e. a piece of unimplanted GaN placed face to face with the sample), the pre-deposition of a capping layer, or annealing in high overpressures of N_2 [7, 9, 30, 31, 32, 33, 34].

2.3.1 Optical Activation by High Temperature Annealing

In this section the correlation of implantation fluence and annealing temperature with the luminescence intensity is discussed.

Fig. 2.13 shows the integrated room temperature cathodoluminescence (CL) intensity of the $^5D_0 \rightarrow {}^7F_2$ Eu emission around 621 nm [21] for the two sample sets described in Sect. 2.2.2 and Sect. 2.2.3 (300 keV Eu implanted into GaN at room temperature and 500 ºC) after annealing for 20 minutes at 1000 ºC in a moderate N_2 overpressure of 4 bars using a proximity cap. As expected, the CL intensity increases with the implantation fluence; however, the simple assumption that doubling the fluence would cause the same incease in CL intensity is not realized. The more severe lattice damage introduced at higher fluences (see 2.2.2, 2.2.3) appears to introduce extra non-radiative de-excitation pathways.

Clearly, the optical activation of Eu ions is improved by the 500 ºC implantation. For 150 keV Tm implantation similar results were found with increasing blue emission for implantation at elevated temperatures [25]. However, the CL intensity starts to decrease for fluences above 2×10^{15} Tm/cm^2 [35]. Tm shows much lower emission intensities than Eu and is possibly more sensitive to lattice damage. We observe that blue *photo*luminescence can only be achieved after annealing GaN:Tm at 1200 ºC [36].

Fig. 2.13 also shows the areal density of substitutional Eu_{Ga} after annealing as determined by RBS/C. A surprisingly good correlation of Eu_{Ga} areal density and CL intensity is observed.

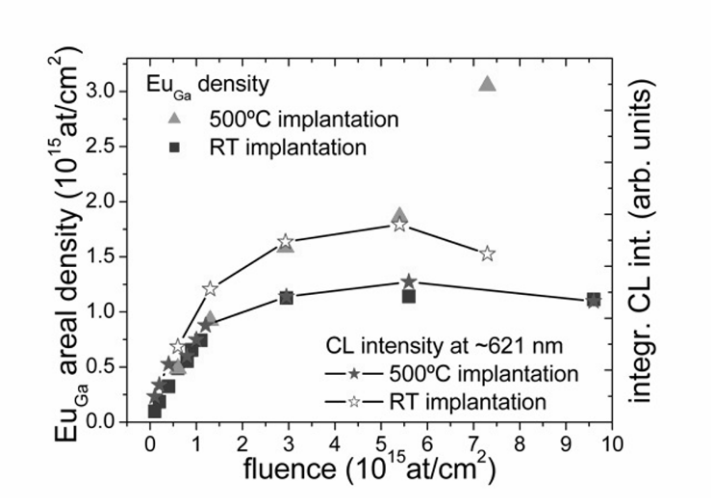

Fig. 2.13. Integrated room temperature CL intensity and the areal density of substitutional Eu_{Ga} of GaN implanted with 300 keV Eu ions at room temperature and 500 ºC to different fluences after annealing at 1000 ºC.

These preliminary results show a complex relationship between structural damage and optical properties, which is reproduced in studies of the CL intensity as a function of the annealing temperature.

GaN was implanted with 300 keV Eu to three different fluences (1×10^{13} at/cm^2, 1×10^{14} at/cm^2 and 1×10^{15} at/cm^2) and annealed at temperatures between 500 ºC and 1200 ºC [21]. For temperatures above 1000 ºC the samples were capped with an epitaxially grown AlN layer as described in detail below. Up to 1000 ºC the CL intensity grows exponentially with annealing temperature for all three fluences (Fig. 2.14). For higher temperature annealing, the CL intensity for the lowest fluences decreases, indicating optimum activation at 1000 ºC; structural degradation (probably due to the out-diffusion of nitrogen) is dominant for higher temperatures. For the sample with the highest Eu doping the CL intensity increases throughout the entire temperature range while the intermediate fluence sample shows highest CL activation for 1100 ºC annealing. The optimum annealing temperature therefore depends on the implantation fluence due to the sensitive balance of defect removal and creation during high temperature annealing.

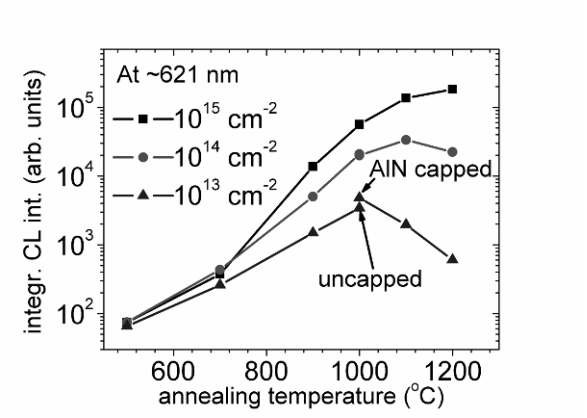

Fig. 2.14. Integrated room temperature CL intensity of GaN implanted with 300 keV Eu ions at room temperature to three different fluences after annealing between 500 and 1200 ºC.

2.3.2 Influence of Annealing Atmosphere

The annealing atmosphere can influence the stability of the GaN surface and thus affect the recovery of the crystal. Lozykowski et al. [37] reported an improvement in luminescence intensity for Pr-implanted GaN annealed at 1100 ºC in NH_3 as compared to samples annealed in N_2. An NH_3-containing atmosphere is present during growth in the MOCVD reactor and may help to stabilize the surface during annealing. At the same time, highly reactive hydrogen, also present when NH_3

dissociates, can damage the surface. Light emission from GaN can also be influenced by the incorporation of hydrogen.

The crucial role of the annealing atmosphere is evident in a comparison of secondary electron images of Er-implanted samples annealed at 1100 ºC in vacuo, in N_2 and in N_2 + NH_3 (Fig. 2.15). After annealing in vacuo or in N_2 at 1000 ºC the surface already shows localized defects with a lateral size around 1 micron. For higher annealing temperature the surface of those samples shows further strong damage and Ga droplets form. In contrast to this, very good results are achieved when using NH_3+N_2: the surface remains smooth even for 1100 ºC annealing.

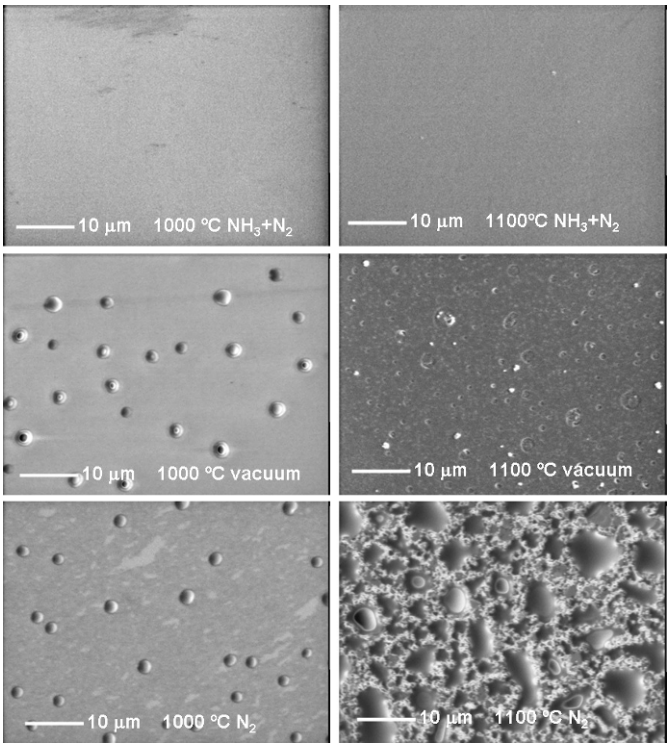

Fig. 2.15. Secondary electron images obtained in the EPMA for Er-implanted samples annealed at 1000 ºC and 1100 ºC in N_2+NH_3, vacuum, and N_2. Annealing in NH_3 containing atmosphere stabilizes the surface.

Fig. 2.16 shows the Ga signal of the RBS/C random and <0001> aligned spectra before and after annealing at 1000 and 1100 ºC in NH_3+N_2. The Er profile (not shown) remains unchanged after annealing. No degradation and indeed a strong removal of implantation damage is evident after annealing at 1100 ºC in NH_3+N_2 while the samples annealed in N_2 or vacuum show strong surface damage and the channelling effect is totally destroyed within a layer as thick as the implanted

region [38]. A sample implanted with Eu and annealed at 1200 ºC in NH_3+N_2 showed a fully restored channelling effect comparable to that of an unimplanted sample [38]; however, at this temperature the surface already shows signs of dissociation and the best results could not always be reproduced. The improved structural properties are reflected in the optical characteristics of the samples. All samples show the typical green emission lines arising from the $^4S_{3/2} \rightarrow {}^4I_{15/2}$ and $^2H_{11/2} \rightarrow {}^4I_{15/2}$ intra-4f shell transition of trivalent Er^{3+} ions. However, for the highly damaged samples, annealed at 1100 ºC in N_2 or vacuum, the CL intensity is very weak. Fig. 2.17 compares the RTCL spectra of samples annealed at 1000 ºC with one annealed at 1100 ºC in NH_3+N_2. The latter, being the sample with better structural properties, clearly shows the higher CL intensity, 50% higher than that of the sample annealed at 1000 ºC.

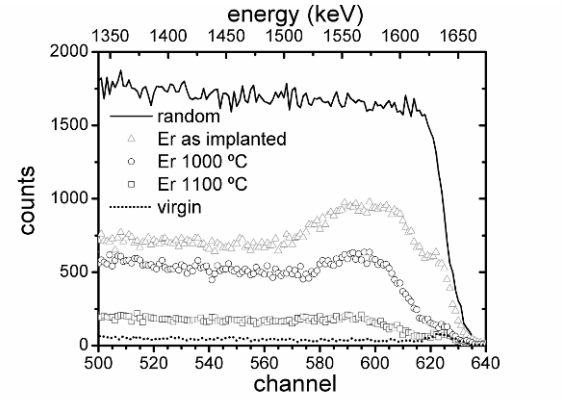

Fig. 2.16. RBS/C random and <0001> aligned spectra showing the Ga signal for Er-implanted GaN before and after annealing at 1000 and 1100 ºC in NH_3+N_2. A virgin sample is shown for comparison.

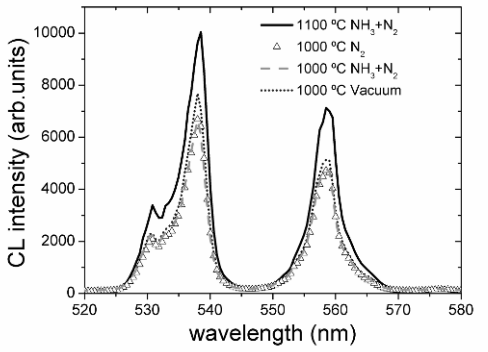

Fig. 2.17. Room temperature CL spectra of Er-implanted GaN annealed at 1000 ºC in three different atmospheres and annealed at 1100 ºC in NH_3+N_2.

2.3.3 Annealing of AlN-Capped Samples

Another way to protect the sample surface, both during implantation and annealing, is to cap it with a material of higher thermal stability. This technique is widely used in III-V semiconductor technology to suppress out-diffusion of the more volatile group V components. Typical capping materials are Si_3N_4 and SiO_2. For nitrides AlN is an obvious capping material, being very stable both chemically and thermally. The random and aligned RBS/C spectra of an AlN-capped and an uncapped sample, implanted with 2×10^{15} Er/cm^2 at 300 keV at room temperature, are shown in Fig. 2.18. The AlN cap was grown by MOCVD directly after the growth of the GaN wafer itself and the implantation was performed through this ~ 10 nm thick AlN layer [34]. The suppression of the typical surface damage peak for the capped sample shows that no NCSL is formed during the implantation. This was confirmed by TEM even for high fluences: Fig. 2.19 shows TEM images of an uncapped and an AlN-capped sample implanted at RT with 4.7×10^{15} Tm/cm^2 and 5.8×10^{15} Tm/cm^2, respectively [39]. A 95 nm thick NCSL forms in the uncapped sample; a region with a high density of planar stacking faults can be seen underneath. For the capped sample, in agreement with RBS/C results, no NCSL forms and the damaged region is deeper suggesting a stronger channelling effect of the implanted ions, since de-channelling by the NCSL is avoided. As in the bulk of uncapped samples stacking faults are formed during the implantation.

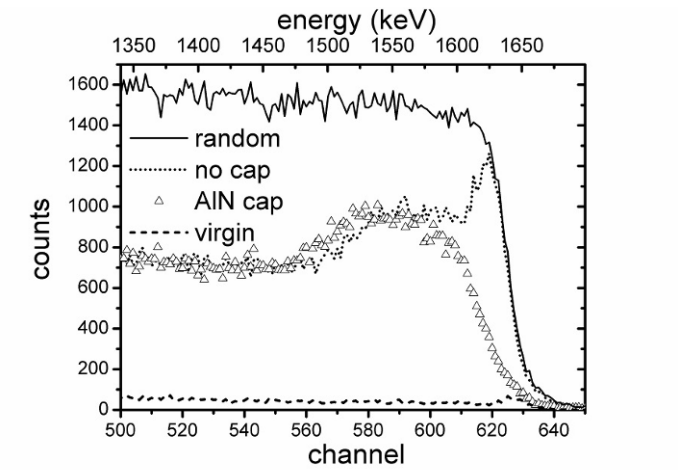

Fig. 2.18. RBS/C random and <0001> aligned spectra after implantation with 2×10^{15} Er/cm^2 into uncapped GaN and GaN capped with a 10 nm AlN layer.

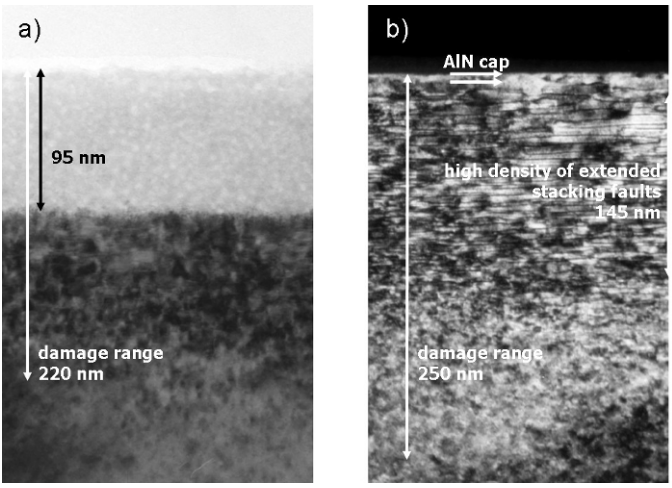

Fig. 2.19. TEM images of as-implanted GaN implanted at room temperature with 300 keV Tm ions. (a) Bright field image of a sample implanted to a fluence of 4.7×10^{15} Tm/cm^2 showing a 95 nm thick nanocrystalline layer on top. (b) Dark field image (g=1 $\bar{1}$ 00) of a sample implanted to a fluence of 5.8×10^{15} Tm/cm^2 through a 10 nm thick AlN layer. No nanocrystalline layer is formed but a region with a high density of extended basal stacking faults can be seen.

Fig. 2.20 presents aligned RBS/C spectra of samples capped with AlN after implantation of 1×10^{15} Eu/cm^2 and annealing at 1000, 1100 and 1300 °C for 20 minutes in N_2 atmosphere as well as the spectrum of a virgin sample for comparison [34]. Here it should be noted that for annealing without an AlN protective layer, GaN already dissociates and Eu diffuses out of the surface for temperatures above 1000 °C. The spectra in Fig. 2.20 already show a very good recovery of the crystal after annealing at 1100 °C, but there is still an elevated level of lattice defects, compared to the virgin sample. Annealing at 1200 °C (not shown) and 1300 °C does not significantly change the aligned spectra within the main damage area. During the dynamic annealing processes very stable extended defects or defect clusters can form in GaN. The TEM images of Fig. 2.21 show that the density of stacking faults is significantly lower after annealing at 1200 ºC compared to annealing at 1000 ºC [39], but to remove them completely, even higher temperatures appear to be called for. In the RBS/C spectra an additional region with increased backscattering yield occurs at the interface to the AlN layer (around channel 625). Already in the virgin sample and in the one annealed at 1100 °C a small peak is present indicating some disorder in the interface region. After annealing at 1200 and 1300 °C this peak increases, proving that an increasing amount of Ga-atoms is displaced from the substitutional site, possibly due to an interaction with defects or Al atoms from the cap. The Eu profile does not change during the annealing process.

It is apparent that the efficacy of the capping layer depends strongly on its structural quality. In fact, SEM images (Fig. 2.22 a and b) of two as-grown AlN-caps grown under the same conditions with slightly different thicknesses (9 and 11

nm, respectively) show surprisingly different morphologies [40]. Crack formation occurs due to the large lattice mismatch between GaN and AlN. Although both cap layers are thicker than the critical layer thickness for plastic relaxation, the crack size and density is much lower for the thinner cap leading to an increased thermal stability. After implantation of 1×10^{15} Eu/cm^2 and annealing at 1300 ºC, only localized damage is visible at the surface (Fig. 2.22c). Fig. 2.22c further shows that this damage is only observed in the implanted part of the sample meaning that, although directly after the implantation no surface damage is visible, the implantation is starting to destroy the capping layer. For the slightly thicker cap the observed degradation is much stronger. Already after annealing at 1200 ºC (Fig. 2.22d) large holes open along the cracks; wavelength dispersive x-ray (WDX) microanalysis (Fig. 2.23) shows that these regions are deficient in N. The degradation of the AlN-cap can be partly suppressed by using additionally an AlN proximity cap during annealing [41].

Fig. 2.24 shows CL spectra of AlN-capped samples annealed between 1000 and 1300 ºC which were taken in selected undamaged regions of the sample. As shown before, the CL intensity exhibits a very strong dependence on the annealing temperature. The intensity of luminescence from a capped and an uncapped sample after annealing at 1000 ºC is comparable. For the AlN-capped samples the integrated Cl intensity of the strongest line increases by a factor of 40 between 1000 and 1300 °C while the low temperature integrated PL intensity even increases by a factor of 100 [42]. An exponential increase of luminescence intensity with annealing temperature was also found for GaN implanted with similar fluences of Tm and Er [36, 43]. These results demonstrate the high potential of the AlN-cap to protect the GaN surface during high temperature annealing; however, more research is needed to obtain reproducible high quality, crack-free capping layers.

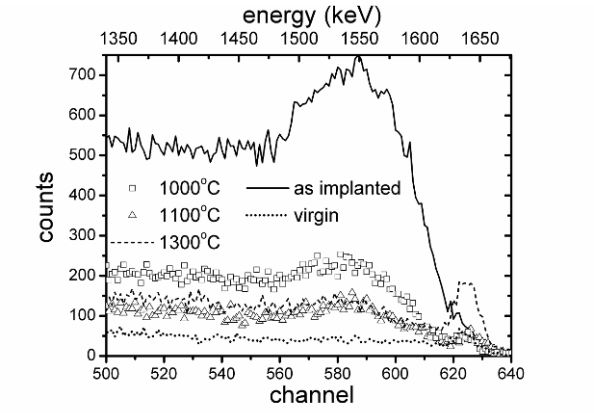

Fig. 2.20. RBS/C <0001> aligned spectra for GaN capped with a 10 nm AlN layer and implanted with 1×10^{15} Eu/cm^2 directly after implantation and after annealing at temperatures from 1000 to 1300 °C.

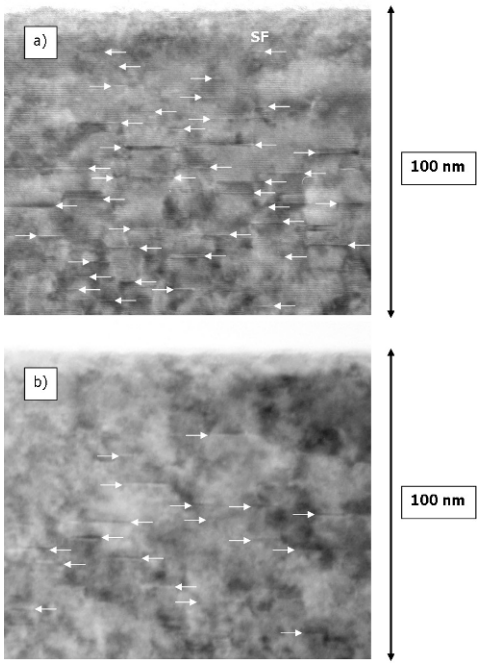

Fig. 2.21. Highly magnified TEM images of samples implanted at room temperature through a 10 nm thick AlN cap to a dose of 5×10^{14} Tm/cm^2 at 150 keV. White arrows show the basal stacking faults; their density is reduced after annealing at 1200 ºC. (a) After annealing at 1000 °C (b) After annealing at 1200 °C

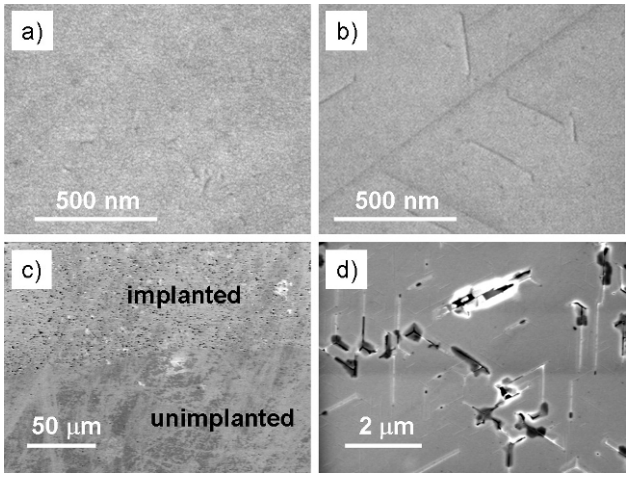

Fig. 2.22. SEM images of the surface of samples (a) with 9 nm AlN cap, unimplanted; (b) with 11 nm AlN cap, unimplanted; **c** sample with 9 nm cap Eu implanted and annealed at 1300 ºC; **d** sample with 11 nm cap Eu, implanted and annealed at 1200 ºC.

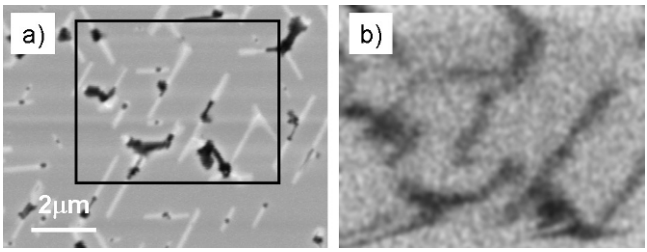

Fig. 2.23. SEM image of (a) the sample with 11 nm cap Eu implanted and annealed at 1200 ºC. (b) Corresponding compositional mapping of nitrogen obtained with WDX.

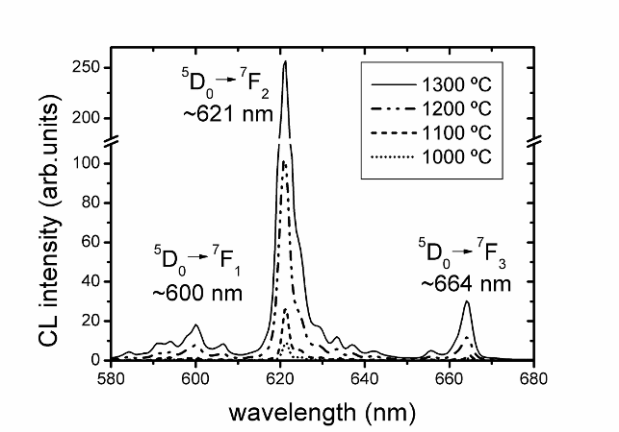

Fig. 2.24. Room temperature CL spectra of AlN-capped GaN implanted with 1×10^{15} Eu/cm^2 after annealing at 1000, 1100, 1200 and 1300 °C. Note the break in the y-axis.

2.3.4 Annealing at Ultrahigh Pressure

GaN epilayers were implanted in random geometry with two different fluences of Eu ions (1×10^{13} at/cm^2 and 1×10^{15} at/cm^2) and annealed at 1000, 1300 and 1450 ºC in a 1 GPa nitrogen overpressure at the Institute of High Pressure Physics, Warsaw, Poland. The RBS/C spectra (Fig. 2.25) for the higher fluence sample show that the damage removal improves for increasing annealing temperature up to 1450 ºC. However, even for this high temperature of annealing damage remains in this sample; higher temperatures (and even higher nitrogen pressures) would be necessary to fully recover the crystalline quality. In contrast to all annealing methods mentioned above, the minimum yield in the Eu-signal also decreases with annealing temperature indicating that the incorporation of Eu on near-substitutional sites is improving. (In fact, similar annealing of a sample implanted at 160 keV in channelling geometry uniquely showed complete recovery of the crystallinity and 100% substitutional incorporation of Eu [44] (see also Chap. 3).

No measurable diffusion of Eu was observed in the present case. For implantation at the much lower fluence of 1×10^{13} at/cm^2, the initial damage is very low and the channelling quality of the virgin sample is already recovered after annealing at 1000 ºC.

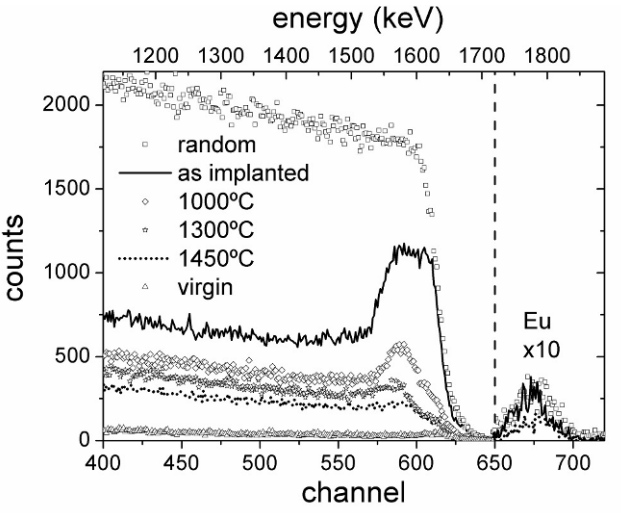

Fig. 2.25. RBS/C random and <0001> aligned spectra for GaN implanted with 1×10^{15} Eu/cm^2 directly after implantation and after annealing at temperatures from 1000 ºC to 1450 °C in ultrahigh nitrogen pressure (1 GPa).

The integrated RTCL intensity at 621 nm as a function of the annealing temperature is presented in Fig. 2.26. For the lower fluence, it is seen to increase strongly for annealing at 1300 ºC in contrast to earlier annealing studies using AlN-capping and low nitrogen pressures (Fig. 2.14) where the CL intensity decreases above 1000 ºC. For the highest temperature, the CL intensity saturates for the high fluence sample and actually decreases for the low fluence sample. This behaviour is partly indicative of a deterioration of the sample at high temperature but is also influenced by the fact that the luminescence in these samples is dominated by a luminescence centre (one of two majority centres [45]) which shows strong luminescence quenching at room temperature. In fact, the low-temperature PL intensity of the low fluence sample increases exponentially in the full range of annealing temperatures and exceeds that of the more strongly doped sample [46].

Although ultrahigh pressure annealing is not easily integrated in industrial production, these measurements emphasize the strong potential to further increase the activation of RE luminescence from implanted GaN by optimizing the annealing procedures.

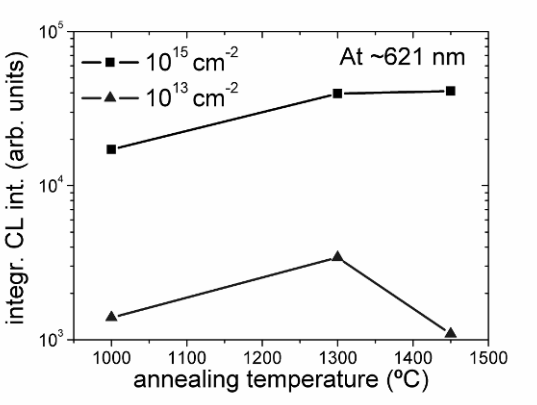

Fig. 2.26. Integrated room temperature CL intensity of GaN implanted with 300 keV Eu ions at room temperature to two different fluences after annealing at temperatures from 1000 ºC to 1450 ºC in ultrahigh nitrogen pressure (1 GPa).

2.4 RE Doping of AlN and AlN-Containing Ternary Alloys

The ternary alloys $Al_xGa_{1-x}N$ and $Al_xIn_{1-x}N$ are promising host candidates for RE ions: their wider band gap allows exploitation of higher lying RE levels and a lower thermal quenching of the luminescence is expected than in GaN. A strong influence of the AlN content in AlGaN alloy on RE emission properties was reported for Eu, Tb, Er and Pr implantation [47, 48, 49]. Eu luminescence intensity can be enhanced significantly in AlGaN when the AlN content is increased to ~ 30%, but declines thereafter [49]. These results are also reproducible for AlGaN templates grown by different techniques [50, 51]. Furthermore, AlGaN ternary alloys are more resistant to implantation damage than GaN [52].

One important advantage of AlN and the AlN-containing ternary alloys over GaN is the suppression of surface nanocrystallization. Fig. 2.27 and 2.28 compare the damage after implantation of 2×10^{15} Eu/cm^2 with two energies into GaN and two ternaries ($Al_{0.3}Ga_{0.7}N$ and $Al_{0.81}In_{0.19}N$). For both implantation energies GaN shows the prominent surface damage peak characteristic of nanocrystallization (note that in the case of 120 keV implantation the two damage peaks are not well resolved) while no surface damage peak is seen in the ternaries [53]. Furthermore, channelling effects are very strong in AlN; channelled implantation can significantly reduce the lattice damage, even at high fluences [54]. Fig. 2.29 shows typical random and <0001> aligned RBS/C spectra after implantation of Eu into AlN with an energy of 300 keV to a fluence of 4×10^{15} at/cm^2 for channelled and random implantation. For channelled implantation the damage profile is extended and the maximum damage level is considerably reduced.

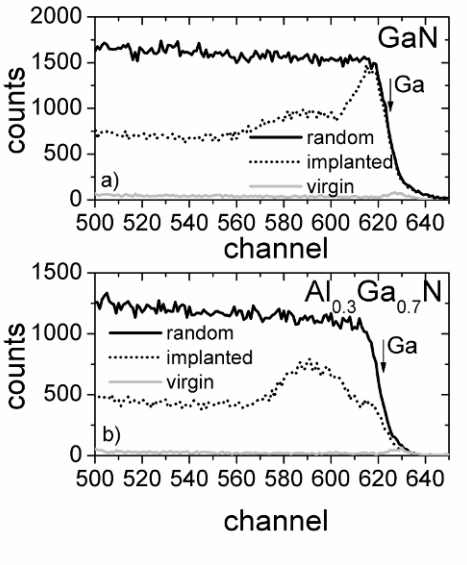

Fig. 2.27. RBS/C random and aligned spectra of samples implanted with 2×10^{15} Eu/cm^2 at an energy of 300 keV : (a) uncapped GaN and (b) $Al_{0.3}Ga_{0.7}N$.

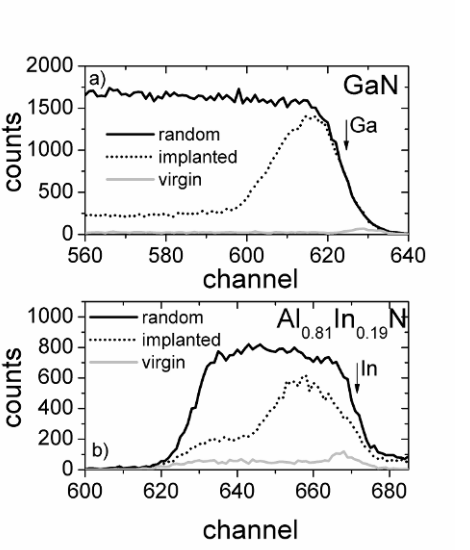

Fig. 2.28. RBS/C random and aligned spectra of samples implanted with 2×10^{15} Er/cm^2 at 120 keV: (a) uncapped GaN and (b) $Al_{0.81}1In_{0.19}N$.

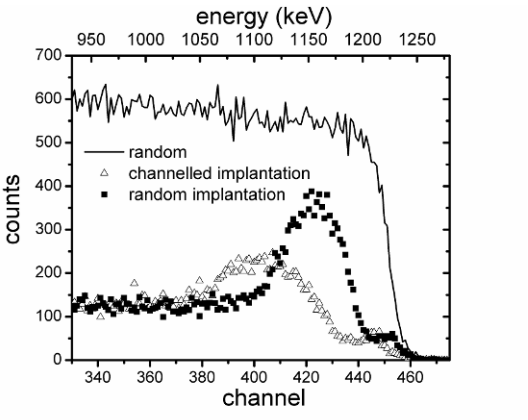

Fig. 2.29. Al signal of a typical random and the <0001> aligned RBS/C spectra after implantation of Eu into AlN at an energy of 300 keV and a fluence of 4×10^{15} at/cm^2 for channelled and random implantation.

Fig. 2.30 presents the RBS/C damage build-up curves for 300 keV Eu channelled and random implantation. The behaviour is similar to GaN, with low damage accumulation for the lowest fluences followed by a regime of steep damage increase. Unlike GaN, however, there is no saturation regime for high fluences: the damage level increases gradually reaching the random level for the highest fluence and random implantation in a region close to the end of range of the implanted ions. In agreement with these results, TEM imaging of this sample (Fig. 2.31) confirms the formation of a buried amorphous layer while the surface and deeper layers remain monocrystalline. Over the entire fluence range the damage level for aligned implantation stays significantly below the value for random implantation.

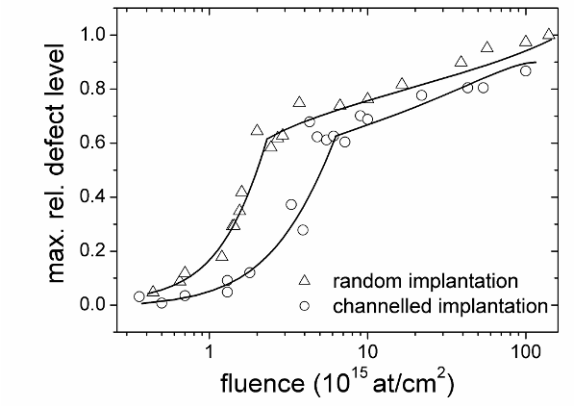

Fig. 2.30. The relative defect concentration in the Al-sublattice as a function of the fluence measured at the maxima of the bulk defect peak for 300 keV random and channelled implantation into AlN.

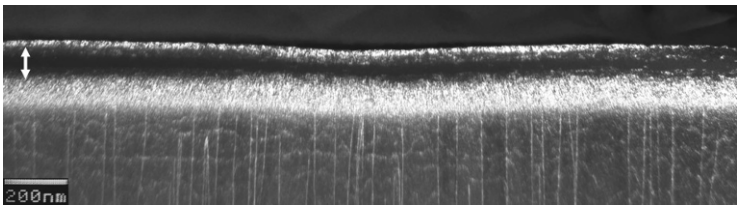

Fig. 2.31. TEM image of AlN sample implanted with 300 keV Eu ions at room temperature in random geometry to a fluence of 1×10^{17} at/cm^2 Eu. The buried amorphous layer shows a dark contrast (white arrow).

In addition to their resistance to radiation damage, AlN-containing alloys also show good thermal stability at temperatures above 1000 ºC, well above the typical growth temperatures of these materials. Efficient optical activation of RE in AlN at temperatures up to 1400 ºC was achieved without any sign of surface degradation [55]. Also the ternaries can be annealed at higher temperatures than GaN without the need of special surface protection. Fig. 2.32 compares RTCL spectra of the blue and IR emissions of Tm-implanted AlN-capped GaN, $Al_{0.11}Ga_{0.89}N$ and $Al_{0.87}In_{0.13}N$ samples, all annealed at 1200 ºC. While for GaN the spectrum shows only one emission line in the blue spectral region, assigned to the $^1G_4\rightarrow{}^3H_6$ transition at 478 nm, the adjacent higher lying level can be excited efficiently for both ternaries and a second blue line at 465 nm is observed, due to the $^1D_2\rightarrow{}^3F_4$ transition [56]. The CL intensity from the ternaries is significantly higher than from GaN. Relatively little work has been done to date on the nitride ternary AlInN and its characteristics as a host for RE. First promising results reveal a strong thermal stability at temperatures well above the growth temperature and improved Eu and Er luminescence intensity when compared to GaN [43, 57].

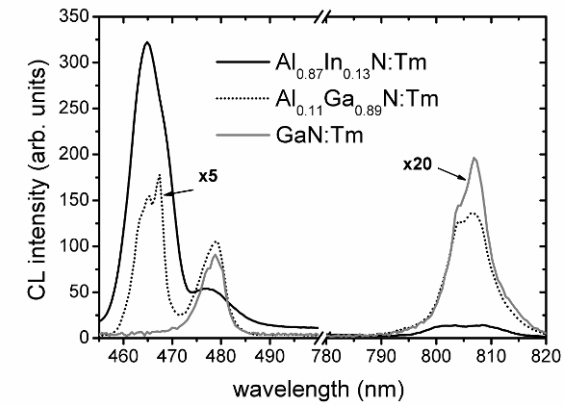

Fig. 2.32. Room temperature CL spectra showing the blue and IR emission of Tm implanted into AlN-capped GaN, $Al_{0.11}Ga_{0.89}N$ and $Al_{0.87}In_{0.13}N$ annealed at 1200 ºC. The implantation fluence and energy were 1×10^{15} at/cm^2 and 300 keV for GaN and AlGaN and 120 keV for AlInN.

2.5 Summary

Ion implantation is a promising technique to dope III-nitride layers with RE ions in a reproducible way and with the facility of lateral patterning. The main drawback of the technique is the correlated radiation damage which needs to be removed by thermal treatment at high temperatures. Special measures to protect the III-N surface from nitrogen loss must be adopted. In this chapter we reviewed the main features of implantation damage build-up in GaN which is characterized by strong dynamic annealing and the formation of two defect regions, one at the surface and one near the end of range of the implanted RE ions. Microscopic investigations of implanted GaN by TEM show that implantation produces mainly stacking faults and point defect clusters. In addition, for room temperature implantation, a highly disordered layer of nanocrystalline material forms at the GaN surface when a critical ion fluence is exceeded. Channelled implantation, implantation at high temperatures and implantation through AlN capping layers all serve to reduce the implantation damage. The two latter are found to prevent nanocrystallization of the surface. In particular the use of an AlN capping layer proves to be effective in preventing surface dissociation and achieving high levels of optical activation during high temperature annealing. Annealing under ultrahigh nitrogen pressures further improves the optical activation of Eu in GaN. First investigations on RE implantation into AlN and AlN-containing ternaries reveal a number of advantages of these materials over GaN, including a strong resistance to radiation damage, high thermal stability and increased RE luminescence yields. Despite considerable progress in the past decade it remains to be established if the problems of annealing implantation damage can be solved efficiently to enable RE implantation to play a useful role in future industrial applications of III-nitrides.

References

1 H. J. Lozykowski, W. M. Jadwisienczak, I. Brown, Appl. Phys. Lett. 74, 1129 (1999).
2 H. J. Lozykowski, W. M. Jadwisienczak, I. Brown, Solid State Comm. 110, 253 (1999).
3 T. Monteiro, C. Boemare, M. J. Soares, R. A. Sa-Ferreira, L. D. Carlos, K. Lorenz, R. Vianden, E. Alves, Physica B 308-310, 22 (2001).
4 J. M. Zavada, R. A. Mair, C. J. Ellis, J. Y. Lin, H. X. Jiang, R. G. Wilson, P. A. Grudowski, R. D. Dupuis, Appl. Phys. Lett. 75, 790 (1999).
5 M. Nastasi and J. W. Mayer, Ion Implantation and Synthesis of Materials, Springer-Verlag Berlin Heidelberg (2006).
6 H. H. Tan, J. S. Williams, J. Zou, D. J. H. Cockayne, S. J. Pearton, R. A. Stall, Appl. Phys. Lett. 69, 2364 (1996).
7 S. J. Pearton, J. C. Zolper, R. J. Shul, F. Ren, J. Appl. Phys. 86, 1 (1999).
8 S. O. Kucheyev, J. S. Williams, S. J. Pearton, Mater. Sci. Eng. R33, 51 (2001).

9 C. Ronning, E. P. Carlson, R. F. Davis, Phys. Rep. 351, 349 (2001).
10 E. Wendler, A. Kamarou, E. Alves, K. Gärtner, W. Wesch, Nucl. Instr. Meth. Phys. Res. B 206, 1028 (2003).
11 S. O. Kucheyev, J. S. Williams, C. Jagadish, Vacuum 73, 93 (2004).
12 A. Vantomme, S. M. Hogg, M. F. Wu, B. Pipeleers, M. Swart, S. Goodman, D. Auret, K. Iakoubovskii, G. J. Adriaenssens, K. Jacobs, I. Moerman, Nucl. Instr. Meth. Phys. Res. B 175, 148 (2001).
13 B. Pipeleers, S. M. Hogg, A. Vantomme, Nucl. Instr. Meth. Phys. Res. B 206, 95 (2003).
14 C. Liu, B. Mensching, K. Volz, B. Rauschenbach, Appl. Phys. Lett. 71, 2313 (1997).
15 B. Pipeleers, S. M. Hogg, A. Vantomme, J. Appl. Phys. 98, 123504 (2005).
16 C. M. Wang, W. Jiang, W. J. Weber, L. E. Thomas, J. Mater. Res. 17, 2945 (2002).
17 F. Gloux, T. Wojtowicz, P. Ruterana, K. Lorenz, E. Alves, J. Appl. Phys 100, 073520 (2006).
18 K. Gärtner, Nucl. Instr. Meth. Phys. Res. B 227, 522 (2005).
19 E. Wendler, K. Gärtner, W. Wesch, Nucl. Instr. Meth. Phys. Res. B 266, 2872 (2008).
20 K. Lorenz, U. Wahl, E. Alves, E. Nogales, S. Dalmasso, R. W. Martin, K. P. O'Donnell, M. Wojdak, A. Braud, T. Monteiro, T. Wojtowicz, P. Ruterana, S. Ruffenach, O. Briot, Optical Materials 28, 750 (2006).
21 K. Lorenz, N. P. Barradas, E. Alves, I. S. Roqan, E. Nogales, R. W. Martin, K. P. O'Donnell, F. Gloux, P. Ruterana, J. Phys. D : Appl. Phys. 42, 165103 (2009).
22 P. Vermaut, P. Ruterana, G. Nouet, H. Morkoç, Phil. Mag. A 75, 239 (1997).
23 P. Vermaut, G. Nouet, P. Ruterana, Appl. Phys. Lett. 74, 694 (1999).
24 S. O. Kucheyev, J. S. Williams, C. Jagadish, J. Zou, G. Li, Phys. Rev. B 62, 7510 (2000).
25 K. Lorenz, U. Wahl, E. Alves, S. Dalmasso, R. W. Martin, K. P. O'Donnell, MRS Symp. Proc. 798, Y 5.4 (2004).
26 K. Lorenz, U. Wahl, E. Alves, T. Wojtowicz, P. Ruterana, S. Dalmasso, R. W. Martin, K. P. O'Donnell, MRS Symp. Proc. 798, Y 5.5 (2004).
27 F. Gloux, P. Ruterana, K. Lorenz, E. Alves, Materials Science and Engineering B 146, 204 (2008).
28 U. Wahl, E. Alves, K. Lorenz, J. G. Correia, T. Monteiro, B. De Vries, A. Vantomme, R. Vianden, Mat. Sci. Eng. B 105, 132 (2003).
29 I. Grzegory and S. Porowski in J. H. Edgar, S. Strite, I. Akasaki, H. Amano, C. Wetzel, *Gallium Nitride and Related Semiconductors*, INSPEC, London, United Kingdom 1999.
30 S. Strite, A. Pelzmann, T. Suski, M. Leszczynski, J. Jun, A. Rockett, M. Kamp, K. J. Ebeling, MRS Internet Journal of Nitride Semiconductor Research 2 (13-15): Art. No. 15 (1997).
31 J. Bartels, K. Freitag, J. G. Marques, J. C. Soares, R. Vianden, Hyperfine Interactions 120-121, 397 (1999).
32 E. Alves , T. Monteiro, J. Soares, L. Santos, M. F. da Silva, J. C. Soares, W. Lojkowski, D. Kolesnikov, R. Vianden, J. G. Correia, Materials Science and Engineering B 81, 132 (2001).
33 T. Monteiro, J. Soares, M. R. Correia, E. Alves, J. Appl. Phys. 89, 6183 (2001).
34 K. Lorenz, U. Wahl, E. Alves, S. Dalmasso, R. W. Martin, K. P. O'Donnell, S. Ruffenach, O. Briot, Appl. Phys. Lett. 85, 2712 (2004).
35 K. Lorenz, U. Wahl, E. Alves, T. Wojtowicz, P. Ruterana, S. Ruffenach, O. Briot, Superlattices and Microstructures 36, 737 (2004).
36 I. S. Roqan, C. Trager-Cowan, B. Hourahine, K. Lorenz, E. Nogales, K. P. O'Donnell, R. W. Martin, E. Alves, S. Ruffenach, O. Briot, MRS Symp. Proc. 892, FF23.13 (2006).

37 H. J. Lozykowski, W. M. Jadwisienczak, I. Brown, MRS Internet J. Nitride Semicond. Res. 5S1, W11.64 (2000).
38 K. Lorenz, E. Nogales, R. Nédélec, J. Penner, R. Vianden, E. Alves, R. W. Martin, K. P. O'Donnell, MRS Symp. Proc. 892, FF23.15 (2006).
39 T. Wojtowicz , F. Gloux, P. Ruterana, K. Lorenz, E. Alves, Opt. Mat. 28, 738 (2006).
40 E. Nogales, R. W. Martin, K. P. O'Donnell, K. Lorenz, E. Alves, S. Ruffenach, O. Briot, Appl. Phys. Lett. 83, 051902
41 E. Nogales, K. Lorenz, K. Wang, I. S. Roq(2006).an, R. W. Martin, K. P. O'Donnell, E. Alves, S. Ruffenach, O. Briot, MRS Symp. Proc. 892, FF24.3 (2006).
42 L. Bodiou, A. Oussif, A. Braud, J. L. Doualan, R. Moncorgé, K. Lorenz, E. Alves, Optical Materials 28, 780 (2006).
43 K. Wang, R. W. Martin, E. Nogales, P. R. Edwards, K. P. O'Donnell, K. Lorenz, E. Alves, I. M. Watson, Appl. Phys. Lett. 89, 131912 (2006).
44 S. F. Song et al., unpublished (2009).
45 K. Wang, R. W. Martin, K. P. O'Donnell, V. Katchkanov, E. Nogales, K. Lorenz, E. Alves, S. Ruffenach, O. Briot, Appl. Phys. Lett. 87, 112107 (2005).
46 I. S Roqan, K. P. O'Donnell, R. W. Martin, P. R. Edwards, S. F. Song, A. Vantomme, K. Lorenz, E. Alves, M. Boćkowski, Phys. Rev. B 80, 023525 (2010).
47 C. J. Ellis, R. M. Mair, J. Li, J. Y. Lin, H. X. Jiang, J. M. Zavada, R. G. Wilson, Mater. Sci. Eng. B 81, 167 (2001).
48 Y. Nakanishi, A. Wakahara, H. Okada, A. Yoshida, T. Ohshima, H. Itoh, phys. stat. sol. b 240, 372 (2003).
49 A. Wakahara, Optical Materials 28, 731 (2006).
50 K. Lorenz, E. Alves, T. Monteiro, A. Cruz, M. Peres, Nucl. Instrum. Meth. Phys. Res. B 257, 307 (2007).
51 K. Wang, K. P. O'Donnell, B. Hourahine, R. W. Martin, I. M. Watson, K. Lorenz, and E. Alves, Physical Review B 80 (2009) 125206.
52 S. O. Kucheyev, J. S. Williams, J. Zou, C. Jagadish, J. Appl. Phys. 95, 3048 (2004).
53 K. Lorenz, E. Alves, I. S. Roqan, R. W. Martin, C. Trager-Cowan, K. P. O'Donnell, I. M. Watson, physica status solidi a 205, 34 (2008).
54 K. Lorenz, E. Alves, F. Gloux, P. Ruterana, M. Peres, A. J. Neves, T. Monteiro, J. Appl. Phys. 107 (2010) 023525.
55 M. Peres, A. Cruz, M. J. Soares, A. J. Neves, T. Monteiro, K. Lorenz, E. Alves, Superlattices and Microstructures 40, 537 (2006).
56 I. S. Roqan, K. Lorenz, K. P. O'Donnell, C. Trager-Cowan, R. W. Martin, I. M. Watson, E. Alves, Superlattices and Microstructures 40, 445 (2006).
57 I. S. Roqan, K. P. O'Donnell, R. W. Martin, C. Trager-Cowan, V. Matias, A. Vantomme, K. Lorenz, E. Alves, I. M. Watson, J. Appl. Phys. 106, 083508 (2009).

Chapter 3
Lattice Location of RE Impurities in III-Nitrides

André Vantomme, Bart De Vries, Ulrich Wahl

Abstract This chapter focuses on the lattice site location of rare earth (RE) ions introduced into group III-nitrides either by ion implantation or doped *in situ* during growth by molecular beam epitaxy (MBE). The lattice site occupied will, to a large extent, govern the luminescence properties of the optically doped semiconductors. An overview of the various possible sites that exist in the wurtzite nitride lattice and of the techniques that can be used to accurately determine the occupied sites will be given. Particular attention will be devoted to channelling techniques, both ion beam channelling and electron emission channelling, which offer direct evidence of the lattice site without the need of further modelling.

Irrespective of the species, the substitutional group III-site (S_{Ga}, S_{Al} or S_{In}) is the only high-symmetry site that has been reported to be occupied by RE in wurtzite material, with the remaining ions being randomly distributed throughout the lattice (so-called *random* sites). With the exception of Eu (for which a second site is suggested, displaced from the S_{Ga} site along the *c*-axis), all REs exhibit a displacement which is larger than the thermal vibration amplitude. The substitutional fraction remains unchanged after thermal annealing, although the REs become better incorporated on the S sites. It will be shown that the obtained fractions are actually lower limits to the real values, since a number of experimental factors may hamper the determination of the lattice site. The role of the sample preparation on the substitutional fraction will be discussed: the implanted fluence,

André Vantomme, Bart De Vries
Instituut voor Kern- en Stralingsfysica and INPAC, Celestijnenlaan 200 D, K.U.Leuven, B-3001 Leuven, Belgium
e-mail: Andre.Vantomme@fys.kuleuven.be

Ulrich Wahl
Instituto Tecnológico e Nuclear, Estrada Nacional 10, 2686-953 Sacavém, Portugal
e-mail: uwahl@itn.pt

the sample temperature during implantation, the implantation geometry, co-doping with light impurities.

Finally, special attention will be devoted to the role of the III-nitride crystal mosaicity (a particular problem for AlN) in determining the lattice site location of implanted REs. Although at first sight, the channelling behaviour appears to have vanished (inferring a small substitutional fraction), advanced analysis of the data, taking the mosaic structure of the nitride into account, allows us to disentangle the effects of substitutionality from those of mosaicity.

3.1 Introduction

As discussed in previous chapters, rare earth (RE) optical dopants can be introduced into nitride hosts either *in situ* during growth (Chaps 4,5,6) or subsequently by ion implantation (Chap. 2). Both approaches incur a number of drawbacks, the most important ones being the limited control over the RE concentration, the limited solid solubility and the risk of precipitation, in the case of *in situ* doping; and implantation-induced lattice damage, in the case of ion implantation. A common issue for all doping techniques is that the functionality of a dopant (be it electrical, magnetic or optical) depends drastically on the lattice site that it occupies within the semiconductor crystal. More specifically, the optical transitions within the 4*f* electronic shells of RE ions, which are forbidden in the free ion, can become allowed if the ion's environment lacks inversion symmetry [1, 2]. The crystal field experienced by the RE first acts as a perturbation on the atomic 4*f* levels, causing a *Stark* splitting of those levels. Next the symmetry of the crystal field at the RE site determines respective radiative intensities by admixing higher-lying states of different parity. Moreover, for efficient injection devices, the RE atom should introduce a trap level in the band gap, which can excite the RE 4*f* level. Hence, it is crucial to know exactly where the REs are located within the nitride lattice and how the incorporation site can be modified by external parameters (e.g. thermal treatment, implantation conditions, co-doping, etc.) in order to maximize into *optically active* sites. It should be mentioned that the (ferro)magnetic response of dilute REs in GaN also depends on the RE lattice site. The colossal magnetic moment observed in GaN:Gd dilute magnetic semiconductors is explained by the interaction of implantation-induced defects surrounding the Gd atoms [3].

In several experiments, lattice sites and RE-defect interaction are assessed *indirectly*, i.e. one aims to deduce the microscopic environment of the RE ion from optical spectroscopy or magnetic studies. Conversely, in this chapter, a systematic structural study of the lattice site location of RE ions in III-nitrides will be presented, emphasizing GaN as a host. Various techniques, either based on ion beam interactions (ion beam channelling and electron emission channelling) or on interaction with electromagnetic radiation (XAFS and hyperfine interactions) will be compared in te*rms* of sensitivity and accuracy.

A comparison between the specific RE lattice sites and the spectroscopic evidence for multiple sites will be discussed in following chapters**,** the question being whether RE emission is due mainly to ions located on a majority site (with a relatively low oscillator strength) or on a minority site with extremely high luminescence efficiency (a so-called *magic* site) [4]. Indeed, it has been proposed by several groups that there is a direct correlation between the RE lattice site and the various peaks detected by luminescence spectroscopy. Kim et al. revealed the presence of distinct Er-related PL (photoluminescence) centres, each characterized by a slightly different crystal field and a site-selective absorption mechanism [5, 6]. However, no information to identify the site configurations could be provided. A PL/PLE (PL excitation) study by Braud et al. indicated two types of optical centers for Er in GaN, originating from isolated RE atoms and RE-defect complexes respectively [7]. Whereas the former are excited directly, excitation of the latter involves a non-radiative energy transfer from defects to Er ions. Similar conclusions were drawn by Pellé et al., who additionally deduced the crystal field strength for Er^{3+} in GaN [8]. Using site-selective combined excitation-emission spectroscopy, Dierolf et al. found two majority GaN:Er sites and several minority sites [9]. Still, according to the authors, *"assigning the [luminescence] peaks to different sites and/or transitions is a challenging task"* and *"assignment of these [peaks] is difficult due to the multiplicity of possible excitation channels"*. Similarly, luminescence studies of Eu-doped GaN led to the conclusion that at least four luminescent sites exist [4, 10, 11], without however being able to unambiguously link the optical sites to specific lattice locations. Consequently, a thorough investigation of the microscopic configuration of RE sites in group III nitrides is indispensable for a full understanding of the excitation and luminescence mechanisms.

3.2 Lattice Sites in Wurtzite Crystals

Group-III nitrides can crystallize in either the wurtzite or zincblende structure, with the wurtzite structure being thermodynamically more stable. In this chapter, we will focus on wurtzite GaN. Each group-III atom is coordinated by four nitrogen atoms; conversely, each nitrogen is coordinated by four group-III atoms, with a stacking sequence ABABAB… of (0001) planes in the [0001] direction (Fig. 3.1) The nitrogen sublattice is equal to the group III sublattice, but is offset by a fraction u of the size of the unit cell along the c-axis. In the geometrically ideal wurtzite lattice this u-parameter equals 3/8.

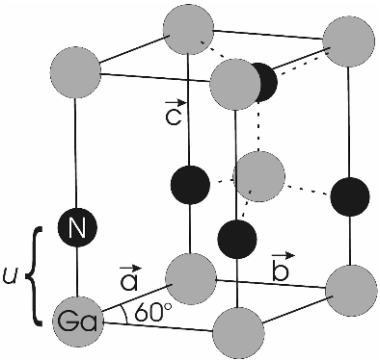

Fig. 3.1. The unit cell of the wurtzite GaN structure [12].

In a depiction of a number of stacked unit cells, Fig. 3.2 presents the most important crystallographic axes and planes in the wurtzite structure, which we use to describe the lattice site of RE ions incorporated in the crystal.

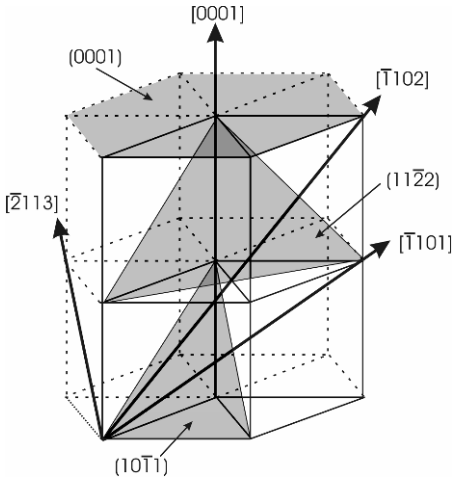

Fig. 3.2. Stacked unit cells (two are marked with full lines), indicating the most important axes and planes of the wurtzite lattice [12].

This basic structural information allows us to define a number of possible lattice sites within the wurtzite crystal. The most trivial position, obviously, is a *substitutional site* whereby the RE either replaces a Ga (or In or Al) atom or a N atom. From the concept of charge equivalence, it is expected that an RE^{3+} ion will replace a Ga atom, i.e. occupy a substitutional Ga site S_{Ga}. Indeed, *ab initio* calculations indicate that the substitutional group-III site is the most energetically favorable position for an isolated RE atom, both in GaN [13] and AlN [14]. However, besides the substitutional sites S_{Ga} and S_N, a large number of highly

symmetric *interstitial sites* can be identified in the wurtzite structure as well. An overview of the most important lattice sites is given in Fig. 3.3. In the lattice location studies presented in this chapter, the following interstitial sites will be considered: the bond-centered sites both within (BC-*c*) and off (BC-*o*) the nitride *c* axis, the antibonding sites AG-*c*, AN-*c*, AG-*o* and AN-*o*, the hexagonal sites HG and HN, and the so-called T and O sites [15].

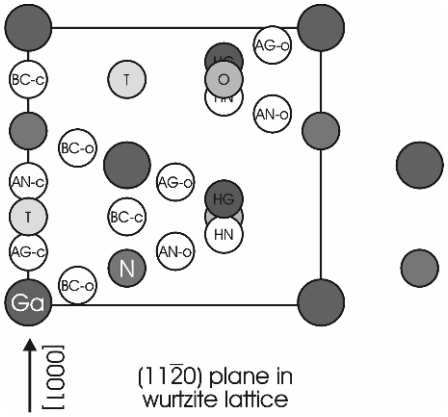

Fig. 3.3. Cross-section through the GaN wurtzite unit cell along the (11$\bar{2}$0) plane, showing the Ga and N lattice positions and the main interstitial sites. Note that the HG and HN sites are very close to the O sites, so the corresponding circles overlap [12].

Experimental studies of lattice location of RE in the elemental semiconductors, Si [16] and Ge [17] and in compound semiconductors such as GaAs [18] and InP [19], indicate that the interaction with intrinsic defects (such as vacancies) or impurities (e.g. oxygen) can result in their eventual incorporation in an interstitial lattice site. Theory [13] supports this model in III-N. Consequently, not only the *perfectly* incorporated lattice sites will be treated, but displacements from the above-mentioned sites have to be taken into account as well.

3.3 Experimental Lattice Site Determination

Although a variety of experimental techniques provide (partial) information on the lattice site of impurities in a host, only a few approaches yield direct evidence of the microscopic structure. The most well-known of these direct techniques is based on the interaction of charged particles with the RE doped nitride, i.e. channelling, which can be performed with an *external* ion beam (ion beam channelling) or with *internal* radioactive probes (emission channelling). Both techniques reveal the lattice site, the symmetry and the displacement of an impurity. Alternatively, using X-ray absorption fine structure (XAFS) or hyperfine

interaction techniques, the separations, coordination numbers and symmetry of the neighbouring atomic shells can be deduced. Obviously, additional modelling is then required to link these parameters to a specific lattice site. All four approaches have their own strengths and weaknesses in terms of the sensitivity (to low/high concentration, multiple sites…) and accuracy that can be achieved.

3.3.1 Ion Beam Channelling

When an energetic, light ion beam – typically MeV He ions – impinges along a major symmetry direction (lattice axis or lattice plane) of a single crystalline host, the probability for a close encounter collision between the incoming ion and the host atoms is drastically reduced. This has a direct consequence in Rutherford backscattering spectrometry (RBS): since the scattering probability decreases by up to two orders of magnitude, the backscattering yield diminishes accordingly [20].

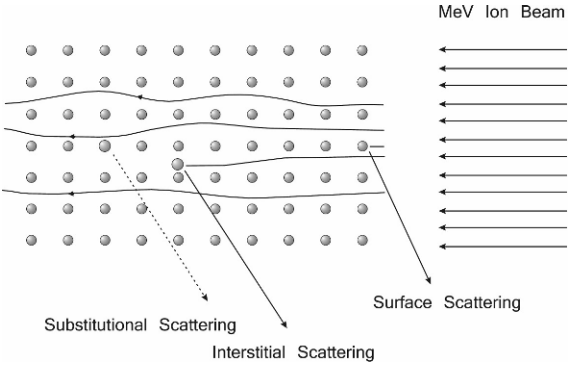

Fig. 3.4. Conceptual scheme of lattice site determination by ion channelling.

This *channelling* effect allows us to determine the lattice site of impurities, as is illustrated in Fig. 3.4 for a substitutional and a random-interstitial impurity. Since the substitutional atom is in line with the atomic rows of the nitride lattice, the probability for backscattering from the impurity atom is very low. Moreover, the dependence of the yield on the angle between the incoming beam and the crystal axis will be the same as for scattering from the host atoms. Any deviation from this angular dependence allows deducing the displacement of the dopant. On the other hand, random interstitial impurities are never positioned "in the shadow" of any atomic row, hence the backscattering yield remains as high as in the case of random beam incidence – no matter the alignment. To provide the lattice site, angular scans (i.e. measuring the backscattering yield as a function of angle of incidence) along at least two crystal directions are required. In order to deduce the

fraction of impurities on a specific site and the displacements from the ideal site, computer simulations using the Monte Carlo code FLUX [21] are performed, where the wurtzite structure is incorporated to simulate the GaN angular scans.

It has to be pointed out that a minimum RE concentration is required to perform this analysis (i.e. to obtain a sufficiently strong RE signal in the backscattering spectra). On the other hand, the implanted RE fluence should not be too high, since implantation-induced defects result in amorphisation of the crystalline host and consequently prevent channelling. In practice, a fluence of the order of 5×10^{14} RE/cm^2 is optimal for these measurements.

3.3.2 Emission Channelling

Rather than investigating the channelling/blocking of incident ions, an alternative approach utilizes the channelling of charged particles *emitted* by radioactive RE atoms implanted into the nitride – this is emission channelling [22]. For RE ions, a variety of isotopes (which emit β^- or conversion electrons) with suitable radioactive lifetimes (optimally a few days to several weeks) and electron energies (of order 30-300 keV) can be produced at on-line isotope separators, such as the ISOLDE facility in CERN, Geneva. It should be remarked that, due to the negative charge of the electrons (as opposed to positive ions used in ion beam channelling – see above), channelling occurs *along* the rows of atoms rather than in the middle of the channels (Fig. 3.5). Consequently, a negatively charged particle will be channeled only if the impurity is located along the row of atoms (Fig. 3.5(a)), resulting in an increased electron yield in this direction. On the contrary, interstitials generally give rise to mixed channelling and blocking effects (Fig. 3.5(b)).

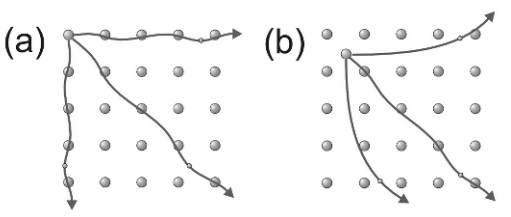

Fig. 3.5. Simplified scheme indicating channelling (black arrows) and blocking (grey arrows) effects for negatively charged particles emitted from (a) substitutional and (b) interstitial impurities.

After implanting the radioactive RE tracers into an epitaxial nitride layer, electron emission patterns around several crystal axes are measured by a position-sensitive detector (Fig. 3.6) or by rotating the sample in front of a collimated detector. The two-dimensional detector has the advantage of recording not only

the intensity along the axis, but also of the surrounding planar channelling or blocking effects. By fitting these experimental patterns to theoretically calculated angular yields, the lattice site of the impurities can be accurately determined.

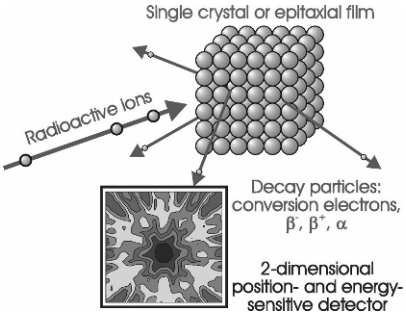

Fig. 3.6. Basic principles of emission channelling experiments using position sensitive detectors [12].

Compared to conventional ion beam channelling, the sensitivity of emission channelling experiments can be higher by up to four orders of magnitude. The reason for this is twofold: (i) by using radioactive probes, the required number of probe atoms can be much lower than with ion beam channelling methods; and (ii) the use of 2D-detectors with large solid angles increases the detection efficiency [23]. Hence, emission channelling is especially suited to study the lattice location of low-fluence impurities (which means isolated impurities with minimal interaction between them), or in systems where conventional ion beam techniques cannot be applied (e.g. for light impurities in a heavy host).

Before analysis the experimental patterns must be corrected for the background caused by electrons that have been backscattered inside the sample or by parts of the vacuum set-up [24]. While a qualitative identification of lattice sites is usually possible from visual inspection of the emission patterns, more precise quantitative results require comparison with theoretical predictions. Thus, the corrected experimental channelling data are compared to simulated patterns by means of a two-dimensional fitting procedure [23]. Theoretical patterns can be calculated using the many-beam approach [22] for electron channelling with the emitting atom on possible lattice sites (with various root-mean-square displacements) including the substitutional and interstitial sites as illustrated in Fig. 3.3.

The principle of emission channelling is illustrated by the example of ^{72}Ga (a β^- emitter with $t_{1/2}$ = 14.10 h) in GaN, where the substitutional Ga site is obviously expected to be in the majority. However, due to the non-equilibrium conditions of the implantation process and the large concentration of point defects which are generated (such as Frenkel pairs), other lattice sites might be populated as well, e.g. anti-sites (Ga_N), interstitials, displaced sites… Typically, the measurements are performed directly after implantation and then repeated after subsequent *in situ* vacuum annealing steps at temperatures up to 900 °C.

Fig. 3.7 shows the *simulated* channelling patterns for 100% occupation of ^{72}Ga emitter atoms on substitutional Ga sites S_{Ga}, substitutional N sites S_N, and the interstitial HG, T and O sites. Since Ga and N atoms are located in the same *c*-axis atomic rows, they give rise to the same emission pattern along this direction. The same reasoning applies to all interstitial sites along the *c*-axis rows, e.g. the T site (cf. Fig. 3.3). Since the HG, HN and O sites are all centered in the hexagon spanned by the *c*-axis atomic rows, they will also produce an identical channelling pattern (different from that of S_{Ga}, S_N and T) with hexagonal symmetry along the [0001] direction. In order to discriminate between these sites, emission patterns along other crystalline directions should be inspected. Typically, the [0001, $\underline{1}$102, $\underline{1}$101] and [$\underline{2}$113] axes are chosen, but there are also other crystallographic directions that work well in this respect, e.g. [$\underline{2}$203, $\underline{3}$302, $\underline{2}$201, $\underline{2}$116] or [$\underline{2}$112] [12]. As can be seen from Fig. 3.7, there is, for every site, at least one angular yield pattern which differs significantly from the others, demonstrating the specificity of the emission channelling technique. By consistent fitting of the results obtained along these different crystal axes, one can accurately determine the lattice site of the radioactive probe atoms.

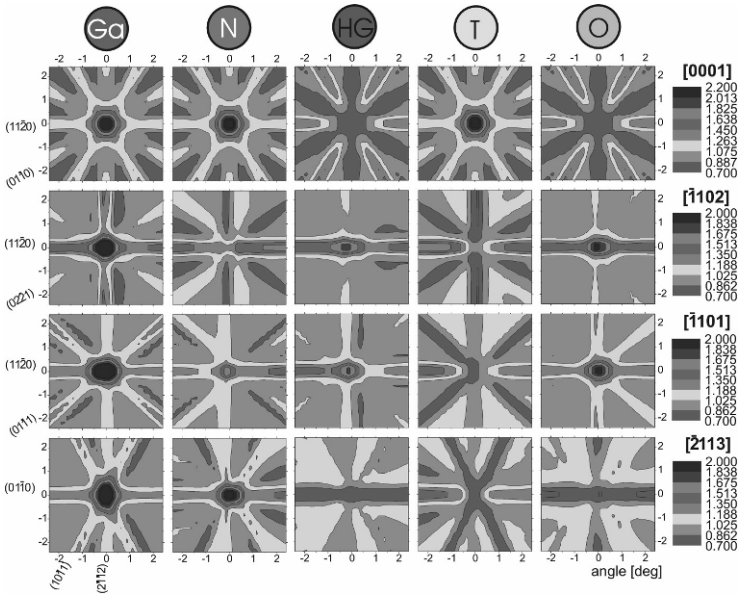

Fig. 3.7. Simulated channelling patterns along the [0001, $\underline{1}$102, $\underline{1}$101] and [$\underline{2}$113] directions for 100% ^{72}Ga emitter atoms on substitutional Ga sites S_{Ga}, substitutional N sites S_N, and the interstitial HG, T and O sites [12].

The axial channelling effect and the intersecting planar effects in the *experimental* β^- pattern along the [0001] direction [Fig. 3.8(a)] immediately suggest that ^{72}Ga is situated along the *c*-axis atomic rows, as can be seen from the projection of

the crystal along the *c*-axis. More quantitative information can be extracted by performing a least-squares fit of this experimental pattern to a set of theoretically calculated patterns. The best two-fraction fit [Fig. 3.8(e)] indeed corresponds to a fraction of 86% of Ga along the *c*-axis rows. The remaining 14% is situated on random (R) sites, which give an isotropic contribution to the emission yield. These R sites correspond to low-symmetry sites or sites with very disordered or amorphous surroundings. The fit procedure further reveals a one-dimensionally projected root-mean-square (*rms*) displacement of atoms, u_1, perpendicular to the [0001] rows of 0.07 Å. Fig. 3.8(b)-(d) show additional emission channelling patterns measured around the [$\underline{1}$102, $\underline{1}$101] and [$\underline{2}$113] axes. These patterns were also fitted to theoretical emission yields: the best fits [Fig. 3.8(f)-(h)] correspond to occupation probabilities of 96%, 91% and 89% for ^{72}Ga on S_{Ga} sites with *rms* displacements of 0.12 Å, 0.09 Å and 0.08 Å perpendicular to the corresponding channelling directions.

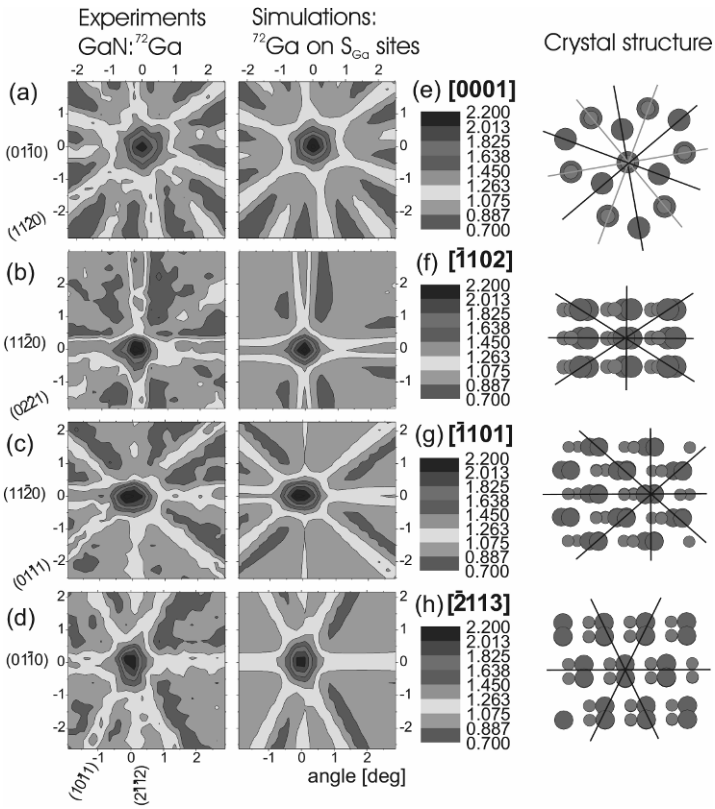

Fig. 3.8. Angle-dependent β^- emission yield from ^{72}Ga in GaN after room temperature implantation, along with the best fits of simulated channelling patterns. The projections of the wurtzite crystal along the four directions used ([0001, $\underline{1}$102, $\underline{1}$101] and [$\underline{2}$113] axes) are shown as well [12].

Subsequent annealing at 600 °C slightly increases the substitutional fraction to about 94%, while the displacement decreases to about 0.06 Å, comparable to the thermal vibration amplitude of Ga in GaN for which values between 0.057 Å and 0.084 Å can be found in the literature [25, 26, 27, 28, 29]. Hence, it can be concluded that immediately after implantation, implanted Ga atoms are slightly displaced from the perfect S_{Ga} sites, while annealing leads to a "perfect" on-site incorporation. It is evident that the initial displacement is a signature of the implantation-induced disorder, which recovers upon annealing at 600 °C [30].

3.3.3 X-Ray Absorption Fine Structure (XAFS)

In XAFS analysis, the absorption of X-rays is measured in the vicinity of a characteristic atomic absorption edge, as a function of the energy of the incident photons (typically originating from a synchrotron source). For energies larger than the absorption edge, photoelectrons are created. Due to the interference of emitted and reflected photoelectrons, a fine structure emerges above the absorption edge (Fig. 3.9).

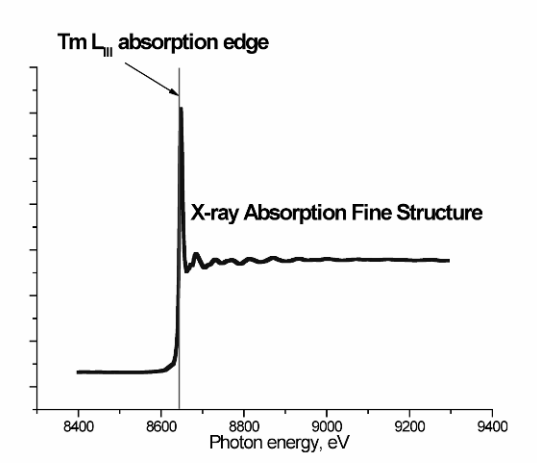

Fig. 3.9. X-ray absorption spectrum in the vicinity of an absorption edge. A fine structure (interference pattern) emerges at energies above the edge [31].

This interference pattern maps the phase shift between the electron waves which depends on on the distance between the atoms. Fourier transformation of the interference pattern (in k-space) yields the radial distribution of the neighbouring atoms. In practice the experimental data are compared to the predicted response of a defined structural model.

The local structure of the probe atom can be mapped (with a typical uncertainty of 0.1 nm), to provide information on the lattice site. One has to keep in mind, however, that the radial distribution function (distances) has to be transformed into a microscopic configuration around the impurity atom – the chosen model is not necessarily unique. Moreover, XAFS, in contrast to emission channelling, is not particularly sensitive to random displacements of a target atom from its lattice site, since such deviations will be averaged out in the total contribution. On the other hand, this technique is sensitive to phase decomposition. In particular, for high RE doping of GaN, the formation of RE-nitrides has been detected.

3.3.4 Hyperfine Interactions

The interactions of the nuclear magnetic dipole moment and the nuclear electric quadrupole moment with internally generated magnetic and electric fields (the so-called hyperfine fields) result in small shifts and/or splittings of the nuclear energy levels. These interactions lead to a *hyperfine structure*, in analogy with the *fine structure* of electronic levels of an atom. Measurement of the nuclear energy splittings yields direct information on the electron distribution around the probe atom, i.e. on the local configuration, from which information on the lattice site can be derived. However, as is the case for XAFS, and in contrast to ion channelling, the information is primarily indirect – a model is required to identify the structure from the measured hyperfine fields. The most common way to access these hyperfine interactions is by measuring, subsequent to the decay of a radioactive probe atom, the energy (Mössbauer spectroscopy) or correlation (PAC, perturbed angular correlation) of emitted electromagnetic radiation. We refer the reader to [32] for more details. Alternatively, by measuring the spin state of an unpaired electron, electron spin resonance probes the interaction of the electron with nearby nuclear spins, hence revealing the lattice location.

3.4 Lattice Site in Wurtzite Crystals

3.4.1 Lattice Location of High-Fluence GaN:RE Implants by RBS/C

RBS/C (Rutherford backscattering and channelling spectrometry) is an established technique to study the depth profile and lattice location of impurities in a host lattice. The lattice (dis)order of the host is probed simultaneously. The efficiency of RBS is lower than that of emission channelling and only *one-dimensional* scans

along a limited number of axes (typically along the [0001] and [10$\underline{1}$1] axes) have been attempted to date.

Lattice location studies have been performed for a variety of RE species implanted into GaN, AlN and various ternary compounds, to a fluence of the order of 5×10^{14} to 1×10^{16} at./cm^2 – the lower limit being set by the sensitivity of the detection, the upper limit by the implantation-induced defect density (ultimately leading to amorphization). Fluences above approximately 5×10^{15} at./cm^2 induce so high a defect concentration that crystal regrowth becomes impossible. Applying specific implantation regimes, such as channeled or high-temperature implantation [33, 34] may help to circumvent such problems or at least to increase the upper limit. At moderate fluence (10^{14} – 10^{15} at./cm^2), the efficient dynamic annealing of GaN prevents the lattice from being completely destroyed.

As an example, we investigate the lattice location of Pr implanted into GaN to a fluence of 7×10^{14} at./cm^2 [35]. The angular scan through the *c*-axis (Fig. 3.10) shows a nearly complete overlap of the Ga and Pr signals, indicating that both the Ga and Pr sublattices are affected to an equal degree by the implantation-induced disorder – both after implantation (not shown) or after subsequent annealing at 1000 °C for 2 minutes [Fig. 3.10(a)]. The minimum (channelling) yield is approximately 30%, compared to about 2% for a virgin nitride layer. Hence, with respect to the *c*-axis, 100% of the Pr ions occupy on average the same lattice site as Ga atoms, but about 30% of them are distributed randomly in the lattice.

The overlap of the scans proves that the implanted REs are shadowed along the [0001] direction. However, since Ga and N form a mixed row along this direction, it is impossible to unambiguously distinguish between the lattice sites along the *c*-axis.

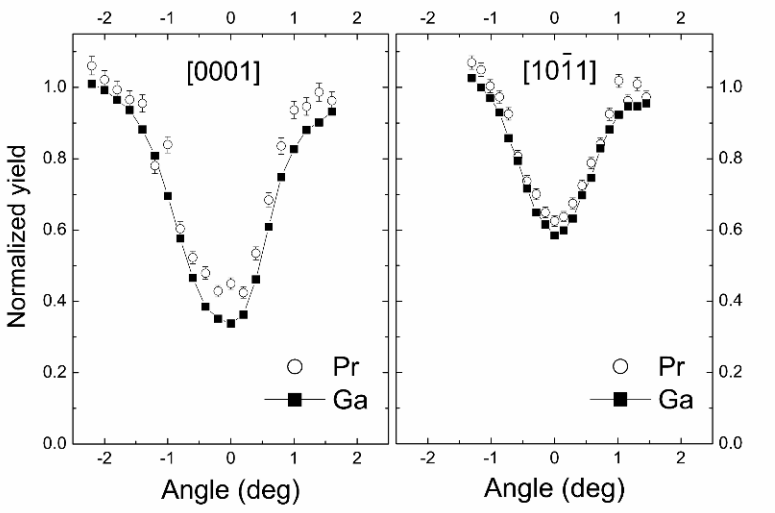

Fig. 3.10. Angular scans across the [0001] and the [10$\underline{1}$1] axis for a Pr implanted GaN sample (7×10^{14} at./cm^2) after annealing at 1000 °C for 2 minutes [35].

For this purpose, scans were performed along the [10$\underline{1}$1] axis, which consist of either pure Ga or pure N atomic rows, hence allowing to distinguish between the Ga and N sites. The large difference in atomic number between the elements results in a much stronger channelling potential for Ga, hence in a much broader angular scan compared to a substitutional N site. RE on an interstitial site such as T, O or H would cause peaks along the [0001] or [10$\underline{1}$1] or both. Hence, the good overlap of the scans for Ga and Pr (Fig. 3.10(b)) proves that Pr is incorporated in Ga sites. Similar experiments have been performed for a wide variety of RE species and the results are essentially the same for Pr, Ce, Eu, Dy, Er and Tm. We refer to [36] for an overview.

Fig. 3.11 compiles the [0001] and [10$\underline{1}$1] angular scans obtained after implanting the abovementioned REs and subsequent annealing at 1000 °C for 2 min in flowing N_2 (except for the Er-implanted sample, which was annealed at 1200 °C for 20 min under 1 GPa N_2 pressure). The solid lines in the figure show computer simulations with the Monte Carlo code FLUX [21], which assume full incorporation of the RE ions on Ga sites. The range of measured minimum yields, between 8% and 44%, scales with the variation in fluence that was used for the various species.

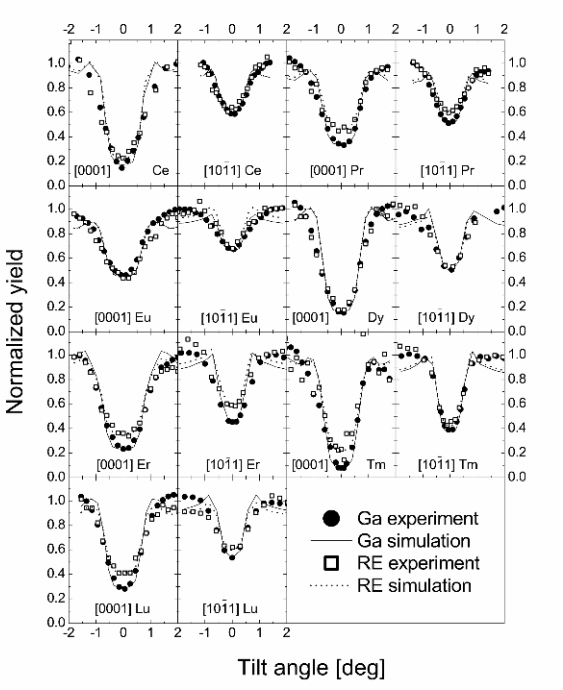

Fig. 3.11. [0001] and [10$\underline{1}$1] scans for Ga and various REs along with the best fits of Monte Carlo simulations for substitutional Ga sites. All REs were implanted with 160 keV at RT up to a fluence of 7×10^{14} at./cm^2 (Ce), 1.2×10^{15} at./cm^2 (Pr), 1.5×10^{15} at./cm^2 (Eu), 8×10^{14} at./cm^2 (Dy), 5×10^{14} at./cm^2 (Er), 7×10^{14} at./cm^2 (Tm) and 9×10^{14} at./cm^2 (Lu). The *rms* displacement used in the simulations was set equal to a representative value of the thermal vibration amplitude of Ga (0.07 Å, except for Eu where an *rms* value perpendicular to [10$\underline{1}$1] of 0.14 Å was used [36].

The fact that the Ga and RE scans overlap indicates that the majority of REs occupies substitutional Ga sites. Taking the Ga signal as a reference, it can be concluded that 97% of Ce, 81% of Pr, 100% of Eu, 96% of Dy, 78% of Er, 83% of Tm and 82% of Lu occupy the same lattice site as Ga. However, one should keep in mind that these may not be *ideal* lattice sites, due to damage remaining after implantation. Furthermore, this retained damage hinders an accurate determination of the *rms* displacement from the ideal substitutional S_{Ga} lattice site. Consequently, the Monte Carlo simulations in Fig. 3.11 do not fully overlap with the Ga angular scans. However, since the angular widths of the Ga and RE scans match, the *rms* displacements of REs must be similar to those of Ga. The simulated RE scans in Fig. 3.11, with the exception of Eu, have been calculated with an *rms* displacement of 0.07 Å.

Among the REs that were investigated, Eu is the exception, as can be clearly seen from the [10$\underline{1}$1] scan (Fig. 3.12), which is much narrower than the Ga scan [35]. From the MC simulation, u_1(Eu) = 0.14 Å was derived, which could also be explained by a Eu displacement of 0.20 Å [= 0.14 Å / sin(46.8°)] along the [0001] direction. Recent work by Bodiou et al. [37] tentatively identifies two luminescence sites for Eu-doped GaN: besides the displaced Eu site mentioned above, a *minority* of the RE ions may be located on S_{Ga} sites, the latter being present in implanted as well as MBE-doped samples. Preliminary experiments show that the *majority* of Eu atoms may be on "ideal" Ga sites when the implantation induced damage is completely removed by a combination of channeled implantation and high-temperature/high-pressure annealing [38]. The specific case of GaN:Eu will be discussed in more detail in Sect. 3.2 of this chapter.

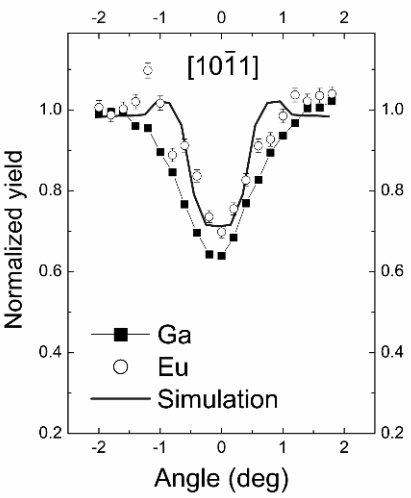

Fig. 3.12. Angular scan across the [10$\underline{1}$1] axis for a Eu implanted GaN sample (5×10^{14} at./cm^2) after annealing at 1000 °C for 2 minutes in flowing N_2 gas. The solid lines are fits obtained with a Monte Carlo simulation [35].

It should be noted that deriving precise values of the RE *rms* displacements by RBS/channelling is difficult, since (i) the azimuthal orientation of the scans are not known accurately enough and (ii) the angular widths are distorted by the retained implantation damage. Consequently, the simulated and experimental Ga scans do not fully overlap (Fig. 3.11). More detailed information about the *rms* displacement of implanted REs is available from emission channelling experiments (see below), where a significantly lower implanted fluence minimizes the impact of implantation damage.

A complementary approach to revealing the local environment of RE dopants in GaN is based on hyperfine interaction measurements. Although experimentally not as straightforward as ^{57}Fe - the workhorse of Mössbauer spectroscopy - several RE atoms have a Mössbauer isotope. Hyperfine interactions reveal the chemical environment (isomer shift) and local symmetry (electric field gradient) around the RE probe atom. Bharut-Ram et al. [39] implanted a GaN sample with 120 keV ^{151}Eu and collected the conversion electron Mössbauer spectra of the 21.6 keV ^{151}Eu transition. The Mössbauer spectra were analysed as two symmetric doublets, which were attributed to Eu on substitutional Ga sites and Eu at or near substitutional sites but with extensive lattice damage, respectively. The quadrupole splittings and annealing behaviour were found to be consistent with hyperfine measurements of ^{96}Ga, ^{71}Ga, ^{111}In and ^{119}Sn [40, 41]. The authors conclude that unambiguous assignment of the two doublets remains difficult without direct lattice site evidence from techniques such as RBS/C or PIXE (particle-induced X-ray emission) [39]. In a similar approach, Ronning et al. combined EC and PAC to investigate the lattice site of ^{111}In and ^{89}Sr in GaN and AlN [42]. Although not focusing on RE dopants, this study confirms that power and sensitivity of the technique in assessing the local surroundings of a dopant, despite the fact that additional input remains necessary to validate the suggested models.

The lattice location of implanted REs has been studied in other group III-nitrides by RBS/channelling as well. Lorenz et al. investigated the incorporation of Eu, Tm and Er in AlN at a fluence of 2.5×10^{15} at./cm^2 [43]. Although very efficient dynamic annealing during implantation of AlN results in a relatively low defect fraction (Chap. 2), simulations of the angular scan using the Monte Carlo code FLUX [21] showed that implanted REs do not occupy an ideal S_{Al} site, as was expected theoretically [14]. Rather, a vibration amplitude (which mimics a random static displacement) of the order of 0.20 Å has to be used to analyze the data. However, it should be noted that the mosaicity of the AlN samples makes the analysis difficult, in particular for channelling scans along off-normal axes. (See Sect. 3.6 of this chapter for a more detailed discussion on the role of mosaicity in the lattice site location of impurities).

Next, the implantation of Eu was studied in a set of ternary $Al_xGa_{1-x}N$ alloys, in the full compositional range [44]. No consistent trend in damage accumulation and near-substitutional fraction was observed with varying AlN content, due perhaps to the variable crystalline quality of the templates. However – and rather surprisingly – the largest perfectly substitutional fraction is obtained for pure GaN, despite the higher damage level.

Implantation of Er in ternary alloys of GaN with InN was investigated by Alves et al. [45]. However, since $In_xGa_{1-x}N$ is much more susceptible to defects than $Al_xGa_{1-x}N$, it was impossible to determine the lattice site for relatively high fluences, i.e. large enough to obtain a sufficiently strong Er signal in the RBS spectra.

3.4.2 Lattice Location of Low-Fluence GaN:RE by EC

RBS/C studies reveal a tendency for the RE implant to occupy a (displaced) substitutional group-III lattice site. However, the sensitivity and accuracy of the technique are limited by, principally, the large defect concentration induced by the implantation. Emission channelling offers an alternative approach, based on the same channelling principle – but one which enables the measurement of very low fluences with a sensitivity that is several orders of magnitude better.

The first EC experiments on RE-implanted nitrides were performed by Dalmer et al. [46], using ^{167}Tm (decaying to ^{167m}Er) and ^{169}Yb (decaying to ^{169*}Tm) to a fluence of 2×10^{13} at./cm^2. The channelling behaviour, measured by recording the emitted electron intensity as a function of tilt angle, along 3 non-coplanar directions, using a Si surface barrier detector, implied a substitutional lattice site. In order to obtain quantitative information, calculated emission yields (using the Many-Beam formalism [22]) were fitted to *one-dimensional cross sections* of the distributions measured along the [111] axis. A good fit was obtained with 90 ± 10% of the emitters assumed to occupy sites displaced from perfect substitutional sites in a Gaussian distribution having a mean deviation of 0.25 Å. From their analysis, no distinction could be made between the S_{Ga} and S_N sites. No increase of channelling was observed after annealing samples at temperatures up to 800 °C.

The first systematic EC study of the lattice site of implanted REs in GaN was done by Wahl et al. [47], who measured the channelling of electrons emitted by the ^{143}Pr ($t_{1/2}$ = 13.58 d) isotope along four crystallographic directions using a position sensitive detector. All experimental patterns were compared to 2D simulations for a variety of lattice sites [48]. Corrections due to backscattered electrons were included in the quantitative analysis, taking the geometrical features of the experimental set-up into account. Immediately after implantation, Pr is found in both substitutional Ga sites and random sites (data not shown). After annealing at 800 °C, S_{Ga} fractions of 78%, 79% 73% and 67% were derived from the emission pattern along the [0001, $\underline{1}$102, $\underline{1}$101] and [$\underline{2}$113] axes respectively, with an *rms* displacement from the ideal site of 0.18 Å, 0.14 Å, 0.10 Å and 0.14 Å respectively. The large *rms* displacements from the four directions and their variation suggest a Pr position somewhat displaced from the Ga site in a specific crystal direction. Allowing an additional fraction of Pr to occupy a second high-symmetry site (i.e. S_N, H_{Ga}, H_N, T, O…) did not significantly improve the fit. Annealing at temperatures up to 900 °C hardly modifies the lattice site compared to the situation after implantation: only a small increase of the substitutional

fraction upon annealing was observed, accompanied by a minor (0.02 Å) decrease of the *rms* displacement from all four axial directions.

A clear view on the specific strengths and possible limitations of lattice site determination by emission channelling is obtained by comparing the above results to EC experiments using a different Pr isotope. Therefore, ^{141}Ce ($t_{1/2}$ = 32.50 d), which finally decays to ^{141*}Pr, was introduced into GaN by implanting the short-lived isotope ^{141}Cs, which decays to ^{141}Ce via the decay chain ^{141}Cs (24.9 s) → ^{141}Ba (18.3 m) → ^{141}La (3.92 h) → ^{141}Ce (32.5 d). Following implantation, the sample was stored for 11 days before starting the experiment, so that 99.6% of the ^{141}La has transformed into ^{141}Ce. One has to bear in mind that during each decay step of this transmutation doping, the daughter nucleus receives a beta recoil energy. If this recoil energy is sufficient to displace an atom from its lattice site, then the daughter nucleus is effectively re-implanted. If not, the daughter's position is determined by (i.e. "inherited from") the mother nucleus. The threshold to displace a Ga atom in GaN is experimentally determined as 19 ± 0.2 eV [49]. Since the last step of the decay chain delivers a recoil energy lower than 20-30 eV, at least a fraction of the probe atoms inherit the lattice site of the implanted precursor. However, this is not a major problem since its impact can be investigated by following the lattice site as a function of annealing temperature: metastable configurations are likely to relax at high temperature.

The ^{141}Ce isotope subsequently decays to ^{141*}Pr by beta decay, and finally to stable ^{141}Pr by emitting a conversion electron (CE) – both steps again accompanied by a recoil energy to the daughter nucleus (Fig. 3.13). An interesting – and powerful – aspect of these experiments is that the combination of beta decay (^{141}Ce) and conversion electron decay (^{141*}Pr) enables us to simultaneously determine the lattice site of Ce and Pr in one single experiment, by separately measuring the beta and conversion electrons.

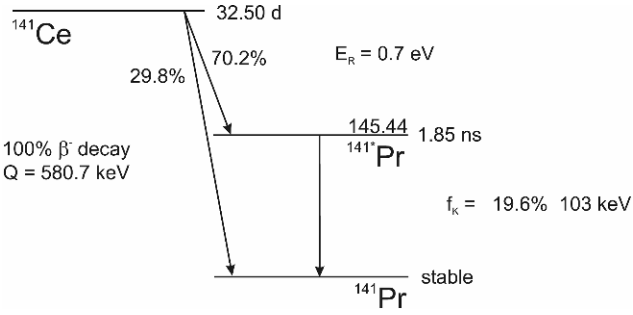

Fig. 3.13. Decay scheme of ^{141}Ce [12].

Fig. 3.14(a)-(d) show the experimental emission yields of the electrons with an energy higher than 108 keV (i.e. only including the ^{141}Ce β^- particles), emitted by ^{141}Ce after vacuum annealing at 900 °C. The resemblance to the ^{72}Ga patterns (Fig. 3.8), i.e. the pronounced axial and planar channelling effects, suggests

substitutionality of the Ce ions. Indeed, the best two-fraction fits [Fig. 3.14(e)-(h)] reveal substitutional fractions of 72%, 55%, 50% and 53% for Ce, with *rms* displacements perpendicular to the corresponding axis of 0.17 Å, 0.10 Å, 0.09 Å and 0.16 Å. The remaining ions occupy random sites, giving a nearly isotropic contribution to the emission yield.

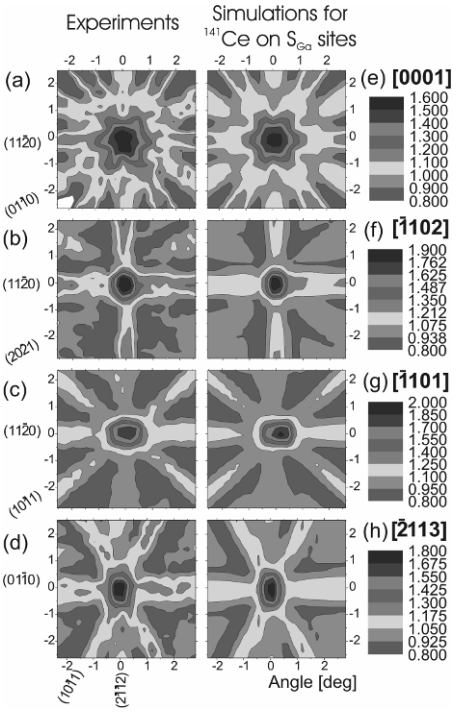

Fig. 3.14. (a-d) Angular dependent β^- emission yields from ^{141}Ce in GaN along 4 channelling directions, following 10 min. annealing at 900 °C. (e-h) Best two-fraction fits of theoretical patterns [12].

By integrating the narrow energy window around 103 keV, corresponding to the conversion electrons emitted by ^{141*}Pr, emission channelling patterns are obtained which provide information on the site of the latter ions. These CE patterns [Fig. 3.15(a)-(d)] are broad compared to the β^- patterns of ^{141}Ce and have a more diffraction-like character. This observation can be classically explained as a consequence of the lower energy of the CE, resulting in larger critical angles [24]. The best fits [Fig. 3.15(e)-(h)] show similar results as for ^{141}Ce with 57%, 64% 60% and 59% of Pr atoms on substitutional Ga sites with *rms* displacements u_1 of 0.16 Å, 0.16 Å, 0.12 Å and 0.20 Å, for the [0001, $\underline{1}$102, $\underline{1}$101] and [$\underline{2}$113] axes respectively. Possible reasons for the slightly lower S_{Ga} values compared to the abovementioned ^{143}Pr experiments will be discussed below.

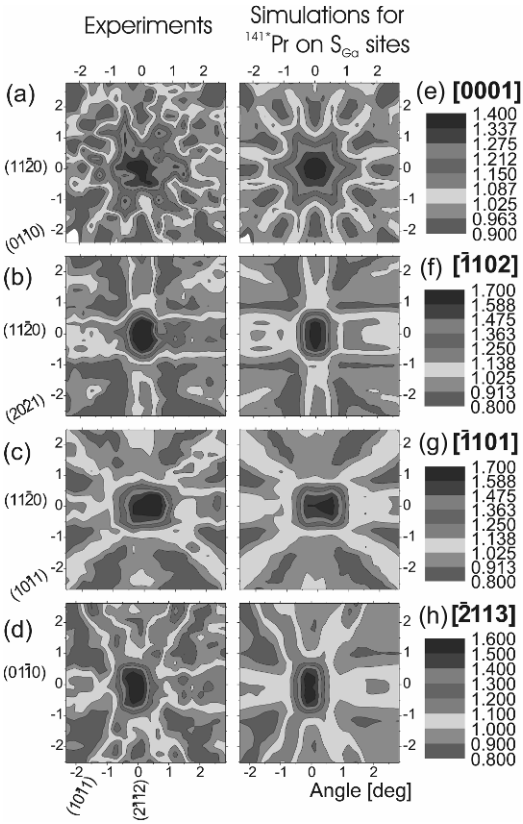

Fig. 3.15. (a-d) Angular dependent conversion electron emission yields from ^{141*}Pr in GaN along 4 channelling directions, following 10 min. annealing at 900 °C. (e-h) Best two-fraction fits of theoretical patterns [12].

This procedure was repeated for each set of channelling patterns measured after each annealing stage for a large number of investigated RE isotopes – resulting in several hundreds of measurements for analysis. Each experimental pattern was fitted to theoretical yields corresponding to the emitter located on various lattice sites and allowing various displacements from the ideal site. It is the combination of (i) the experimental analysis of the anisotropic emission in four directions, (ii) the detailed theoretical simulations of all patterns, and (iii) inclusion of corrections for backscattered electrons, which finally allows a quantitative determination of the lattice sites.

Fig. 3.16 summarizes the deduced substitutional fractions and *rms* displacements of all REs investigated, as a function of annealing temperature. In all cases, the majority of RE atoms (50-95%) are found on substitutional Ga sites, with the remainder located on random sites. These random fractions can be caused by (i) RE atoms occupying many different lattice sites of low symmetry, (ii) imperfections in the GaN crystal quality (either due to the implantation or due to an

imperfect growth), (iii) insufficiently accurate corrections for electrons backscattered from the sample and the chamber walls. The possibility of high-symmetry sites other than S_{Ga} (see Fig. 3.3) was investigated by introducing additional fractions into the fitting procedure. Although none of these additional sites significantly improved the fit quality, the possibility cannot be fully excluded that small fractions (< 5%) of RE atoms occupy S_N, HG or O sites.

Compared to the as-implanted state, the substitutional fractions hardly change after the vacuum annealing sequences up to 900 °C. Another observation is that the *rms* displacements from the perfect Ga site are larger than the thermal vibration amplitude of Ga in GaN, u_1(Ga)=0.057-0.084 Å. Compared to the as-implanted state, the *rms* displacements decrease slightly with increasing annealing temperature, indicating a better incorporation of the RE atoms into the substitutional Ga site. Further, for each experiment and isotope, different u_1 values are observed perpendicular to the four channelling directions, which may indicate that the different RE elements experience small static displacements along well-defined crystallographic directions. However, the differences are typically of the same order of magnitude as the estimated experimental uncertainty, which is around 0.02–0.03 Å.

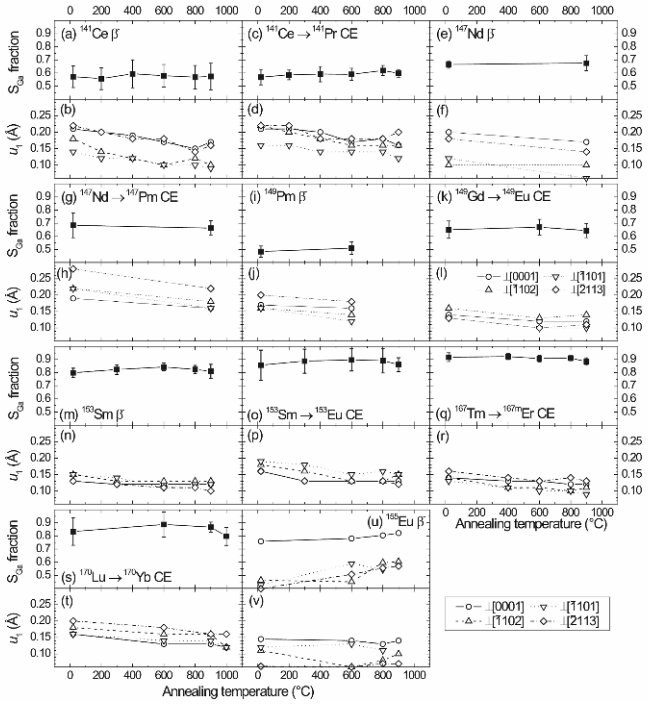

Fig. 3.16. Fraction of RE ions on substitutional Ga sites and their *rms* displacements u_1 perpendicular to the channelling directions, as a function of annealing temperature. The vertical scale offset of the *rms* displacements corresponds approximately to the Ga thermal vibration amplitude u_1(Ga) = 0.057-0.084 Å.

In order to clearly demonstrate the systematic trends in the experimental data, Fig. 3.17(a) summarizes the extracted substitutional fractions in one graph, while Fig. 3.17(b) shows the *rms* displacements (data compiled from [24, 47, 50, 51, 52]). The data points in these graphs represent the averages of the S_{Ga} fractions and displacements obtained for the four different channelling directions, except for ^{155}Eu for which only the *c*-axis results are plotted (see below).

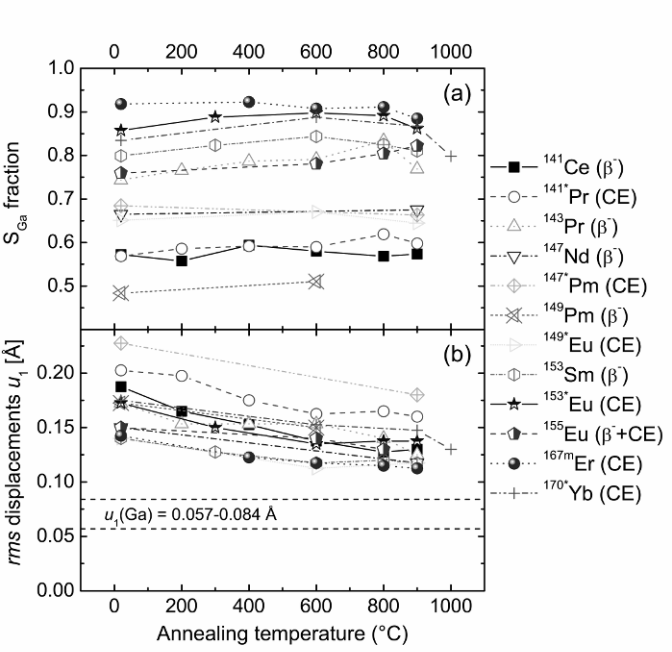

Fig. 3.17. Comparison of the emission channelling experiments using RE probe atoms: (a) fraction of RE atoms on substitutional Ga lattice sites as a function of temperature (b) *rms* displacements from the perfect Ga site as a function of annealing temperature. The region between the dotted lines indicates the thermal vibration amplitude of Ga in GaN.

First, we would like to address the differences in substitutional fractions observed for the various RE elements, as shown in Fig. 3.17(a). In particular, the fact that different isotopes of the same element (e.g. ^{147*}Pm and ^{149}Pm, or ^{149*}Eu, ^{153*}Eu and ^{155}Eu) produce different results, seems puzzling at first sight. The explanation for this lies probably in the fact that, in fitting any emission channelling pattern, an isotropic component always has to be included, which is given by one minus the sum of all other fitted fractions (here: only the RE_{Ga} fraction) [23]. This isotropic contribution will correspond to the fraction of emitter atoms on random sites only if the scattering background and the emitter depth profile are known exactly and only if there is no increased dechannelling due to defects in the crystal. As a

result, the presence of defects or uncertainties in the scattering background or depth profile will invariably lead to errors in the fitted fractions.

For the CE experiments with $^{167}Tm \rightarrow {}^{167m}Er$ and $^{170}Lu \rightarrow {}^{170*}Yb$, the scattering background was extracted from the experimental energy spectra, which is a procedure that should give quite accurate results. As is shown in Fig. 3.17(a), both isotopes display substitutional fractions of 85–95%. On the other hand, the background correction factors for the other experiments (β emitter) were calculated by the Monte-Carlo simulations described in the experimental section. These simulations often underestimate the scattering [24], leading to an underestimation of the substitutional fraction. This implies that the data points shown in Fig. 3.17(a) can be interpreted as lower limits to the actual substitutional fractions.

A second cause of an underestimation of the actual substitutional fraction is the presence of mosaicity in GaN layers, which will be discussed in detail at the end of this chapter. However, as opposed to AlN, the impact of mosaicity on the determination of the lattice site of impurities in GaN is rather small [24]. Since the two properly corrected experiments with $^{167}Tm \rightarrow {}^{167m}Er$ and $^{170}Lu \rightarrow {}^{170*}Yb$ were performed on good quality samples (with reduced mosaicity) and show RE_{Ga} fractions of 80–95%, we believe that in similar experiments comparable fractions of RE atoms are actually located on Ga sites, despite the lower RE_{Ga} fractions obtained from the fitting. Finally, the presence of point defects in the material can lead to an additional underestimation of the fraction. Due to the very efficient dynamic annealing of GaN, it is of minor importance for the fluence range around 10^{13} at./cm^2. However, it is the most likely reason why the off-normal directions yield a much lower S_{Ga} fraction compared to the *c*-axis measurement of the ^{155}Eu sample, which was implanted to a ten times larger fluence, i.e. 1.6×10^{14} at./cm^2 [see Fig. 3.16(u)].

Since the (unknown) electron scattering contribution and the mosaic spread depend only on the characteristics of the probe isotope and the sample quality, it is still possible to extract information on the annealing behavior from the *relative* differences between the RE_{Ga} fractions at different annealing temperatures. This shows that, irrespective of the chosen RE isotope, the RE_{Ga} fraction is hardly influenced by annealing at temperatures up to 900 °C, which indicates that the implanted RE atoms are stable on substitutional Ga sites up to at least that temperature. On the other hand, the higher annealing temperatures (1000 and 1100 °C) used in the $^{170}Lu \rightarrow {}^{170*}Yb$ experiment [data not shown in Fig. 3.16(s)-(t)] seem to have a detrimental effect on the substitutional fraction. It is well known that epitaxial GaN starts decomposing from about 1000 °C onwards in atmospheric pressure, leading to a loss of nitrogen in the surface layer (cf. Chap. 2). The decrease in S_{Ga} fraction can be explained by a combination of enhanced dechannelling of electrons in a thin damaged surface layer, and migration/precipitation of the probe atoms.

In contrast to the substitutional fractions, the deduced *rms* displacements are not affected by the scattering background. The values shown in Fig. 3.17(b) can therefore be interpreted as quantitative information on the mean spread of the RE atoms around the perfect Ga site. A first observation is that all *rms* displacements are

larger than that expected to arise from thermal vibration. The extra displacement is most likely caused by the presence of point defects in the vicinity of the RE atoms. This is not unexpected, since many vacancies and interstitials are produced during implantation of heavy RE ions. Further support for this assumption comes from theoretical calculations [13] that have shown that substitutional RE atoms tend to bind to vacancies, interstitials and oxygen impurities in GaN. Ga and N vacancies both pull the RE atoms from the substitutional lattice site by about 0.2 Å, which corresponds to the *rms* displacements observed in the measurements. Of all the investigated defects, the RE-nitrogen vacancy (V_N) complex has the largest binding energy: RE_{Ga}–V_N pairs are stable to around 1000 °C, with the other defect complexes starting to dissociate already at lower temperatures (these findings have been further supported by DLTS measurements of Eu-implanted GaN [53]). In line with these calculations, we observe that the displacements do not decrease to the level of the vibration amplitude even after 1000 °C annealing, which suggests an incomplete annealing of the surrounding lattice damage. However, the *rms* displacements do decrease slightly, which indicates at least a partial break-up of RE-defect complexes, resulting in a better incorporation into the Ga sites. Ronning et al. further underline the fact that point defects remain present, even after high-temperature annealing at 800-1000 °C [42]. An even higher annealing temperature than 1000 ºC is indispensable to remove all remaining defects. Indeed, De Vries et al. [54] showed that Ca, an electrical dopant in GaN, is better incorporated after high pressure/high temperature annealing – up to 1.0 GPa N_2 pressure and 1200 °C. Preliminary RBS/C results on Eu-implanted GaN further confirm that high pressure/high temperature annealing, preferably in combination with a channelling implantation geometry to further reduce defect production (see below), is required to fully incorporate the dopant in an S_{Ga} site [38].

The presence of RE-defect complexes can also explain the multitude of optical centers that have been observed by photoluminescence excitation experiments (see [36] and references therein and Chaps 7 and 8). Since lattice location experiments reveal that the majority of RE ions are located on, or near, S_{Ga} sites, it seems likely that the observed multiple luminescence spectra are due to centers where the RE atoms occupy the Ga site but are surrounded by different atomic configurations caused by nearby defects. This hypothesis has already been put forward by several authors [4, 5, 36].

For the specific case of Eu doping, RBS/C [35, 55] measurements have indicated that the Eu atoms are displaced from the S_{Ga} site along the *c*-axis by 0.2 Å. While the size of the displacement is in accordance with the EC observations of three different Eu isotopes, the preferred displacement direction is not (see Fig. 3.16(v)). Introducing static displacements (either along or perpendicular to the *c*-axis) or larger *rms* displacements, consistently resulted in a worse fit to the data. Allowing a second site suggested that approximately 1/3 of the ^{155}Eu ions on high-symmetry sites occupy a position shifted along the *c*-axis, away from S_{Ga}, towards the antibonding site AG-c. The magnitude of the displacement is about 50-100% of the S_{Ga} – AG-c distance, i.e. 0.5-1.0 Å, although an unambiguous proof from the current experimental data remained impossible.

Bang et al. [56] have reported a similar displacement in Eu-doped MBE-grown layers measured by XAFS, while Katchkanov et al. [57] found Eu only on regular Ga sites. It should be pointed out that XAFS, in contrast to EC, is not particularly sensitive to random displacements. On the contrary, when doping GaN with 2% Tb, XAFS indicated the incorporation onto ideal Ga sites [56]. Similarly, an RBS/C study along the [0001] axis of the lattice site of a low concentration (0.15%) of Er in MBE-grown GaN reported a majority of the REs (84%) on S_{Ga} sites, in agreement with Er-implanted GaN. However, a substitutional fraction of merely 30% was derived from the [10$\underline{1}$1] axial scan. This discrepancy was assigned to the poor surface condition and columnar structure of the sample [58].

3.5 RE Lattice Site Dependence on Experimental Parameters

3.5.1 Dependence on the Fluence

As illustrated in the previous section, typical implanted fluences necessary for RBS/channelling studies are often orders of magnitude larger than emission channelling requires. In order to compare the results obtained by both approaches, and to further elucidate the dependence of the lattice site on the total implanted fluence, several groups have focused on this topic.

For all fluences studied, only one high-symmetry site is detected for RE ions in the GaN lattice, viz. the (near-)substitutional Ga site S_{Ga}. The remaining ions reside on so-called random sites (see above). Using fluences from 1×10^{14} to 8×10^{15} at./cm^2, Lorenz et al. investigated the dependence of the substitutional fraction for 150 keV Tm ions [59]. At low fluences, a substitutional fraction of typically 80% or larger is obtained. However, as the fluence increases, the angular scans become significantly narrower due to the interactions with defects. From the analysis with the Monte Carlo ion beam simulation code FLUX [21], it is deduced that the fraction of Tm ions incorporated in Ga sites rapidly decreases, to finally vanish around 2×10^{15} cm^{-2} (Fig. 3.18).

Pipeleers et al. systematically determined the substitutional fraction of Er in GaN (using implantation energies of 80 and 170 keV) from measurements along the [0001] axis, i.e. without performing full triangulation [60]. In order to compare the results obtained with both energies, the fluence was normalized in units of *dpa* (displacements per atom). They found that the overall trend does not depend on the energy (Fig. 3.19): at a fluence below 1.5 *dpa* (corresponding to approximately 1×10^{14} Er/cm^2 for 80 keV), nearly all Er ions occupy a substitutional site. At higher fluences, the substitutional fraction rapidly decreases. When interpreting the fluence dependence of these two studies, it should be kept in mind that in an RBS/channelling experiment, the substitutional fraction is determined from a comparison of the minimum yield (i.e. channelling behaviour) in the RE signal

and the Ga signal respectively. Hence, the substitutional fraction f_s reflects the fraction of ions that reside in an environment comparable to that of the Ga atoms. Since the defect fraction in the GaN lattice increases with increasing implantation fluence, the channelling behaviour in the nitride (i.e. the reference signal) rapidly deteriorates. From a comparison of the above results with the defect accumulation upon implantation (Chap. 2), it is clear that the substitutional fraction is closely linked to the defect concentration.

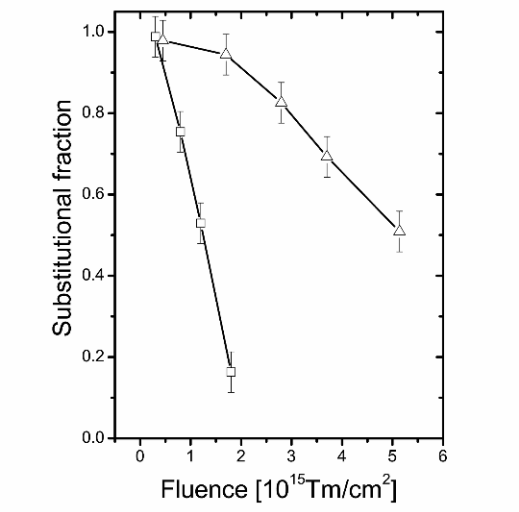

Fig. 3.18. Fraction of Tm incorporated in Ga sites as a function of Tm fluence after implantation at RT (□) and 500 °C (Δ). The results after high-temperature implantation will be discussed further in the text [59].

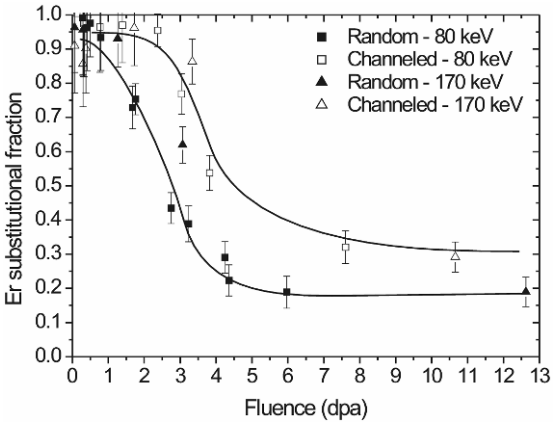

Fig. 3.19. Fraction of Er ions occupying a substitutional Ga position in the GaN crystal as a function of fluence, after implantation at 80 keV and 170 keV. The solid lines are a guide to the eye [60].

Benefiting from the superior sensitivity of EC is not straightforward in the case of high-fluence implantations. On the one hand, the low radioactive beam currents available would result in an unrealistically long implantation time, and on the other hand, the radiation level of the samples would then be unacceptably high. However, pre-implanting the sample with a fluence of 5×10^{14} at./cm^2 stable ^{166}Er ions allows to subsequently perform an emission channelling experiment under standard conditions, i.e. implanting with 2×10^{13} ^{167}Tm/cm^2 [61]. The ^{167}Tm decays to the ^{167m}Er isotope, which finally decays to the ^{167}Er ground state. The CE emitted during the latter transition are used to determine the Er lattice site. As can be seen from Fig. 3.20, the clear axial and planar channelling effects reveal that - despite the large fluence - a considerable fraction of ^{167m}Er atoms occupies substitutional sites. The theoretical fits to the data suggest that although 52% of the Er is aligned with the *c*-axis, only 35%, 31% and 32% occupy a substitutional site – as derived from the measurements in the other 3 directions. Fig. 3.20 shows further that the experimental patterns for the 3 non-normal directions are systematically broadened compared to the theoretical simulations. This broadening is most pronounced in the direction along which the GaN has been rotated to reach the off-normal channelling directions.

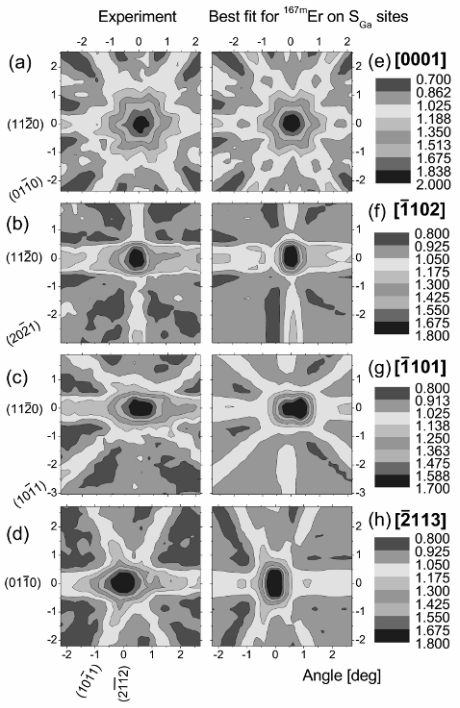

Fig. 3.20. (a-d) Experimental and (e-h) theoretical emission channelling patterns from ^{167m}Er in GaN that was pre-implanted with 5×10^{14} ^{166}Er/cm^2. The sample was annealed at 900 °C prior to the emission channelling experiment [61].

The poor quality of the fit causes the Er_{Ga} fractions estimated from these directions to be much lower than the one derived from the [0001] direction. Allowing a fraction of Er on another high-symmetry site does not significantly improve the fits. On the other hand, the origin of this broadening, which is not present in the case of low implantation fluences, can be found in the elastic strain which is induced during high-fluence implantations. From strain analysis of the sample, an "uncertainty" (i.e. variation) in the inclination angle for the off-normal axes of approximately 0.14° to 0.32° was obtained – of comparable magnitude to the broadening of the emission patterns [61].

Taking the [0001] aligned fraction as the substitutional Er_{Ga} fraction, the results suggest that already after implantation about 40% of the Er atoms are located on substitutional sites (Fig. 3.21), fewer than for low fluence implantations (2×10^{13} at./cm^2), but comparable to the fractions derived from RBS/C measurements. With increasing annealing temperature, the disorder gradually reduces, resulting in an improved channelling effect, hence a larger substitutional fraction. It should be noted that, due to the poor agreement of measurements and simulations, an accurate determination of the *rms* displacements proves impossible in this case.

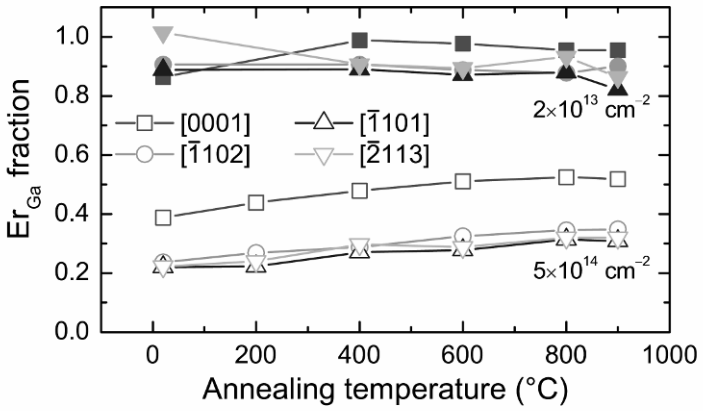

Fig. 3.21. Substitutional fraction of ^{167m}Er deduced from 4 channelling directions. The fractions are shown as a function of annealing temperature for a GaN sample that was pre-implanted with 5×10^{14} ^{166}Er/cm^2 (open symbols) and for a sample implanted with 2×10^{13} ^{167m}Er/cm^2 only (filled symbols) [61].

As mentioned above, implanting at high fluences results in heavily damaged or even amorphous GaN, making lattice location studies virtually impossible. However, RE concentrations up to several atomic percent can be achieved – without drastically affecting the crystalline quality – by doping the nitride *in situ*, i.e. during MBE growth. Similar to the case of implanted REs, the only high-symmetry site that could be revealed by MC simulation of the [0001] and [10$\underline{1}$1]

angular scans was the substitutional Ga site [58]. Besides RBS/C studies, a number of XAFS investigations of MBE-doped GaN have been reported. Katchkanov et al. studied the local surroundings and coordination number of Er [57], Eu [57] and Tm [62] in MBE-doped GaN. For the lowest concentrations (≤ 0.5 at.%), Tm is found only on substitutional Ga sites. At an intermediate concentration (1-2 at.%), a substantial fraction of the Tm ions resides in TmGaN clusters. Finally, the formation of pure TmN is observed for a dopant concentration of approximately 3.4 at.%. A comparable intermediate and high concentration regime is found for Er doping, further underlining the strong tendency of REs in GaN to agglomerate, initially in REGaN clusters with a locally high RE concentration, and in pure RE nitrides at still higher doping level. On the other hand, based on a combined RBS/C and XAFS investigation, Bang et al. report mostly substitutional sites for 2 at.% Tb and Eu doped GaN [63]. The origin of the discrepancy with the above-mentioned results is most likely related to the different growth conditions of the GaN layers.

Finally, one has to bear in mind that any direct (qualitative and quantitative) comparison between XAFS and RBS/C or EC is only possible after disentangling dynamic thermal contributions, from those due to static atomic displacements [4].

3.5.2 Dependence on the Implantation Geometry

Since nuclear collisions are the cause of lattice defect production during ion implantation, the channelling of REs is expected to decrease the defect fraction. Indeed, as illustrated in Chap. 2, applying a channelling implantation geometry can drastically reduce the retained defect fraction [33]. Given the intimate relation between disorder and substitutional fraction, an effect on the latter property is expected as well. Pipeleers et al. [60, 64] carried out a systematic study of the implantation of Er into GaN, as a function of both fluence and the angle between the ion beam and the sample *c*-axis. As evidenced in Fig. 3.19, the substitutional fraction remains at a level above ~ 90% for a fluence up to 3 *dpa*, i.e. double that due to implantation at random incidence. In particular f_s remains significantly larger for channelled implantation [60] for fluences between 2.5 and 5 *dpa* (of the order of several times 10^{14} at./cm^2, a very relevant dopant concentration from the luminescence point of view). These authors further showed that, due to the relatively low implantation energies and the large mass of RE ions, the critical angle for channelling is of the order of several degrees (e.g. 7.5° for 80 keV Er atoms). Consequently, the sample alignment is not extremely critical. Indeed, as shown in Fig. 3.22, the substitutional fraction remains nearly unaffected for misalignments of the ion beam up to 6° and 2.5° for 80 keV and 160 keV beams, respectively. On the other hand, incorporating an offset of 7 to 10°, commonly used to “minimize” channelling effects, results in a considerably lower substitutional fraction [64].

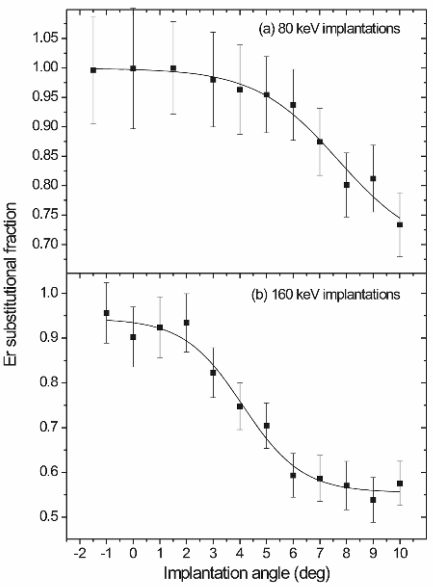

Fig. 3.22. Fraction of Er ions occupying a substitutional Ga position in the GaN crystal as a function of incident angle, after implantation at (a) 80 keV (2.5×10^{14} Er/cm^2) and (b) 160 keV (5.0×10^{14} Er/cm^2) [64].

Finally, the dependence of lattice site occupation on the implantation geometry was explored by performing 60 keV ^{167}Tm implantations, using emission channelling from the ^{167m}Er daughter nuclei to investigate the RE location. To enhance the accuracy of the analysis, a total of nine independent channelling directions was used and compared to implantations using random beam incidence on an identical sample in an identical experimental set-up. After room temperature implantation, both samples show comparable amounts (~ 90%) of ^{167m}Er substitutional on Ga sites (Fig. 3.23).

While the difference in substitutional fraction between the two implantation geometries is still within the experimental error for annealing at 400 °C, the advantage of channelling increases noticeably above that temperature. Moreover, whereas the randomly implanted sample shows a nearly constant substitutional fraction or even a minor decrease as a function of annealing temperature, the channelled-implanted S_{Ga} fraction increases monotonically up to 100%. One explanation is that this behavior relates to the different damage creation processes for the two geometries. Random implantation at low fluences is known to introduce damage mainly very close to the surface, while during channelled implantation, a larger penetration depth results in a lower 'more spread-out' defect concentration (Chap. 2 and [60]). This permits properly annealing out the lattice damage in the channel-implanted sample. The random-implanted sample has denser surface damage, which can even cause further degradation during

high temperature annealing. A damaged surface layer will cause an apparent decrease in the substitutional fractions as a result of the enhanced dechannelling of electrons.

Despite the enhanced substitutional fraction after channelled implantation, the *rms* displacements behave exactly the same upon annealing as for random implantation, i.e. they decrease as a function of annealing temperature, but not quite to the level of the thermal vibration amplitude (Fig. 3.23). However, the *rms* displacements after channelled implantation seem to be consistently higher than in the randomly implanted sample. Most likely, this deviation is – at least partially – correlated (i) to the deeper profile (causing more dechannelling) and (ii) to errors in the depth profile of the channel-implanted Er probes used in the EC simulations. Nevertheless, the increase of the S_{Ga} fraction in case of channelled implantation is due to a reduction in damage production.

The fact that the local structure surrounding the RE depends on the implantation geometry is further highlighted by the fact that certain specific defect levels in the GaN band gap exclusively appear in either random or channelled implanted samples [53] and that both geometries result in different luminescent centers [7].

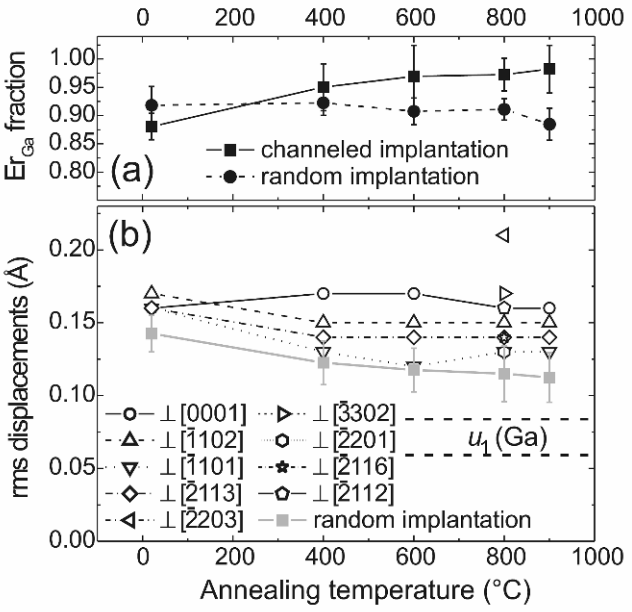

Fig. 3.23. (a) Fraction of ^{167m}Er ions occupying a substitutional Ga position in the GaN crystal as a function of annealing temperature. (b) Root-mean-square displacements perpendicular to the channelling axes as a function of annealing temperature. The data points represent an average of the S_{Ga} fractions derived from emission channelling measurements along nine independent directions. The region between the dotted lines (0.057-0.084 Å) indicates the thermal vibration amplitude of Ga in GaN [12].

3.5.3 Dependence on the Implantation Temperature

Raising the sample temperature during implantation promotes dynamic annealing, which is the *in situ* recovery of induced damage (Chap. 2). Consequently, a drastically lower defect fraction may be obtained after implantation, as illustrated by comparing RT and 450 °C Er implantation [33] and RT and 500 °C Tm implantation [59]. The reduced defect fraction is expected to manifest in an enhanced substitutional fraction. Indeed, as shown in Fig. 3.18, the decrease in f_s with increasing fluence is averted when implanting Tm at 500 °C [59]. In particular, at fluences where no more substitutional Tm is observed after random implantation (above ~ 2.5×10^{15} at./cm^2), the majority of the implanted ions is still located on a S_{Ga} site after high-temperature implantation.

Although the substitutional fraction eventually decreases in case of high-temperature implantation as well, the *absolute* number of substitutional REs in the nitride is increasing, as shown for Eu [65] and Er [64] implantation. A direct correlation between the density of substitutional ions and the luminescence intensity has been suggested by these studies: both quantities increase in a similar way with increasing fluence. At higher fluence, the number of substitutional RE atoms finally saturates, at a local concentration below 1 at.%, i.e. unexpectedly low compared to MBE-doped samples [65].

Combining high implantation temperature with a channeled ion beam geometry results in a further reduction of the damage [33, 59], and consequently in a larger substitutional fraction.

3.5.4 Co-Implantation of RE and O or Other Impurity

Perturbations in the crystal field, either due to interaction with defects (as described above) or impurities, can enhance site-selective spectral redistributions of the RE radiative transitions. In tetrahedral or hexagonal symmetry, not all RE dipole transitions are forbidden. The different local crystalline environment results in different optical activation. In the case of Er-doped Si and AlGaAs, the symmetry and co-ordination of the emitting site can change after co-doping the substrate with light impurities, such as carbon, nitrogen, oxygen, fluorine or sulphur. Typical co-dopant concentrations exceed that of the RE by up to one order of magnitude, and implantation energies are adapted to best overlap the depth profiles of the dopants.

With respect to the effect of O on Er luminescence in GaN, contrary results are found in the literature [36]. Some papers state a beneficial influence of oxygen or even a requirement to obtain luminescence [66, 67, 68, 69]. Focusing on the IR emission spectrum of GaN:Er, several groups have reported *"little or no 1.54 μm luminescence without O co-doping"* [66] or *"oxygen appears to be necessary for the luminescence of Er in GaN"* [67], whereas Alves et al. reported a doubling of

PL intensity for a sample containing oxygen [68]. On the other hand, Citrin et al. report no effect of co-doping on the Er-related luminescence [70], while a number of groups even reported a negative impact [35, 55, 71, 72]. The authors link the lower luminescence yield to the higher degree of disorder in case of oxygen co-implanted nitrides, possibly related to the high annealing temperature (1200 °C) used in their study [35]. Co-doping with C [73] or F [69] has also been reported to increase the luminescence yield.

However, in none of the reported papers could the specific role of the impurity be elucidated. Earlier work on the influence of oxygen co-doping on the incorporation of Er in Si revealed that the RE lattice site depends on the oxygen concentration [16]. Whereas a majority of Er occupies a near-tetrahedral position after annealing up to 600 °C, above 800 °C this lattice site remains stable in oxygen-lean float zone Si, but changes to low-symmetry sites in oxygen-rich CZ-Si, indicating a strong RE-O interaction.

In order to ascertain whether oxygen also modifies the lattice site of Er in GaN, lattice location studies have been performed with RBS/C and emission channelling. Using RBS/C in combination with Monte Carlo simulations, Alves et al. concluded that the presence of oxygen may stabilize the Er in the Ga sites (at least up to a temperature of 900 °C), probably through the formation of Er-O complexes [68]. However, the effect seemed to be of minor importance.

In their early emission channelling work, Dalmer et al. studied the impact of oxygen co-doping on the lattice site of ^{167}Er and ^{169}Tm ions by measuring the [0001] emission yield [46]. According to the one-dimensional fits of the spectra, approximately 90% of the emitters are located along the [0001] directions with a root-mean-square displacement of 0.25 Å, whether using a virgin sample or a previously oxygen co-implanted sample – within the experimental accuracy, the channelling effects are comparable in both cases. However, since no other crystallographic directions were measured, a complete determination of the lattice site could not be made. Nevertheless, these authors observed different lines and drastically different line intensities in the luminescence spectra if oxygen is present [46]. Hence, they concluded that the differences in the PL spectra are due to oxygen present in the immediate neighbourhood of the RE atoms without affecting their lattice sites.

In order to explore the effect of co-doping on the RE lattice site, a systematic EC investigation was performed by De Vries et al. [52]. Three *identical* MOCVD-grown samples were doped with ^{167m}Er (by means of ^{167}Tm implantation) to a fluence of 2.0×10^{13} at./cm^2 : one virgin layer and two that were pre-implanted with 11 keV ^{16}O or 8 keV ^{12}C respectively, both to a fluence of 5.0×10^{14} at./cm^2. The O and C implantation energies were chosen such that their peak concentrations overlap with the one of ^{167m}Er, resulting in Er:O and Er:C concentrations of ~ 1:14. Subsequently, the angular electron emission patterns were measured at room temperature along the [0001, $\underline{1}$102, $\underline{1}$101] and [$\underline{2}$113] axes for the as-implanted state as well as after isochronal (10 min) vacuum annealing steps up to 900 °C. Note that the authors started with three identical samples that were measured using the same experimental setup under the same conditions. Consequently, any

systematic errors (e.g. the electron scattering background or the sample quality mentioned above), should be equal for these three measurements. Additionally, because only low fluences of ^{167}Tm are implanted, clustering of probe atoms is avoided. Any difference in the results between the samples should therefore depend only on the influence of oxygen or carbon on isolated Er/Tm atoms in the GaN crystal.

Fig. 3.24(a)-(d) show the normalized angular emission yields of conversion electrons along the [0001, $\underline{1}$102, $\underline{1}$101] and [$\underline{2}$113] axes of the GaN sample co-implanted with oxygen after 900 °C annealing. The central axial channelling peaks and the intersecting planar channelling effects are direct evidence that a substantial fraction of the emitter atoms are situated on substitutional sites. The best fits [Fig. 3.24(e)-(h)] of theoretical patterns to the experimental ones result in an average of 89(3)% ^{167m}Er atoms on Ga sites, with an average *rms* displacement of 0.19 Å, the remainder being located on random sites or low symmetry sites, which shows that no fundamentally different lattice site is occupied by Er in the presence of oxygen.

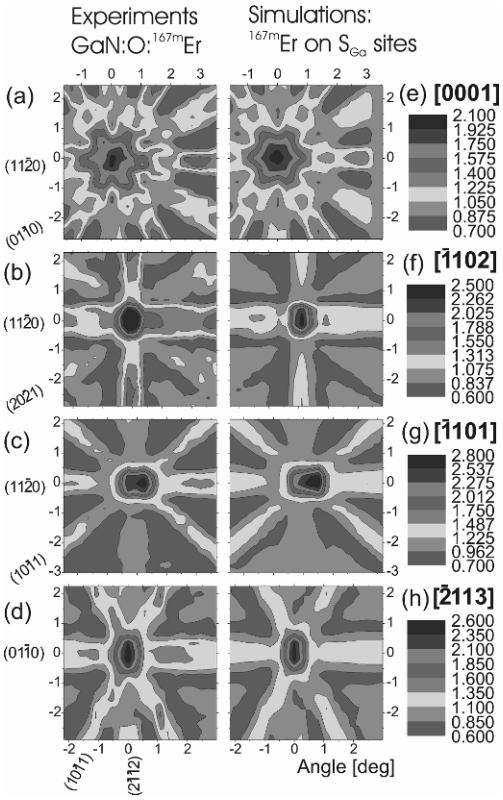

Fig. 3.24. Electron emission channelling patterns of ^{167m}Er in GaN:O following 900 °C vacuum annealing. (a-d) Experimental spectra; (e-h) best fits of theoretical spectra [12].

An overview of the substitutional fractions for all three samples as a function of annealing temperature is given in Fig. 3.25(a). It is observed that large fractions (~ 90%) of ^{167m}Er are located on S_{Ga} sites already after room-temperature implantation for all three samples. The remainder of the Er atoms is located on random or low-symmetry sites, although the presence of small fractions (< 5%) of Er on other high symmetry sites would also be in agreement with the analysis. Annealing at up to 900 °C influences the substitutional fractions only slightly, with intermediate temperatures giving the highest yields. From these results it is obvious that the presence of O or C does not noticeably influence the lattice site occupied by Er in GaN, at least not for low fluences of 2.0×10^{13} cm^{-2}, in striking contrast to the case of O in Si [16]. This result agrees with theoretical calculations [13] that have shown that the Er-O binding energy is relatively weak (390 meV) in GaN, compared to the strong Er-N bonds.

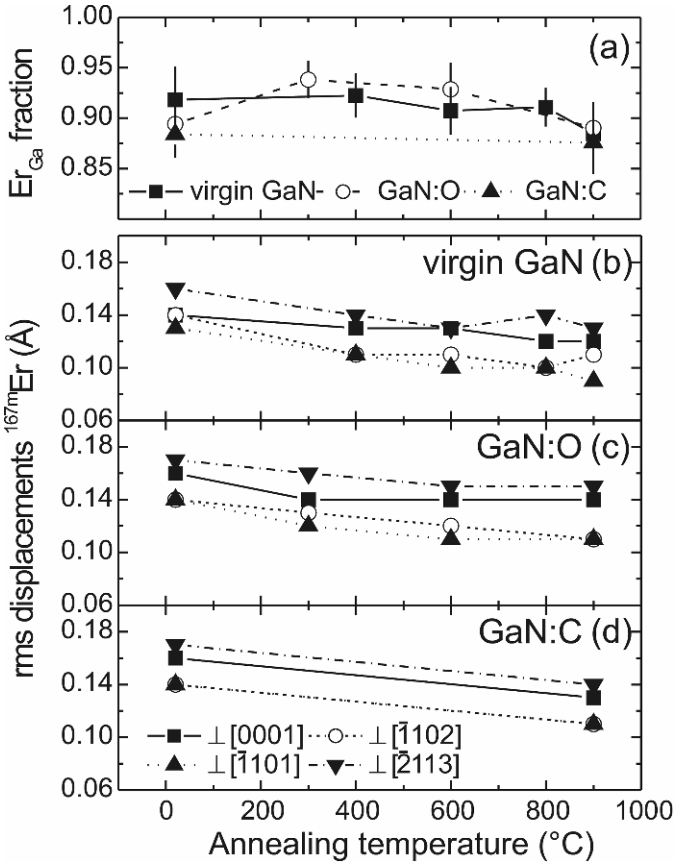

Fig. 3.25. (a) S_{Ga} fraction for ^{167m}Er in virgin GaN, GaN:O and GaN:C, as a function of annealing temperature (averaged values over the four channelling axes). (b-d) *rms* displacements from the perfect S_{Ga} in a direction perpendicular to the channelling axes [52].

The *rms* displacements $u_1(^{167m}\mathrm{Er})$ from the ideal S_{Ga} sites were also deduced [Fig. 3.25(b)-(d)]. A first observation is that the annealing behavior of all three samples shows the same general trends that were discussed in the previous section: the displacements are larger than the thermal vibration amplitude $u_1(\mathrm{Ga})$ = 0.057-0.084 Å, and decrease as the annealing temperature increases.

The fact that the same behavior is observed, regardless of co-implantation, agrees with the theoretical prediction of a weak Er-O binding energy in GaN. Most likely this decreasing trend can be attributed to the gradual removal of crystal defects (e.g. Ga or N vacancies) in the vicinity of the Er atoms. This assumption is supported by the observation that for all measurement axes the *rms* displacements in the co-implanted samples are slightly larger than those in the virgin sample. One expects that the additional implantation of O or C increases the number of crystal defects, hence also the probability that an Er atom ends up in a disordered environment (cf. Sect. 3.5.1 on fluence dependence). The differences are, however, of the same order of magnitude as the experimental sensitivity. Even after 900 °C annealing, a small difference remains between the co-implanted and virgin samples, again suggesting that these annealing conditions are not sufficient to remove all implantation damage.

As a final note, it should be pointed out that for all three samples, slightly different u_1 values are observed along the four axes, with: $u_{\perp [2\bar{1}\bar{1}3]} > u_{\perp [0001]} > u_{\perp [1\bar{1}02]} = u_{\perp [1\bar{1}01]}$. This could suggest that a preferential crystal axis for displacement of Er atoms might exist. However, the differences do not exceed the experimental uncertainty. Since a similar displacement behavior is found in all samples, the influence of oxygen and carbon on Er in GaN must be small.

3.6 The Effect of Sample Mosaicity on Determining the Lattice Sites: AlN vs. GaN

As mentioned previously, the lattice site occupancies S_{III} of implanted RE ions in AlN and $Al_xGa_{1-x}N$ alloys does not reach values comparable to those obtained for GaN (cf. RBS/C studies by K. Lorenz et al. [43, 44]). The specific problems with respect to AlN alloys are illustrated in more detail by the emission channelling investigations of Vetter et al. [74] and De Vries et al. [75].

Vetter et al. measured two-dimensional emission patterns of ^{169}Tm (the decay product of implanted ^{169}Yb), along the [0001] and [$\bar{2}$113] axes in AlN. The simulations revealed about 69% of the emitters on an S_{Al} site with a mean static displacement of 0.24 Å [74], i.e. significantly less substitutionality compared to typical cases of GaN. Moreover, the agreement between the experimental and simulated patterns was inferior to that found for RE-doped GaN.

Using the ^{167m}Er emission probe, De Vries et al. [75] investigated the lattice location of Er in AlN in detail. They measured the emission pattern along 4 crystallographic axes, immediately after implantation as well as after isochronal

annealing for 10 min. in vacuum at 600 and 900 °C and after tube furnace annealing for 10 min. at 1050 °C in a N_2 atmosphere.

Fig. 3.26(a)-(d) show the experimental emission yields of CE around the [0001, $\underline{1}$102, $\underline{2}$113] and [$\underline{1}$101] axes after annealing at 900 °C. Note that the channelling effects have been ordered by the increasing inclination angle with respect to the surface normal, $\theta = 0°$, 28.0°, 31.6° and 46.8°, respectively. Similar to the experiments of Vetter et al., the patterns are significantly broadened, masking the fine structure of the channelling behaviour. When fitting the experimental patterns to 2D theoretical emission yields calculated assuming a perfect crystal lattice, the best results are obtained for Er on Al sites [Fig. 3.26(e)-(h)] with the remaining Er atoms occupying random sites. A first visual inspection of the patterns already shows that the experimental channelling effects are broader than the theoretical effects, and that the overall agreement becomes increasingly worse for larger inclination angles.

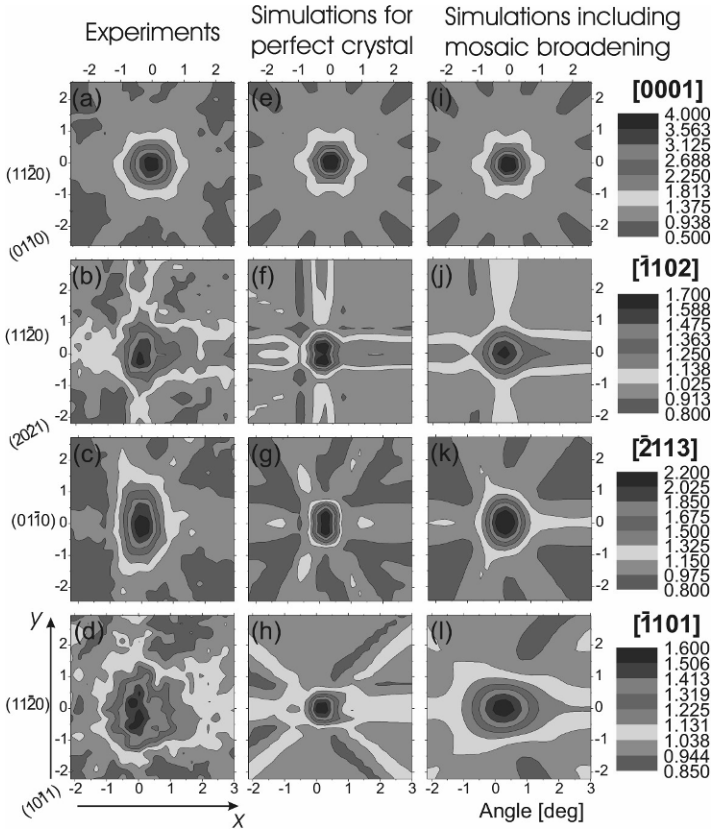

Fig. 3.26. (a-d) Experimental emission channelling patterns for ^{167m}Er in AlN. (e-h) Best fits of theoretical emission yields assuming a *perfect* AlN crystal. (i-l) Best fits of theoretical patterns including the broadening due to the AlN *mosaicity* [12].

GaN epitaxial films are usually not continuous 2D layers, but consist of a mosaic of single-crystalline domains of micrometer size, with a large concentration of stacking faults at their boundaries. As a consequence, the domains have slightly different crystallographic orientations – generally referred to as mosaic structure, or mosaicity in general. If the average mosaic spread becomes comparable in magnitude to the angular resolution of the channelling measurement — about 0.24° in this case — it will directly affect the outcome of the experiment.

The misorientation can be split up into two components: mosaic *tilt* and *twist*, i.e. out-of-plane and in-plane misalignment [Fig. 3.27(a) and (b)] respectively.

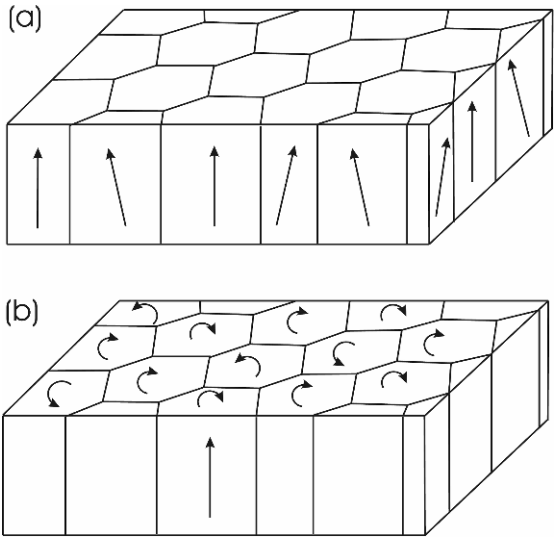

Fig. 3.27. Schematic of a mosaic layer, depicting the columnar domains and the (a) tilt and (b) twist components of their crystallographic orientations [12].

In practice, the convolution of tilt and twist has to be taken into account, as proposed in the phenomenological model of Srikant et al. [76]. Due to mosaicity, the crystallographic directions of the lattice are no longer perfectly determined, as in an ideal crystal, but involve a distribution of angles between various axes and planes. These distributions are reflected in XRD measurements as variations in planar directions and in channelling as variations in axial directions.

By collecting X-ray rocking curves from up to 7 different crystal planes, De Vries et al. determined the mosaicity of the GaN and AlN samples used in their lattice location studies [75]. Their results show that the convoluted broadening (combining *tilt* and *twist* contributions) (i) increases for crystallographic directions that are further away from the perpendicular *c*-axis, and (ii) is significantly larger for AlN (up to 1.5° broadening) than for GaN (typically ~ 0.20°-0.25°). Taking into account the experimental angular resolution is only 0.24°, it is obvious that a limited effect of the mosaicity is expected for lattice location studies in GaN,

whereas a significant impact can be expected for AlN. Meanwhile, it has become possible to grow structurally better AlN samples, thus reducing the effect of mosaicity on channelling measurements.

Re-examining the experimental results [Fig. 3.26(a)-(d)] reveals the influence that mosaicity exerts on emission channelling measurements. Fig. 3.28(a) shows the Er_{Al} fractions deduced from the fitting procedure as a function of annealing temperature, assuming a perfect crystal. A comparison of the results of the four channelling axes indicates that the estimated fractions drastically decrease with increasing inclination angle θ. This is, of course, not a physical effect but an artefact of the progressively worse agreement between theory and experiment, and illustrates that, if a large mosaic spread is ignored, the analysis can produce meaningless or wrong results.

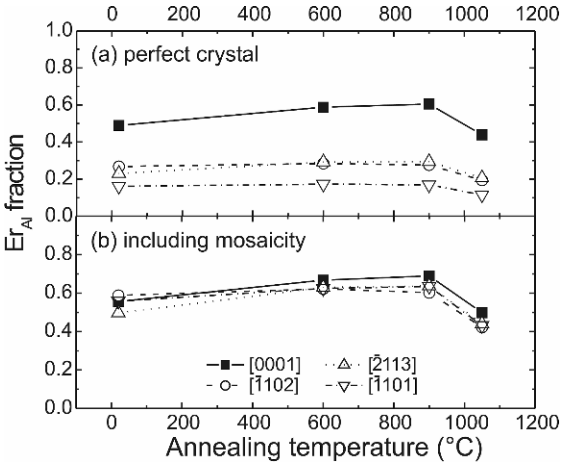

Fig. 3.28. Fraction of ^{167m}Er on Al positions as a function of annealing temperature, deduced from a fit to theoretical simulations (a) assuming a perfect crystal and (b) including the broadening due to mosaicity [12].

In order to check if this behavior can be fully explained by the mosaicity of the AlN layer, the fitting procedure was repeated with another set of theoretical emission yields that include the mosaic broadening. This was achieved by convoluting the simulations for a perfect crystal with Gaussian distributions with FWHM W_G according to the values measured by X-ray rocking curves. The best fits of the "corrected" simulations to the experimental patterns are shown in Fig. 3.26(i)-(l) and correspond to Er on Al sites. It is obvious that these theoretical yields display a significantly better agreement to the experiments than the ones that assume a perfect crystal structure. Furthermore, as can be seen in Fig. 3.28(b), the fitting procedure with the corrected simulations results in equal substitutional Er fractions along the four crystal axes, within the experimental error bars of about 10%.

This new approach allows the extraction of physical information on the lattice site location of impurities in highly mosaic layers. For this specific case, the data in Fig. 3.28(b) show that already after room-temperature implantation the majority (~ 55-60%) of Er atoms are located on Al sites, with the remainder situated on random sites. Including a third fraction in the fitting procedure does not considerably improve the fit quality, although it cannot be excluded that less than 5% of the Er atoms are located on other high-symmetry sites. The largest Er_{Al} fraction of about 65% is obtained after vacuum annealing at up to 900 °C. However, this fraction decreases after annealing at 1050 °C in N_2, which is unexpected, considering that AlN is expected to be more resistent to high temperatures than GaN.

With the emission channelling technique one can in principle also deduce the root-mean-square displacements from the ideal Al lattice sites, as was extensively demonstrated for GaN in the previous chapter. However, the large mosaic broadening leads to a loss of sensitivity in the experimental emission patterns of the AlN samples, which precludes this.

3.7 Conclusions

Since the precise lattice site of RE ions introduced in a group III-nitride determines the crystal field experienced, it is expected to govern the Stark splitting of the 4*f* levels and the intensity of the luminescence. In all studies published to date, using a wide variety of RE species, concentrations, experimental parameters and analytical techniques, basically just one lattice site has been reported, i.e. the substitutional site, RE_{III}, denoted S_{III} in the foregoing. Within the sensitivity of the techniques (of the order of 5% of the estimated fractions), no other high-symmetry site could be identified. The fraction of substitutional REs varies from nearly 100% to 0%, the remaining ions being positioned on so-called "random" sites. The major limitation to incorporating REs on high-symmetry lattice sites is the creation of implantation-induced defects in the case of ion implantation doping, and clustering and RE nitride formation in the case of *in situ* doping with MBE. It should be noted that all RE do not occupy the perfect substitutional position; rather they are (randomly) displaced around this position. Although additional thermal annealing does not result in an increased substitutional fraction, the average displacement decreases – the RE ions are thus better incorporated on the sites due to the removal of lattice defects from their vicinity. Still, the displacement remains larger than the thermal vibration amplitude in the group III-nitride. All RE species studied show the same behaviour, the only exception being Eu, for which a second site has been reported, i.e. a position in which the Eu ion is displaced along the *c*-axis, towards the AG-*c* antibonding site.

There are two major approaches to assess the lattice site of RE ions in the semiconductor lattice. A first group of techniques relies on the symmetry and coordination around the RE and on the distances to the neighbouring atoms, to model the III-N:RE incorporation. The main examples are X-ray absorption fine structure measurements

and hyperfine interaction studies. Although very sensitive to small variations of the lattice site, the models derived from these measurements may not always be unique and these techniques are not particularly sensitive to random displacements. Alternatively, channelling of energetic charged particles provides direct information on the dopant lattice site. Conventional ion-beam channelling is an ideal approach for relatively high RE concentrations, whereas emission channelling allows determining the site of very low dopant populations, i.e. where no interaction between neighbouring RE ions is present. In all cases, the obtained fractions are lower limits, due to the presence of defects and elastic strain in the nitride (hampering the channelling of the charged particles), mosaic structure of the host (in particular for AlN), electron scattering from the vacuum chamber, etc. Hence, care should be taken when comparing substitutional fractions from different studies.

To a large extent, the substitutional fraction can be tailored by adjusting the experimental parameters during implantation or MBE growth. More specifically, a larger fraction of REs occupies a substitutional group III-site when either (i) a lower fluence is used, (ii) the implantation is performed at an elevated temperature or (iii) in channelling geometry, or a combination of these three. It is clear that we must strive for a minimum defect concentration in order to obtain a maximum substitutional fraction. In contrast to other RE-doped semiconductors, co-doping with light impurities such as C, O or F does not alter the lattice site of RE in GaN.

In conclusion, the lattice sites of REs in III-nitrides – i.e. (displaced) RE_{III} or random sites – have been well established and the tailoring of the substitutional fraction and *rms* displacement by adjusting a variety of experimental parameters has been elucidated. These results can pave the way to understanding how the luminescent properties of the nitride can be tuned by modifying the RE lattice site.

Acknowledgements

This work was supported by the Fund for Scientific Research, Flanders (FWO), the Concerted Action of the K.U.Leuven (GOA/2009/006), the Inter-university Attraction Pole (IUAP P6/42), the Center of Excellence Programme (INPAC EF/05/005) and by the European Commission through the RENiBEl (Rare Earth doped Nitrides for high Brightness Electroluminescent emitters) network (Contract No. HPRNCT-2001-00297). The authors want to thank Katharina Lorenz, Eduardo Alves, Kevin O'Donnell and Stefan Decoster for providing figures for this chapter and for their constructive discussions.

References

1. B.R. Judd, Phys. Rev. 127, 750 (1962).
2. G.S. Ofelt, J. Chem. Phys. 37, 511 (1962).
3. S. Dhar, T. Kammermeier, A. Ney, L. Pérez, K.H. Ploog, A. Melnikov and A.D. Wieck, Appl. Phys. Lett. 89, 062503 (2006).
4. K.P. O'Donnell and B. Hourahine, Eur. Phys. J. Appl. Phys. 36, 91 (2006).
5. S. Kim, S.J. Rhee, D.A. Turnbull, E.E. Reuter, X. Li, J.J. Coleman and S.G. Bishop, Appl. Phys. Lett. 71, 231 (1997).
6. S. Kim, S.J. Rhee, D.A. Turnbull, X. Li, J.J. Coleman, S.G. Bishop and P.B. Klein, Appl. Phys. Lett. 71, 2662 (1997).
7. Braud, J.L. Doualan, R. Moncorgé, B. Pipeleers and A. Vantomme, Mat. Sci. Eng. B105, 101 (2003).
8. F. Pellé, F. Auzel, J.M. Zavada, D.S. Lee and A.J. Steckl, Mat. Sci. Eng. B105, 126 (2003).
9. V. Dierolf, C. Sandmann, J. Zavada, P. Chow and B. Hertog, J. Appl. Phys. 95, 5464 (2004).
10. K. Wang, R.W. Martin, K.P. O'Donnell, V. Katchkanov, E. Nogales, K. Lorenz, E. Alves, S. Ruffenach and O. Briot, Appl. Phys. Lett. 87, 112107 (2005).
11. L. Bodiou, A. Oussif, A. Braud, J.-L. Doualan, R. Moncorgé, K. Lorenz and E. Alves, Opt. Mat. 28, 780 (2006).
12. B. De Vries,PhD thesis, Katholieke Universiteit Leuven, 2006 (can be downloaded from http://fys.kuleuven.be/iks/nvsf/files/thesis-bartdv.pdf
13. J.-S. Filhol, R. Jones, M. J. Shaw, and P. R. Briddon, Structure and electrical activity of rare-earth dopants in GaN, Appl. Phys. Lett. 84, 2841 (2004).
14. S. Petit, R. Jones, M. J. Shaw, P. R. Briddon, B. Hourahine, and T. Frauenheim, Electronic behavior of rare-earth dopants in AlN: a density-functional study, Phys. Rev. B 72, 73205 (2005).
15. P. Boguslawski, E.L. Briggs and J. Bernholc, Phys. Rev. B51, 17255 (1995).
16. U. Wahl, A. Vantomme, G. Langouche, J.G. Marques, J.G. Correia and the ISOLDE Collaboration, Phys. Rev. Lett. 79, 2069 (1997).
17. S. Decoster, B. De Vries, U. Wahl, J.G. Correia and A. Vantomme, Appl. Phys. Lett. 93, 141907 (2008).
18. U. Wahl, A. Vantomme, G. Langouche and the ISOLDE Collaboration, Nucl. Instr. Meth. B148, 492(1999).
19. U. Wahl, A. Vantomme, G. Langouche, J.P. Araújo and the ISOLDE Collaboration, Nucl. Instr. Meth. B 175-177, 262 (2001).
20. L.C. Feldman, J.W. Mayer and S.T. Picraux, "*Materials Analysis by Ion Channeling*" (Academic Press, NY, 1982).
21. P.J.M. Smulders and D.O. Boerma, Nucl. Instr. Meth. B29, 4332 (1987).
22. H. Hofsäss and G. Lindner, Phys. Rep. 201, 121 (1991).
23. U. Wahl, J.G. Correia, A. Czermak, S.G. Jahn, P. Jalocha, J.G. Marques, A. Rudge, F. Schopper, J.C. Soares, A. Vantomme, P. Weilhammer and the ISOLDE Collaboration, Nucl. Instr. Meth. A 524, 245 (2004).
24. B. De Vries, U. Wahl, E. Rita, J.P. Araújo, S. Pereira, J.G. Correia and A. Vantomme, unpublished.
25. H. Schulz, K.H. Thiemann, Solid State Comm. 23, 815 (1977).
26. A. Yoshiasa, K. Koto, H. Maeda, and T. Ishii, Jpn. J Appl. Phys. 36, 781 (1997).
27. X. Xiong and S.C. Moss, J. Appl. Phys. 82, 2308 (1997).

28. X.L. Chen, J.K. Liang, Y.P. Xu, T. Xu, P.Z. Jiang, Y.D. Yu, and K.Q. Lu, Mod. Phys. Lett. B 13, 285 (1999).
29. W. Paskowicz, S. Podsiadlo, and R. Minikayev, J. Alloy Comp. 382, 100 (2004).
30. C. Ronning, E. P. Carlson and R. F. Davis, Phys. Rep. 351, 349 (2001).
31. K.P.O'Donnell, V. Katchkanov, K. Wang, R.W. Martin, P.R. Edwards, B. Hourahine, E. Nogales, J.F.W. Mosselmans, B. De Vries and the RENiBEl Consortium, Mater. Res. Soc. Symp. Proc. 831, E9.6.1 (2005).
32. G. Schatz and A. Weidinger, *Nuclear Condensed Matter Physics*, translated by J.A. Gardner, John Wiley and Sons, U.K. (1996).
33. A. Vantomme, S.M. Hogg, M.F. Wu, B. Pipeleers, M. Swart, S. Goodman, D. Auret, K. Iakoubovskii, G. Adriaenssens, K. Jacobs and I. Moerman, Nucl. Instr. Meth. B 175-177, 148 (2001).
34. K. Lorenz, E. Alves, U. Wahl, T. Monteiro, S. Dalmasso, R.W. Martin, K.P. O'Donnell and R. Vianden, Mat. Sci. Eng. B105, 97 (2003).
35. E. Alves, K. Lorenz, R. Vianden, C. Boemare, M.J. Soares and T. Monteiro, Mod. Phys. Lett. 15, 1281 (2001).
36. U. Wahl, E. Alves, K. Lorenz, J.G. Correia, T. Monteiro, B. De Vries, A. Vantomme and R. Vianden, Mat. Sci. Eng. B105, 132 (2003).
37. L. Bodiou, A. Braud, J.-L. Doualan, R. Moncorgé, J.H. Park, C. Munasinghe, A.J. Steckl, K. Lorenz, E. Alves and B. Daudin, J. Appl. Phys. 105, 043104 (2009).
38. S.F. Song, I.S. Roqan, R.W. Martin, K.P. O'Donnell and A. Vantomme, unpublished (2010).
39. K. Bharut-Ram, H. Hofsäss and C. Ronning, Hyp. Int. 184, 213 (2008).
40. K. Lorenz, F. Ruske and R. Vianden, Appl. Phys. Lett. 80, 1 (2002).
41. M. Fanciulli, M. Lindroos, G. Weyer and T.D. Moustakas, Mat. Sci. Forum. 196-201, 61 (1995).
42. C. Ronning, M. Dalmer, M. Uhrmacher, M. Restle, U. Vetter, L. Ziegeler, H. Hofsäss, T. Gehrke, K. Järrendahl, R. F. Davis and the ISOLDE Collaboration, J. Appl. Phys. 87, 2149 (2000).
43. K. Lorenz, E. Alves, T. Monteiro, M.J. Soares, M. Peres and P.J.M. Smulders, Nucl. Instr. Meth. B242, 307 (2006).
44. K. Lorenz, E. Alves, T. Monteiro, A. Cruz and M. Peres, Nucl. Instr. Meth. B257, 307 (2007).
45. E. Alves, U. Wahl, M.R. Correia, S. Pereira, B. De Vries and A. Vantomme, Nucl. Instr. Meth. B206, 1042 (2003).
46. M. Dalmer, M. Restle, A. Stötzler, U. Vetter, H. Hofsäss, M.D. Bremser, C. Ronning, R.F. Davis and the ISOLDE Collaboration, Mat. Res. Soc. Symp. Proc. 482, 1021 (1998).
47. U. Wahl, A. Vantomme, G. Langouche, J.P. Araújo, L. Peralta, J.G. Correia and the ISOLDE Collaboration, J. Appl. Phys. 88, 1319 (2000).
48. U. Wahl, J.G. Correia, S. Cardoso, J.G. Marques, A. Vantomme, G. Langouche and the ISOLDE Collaboration, Nucl. Instr. Meth. B136, 744 (1998).
49. A. Ionascut-Nedelescu, C. Carlone, A. Houdayer, H.J. von Bardeleben, J.-L. Cantin and S. Raymond, IEEE Trans. Nucl. Sci. 49, 2733 (2002).
50. B. De Vries, U. Wahl, A. Vantomme, J.G. Correia and the ISOLDE Collaboration, Phys. Stat. Sol. (c) 0, 453 (2002).
51. B. De Vries, U. Wahl, A. Vantomme, J.G. Correia and the ISOLDE Collaboration, Mater. Sci. Engin. B105, 106 (2003).
52. B. De Vries, V. Matias, A. Vantomme, U. Wahl, E.M.C. Rita, E. Alves, A.M.L. Lopes, J.G. Correia and the ISOLDE Collaboration, Appl. Phys. Lett. 84, 4304 (2004).

53. M. Mamor, V. Matias, A. Vantomme, A. Colder, P. Marie and P. Ruterana, Appl. Phys. Lett. 85, 2244 (2004).
54. B. De Vries, A. Vantomme, U. Wahl, J.G. Correia, J.P. Araújo, W. Lojkowski, D. Kolesnikov and the ISOLDE Collaboration, J. Appl. Phys. 100, 023531 (2006).
55. T. Monteiro, C. Boemare, M.J. Soares, R.A. Sá Ferreira, L.D. Carlos, K. Lorenz, R. Vianden and E. Alves, Physica B308-310, 22 (2001).
56. H. Bang, S. Morishima, Z. Li, K. Akimoto, M. Nomura and E. Yagi, J. Cryst. Growth 237-239, 1027 (2002).
57. V. Katchkanov, J.F.W. Mosselmans, S. Dalmasso, K.P. O'Donnell, R.W. Martin, O. Briot, N. Rousseau and G. Halambalakis, Mat. Res. Soc. Symp. Proc. Vol. 798, Y5.10.1 (2004).
58. K. Lorenz, R. Vianden, R. Birkhahn, AlJ. Steckl, M.F. da Silva, J.C. Soares and E. Alves, Nucl. Instr. Meth. B161-163, 946 (2000).
59. K. Lorenz, U. Wahl, E. Alves, T. Wojtowicz, P. Ruterana, S. Dalmasso, R.W. Martin, K.P. O'Donnell, S. Ruffenach, O. Briot and A. Vantomme, Mat. Res. Soc. Symp. Proc. 798, Y5.5.1 (2004).
60. B. Pipeleers, S.M. Hogg and A. Vantomme, J. Appl. Phys. 98, 123504 (2005).
61. U. Wahl, B. De Vries, S. Decoster, A. Vantomme and J.G. Correia, Nucl. Instr. Meth. B 267, 1340 (2009).
62. V. Katchkanov, J.F.W. Mosselmans, S. Dalmasso, K.P. O'Donnell, S. Hernandez, K. Wang, R.W. Martin, O. Briot, N. Rousseau, G. Halambalakis, K. Lorenz and E. Alves, Superlattices and Microstructures 36, 729 (2004).
63. H. Bang, S. Morishima, Z. Li, K. Akimoto, M. Nomura and E. Yagi, J. Phys.: Condens. Matter 13, 10837 (2001).
64. B. Pipeleers, S.M. Hogg, M. Swart and A. Vantomme, unpublished.
65. K. Lorenz, N. Barradas, E. Alves, I.S. Roqan, E. Nogales, R.W. Martin, K.P. O'Donnell, F. Gloux and P. Ruterana, J. Phys. D: Appl. Phys. 42, 165103(2009).
66. R.G. Wilson, R.N. Schwartz, C.R. Abernathy, S.J. Pearton, N. Newman, M. Rubin, T. Fu and J.M. Zavada, Appl. Phys. Lett. 65, 992 (1994).
67. C.H. Qiu, M.W. Leksono, J.I. Pankove, J.T. Torvik, R.J. Feuerstein and F. Namavar, Appl. Phys. Lett. 66, 562 (1995).
68. E. Alves, M.F. da Silva, J.C. Soares, R. Vianden, J. Bartels and A. Kozanecki, Nucl. Instr. Meth. B147, 383 (1999).
69. J.T. Torvik, C.H. Qiu, R.J. Feuerstein, J.I. Pankove and F. Namavar, J. Appl. Phys. 81, 6343 (1997).
70. P.H. Citrin, P.A. Northrup, R. Birkhan and A.J. Steckl, Appl. Phys. Lett. 76, 2865 (2000).
71. V.Y. Davydov, V.V. Lundin, A.N. Smirnov, N.A. Sobolev, A.S. Usikov, A.M. Emel'yanov, M.I. Makoviickhuk and E.O. Parshin, Semiconductors 33, 1 (1999).
72. S.F. Song, W.D. Chen, C. Zhang, L. Bian, C.C. Hsu, B. Ma, G.H. Li and J. Zhu, J. Appl. Phys. 96, 4930 (2004).
73. M. Overberg, C.R. Abernathy, J.D. MacKenzie, S.J. Pearton, R.G. Wilson and J.M. Zavada, Mater. Sci. Eng. B81, 121 (2001).
74. U. Vetter, M.R. Reid, H. Hofsäss, C. Ronning, J. Zenneck, M. Dietrich and the ISOLDE Collaboration, Mat. Res. Soc. Symp. Proc. 743, L6.16.1 (2003).
75. B. De Vries, U. Wahl, E. Rita, S. Ruffenach, O. Briot, J.G. Correia and A. Vantomme, unpublished.
76. V. Srikant, J.S. Speck and D.R. Clarke, J. Appl. Phys. 82, 4286 (1997).

Chapter 4
Electroluminescent Devices Using RE-Doped III-Nitrides

Akihiro Wakahara

Abstract The III-nitride semiconductors doped with RE atoms appear to be excellent materials for thin film optical device applications. The spectral coverage extends from UV to infrared and thus light-emitting devices suitable for full-color displays, solid-state lasers, and optical telecommunication fields are expected. This chapter reviews the current status of electrically pumped light-emitting devices based on RE-doped GaN, such as AC- and/or DC-biased electroluminescent (EL) devices and 'p-n' junction based light-emitting diodes. The different excitation mechanisms are reviewed.

4.1 Introduction

Rare earth (RE) doped semiconductors have recently been developed for efficient light-emitting devices, from solid-state lasers to color displays to optical fiber telecommunications [1]. The advantage of such devices comes from the fact that the luminescence originates from a transition within a partially filled 4*f* shell, which is shielded from the surrounding host material by completely filled valence shells. This results in very sharp, temperature-insensitive optical emission at wavelengths determined only by the RE 4*f* shell energy structure.

RE doping of conventional semiconductors (Si, GaAs, etc.) suffers from limited solubility and strong temperature quenching of the light emission, which is a key issue for room temperature operation. The wide-gap semiconductors are attractive RE hosts for room-temperature device applications because the emission

Akahiro Wakahara
Toyohashi University of Technology, Dept Electrical and Electronic Engineering, 1-1 Hibarigaoka, Tempaku, Toyohashi, Aichi 441-8580, Japan
wakahara@eee.tut.ac.jp

efficiency appears to increase with the bandgap value [2]; group-III nitrides, in particular GaN, are especially advantageous, providing efficient carrier generation to excite the RE atoms, high solubility of RE dopants, and they are thermally and chemically robust. In addition, RE-doped wide gap III-N semiconductors allow light emission at visible wavelengths for full-color display applications due to their high transparency in the visible spectral region. Photoluminescence (PL) and electroluminescence (EL) from RE-doped GaN have been demonstrated in blue [3, 4, 5], green [4, 6, 7, 8, 9, 10], red [10, 11, 12, 13, 14, 15, 16, 17, 18, 19], turquoise [20], yellow, and orange [21] colors. A strong argument in favor of utilizing RE doping of III-nitrides is that integration of the primary colors on a single substrate would allow the development of future generations of flat panel displays.

Fig. 4.1 illustrates the full-color capability of EL-devices with RE-doped GaN on the Commission International d'Eclairage (CIE) chromaticity diagram. The solid triangle in the diagram defines the full-color capability of emission from GaN doped with Eu (red), Er (green), and Tm (blue). The 'full-color' CIE triangle of the European Broadcasting Union (EBU) is shown for comparison [22]. Besides, the *infrared* emission of GaN:Er at 1.54 μm is very promising for optical fiber communication applications. In this chapter, electrically pumped light-emitting devices based on RE-doped GaN will be treated.

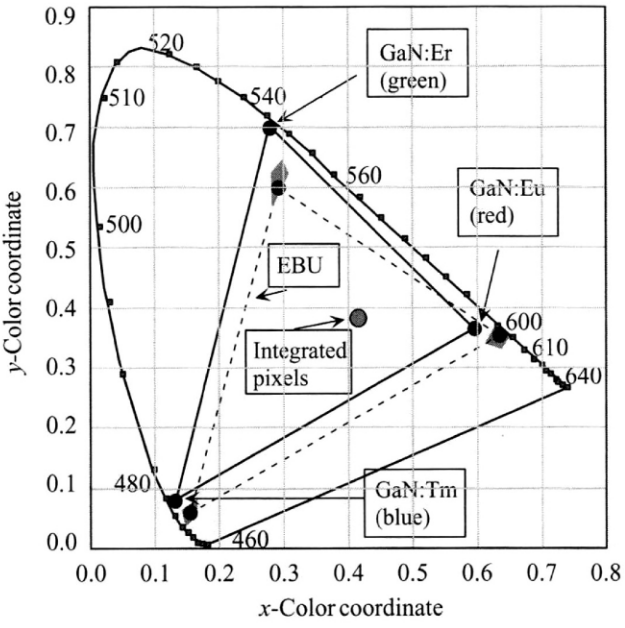

Fig. 4.1. CIE x-y chromaticity diagram showing the locations of the blue, green, and red emission from the individually biased pixels in an integrated GaN:RE-based EL-device and from simultaneously biasing all three pixels in the device. Also shown are the coordinates of the CIE triangle recommended by the European Broadcasting Union (dashed line). Reprinted with permission from [22]. Copyright (1997) American Institute of Physics."

4.2 General Treatment of EL devices

The two main types of EL devices are distinguished by their generation of light at "high-voltage" or "low-voltage". The different excitation processes involved are illustrated in Fig. 4.2.

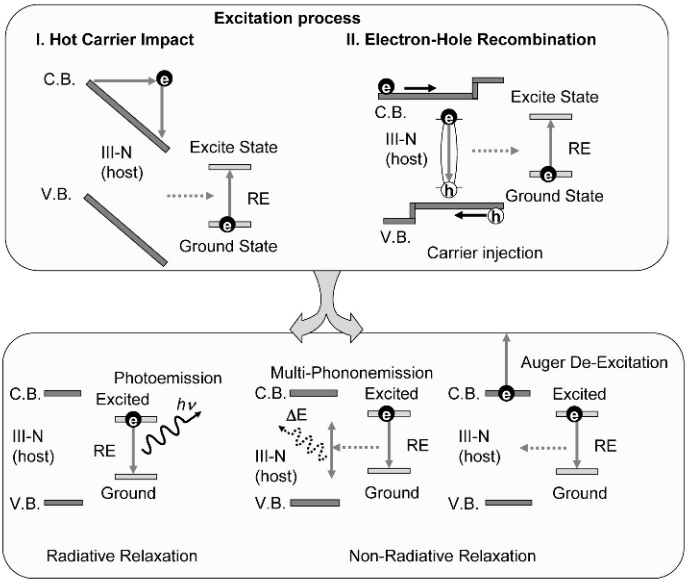

Fig. 4.2. Electrical excitation and relaxation processes.

For the high-voltage EL devices, the layer thickness of luminescent material is typically of order 1μm, and thus high electric fields are present even if the applied voltage is relatively small (<100 V). Electrons, accelerated in the material, excite the luminous centers, such as RE ions, by impact excitation. In the case of low-voltage EL devices, electrons (holes) are injected into an active layer doped with RE by using a p-n junction forward biased to V_F; when they recombine, the captured electron-hole pairs excite the RE ions. In this excitation process, the difference between $eV_F \sim E_g$ and an energy loss caused by Joule heating is the energy available for excitation of RE ions.

In the general case of excitation of luminescence via a host, the luminescence efficiency (energy efficiency) η can be expressed as:

$$\eta = \frac{E_{em}}{E_{exc}} \eta_t \eta_{RE} \eta_{esc} \tag{1}$$

where, η_t is the probability of energy transfer from the host lattice to the RE, η_{RE} is the quantum efficiency of the RE transition, E_{em} is the emitted photon energy

and E_{exc} is the energy available for the excitation of the luminescence. η_{esc} is the photon escape probability, the ratio of the number of photons emitted to the number generated in the material. This equation means that the maximum efficiency of EL phosphors is affected by host and dopant properties.

For high-voltage EL, the energy efficiency η for devices with hot carrier excitation is given by:

$$\eta = E_{em} s \tilde{N} e F \tag{2}$$

where s is the cross-section for impact excitation, $\tilde{N}$ the concentration of luminescent centers, and F the applied electric field. Neglecting possible energy loss by phonon emission, the mean energy acquired from the electric field by the carrier between impact excitation events equals $eF/s\tilde{N}$. If we assume that the cross-section of GaN:Eu is approximately the atomic dimension, squared, i.e., $s = 10^{-16}$ cm^2 and the other parameters are taken as values typical for GaN:Eu devices, E_{em} = 2 eV, $\tilde{N} = 10^{20}$ cm^{-3} and F = 1 MV/cm, an energy efficiency of about 2% is estimated from Eq. (2) In real EL devices, we also have to take Stokes' shift, light trapping, and concentration quenching effects into account. All of these phenomena reduce the energy efficiency.

4.3 III-N:RE EL Devices

An alternating current (AC)-biased dielectric/phosphor/dielectric layered structure [23] allows reliable high field operation by current-limiting the electrical breakdown of the phosphor layer. Thin-film AC-biased EL devices using AlGaN:Er [24, 25] GaN:Eu, GaN:Nd [26], and GaN:Tm [27] have been demonstrated. The basic structure of an AC-biased EL device is shown in Fig. 4.3 [24]. The structure is composed of a 200nm-thick Indium-Tin-Oxide (ITO) transparent electrode, a 300 nm-thick dielectric, a 600nm-thick active layer of GaN:Er, a 300nm-thick lower dielectric layer, all mounted on a p^+-Si substrate. Al_2O_3, AlN, Si_3N_4, and/or SiON were utilized as the dielectrics because of their similar permittivity to GaN (Er ~ 8). In common with other thin-film EL device structures, the final Al_2O_3/GaN:Er/Al_2O_3/ITO film stack is subject to significant light piping in the phosphor and dielectrics [28]. Also, the surface roughness of the GaN:Er film has a strong influence on the out-coupling of light. The use of polished substrates with RF sputtered dielectrics subjects the AC-biased EL devices to significant light guiding within the phosphor layer. Although substrate roughness improves the out-coupling of light, surface roughness of the dielectric layer degrades the reliability of the AC-biased EL devices. If the surface is too rough, high-field points, created at surface 'peaks', can result in premature electrical breakdown of the insulating dielectric layers.

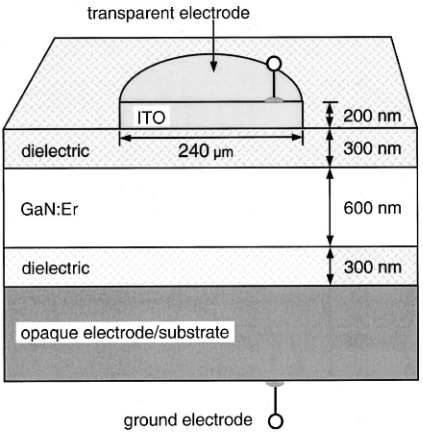

Fig. 4.3. Illustration of AC-biased green EL device structure. The device is composed of polycrystalline GaN:Er phosphor and ITO dot contact. The emission area is 1.8×10^{-3} cm^2 emission. The dielectric layers capacitively couple an alternating voltage to the GaN:Er layer. Reprinted with permission from [24]. Copyright (2000) American Institute of Physics.

A strong visible emission of Er was demonstrated from GaN:Er AC-biased EL devices as shown in Fig. 4.4. The electric field applied to Al_2O_3 /GaN:Er/Al_2O_3 layers at the peak voltage (V_p) of 180V is about 1.5 MV/cm, suitable for exciting Er^{3+} in GaN [25]. The two green emission peaks at 537/558 nm are essentially identical to those reported for PL of epitaxially grown GaN:Er and originate from the $^2H_{11/2}$ - $^4I_{15/2}$ and $^4H_{3/2}$ - $^4I_{15/2}$ transitions of Er^{3+}. The spectrum also contains a strong violet peak at 415 nm ($^2H_{9/2}$- $^4I_{15/2}$) and a weaker ultraviolet peak at 389 nm ($^4G_{11/2}$- $^4I_{15/2}$). The violet emission indicates that hot carriers can gain up to ~3 eV energy in the 1.5 MV/cm applied field. A maximum luminance value of 300, 60, and 15 cd/m^2 has been reported for GaN:Er and AlGaN:Er AC-biased EL devices driven by square wave modulation at 180 V with frequencies of 100, 10, and 1 kHz, respectively [25]. The emitted intensity initially increases linearly with frequency, then tends to saturate. The saturation trends can be explained in terms of the long spontaneous emission lifetimes of the visible (~10 ms) and IR (~1ms) Er^{3+} emissions.

Fig. 4.5 shows the proposed excitation mechanism for RE-doped EL devices with the double dielectric layer structure [27]. When the applied electric field reaches a threshold in the RE-doped GaN layer, breakdown occurs by avalanche and Zener mechanisms [29]. Electrons trapped in the interface states between the GaN:RE and the cathode-side dielectric layers are injected into the GaN conduction band by field-assisted tunneling. These electrons are accelerated by the electric field (> 1MV/cm) and gain kinetic energy; the 'hot' electrons directly excite electrons from the ground state to higher levels of the *4f* shell of RE^{3+} by the impact-excitation mechanism. Since the average energy of the hot electron is expected to be proportional to the applied electric field, a significant energy for

the impact excitation of the RE^{3+} above the turn-on voltage is obtained. According to this model, luminance would depend strongly on the pulse width. Actually, the device brightness under bipolar biasing is much stronger than for monopolar biasing at the same duty ratio [24]. In the case of monopolar pulse bias, electrons injected from the cathode-side interface move to the anode-side during the pulse. When the pulse is off, only the electrons not trapped at the interface, and/or those thermally emitted from the trap, are free to diffuse back. These electrons will excite RE ions during the next pulse, if the pulse width is long enough to achieve full acceleration. On the other hand, in bipolar biasing, trapped electrons at the anode-side interface can be injected in reverse bias.

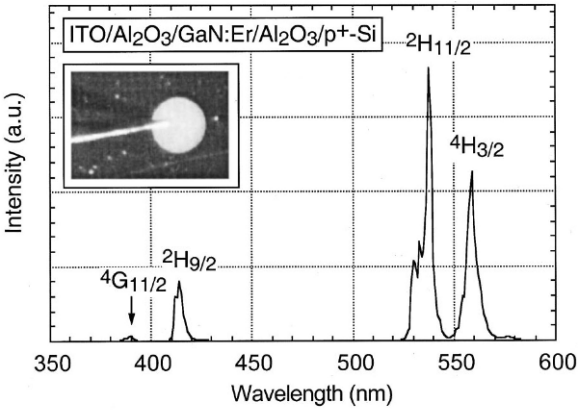

Fig. 4.4. Electroluminescent spectrum from ITO/Al2O3/GaN:Er/Al2O3 on p+-Si driven by a square wave with 180V at 10kHz. All emission peaks originated from Er3+ states. Reprinted with permission from [24]. Copyright (2000) American Institute of Physics.

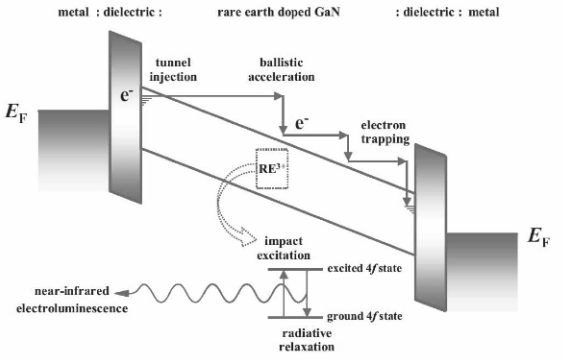

Fig. 4.5. The excitation mechanism of RE-doped EL devices with double dielectric layered structure. Reprinted with permission from [27].

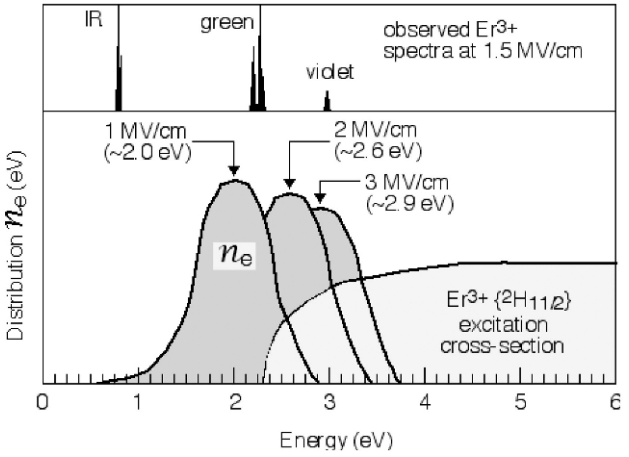

Fig. 4.6. Qualitative plot of electron energy distribution for various electric fields applied to GaN. The electron distributions were estimated based on average energy using Monte Carlo calculations of high field transport in GaN. Reprinted with permission from [25].

Heikenfeld and Steckl calculated a qualitative plot of electron energy distribution in GaN at several applied field strengths [25] from Monte Carlo calculations of high field transport in GaN [30]. As can be seen in Fig. 4.6 the calculations show that at the applied electric field of ~2 MV/cm the average carrier can excite the blue (2.6 eV) emission. This indicates that the minimum field strength required for GaN:RE ELDs is an order of magnitude lower than the 1-2 MV/cm required for II-VI:RE based ELDs. The external power efficiency, η_{ex}, of EL devices can be obtained by dividing the measured optical output power by the input electric power. The external power efficiency of the Tm-, Nd-, and Er-doped GaN EL devices at 40 V above the turn-on voltage were reported to be $\sim 1 \times 10^{-6}$, $\sim 1 \times 10^{5}$, and $\sim 4 \times 10^{-6}$, respectively [27].

EL devices without dielectric layers are suitable to overcome the limitation of trap concentration on the emission intensity. Schottky contact EL devices with GaN:RE (RE: Er [9, 31], Eu [12], Pr [13] and Tm [3]) have been reported. Fig. 4.7 shows an example of a Schottky contact EL device fabricated on a Si (111) substrate. By utilizing an Al ohmic contact to the Si substrate, the series resistance was minimized and the resistance of the device decreases proportionally with decreasing GaN:RE thickness. For bright EL devices, the use of a highly conductive GaN:RE layer is not a viable approach for reduction of the operation voltage, since the field strength will be compromised and most carriers will not have enough energy to impact-excite RE ions regardless of how much current flows through the EL device.

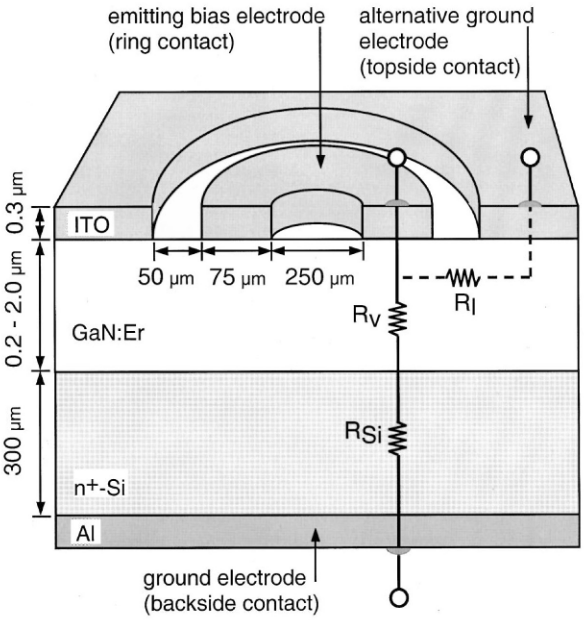

Fig. 4.7. Schematic diagram of GaN:Er EL device structure. Reprinted with permission from [31]. Copyright (2000) American Institute of Physics.

Heikenfeld et al. demonstrated low-voltage operation of a GaN:Er green EL device using a 100 nm buffer layer and a 200 nm-thick GaN:Er followed by a 100nm-thick buffer layer on n^+-Si substrate [31]. Top electrode and bottom contacts were ITO and Al, respectively. They detected green emission at 5 V from the GaN:Er by using a photomultiplier tube. The minimum energy required for excitation of Er to the $^2H_{11/2}$ level [32] is approximately $E_{exe} \sim 2.3$ eV. The voltage efficiency, defied as E_{exe}/V_f, at the optical turn-on voltage ($V_f \sim 6$V) was 38%. The minimum field strength for a GaN:Er EL device with a 300 nm phosphor layer was reported to be only ~0.2 MV/cm.

Based on the device technology described above, a three-color laterally integrated EL device was fabricated by a combination of MBE growth of RE-doped GaN and a lift off process using a spin-on-glass (SOG) mask [33]. Fig. 4.8 shows the schematic processing flow for the demonstrated three-color integrated EL device. A thick SOG on Si wafer was used as a mask for lift-off of each pixel. RE-doped GaN pixels were grown by MBE after the sufficient outgas process for SOG. The lift-off of GaN:RE layer was carried out with HF. These procedures are repeated to obtain the required layers for color integration. Finally ITO electrodes were formed on GaN:RE pixels using lift-off with conventional photoresist and annealed in N_2 ambient to form contacts.

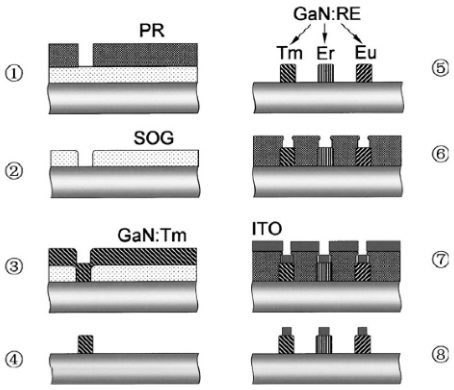

Fig. 4.8. Schematic diagrams indicating the steps for the SOG lift-off process. Reprinted with permission from [33]. Copyright (2003) American Institute of Physics.

Fig. 4.9 shows a photograph of the laterally integrated three-color GaN:RE EL devices. Fig. 4.9(b) shows the GaN:RE EL devices in operation under DC bias. Blue, green, and red emission was observed from the laterally integrated single chip EL device. This integrated EL device showed the CIE coordinates of (0.13, 0.09) for blue emission, (0.28, 0.70) for green, and (0.60, 0.37) for red. The combined emission from all three integrated pixels results in CIE coordinates of (0.42, 0.38). These coordinates correspond to Planck emission at a temperature of ~3000 K and a color rendering index of ~85.

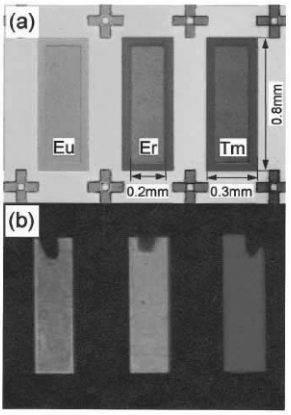

Fig. 4.9. Laterally integrated RE-doped GaN EL devices containing primary colors. (a) Microphotograph of the fabricated devices, (b) Light emission under the DC bias condition from the integrated EL devices doped with Tm, Er, and Eu. Reprinted with permission from [33]. Copyright (2003) American Institute of Physics.

Recently, Okada et al. fabricated a light emitting field effect transistor (FET) based on the AlGaN/GaN high-electron mobility FET (HEMT) structure with spatially selective doping of luminescent RE ions in the channel [34]. The layer structure comprised a 25 nm thick $Al_{0:25}Ga_{0:75}N$ barrier and a 3 μm thick GaN layer on a sapphire substrate. Eu ion implantation was carried out at an implantation energy which locates the impurity in an active two-dimensional electron gas (2DEG). Fig. 4.10 shows the device structure and photograph of the operating device. The fabricated device showed good transistor *I–V* characteristics with gate control. By applying a drain bias of 20 V, red emission from Eu ion was demonstrated. Applying a pinch-off bias to the Schottky gate decreased the luminescence intensity, which indicates that the electrons in the channel accelerate by the high electric field at drain side gate edge and excite the Eu ions. Direct modulation of the luminescence can be made by changing the field under the gate. According to a computer simulation by Hu *et al*, the electric field for an AlGaN/GaN HEMT with L_G = 5 μm has a maximum value of ~ 60 kV/cm at V_{DS} = 10 V [35]. This field is far lower than the theoretically critical electric field of 1 ~ 2 MV/cm for impact excitation in GaN:Er [25], but close to that observed in practical GaN:Er EL devices [31].

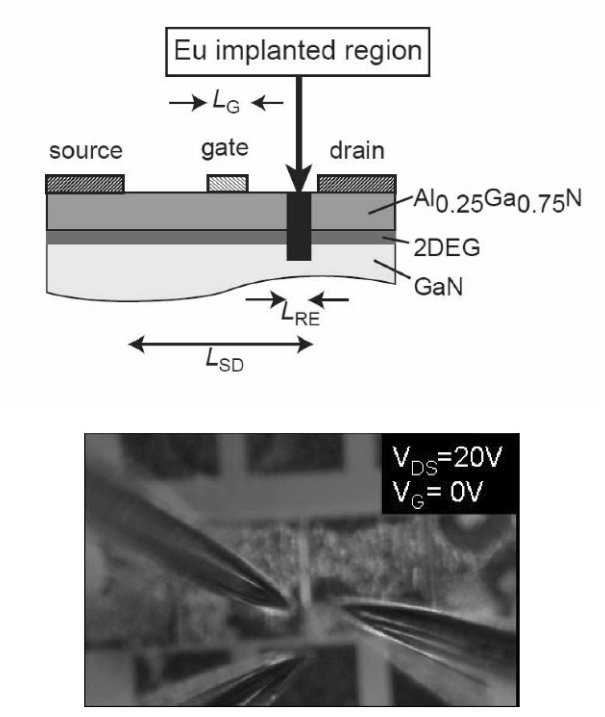

Fig. 4.10. Schematic cross-section of light emitting FET based on spatially selective doping of Eu in AlGaN/GaN HEMT structure. [34]

4.4 Light Emitting Diode with RE-doped GaN Active Layer

Although the light emitting diode (LED) based on current injection in a p-n junction is a ubiquitous device, very few publications report LEDs containing RE-doped GaN. Zavada and co-workers demonstrated a III–N double heterostructure LED [36]. The device was composed of Si-doped n-$Al_{0.12}Ga_{0.88}N$, a 20nm layer of GaN co-doped with Er, and O, and Mg-doped p-$Al_{0.12}Ga_{0.88}N$ on sapphire substrate, as shown in Fig. 4.11. The Er concentration was reported to be only 10^{18} cm^{-3}. EL emission lines representative of the GaN:Er system (green: 539 nm, 559 nm, infrared: 1000 nm, 1530 nm) were recorded under both forward and reverse bias conditions. In their report, the EL under reverse bias was five to ten times more intense than that under forward bias (see Fig. 4.12). Under reverse bias, the Er^{3+} ions would be excited by hot electrons from the junction, while the excitation mechanism for forward bias is not fully understood. The brightness of the LEDs was approximately 2.5 W/m^2 at 300 K.

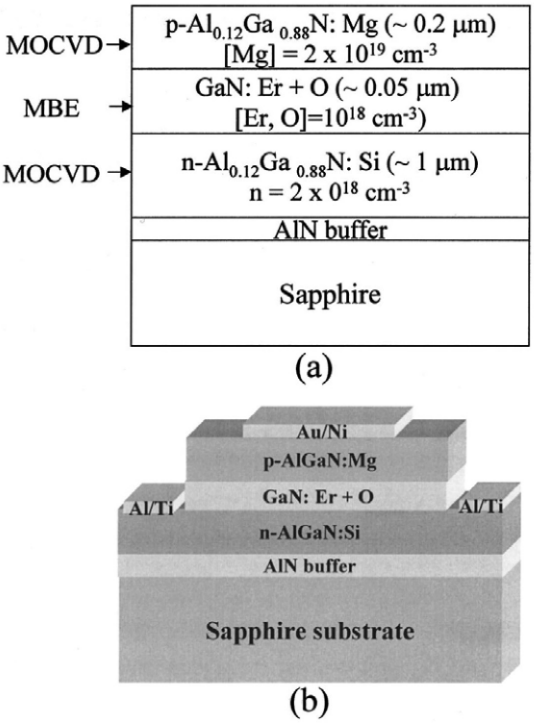

Fig. 4.11. (a) Layer structure of III–N double heterostructure for LED and (b) Schematic drawing of the processed LED. Reprinted with permission from [36]. Copyright (2004) American Institute of Physics.

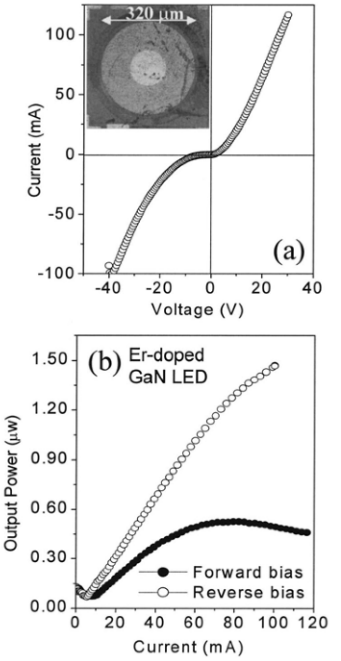

Fig. 4.12. (a) *I –V* characteristics at 300 K of the Er-doped GaN LED, the inset shows an optical micrograph of the LED, (b) Output power, integrated over the visible spectrum, under reverse bias (open circles) and under forward bias (solid dots) conditions. Reprinted with permission from [36]. Copyright (2004) American Institute of Physics.

More recently, Nishikawa et al. realized red emission from a GaN LED with Eu-doped active layer under current injection [37]. Their diode structure consists of a 20-nm-thick Mg-doped GaN contact layer, an 80-nm-thick Mg-doped GaN layer with a doping concentration of 7×10^{19} cm^{-3}, a 20-nm-thick Mg-doped $Al_{0:1}Ga_{0:9}N$ electron-blocking layer, a 300-nm thick Eu-doped GaN layer and a 3-μm-thick n-type Si-doped GaN layer with doping concentration of 4×10^{18} cm^{-3}, as shown in Fig. 4.13. The Eu concentration was about 7×10^{19} cm^{-3}. The current increased remarkably at forward voltages greater than 3 V, which is close to the built-in potential of the GaN-based p–n junction. The leakage currents for both the forward and the reverse characteristics were relatively high because of the n-type electrode. Even at an applied voltage as low as 3 V, red emission was easily visible to the naked eye under normal lighting conditions. Increasing the applied voltage caused the emission intensity to increase, while no luminescence was observed in the reverse bias condition, indicating that the observed luminescence in the forward bias was not due to the impact excitation of Eu^{3+} ions by hot carriers, but rather was caused by the energy transfer from the GaN host to the Eu^{3+} ions. The output power, integrated over the $^5D_0$–$^7F_2$ transition region was reported to be 1.3 mW at a DC current of 20 mA.

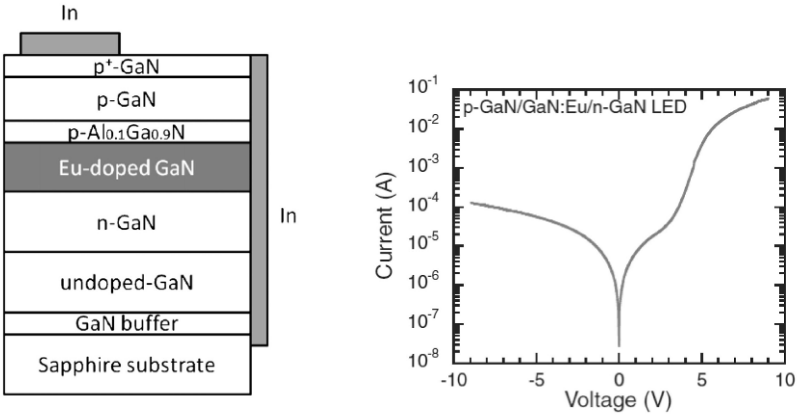

Fig. 4.13. Schematic drawing of the device structure and I-V characteristics of the GaN:Eu LED. Reprinted with permission from [37].

4.5 Summary

An RE-doped III-Nitride electroluminescent device demonstrated potential for high performance applications in flat panel displays with low temperature sensitivity. There are however several competing technologies for display development, such as plasma display panel (PDP), liquid crystal display (LCD), organic LED, etc. The fabrication cost of III-Nitride based ELDs is high compared with organic ELDs because of the high temperature and vacuum processes involved in maufacture, especially for increasing screen sizes. To overcome this drawback, deposition of high quality GaN:RE using sputtering technology may be key.

The recent development of current injection LEDs with RE-doped III-Nitride active layers opens a new paradigm for optoelectronic integration. RE-doped emitters have temperature-stable emission properties, which is an essential requirement for large scale integrated light emitters, in which operating temperature changes dynamically due to the highly developed power management architecture. Also LEDs with RE-doped active layers are expected to have potential application in spin-LEDs, and as qubits for quantum computation. To explore these new fields, we will require improvements in quantum efficiency and progress of the device fabrication process, in addition to fundamental investigations for deeper understanding of the basic operating principles of RE-doped devices.

References

1. For a review of photonic applications of RE-doped semiconductors, see A. J. Steckl and J. M. Zavada, MRS Bulletin 1999, **24** (9), p. 16, and articles therein.
2. P.N. Favennec, H.L'Haridon, M.Salvi, D.Mountonnnet, and Y.Le Guillou, Electronn. Lett. **25** (1989) 718.
3. A.J. Steckl, M. Garter, D.S. Lee, J. Heikenfeld, and R. Birkhahn, Appl. Phys. Lett., **75** (1999) 2184.
4. D.S. Lee and A.J.Steckl, Appl. Phys. Lett., **81** (2002) 2331.
5. D.S. Lee and A.J.Steckl, Appl. Phys. Lett., **82** (2003) 55.
6. A.J. Steckl and R. Birkhahn, Appl. Phys. Lett., **73** (1998) 1700.
7. R. Birkhahn and A.J. Steckl, Appl. Phys. Lett., **73** (1998) 2143.
8. M.J. Garter, J. Scofield, R. Birkhahn and A.J. Steckl, Appl. Phys. Lett., **74** (1999) 182.
9. A.J. Steckl, M. Garter, R. Birkhahn, and J. Scofield, Appl. Phys. Lett., **73** (1998) 2450.
10. L.C. Chao, B.K. Lee, C.J. Chi, J. Chyr, and A.J. Steckl, J. of Vac. Sci. & Technnology B, **17** (1999) 2791.
11. S. Morishma, T. Maruyama, M. Mmaka, Y. Masumoto, and K. Akimoto, Physica Status Solodi (a), **176**, (1999) 113.
12. R. Birkhahn, M. Garter, and A.J. Steckl, Appl. Phys. Lett., **74** (1999) 2161.
13. J. Heikenfeld, M.J. Garter, D.S. Lee, R. Birkhahn, and A.J. Steckl, Appl. Phys. Lett., **75** (1999) 1189.
14. Z. Li, H. Bang, G. Piao, J. Sawahata, and K. Akimoto, J. Crystal Growth, **240** (2002) 382.
15. H.J. Lozykowski, W.M. Jadwisienczak, and I. Brown, J. Appl. Phy., **88** (2000) 210.
16. T. Monteiro, C. Boemare, M.J. Soares, R.A. SaFerreira, L.D. Carlos, K. Lorenz, R. Vianden, and E. Alves, Physica B, **308-310** (2001) 22-25.
17. H. J. Lozykowski, W.M. Jadwisienczak, J. Han, and I. Brown, Appl. Phys. Lett., **77** (2000) 767.
18. L.C. Chao and A.J. Steckl, Appl. Phys. Lett., **74** (1999) 2364.
19. J.M. Zavada, R.A. Mair, C.J. Ellis, J.Y. Lin, H.X. Jiang, R.G. Wilson, P.A. Grudowski, and R.D. DuPuis, Appl. Phys. Lett., **75** (1999) 790.
20. A.J. Steckl and J.M. Zavada, Materials Research Society Bulletin, **24** (1999) 33.
21. D.S. Lee, J. Heikenfeld, R. Birkhahn, M.J. Garter, B.K. Lee, and A.J. Steckl, Appl. Phys. Lett., **76** (2000) 1525.
22. J.T. Torvik, C.H. Qiu, R.J. Feuersteum, J.I. Pankov, and F. Namavar, J. Appl. Phys., **81** (1997) 6343
23. M. J. Russ and D.I. Kennedy, J. Electrochem. Soc., **114** (1967) 1066.
24. J. Heikenfeld and A.J. Steckl, Appl. Phys. Lett., **77** (2000) 3520.
25. J. Heikenfeld and A.J. Steckl, MRS Symposium Proceedings, **639** (2000) G10.4
26. J.H. Kim and P.H. Holloway, Appl. Phys. Lett., **85** (2004) 1689.
27. J.H. Kim and P.H. Holloway, Adv. Mater. **17**(1) (2005) 91.
28. R. Mueller-Mach, G.O. Mueller, M. Leskela, W. Li, and M. Ritala, in *Electroluminescence II*, edited by G.O. Meuller (Academic, San Diego, 2000), Chaps. 2 and 3.
29. J.F. Wager and P.D. Keir, Annu. Rev. Mater. Sci., **27** (1997) 223
30. E. Bellotti, I.H. Oguzman, J. Kolnik, K.F. Brennan, R. Wang, and P.P. Ruden., Mat. Res. Soc. Symp. Proc. **Vol. 468** (1997) 457.

31. J. Heikenfeld, D.S. Lee, M. Garter, R. Birkhahn, and A.J. Steckl, Appl. Phys. Lett., **76** (2000) 1365
32. J.I. Pankove and R.J. Feuerstein, Mater. Res. Soc. Symp. Proc. **301**, (1993) 287.
33. Y.Q. Wang and A.J. Steckl, Appl. Phys. Lett., **82** (2003) 502
34. H. Okada, K. Takemoto, F. Oikawa, Y. Furukawa, A. Wakahara, S. Sato, and T. Ohshima, Phys. Status Solidi (c), **S2** (2009) S631
35. W.D. Hu, X.S. Chen, Z.J. Quen, C.S. Xia, W. Lu, and P.D.Ye, J. Appl. Phys., **100** (2006) 074501.
36. J.M. Zavada, S.X. Jin, N.Nepal, J.Y. Lin, and H.X. Jiang, P. Chow and B. Hertog, Appl. Phys. Lett., **84** (2004) 1061.
37. A. Nishikawa, T. Kawasaki, N. Furukawa, Y. Terai, and Y. Fujiwara, Appl. Phys. Express, **2** (2009) 071004

Chapter 5
Er-Doped GaN and $In_xGa_{1-x}N$ for Optical Communications

R. Dahal, J. Y. Lin, H. X. Jiang, J.M. Zavada

Abstract Considerable research effort has been devoted recently to the incorporation of RE ions, in particular Er^{3+}, into wide bandgap III-nitride semiconductors. Significant progress has been achieved in terms of material growth and the understanding of fundamental optical properties of GaN:Er using photoluminescence (PL), photoluminescence excitation (PLE), and electroluminescence (EL) spectroscopies. Initially, poor crystalline quality of doped material resulted in very poor emission efficiency in the visible and infrared regions. Several growth techniques are now available to grow Er-doped GaN with reasonable crystalline quality and significantly improved optical emission at 1.54 μm has been demonstrated. In this chapter, we summarize major research on Er-doped GaN grown by different techniques. Very recent progress on Er-doped InGaN alloys, in particular those grown by metal organic chemical vapor deposition (MOCVD) in the authors' laboratory, is reviewed. Electrical and optical properties are described as well as preliminary demonstrations of emitter and optical waveguide amplifiers operating in a 1.54 μm communication window. Perspectives and future challenges in material issues, design and fabrication of novel photonic devices of Er-doped nitride semiconductors for applications in optical communications are discussed.

R. Dahal, J. Y. Lin and H. X. Jiang
Department of Electrical & Computer Engineering, Texas Tech University, Lubbock, TX 79409, e-mail: hx.jiang@ttu.edu

J. M. Zavada
Department of Electrical & Computer Engineering, North Carolina State University, Raleigh, NC 27695-7911

5.1 Introduction

The incorporation of RE atoms into solid hosts has received attention in the last 30 years due to the potential applications of RE-doped materials in optoelectronic semiconductor devices. Much of the research done on RE doping has focused on the element Erbium. Er^{3+} has sharp spectral emissions from the visible to near infrared region due to the intra-*4f* transitions depicted in Fig. 5.1 [1]. The transition from the first excited ($^4I_{13/2}$) to the ground state ($^4I_{15/2}$) at ~ 1.54 μm falls within the minimum loss window of silica fibers for optical communications. Er^{3+} suffers from low emission efficiency in narrow bandgap semiconductor hosts at room temperature due to a strong thermal quenching effect; it has been well established that the thermal stability of Er emission improves with an increased energy gap and better crystalline quality of the host [2, 3, 4, 5]. Furthermore, it has also been suggested that the environment created by more ionic hosts increases the emission efficiency of intra-*4f* Er^{3+} transitions [3, 6, 7]. III-nitride wide bandgap semiconductors therefore appear to be excellent host materials for Er ions, not only due to their structural and thermal stability but also to the recent advancements in growth techniques of high-quality samples with both n- and p-type conductivities.

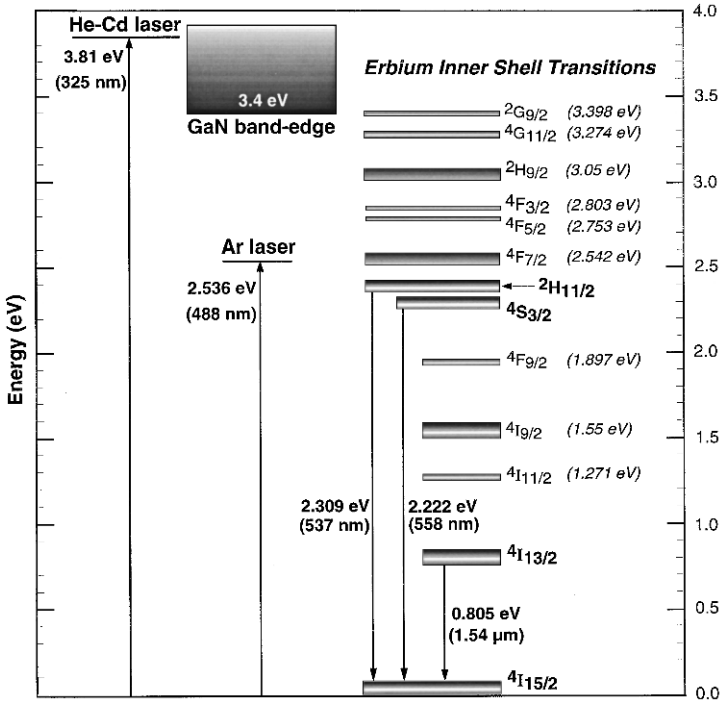

Fig. 5.1. Energy levels relevant to PL and EL of GaN:Er films: Er 4*f* energy levels, GaN bandgap energy and excitation laser photon energies.

In earlier times, Er was incorporated into GaN through ion implantation and reactive sputtering. Ion implantation creates lattice damage that often requires to be healed by post-implantation annealing. However, complete recovery of the implantation damage is difficult to achieve. Research done in the late 1990s on GaN:Er focused on photoluminescence (PL), and photoluminescence excitation spectroscopy (PLE). While the GaN was of poor quality, strong Er-related PL emissions at visible wavelengths (537 and 558 nm) were reported [1, 7, 8, 9, 10, 11, 12] in addition to weak PL emission at 1.54 μm. Techniques for the doping of III-nitrides now include *in situ* processes such as molecular beam epitaxy (MBE) and metal organic chemical vapor deposition (MOCVD). *In situ* incorporation of Er into semiconductors produces epilayers of high crystalline quality and improved Er-related emission compared to implanted samples.

5.2 Er Doping of GaN and InGaN by Ion Implantation

This section summarizes the work done on ion-implanted GaN:Er and InGaN:Er for 1.54 μm emission applications. Ion implantation was one of the earliest methods for incorporating Er atoms into GaN hosts. Since ion implantation is a non-equilibrium process, it is not limited by solubility constraints or by surface chemistry. Furthermore, the precise control of dosage and doping profile offered by implantation of heavy ions is very attractive in semiconductor device fabrication. Complex profiles can be achieved by multi-energy implants.

In GaN implanted with Er, the majority of Er^{3+} ions are substitutional on Ga sites. The influence of site on the PL emission and the optical excitation mechanism has been the subject of widespread discussion. Furthermore, the optimization of Er concentration and post-implantation annealing and the influence of co-doping with O, F, etc. has generated a considerable amount of research. However, the results from different groups are not consistent and in some cases even contradictory, which may relate to differing crystalline quality, mainly the presence of defects and dislocations in GaN produced by different growth techniques, (sputtering, MBE, and MOCVD) as well as the use of non-standardized excitation conditions to study the optical properties.

Wilson et al. [7] studied GaN grown by MBE on GaAs and sapphire substrates. Er was implanted at room temperature with a fluence of $2\times10^{14}cm^{-2}$ at 300 keV, and O was co-implanted at 40 keV with a fluence of 1×10^{15} cm^2 to enhance the optical activation of Er. The PL spectra obtained with below-bandgap excitation by a 457.9 nm argon ion laser at different temperatures is shown in Fig. 5.2. Torvik et al. [13] reported electroluminescence (EL) at 1.54 μm from metal-insulator-n (m-i-n) GaN diode structures grown on R-plane sapphire substrates. The active layer of the diode was co-implanted with Er and O in Zn-doped insulating GaN. Implantation of Er at 350 keV and O at 80 keV, with fluences of 1×10^{15} and 1×10^{16} ions cm^2 respectively was used, followed by annealing at 800^0C for 45 minutes under NH_3 gas flow. They reported a ×10 increase in 1.54 μm emission intensity with O co-implantation. The

EL intensity at 1.54 μm under reverse bias was 3 times stronger than that with 980 nm laser excitation. In addition, the electrical excitation cross-section of Er^{3+}, 6×10^{-16} cm^2 under reverse bias, was five orders of magnitude greater than that of optical resonance excitation by a 980 nm laser ($5\times10^{-21}cm^2$). No EL was observed at 1.54 μm under forward bias. The EL and PL spectra of m-i-n-GaN diodes are shown in Fig. 5.3. Later, the same group studied [14] PL, cathodoluminescence (CL), and EL from Er- and O- co-implanted n-type GaN grown by halogen chemical vapor evaporation (HVPE) on R-plane sapphire substrates (with electron mobility 150 cm^2/Vs and concentration 1×10^{18} cm^{-3}). The optimum ratio of O to Er was studied in the range from 5:1 to 10:1(Er ~ $2\times10^{15}cm^{-2}$ and O ~ 1×10^{16} cm^2) for the strongest emission at 1.54 μm. Lifetime measurements of 1.54 μm emission were made under different optical and impact excitation conditions. The results are shown in Fig. 5.4 and Fig. 5.5, respectively. The measured lifetimes for 1.54 μm emissions were 2.33, 2.15 and 1.74 ms for resonance excitation with 980 nm lasers, above-bandgap excitation at 337 nm, and EL under reverse bias, respectively. The shorter lifetimes for above-bandgap excitation and EL under reverse bias may be related to an increase in non-radiative channels due to interactions between excited Er ions and the GaN host.

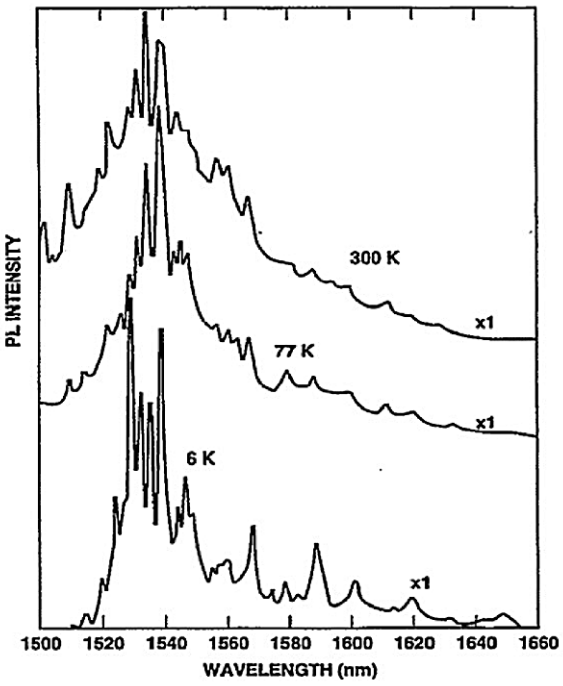

Fig. 5.2. PL spectra of Er-implanted GaN measured at different temperatures.

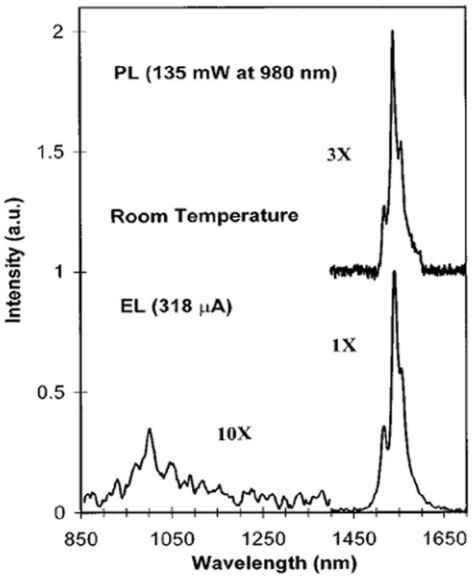

Fig. 5.3. EL (lower) and PL (upper) spectra with 980 nm excitation.

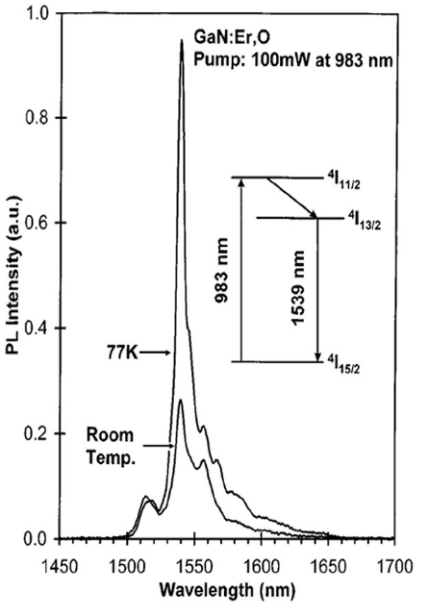

Fig. 5.4. PL spectra at different temperatures with resonant excitation by 983 nm laser.

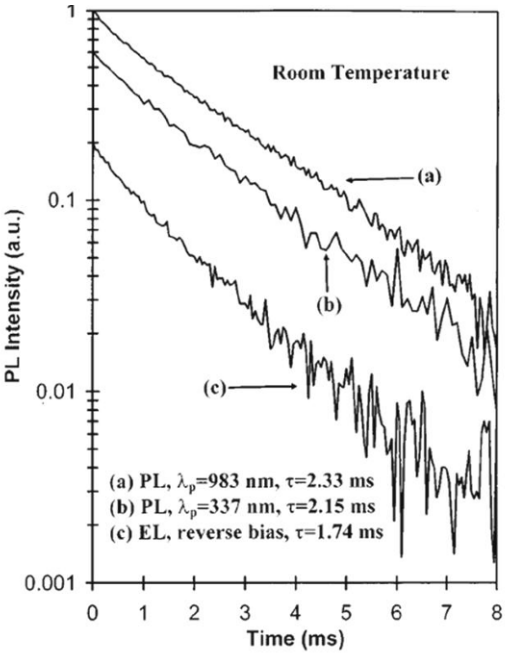

Fig. 5.5. Decay of 1.54 μm emission of GaN:Er for different excitation wavelengths.

Kim et al. [15] performed PLE experiments on 1.54 μm emission from Er-implanted GaN grown by MOCVD on c-plane sapphire substrates and observed three distinct PL spectra, two related to absorption by defects and background impurities or their complexes, and the third to an exciton bound to an Er-related trap. Thaik et al. [16] studied the PL of Er-implanted GaN grown by reactive ion-beam MBE. Er was implanted at 300 keV to a fluence of 2×10^{14} cm^2 and O later co-doped at 40 keV to a fluence of 1×10^{15} cm^2. The post implantation annealing temperature was 650 ºC. They observed strong 1.54 μm emission from the GaN:Er,O layer using both below (488 nm) and above (325 nm) bandgap excitations. The thermal stability of above-bandgap excitation was better than that of below-bandgap excitation. Their results are shown in Fig. 5.6 and Fig. 5.7, respectively. Kim et al. suggested in subsequent work [9] an increase in excitation efficiency of Er^{3+} in GaN by appropriate co-dopants. Their results showed an enhancement of the intensity of the 1554.8 nm emission under 404 nm excitation. Er was implanted into MOCVD GaN at 280 keV with a fluence of 4×10^{13} ions cm^{-2} and the post implantation annealing was done at 900 ºC for 90 min under flowing nitrogen. The results are shown in Fig. 5.8.

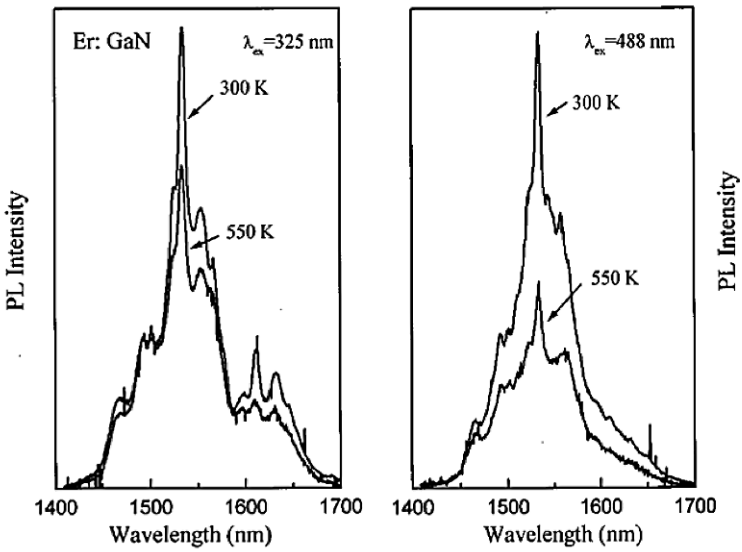

Fig. 5.6. PL spectra at different temperatures with above-bandgap (left) and below-bandgap (right) excitation.

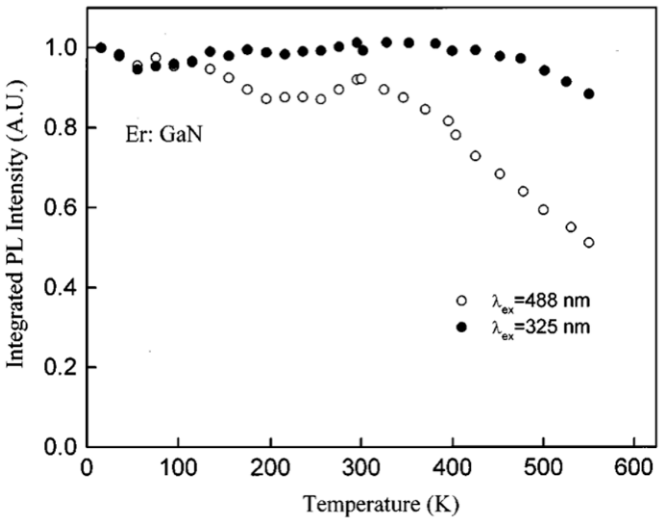

Fig. 5.7. Thermal quenching of 1.54 μm emission with above-bandgap (325 nm) and below-bandgap (488 nm) excitation.

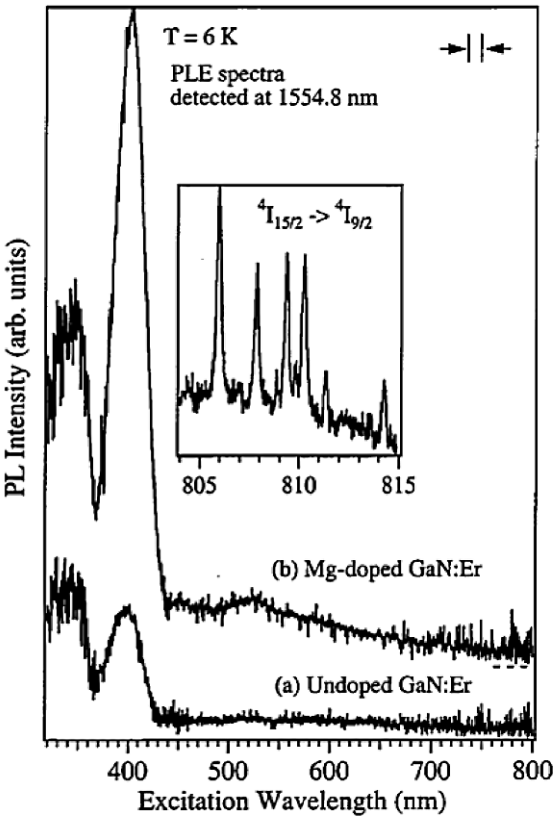

Fig. 5.8. PLE spectra of 1.5548 μm emission from GaN:Er epilayers with and without Mg co-doping.

Correia et al. [17] studied PL of Er-implanted $In_{.07}Ga_{.93}N$ grown on sapphire substrates by MOCVD. Er was implanted at 150 keV with a fluence of 1×10^{15} ions cm^2 and annealed at 400 ºC for 30 min *in vacuo*. Under below-bandgap excitation at 488 nm they observed a complex temperature dependence of the main peak at 1535.3 nm with two thermal activation energies of 33 ± 4 and 189 ± 86 meV. Their results are shown in Fig. 5.9 and Fig. 5.10, respectively.

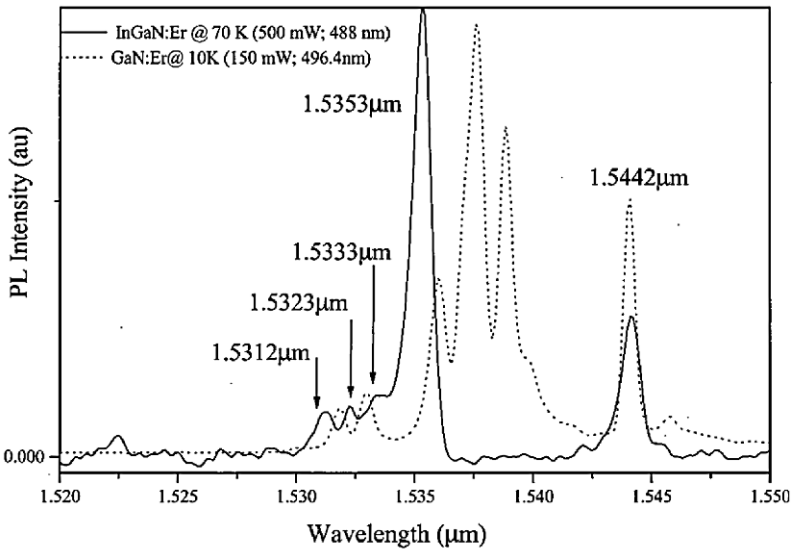

Fig. 5.9. PL at 70 K of Er-implanted GaN (dashed line) and InGaN (solid line).

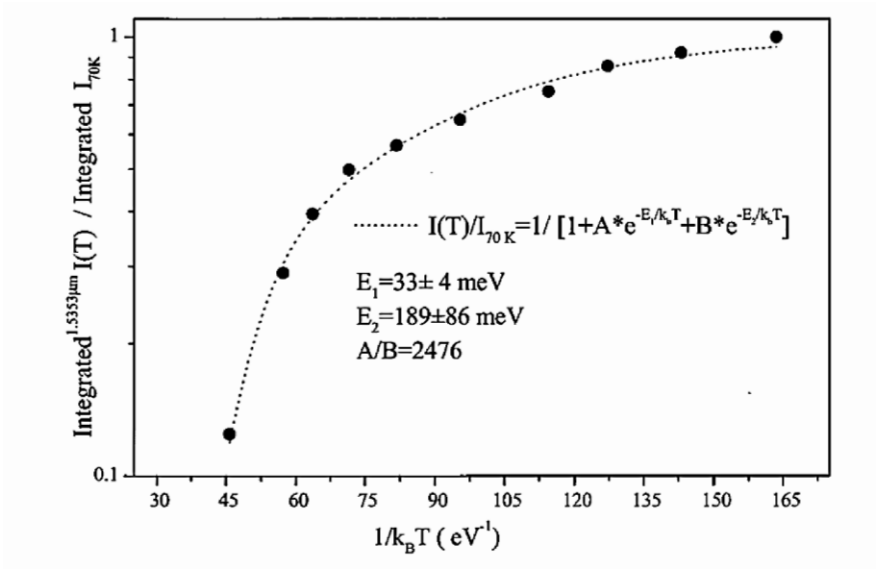

Fig. 5.10. Arrhenius plot of PL emission at 1535.3 nm of Er-implanted $In_{.07}Ga_{.93}N$.

Zavada et al. [18] studied the influence of annealing temperature on the 1.54 μm emission of MOCVD GaN films co-implanted with Er and O at 300 and 40 keV with fluences of 5.7×10^{13} and 1.2×10^{15} ions cm^2, respectively. This was the first report on O, Er co-implantation in GaN grown by MOCVD. Different optimum annealing temperatures for 1.54 μm emission were ascribed to different energy transfer mechanisms for below and above-bandgap excitations. The PL spectra with below (442 nm) and above-bandgap (351.1 and 363.8 nm) excitation are presented in Fig. 5.11 and Fig. 5.12, respectively. Lu et al. [19] reported the influence of annealing on the properties of Er-implanted GaN films grown on SiC and Si substrates by MBE. Er was implanted at 180 keV with fluences varying from 5×10^{13} to 5×10^{15} cm^{-2}. They found that the optimum annealing temperature was 950 ºC. The PL at 1.54 μm obtained by below-bandgap excitation (488 nm) is shown in Fig. 5.13. They also studied the dependence of 1.54 μm emissions on implantation dose (Fig. 5.14). The PL intensity tends to saturate beyond an Er fluence of 5×10^{14} cm^{-2}, due to the greater crystal damage that occurs with higher implantation doses.

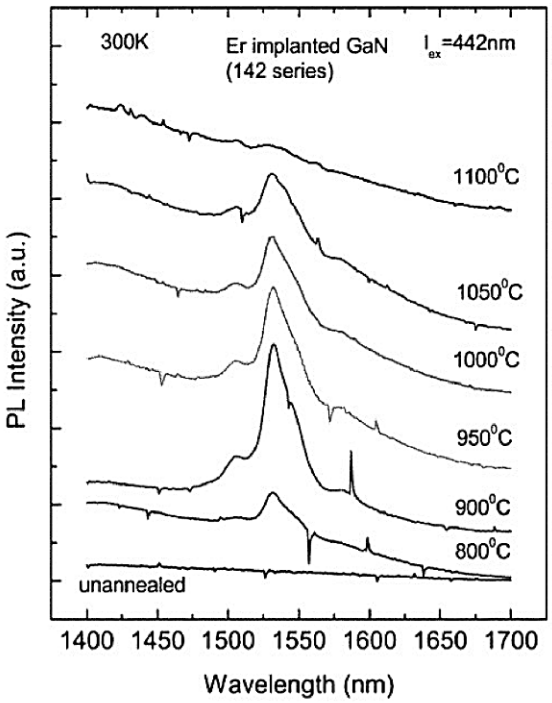

Fig. 5.11. Annealing temperature dependence of PL spectra of GaN co-implanted with Er,O under below-bandgap excitation (442 nm).

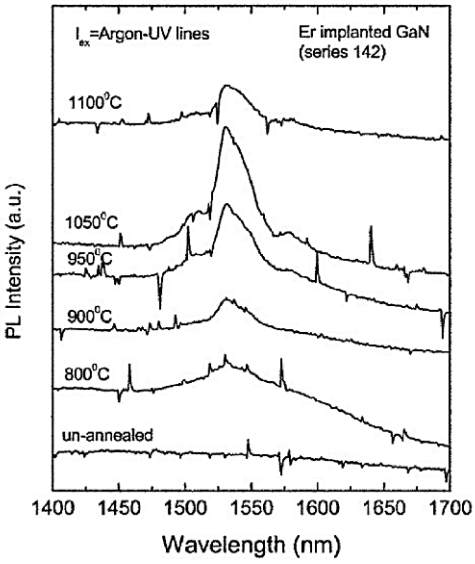

Fig. 5.12. Annealing temperature dependence of PL spectra of GaN co-implanted with Er,O under above-bandgap excitation (351.1-363 nm).

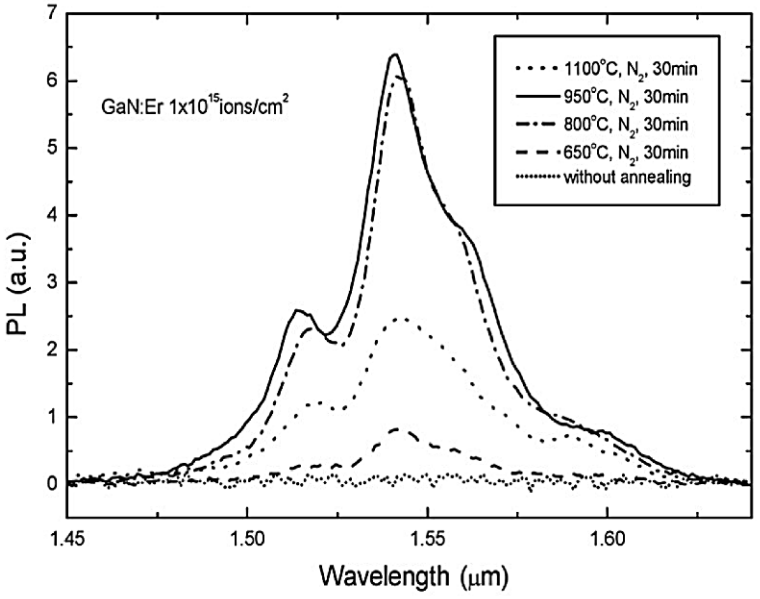

Fig. 5.13. Annealing temperature dependence of PL spectra of Er-implanted GaN under N_2 gas flow.

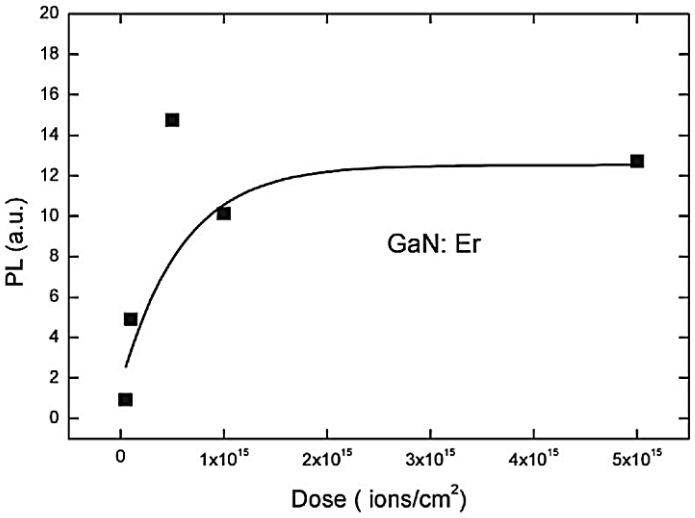

Fig. 5.14. Implantation dose dependence of 1.54 μm GaN:Er emission intensity.

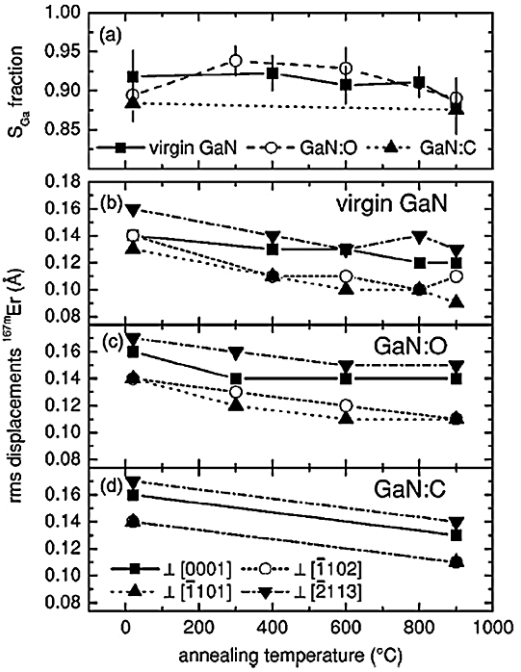

Fig. 5.15. Annealing temperatures dependence of substitutional fraction and average Er atom displacements from the Ga lattice site in Er-implanted GaN.

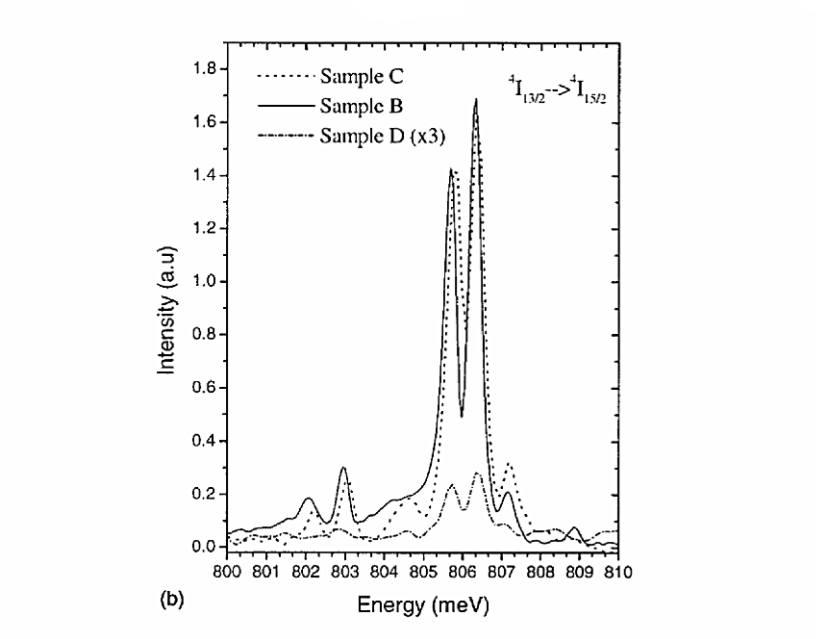

Fig. 5.16. PL spectra of GaN:Er (Er ~ 1×10^{15} cm^{-2}) implanted at 550 ºC (sample **B**, at room temperature (sample **C**, at room temperature with O co-implantation (sample **D**.

De Vries et al. [20] studied the influence of O and C co-implantation on the occupation site of Er in GaN by using emission channelling techniques. They suggested that 90% of implanted Er ions occupy Ga lattice sites and co-implanting with O or C does not significantly affect the incorporation of Er into Ga sites in the case of low-dose Er implantation (< 2.0×10^{13} cm^{-2}). They further observed that annealing up to 900 °C does not change the occupancy of Ga sites by Er ions. The only noticeable effect due to O or C implantation is a small (average) displacement of Er atoms, which is shown in Fig. 5.15.

Monteiro et al. [21] studied emission from Er-implanted GaN grown by MOCVD with and without subsequent O co-implantation. Rutherford back scattering (RBS) experiments showed better recovery of damage caused by implantation for the samples without O co-implantation compared to co-implanted samples. This conclusion was further supported by observing the highest intensity (and narrowest line width) of the 1.54 μm emission from samples without O co-implantation. PL measurements were carried out at 4.2 K using below-bandgap excitation (496.4 nm) and the spectra are shown in Fig. 5.16. The observation of a broad yellow band (at ~ 2.1 eV) in O co-implanted samples indicated the presence of defects. Their results contradict the earlier results of Torvik et al. [14]. Similar contradictory results were also reported by Song et al. [22], who performed Raman scattering and PL studies of Er-implanted and Er, O co-implanted GaN grown on sapphire substrates by MOCVD. The Er was implanted at 400 keV with

fluences ranging from 3×10^{13} to 3×10^{15} ions cm^{-2}. O was co-implanted in one sample at 80 keV with a fluence of 3×10^{13} ions cm^{-2}. These implantation fluences are in the same range used in other reported works. However, the PL spectra, shown in Fig. 5.17, revealed that the intensity at 1.54 μm for the Er-only sample is more than an order higher than that from Er, O co-implanted samples with the same Er doping.

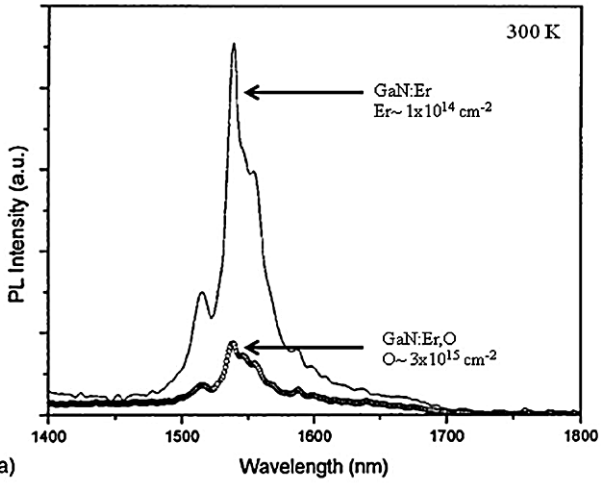

Fig. 5.17. Room temperature PL spectra of Er implanted GaN with and without O co-implantation.

While electrical properties are very important for semiconductor devices, very few such results have been reported on Er-implanted GaN. Song et al. [23] reported the electrical characterization of Er-implanted GaN grown on sapphire substrates by MOCVD. The room temperature free-electron concentration, Hall mobility, and resistivity of unimplanted template material were 2.1×10^{17} cm^{-3}, 437 cm^2/Vs, and 0.063 Ω cm, respectively. After Er implantation at 400 keV to a fluence of 3×10^{15} ions cm^{-2}, the resistivity increased to 10^7 Ω cm due to implantation-generated defects and electron traps, which reduce free carrier concentration and mobility. The implanted samples were annealed at 900 ºC for 30 min in nitrogen. After annealing, electron concentration, Hall mobility and resistivity of the samples were found to be 9.82×10^{16} cm^{-3}, 96 cm^2/Vs, and 0.67 Ω cm, respectively. Even after post-implantation annealing, an increase in resistivity by an order of magnitude, a decrease in free electron concentration by 50% and of mobility by a factor of 4, indicate that the implantation caused significant impairment of the crystalline quality, which could not be recovered completely by post implantation annealing at 900 ºC. The crystalline and optical quality degradation due to implantation imposes a major challenge to the realization of current injected functional devices based on GaN:Er material prepared by this method.

From these results on Er-implanted GaN host semiconductors grown by different methods, it is apparent that the 1.54 μm emission intensity not only depends on the excitation mechanism (above vs. below-bandgap excitation), but also on the crystalline quality and the impurities present in the GaN host semiconductors. For GaN samples grown by MOCVD, co-implantation of O with Er does not enhance the optical activity of Er^{3+} emission centers; rather it increases the non-radiative recombination centers and thus decreases emission intensity at 1.54 μm. In MOCVD grown samples, high concentrations of O may already be present (particularly in samples grown earlier). Er implantation may further degrade the crystalline quality which cannot be fully recovered with post implantation annealing.

5.3 *In Situ* Er Doping of GaN by MBE and HVPE

In situ doping of nitride materials during epitaxial growth has several important advantages for photonic device development including the avoidance of implantation damage and a more homogeneous doping profile. Furthermore, with *in situ* doping, Er can be selectively incorporated into active layers such as quantum wells (QWs) and quantum dots (QDs) of light emitting diodes (LEDs), laser diodes (LDs), and in the core region of planar waveguide amplifiers for photonic device applications. MBE and Hydride Vapor Phase Epitaxy (HVPE) are well-established growth techniques for III-nitride materials and devices [24, 25]. For *in situ* Er^3doping using these methods, challenges arise for efficient Er^{3+} emissions concerning the crystalline quality, electrical and optical properties and electrical activity of Er^{3+}. In this section we summarize the important results.

Mackenzie et al. [24] were the first to incorporate Er into GaN on sapphire and Si substrates during epitaxial growth by Metallorganic Molecular Beam Epitaxy (MOMBE). The Er concentration measured by secondary ion mass spectrometry (SIMS) was 3×10^{18} cm^{-3}. They also observed the presence of unintentionally incorporated O and C. The PL spectra centered at 1.54 μm, using 488 nm below-bandgap excitation, are compared in Fig. 5.18 for Er-doped GaN grown on sapphire and Si substrates under identical conditions. The influence of background O and C concentrations on the optical activity of Er^{3+} was also studied by monitoring the PL intensity at the 1.54 μm region and the thermal quenching behavior of PL intensity. The results are shown in Fig. 5.19 and Fig. 5.20, respectively. With the same concentration of Er, the PL intensity at 1.54 μm is more than two orders of magnitude higher for background concentrations of O and C increased from < 10^{19} cm^{-3} to 10^{20} cm^{-3} (O) and 10^{21} cm^3 (C), respectively. For samples with higher O and C levels in GaN:Er grown on sapphire, the PL intensity quenched by only 10% when temperature increased from 15 to 300 K, while for samples with lower O and C concentration, the quenching increased to 85%. For these samples, a detailed study of the crystalline quality was not reported. The excitation laser line (488 nm) is below the bandgap of the host and the energy transfer process for the

1.54 μm emission was likely to be due to the defects in the intermediate state of the energy transfer mechanism. The enhanced optical emission at 1.54 μm observed in GaN:Er samples with higher concentrations of impurity elements, such as O and C, could be related to the more ionic state of local bonds because the impurity elements form ligands with Er which change the local bonds into a more ionic state.

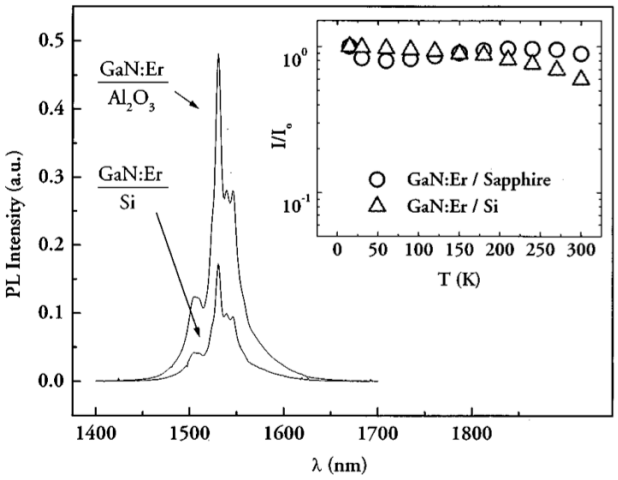

Fig. 5.18. PL spectra of MBE-grown GaN:Er films on Al_2O_3 and Si substrates. Inset compares the thermal quenching of 1.54 μm emission from GaN:Er grown on Al_2O_3 (open circle) and Si (open triangle).

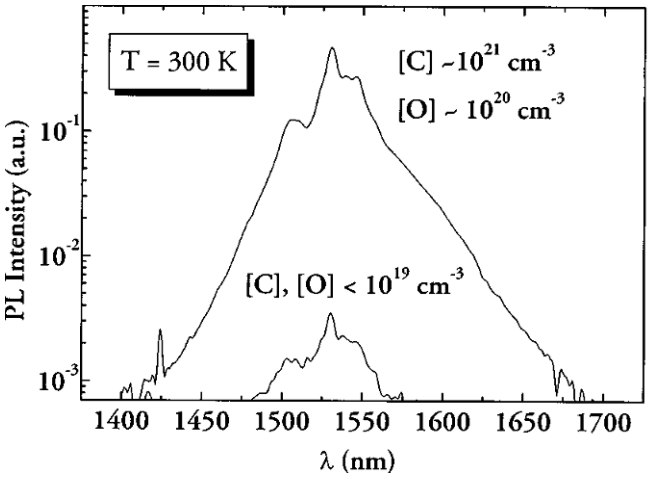

Fig. 5.19. PL spectra of MBE-grown GaN:Er epilayers with different impurity (O and C) concentrations.

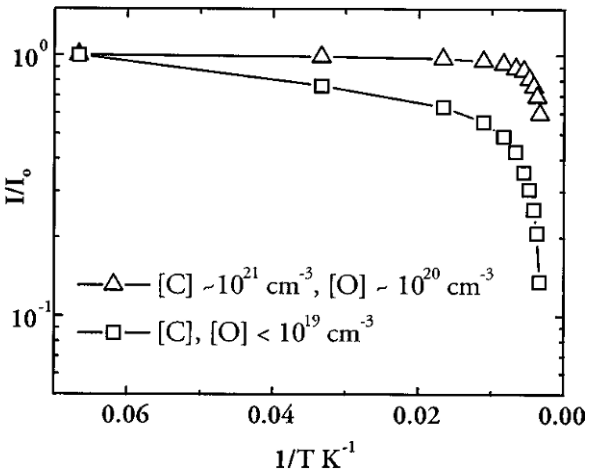

Fig. 5.20. Quenching behavior of 1.54 μm emission from MBE-grown GaN:Er epilayers with different impurity (O and C) concentrations.

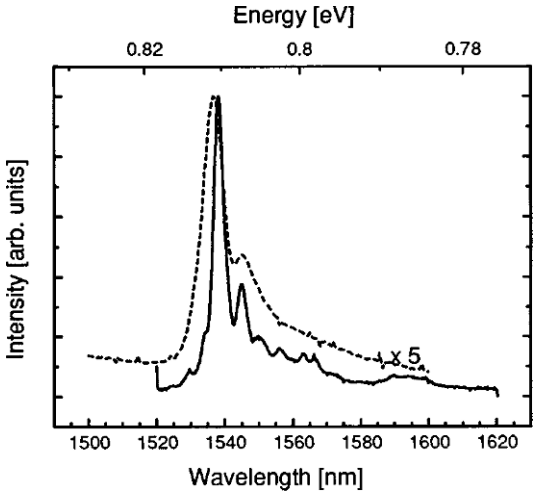

Fig. 5.21. PL spectra at 11 K of *in situ* Er-doped GaN grown by HVPE (solid line) and Er-implanted HVPE-grown GaN (dashed line).

Hansen et al. [25] reported *in situ* doping of Er in GaN by HVPE. A 20 μm thick GaN film was grown using a V/III ratio of 30 at a substrate temperature of 1030 ºC. The Er concentration determined by SIMS was 2×10^{19} cm^{-3} near the top surface (to a depth of 0.1 μm) and decreased to 1×10^{18} cm^{-3} throughout the remaining epilayer. The PL emission with 488 nm laser excitation was, at 1536.5 nm, blue shifted by 2.5 nm compared to ion-implanted GaN, also grown by HVPE with Er and O co-implantaton at average concentrations of 5.3×10^{19} cm^{-3} and 3.4×10^{20} cm^{-3}, respectively. PL intensity of the *in situ* Er-doped material was 5

times weaker than that of implanted samples (see Fig. 5.21). Decay times were significantly longer for Er+O co-implanted samples (~ 2.9 ± 0.1 ms) than for samples doped *in situ* (~ 2.1 ± 0.1 ms). It was suggested that the difference in lifetimes could be due to different excitation mechanisms related to different Er^{3+} centers in the samples.

Overberg et al. [26] studied the influence of C co-doping on surface morphology and 1.54 μm PL intensity of GaN:Er epilayer grown by MBE. Fig. 5.22 shows the integrated PL intensity at 1.54 μm as a function of CBr_4 flow rate. The optimum CBr_4 flow rate for smooth surface morphology and enhanced 1.54 μm PL intensity was determined. They suggested that formation of an Er-C complex initially increases the PL intensity; however increased C concentrations create defects, which increased non-radiative recombination and reduced emission intensity at 1.54 μm.

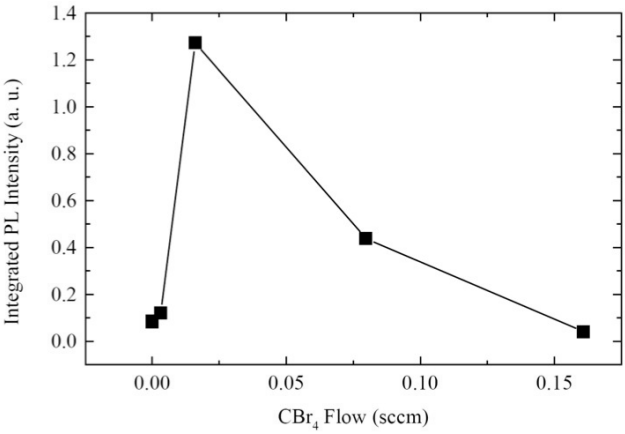

Fig. 5.22. Integrated PL intensity at 1.5 μm for Er, O co-doped GaN grown by MBE, as a function of CBr_4 flow rate.

A two-step growth process was adopted to grow GaN:Er/AlGaN single heterostructures (SH) and AlGaN/GaN:Er/AlGaN double heterostructures (DH) [7, 27]. It combines growth by MOCVD of AlGaN n- and p-layers with MBE growth of active layers. In the SH an Er-doped GaN epilayer was grown by MBE on an MOCVD-grown 1 μm thick $Al_{0.12}Ga_{0.88}N$/sapphire template. For the DH, a 200 nm $Al_{0.12}Ga_{0.88}N$ layer was grown on top of a previously grown SH. Samples with GaN:Er thicknesses of 7 and 200 nm were studied. Fig. 5.23 compares PL spectra at 1.54 μm of SH (dotted line) and DH (solid line) structures with 200 nm GaN:Er active layers. The excitation wavelength (496.5 nm) is below the bandgap of GaN. The comparable PL intensity for SH and DH structures indicates no influence of confinement. However, with above energy gap excitation (336 to 363 nm) a significant difference was noticed, as shown in Fig. 5.24: the PL of the DH was 3

times more intense than that of the SH. Under above-bandgap excitation, Er^{3+} is excited by photo-generated excitons or charge carrier pairs and the improved PL emission efficiency in DH could be related to the better confinement of excitons or carriers by band offsets between GaN:Er and $Al_{0.12}Ga_{0.88}N$ layers as well as reduced surface recombination and greater probability of e-h pair recombination near Er related complexes. In subsequent work, Zavada et al. [7] studied EL of GaN:Er,O LEDs using DH structures prepared by two-step growth. The layer structure was p-$Al_{0.12}Ga_{0.88}N$/GaN:Er,O/n-$Al_{0.12}Ga_{0.88}N$ on sapphire substrates with p- and n-$Al_{0.12}Ga_{0.88}N$ MOCVD layers and GaN:Er, O MBE layer. The concentrations of Er and O in the active layer were ~ 10^{18} cm^{-3}. The EL spectrum measured at 10 K under reverse bias is shown in Fig. 5.25.

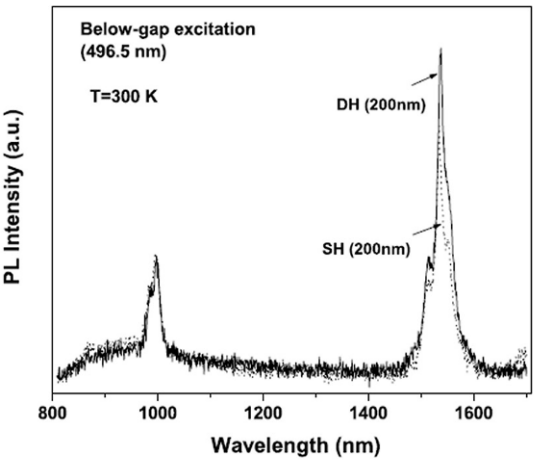

Fig. 5.23. Room temperature PL spectra of a 200 nm GaN:Er/AlGaN SH (dotted line) and a 200 nm AlGaN/GaN:Er/AlGaN DH (solid line) under below-bandgap excitation (496.5 nm).

Though many groups have reported PL, PLE, and EL of Er-doped GaN, there are few reports on the influence of crystalline quality on the optical properties. Chen et al. [28] doped MBE GaN with Er to concentrations varying from 0.1 to 7 at% as determined by RBS. Reflection high-energy electron diffraction (RHEED) patterns were used to monitor the crystalline quality during growth. Representative patterns for Er concentrations of 1, 2, 4, and 7 at% are shown in Fig. 5.26. Optical quality was monitored by measuring the PL transition at 558 nm from $^4S_{3/2}$ to the ground state ($^4I_{15/2}$). The PL intensity increases with increasing Er concentration up to 4 at% and then decreases (Fig. 5.27). A typical spotty RHEED pattern is observed up to 4 at% Er which indicates single crystalline growth. However, a ring-like pattern indicated polycrystalline growth for the 7 at% sample. A decrease in PL intensity beyond 4 at% of Er could therefore be related to the degradation of crystalline quality which generates non-radiative centers.

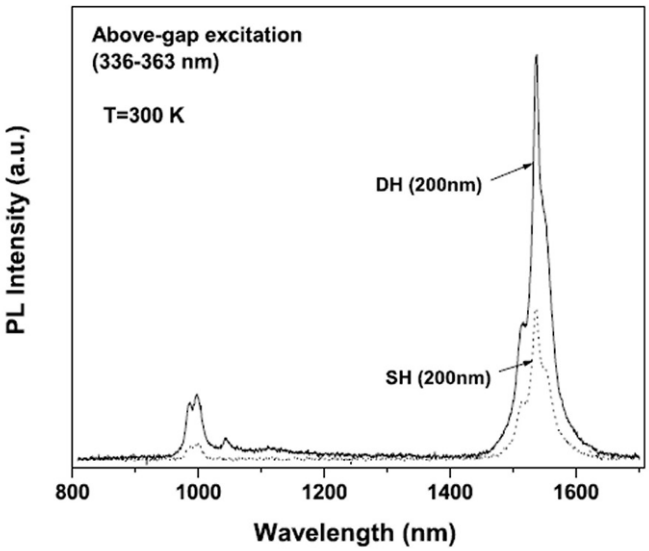

Fig. 5.24. Room temperature PL spectra of a 200 nm GaN:Er/AlGaN SH (dotted line) and a 200 nm AlGaN/GaN:Er/AlGaN DH (solid line) under above-bandgap excitation (336 -363 nm).

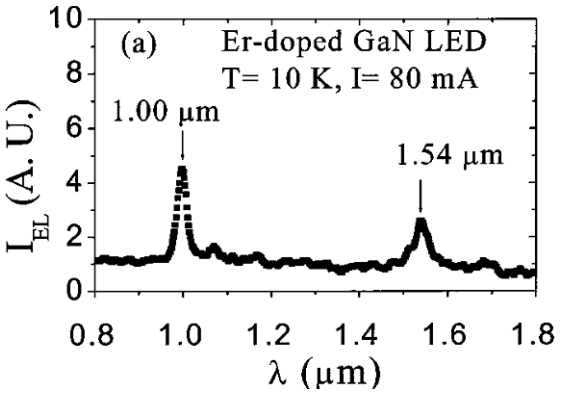

Fig. 5.25. EL spectrum of Er-doped nitride LED grown by two-step growth (MBE & MOCVD) at 10 K under reverse bias with a driving current of 80 mA.

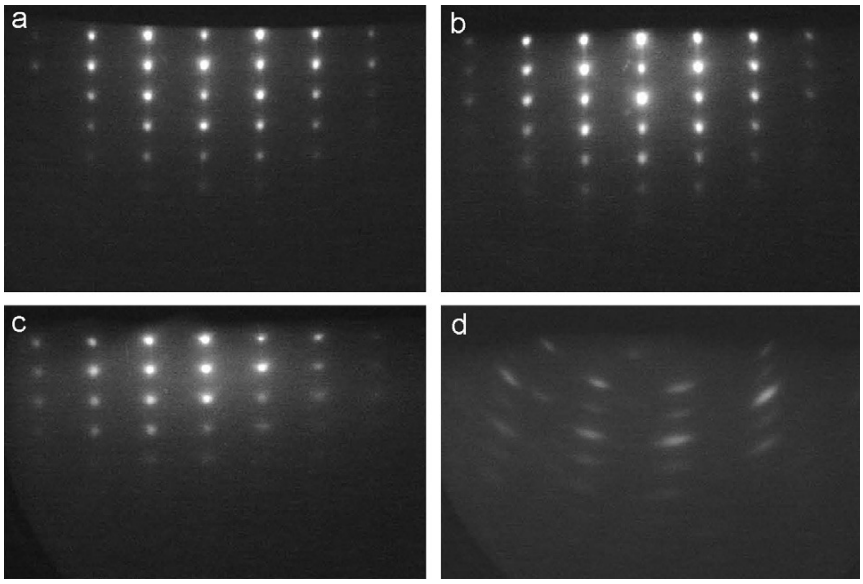

Fig. 5.26. RHEED patterns of *in situ* doped GaN:Er grown by MBE with Er concentrations of (a) 1 at%, (b), 2 at%, (c) 4 at%, and (d) 7 at%, respectively.

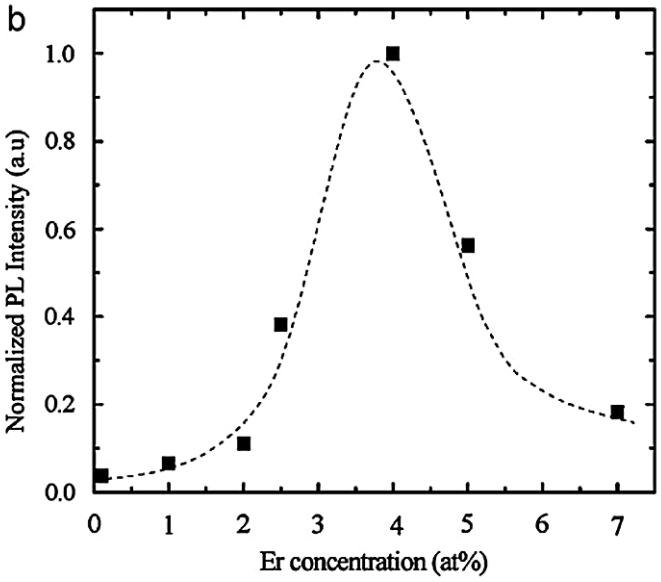

Fig. 5.27. Er concentration dependence of PL intensity at 77 K of *in situ* doped GaN:Er grown by MBE.

Positron annihilation techniques have been used to study vacancy-type defects in MBE-grown GaN:Er [29]. A clear correlation between the defect concentration and the PL intensity at 511 nm was observed. The major defect species identified by positron annihilation was the Ga vacancy (V_{Ga}) that increased with Er concentration.

5.4 MOCVD Growth of Er-Doped III-Nitrides

In this section, we summarize recent progress on the growth of III-N:Er epilayers by MOCVD, and their optical, crystalline, and electrical properties. Most prior research work has focused on samples doped either by ion implantation or *in situ* by using MBE or HVPE. One challenging problem of MBE GaN:Er devices is the requirement to produce IR emission at 1.54 μm via injection of electrons under high field reverse bias [7]. Furthermore, these devices suffer from competing emission in the visible region, severely limiting their prospects for optical communication applications. MOCVD is an alternative well-established growth method for III-nitrides, and almost all commercial III-nitride photonic devices are grown by MOCVD. However, a major problem in incorporating Er ions into III-nitride materials using MOCVD is the low vapor pressure of available Er precursors.

Recently, Er-doped GaN and InGaN epilayers have been grown by MOCVD [30, 38, 41, 42]. Growth begins with deposition of a thin GaN buffer layer on sapphire, followed by a GaN template with thickness ~1.5 μm and an Er-doped GaN layer, both grown at 1040 ºC. The Er-doped $In_xGa_{1-x}N$ ($0 < x < 0.2$) sample structure was very similar [30]. Growth of the epilayer began with a thin GaN buffer layer and a 1.5 μm GaN epi-template followed by a 300 nm $In_xGa_{1-x}N$:Er ($0 < x < 0.2$) layer grown at 760 ºC. The InN content of the Er-doped InGaN epilayers was determined from the x-ray diffraction (XRD) peak positions of θ-2θ Ω scans. The full width at half maximum (FWHM) of XRD rocking curves of the (002) plane was utilized to determine the crystalline quality. A Quesant Q-scope 250 atomic force microscope (AFM) was used to characterize the surface morphology, and the optical properties were determined by PL spectroscopy. Fig. 5.28 shows the Er profile for one of our epilayers as probed by SIMS.

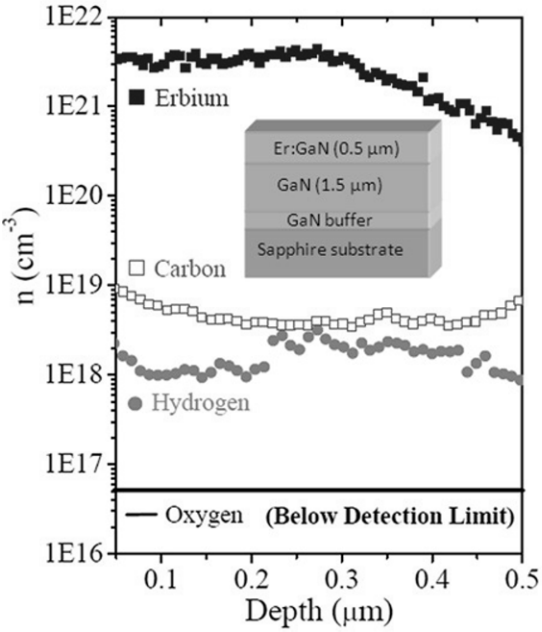

Fig. 5.28. Er, C and H SIMS profiles of Er-doped GaN grown by MOCVD. The inset shows the layer structure.

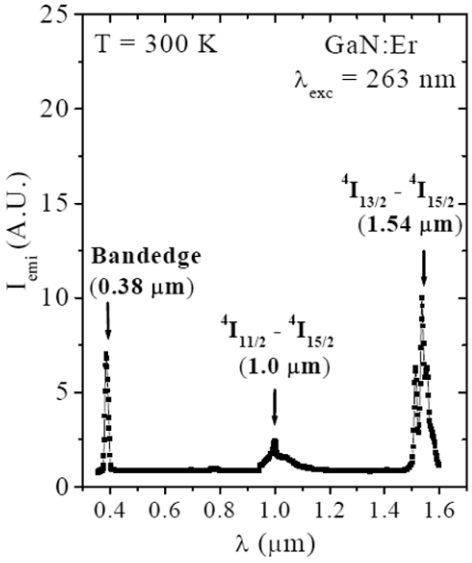

Fig. 5.29. Room temperature PL spectrum with 263 nm excitation of MOCVD-grown GaN:Er.

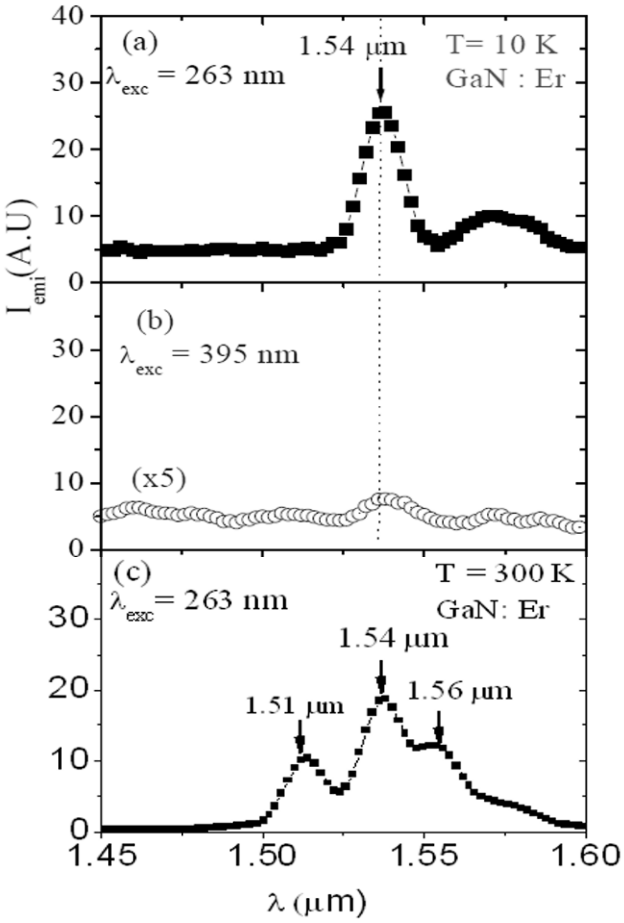

Fig. 5.30. PL spectra at 10 K of GaN:Er with (a) above bandgap (263 nm) and (b) below-bandgap (395 nm) excitation; (c) PL spectrum at RT with λ_{exc} = 263 nm.

5.4.1 Er-Doped GaN

Fig. 5.29 is a room temperature PL spectrum of Er-doped GaN covering wavelengths in the visible and IR regions, for an excitation wavelength (λ_{exc}) of 263 nm. Two emission lines are observed at 1.0 and 1.54 μm, with a full width at half maximum of 10.2 and 11.8 nm, respectively, corresponding to intra-*4f* transitions from the $^4I_{11/2}$ (second excited state) and the $^4I_{13/2}$ (first excited state) to the $^4I_{15/2}$ (ground state), respectively. The intensity of 1.54 μm emission is much stronger than that of the 1.0 μm emission. Fig. 5.29 also shows that virtually no visible emission is observed from Er-doped GaN epilayers grown by MOCVD. This is in

sharp contrast to the results of Er-doped GaN obtained by MBE or ion implantation, which exhibit the dominant intra-4f Er^{3+} transitions from the $^2H_{11/2}$ (537 nm) and $^4S_{3/2}$ (558 nm) levels to the $^4I_{15/2}$ ground state [1, 31, 32].

Fig. 5.30 compares PL spectra of Er-doped GaN excited at 10 K with (a) above-bandgap excitation (λ_{exc} = 263 nm) and (b) below-bandgap excitation (λ_{exc} = 395 nm). PL intensity of the 1.54 μm emission with λ_{exc} = 263 nm excitation is observed to be an order of magnitude larger than that with λ_{exc} = 395 nm, indicating that the generation of electron-hole (*e-h*) pairs with above-bandgap excitation results in a more efficient energy transfer to Er centers than that through defect centers. Thus, optical amplifiers and emitters operating at 1.54 μm should be more efficient with above-bandgap excitation. Further, it is evident that the 1.54 μm emission is dominant at low temperatures (see Fig. 5.30(a)). As the temperature is increased, two additional emission peaks appear at 1.51 and 1.56 μm (see Fig. 5.30(c)). The presence of multiple peaks near 1.54 μm in GaN:Er may allow broadband optical amplification at room temperature in the main c-band telecommunication wavelength.

A general understanding of the excitation dynamics of the 1.54 μm emission of Er-doped GaN is essential for further improving the material quality. One problem for narrow bandgap semiconductors (NBGS) is the large thermal quenching of the emission. A proposed mechanism of this is an Er-related trap level in the energy bandgap, with an Auger energy transfer via bound carriers or excitons [33, 34, 35]. If the thermal energy of the environment becomes large enough, the carriers or excitons dissociate from the Er centers, resulting in a dramatic drop in energy transfer efficiency which causes thermal quenching of emission.

Fig. 5.31 plots the integrated PL emission intensity (I_{int}) of the 1.54 μm emission line from Er-doped GaN between 10 and 450 K with λ_{exc} = 263 nm. The Er emission has a 20% decrease in I_{int} between 10 and 300 K, which represents the lowest reported degree of thermal quenching for any RE-doped semiconductor [30]. This also provides a better understanding of the low degree of thermal quenching in wide bandgap semiconductors (WBGS). It is well established that for semiconductors, donor ionization energy increases with energy bandgap. The low degree of thermal quenching for Er-doped WBGS may be related to this behavior. For NBGS, the electrons or excitons are loosely bound to the Er trap and can be detached at low temperature. This decreases the efficiency of energy transfer to the *4f* electrons via an Auger-like process. However, for WBGS, the photo-generated electrons or excitons remain bound to the Er trap at higher temperatures since the binding energy is larger. The Auger energy transfer between bound electrons or excitons and *4f* electrons can still occur, and the subsequent thermal quenching is dramatically reduced.

The inset in Fig. 5.31 is an Arrhenius plot of the integrated PL emission intensity at 1.54 μm between 10 and 450 K, fitted by the equation,

$$I_{\text{int}} = \frac{I_0}{1 + ce^{-\frac{E_0}{kT}}} \tag{1}$$

where I_0 is the integrated intensity at low (zero) temperature, c is a fitting constant, E_0 is the activation energy of thermal quenching, and k is the Boltzmann constant. An activation energy of E_0=191 ± 8 meV was determined from the least squares fit of data to Eq. (1).

A dominant near-bandedge emission at 3.23 eV was observed at 300 K, which is red-shifted by 0.19 eV from the 3.42 eV bandedge of undoped GaN (Fig. 5.32 (a)). The difference in transition energy of the bandedge emissions for undoped and Er-doped GaN at room temperature (3.42 – 3.23 = 0.19 eV) equals the estimated thermal activation energy. In order to further clarify the nature of the transition, the decay lifetime was measured by time-resolved PL [36]. The inset in Fig. 5.32 (b) shows the temporal response at 10 K. The lifetime was determined to be 200 ps, which suggests that the emission at 3.23 eV is an impurity-to-band transition [37]. Thus, the 3.23 eV emission line is believed to be due to the recombination between electrons bound to the Er_{Ga}-V_N complex and free holes in the valence band [38]. Here Er_{Ga} represents the substitution of Er on a Ga site and V_N is the nitrogen vacancy. The density functional study of Er-doped GaN by Fihol et al. showed that Er_{Ga}-V_N complexes in GaN have a half-filled energy level approximately 0.2 eV below the conduction band [38]. This theoretical calculation is in good agreement with our experimental results. Our experimental results also match reasonably well with those of Song et al., who used deep level transition spectroscopy (DLTS) to measure a level 0.188 eV below the conduction band [23]. Thus, we conclude that the exchange of energy between the electrons bound to the Er_{Ga}-V_N complex and the 4*f* cores states of Er is the dominant excitation mechanism of 1.54 μm emission in MOCVD-grown Er-doped GaN using above-bandgap excitation.

An important consideration for the realization of practical photonic devices is the effect of Er incorporation on the electrical properties of GaN. Doping GaN with Er may introduce defects that are detrimental to the required electrical conductivity. In Fig. 5.33, we plot the optical and electrical properties (integrated 1.54 μm emission intensity, resistivity, electron mobility, and free electron concentration) of MOCVD grown Er-doped GaN as functions of Er concentrations in the range $(0.2–1)\times10^{21}$ cm^{-3}. The electrical properties are unchanged with an increase in Er concentration. In fact, the values of mobility (~200 cm^2/V s), electron concentration ($\sim2\times10^{17}$ cm^{-3}), and resistivity (~0.2 Ω cm) are comparable to those of high-quality undoped MOCVD-grown GaN (400 cm^2/V s, 2×10^{17} cm^{-3}, 0.05 Ω cm). The slightly higher resistivity of Er-doped GaN is attributed to the slight decrease in electron mobility; however the free electron concentration is unchanged. These results can be explained if we consider the bonding nature of Er within a GaN host. It has been reported that the majority of Er atoms occupy the Ga sites within the hexagonal Wurtzite structure [3]. It is also known that the normal charge state of Er ions inside an ionic host is Er^{3+} [39, 40], the same as that of Ga atoms inside the GaN structure. This implies that the incorporation of Er atoms into GaN is essentially isoelectronic doping, and should not affect the free electron concentration. However, Er atoms act as scattering centers, thereby reducing the electron mobility.

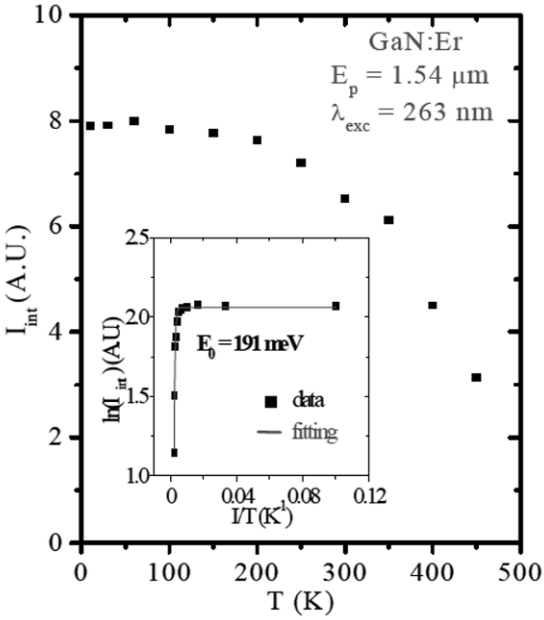

Fig. 5.31. Integrated emission intensity of MOCVD-grown GaN:Er at different temperatures. The inset is an Arrhenius plot of PL intensity.

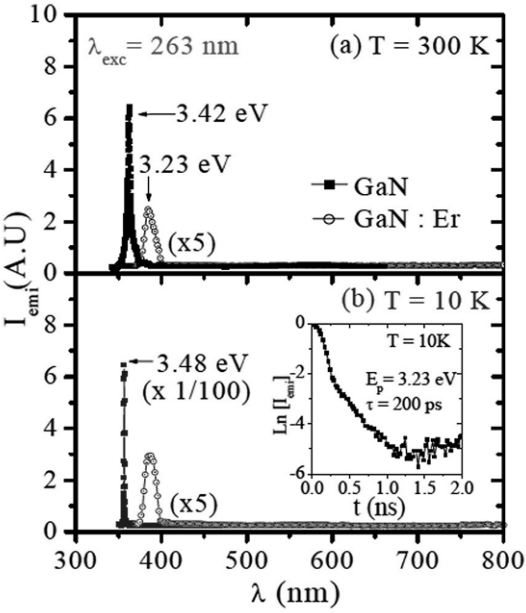

Fig. 5.32. PL spectra of undoped and Er-doped GaN epilayers at (a) room temperature and (b) 10 K. The inset shows PL decay of the 3.23 eV transition.

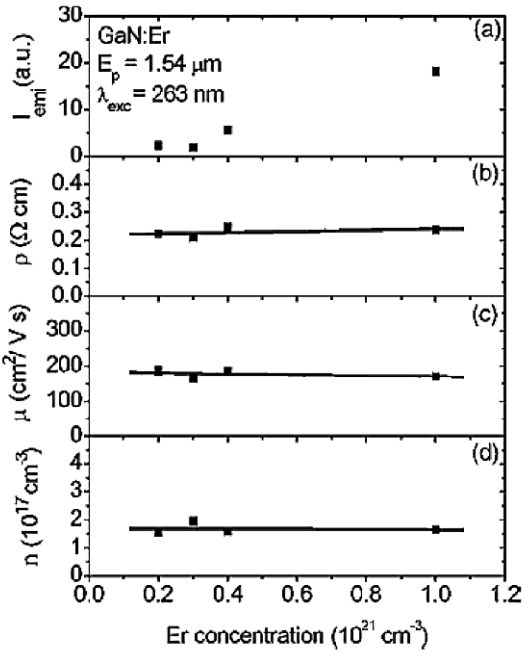

Fig. 5.33. Optical and electrical properties of MOCVD-grown GaN:Er as functions of Er concentration.

5.4.2 Er-Doped InGaN

Recent progress in high-efficiency InGaN-based LEDs and LDs, operating in the blue/green spectral region, has motivated research on Er-doped InGaN with the possibility of either monolithic integration of Er-doped InGaN layers or the incorporation of Er ions into InGaN active layers in heterostructures. The incorporation of Er into InGaN is more challenging than that into GaN mainly due to the lower growth temperature of InGaN and the poor crystalline quality that occurs with high InN content. In this section we discuss the growth of Er-doped InGaN and compare its crystalline quality, surface morphology, and optical properties with those of GaN:Er layers.

Er-doped InGaN was grown on GaN/sapphire templates by MOCVD using the same growth conditions (Er and NH_3 flow rates) as GaN:Er but at a lower growth temperature. Fig. 5.34 shows a θ-2θ XRD scan of an InGaN:Er sample grown on a 1.2 μm GaN/sapphire template at a growth temperature of 760 ºC (cf. 1040 ºC for GaN:Er). Er concentration was of order 10^{21} cm^{-3} for both layers. The (002) diffraction peaks at 34.36 and 34.52 degrees correspond to $In_{.05}Ga_{.95}N$ and GaN, respectively. Atomic Force Microscope (AFM) images of Er-doped $In_{.05}Ga_{.95}N$ and GaN are compared in Fig. 5.35. The root mean square (RMS) surface rough-

ness of Er-doped $In_{.05}Ga_{.95}N$ is higher than that of Er-doped GaN (4 nm compared to 2 nm). Although Er-doped $In_{.05}Ga_{.95}N$ has a relatively rough surface, (002) XRD rocking curves (Fig. 5.36) reveal that the crystalline quality of Er-doped $In_{.05}Ga_{.95}N$ (462 arcsec) is almost the same as that of Er-doped GaN (450 arcsec).

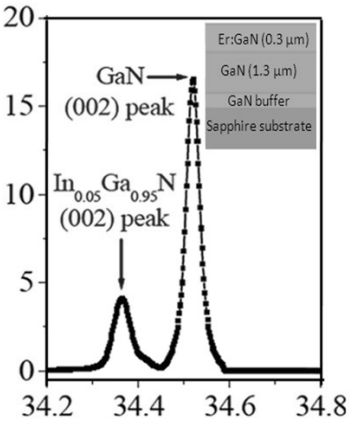

Fig. 5.34. XRD scan for (002) lines of $In_{0.05}Ga_{0.95}N$:Er. The inset shows the epilayer structure.

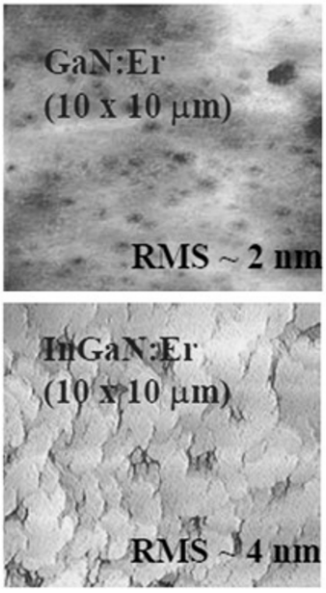

Fig. 5.35. AFM images of GaN:Er and $In_{0.05}Ga_{0.95}N$:Er.

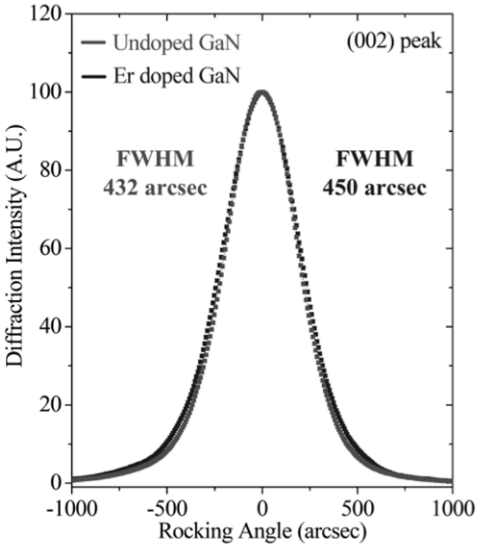

Fig. 5.36. XRD rocking curve of $In_{0.05}Ga_{0.95}N$:Er sample.

Room temperature PL spectra of Er-doped $In_{.05}Ga_{.95}N$ and GaN epilayers for an excitation wavelength λexc = 263 nm are shown in Fig. 5.37. The 1.54 μm PL emission intensity is about an order of magnitude smaller in the $In_{.05}Ga_{.95}N$:Er sample. The drop was attributed to the much lower growth temperature resulting in a relatively poor crystalline quality and decrease in optically active Er^{3+} emitting centers .

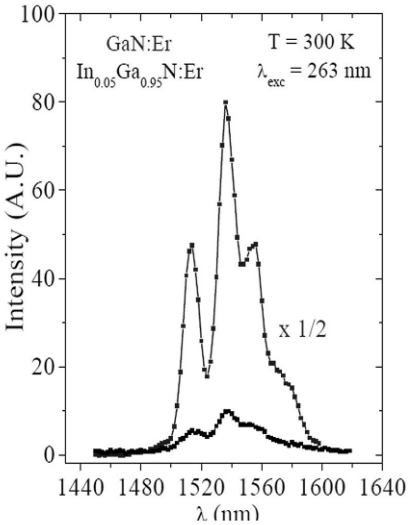

Fig. 5.37. PL spectra of Er-doped GaN and $In_{0.05}Ga_{0.95}N$ grown by MOCVD.

In order to investigate the dependence of 1.54 μm PL intensity on InN fraction, Er-doped InGaN epilayers, with InN content at a fixed growth temperature (T_G = 760 ºC) but varying growth pressures (P_G), and NH_3 and Ga flow rates. The InN content and the crystalline quality of these samples were monitored by XRD. As growth pressure increases, the InN fraction increases from 5 to 16%. The increase in InN content is most likely a result of the larger sticking coefficient for In at higher pressures as predicted by Henry's law. Fig. 5.38 shows PL spectra of $In_xGa_{1-x}N$:Er; the intensity of 1.54 μm PL decreases significantly with increasing P_G. As InN content increases, we also expect the dislocation density to increase as a result of a larger lattice mismatch between InGaN:Er and the underlying GaN, leading to an increase in non-radiative recombination.

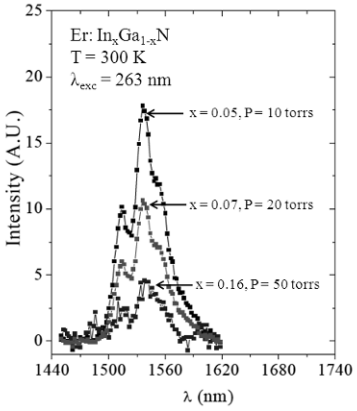

Fig. 5.38. PL spectra of $In_xGa_{1-x}N$:Er grown by MOCVD with different x.

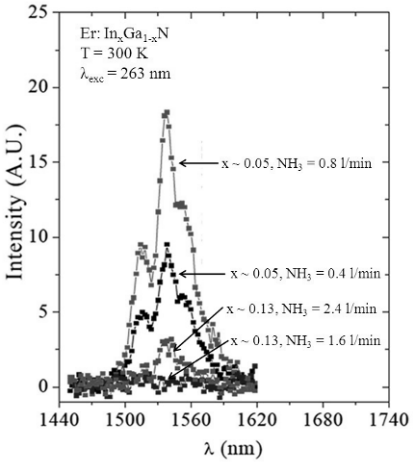

Fig. 5.39. PL spectra of $In_xGa_{1-x}N$:Er epilayers grown by MOCVD at different NH_3 flow rates.

We also show the dependence of 1.54 μm emission intensity on NH_3 flow rate (Fig. 5.39). The PL intensity increases with increasing flow rate from 0.4 to 0.8 l/min, (InN fraction about 5%). However, PL intensity decreases for further increase in flow rate, mainly due to an increase in InN content (5% for 0.4 to 0.8 l/min vs 13% for 1.6 to 2.4 l/min). Fig. 5.40 shows the dependence of PL intensity of InGaN:Er samples grown at different Ga flow rates. PL intensity increases with increasing Ga flow rate. This increase in PL intensity is related to a decrease in InN content, and hence improved material quality.

The data in Fig. 5.38, Fig. 5.39, and Fig. 5.40 clearly indicate that the emission intensity at 1.54 μm in Er-doped InGaN epilayers significantly decreases with increasing InN fraction. In order to understand the mechanism responsible, PL measurements of $In_xGa_{1-x}N$:Er for $0 < x < 0.16$ were carried out at 10 K in both IR and visible spectral regions [41]. The results shown in Fig. 5.41 (a) and Fig. 5.41 (b) clearly reveal that an increase in InN fraction, causing a rapid reduction of 1.54 μm emission intensity, is accompanied by the emergence of new emission in the visible spectral region. In sharp contrast to the case of GaN:Er, in which only a weak band-edge emission at 3.23 eV is observed [30], three strong emission lines emerge: relatively weak red and yellow bands, centered around 1.86 and 2.10 eV appear in $In_xGa_{1-x}N$:Er at low x; a third emission peak at higher energy becomes more prominent and red-shifts with increasing x (2.95, 2.77 and 2.61 eV for x=0.05, 0.10 and 0.15, respectively).

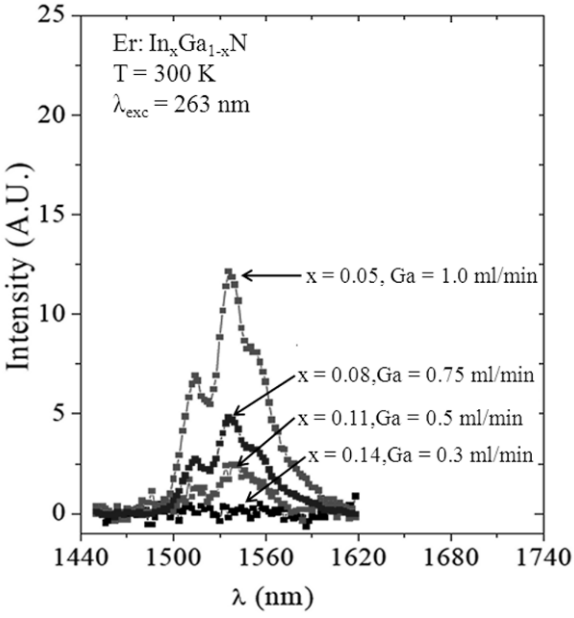

Fig. 5.40. PL spectra of $In_xGa_{1-x}N$:Er grown by MOCVD at different Ga flow rates.

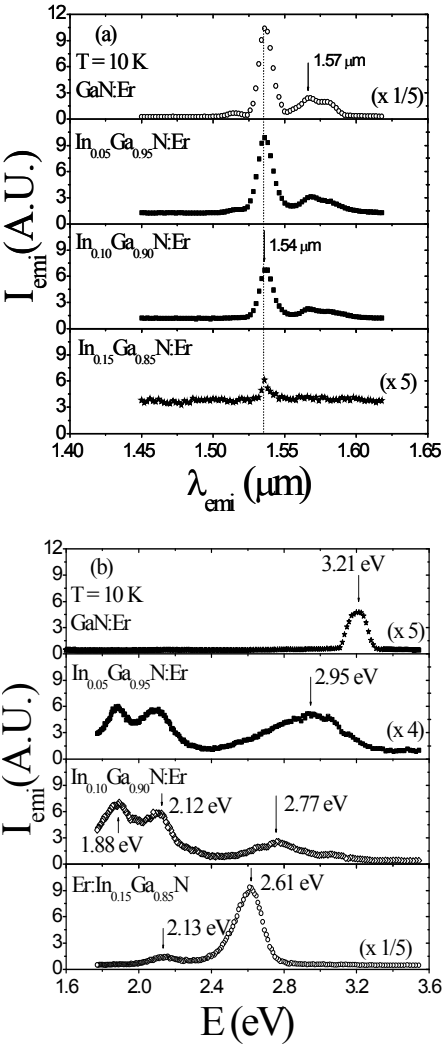

Fig. 5.41. PL spectra at 10 K of MOCVD-grown GaN:Er and $In_xGa_{1-x}N$:Er in (a) 1.54 μm and (b) visible spectral regions.

Although the origins of these visible transitions are not fully understood, the spectral peak positions suggest that they are related to deep levels (such as cation and anion vacancies and their complexes). A negative correlation between IR and deep level emission is revealed in Fig. 5.42; the relationship is described by an exponential dependence:

$$I_{1.54\mu m} = ae^{-\beta I_{imp}} \tag{2}$$

where a and β are fitting parameters and I_{imp} denotes the integrated emission intensity of all observable transition lines in the visible spectral region. The results clearly demonstrate that deep levels are more readily incorporated into InGaN:Er with higher InN contents (and lower bandgaps), and that Er-related emission intensities at 1.54 μm decrease exponentially with their concentration (proportional to I_{imp}). The presence of deep level centers in the host material offers alternative recombination routes in the visible spectral region and inhibits the energy transfer to the Er atoms. The low growth temperature (760 ºC), limited by weak In-N bonding, tends to generate more native defects in InGaN:Er such as nitrogen vacancies due to the insufficient decomposition of NH_3. Furthermore, as InN content increases, the lattice mismatch between the InGaN:Er layer and the underlying GaN also increases, resulting in more dislocations. As the dislocation density increases, the number of non-radiative recombination centers also increases, thus reducing the PL intensity at 1.54 μm. The mechanism responsible for the drop in Er-related PL intensity as a function of increasing In-content seems similar to that for InGaN-based LEDs varying from blue to green.

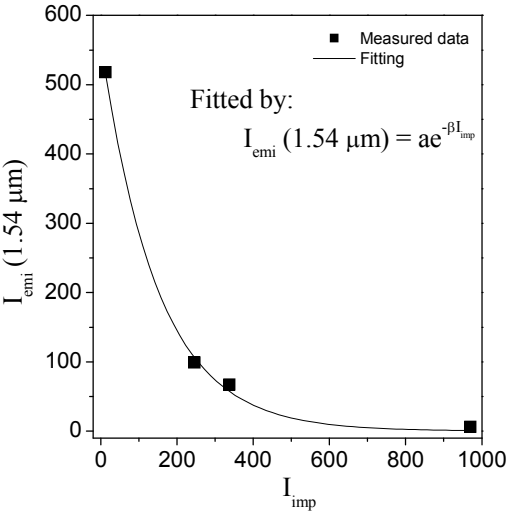

Fig. 5.42. PL emission intensity at 1.54 μm as a function of integrated emission intensity, I_{imp}, of all observable impurity lines in the visible spectral region of $In_xGa_{1-x}N$:Er for x = 0, 0.05, 0.10 and 0.16, respectively. Solid line is the least squares fit of data to Eq. (**2**).

An Arrhenius plot of the $In_{.10}Ga_{.90}N$:Er IR emission is shown in Fig. 5.43(a); an activation energy (E_A) of about 66 meV is determined from a fit to this plot. Fig. 5.43(b) clearly shows that E_A decreases continuously with decreasing energy band-gap (increasing InN fraction).

Detailed understanding of the relationship between 1.54 μm emission and the excitation energy in Er-doped InGaN/GaN semiconductors is interesting from both a fundamental scientific perspective and efficient photonic device applica-

tions. In order to provide insight into the excitation mechanisms, Er-doped GaN and $In_{.06}Ga_{.94}N$ epilayers were grown by MOCVD for optical studies, including PL emission, PLE, and absorption spectroscopy [30, 36, 42]. Fig. 5.44(a) shows room temperature emission spectra of an Er-doped GaN epilayer under optical excitation using different wavelengths. The results clearly demonstrate that the 1.54 μm emission intensity (I_{emi}) increases sharply as the excitation energy (E_{exc}) is tuned to the bandgap of GaN. This point is corroborated by the PLE spectrum (Fig. 5.44 (b)) which shows an onset for obtaining efficient 1.54 μm emission around 3.35 eV or $\lambda_{exc} \leq 370$ nm. The emission intensity begins to saturate for $E_{exc} > 3.4$ eV ($\lambda_{exc} < 362$ nm). Fig. 5.44(b) also shows an optical absorption spectrum of Er-doped GaN; a strong correlation between absorption and PLE is evident near the energy bandgap of GaN. These results clearly demonstrate that Er^{3+} ions can be excited very efficiently through electron-hole pair mediated processes in GaN:Er epilayers. Er-doped InGaN exhibits a similar trend. The onset for obtaining efficient emission is reduced because of the smaller bandgap of $In0._{06}Ga_{0.94}N$ (3.18 eV) [42].

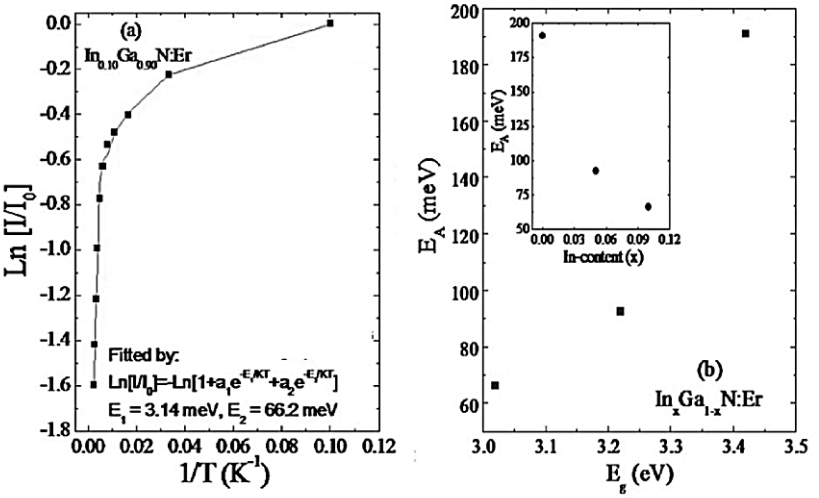

Fig. 5.43. (a) Arrhenius plot of the integrated 1.54 μm emission intensity between 10 and 400 K for $In_{0.10}Ga_{0.90}N$:Er; (b) The thermal activation energy (E_A) of the 1.54 μm emission line as a function of the band-gap energy of InGaN. The inset shows E_A as a function of In-N fraction.

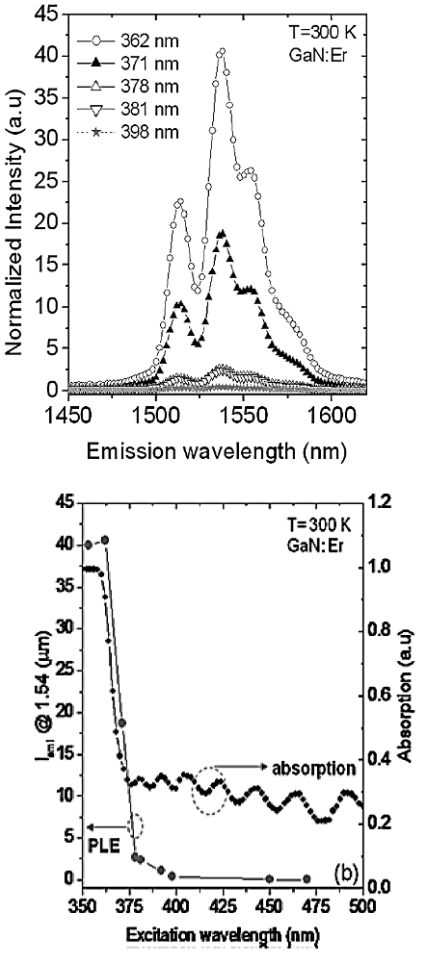

Fig. 5.44. (a) Room temperature PL spectra of MOCVD-grown GaN:Er epilayers. The excitation sources were III-nitride near-UV LEDs with wavelengths spanning the GaN bandgap. The emission intensities are normalized to the LED power output. (b) PLE spectra of 1.54 μm emission (left axis) and absorption spectrum (right axis) of GaN:Er.

5.5 Current-Injected 1.54 μm LEDs Based on GaN:Er

The recent progress on the growth of high optical quality, *in situ* doped InGaN/GaN:Er with predominant 1.54 μm emission naturally leads to research on practical devices. The first chip-scale current-injected 1.54 μm emitter was fabricated by successfully integrating an Er-doped GaN epilayer with a 365 nm nitride LED [42]. The emitter layer structure is shown in Fig. 5.45. Fig. 5.46 shows the room temperature EL spectrum under forward bias for a range of injection currents. The emission intensity increases linearly with input current and

virtually no visible Er-related emission was observable. The intensity of the 1.54 μm emission decreases between 10 and 300 K by less than 15% (Fig. 5.47), which represents the lowest thermal quenching ever reported for an Er-doped semiconductor device.

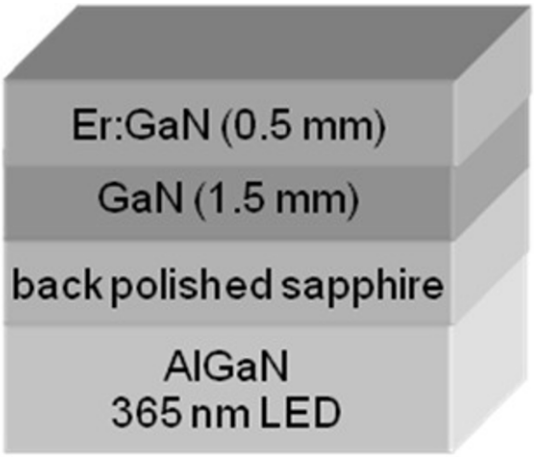

Fig. 5.45. Schematic layer structure of a 1.54 μm emitter using GaN:Er.

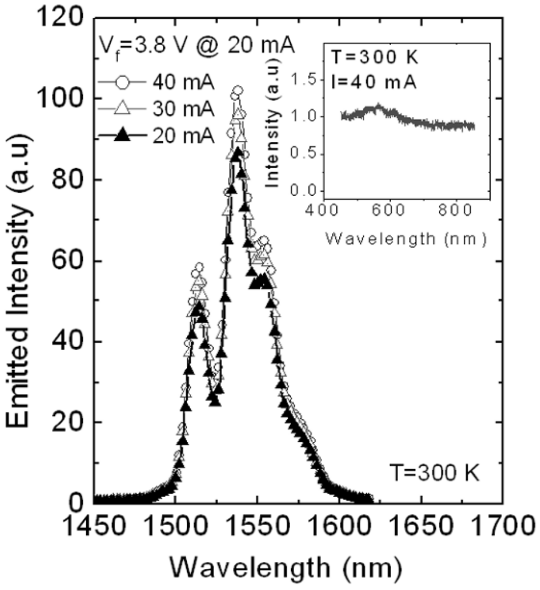

Fig. 5.46. EL spectra of GaN:Er LED with different injection currents.

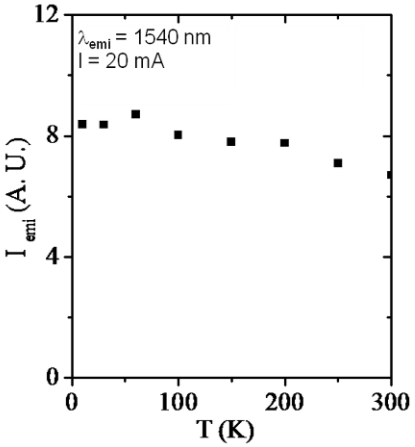

Fig. 5.47. Temperature dependence of 1.54 μm emission of GaN:Er LED.

The successful heterogeneous integration of blue and IR light emitters suggests that it is feasible to grow Er-doped nitride layers directly on either the top or back side of polished sapphire substrates of UV/blue/green nitride LED structures to achieve electrically driven emission at 1.54 μm. Such a development would require further improvements in GaN:Er and InGaN:Er epilayer material quality and device architecture. It also appears feasible to obtain current-injected optical amplification from Er-doped nitride amplifiers (EDNAs) based on a GaN:Er waveguide layer deposited on top of a completed III-nitride UV emitter structure or AlGaN/(In)GaN:Er/AlGaN p-i-n quantum well structure, as described in the next section.

5.6 Er-Doped Nitride Amplifier (EDNA) Development

Planar waveguide amplifiers based on Er-doped GaN/AlGaN, a key component of chip-size photonic integrated circuits (PICs) operating in the c-band communication wavelength, are expected to show better performance in terms of linear gain response, temperature stability and low noise. Furthermore, the GaN material system is essentially transparent in optical communication wavelength windows since the material bandgap is far from the signal wavelength. Er-doped III-nitride waveguide amplifiers have great potential applications in dense PICs with multiple functionalities to full color display systems, which cannot be obtained either with silica glass or narrow gap semiconductor materials such as InGaAsP.

Recently, we have carried out measurements using optical excitation of PL to study the propagation loss and the preliminary amplification effects in AlGaN/GaN:Er/AlGaN waveguide heterostructures [43]. To measure loss, one end of a fabricated waveguide was excited from the top side by a 371 nm laser with

beam spot diameter of ~10 μm. 1.54 μm light generated within the waveguide by the intra-4*f* transition of Er^{3+} propagated through the core, and was detected at the far end using a tapered fiber coupler with an InGaAs detector and monochromator. The PL signal at the exit facet of the waveguide is plotted in Fig. 5.48 as a function of laser excitation spot distance, d. The inset in Fig. 5.48 shows the optical set-up.

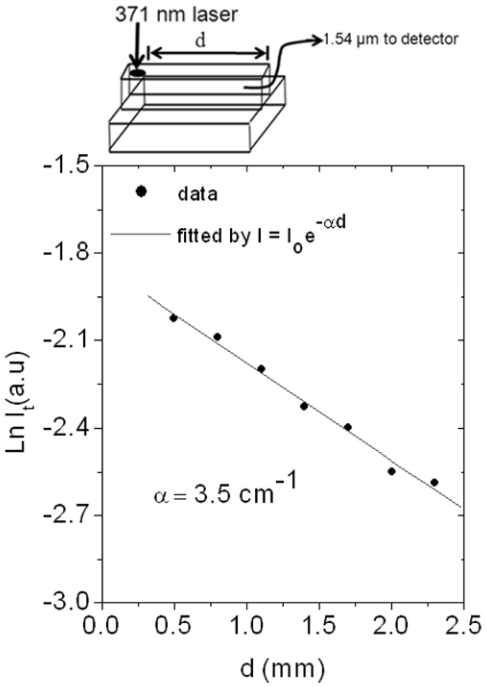

Fig. 5.48. Optical loss measurement for GaN:Er waveguide amplifier.

The collected intensity is given by

$$I_t = I_0 \exp(-\alpha d) \tag{3}$$

where I_0 is the PL emission intensity measured at the excitation spot, d is the optical path length, and α is the optical loss. The optical loss at 1.54 μm was found to be 3.5 cm^{-1}. This relatively small value indicates good material quality of the GaN:Er layer, and is comparable to a value of 4.45 cm^{-1} reported for undoped GaN ridge waveguide devices at 488 nm [44].

The low optical loss at 1.54 μm promises high potential for optical amplification using GaN:Er waveguides. The setup for measuring optical amplification and the experimental results are illustrated in Fig. 5.49. In the absence of an input signal (bottom panel), excitation of the Er-doped GaN waveguide by a 365 nm

LED produces an emission spectrum that is identical to the EL spectrum (Fig. 5.46) of a 1.54 μm LED [42]. In the presence of a 1544 nm input signal (top panel), excitation by the 365 nm LED induces a considerable amplification (2x) solely at the signal wavelength of 1544 nm, despite the fact that the waveguide length is only 3 mm long. This result demonstrates that the current-injected optical waveguide amplifier operating at 1.54 μm region based on Er-doped III-nitride semiconductors could be achieved by further optimization of the waveguide structures.

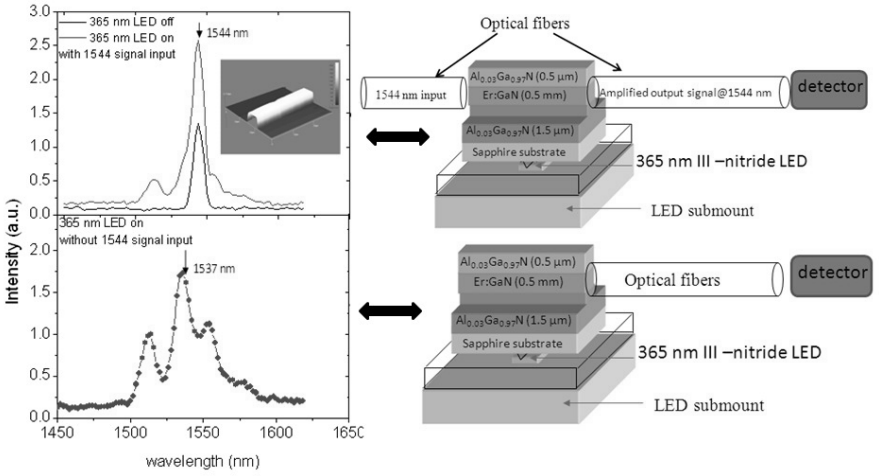

Fig. 5.49. Experimental setup (right) for measuring amplification in an Er-doped GaN waveguide . The waveguide has an emission peak at 1537 nm when pumped by a nitride LED at 365 nm (bottom panel). With a 1544 nm signal input (top panel), the 365 nm LED pump induces a 2x signal enhancement at the signal wavelength.

Integration of a large number of optical components is an important goal of PIC technology. A variety of optical structures such as optical couplers, Wavelength Division Multiplexing (WDM) multiplexers/demultiplexers and photonic crystals have already been demonstrated on 2-Dimensional (2D) PIC in semiconductors other than III-N. Based on the results for Er-doped nitride semiconductor devices, various optical circuit configurations can be explored on the GaN PIC platform. For example, an important issue of travelling wave optical amplifiers is the facet reflection, which might introduce multi-pass interference and self-oscillation. In order to integrate nitride guided-wave devices with photonic devices made of other materials, such as silicon and InP, reflections at the input and output interfaces have to be minimized. Grating-assisted directional couplers at the input and the output ports of the Er-doped nitride-based amplifier need to be investigated for this purpose. The optical gain in Er-doped GaN waveguides may also be used to create unique laser sources.

5.7 Summary

In this chapter we have described Er doping of GaN and InGaN wide bandgap semiconductors with an emphasis on recent progress using MOCVD. The crystalline quality, optical properties and 1.54 μm emission of in situ Er-doped $In_xGa_{1-x}N$ for $x < 0.2$ were discussed. Encouraging results on photonic devices, IR emitters and optical waveguide amplifiers operating at 1.54 μm were presented. Monolithic integration of Er-doped InGaN/GaN epilayers with nitride light emitting diodes (LEDs) and laser diodes (LDs) with emission wavelength matching the bandgap of host nitride materials opens the possibility of realizing planar waveguide amplifiers and emitters operating in the c-band communication window (1530-1550 nm). Optical or current injected waveguide amplifiers based on Er-doped InGaN/GaN are expected to have better performance in terms of linear gain, temperature stability and low noise, than either Er-doped silica glasses or narrow bandgap semiconductor materials such as InP. Devices are expected to be electrically pumped, chip-scale, integratable, and low-cost. Electrically pumped optical amplifiers possess both the semiconductor advantages of small size, electrical pumping, ability for photonic integration, etc. and the fiber advantage of minimal crosstalk between different wavelength channels in WDM. Integration is then possible with other functional optical devices, such as wavelength routers, optical switches, light sources, and detectors, to build monolithic PICs. This prospect becomes especially attractive if Er-doped III-nitride materials can be grown on large area silicon substrates compatible with the standard processes of CMOS technology and could open up unprecedented applications including those envisioned for Si photonics.

Acknowledgements

This work was supported by NSF (Grant No: ECCS-0823894) and ARO (Grant No: W911NF-09-1-0277). H. X. Jiang and J. Y. Lin would like to acknowledge the support of Edward Whitacre and Linda Whitacre endowed chairs through the AT&T foundation. We would also like to acknowledge Dr. J. Li, Dr. C. Ugolini, Dr. Neeraj Nepal, B. N. Pantha, A. Sedhain and Dr. P. Chow (SVTA) for their contributions to this work.

References

1. A. J. Steckl and R. Birkhahn, Appl. Phys. Lett. 73, 1700 (1998).
2. P. N. Favennec, H. L'Haridon, M. Salvi, D. Moutonnet, and Y. Le Guillou, Electron. Lett. 25, 718 (1989).
3. J. M. Zavada and Dahua Zhang, Solid-State Electron. 38, 1285 (1995).
4. M. R. Brown, A. F. J. Cox, W. A. Shand, and J. M. Williams, Advances in Quantum Electronics 2, 69 (1974).
5. H. Ennen, J. Schneider, G. Pomrenke, and A. Axmann, Appl. Phys. Lett. 43, 943 (1983).
6. R. Birkhahn, M. Garter, and A. J. Steckl, Appl. Phys. Lett. 74, 2161 (1999).
7. R. G. Wilson, R. N. Schwartz, C. R. Abernathy, S. J. Pearton, N. Newman, M. Rubin, T. Fu, and J. M. Zavada, Appl. Phys. Lett. 65, 992 (1994).
8. J. M. Zavada, S. X. Jin, N. Nepal, J. Y. Lin, H. X. Jiang, P. Chow, and B. Hertog, Appl. Phys. Lett. 84, 1061 (2004).
9. S. Kim, S. J. Rhee, X. Li, J. J. Coleman, and S. G. Bishop, Appl. Phys. Lett. 76, 2403 (2000).
10. J. T. Seo, U. Hommerich, J. D. MacKenzie, C. R. Abernathy, and J. M. Zavada, J. Kor. Phys. Soc. 36, 311 (2000).
11. K. P. O'Donnel and B. Hourahine, Eur. Phys. J. Appl. Phys. 36, 91 (2006).
12. U. Hommerich, M. Thaik, R. N. Schwartz, R. G. Wilson, J. M. Zavada, S. J. Pearton, C. R. Abernathy, and J. D. MacKenzie, Electrochem. Soc. Proc. 98-2, 110 (1998).
13. J. T. Torvik, R. J. Feuerstein, J. I. Pankove, C. H. Qiu, and F. Namavar, Appl. Phys. Lett. 69, 2098 (1996).
14. J. T. Torvik, C. H. Qiu, R. J. Feuerstein, J. I. Pankove, and F. Namavar, J. Appl. Phys. 81, 6343 (1997).
15. S. Kim, S. J. Rhee, D. A. Turnbull, E. E. Reuter, X. Li, J. J. Coleman, and S. G. Bishop, Appl. Phys. Lett. 71, 231 (1997).
16. M. Thaik, U. Hommerich, , R. N. Schwartz, R. G. Wilson, and J. M. Zavada, 71, 2641 (1997).
17. M. R. Correia, S. Pereira, A. Cavaco, E. Pereira, and E. Alves, Appl. Phys. Lett. 80, 4504 (2002).
18. J. M. Zavada, R. G. Wilson, U. Hommerich, M. Thaik, J. T. Seo, C. J. Ellis, J. Y. Lin, and H. X. Jiang, Electronic Materials, 32, 382 (2003).
19. F. Lu, A. Rizzi, R. Carius, and C. H. Lei, J. Phys. D: Appl. Phys. 37, 1544 (2004).
20. B. D. Vries, V. Matias, A. Vantomme, U. Wahl, E. M. C. Rita, E. Alves, A. M. L. Lopes, and J. G. Correia, Appl. Phys. Lett. 84, 4304 (2004).
21. T. Monterio, J. Soares, M. R. Correia, and E. Alves, J. Appl. Phys. 89, 6183 (2001).
22. S. F. Song, W. D. Chen, C. Zhang, L. Bian, C. C. Hsu, B. Ma, G. H. Li, and J. Zhu, J. Appl. Phys. 96, 4930 (2004).
23. S. F. Song, W. D. Chen, C. Zhang, L. Bian, C. C. Hsu, B. Ma, L. W. Lu, Y. H. Zhang, and J. Zhu, Appl. Phys. Lett. 86, 152111 (2005).
24. J. D. MacKenzie, C. R. Abernathy, S. J. Pearton, U. Hommerich, J. T. Seo, R. G. Wilson, and J. M. Zavada, Appl. Phys. Lett. 72, 2710 (1998).
25. D. M. Hansen, R. Zhang, N. R. Perkins, S. Safvi, L. Zhang, K. L. Bray, and T. F. Keuch, Appl. Phys. Lett. 72, 1244 (1997).
26. M. E. Overberg, C. R. Abernathy, S. J. Pearton, R. G. Wilson, and J. M. Zavada, (http://nsr.mij.mrs.org/5S1/W11.62/article.pdf).
27. J.M. Zavada, J.Y. Lin, H.X. Jiang, P. Chow, B. Hertog, U. Hömmerich, Ei Ei Nyein, and H.A. Jenkinson, Mat. Sci. Eng. B105, 118 (2003).

28. S. Chen, J. Seo, J. Sawahata, and K. Akimoto, J. crystal Growth, 311, 2042 (2009).
29. A. Uedono, C. Shaoqiang, S. Jongwon, H. Nakamori, N. Honda, S. Tomita, K. Akomoto, H. Kudo, and S. Ishibashi, J. Appl. Phys. 103, 104505 (2008).
30. C. Ugolini, N. Nepal, J. Y. Lin, H. X. Jiang, and J. M. Zavada, Appl. Phys. Lett. 89, 151903 (2006).
31. R. H. Birkhahn, R. Hudgins, D. S. Lee, B. K. Lee, A. J. Steckl, A. Saleh, R. G. Wilson, and J. M. Zavada, MRS Internet J. Nitride Semicond. Res. 4S1, G3.80 (1999).
32. C. S. Son, S. Kim, Y. H. Kim, I. K. Han, Y. T. Kim, A. Wakahara, I. H. Choi, and H. C. Lopez, J. Korean Phys. Soc. 45, 955 (2004).
33. H. J. Lozykowski, Phys. Rev. B 48, 17758 (1993).
34. H. Przybylinska, A. Kozanecki, V. Glukhanyuka, W. Jantsch, D. J. Asc, and K. Lischka, Physica B 308, 310 (2001)
35. A. R. Zanatta, Appl. Phys. Lett. 82, 1395 (2003).
36. C. Ugolini, N. Nepal, J. Y. Lin, H. X. Jiang, and J. M. Zavada, Appl. Phys. Lett. 90, 051110 (2007).
37. M. Smith, G. D. Chen, J. Y. Lin, H. X. Jiang, A. Salvador, B. N. Sverdlov, A. Botchkarev, H. Morkoc, and B. Goldenberg, Appl. Phys. Lett. 68, (1996).
38. J. S. Fihol, R. Jones, M. J. Shaw, and P. R. Briddon, Appl. Phys. Lett. 84, 2841 (2004).
39. B. Wybourne, Spectroscopic Properties of Rare Earths (Interscience, NewYork, 1965), pp. 3–8.
40. S. Hufner, Optical Spectra of Transparent Rare Earth Compounds (Academic, New York, 1978), pp. 14–16.
41. A. Sedhain, C. Ugolini, J. Y. Lin, H. X. Jiang, and J. M. Zavada, Appl. Phys. Lett. 95, 041113 (2009).
42. R. Dahal, C. Ugilini, J. Y. Lin, H. X. Jiang, and J. M. Zavada, Appl. Phys. Lett. 93, 033502 (2008).
43. R. Dahal, C. Ugilini, J. Y. Lin, H. X. Jiang, and J. M. Zavada, Appl. Phys. Lett. 95, 111109 (2009).
44. O. Skorka, B. Meyler, and J Salzman, Appl. Phys. Lett. 84, 19 (2004).

Chapter 6
Rare-Earth-Doped GaN Quantum Dots

B. Daudin

Abstract The *in situ* doping of GaN quantum dots (QD) with RE ions with a view to visible light emission applications is discussed. It is shown that *in situ* doping is complicated by the influence of RE atoms on the physical mechanism responsible for QD formation. The cases of Eu, Tm and Tb are described in detail. In particular it is demonstrated that RE can be efficiently incorporated in QDs, at concentrations in the 1% range. Next, the optical properties of RE-doped GaN QDs are described. Photoluminescence properties are found to be different from those observed in doped thick layers, which is ascribed to carrier confinement effects and to the peculiar strain state in GaN QD. Studies of photoluminescence dynamics show that the energy transfer from carriers in quantum dots to RE^{3+} ions is very fast, whereas RE^{3+} photoluminescence decay exhibits trends similar to those found for thick layers.

6.1 Introduction

Rare earth (RE) doped III-V semiconductors are of potential interest for the realization of electroluminescent devices [1, 2] and novel semiconductor lasers [3, 4] as they offer the opportunity to combine the electrical excitation of the host material and the remarkable optical properties of RE ions. More precisely, and limiting ourselves to III-V nitrides, RE doping of GaN appears to be an alternative way for the realization of light-emitting diodes (LEDs) in the visible range, and it has spurred interest in GaN doped with Eu, Sm or Pr (red emission), Tm (blue), and Er, Ho, or Tb (green) [5, 6, 7, 8, 9, 10, 11, 12]. The RE doping option is particularly attractive in the case of red and green light as a possible way to elude

CEA-CNRS group « Nanophysique et Semiconducteurs »,
Institut Néel/CNRS-Univ. J. Fourier and
CEA Grenoble, INAC, SP2M, 17 rue des Martyrs, 38 054 Grenoble, France
bruno.daudin@cea.fr

problems related to the growth of InGaN with high InN content. However, a restriction to the use of RE ions is their relatively low luminescence efficiency, which is partly due to the low concentration of RE ions combined with non-radiative carrier recombination. This is particularly crucial in the case of nitride semiconductors where the lack of adapted substrates results in a high density of dislocations. A possible way to overcome these difficulties consists of using quantum dots (QDs) doped with RE material. As a matter of fact, it is expected that the strong confinement of carriers in dots will enhance their recombination in the vicinity of RE ions, thus improving luminescence efficiency in the visible range. It has been demonstrated that molecular beam epitaxy (MBE) growth of GaN at high temperature (710–750°C) under N-rich conditions obeys the Stranski–Krastanow (SK) growth mode, with three dimensional (3D) islanding observed above a critical thickness of about 2 monolayers (MLs) [13, 14]. Due to the large difference in band gap energy between AlN and GaN, strong confinement of carriers in GaN QDs is expected, which leads to a remarkable persistence of photoluminescence (PL) up to room temperature despite the high density of dislocations in the surrounding AlN matrix [15], strongly supporting the idea that doping GaN QDs with RE materials should dramatically enhance their luminescence efficiency.

It is currently accepted that the remarkable optical properties of InGaN-based LEDs is due to the presence of localization centers in the active region, i.e. in the InGaN quantum wells. Although the microscopic nature of these localization centers is not clear and is still a matter of debate [16], they are likely responsible for the high quantum efficiency of visible nitride LEDs, despite the high density of dislocations and related non radiative recombination centers. However, it should be noted that the beneficial existence of the localization centers also results in a non-negligible spreading of LED emission wavelength, which may be detrimental to applications. Then, doping QDs with RE ions may be viewed as an innovative solution to engineer localization centers, with the consequence of minimizing non-radiative recombination, while taking advantage of the very stable RE emission, which leads to well defined chromaticity.

It is the aim of this chapter to discuss growth by molecular beam epitaxy of GaN QDs *in situ* doped with RE ions. After describing the conditions leading to the formation of GaN QDs according to the Stranski-Krastanow (SK) growth mode, we will discuss the conditions leading to incorporation of Eu, Tm and Tb for red, blue and green emission, respectively. The optical properties of doped GaN QDs will be discussed, before an evaluation of their potential for device applications.

Finally, it is worth mentioning that the excitation mechanisms leading to the luminescence of RE^{3+} ions in III-N compounds remain unclear. In particular, the impact of the doping method, i.e. whether it is performed *in situ* during growth or post-growth by ion implantation should be clarified. Comparative studies on the effect of doping techniques are indeed very scarce in the literature. *In situ* doping of MBE-grown GaN with Nd has recently been reported

[17]. One conclusion of this work is that most Nd atoms sit on the same site within the GaN matrix, with a reduced influence of defect-assisted transitions involving multiple sites. In a similar way, concerning Eu-doping, it will be shown in detail in Sect. 6.3.1 that implantation-induced structural defects lead to the existence of multiple sites for Eu. By contrast, Eu incorporation in MBE leads to a reduced number of incorporation sites and, of course, to the absence of implantation defects, likely leading to the existence of peculiar excitation processes. Furthermore, it should be mentioned that the GaN growth process itself may lead to different RE incorporation sites. Whereas a photoluminescence excitation (PLE) study for a below-bandgap excitation in Er-doped GaN reported [18] some similarities between ion-implanted and *in situ* doped GaN samples in case of Er resonant excitation, another comparison between Er-doped GaN prepared by metal-organic molecular beam epitaxy (MOMBE) and solid-source molecular beam epitaxy (SSMBE) shows green PL signal only from SSMBE samples [19].

It will also be a goal of this chapter to enlighten the issue of doping technique, which is of crucial importance in view of possible applications.

6.2 Growth of GaN QDs

6.2.1 Undoped Dots

It is now well known that GaN deposited on AlN obeys the Stranski-Krastanow (SK) growth mode, with formation of 3-dimensional islands for a GaN amount larger than a critical thickness of about 2.3 monolayers (MLs) [13, 14]. However, as extensively discussed [20], occurrence of this growth mode strongly depends on the Ga/N ratio, which directly controls surface kinetics of the growing material. As a matter of fact, it has been found that SK growth is observed when growing GaN in N-rich conditions (Ga/N<1), associated with low adatom mobility [21]. In the extreme case of Ga/N >> 1, a Ga bilayer is rapidly formed on growing GaN. The existence of this self-regulated Ga bilayer has been demonstrated both theoretically [22, 23] and experimentally [24]. It results in the opening of a new diffusion path for N between the two Ga layers and is also associated with a deep change in surface kinetics. Then, when the Ga flux is high enough that this Ga bilayer is completed before reaching the critical thickness, the 2D/3D transition is found to be inhibited and no QD formation is observed but rather a plastic strain relaxation of the GaN layer, providing a clue that formation of misfit dislocations is energetically more favorable in such growth conditions [25]. It should be noted at this stage that the nature of the active N source is a determinant parameter of GaN growth by MBE. When using

ammonia as the source, it has been demonstrated that QD formation only occurs with growth interruption [26], suggesting that GaN 2D growth is stabilized in the presence of ammonia, in a way phenomenologically similar to what is found to occur in the presence of a Ga bilayer. As will be shown later, depending on growth temperature and flux, Eu also tends to segregate during GaN growth, which modifies the surface energy and may affect the SK transition, eventually inhibiting it.

As AlN is highly insulating, the practical realization of LEDs with RE^{3+}-doped GaN QDs in the active region requires us to grow them on AlGaN, with an Al content low enough to make n-type and p-type electrical doping possible. However, the requirements to obtain a high doping level, namely a low Al content, also implies the reduction of the lattice mismatch between GaN and AlGaN, eventually leading to a suppression of the SK transition and of GaN QDs formation. The growth of GaN QDs by plasma-assisted MBE on an $Al_xGa_{1-x}N$ layer (x=0.26−1.0) has been studied in detail [27]. It has been found that the relaxation mechanisms of QDs were different on AlN and AlGaN surfaces, even if they had the same lattice parameter, emphasizing the role of the chemical nature of the substrate in the total energy balance leading to spontaneous 3D islanding of GaN.

The observation by atomic force microscopy of GaN QDs grown on AlGaN revealed that their size was related to the Al content of AlGaN barrier. A size bimodality was found for an Al content ranging from 100 to 80%. The suppression of GaN QD bimodality for an Al content lower than 80% suggested a decrease in adatom diffusion length as the Al content decreases. However, this would lead to the formation of smaller dots for lower Al content. Although a minimum in dot height and diameter is observed for Al content between 60% and 70%, further decrease in the Al content leads to an increase in the dot size. Thus, it was concluded that the morphology of GaN QDs grown on AlGaN does not primarily depend on kinetics, but is related to the chemical dissymmetry of the $GaN/Al_xGa_{1-x}N$ interface.

In addition, it has been demonstrated that, for a given lattice mismatch, the lower the Al content, the smaller the aspect ratio of GaN QDs, i.e. the smaller the elastic strain energy relaxation, which was attributed to the role of interface energy, making less favorable the formation of GaN QDs on AlGaN barrier with low Al content [27].

In conclusion of this section, it appears that the formation of GaN QDs on AlGaN is a complex process driven by both the GaN/AlGaN lattice mismatch and the interface energy, which determines the morphological/structural properties of the nanostructures and also, consequently, their optical properties. As a matter of fact, it will be shown in the following sections that an efficient energy transfer from GaN matrix to RE^{3+} ions implies particular conditions for QD energy emission, as an illustration that GaN QDs morphology control is a necessary tool for optimal engineering of RE^{3+} emission.

6.2.2 Rare-Earth-Doped Dots

6.2.2.1 Eu-Doped Dots

A characteristic 2×2 surface reconstruction has been observed when growing thick GaN layers by plasma-assisted MBE, in the presence of an Eu flux [28]. This reconstruction has been assigned to surface segregation of Eu during growth. In addition, it has been found that the presence of a thin Eu layer on the growing surface drastically changed the surface kinetics and results in a decrease in the GaN growth rate, which has been assigned to an increase in Ga adatom mean free path and increased desorption probability in the presence of Eu [28].

It has been furthermore demonstrated that the change in surface kinetics induced by the presence of Eu deeply affects GaN QDs formation. The samples designed for this study consisted of a stack of several planes of GaN QDs, grown at 720 °C in N-rich conditions (Ga/active N flux was about 0.65). Each plane of dots corresponded to a nominal deposit of 2.4 monolayers of GaN. During the growth of GaN QDs, the sample was exposed to Eu flux. The last plane of dots was left uncapped on the surface for AFM analysis. The Eu content of the QDs was measured by Rutherford backscattering spectrometry (RBS). The influence of Eu on GaN QD nucleation is illustrated in Fig. 6.1. An AFM image of undoped GaN QDs is shown in Fig. 6.1(a) The effect of 1% Eu doping, as shown in Fig. 6.1(b), is a lower density of bigger dots, while a further increase of Eu content up to 2.2% results in a larger density of smaller dots as seen in Fig. 6.1(c). The variation of both density and average dot diameter as a function of Eu content (corrected for tip dimension effects) is further illustrated in Fig. 6.2. A decrease in the density of dots correlated with an increase of their size is observed for concentrations of Eu up to about 1.6%. Next, density is found to increase again while dimensions decrease. For about 3% of Eu, no more 2D/3D transition was observed, i.e., the spontaneous 3D islanding of GaN was completely inhibited.

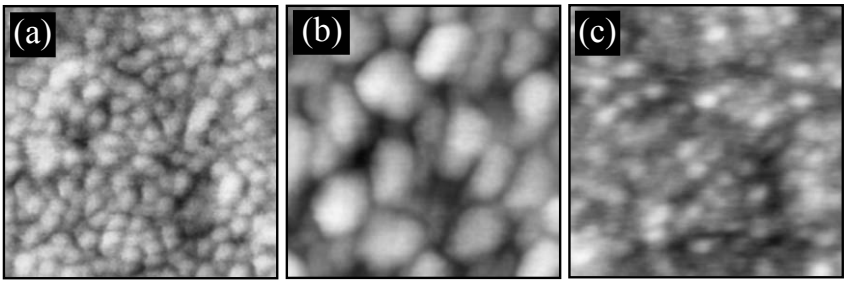

Fig. 6.1. AFM images of (a) GaN QDs, (b) GaN QDs doped with 1%, and (c) 2.8% of Eu. Areas of images are 150 nm × 150 nm (after [28]).

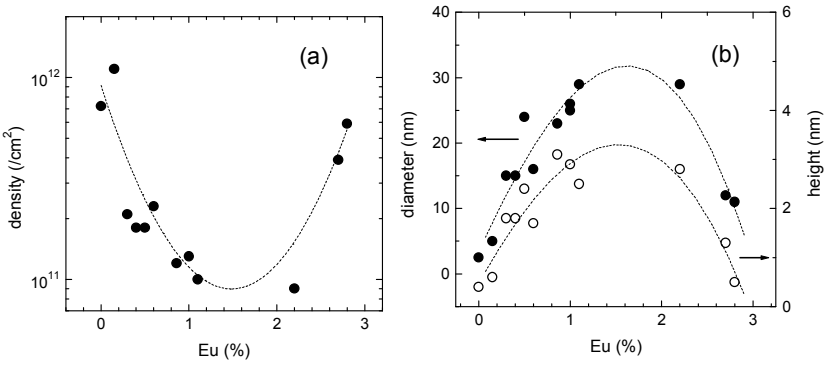

Fig. 6.2. (a) Density of Eu-doped GaN QDs as a function of their Eu content, (b) diameter and height of Eu-doped GaN QDs as a function of their Eu content. The growth temperature was 730 °C (after [28]).

The tendency of Eu to segregate on the growing surface makes the issue of its incorporation in GaN QDs a crucial one. Is Eu *really* incorporated in dots? Is it perhaps preferentially incorporated in the surrounding AlN matrix? Is it incorporated in both?

These issues, which are as crucial from a basic point of view as for device realization have been addressed by performing extended X-ray absorption fine structure (EXAFS) experiments which provide information on the local environment of Eu^{3+} ions [29]. EXAFS results obtained for a sample with 2.7% Eu-doped QDs are presented in Fig. 6.3. In order to quantitatively determine if Eu has been substitutionally incorporated inside GaN or AlN, the chemical nature of the second nearest neighbor shell of Eu had to be assessed: either 12 Ga atoms for Eu inside GaN QDs or 12 Al for Eu inside the AlN matrix. In Fig. 6.3, the peak around 2.6 Å corresponds to the second nearest neighbor shell which consists of heavier elements. Therefore, EXAFS analysis was conducted on this second peak by Fourier backtransform (lower part in Fig. 6.3), with R ranging from 2.2 to 3.1 Å. Results of the fitting procedure in Fig. 6.3 clearly show a good agreement with experimental data if Eu is assumed to be incorporated inside GaN QDs. By contrast, assuming Eu incorporation in AlN leads to poor agreement: the EXAFS oscillation amplitude is too large at low q and too small at high q, as evidence that Al is too light to be a backscatterer. Therefore, it appears clear that the second nearest neighbor shell of Eu consists of Ga, which unambiguously demonstrates that Eu is incorporated inside GaN QDs and not in the surrounding AlN matrix [29].

It should be noted in addition that the best fit to experiment was found to be consistent with a 1.7% contraction of GaN around Eu^{3+}: this feature is also in agreement with the hypothesis that Eu^{3+} is substitutionally incorporated inside

GaN QDs, and experiences a compressive stress due to the 2.5% lattice mismatch between GaN and AlN.

Hence, to summarize this section, it appears that Eu can be effectively incorporated in GaN QDs, at concentrations up to about 3%. The tendency of Eu to segregate on the surface of growing GaN and AlN limits incorporation at higher concentrations; a drastic change in growth mode for high Eu flux inhibits QDs formation. It should be noted at this stage that Eu can also be incorporated in InGaN QDs which have been grown on GaN [30].

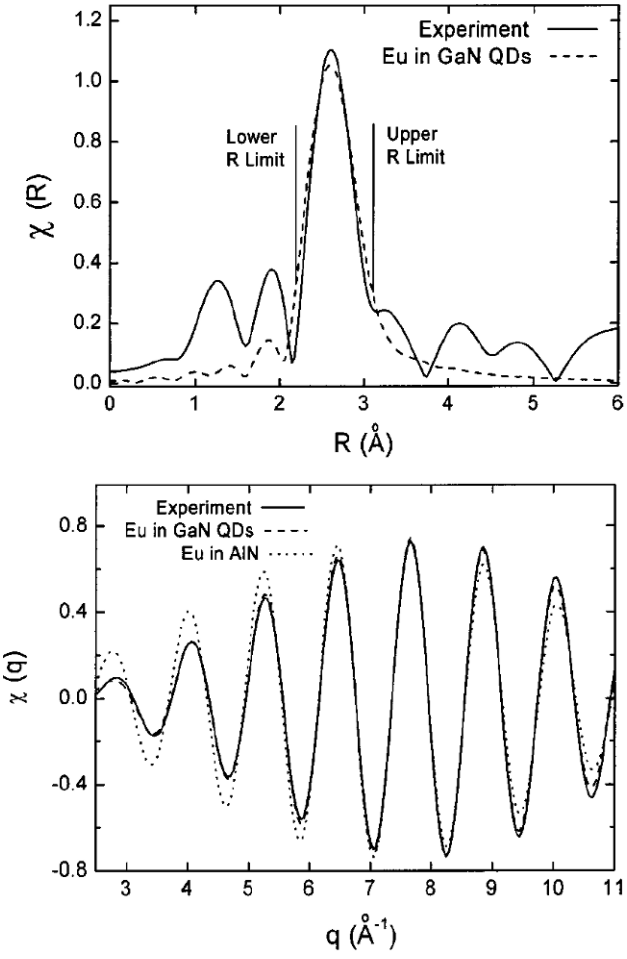

Fig. 6.3. Comparison between experimental (solid line) and calculated EXAFS spectra in *R* space (top part, not phase corrected) and *q* space (bottom part, with *R* ranging from 2.2 to 3.1). The dashed line (dotted line) represents simulation assuming Eu incorporation into GaN QDs (AlN matrix), (after [29]).

6.2.2.2 Tm-Doped Dots

Along the same lines as above, the incorporation of Tm in GaN QDs has been studied in order to take advantage of the blue emission of Tm^{3+} ions [31]. Results of AFM experiments to study the morphology of GaN QDs, namely their height, diameter, and density as a function of Tm content are shown in Fig. 6.4. A minimum in diameter and a maximum in density are observed for a Tm content of about 2%. A decrease of the QD height by a factor of 2 is observed for Tm concentrations higher than 4%. As in the case of Eu discussed in the previous section, these features indicate changes in adatom kinetics induced by the presence of Tm. However, the variations in QD morphology are significantly smaller than in the case of Eu-doped QDs. It has to be recalled that Eu, when incorporated in GaN at a concentration higher than 3%, inhibits the SK transition and the nucleation of GaN QDs. By contrast, in the case of Tm doping, GaN QDs are observed for Tm content higher than 10%, as measured by RBS.

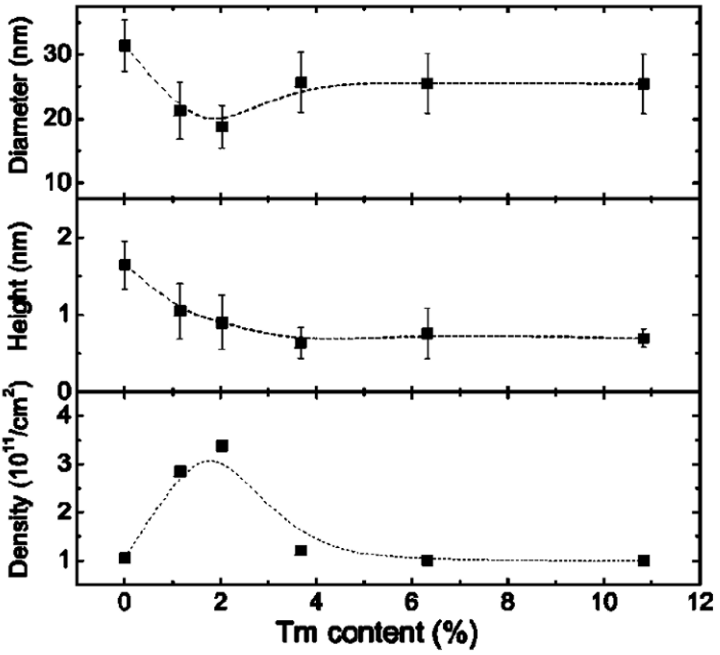

Fig. 6.4. Diameter, height, and density of QDs measured for samples containing different Tm concentrations. The dashed lines are guides to the eye. The error bars are calculated from Gaussian fits (after [31]).

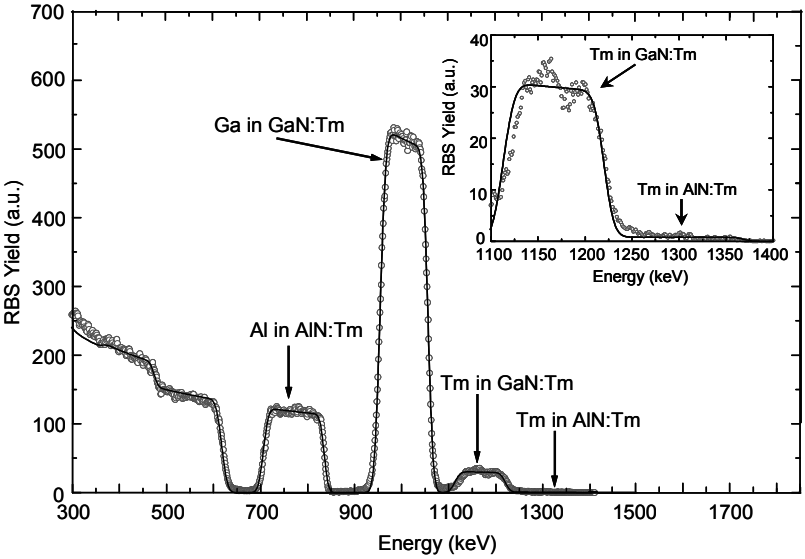

Fig. 6.5. RBS spectrum of a sample containing a 104 nm GaN:Tm layer with 180-nm-thick AlN:Tm on top. Acceleration voltage of the He ions, 1.5 MeV. Tm content inside GaN, 1.2%.

As discussed extensively in [31], RBS leads to the determination of Tm content normalized to the GaN content but does not provide precise information on the location of incorporated Tm. Thus, in order to determine the incorporation yield of Tm in both AlN and GaN, a sample was especially designed, which consisted of a 104-nm thick GaN layer grown on an AlN template and capped by a 180-nm-thick AlN film. During the growth of both AlN and GaN layers, the Tm flux remained constant. An RBS spectrum corresponding to the sample described above is shown in Fig. 6.5. Quantitative analysis demonstrated that Tm was mostly incorporated in the GaN layer whereas the incorporation in AlN was negligible.

In addition to these experiments, the issue of incorporation of Tm in GaN QDs was addressed by performing EXAFS experiments [31]. The results lead to the conclusion that Tm is located in a Ga or Al substitutional site, with four nitrogen atoms as the first neighbors. To further determine whether Tm is incorporated within GaN or AlN, the chemical nature of the second-nearest-neighbor shell of Tm had to be determined. This second-nearest-neighbor shell consists of 12 Ga or 12 Al, depending if Tm is incorporated in GaN or AlN, respectively. Actually, the optimum fit of the data was obtained using 3 Ga atoms and 9 Al atoms.

Combining these results and RBS ones, it was finally concluded that Tm probably incorporates in GaN QDs, at the interface between the dots and the AlN barrier [31].

6.2.2.3 Tb-Doped Dots

Tb^{3+} ions luminesce in the green wavelength region. Thus, in order to complete the available chromatic gamut, the incorporation of Tb in GaN QDs was studied, using a strategy similar to that previously described in the case of Eu and Tm [32]. As in the case of Eu and Tm, it was found that Tb had a significant influence on adatom kinetics, with consequences on the morphology of GaN QDs. As a matter of fact, as shown in Fig. 6.6 for a growth temperature of 700 °C, the dot density and diameter were constant up to 3.6% Tb content (measured by RBS), whereas the dot height rapidly decreases to half of the height of undoped QDs for a Tb content of 0.5% and remains constant with increasing Tb content. Further increase of Tb content above 3.6 % was found to result in a disappearance of dots, a feature assigned to a dramatic decrease in GaN growth rate in the presence of Tb. For a growth temperature of 760 °C, no QDs are found on the surface for Tb contents higher than 2%. The changes in GaN QDs nucleation process was found to be particularly marked at higher temperature: both QD density and size strongly decreased as a function of Tb flux, the density being found to drop by about one order of magnitude for a Tb content of about 2%.

As a conclusion of Sect. 6.2, it has to be emphasized that the change in adatom kinetics induced by the presence of an additional RE flux during the growth of GaN QDs is a general feature, which deeply perturbs QD formation. Eventually, for high RE flux, it was found that the SK transition could be completely suppressed, as an intrinsic limitation to the *in situ* doping of GaN or InGaN QDs by RE ions. However, using AFM data, a rough estimation of the total number of RE ions present in dots could be made: in all cases, the highest doping level compatible with dot formation corresponds to several tens of ions in each dot, high enough for practical applications, provided that clustering effects are absent.

6.3 Optical Properties

6.3.1 Eu-Doped GaN QDs Embedded in AlN

Optical properties of RE-doped GaN QDs have been studied and compared to the results obtained on a thick GaN layer, for the same Eu flux during growth. Normalized photoluminescence (PL) intensities for a Eu-doped GaN layer, undoped GaN QDs and Eu-doped GaN QDs are shown in Fig. 6.7 as a function of inverse temperature. It has to be noted that for all samples optical excitation was provided by the fourth harmonic (266 nm) of a Nd:YAG pulsed laser, too low in photon energy to excite AlN, so that the electron-hole pairs are directly photogenerated in GaN [29].

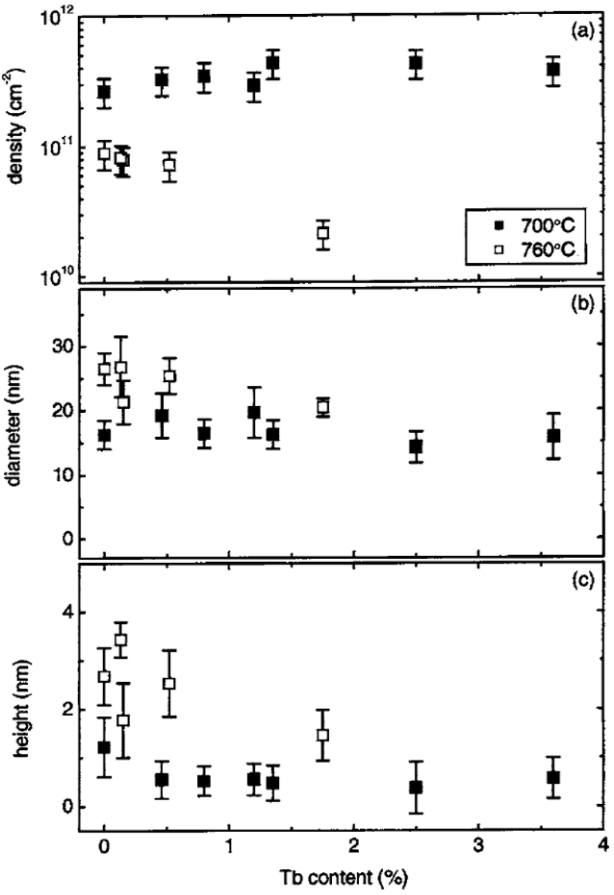

Fig. 6.6. (a) Density, (b) diameter, and (c) height of Tb-doped GaN QDs as a function of their Tb content. Solid and open squares correspond to the lower (700 °C) and higher (760 °C) growth temperatures, respectively. Tb content was determined by RBS (after [32]).

The PL spectra of Eu-doped samples are dominated by Eu^{3+} transitions at around 622 nm. For the thick GaN layer doped with Eu a decrease of PL intensity by almost two orders of magnitude is observed between 10 and 300 K, consistent with an increase of non-radiative carrier recombination at higher temperature, which is ascribed to a decrease in carrier-mediated energy transfer between the GaN matrix and Eu ions [6, 33]. As shown in Fig. 6.7 the 340 nm PL band of undoped QDs exhibits a weak decrease, by about 30%, between 10 and 300 K [15]. By way of contrast, the PL intensity of GaN QDs doped with Eu is almost constant as a function of the temperature.

At first sight, this behavior could suggest that carrier recombination through Eu excitation is fast enough to be dominant over other possible processes. However, this is contradictory with the very long PL decay times of Eu-doped GaN, in the 30–240 μs range, depending on the local symmetry of Eu sites [33]. Despite such a long radiative recombination time, it is still possible that trapping of carriers by Eu atoms is consistent with a rapid localization of carriers in the vicinity of Eu atoms prior to recombination, which would tend to exclude or reduce nonradiative recombination paths. Actually, it is possible that carrier trapping by Eu ions is more effective in defect-free Eu-doped GaN QDs than in Eu-doped GaN thick layers. It is also possible that Eu-trapped carriers in QDs are more localized than carriers trapped in undoped QDs, making them less sensitive to non-radiative recombination as evidenced by the reduced quenching of PL between 4 K and room temperature for Eu-doped QDs, with respect to undoped QDs [29].

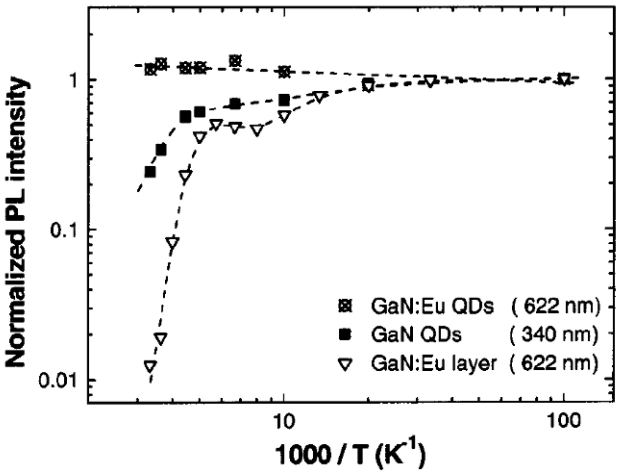

Fig. 6.7. Temperature dependence of the PL intensity for Eu-doped GaN QDs, undoped GaN QDs, and the Eu-doped GaN thick layer. The wavelength at 10 K of the integrated peak was 622, 340, and 622 nm, respectively (after [29]).

Now considering the case of Eu-implanted material, detailed studies on Eu^{3+} excitation have led to the conclusion that under above-bandgap excitation the Eu luminescence at 10K arises predominantly from two different Eu sites in implanted GaN:Eu samples annealed at 1100 °C and above [34, 35]. Furthermore, photoluminescence studies of MBE samples consisting of in-situ Eu-doped thick GaN layers also led to suggest the existence of multiple Eu sites [36, 37]. More precisely, a study of stimulated emission in GaN:Eu *in-situ* doped MBE samples has allowed one to identify two main sites, namely Eu_x emitting at ~ 620 nm, producing stimulated emission and exhibiting a fast decay time constant, and Eu_y emitting at 621 nm, producing only spontaneous emission and having a slower decay time constant [38].

All these results raise the question of the nature of Eu sites in *in situ* doped GaN QDs and has motivated a detailed comparison between implanted and in-situ doped samples [39]. This work demonstrated that, independently of Eu-doping method, PL could be assigned to the presence of two distinct Eu sites, namely Eu_1 and Eu_2, with Eu_2 ions being more efficiently excited via the host matrix than Eu_1 ions. It was found that PL spectra associated with the Eu_1 site were very similar in implanted and MBE samples, whereas PL spectra associated with the Eu_2 site were markedly different. As a further conclusion, it was suggested that Eu_1 ions in both MBE and implanted samples occupy Ga substitutional sites with a carrier trap located in the second or third neighbouring shell, while Eu_2 ions are located on a site distorted by a much closer local defect, which is electrically active as a carrier trap. The close proximity of the carrier trap to the Eu_2 ions explains the higher excitation efficiency of this Eu center in comparison to Eu_1 ions. The lattice distortion introduced by the local defect close to Eu_2 ions is not the same in implanted and *in-situ* doped samples giving rise to a different PL spectrum. Consistent with such a view, Eu luminescence in Eu-doped GaN QDs exhibits similarities with Eu_1 ions spectroscopic features observed both in implanted and *in situ* doped GaN samples. However, the broad Eu PL spectrum indicates that Eu ions in GaN quantum dots occupy distorted Ga substitutional sites, consistent with the wide strain distribution assigned to the size distribution of GaN QDs.

As a concluding remark of this section, it appears that RE implantation and *in situ* doping are *not* equivalent. The PL efficiency of Eu-doped GaN QDs has been assigned to the Eu_1 center, whereas PL in implanted samples is mostly assigned to Eu_2 centers. The close proximity of the carrier trap to the Eu_2 ions explains the higher excitation efficiency of this Eu center in comparison to Eu_1 ions. Then, paradoxically, defects induced by implantation may be an advantage for achieving efficient RE excitation in practical devices, while the control of implantation defects through annealing opens the way to defect engineering as a tool for enhancing luminescence efficiency through optimized incorporation of RE on specific sites.

6.3.2 Eu-Doped InGaN QDs Embedded in GaN

To overcome the difficulties of current injection into GaN:RE QDs grown on insulating AlN for electroluminescent device applications, a special interest has been paid to Eu-doped InGaN QDs grown on GaN [30].

Room temperature PL spectra in the red spectral range corresponding to the $^5D_0 \rightarrow {}^7F_2$ transition of Eu^{3+} ions are shown in Fig. 6.8 for three different samples, namely a thick GaN:Eu layer, GaN:Eu QDs, and InGaN:Eu QDs. For these three samples, above-band-gap excitation at 360, 300, and 360 nm, respectively, was used. It was found that the PL spectrum of InGaN:Eu QDs exhibits several lines at around 620, 622, and 633.5 nm. The spectrum for InGaN:Eu QDs is quite similar

to that of the GaN:Eu thick layer, in contrast to that of GaN:Eu QDs, which shows only an intense line at 622.5 nm. Compared to the GaN:Eu layer, RE lines are slightly broader in the spectrum corresponding to InGaN:Eu QDs, due to internal strain and electric field distributions [32].

From results in Fig. 6.8 and additional photoluminescence excitation (PLE) measurements, it was concluded that Eu ions can occupy different sites in Eu-doped GaN layer and InGaN QDs. It was further suggested that the 622 nm line in the PL spectrum of InGaN:Eu QDs sample could be assigned to Eu ions in InGaN QDs, and the 620 and 633.5 nm lines to Eu ions in the GaN barrier layer. Then, contrary to the case of Eu-doped GaN QDs in AlN discussed in the previous section, it appears that RE dopants are present in both InGaN QDs and the GaN barrier. Such a spreading of RE dopants has been assigned to segregation effects during growth, similar to the case of Tm-doped GaN/AlN QDs which will be discussed in the next section [31].

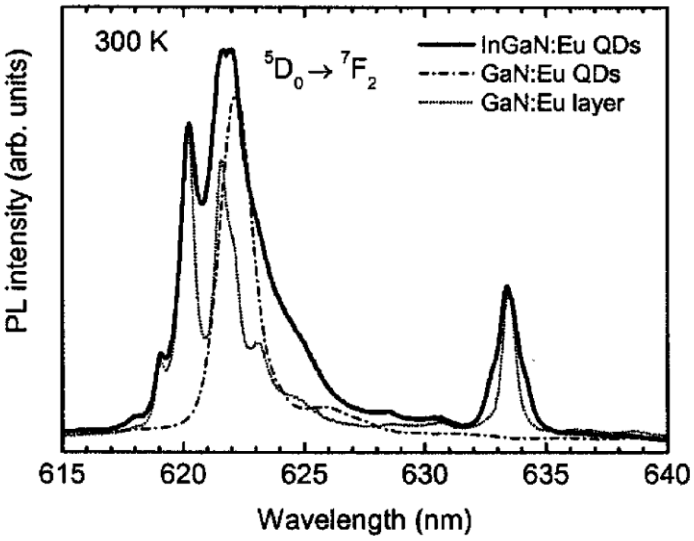

Fig. 6.8. PL spectra of InGaN:Eu QDs (solid line), GaN:Eu QDs (dashed dotted line), and GaN:Eu layer (dotted line) measured at 300 K and for excitations at 360, 300, and 360 nm, respectively (after [30]).

6.3.3 Tm-Doped Dots

Cathodo- and photoluminescence of Tm-doped GaN QDs, of Tm-doped GaN and Tm-doped AlN are compared in Fig. 6.9. First of all, it has to be noted in Fig. 6.9 (a) that the PL spectrum at 5 K of a GaN:Tm thick layer with a 2% Tm content is dominated by a near band-edge emission at 355 nm, a strong broad-

band at 390 nm, and a yellow band at 575 nm. The 390 nm band, not observed in undoped samples, could be related either to some defects induced by Tm doping or to Tm^{2+} ions since divalent RE ions are known to be more sensitive to local crystal field effects than trivalent RE ions. Additional sharp lines at 480 and 805 nm (not shown) are also observed with considerably weaker intensity. These lines have been assigned to transitions originating from the $^1G_4$ and $^3H_4$ levels of Tm^{3+} (see Fig. 6.10) [31]. In this diagram it can be seen that the $^1D_2$ level is nearly resonant with the band gap of GaN. However, no transitions related to this level are observed, in agreement with literature results [40, 41].

Turning back to Fig. 6.9a, it appears that the spectrum corresponding to Tm-doped GaN QDs is very different from the one corresponding to a GaN thick layer. First of all, it extends further into the ultraviolet, well above the band gap of bulk GaN. Consistent with results reported in Sect. 6.2.2.2, which establish that Tm doping results in the formation of small GaN QDs, it is expected that carrier confinement should be dominant over the quantum confined Stark effect [15] in these samples, so that the band at 320 nm in Fig. 6.9a has been assigned to the radiative recombination of electron-hole pairs in QDs [31].

For Tm-doped GaN QDs, intense sharp lines related to the $^1I_6$, $^1D_2$, and $^1G_4$ levels in the blue-green region (450–550 nm) are observed (see the energy diagram in Fig. 6.10 and note the position of the emission energy of the dots). Interestingly these lines have also been observed in Tm-doped AlGaN alloys, but only for an Al content larger than about 30%, i.e. for an energy gap larger than about 4 eV (310 nm) [40, 41]. Then, the observation of such lines assigned to the emission of Tm ions incorporated in GaN QDs is a clue that band-gap engineering in semiconductor nanostructures can be used as an alternative way to tune the optical properties of RE ions.

In Fig. 6.9b, it can be seen that Tm^{3+} lines in QDs are spectrally broader and redshifted by about 2–3 nm in the blue-green region when compared to those in AlN:Tm samples. The minimum full width at half maximum (FWHM) is about 1.2 and 0.3 nm in GaN:Tm QDs and in AlN:Tm, respectively. This broadening of the emission lines has been assigned to i) the compressive strain experienced by Tm ions in QDs and ii) the huge internal electric field in GaN QDs embedded in AlN [15]. As this electric field is not uniformly distributed in GaN QDs it is expected that it will induce a spectral broadening of Tm^{3+} lines. It should be noted that a Stark shift of about 200 kHz/ (V/cm) has been reported for the $^4I_{15/2}$-$^4F_{9/2}$ line of Er^{3+} in $YAlO_3$ by application of an external electric field of 200 V/cm [42]. If speculating that a similar Stark effect can be observed in GaN QDs, a shift of the order of 0.1 nm would be expected for transition lines in the blue. This value is smaller by one order of magnitude than the measured value but it has to be considered that electric fields in QDs are in the MV/cm range, namely four orders of magnitude larger than the external applied field in the work reported in [42]. For such large electric fields, it is reasonable to assume that nonlinear Stark effects could take place and induce a larger spectral shift [31].

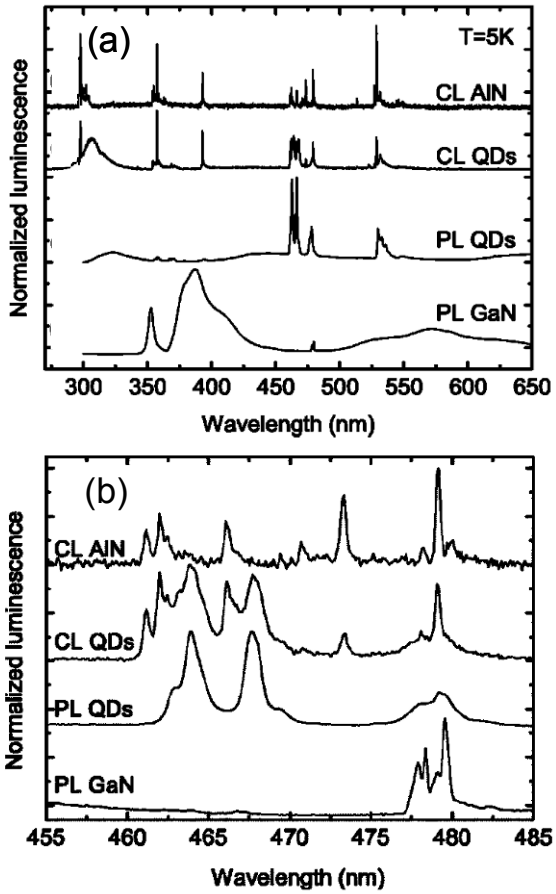

Fig. 6.9. From bottom to top: PL of a GaN:Tm layer; PL of GaN:Tm QDs; CL of GaN:Tm QDs; CL of AlN:Tm at 5 K. In case of the PL spectra, a long-pass filter at 300 nm was used to protect the monochromator from direct laser exposure (after [31]).

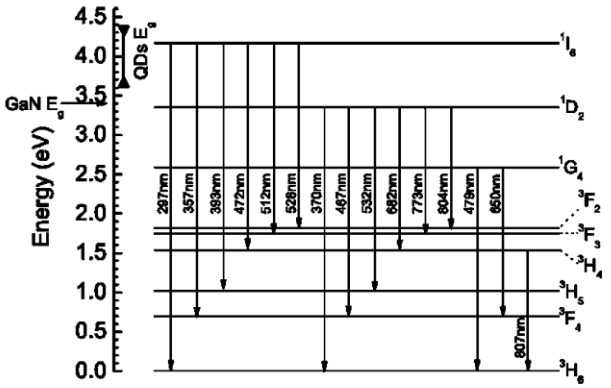

Fig. 6.10. Energy diagram of Tm3+ ions and observed transitions in AlN host. The energetic position of intra-QD transitions is marked with the arrow on the energy scale. The band gap of GaN at 3.4 eV is also indicated in the figure (after [31]).

6.3.4 Tb-Doped GaN QDs

Photoluminescence spectra of samples consisting of ten stacked planes of GaN:Tb QDs, which were separated from each other by an 8 nm thick AlN spacer are shown in Fig. 6.11. The broad peak around 350 nm corresponds to the band edge emission of GaN QDs, which was found to progressively blueshift, as a consequence of dot height reduction associated with increasing Tb content [32], as shown in Sect. 6.2.2.3. The narrow lines at 490, 550, 580, and 620 nm are assigned to the $^5D_4 \rightarrow {}^7F_J$ (J= 6,5,4,3, respectively) intra-4*f* transitions of Tb^{3+} ions, schematically shown in Fig. 6.12.

These results are significantly different from literature data. Indeed, the PL spectrum of a Tb-doped GaN thick layer at 77 K reported by Bang et al. [12] showed only a very weak $^5D_4 \rightarrow {}^7F_5$ transition, while other lines were not identified. The authors explained this poor radiative quantum efficiency by means of EXAF measurement, which revealed that the Tb ion occupies a Ga site in the tetrahedral coordination and that the bond length of Tb-N was the same as that of Ga-N. This highly symmetrical structure suppresses the inner-4*f* transition of Tb, because the inner-4*f* transition of RE ion is intrinsically forbidden.

On the other hand, an optical study of Tb^{3+} ions implanted in GaN layers has also been reported, wherein the transitions of $^5D_3 \rightarrow {}^7F_J$ and $^5D_4 \rightarrow {}^7F_J$ were both observed [43, 44]. This could be due to the fact that the local symmetry of Tb^{3+} ions in this type of material system can be as low as D_2 [44].

In the case of Tb-doped GaN QDs reported here, transitions from the $^5D_3$ and $^5D_4$ excited states have been observed at low temperature (T<200 K), whereas only transitions from $^5D_4$ remain visible at room temperature as shown in Fig. 6.11. It should be noted that the $^5D_4$-related transitions exhibit a nearly tempera-

ture-independent luminescence from 10 K to room temperature, supporting the hypothesis of Tb incorporation in GaN QDs.

The discrepancies with respect to the case of Tb-doped or Tb-implanted GaN thick layers have been ascribed to specific changes in local site symmetry resulting from the internal strain as well as internal electric field that is experienced by the GaN QDs in an AlN matrix. In line with these views, the absence of transitions from the excited state $^5D_3$ at room temperature, could be possibly related to the energy transfer mechanism between RE ions and host material, since the nature of the defects induced by Tb doping is likely different from those generated in the implantation process.

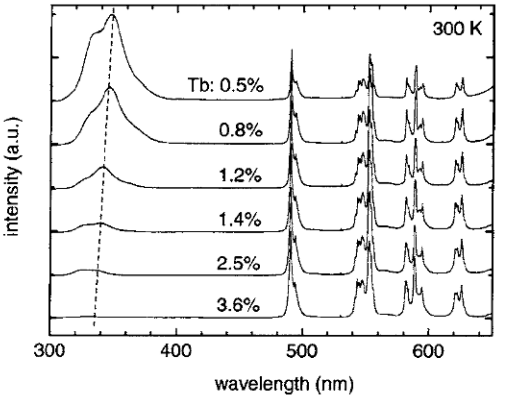

Fig. 6.11. PL spectra of Tb-doped GaN QDs measured at room temperature with different Tb contents. The dashed line is a guide for the eye. The Tb content is indicated on each spectrum (after [32]).

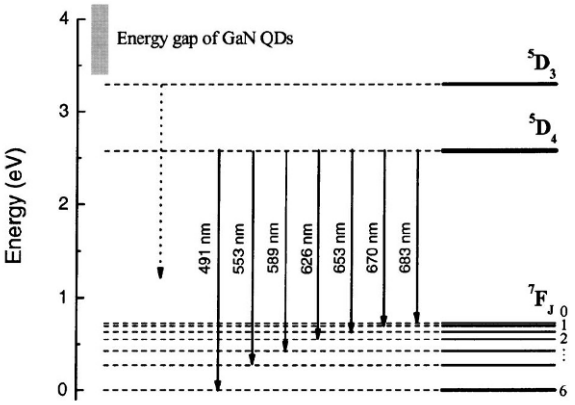

Fig. 6.12. Energy diagram for intra-4*f* transitions of Tb^{3+} ions found at room temperature in Tb-doped GaN QDs. The gray band indicates a range of the energy gap of GaN QDs (after [32]).

The variations in PL intensity as a function of Tb content shown in Fig. 6.11 are quantitatively analyzed and plotted in Fig. 6.13. It is found that the band edge emission of GaN QDs strongly decreases for increasing Tb content. This behavior could be correlated to an improved efficiency of the luminescence from Tb^{3+} ions for increasing doping level. However, it clearly appears in Fig. 6.13 that the integrated PL intensity of Tb^{3+} lines remains constant regardless of the Tb content. This suggests that the band edge emission of GaN QDs comes from undoped QDs and that its decay with increasing Tb doping results from the relative decrease of the undoped QDs density with respect to the doped ones. It can also be concluded that luminescence from Tb^{3+} ions is roughly independent of concentration, suggesting that the maximum doping level is limited by clustering effects [32].

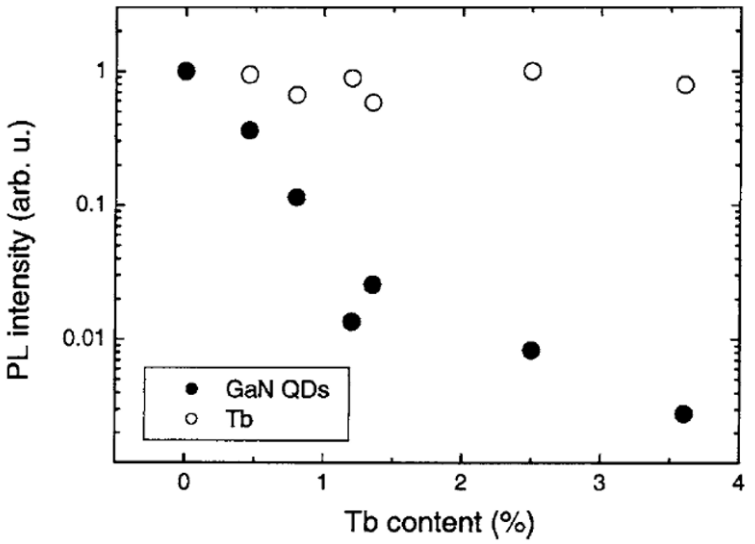

Fig. 6.13. Integrated PL intensity of GaN QDs and Tb^{3+} ions as a function of Tb content. Solid and open circles correspond to GaN QDs and Tb^{3+} ions, respectively (after [32]).

6.3.5 Photoluminescence Dynamics of RE-Doped GaN QDs

As previously mentioned, the excitation mechanisms of RE^{3+} in solid hosts is not clear and is expected to depend to some extent on the doping method. Concerning in-situ doping, it has been shown in the previous sections that the peculiar RE^{3+} symmetry associated with incorporation in strained GaN QDs could lead to specific excitation mechanisms. Fig. 6.14 shows a schematic model of RE^{3+} excitation in GaN. It is assumed that after band to band excitation of the semiconductor (1) the generated free electron can be captured by a RE related trap (2).

Then a hole from the valence-band is bound due to the resulting Coulomb interaction (3). The recombination energy is then used to excite the RE^{3+} ion from the ground state to the excited state in a so called Auger process involving electrons from the 4*f*-shell of the RE atom (4). It is understandable that the energy between excited state and ground state has to be well defined. Too low recombination energy from the recombining electron-hole pair would not yield any excitation of the RE^{3+} ion. On the other hand, the use of too wide band-gap would lead to complex processes, the excess energy being released by the generation of phonons, as experimentally established by Taguchi and coworkers [45].

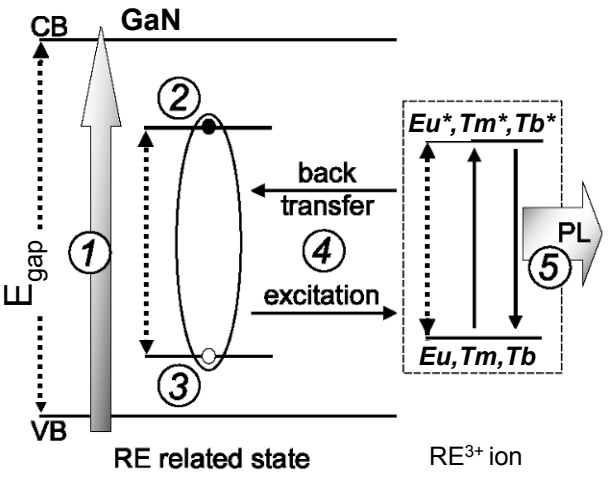

Fig. 6.14. Model of excitation of RE^{3+} ions in GaN host. After band to band excitation **1** the generated free electrons can be captured by an RE-related trap **2**. Binding of the hole **3** forms an electron hole pair on the trap. Non radiative recombinations of the pair leads to excitation of the RE^{3+} ion **4**, producing the observed PL **5**. An energy backtransfer can lead to a deexcitation of the RE^{3+} ion.

Returning to the ultimate step of the energy transfer process shown in Fig. 6.14, the excited state of the RE^{3+} atom can relax to the ground state which is associated with the light emission (5). However, an energy backtransfer process can also occur, leading to deexcitation of the RE^{3+} ion. In such a situation the free energy can be used again to excite an RE^{3+} ion, either the same or possibly a neighboring ion in the case of samples with high RE content. Another possibility is that an electron from the valence band can be generated with band edge related luminescence as the result. For matching the energy difference between trap level and conduction band a multiphonon process has been proposed [46].

The processes discussed above occur on different time scales. In the case of Yb^{3+} ions, the rise time has been measured to be between 1 μs and 10 μs depending on the generation rate [47, 48], whereas the decay time is between 7 μs and 12 μs. Note that for other RE atoms the decay time can be much longer as it depends

strongly on the transition itself. In terms of the above description the rise time includes processes (1) to (3). For the decay time, only the internal process has to be considered.

All RE^{3+} ions other than Yb^{3+} have more than one excited state so that the energy transfer mechanism is more complicated. At first the electron from the excited RE^{3+} ion can relax radiatively or with phonon emission to lower lying excited states. Also cross-relaxation processes can occur, which means that energy from an excited RE^{3+} ion is transferred, after radiative relaxation to a ground state, to another RE^{3+} ion, which is typically located close to the first ion in the lattice. This has of course detrimental effects on the optical output of the observed emission line as the cross-excited luminescence is at the same (or lower) emission energy. Cross-relaxation processes typically yield long decay times of the emission lines which will be discussed later in more detail for the case of Eu-doped QDs. This phenomenon has been experimentally established for Eu^{3+} ions in insulators [49].

In the specific case of Eu-doped GaN QDs, time resolved measurements have been performed on two samples consisting of ten stacks of GaN:Eu QDs embedded in AlN. Eu doping levels were 1.6% and 0.4%, respectively [50]. The results are shown in Fig. 6.15 (a). They have been fitted to a double exponential decay, the first decay time (8 μs) originating from the experimental setup and the second one from the Eu^{3+} ions. A good fit to the experimental data was found over more than two orders of magnitude. Fig. 6.15 (b) shows the temperature dependence of the decay time of the $^5D_0 \rightarrow {}^7F_2$ transitions of GaN:Eu QDs for the two Eu concentrations. At first it appears that the decay time is consistently about 20% longer in the sample with more Eu, being about 280 and 330 μs at 5K for 0.4 % and 1.6 % Eu content, respectively. This can be tentatively explained by possible cross-relaxation processes between Eu^{3+} ions, i.e. after RE excitation a backtransfer occurs to the trap level or to another excited state of a neighboring RE ion. Such a mechanism has been invoked in Eu-doped fluoride glasses [49]. In addition to this concentration-dependent effect, an increase of about 20 % of the decay time can be observed for the two samples between liquid helium temperature and 250 K.

This is a surprising feature as the decay time is usually found to decrease with temperature due to non-radiative mechanisms. It could be assigned to the occurrence of higher cross-relaxation rates with temperature. However, such a process is unlikely for samples with low RE concentrations. The peculiar variation of decay time as a function of temperature in the case of moderately Eu-doped (0.4%) GaN QDs then raises the question of microscopic Eu location in GaN QDs. Since the cross-relaxation rate is expected to depend not only on the absolute Eu content in GaN QDs, but also on the distance between two Eu ions. It is possible that Eu is not homogeneously incorporated into QDs. It is also possible that the strain field in dots and the associated internal electric field affects the decay time of PL, however a full explanation of these experimental results is still speculative.

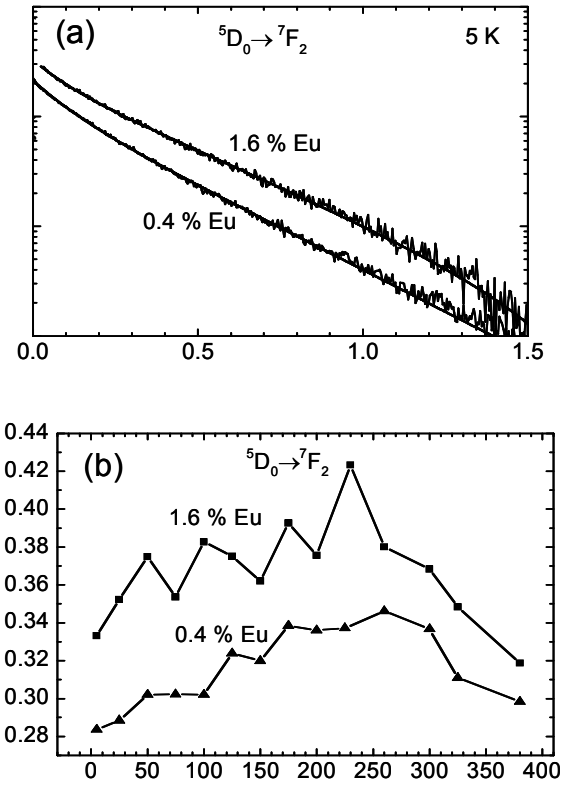

Fig. 6.15. (a) Time resolved PL signal of the $^5D_0 \rightarrow {}^7F_2$ transtion measured at 5 K for GaN:Eu QDs with a concentration of 1.6% and 0.4%. Fitting of the measurements with double exponential decay are plotted bold. (b) Decay times as a function of temperatures of the two samples (after [51]).

Coming back to the dependences shown in Fig. 6.15b, a decreasing decay time is observed for the two Eu concentrations under consideration for temperatures higher than 250 K, indicating that non-radiative processes play a role in QDs at elevated temperatures.

Photoluminescence dynamics has also been studied for Tm-doped GaN QDs [51]. In the blue and green spectral regions of Tm^{3+} emission, which are of interest for applications, two sets of transitions exhibit emission lines at very similar energies in steady-state PL spectra, but distinct decay times have been observed. The measured decay time values are ~ 0.5 μs for the emissions at 466.3 nm, 469.7 nm, 534.5 nm, 537.5 nm and ~ 1.2 μs for the emission at 532 nm [51]. As shown in Fig. 6.16a, the former emission group has been identified as resulting from the $^1I_6$ level ($^1I_6 \rightarrow {}^3H_4$ for the 466.3 nm and 469.7 nm lines, and $^1I_6 \rightarrow {}^3F_3$ for the 531 nm, 534.5 nm and 537.5 nm lines (see Fig. 6.10).

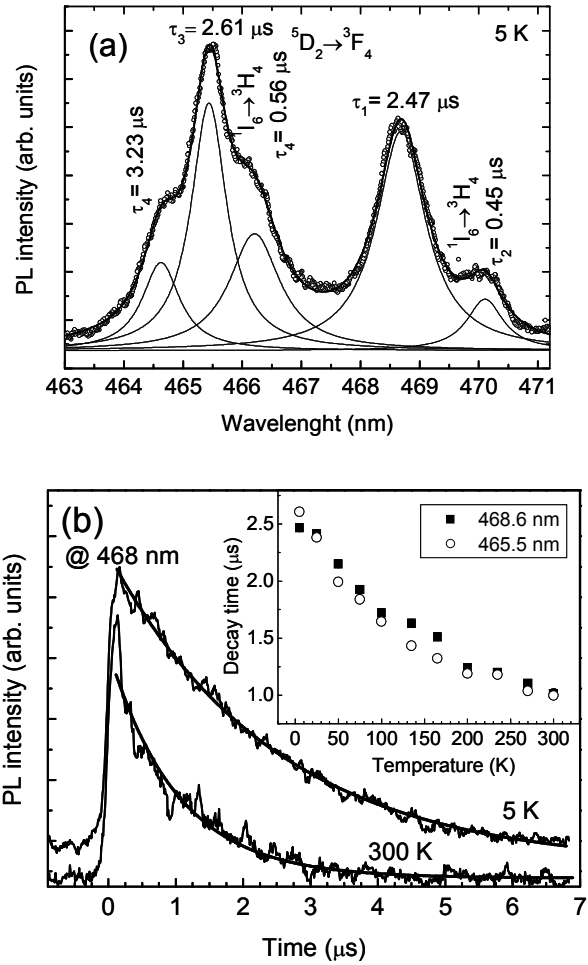

Fig. 6.16. (a) The open circles correspond to the PL from GaN:Tm QDs measured at 5 K with the time resolved setup (see experimental part). The spectrum has been fitted with a multiple Lorentzian containing 5 peaks. Measured decay times and assigned transitions are also indicated in the figure. (b) Time resolved PL signal of the $^1D_2$-$^3F_4$ transition measured at 468 nm at 5 K (upper curve) and 300 K (lower curve). Fitting of the measurements with mono exponential decay are plotted bold. The inset shows decay times for the $^1D_2$-$^3F_4$ transition at 468 nm and 465 nm as a function of temperatures (after [51]).

As the emission lines overlap in the 463-471 nm range, the quantitative determination of decay times was achieved after deconvolution of the various components using a multiple Lorentzian curve fit (Fig. 6.16a). For the two strongest isolated lines (at 465.5 nm and 468.6 nm), the PL decays could be well fitted with a monoexponential function. The results for the 468.6 nm emission line at 5 K and

300 K are shown in Fig. 6.16b. The decay time, about 2.6 μs at 5K, exhibits a continous decrease to 1 μs at room temperature.

For the two main blue emission lines at 468.6 nm and 465.5 nm and the one at the higher energy side (464.5 nm) the decay times obtained at 5 K are similar, respectively 3.2 μs, 2.6 μs and 2.5 μs. This is to be expected since the three lines all originate from the Stark-splitting of the $^1D_2 \rightarrow {}^3F_4$ transition in C_{3v} symmetry. However, it is worth noting that there is a trend to longer decay time for the higher-energy Stark component. This behaviour has also been observed for the Stark-splitting components of the $^1I_6 \rightarrow {}^3H_4$ transition that results in the 466.2 nm (0.56 μs) and 470 nm (0.45 μs) lines as well as in the case of the $^1I_6 \rightarrow {}^3F_3$ transition that results in the 531.6 nm (1.2 μs), 534.5 nm (0.6 μs) and 537.5 nm (0.5 μs) lines. There is no satisfactory explanation of this result at the present time.

Furthermore, it should be noted that the decay time of the $^1D_2 \rightarrow {}^3F_4$ transition at 5 K has been found to be ~ 2.6 μs which is longer than those for the $^1I_6 \rightarrow {}^3F_3$ (1.2 μs). This is likely due to the fact that the $^1D_2 \rightarrow {}^3F_4$ transition is spin-forbidden as is the $^1I_6 \rightarrow {}^3F_3$ transition. In addition the $^1D_2$ state is located far below $^1I_6$ so that energy released from the $^1D_2$ transitions to any manifolds is far from resonance with the fundamental energy of the host material or near-fundamental-edge traps that favor the back-energy transfer and contribute to the reduction of the measured decay time. Interestingly, a similar trend, i.e. a longer decay time for the $^1D_2$ excited state compared to $^1I_6$ was observed in Tm-doped AlGaN [41]. Although the longest decay time has been found for emissions resulting from the $^1D_2 \rightarrow {}^3F_4$ transition, which is assigned to a reduced energy back-transfer to the host material, a reduction of the decay time has been found with increasing temperature, from ~ 2.6 μs at 5 K to ~ 1 μs at 300 K (see the inset in Fig. 6.16b). This reduction in decay time can be attributed to an increase in non-radiative recombination with increasing temperature due to an increased back-transfer to the host [48]. However, this increase in the non-radiative recombination rate is not correlated with a corresponding decrease in luminescence intensity. Indeed, from 4 K to 300 K, the luminescence intensity for the $^1D_2 \rightarrow {}^3F_4$ transition was found to be constant within ± 20% (29). As PL experiments were performed in the low excitation regime, i.e. well below saturation of the transitions, this suggests that the excitation efficiency of the $^1D_2$ level increases with increasing temperature and that this effect compensates to some extent the non-radiative losses. In particular, $^1D_2$ could benefit from depopulation of $^1I_6$ with temperature. Then, the following excitation scheme for the 468 nm emission has been proposed: (i) photo-excited/generated carriers (in host GaN QDs) → (ii) traps (isoelectronic Tm^{3+} ions) → (iii) 4*f*-electrons of Tm^{3+} ions (by near resonant energy transfer to high-lying states like $^1I_6$ and $^3P_1$ and/or non-resonant process to $^1D_2$) → (iv) transitions (e.g $^1D_2 \rightarrow {}^3F_2$) to emit light. One can expect that processes (i) – (iii) occur on a nanosecond timescale and contribute to the rise-time in the time-resolved PL measurement. From the time-resolved spectra taken at 5 K and 300 K (Fig. 6.16b), it appears that the rise-time is shorter than 50 ns. This value can be accounted for by the energy transfer from GaN QDs to the 4*f*-electrons of Tm^{3+} ions. As the energy transfer

processes from the QDs to the RE^{3+} ions take place faster than other non-radiative processes, one can practically expect high efficiency luminescence from the RE-doped GaN QDs. This conclusion also holds for Eu-doped GaN QDs, with an Eu content in the 1% range and for Tb-doped GaN QDs, with a Tb content in the 3.5% range. It is consistent with the fact that the fundamental level emission for GaN QDs doped with Tm (Eu, Tb) is not observed because energy transfer processes to Tm^{3+} (Eu^{3+}, Tb^{3+}) ions are much faster than other possible processes in QDs.

As a conclusion of this section, it appears that the energy transfer from GaN QDs matrix to RE^{3+} ions is sufficiently fast to not be a limitation for practical applications. By contrast, the efficiency of visible emission of RE-doped GaN QDs can be limited by the RE^{3+} luminescence decay time. Although this is a minor inconvenience in the case of Tm, decay times of ~ 350 μs measured for Eu may be detrimental to the efficiency of practical devices. However, it should be recalled that each GaN dot contains several tens of Eu^{3+} ions on average. This is expected to compensate to some extent the aforementioned inconvenience if cross-relaxation processes between Eu^{3+} ions are not deleterious, as inferred from experimental results reported above.

6.4 Electroluminescence of Rare Earth-Doped GaN QDs

At this stage, it appears that RE-doped GaN QDs embedded in AlN matrices offer potential as efficient visible light emitters. Fig. 6.17 shows the results of optical pumping of Eu-, Tm-, and Tb-doped GaN QDs for red, blue, and green light emission, respectively. White light produced by optically pumping a stack of GaN dot planes doped with Eu, Tm or Tb is also shown. It is worth noting that in this case, the desired chromaticity can be obtained by an appropriate balance between the number of GaN QDs planes doped with the different RE. However, the insulating characteristics of AlN make such heterostructures unsuitable for electro-optical applications. This difficulty has been overcome by growing RE-doped GaN QDs on AlGaN template layers, with an AlN content as low as 34% [27]. It has to be recalled that GaN QDs grow on AlN because the ~ 2.5% in-plane lattice mismatch leads GaN to experience a compressive stress which is relaxed through the formation of 3D islands. Hence, the formation of GaN QDs on AlGaN has to satisfy two contradictory conditions: on the one hand, the AlN content of AlGaN has to be sufficiently low to make both n-type and p-type doping feasible. On the other hand, the AlN content of AlGaN has to be sufficiently high to ensure that GaN grown on it will experience a compressive stress high enough to trigger the SK mechanism.

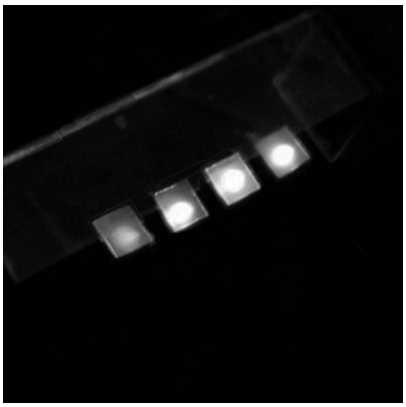

Fig. 6.17. PL of samples containing (from left to right) 100 stacks of GaN:Tm QDs for blue emission, 100 stacks of GaN:Eu QDs for red emission, 100 stacks of GaN:Tb QDs for green emission and 24 × [4 stacks of GaN:Tm QDs, 6 stacks of GaN:Tb QDs and 2 stacks of GaN:Eu QDs] for white emission. Embedding material is AlN.

It has been found experimentally (see Fig. 6.18) that the elastic strain relaxation of AlGaN layers up to an AlN content as low as 34 % can be drastically delayed when deposited on AlN [27]. For this purpose, several samples consisting of 150 nm-thick $Al_xGa_{1-x}N$ layers differing only in AlN content were grown on AlN. The *a* and *c* lattice parameters of these samples measured by high resolution X-ray diffraction are shown as solid circles in Fig. 6.18. The lattice parameters of strain-free $Al_xGa_{1-x}N$ alloys are represented as solid lines in the figure, using Vegard's law and the lattice parameters of strain-free AlN and GaN [52].

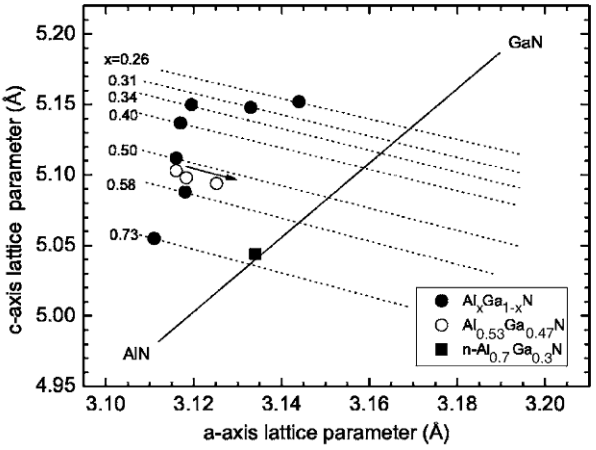

Fig. 6.18. Lattice parameter variations analyzed by XRD. Solid circles:$Al_xGa_{1-x}N$ layers with *x* varying between 0.73 and 0.26, open circles: $Al_{0.53}Ga_{0.47}N$ layers of 300, 600, and 900 nm thickness, with the arrow indicating the increase of the thickness, and closed square: 1.6-µm-thick Si-doped $Al_{0.7}Ga_{0.3}N$ layer deposited by MOVPE. The solid line between AlN and GaN corresponds to the expected behavior of the fully relaxed $Al_xGa_{1-x}N$ layers (after [27]).

If the $Al_xGa_{1-x}N$ layers were completely relaxed, one would expect to find *a* and *c* lattice parameter values on the full line connecting AlN and GaN in Fig. 6.18. This is indeed found in the case of a thick $Al_{0.7}Ga_{0.3}N$ layer. By contrast, in the case of 150 nm-thick $Al_xGa_{1-x}N$ layers, their strain state which is imposed by the underlying AlN template makes possible the growth of GaN SK QDs for an AlN content as low as 34%.

It was furthermore found that the morphology of GaN QDs was affected by the change in surface energy. When grown on AlGaN [27], a bimodality of GaN QDs was observed for AlN contents between 100 and 80%. Monomodal GaN QDs formed with a continuously decreasing aspect ratio between 75% and 34% Al content. Below 34 % AlN content, no dots could be grown, providing evidence that the lattice mismatch is not the sole factor governing QD formation and as a practical limitation for the achievement of LEDs with RE-doped GaN QDs in the active region.

6.5 Conclusion

In conclusion, it appears that *in situ* doping of GaN QDs with RE ions can be successfully used to realize potentially efficient LEDs. The possibility to engineer the band gap energy of GaN QDs by controlling the morphology of the dots and the additional option of depositing them on AlGaN make this technique of particular interest for applications. However, *in situ* incorporation efficiency depends on kinetical parameters which may be a serious limiting factor to QDs formation and to the control of their morphology, as has been shown above in the case of Eu^{3+}.

Despite these limitations, *in situ* incorporation of RE^{3+} ions in III-N heterostructures appears to offer advantages over conventional implantation techniques, as it results in spatial localization of the dopants, limiting their incorporation to the active region of the device, and avoids the implantation damage which requires annealing at high temperatures.

One intrinsic limitation to RE-based LEDs, namely the long photoluminescence decay times, can be overcome to some extent by increasing the number of RE ions in each QD. As a whole, the chromatic stability of RE emission combined with the limited quenching which results from carrier confinement in QDs makes them a particularly attractive solution for the realization of nitride-based green and red LEDs, a wavelength range for which bad homogeneity of InGaN QW composition makes the conventional approaches difficult to apply.

Acknowlegements

I gratefully acknowledge my colleagues of CEA-INAC for fruitful discussions. Special thanks to Dr. T. Andreev and Dr. Y. Hori who have performed the experiments reported in this review. Dr. O. Oda, from NGK Insulators, Japan, is acknowledged for financial and intellectual support. The support of DOWA Mining, Japan, was equally appreciated.

References

1. Rare-Earth Doped Materials for Photonics, Proceedings of E-MRS Symposium, Spring 2003 (P. Ruterana, editor) Mater. Sci. Eng. B 105, Elsevier (2003).
2. A.J. Steckl, J.C. Heikenfeld, D.S. Lee, M.J. Garter, C.C Baker, Y. Wang and R. Jones, Rare-Earth-Doped GaN: Growth, Properties, and Fabrication of Electroluminescent Devices, IEEE J. Sel. Top. Quant. Electron. 8, 749 (2002).
3. J. H. Park and A. J. Steckl, Laser action in Eu-doped GaN thin-film cavity at room temperature, Appl. Phys. Lett. 85, 4588 (2004).
4. J. H. Park and A. J. Steckl, Demonstration of a visible laser on silicon using Eu-doped GaN thin films, J. Appl. Phys 98, 056108 (2005).
5. D. S. Lee and A. J. Steckl, Enhanced blue and green emission in rare-earth-doped GaN electroluminescent devices by optical photopumping, Appl. Phys. Lett. **81**, 2331 (2002).
6. S. Morishima, T. Maruyama, and K. Akimoto, Epitaxial growth of Eu-doped GaN by gas source molecular beam epitaxy,J. Cryst. Growth **209**, 378 (2000)
7. S. Morishima, T. Maruyama, M. Tanaka, Y. Masumoto, and K. Akimoto, Growth of Eu Doped GaN and Electroluminescence from MIS Structure, Phys. Status Solidi A 176, 113 (1999)
8. K. Hara, N. Ohtake, and K. Ishii, Green Emission from Tb-Doped GaN Grown by MOVPE, Phys. Status Solidi B **216**, 625 (1999)
9. A. J. Steckl, M. Garter, D. S. Lee, J. Heikenfeld, and R. Birkhahn, Blue emission from Tm-doped GaN electroluminescent devices, Appl. Phys. Lett. 75, 2184 (1999)
10. H. J. Lozykowski, M. Jadwisienczak, and I. Brown, Visible cathodoluminescence of GaN doped with Dy, Er, and Tm, Appl. Phys. Lett. 74, 1129 (1999)
11. Z. Li, H. Bang, G. Piao, J. Sawahata, and K. Akimoto, Growth of Eu-doped GaN by gas source molecular beam epitaxy and its optical properties, J. Cryst. Growth 240, 382 (2002)
12. H. Bang, S. Morishima, Z. Li, K. Akimoto, M. Nomura, and E. Yagi, MBE growth of Eu- or Tb-doped GaN and its optical properties, J. Cryst. Growth 237–239, 1027 (2002)
13. B. Daudin, F. Widmann, G. Feuillet, Y. Samson, M. Arlery, and J. L. Rouvière, Stranski-Krastanow growth mode during the molecular beam epitaxy of highly strained GaN, Phys. Rev. B 56, R7069 (1997)
14. F. Widmann, B. Daudin, G. Feuillet, Y. Samson, J. L. Rouvière, and N. Pelekanos, Growth kinetics and optical properties of self-organized GaN quantum dots, J. Appl. Phys. 83, 7618 (1998)
15. J. Simon, N. T. Pelekanos, C. Adelmann, E. Martinez-Guerrero, R. André, B. Daudin, L. S. Dang, and H. Mariette, Direct comparison of recombination dynamics in cubic and hexagonal GaN/AlN quantum dots, Phys. Rev. B **68** 035312 (2003)

16. see for instance R. A. Oliver, B. Daudin, Intentional and unintentional localization in InGaN, Philosophical Magazine, 87, 1967 (2007) and references therein.
17. E.D. Readinger, G. D.Metcalfe, H. Shen and M. Wraback, GaN doped with neodymium by plasma-assisted molecular beam epitaxy, Appl. Phys. Lett. **92**, 061108 (2008)
18. A. M. Mitofsky, G.C. Papen, S. G. Bishop, D.S. Lee, and A. J. Steckl, Comparison of Er^{3+} photoluminescence and photoluminescence excitation spectroscopy in in-situ doped GaN:Er and Er-implanted GaN, Proc. Mat. Res. Soc. Symp., 639, G6.26 (2001).
19. U. Hömmerich, J.T. Seo, C.R. Abernathy, A.J. Steckl, J.M. Zavada, Mat. Sc. and Eng. B, Spectroscopic studies of the visible and infrared luminescence from Er doped GaN, 81, 116 (2001).
20. B. Daudin, Polar and non polar GaN quantum dots, J. of Physics: Cond. Matter, J. Phys.: Condens. Matter **20** (2008) 473201
21. T. K. Zywietz, J. Neugebauer, M. Scheffler, Adatom diffusion at GaN (0001) and ($000\bar{1}$) surfaces, Appl. Phys. Lett. 73, 487 (1998)
22. J.E. Northrup, J.Neugebauer, R. M. Feenstra,,A.R. Smith, The laterally contracted Ga bilayer model structure of GaN(0001), Phys. Rev. B **61**, 9932 (2000*)*
23. J. Neugebauer, T. K. Zywietz, M. Scheffler, J. E. Northrup, H. Chen, and R. M. Feenstra, Adatom Kinetics On and Below the Surface: The Existence of a New Diffusion Channel, Phys. Rev. Lett. 90, 056101 (2003)
24. C. Adelmann, J. Brault, D. Jalabert, P. Gentile, H. Mariette, Guido Mula, and B. Daudin, Dynamically stable gallium surface coverages during plasma-assisted molecular-beam epitaxy of (0001) GaN, J. Appl. Phys. 91, 9638 (2002).
25. N. Gogneau, D. Jalabert, and E. Monroy, T. Shibata, M. Tanaka, B. Daudin, Structure of GaN quantum dots grown under "modified Stranski–Krastanow" conditions on AlN, J. Appl. Phys. 94, 2254 (2003).
26. B. Damilano, N. Grandjean, F. Semond, J. Massies and M. Leroux, From visible to white light emission by GaN quantum dots on Si(111) substrate, Appl. Phys. Lett. 75 962, (1999).
27. Y. Hori, O. Oda, E. Bellet-Amalric, and B. Daudin, GaN quantum dots grown on $Al_xGa_{1-x}N$ layer by plasma-assisted molecular beam epitaxy, J. Appl. Phys., 102, 024311 (2007)
28. Y. Hori, D. Jalabert, T. Andreev, E. Monroy, M. Tanaka, O. Oda and B. Daudin, Morphological properties of GaN quantum dots doped with Eu, Appl. Phys. Lett. 84, 2247 (2004)
29. Y. Hori, F. Enjalbert, E. Monroy, D. Jalabert, Le Si Dang, X. Biquard, M. Tanaka, O. Oda and B. Daudin, GaN quantum dots doped with Eu Appl. Phys. Lett. 84, 206 (2004)
30. Thomas Andreev, Nguyen Quang Liem, Yuji Hori, Eva Monroy, Bruno Gayral, Mitsuhiro Tanaka, Osamu Oda, Daniel Le Si Dang and Bruno Daudin, Eu locations in Eu-doped InGaN/GaN quantum dots, Applied Physics Letters **87**, 021906 (2005)
31. T. Andreev, Y. Hori, X. Biquard, E. Monroy, D. Jalabert, A. Farchi, M. Tanaka, O. Oda, Le Si Dang, and B. Daudin, Optical and morphological properties of GaN quantum dots doped with Tm, Phys. Rev. B 71, 115310 (2005).
32. Y. Hori, T. Andreev, D. Jalabert, E. Monroy, Le Si Dang, M. Tanaka , O. Oda and B. Daudin, GaN quantum dots doped with Tb, Applied Physics Letters 88, 053102 (2006)
33. E. E. Nyein, U. Hömmerich, J. Heikenfeld, D. S. Lee, A. Steckl, and J. M. Zavada, Spectral and time-resolved photoluminescence studies of Eu-doped GaN, Appl. Phys. Lett. 82, 1655 (2003).
34. L. Bodiou, A. Oussif, A. Braud, J-L. Doualan, R. Moncorgé, K. Lorenz, E. Alves, Effect of annealing temperature on luminescence in Eu implanted GaN, Optical Materials, 28, 780 (2006).

35. K. Wang, R. W. Martin, K. P. O'Donnell, V. Katchkanov, E. Nogales, K. Lorenz, E. Alves, S. Ruffenach, and O. Briot, Selectively excited photoluminescence from Eu-implanted GaN, Appl. Phys. Lett., 87, 112107 (2005).
36. Ei Ei Nyein, U. Hömmerich, C. Munasinghe, A. J. Steckl, J. Zavada, Excitation Wavelength Dependent and Time-Resolved Photoluminescence Studies of Europium Doped GaN Grown by Interrupted Growth Epitaxy (IGE), Proc. Mat. Res. Soc. Symp., 866, V3.5, 67 (2005).
37. H. Peng, C.W. Lee, H. O. Everitt, C. Munasinghe, D. S. Lee, and A.J. Steckl, Spectroscopic and energy transfer studies of Eu^{3+} centers in GaN, J. Appl. Phys. 102, 073520 (2007).
38. H. Park and A. J. Steckl, Site specific Eu^{3+} stimulated emission in GaN host, Appl. Phys. Lett. 88, 011111 (2006).
39. L. Bodiou, A. Braud, J.-L. Doualan, R. Moncorgé, J. H. Park, C. Munasinghe, A. J. Steckl, K. Lorenz, E. Alves and B. Daudin, Optically active centers in Eu implanted, Eu in-situ doped GaN and Eu-doped GaN quantum dots, J. Appl. Phys., in press (2009)
40. D. S. Lee, A. J. Steckl, Enhanced blue emission from Tm-doped $Al_xGa_{1-x}N$ electroluminescent thin films, Appl. Phys. Lett. **83**, 2094 (2003)
41. U. Hömmerich, Ei Ei Nyein, D. S. Lee, A. J. Steckl, J. M. Zavada, Photoluminescence properties of in situ Tm-doped $Al_xGa_{1-x}N$, Appl. Phys. Lett. **83**, 4556 (2003)
42. Y. P. Wang and R. S. Meltzer, Modulation of photon-echo intensities by electric fields: Pseudo-Stark splittings in alexandrite and $YAlO_3:Er^{3+}$, Phys. Rev. B 45, 10119 (1992)
43. H. J. Lozykowski and W. M. Jadwisienczak, Photoluminescence and cathodoluminescence of GaN doped with Tb, Appl. Phys. Lett. 76, 861 (2000).
44. J. B. Gruber, B. Zandi, H. J. Lozykowski, and W. M. Jadwisienczak, Spectra and energy levels of $Tb^{3+}(4f^8)$ in GaN, J. Appl. Phys. 92, 5127 (2002).
45. A. Taguchi, K. Takahei, and Y. Horikoshi, Multiphonon-assisted energy transfer between Yb 4f shell and InP host, J. of Appl. Phys. **76**, 7288 (1994).
46. A. Taguchi and K. Takahei, Band-edge-related luminescence due to the energy backtransfer in Yb-doped InP, J. of Appl. Phys. **79**, 3261 (1996).
47. H. J. Lozykowski, Kinetics of luminescence of isoelectronic rare-earth ions in III-V semiconductors, Phys. Rev. B **48**, 17758 (1993).
48. H. J. Lozykowski, A. K. Alshawa, and I. Brown, Kinetics and quenching mechanisms of photoluminescence in Yb-doped InP, J. Appl. Phys. **76**, 4836 (1994).
49. M. Dejneka, E. Snitzer, and R. E. Riman, Blue, green and red fluorescence and energy transfer of Eu^{3+} in fluoride glasses, J. of Luminescence **65**, 227 (1995).
50. T. Andreev, Growth and optical properties of GaN and InGaN quantum dots doped with rare earth ions, Thesis, Université Joseph Fourier (2006), Grenoble, France
51. Thomas Andreev, Nguyen Quang Liem, Yuji Hori, Mitsuhiro Tanaka, Osamu Oda, Daniel Le Si Dang, Bruno Daudin, and Bruno Gayral, Optical study of excitation and deexcitation of Tm in GaN quantum dots, Phys. Rev. B **74**, 155310 (2006)
52. S. Strite and H. Morkoç, GaN, AlN, and InN : A review, J. Vac. Sci. Technol. B **10**, 1237 (1992)

Chapter 7
Visible Luminescent RE-doped GaN, AlGaN and AlInN

Robert Martin

Abstract Study of the luminescence of Rare Earth ions introduced into III-nitride semiconductor hosts produces a wealth of important information. This chapter describes investigations of photoluminescence and cathodoluminescence spectroscopy on a range of RE-implanted samples, with hosts including GaN, AlGaN and AlInN. Raising the post-implantation annealing temperature is shown to lead to a dramatic increase in RE luminescence intensity, and methods to allow annealing well above the growth temperature of the host are discussed. The high-brightness samples that result enable the resolution of additional fine-structure in the luminescence from GaN:Eu and clarification of multiple sites for the RE. Measurements for AlGaN hosts covering the entire composition range point to the importance of core-excitons in the luminescence process. Adding in information from X-ray microanalysis and high spatial resolution luminescence mapping reveals further details of the effects resulting from annealing and of changes in host composition.

7.1 Introduction to Luminescence of RE-Doped GaN

The study of the bright, sharp-line intra-*4f* shell luminescence characteristic of rare earth (RE) ions in inorganic hosts has a long and prolific history. Furthermore there are several major applications of the emission, in phosphors (for displays and lighting, e.g. Y_2O_2S:Eu red pixels in cathode ray tubes), telecomms (Er-doped amplifiers for optical fibre technology) and solid state lasers (e.g. YAG:Nd). Employment of III-nitride semiconductors as the host materials has generated particularly bright RE-related luminescence and much interesting physics [1]. The development of the field was

SUPA Department of Physics,
Strathclyde University
Glasgow
r.w.martin@strath.ac.uk

signposted by the classic 1989 paper of Favennec et al. [2], who compared the 1.54 μm infra-red (IR) luminescence from erbium ions implanted in a range of semiconductor hosts. The emission is due to transitions between $^4I_{13/2}$ and $^4I_{15/2}$ levels of Er^{3+}. The authors reported similar intensities for Er luminescence at 77 K in hosts with a wide range of band-gaps (0.8 to 2.4 eV) but demonstrated that the fall-off in intensity with rising sample temperature depends dramatically on the band-gap, as shown in Fig. 7.1. Strong thermal quenching prevents bright RE emission at room temperature from the semiconductor hosts Si and GaAs, shown as b and d in the figure; g is CdS. Extrapolating the "Favennec rule" to GaN (band gap 3.4 eV at 300K) and the even larger gaps presented by AlN-containing semiconductors suggested clear benefits for RE emission from III-nitride hosts.

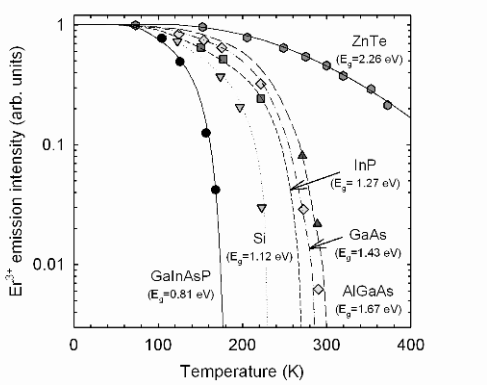

Fig. 7.1. Intensity of Er^{3+} emission for a range of hosts in order of increasing band-gap: 1. GaInAsP; 2. Si; 3. InP; 4. GaAs; 5. AlGaAs; 6. ZnTe; 7. CdS. Adapted from [2].

IR luminescence of Er-doped GaN has been reported by a number of groups, with notable early work on ion-implanted material by Wilson et al. [3] and on Er-doped molecular beam epitaxial (MBE) material by MacKenzie et al. [4]. In the late 1990s, emission was reported across the entire visible spectrum for GaN doped with various REs. Relatively strong luminescence lines in the red, green, and blue spectral regions can be achieved by doping GaN with Eu or Pr, Er or Tb and Tm, respectively. This chapter concentrates on such visible emissions from RE-doped III-nitrides, in particular the red luminescence from III-N:Eu which proves to be particularly sharp and intense.

Green emission from MBE-grown GaN:Er was reported in 1998 by Steckl, Birkhahn and co-workers [5]. Soon afterwards the same group reported red emission of Pr- and Eu-doped GaN [6, 7] and sharp blue emission from GaN:Tm [8]. At a similar time Lozykowski et al. reported the visible luminescence spectra of Dy, Er, and Tm implanted into GaN [9]. Many sharp intra-*4f* emissions in the range 350 – 850nm are reproduced in Fig. 7.2.

The subsequent achievement of electroluminescent (EL) emission at each of the RGB primary colours paved the way for prototype light-emitting devices, such as flat-panel displays and LEDs [1], and was further developed in the demonstration of an

optically pumped red laser based on GaN:Eu [10, 11]. The contemporaneous development of blue and green lasers based on InGaN/GaN seems unlikely at present to deliver red lasers. Eu doping may therefore provide the route to all-nitride full primary colour lasing.

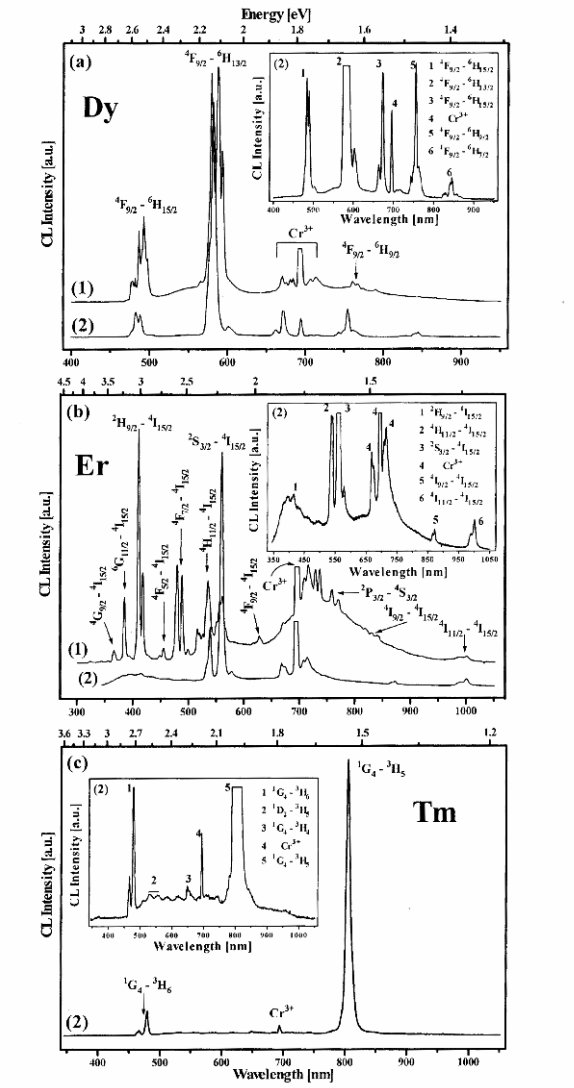

Fig. 7.2. Cathodoluminescence spectra of Si-doped GaN [spectrum (1)], and undoped GaN [spectrum (2)] epilayers grown by MOCVD on sapphire implanted with Dy^{3+} (a); Er^{3+} (b) and Tm^{3+} (c) annealed in N2 for 30 minutes at 1100 °C, and measured at 200 K. The main emission lines are shown with transition assignment. The inset in [(a), (b) and (c) is an enlargement of spectrum (2) to show details of the lower intensity emission lines for undoped Si with GaN in the investigated spectral range of 350–1050 nm. Reprinted with permssion from [9]. Copyright (1999) American Institute of Physics.

A number of early reports describe the optical properties of visibly emitting RE ions in AlN and AlGaN, for instance [12, 13, 14]. Here the wider band-gap of the AlN-containing material offers a number of potential advantages. The optical emission of Eu-implanted AlGaN over the whole alloy composition range will be discussed in Section 7.6.

The defect structures responsible for the luminescence and the mechanisms of RE excitation in III-nitride hosts continue to be poorly understood. Greater understanding and control of the properties of RE-doped nitrides will be important for the achievement of more optically efficient materials. This chapter considers the properties of various luminescent REs (principally Eu- and Er-) in a range of wide band-gap hosts: namely GaN, AlGaN and AlInN. Section 7.2 describes the sample preparation and the experimental techniques are introduced in Section 7.3, followed by a discussion of the GaN:Eu luminescence spectrum and how it can be modified by sample annealing (Sections 7.4 and 7.5). The concluding sections cover the luminescence properties of Eu in ternary nitride hosts (7.6 for AlGaN and 7.7 for AlInN)

7.2 Preparation of Samples

RE-doped III-nitrides can be prepared by solid source MBE [1], by MOVPE (see Chap. 5 by H. Jiang) and by sputtering [12] but this chapter will focus on samples doped by ion implantation. Implantation facilities are generally also applicable to a range of analytical techniques, such as Rutherford Back-scattering Spectrometry (RBS) [15, 16, 17]. The implantation of fast ions inevitably introduces lattice damage of the host through atomic displacements and an annealing step is generally required to repair some of this damage. Subsequent sections will discuss the effects of annealing on the optical spectra of ion-implanted III-N semiconductors.

Details of the ion-implantation and of the associated characterization techniques are given in Chap. 2 by K. Lorenz.

7.3 Cathodoluminescence and X-Ray Microanalysis

Simultaneous measurement of the incorporation of RE ions and of their luminescence spectrum is very valuable in the study of RE-doped semiconductors. It can be achieved by using a combination of wavelength dispersive X-ray (WDX) microanalysis and cathodoluminescence (CL) spectroscopy in a modified electron probe micro-analyser (EPMA) [18, 19]. Spatial resolution of the combined technique can approach 100 nm and hyperspectral mapping, using three WDX channels and 1024 CL channels, can be usefully performed on areas ranging from a few microns to many millimetres square [20]. A schematic of the Cameca

SX100 instrument used for these measurements at Strathclyde University is shown in Fig. 7.3. The built-in optical microscope, coaxial and confocal with the electron beam, allows optical monitoring of the excited region. We have modified the EPMA by introducing an optical spectrometer, equipped with a cooled silicon CCD detector array, in the light path of the optical microscope. CL spectral maps may be collected at the same time as the WDX intensity maps and then treated computationally to extract two-dimensional images representing various aspects of the CL data, such as spectrally integrated intensity, peak wavelength, peak width or chromaticity and the information combined mathematically with the X-ray information to extract further information on correlations and principal spectral components [21].

RE-implanted GaN can produce blue (Tm), green (Er) and red (Eu) luminescence corresponding to the intra 4*f*(n) shell electron transitions of the specified RE ions. Fig. 7.4 shows room temperature CL spectra of GaN films implanted with each of the 3 RE elements, taken with an electron beam voltage of 10 kV. An additional spectrum, of an un-annealed Tm sample, is shown to illustrate the general need to anneal samples in order to promote luminescence.

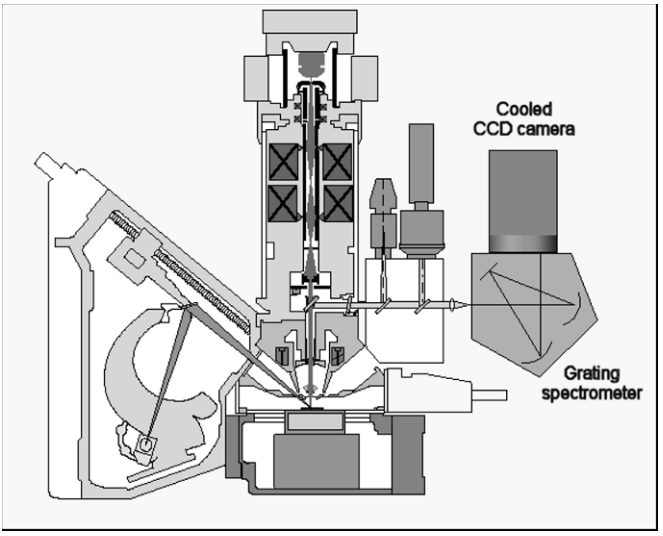

Fig. 7.3. Schematic of the Cameca SX100, modified for CL spectroscopy (adapted from image on Cameca website: www.cameca.com).

The spectra have been offset vertically for clarity. The characteristic sharp transitions associated with each of the different RE elements are seen, along with the GaN band edge (BE) emission at ~ 363 nm and the sharp line at ~ 693 nm due to Cr^{3+} in the sapphire substrate (the R-line of the ruby laser). The interference fringes result from multiple reflections due to refractive index mismatches at the air/GaN/sapphire interfaces.

The main transitions of Eu-implanted GaN are observed at ~620 nm ($^5D_0$-$^7F_2$) while those of the Er-implanted samples appear at 537 nm ($^2H_{11/2}$-$^4I_{15/2}$) and 558 nm ($^4S_{3/2}$-$^4I_{15/2}$). In the Tm-implanted samples, two main lines are observed at 477 nm ($^1G_4$-$^3H_6$) and at 805 nm ($^1G_4$-$^3H_3$).

EPMA provides an excellent basis for CL spectroscopy and can also be used to quantify material composition and RE incorporation in the host. Er and Tm were quantified by detecting the M_α X-rays diffracted by a thallium acid phthalate (TAP, 2d = 25.75 Å) crystal in comparison with Er- and Tm-doped glass standards. The Eu content was quantified by detecting the L_α X-rays diffracted by a large area pentaerythritol (PET, 2d = 8.75 Å) crystal and standardized using Eu-doped glass. A second TAP crystal and a large area synthetic pseudo crystal (2d = 60 Å) were employed to diffract the Ga (or Al) L_α and N K_α X-rays respectively. A thick undoped GaN epilayer was used as a standard for both the Ga and N elements. Indium was quantified using the PET crystal and an InP standard.

These techniques will be exemplified by the study of Eu- and Er-implanted samples of MOVPE-grown GaN on sapphire using channelled implantation along the growth axis under different conditions (energies of 80 keV and 170 keV and fluences ranging from 10^{14} cm^{-2} to 10^{15} cm^{-2}). A high temperature annealing step follows the implantation [22].

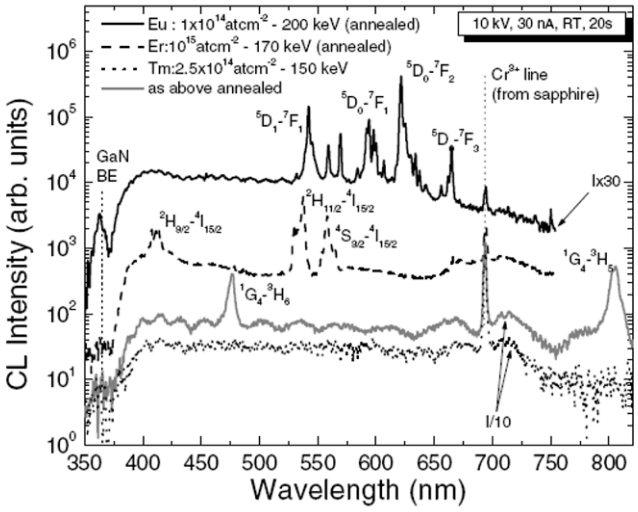

Fig. 7.4. Room temperature CL spectra of GaN films implanted with each of the different RE ions after annealing. The spectrum from an unannealed GaN:Tm sample is also shown.

RE doping by implantation, beside its numerous advantages (no solubility limit, dose control, no impurity introduction, etc.), leads to a very thin doped layer and to the creation of damage. Simulations performed with the SRIM 2000 software [23] indicate that for implantation energies in the range 80 -170 keV the majority of the ions reside within a depth of between 30 and 80 nm. In order to obtain the depth profile of the implanted RE in the GaN host, composition measurements using WDX analysis were performed as a function of the incident electron beam voltage. The energy threshold for the generation of the Eu L_α X-rays, 7 kV, corresponds to a probed depth of 200 nm in GaN. Therefore, it is not possible to confine the WDX measurement to the RE-containing layer. Measurements are used in combination with computer software which simulates a layered structure. In the case of Er, the lower threshold for the M_α X-rays, 2 kV, allows the excitation to be confined to the implanted region, thereby increasing the accuracy of the results. Fig. 7.5 shows the ratio of the X-ray counts measured on the sample to that from a standard (I_x/I_0) as a function of electron beam voltage for Eu- and Er-implanted GaN samples. The lines show simulated profiles calculated using software supplied with the Cameca EPMA with the assumption of a single uniform layer of RE-doped GaN layer. While this assumption clearly does not match the depth profile of the implanted ions it does allow estimates of the average ion concentrations and implant depth.

The Ga and N signals are not shown but are very close to unity at all voltages, due to the similarity of the sample and standard. The values for the RE concentration and thickness obtained from the fitted lines shown in Fig. 7.4, are reported in Table 7.1.

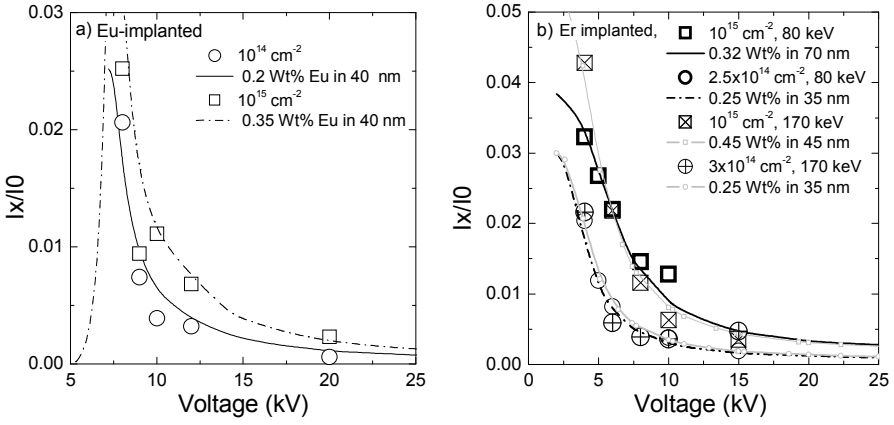

Fig. 7.5. WDX data measured as a function of electron beam voltage for (a) Eu- and (b) Er-implanted GaN samples. The lines are the theoretical profiles assuming a single uniform layer of RE-doped GaN layer. Reprinted with permission from [22]. Copyright (2003) Institute of Physics Publishing.

Table 7.1. Thicknesses and weight percentages extracted from the fit of the RE concentration measured as a function of the beam voltage for the different samples.

	#Eu1 : 10^{14} cm^{-2} 200 keV	#Eu2 : 10^{15} cm^{-2} 200 keV	#Er1 : 3×10^{14} cm^{-2} 170 keV	#Er2 : 10^{15} cm^{-2} 170 keV	#Er3 : 2.5×10^{14}cm^{-2} 80 keV	#Er4 : 10^{15} cm^{-2} 80 keV
RE thickness	40 ± 5 nm	40 ± 5 nm	35 ± 5 nm	45 ± 5 nm	30 ± 5 nm	70 ± 5 nm
RE concentration (Weight%)	0.20±0.02	0.35±0.02	0.25±0.02	0.45±0.05	0.25±0.05	0.32±0.02

The thicknesses obtained for the implanted zone are in agreement with the SRIM simulations though slightly smaller in the case of the samples implanted with an energy of 170 keV. Rutherford back scattering measurements performed on the Eu-implanted samples also confirmed these results [24]. The expected increase in concentration of both elements, Er and Eu, with fluence is seen in the case of samples implanted at the same energy. The WDX analyses allow us to determine Eu and Er concentrations down to ~0.2 % and 0.3 % by weight, which correspond to atomic concentrations of ~ 0.06 % and 0.08 %, respectively, in very thin layers.

The mapping capability of the modified microprobe can be used to explore variations in material composition and their correlation with RE-related luminescence. Fig. 7.6 shows WDX and CL maps acquired over a region of about 20 μm^2 for a Eu-doped GaN sample capped with a thin layer of AlN (see Section 7.4 for more details). In this case the AlN cap is non-ideal and shows cracks in the back-scattered electron image (Fig. 7.6(a)) [25]. A full spectrum, similar to that in Fig. 7.6(d) is collected at each pixel in the map and can be represented by a variety of 2D-images such as the plot of the intensity of the $^5D_0 - {}^7F_2$ line shown in Fig. 7.6.(e). These can then be correlated with the WDX maps plotting the intensity of specific X-ray lines.

The sample has been annealed at 1200 ºC but in areas where no cracks are present, the AlN provides good protection and no loss of N or Ga is evident. In the vicinity of damaged regions, however, the composition maps show that N is lost all along the cracks, while Al and Ga are deficient only when holes are formed. This reveals a dissociation mechanism with two steps: first, N outdiffuses through cracks, and then a breach forms in the AlN cap through which Ga from the underlayer is also lost. The CL map of the intensity of the Eu-emission line shows this to be reduced in the regions where nitrogen is severely deficient, below the AlN cracks. The Eu X-ray intensity map does not show a reduction near the cracks but only where holes are formed. Thus, the decrease in the CL intensity is related not to Eu loss but to N deficiency. Somewhat surprisingly, an increased CL intensity is sometimes observed around the holes [25].

The simultaneous CL and WDX mapping provides a very useful tool for RE-doped samples allowing the RE composition and luminescence to be correlated on a sub-micron scale and also correlated with subtle changes in the host properties.

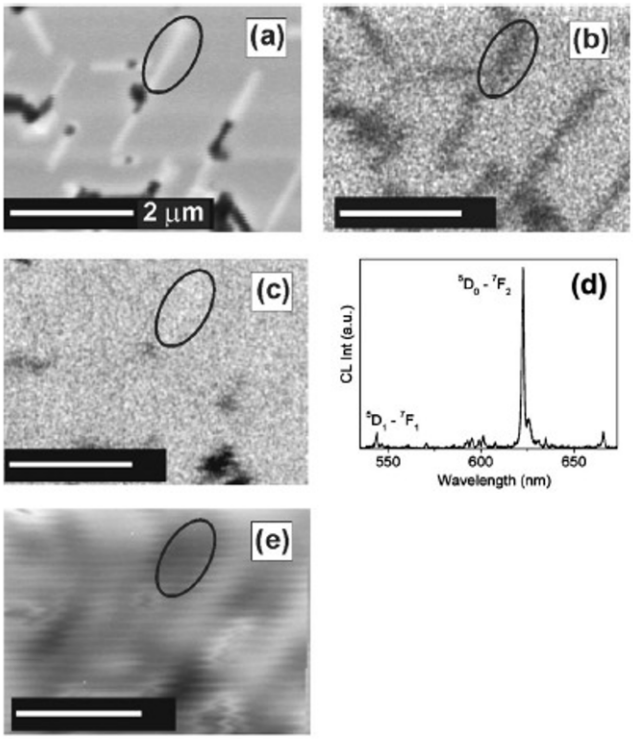

Fig. 7.6. (a) Back-scattered electron image of Eu-implanted AlN-capped sample of GaN after annealing at 1200 °C, and corresponding compositional mappings obtained with WDX of (b) N and (c) Ga signals. (d) Spectrum obtained in this area showing the Eu-related sharp line cathodoluminescence. (e) CL map showing the integrated $^5D_0$– $^7F_2$ intensity corresponding to the same area (dark, ~1500 counts, bright, ~5500 counts). The ellipse shows a Ga-rich area associated with decreased emission efficiency. Reprinted with permission from [25]. Copyright (2006) American Institute of Physics.

7.4 Annealing Temperature Dependence of RE Luminescence

Ion implantation represents an attractive tool for selective area doping, dry etching or electrical isolation and is a key technology in semiconductor industry. The build-up of implantation damage in GaN has recently been investigated and reviewed. [26, 27]. As shown in Fig. 7.4, ion-implanted samples must be annealed to counteract this damage. In this respect the thermal robustness can be a specific advantage of the III-nitrides. Bare GaN can be annealed up to around 900 ºC without damage and, as will be discussed below, AlGaN can be safely annealed at even higher temperatures. (InGaN is found to be much less robust but section 7.7 describes some surprising results for AlInN which shows resistance to thermal damage at temperatures well above its growth temperature (approximately 800 ºC)). Nevertheless further advantages are

expected to follow from annealing samples at even higher temperatures. To some extent the material breakdown that tends to occur can be prevented by means of proximity caps and N_2 over-pressure but a simpler method of protection presents itself and is now discussed.

Hard materials generally show rather poor recovery of lattice damage, even at very high annealing temperatures. The best results are achieved by combining very high temperatures with large nitrogen overpressures (10 kbar) [26, 27]. Although this technique is not suitable for industrial use, it was shown that complete recovery of ion-bombarded GaN occurs for annealing temperatures in excess of 1400 °C. An easier method is to anneal samples provided with an AlN capping layer. High electrical activation of implanted dopants has been achieved by this method [26, 27, 28]. In most cases, the cap layer was deposited after implantation by reactive sputtering. Further benefits accrue from using Eu-implanted GaN capped with a thin (10 nm) *in situ* AlN layer, grown epitaxially by metalorganic chemical vapour deposition (MOCVD) prior to the implantation [29]. This layer serves as a protective cap both during the implantation and during post-annealing, and leads to significantly increased luminescence intensity, compared to non-capped samples. After annealing, the AlN layer can be easily removed with a KOH-based etchant [26] but it could also be beneficial to keep it in place for electroluminescence devices (ELD).

The benefits of the *in situ* AlN cap and high temperature annealing were demonstrated using Eu ion implantation of AlN/GaN/sapphire structures which were annealed for 20 min at 1100, 1200, and 1300 °C in a conventional tube furnace using a modest overpressure of nitrogen gas. The structural properties of the samples were analyzed using Rutherford Backscattering Spectrometry/Channelling (RBS/C) and the optical activation of the RE ions by room temperature CL spectroscopy [29].

The damage build-up during implantation is evident in the RBS/C results shown in Fig. 7.7. The Ga signal of a typical random spectrum and aligned spectra, after Eu implantation with and without the AlN cap, are shown along with an aligned spectrum for an unimplanted (virgin) sample.

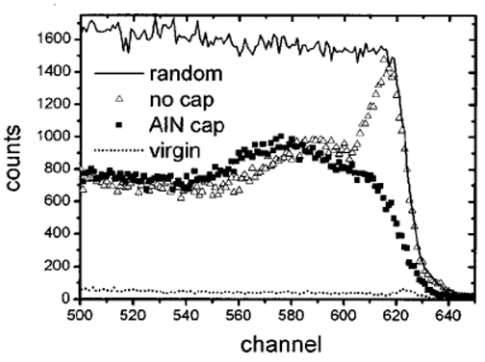

Fig. 7.7. RBS/C random and [0001] aligned spectra after implantation with 2×10^{15} Eu/cm^2 into uncapped GaN and GaN capped with a 10 nm AlN layer. Reprinted with permission from K. Lorenz, U. Wahl, E. Alves, S. Dalmasso, R. W. Martin, K. P. O'Donnell, S. Ruffenach, and O. Briot, Appl. Phys. Lett. **85**, 2712. Copyright (2004) American Institute of Physics.

The uncapped sample undergoes the typical damage build-up reported for various implanted species including RE ions. [27, 30]. There are two damage regions: one near the sample surface takes the form of a thin amorphous layer, confirmed by RBS/C and TEM studies following thulium implantation; another forms deeper inside the crystal at the end of range of the implanted ions [16]. In the literature two hypotheses are advanced for the origin of the surface peak [26]. The first is that the surface acts as a sink for migrating point defects, resulting in an amorphous layer that grows gradually with the implanted ion dose; the second is that the surface amorphous layer results from preferential sputtering of nitrogen by the ion beam. The AlN-capped sample in Fig. 7.7 shows a very different behaviour with no surface peak in the RBS spectrum. Amorphization has therefore been suppressed by use of the cap, favouring the second hypothesis.

In general no Eu luminescence is observed directly after implantation. After annealing CL spectroscopy reveals characteristic red Eu emission shown in Fig. 7.8. The CL intensity exhibits an exponential dependence on annealing temperature.

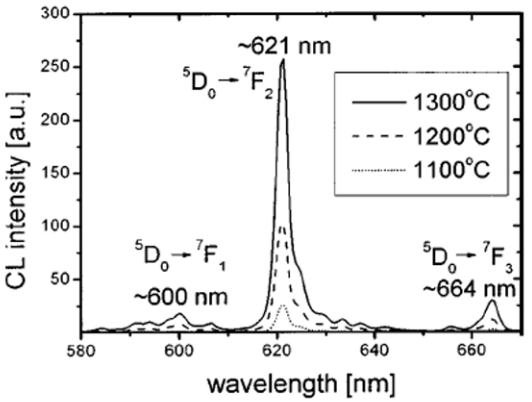

Fig. 7.8. Room temperature CL spectra of AlN-capped GaN implanted with 1×10^{15} Eu/cm^2, taken with a beam voltage of 10 kV and a current of 10 nA, after annealing at 1100, 1200, and 1300 °C. Reprinted with permission from K. Lorenz, U. Wahl, E. Alves, S. Dalmasso, R. W. Martin, K. P. O'Donnell, S. Ruffenach, and O. Briot, Appl. Phys. Lett. **85**, 2712. Copyright (2004) American Institute of Physics.

The intensity of luminescence from a capped and an uncapped sample after annealing at 1000 °C is comparable, since this temperature is only just high enough to promote thermal breakdown of GaN. Dissociation of the GaN surface becomes clearly visible after 1100 ºC annealing and the luminescence intensity becomes very inhomogeneous. For the AlN-capped samples the intensity of the strongest line increases by an order of magnitude between 1100 and 1300 °C. This improvement in luminescence output represents a considerable improvement on previous work and enables the identification of additional fine structure in the luminescence spectrum of GaN:Eu, as discussed in Section 7.5.

The strong increase in luminescence intensity is surprising, given the small change observed in the RBS spectra. Implanted Eu ions are on average incorporated on a site slightly displaced from the Ga site [15]. In this case the backscattering yield from Eu in the aligned measurement has not changed significantly with annealing temperature and the increase in CL intensity cannot be due to the presence of a larger substitutional fraction of Eu on Ga sites. However, it is possible that, at the high annealing temperatures used here, the displacement of Eu ions from the perfect substitutional site changes. Another possible explanation for the increase in luminescence intensity could be the interaction of Eu with certain kinds of defects to form more optically active centres.

Nogales et al. [31] examined the protective ability of various AlN caps on a micro-scale and demonstrated the importance of having the correct thickness and structure in order to suppress thermal breakdown of the nitride hosts at very high temperature. Typical data from this study were presented in section 7.3.

7.5 Site Multiplicity in GaN:Eu Revealed by Photoluminescence Spectroscopy

The ultra-high temperature annealing introduced in the previous section results in extremely bright RE-related luminescence from ion-implanted III-nitride samples, paving the way for in-depth studies of the spectral properties of the luminescent RE ions. In this section a high resolution study of Eu luminescence in GaN will be described. Photoluminescence (PL) and PL excitation (PLE) data will be used, measured at cryogenic temperatures to maximize the PL intensity and minimize the linewidths. The question to be addressed is the extent to which the optical spectroscopy can provide information on the number, nature and relative efficiencies of RE sites for a given host material. After setting the scene for this type of study, information gained from combined PL/PLE studies of Eu-implanted GaN, annealed at very high temperatures, will be presented.

Nyein et al. [32] inferred the existence of different Eu- related optically active centres in GaN from the observation that the PL decay dynamics and thermal quenching depend on the energy of excitation. PLE spectroscopy by the same workers revealed five absorption lines in the spectral region from 570 to 590 nm associated with the 'sensitive' $^7F_0$–$^5D_0$ transition. Selective excitation of PL by resonant pumping into these lines changes the envelope of the near-620 nm spectral emission, although individual lines were not resolved [33]. PLE is also a useful technique to study the excitation transfer from the host GaN, via such processes as carrier-mediated excitation, excitation by excitons, and defect-mediated excitation. For example, PLE studies of GaN:Eu at 300 K revealed the existence of a sub-gap absorption band at 400 nm [32] (although subsequent measurements indicate that this is associated with a broad background luminescence which underlies the near-620 nm PL, rather than with the sharp line Eu PL

itself [34]). Temperature-dependent and excitation wavelength-dependent PL decay transients were later explained in terms of different energy transfer pathways [35, 36]. By using the systematic approach of combined excitation-emission spectroscopy (CEES), Dierolf et al. presented a detailed assignment of PL and PLE peaks for two dominant Er^{3+} sites and several minor ones in GaN:Er [37]. The identified sites differ strongly in their excitation and energy transfer efficiencies. Chap. 8 updates these results.

Turning now to look specifically at the red emission of GaN:Eu, I will focus on the fine structure of the $^5D_0$–$^7F_2$ multiplet with a view to identifying the origin of the different components. The majority of RE ions incorporated into GaN have been shown to substitute for Ga: the C_{3v} site symmetry is expected to remain intact as charge compensation is not required. The high symmetry leads to an expectation that the $^5D_0$–$^7F_2$ transition will split into a maximum of three lines.

Fig. 7.9 shows PL spectra of the red emission lines for a series of AlN-capped GaN:Eu samples implanted with the same fluence of 1×10^{15} at/cm^2 and annealed at 1000, 1100, and 1300 ºC, respectively. Similar to results presented in section 7.4, a dramatic increase in emission intensity is seen when the anneal temperature increases from 1000 to 1300 ºC. The higher spectral resolution reveals significant changes in the spectral pattern. For the sample annealed at 1300 ºC, the emission is split into 3 strong lines and a number of weaker ones. The strongest peak, at 620.8 nm, is followed by relatively strong peaks at 621.7 nm and 622.5 nm. By contrast the middle peak is the strongest in spectra taken after annealing at 1000 and 1100 ºC and the 620.8 nm peak is not visible at all in the spectrum of the 1000 ºC sample.

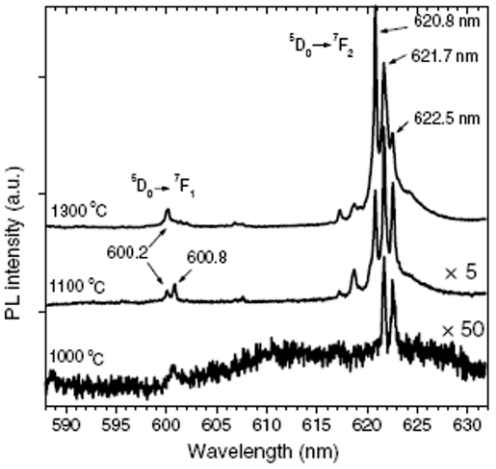

Fig. 7.9. 15 K PL spectra of AlN-capped GaN samples implanted with 1×10^{15} Eu/cm^2 and annealed at 1000, 1100, 1300 ºC. The 325 nm line of a He–Cd laser was used as the excitation source. Reprinted from Opt. Mater. **28**, K. Wang, R. W. Martin, E. Nogales, V. Katchkanov, K. P. O'Donnell, S. Hernandez, K. Lorenz, E. Alves, S. Ruffenach, and O. Briot, 797. Copyright (2006) with permission from Elsevier.

Turning attention to the $^5D_0$–$^7F_1$ transition, the peak at 600.2 nm is seen to increase much faster than the peak at 600.8 nm as the annealing temperature increases and dominates after annealing at 1300 ºC. The PL intensity of these peaks clearly have different dependencies on the anneal temperature, suggesting the existence of at least two different Eu sites. The annealing promotes damage recovery, and maybe other effects in the lattice, which impact on the emission efficiency of these different centres in different ways. The Eu centre responsible for the peak at 620.8 nm requires more thermal energy to form than the other peaks but as the annealing proceeds it becomes dominant. It should be noted that the PL spectra of GaN:Eu also show in general a set of near-band-edge peaks in the wavelength range from 370 to 400 nm [38], to be discussed further in section 7.6.

The spectra in Fig. 7.9 were excited conventionally by the 325 nm line of a 10 mW HeCd laser; it proves informative to tune this excitation wavelength, as can be achieved by replacing the laser with monochromated light from a Xe arc lamp. Although the excitation intensity is considerably reduced (the monochromated output is about 1 mW per mm slit width) the high brightness of the AlN-capped GaN:Eu samples allows excellent PL spectra to be obtained. Examples are shown in Fig. 7.10 for excitation at 356 nm (matching the GaN band-gap) and at 385 nm (0.25 eV below the gap). The sample is the one annealed at the highest temperature.

The PL spectrum excited with light resonant with the GaN band-edge shows the three main peaks described above, at 620.8, 621.7, 622.5 nm along with three minor peaks at 617.2 nm, 618.7 nm and 619.3 nm. Shoulders also appear in the wavelength range 623–625 nm. The first main peak at 620.8 nm, with a FWHM of 0.4 nm, is the dominant one and the third line at 622.5 nm is weak. More importantly, the middle line is now seen to consist of two components with a peak at 621.7 nm and a shoulder at 621.9 nm. In previously published works the splitting of the central peak had not been clear bearing testament to the benefits of high temperature annealing.

With excitation tuned below the host band gap, the PL spectrum changes markedly (Fig. 7.10). The line at 620.8 nm is now the weakest of the four main ones and the peak at 622.5 nm is enhanced. Moreover, the middle peak becomes much sharper and is slightly blue shifted to 621.6 nm, due to the selective enhancement of one of the pair of unresolved lines. The minor peaks in the shorter wavelength range from 617 to 620 nm disappear completely and the intensity of the unresolved emission in the longer wavelength range from 623 to 625 nm is also reduced. The spectra clearly show emission in the $^5D_0$–$^7F_2$ transition region to consist of four main lines, one of which is not completely resolved [39, 40, 41].

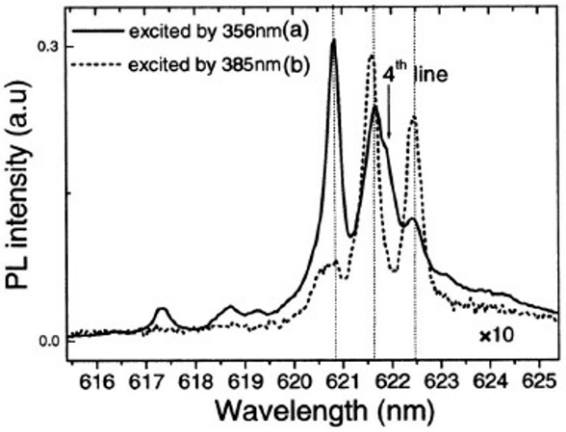

Fig. 7.10.15 K PL spectra of AlN-capped GaN implanted with 2×10^{15} Eu/cm^2, after annealing at 1300 °C. Excited above band gap (solid line) and below band gap (dotted line) by light from a monochromated Xenon lamp. Reprinted with permission from K. Wang, R. W. Martin, K. P. O'Donnell, V. Katchkanov, E. Nogales, K. Lorenz, E. Alves, S. Ruffenach, and O. Briot, Appl. Phys. Lett. **87**, 112107. Copyright (2005) American Institute of Physics.

Consider now PLE spectra detected at the three wavelengths marked by vertical lines in Fig. 7.10. The spectra, shown in Fig. 7.11 after normalization to the signal height at 356 nm, clearly demonstrate above-gap excitation (<355 nm) and an exciton-like absorption peak at 356 nm. The significant difference between the three traces is the appearance of a broad excitation band centred at about 385 nm for the emission at 621.7 nm (unresolved doublet) and 622.5 nm (singlet). Some weak structures can also be observed within the band near 372 and 385 nm. The PLE spectrum detected at 621.7 nm collects light from two emission peaks to produce an excitation spectrum that is roughly the average of the other two. It can be seen that the broad below-gap band excites only the line pair at 621.7 and 622.5 nm. These data separate the lines in the multiplet into two pairs of two strong lines, whose identification points to at least two sites (Eu1 and Eu2) for luminescent Eu in GaN. The site producing the lines at 621.7 and 622.5 nm shall be referred to as Eu1, and will be found to also be dominant in $Al_xGa_{1-x}N$:Eu with $x > 0.15$ [42]. It appears to be the same centre found in implanted GaN annealed at low temperature. The second luminescent centre (Eu2), involving lines near 620.8 and 621.5 nm can be excited *only* by light above the band gap and becomes dominant in GaN samples annealed at higher temperatures.

Symmetry considerations lead one to expect triplets rather than doublets and it is likely that the third lines are either hidden under the stronger ones or appear as one of the weaker lines seen in the PL spectra. Recent work by

Roqan, O'Donnell et al. on high-pressure annealed GaN:Eu, where the damage induced by implantation is completely removed has produced spectra with a pure Eu2 nature, considerably reduced linewidths and further splittings [34]. The longer wavelength component of Eu2 is now seen to be composed of two lines and the Eu2 luminescence shown to be related to the principal Eu-on-Ga substitutional site, without any associated defects.

Selectively excited PL in the regions near 602 nm ($^5D_0$–$^7F_1$) and 664 nm ($^5D_0$–$^7F_3$) have also been investigated and show similar results [40].

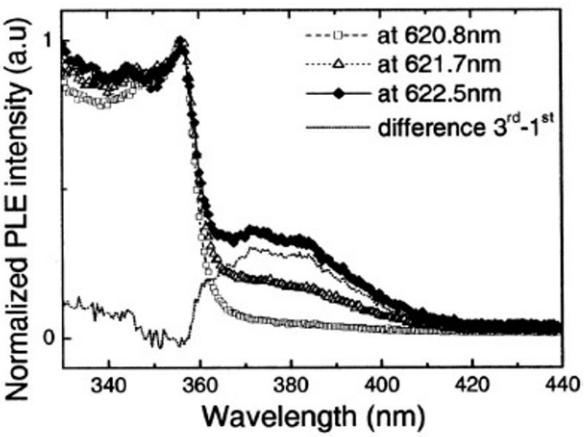

Fig. 7.11. 15 K normalized PLE spectra of AlN-capped GaN implanted with 2×10^{15} Eu/cm^2, after annealing at 1300 °C, detected at the three main peaks, 620.8 nm, 621.7 nm, and 622.5 nm. Also shown (dotted line) is the difference between the first and last PLE spectra. Reprinted with permission from K. Wang, R. W. Martin, K. P. O'Donnell, V. Katchkanov, E. Nogales, K. Lorenz, E. Alves, S. Ruffenach, and O. Briot, Appl. Phys. Lett. **87**, 112107. Copyright (2005) American Institute of Physics.

Measuring the temperature and excitation intensity dependences of the PL and PLE spectra, such as those in Fig. 7.10 and 11 provides extra information [40, 41]. Above-gap excited PL spectra measured from 15 to 297 K demonstrate different thermal quenching rates for the three main peaks, with the peak at 620.8 nm quenching much faster than the other two [38]. Below-gap excitation at 385 nm reduces the strong lines in the multiplet to the emission pair at 621.7 and 622.5 nm. Fig. 7.12 shows the quenching behaviour of this pair.

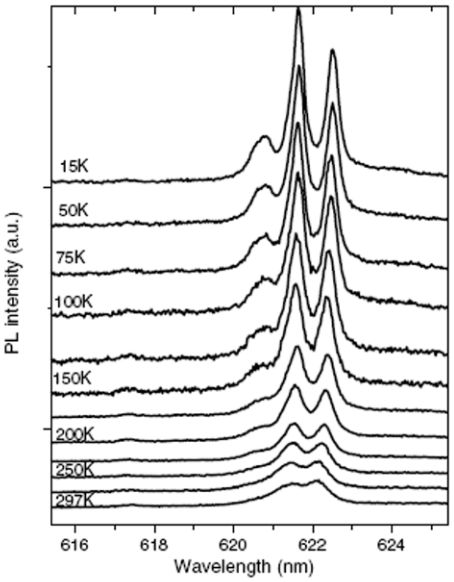

Fig. 7.12. PL spectra excited by 385 nm light from 15 to 297 K. Reprinted from Opt. Mater. **28**, K. Wang, R. W. Martin, E. Nogales, V. Katchkanov, K. P. O'Donnell, S. Hernandez, K. Lorenz, E. Alves, S. Ruffenach, and O. Briot, 797. Copyright (2006) with permission from Elsevier.

Thus, high resolution PL/PLE spectroscopy can be used to break down an RE multiplet into sets of different lines with different excitation pathways. These then point to different Eu centres within the GaN lattice, possibly involving interaction with different types of defects. The latest results [34] indicate that Eu2 is the pure substitutional site (Eu_{Ga}) whilst Eu1 involves the substitutional Eu ion in association with another defect.

7.6 Luminescence of Eu Ions in AlGaN across the Entire Alloy Composition Range

The previous section explored the luminescence of Eu implanted into GaN and focussed on the fine structure in the $^5D_0$-$^7F_2$ multiplet. Attention is now turned to the luminescence of Eu ions in wider gap III-N alloys with a view to providing a model for the excitation-emission process.

The "rule" of Favennec *et al.* indicates that materials with wider bandgaps show lower thermal quenching of RE luminescence [2]. The observation of comparatively intense RE luminescence from III-nitride hosts points the way to the use of AlN-rich hosts such as AlGaN and AlInN. The band-gap of AlN has a value of 6.2 eV. The work of Wakahara demonstrated that $Al_xGa_{1-x}N:Eu^{3+}$

luminescence efficiency improves as the AlN fraction *x* increases from 0 to ~0.3 but decreases at higher values [14]. Lee and Steckl [43] and Hommerich et al. [44] had earlier reported similar behavior for $Al_xGa_{1-x}N$:Tm, with maximum emission occurring in the range $0.6<x<0.8$. Subsequently Wang et al. [42] investigated PL and PLE spectra of Eu-implanted $Al_xGa_{1-x}N$ across the entire alloy composition range and developed a model of the nature of the luminescent sites.

Current spectroscopic models of RE ions in solids derive from descriptions of free *4f*-states, with large spin-orbit coupling, perturbed by crystal fields. On this basis, atomic term identifiers are assigned to experimental emission lines [45]. The relatively small perturbation of host-ion interactions plays an essential role in *enabling* luminescence, by relaxing selection rules [46]. However, the search for chemical trends in the values of the several parameters that quantify the interaction has had mixed results. At the same time, there is confusion regarding the mechanism of excitation energy transfer from extended to localized states at light-emitting centres in RE-doped semiconductors. The emphasis here has been either on the atomic properties of RE ions or on the defect physics of the hosts. Aligning the energy levels of the RE ions with the band diagram of the host [47, 48] corresponds to a model of excitation via charge transfer from nearest neighbours (ligands) to the RE *4f* shell. An alternative description regards the RE^{3+} ion as an isoelectronic trap, which localizes a carrier; the charged centre subsequently binds a carrier of opposite sign to form a localized exciton, which then excites the *4f* shell [49, 50]. Excitation models requiring a further 'RE-related defect' which may be a 'carrier trap' [51] to mediate the excitation process also feature in the literature [52]. Wang et al. [42] demonstrated that aspects of both descriptions are important to describe the RE luminescence and attempt to present a unified description of the phenomenology, as described in this section.

The proposed excitation model for $Al_xGa_{1-x}N:Eu^{3+}$ formally equates charge transfer with isoelectronic exciton creation and thus avoids the need for sensitizing defects. The entire sharp line emission is ascribed to the annihilation of excitons at Eu ions. Similar experimental findings for Dy-, Tm- and Pr-doped samples [53, 54] suggest that excitonic processes feature strongly in the optical spectroscopy of light-emitting RE-doped nitrides.

The complete composition range of $Al_xGa_{1-x}N$ was covered by two series of samples. One series of ~700 nm thick $Al_xGa_{1-x}N$ epilayers with low AlN molar fractions ($x \leq 0.22$) was grown by metal organic vapor phase epitaxy (MOVPE) Another series of nominally 500 nm thick $Al_xGa_{1-x}N$ layers with AlN fractions, $0.07 \leq x \leq 1$, were grown by hydride vapour phase epitaxy (HVPE). Eu ions were implanted into each sample to a fluence of 1×10^{15} at/cm^2 along the surface normal, with a beam energy of 300 keV. Post-implantation annealing was performed in N_2 at temperatures from 1000-1300 ºC. All the samples were protected using an unimplanted AlN proximity cap during annealing in order to inhibit out-diffusion of nitrogen. A thin epitaxial AlN capping layer additionally protects the GaN sample as described earlier. High-resolution PL spectra were taken at 15 K in the vicinity of the $^5D_0$-$^7F_2$ transition (~622 nm in GaN) and PLE spectra obtained by monitoring selected lines of this transition while scanning the excitation wavelength.

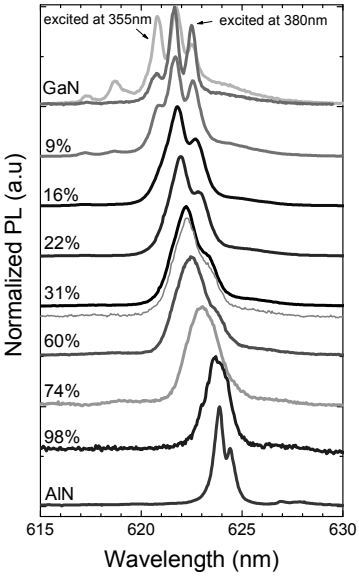

Fig. 7.13. High resolution 15 K PL spectra of the $^5D_0$-$^7F_2$ transition of implanted $Al_xGa_{1-x}N$:Eu over the whole alloy composition range. Reprinted with permission from K. Wang, K. P. O'Donnell, B. Hourahine, R. W. Martin, I. M. Watson, K. Lorenz, and E. Alves, Phys. Rev. B. Copyright (2009) the American Physical Society.

Fig. 7.13 plots PL spectra in the region of the $^5D_0$-$^7F_2$ transition for nine samples, normalized to the intensity of the highest peak. For two samples, two PL spectra are shown, corresponding to excitation above and below the band-gap. In the other cases the excitation wavelengths used were those of the $Al_xGa_{1-x}N$ bandgaps, as determined by PLE spectra, except for AlN, excited by 325 nm laser light, and $Al_{0.98}Ga_{0.02}N$, excited at 345 nm by the Xe lamp.

PL spectra of all samples also feature a broad UV band [38] with an integrated PL intensity roughly equal to the sum of *all* the visible sharp-line emissions. As described in Section 7.5 [39, 40, 41], and shown in Fig. 7.13, two distinct Eu spectra occur when GaN:Eu is excited above and below the band edge. Selectively excited spectra for $Al_{0.07}Ga_{0.93}N$:Eu are shown in Fig. 7.14(a) and demonstrate a similar situation, indicating at least two Eu centres in these samples. The peak at 620.8 nm is clearly observed for excitation at energies above the band edge (343 nm), but its intensity decreases dramatically for sub-gap excitation (e.g. 365 or 380 nm). Fig. 7.14(b) shows similar results for $Al_{0.09}Ga_{0.91}N$:Eu, although the decrease in intensity of the extra line is less pronounced. However, for $Al_xGa_{1-x}N$ hosts with $x > 0.15$, excitation above or below the band edge results in almost identical spectral patterns. Additional lines seen for $0 < x < 0.15$ samples resemble those in GaN that can only be excited by above-bandgap light.

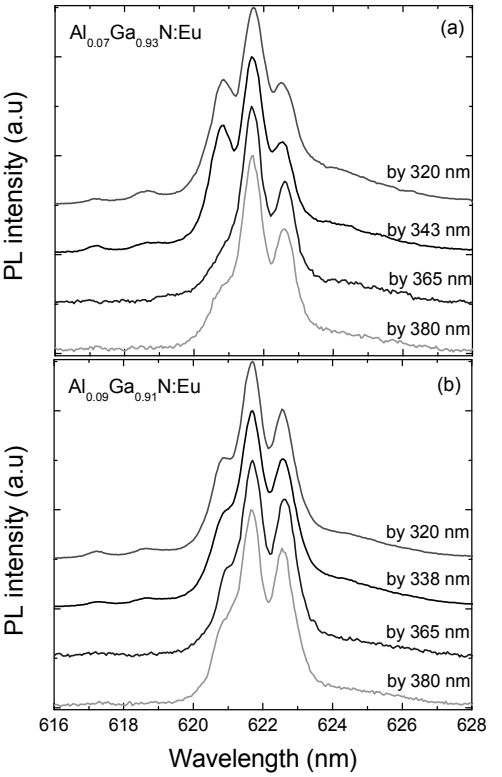

Fig. 7.14. Selectively excited 15 K PL spectra of Eu $^5D_0$-$^7F_2$ emission for (a) $Al_{0.07}Ga_{0.93}N$:Eu and (b) $Al_{0.09}Ga_{0.91}N$:Eu. Reprinted with permission from K. Wang, K. P. O'Donnell, B. Hourahine, R. W. Martin, I. M. Watson, K. Lorenz, and E. Alves, Phys. Rev. B. Copyright (2009) the American Physical Society.

Finally, annealing $Al_xGa_{1-x}N$:Eu with $x > 0.15$ at high temperatures strongly influences the line intensities but does not alter the spectral pattern. As seen earlier, in GaN:Eu, the two dominant Eu centers have very different annealing dependences [40].

These observations are all consistent with the presence in $Al_xGa_{1-x}N$ samples with $x > 0.15$ of a single luminescent Eu centre, which can be excited both above and below the host band gap. The Eu centre in GaN excited by light both below and above the band-gap, which is referred to as Eu1, dominant in $Al_xGa_{1-x}N$ with $x > 0.15$, appears to be the same as that found in GaN annealed at low temperature. The additional Eu luminescence spectrum (Eu2), found in $Al_xGa_{1-x}N$ samples with $x < 0.15$ can *only* be excited above the gap and becomes dominant in GaN samples annealed at higher temperatures [40, 41] *or* higher pressures [34].

Fig. 7.15 shows the integrated PL and CL intensities as a function of AlN fraction, normalized to that of GaN:Eu. The PL spectra were obtained by excitation at the band edge (except for AlN:Eu, which is excited at 350 nm) and the resulting intensity adjusted according to the intensity of the incident excitation light. The intensity increases in the low Al content region and reaches a maximum at around x = 0.2-0.3. Wakahara et. al. [14] reported an increase of more than one order of magnitude for $Al_{0.4}Ga_{0.7}N$:Eu compared to GaN:Eu and a decrease for x > 0.4. It should be noted that the amount by which the PL intensity increases will depend on the annealing conditions.

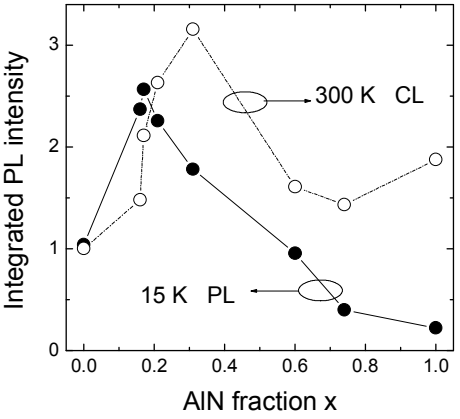

Fig. 7.15. The integrated 15 K PL (left) and 300 K CL (right) intensity of $^5D_0$-$^7F_2$ transition of Eu luminescence from 615 to 630 nm as a function of AlN fraction. Reprinted with permission from K. Wang, K. P. O'Donnell, B. Hourahine, R. W. Martin, I. M. Watson, K. Lorenz, and E. Alves, Phys. Rev. B. Copyright (2009) the American Physical Society.

The linewidths of the component lines of the $^5D_0$-$^7F_2$ emission multiplet show marked variations with composition. In order to extract the component linewidths, the emission spectra were decomposed into 2 or 3 Lorentzians, depending on the value of *x*. Fig. 7.16 plots the full width at half maximum (FWHM) of the fitted components as a function of AlN fraction. The asymmetrical variation in linewidth as a function of composition is strongly reminiscent of that observed for bound excitons in semiconductor alloys [55]. We fit to the extracted linewidth data an expression adapted from that derived in [56]:

$$\sigma(x) = \sigma_0 + \frac{dE_g(x)}{dx}\sqrt{\frac{8\ln(2)x(1-x)}{(4\pi/3)R_{ex}^3 K}} \qquad (1)$$

K is the cation/anion number density, $\sqrt{2}/a_0^3$ for the wurtzite lattice, with a_0=3.15 Å the *average* a-plane lattice constant (for simplicity). The residual linewidth, σ_0,

is taken to be 1.4 meV for all samples. RBS estimates of residual lattice disorder agree with this assumption. The fit is seen to be exceptionally good, with small scatter in the component linewidths for a given composition.

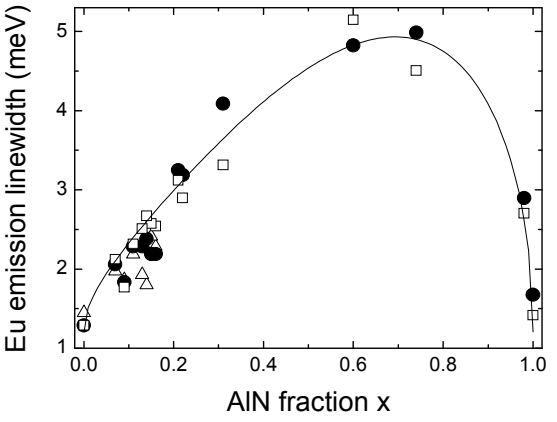

Fig. 7.16. FWHM of the main emission lines of the Eu $^5D_0$-$^7F_2$ transition as a function of AlN molar fraction. The triangles, circles and squares correspond to the lower, central and upper wavelength lines of the PL "triplet", respectively. The solid line is described in the text and is a fit to the circular data points. Reprinted with permission from K. Wang, K. P. O'Donnell, B. Hourahine, R. W. Martin, I. M. Watson, K. Lorenz, and E. Alves, Phys. Rev. B. Copyright (2009) the American Physical Society.

Using experimental band-gaps and bowing parameter of E_g(GaN, AlN) = 3.5 eV, 6.2 eV and b = -1.5 eV to determine dE_g/dx, we estimate a mean exciton radius, R_{ex}, of ~10 nm. More important than this magnitude is the fact that the asymmetric dependence of linewidth on x shows the influence of alloy disorder through the binomial term in Eq. (1) with an energy scaling that depends only on the bowing parameter, b.

Similar broadening is observed in spectra of Dy:$Al_xGa_{1-x}N$ [53], which also shows a small upshift in peak energy, in Tm:$Al_xGa_{1-x}N$ [53], which has no measurable peak shift and in Pr:$Al_xGa_{1-x}N$ [54]. These observations suggest an excitonic aspect of Eu, Pr, Dy and Tm emissions in $Al_xGa_{1-x}N$. The maximum broadening of Eu:$Al_xGa_{1-x}N$ emission lines (~3.5 meV at x ~ 0.75) is ~10 times smaller than that of band-edge excitons [56]. For such excitons, the emission energy is naturally associated with the optical band gap; but the *peak* energy of the $^5D_0$-$^7F_2$ transition of Eu is found to be almost independent of the host composition: it decreases by only 7 meV between GaN and AlN. We note that a strikingly similar asymmetry of the magnetic moment of Tm:$Al_xGa_{1-x}N$ has been recently reported by Nepal et al. [57].

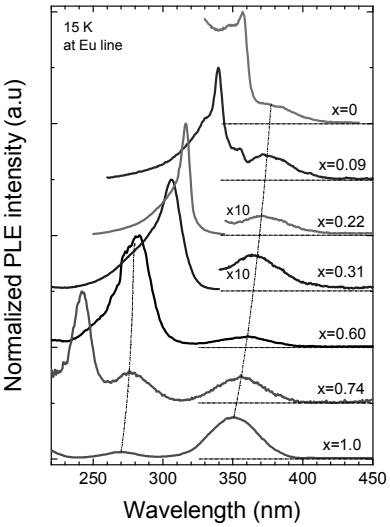

Fig. 7.17. 15 K PLE spectra of Eu:$Al_xGa_{1-x}N$ detected at the peak of the $^5D_0$-$^7F_2$ luminescence, apart from the case of GaN for which the long wavelength line was used. All spectra, except AlN, were normalized to the band-edge peak. The dashed lines are guides for the eye, charting the evolution of the X_1 and X_2 features. Reprinted with permission from K. Wang, K. P. O'Donnell, B. Hourahine, R. W. Martin, I. M. Watson, K. Lorenz, and E. Alves, Phys. Rev. B. Copyright (2009) the American Physical Society.

Fig. 7.17 compares PLE spectra of Eu:$Al_xGa_{1-x}N$ samples, detected at the strongest peak of the $^5D_0$-$^7F_2$ luminescence apart from that for GaN, x = 0, for which the long wavelength peak at 622.5 nm was used to avoid mixing in the second Eu component. The PLE spectra are normalized to the excitation peak at the band edge, except in the case of AlN, for which the band-edge onset near 200 nm (6.2 eV) is beyond the reach of our excitation lamp. All spectra show at least one 'below-gap' excitation band, which we label X_1, whose peak energy up-shifts linearly with increasing x as plotted in Fig. 7.18. The shift, from 3.26 eV for GaN to 3.54 eV for AlN, is only a tenth of the band-gap widening. As a consequence the excitation feature lies close to the band edge for GaN but approaches mid-gap for AlN. For low AlN fractions, X_1 overlaps the strong band-edge absorption, but it is resolved even for GaN. Its FWHM is approximately constant, with a value near 0.4 eV across the whole composition range. As the AlN fraction increases, a second feature (X_2 on Fig. 7.18), with a similar FWHM to X_1, emerges below the shifting gap at x~0.6. Eu in $Al_xGa_{1-x}N$ thus introduces two excitation bands, both of which may lead to PL of Eu1 centres.

In the absence of microscopic information on defect structure, we shall provide a description of the $X_{1,2}$ bands as *excitonic* features associated with Eu1 centres. In light of observing similar PLE data from a wide range of different samples it can be seen that the involvement of "sensitizing defects" in the excitation process of AlGaN:Eu_I is an unnecessary complication. Many, perhaps all, RE-doped wide

band gap solids feature strong UV absorption peaks, similar to X_1 here, which are usually assigned to "electrons… excited from a neighbouring anion orbital onto the dopant ion" [58]. Furthermore the obvious candidate species for a sensitizing defect, the native lattice point defects created during implantation, would be expected to show much stronger shifts in energy of $X_{1,2}$ with composition, due to the strong valence- or conduction-band-like character of their associated states. By trapping an exciton, Eu1 centres can act as their own sensitizer.

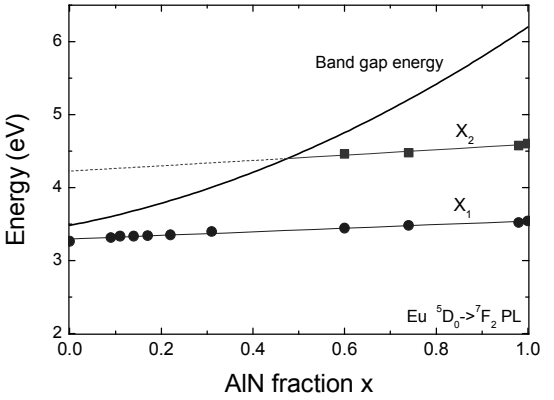

Fig. 7.18. Excitation energies of Eu:$Al_xGa_{1-x}N$ derived from PLE as a function of AlN molar fraction. The x-axis corresponds to the PL used to monitor the excitation spectra. Reprinted with permission from K. Wang, K. P. O'Donnell, B. Hourahine, R. W. Martin, I. M. Watson, K. Lorenz, and E. Alves, Phys. Rev. B. Copyright (2009) the American Physical Society.

In the language of semiconductor physics, electron transfer from a nitrogen ligand to a neighbouring RE ion produces a core exciton, favoured by the strong exciton binding energy in wide gap III-nitrides. The charge transfer state is analogous to a core exciton on account of the large separation of electron and hole which enhances the oscillator strength of the transition. A charge transfer into the empty *5d*-shell of the RE would leave the *4f* optical core states of the RE essentially unchanged. Such an entity will be referred to as a *d*-exciton. The excess energy in this *d*-exciton can then be transferred to the *4f* shell leading to the characteristic sharp line RE^{3+} emission. At the same time, the UV emission band [38] may be ascribed to internal recombination of *d*-excitons. The anomalous loss, in the context of the Favennec rule, of luminescence efficiency of the sharp lines at high values of *x* reflects the emergence of X_2, whose higher energy opens the possibility of extra energy losses in the excitation-emission cycle.

The general form of the fitting used in eq. (1) applies to a state with sufficient spatial extent to sample the composition fluctuations of an alloy and therefore be sensitive to "local" band-gap variations. If variations in the crystal field, due to local compositional fluctuations, were responsible for broadening the line, the variation of linewidth might be expected to be symmetric about x = 0.5. For

ordinary alloy excitons, the transition energy can be very closely identified with the band gap; this is obviously not true for the $^5D_0$-$^7F_2$ PL component lines, which shift by only 7 meV between GaN and AlN. (Dy- and Tm-related PL lines in $Al_xGa_{1-x}N$ shift by even smaller amounts, but still broaden considerably). Fig. 7.16 thus demonstrates that a spatially extended state is involved in the $^5D_0$-$^7F_2$ luminescence, associated with the de-excitation of the extended *d*-exciton. It is interesting to compare this situation with the case of transition metal (TM) ions in II-VI compounds, where capture of a conduction band electron by TM^{3+} results in TM^{2+} emission [59].

This exciton picture, combined with the estimated "exciton" size implies that these centers are closer in character to isoelectronic exciton traps [50, 60] than a defect perturbed by a crystal field. Unlike conventional isoelectronic centres however, the complexities of the rare-earth electron configuration must also be considered. Additionally the presence of the X_2 excitation band must still be explained. Lozykowski et al. [60] have argued that clustering of RE ions is responsible for a series of PLE features, which would correspond to the series of excitation features $X_{1,2...n}$; however such clustering would lead to characteristic features in the emission spectra of some RE ions [61] and there is still the problem of excitation transfer from cluster to single ion to contend with. Moreover, EXAFS studies of GaN:Eu, even at rather large doping levels, have shown only isolated Eu_{Ga} [45]. The host-independent and almost RE-independent, X-band energies suggest an alternative origin, as the $5d^1$ configuration splits into high and low spin states, separated by ~1 eV according to [47, 48].

The second luminescent Eu site (Eu2), which appears in the low AlN content ($x < 0.15$) $Al_xGa_{1-x}N$ samples, is subject to a very different excitation path involving only light with energy greater than the band gap. The excitation/emission cycle of this defect is the focus of ongoing studies.

7.7 Luminescence of RE Ions in AlInN Hosts

The previous section discussed RE emission using AlGaN as a host, with the wider band gap of this material offering notable further advantages for RE doping. The other AlN-containing III-nitride alloy, AlInN, also affords potential as a wide-gap RE host and has the additional advantage that it can be lattice matched to GaN, for an InN fraction of 16%–17% [17, 62]. The band gap of $Al_{0.83}In_{0.17}N$ is about 4.3 eV [62, 63]. This section describes the use of AlInN as a host material for RE light emission. The optical properties of four series of Eu and Er implanted AlInN/GaN and GaN samples, each annealed at different temperatures in the range from 700 to 1300 °C, are investigated using CL spectroscopy.

AlInN layers, nominally 130 nm thick, were grown at Strathclyde University by Dr. I.M. Watson on GaN-on-sapphire buffers. The layer used for Eu implantation was grown at a set point of 840 °C with an InN fraction estimated as 15±2 at.%. That used for Er implantation was grown at 820 °C with an InN fraction

estimated as 17±2 at.%. Eu and Er ions were implanted into the AlInN/GaN bilayers using a 120 keV beam to a nominal dose of 1×10^{15} at./cm^2 with the beam tilted 10° away from the surface normal in order to minimize channelling. The implanted samples were then annealed at different temperatures in the range from 700 to 1300 °C for 20 min in a conventional tube furnace filled with nitrogen gas at 4 bar overpressure. When the annealing temperature exceeds the growth temperature of the host materials, some decomposition is expected: principally, loss of In from AlInN and N loss from GaN.

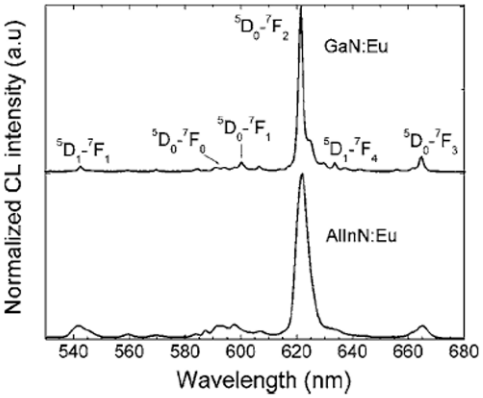

Fig. 7.19. RTCL spectra of Eu implanted GaN and AlInN annealed at 1100 °C and normalized to the intensity at 622 nm. Reprinted with permission from K. Wang, R.W. Martin, E. Nogales, P. R. Edwards, K. P. O'Donnell, K. Lorenz, E. Alves and I. M. Watson, Appl. Phys. Lett. **89**, 131902. Copyright (2006) American Institute of Physics.

Fig. 7.19 compares typical RTCL spectra of Eu:AlInN and GaN:Eu samples, both annealed at 1100 °C. The emission lines can be assigned to the intra-4*f* shell transitions of Eu ions, marked on the figure. The spectra are normalized to the peak of the strongest emission line at 622 nm, which we know to be composed of several lines (see previous sections of this chapter).

All of the Eu emission lines appear at roughly the same spectral positions for the two different hosts, with the strongest line showing only a very slight *redshift* for Eu:AlInN compared to GaN:Eu. The main difference between the spectra is in the width of the emission lines. The FWHM of the main peak increases from ~2 nm for GaN to ~5 nm for AlInN. Moreover, it is found that the broadening of the emission lines does not change with the annealing temperature, indicating that the width is not likely to be a function of annealing damage, but is associated with some aspect of the loval environment which is insensitive to annealing. Thus, it can be inferred that it is alloy disorder that increases the width of Eu emission lines in AlInN, relative to GaN. Similar data and conclusions apply to Er-implanted AlInN, although in this case the broadened AlInN:Er peaks are slightly *blueshifted* with respect to GaN:Er. [64].

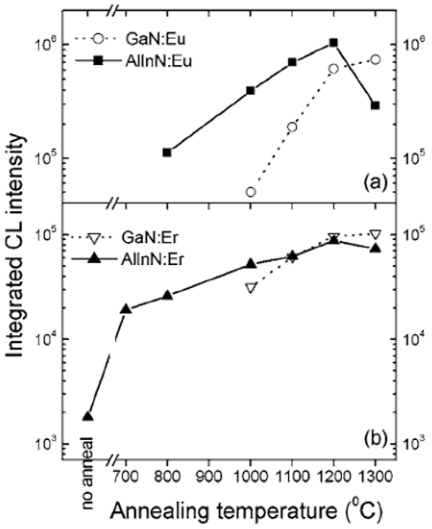

Fig. 7.20. Integrated RTCL intensity of (a) Eu-implanted GaN and AlInN (b) Er implanted GaN and AlInN annealed at different temperatures and measured under the same conditions. Reprinted with permission from K. Wang, R.W. Martin, E. Nogales, P. R. Edwards, K. P. O'Donnell, K. Lorenz, E. Alves and I. M. Watson, Appl. Phys. Lett. **89**, 131902. Copyright (2006) American Institute of Physics.

The variation of the integrated CL intensity of the main RE emission lines with annealing temperature is shown in Fig. 7.20. The integrated CL intensity (610–635 nm) of AlInN:Eu increases by one order of magnitude as the annealing temperature is increased from 800 to 1200 °C. It is noticeable that the integrated CL intensity of AlInN:Eu is several times stronger than that of GaN:Eu except for 1300 °C annealing. Moreover, some of the as-implanted AlInN:Eu samples emit red light whereas GaN:Eu does not show any detectable emission prior to annealing.

The integrated CL intensity (510–580 nm) of the AlInN:Er samples increased by a factor of about 5 in the annealing temperature range from 700 to 1200 °C. The significant drop in CL intensity for the sample annealed at 1300 °C is due to decomposition of the ternary alloy. It is worth mentioning again that the as-implanted AlInN:Er was found to emit green light whereas GaN:Er did not show any emission prior to annealing. The integrated CL intensity of AlInN:Er is very close to that of GaN:Er annealed at the same temperatures. By way of comparison, the optimized integrated CL intensity of Eu luminescence from both hosts is similar and one order of magnitude stronger than Er luminescence from the same hosts.

SEM images of AlInN:Eu give clues to explain the rapid reduction in CL intensity of the AlInN sample annealed at 1300 °C. The sample annealed at 1000 °C has a very clear and homogeneous background with some pits distributed across

its surface, which are also seen in the as-grown samples. When the anneal temperature is increased to 1200 °C, the background of the SEM image shows a mixture of dark and light regions, suggesting that some decomposition of the AlInN has occurred. However, the CL intensity of Eu emission still increases in spite of the obvious deterioration of the sample. The SEM image of AlInN:Eu annealed at 1300 °C shows extra features and the CL intensity of this sample is much reduced.

WDX measurements of sample composition reveal that the InN fraction is constant at 17% when the annealing temperature is 1100 °C. A slight decrease, to 16% InN, is observed for annealing at 1200 °C but severe decomposition with significant In loss (measured InN fraction down to 10%, accompanied by a compensating Ga signal) was observed for samples annealed at 1300 °C [64]. It is, however, remarkable that the implanted sample is able to withstand annealing at up to 400 °C above the AlInN growth temperature.

Further work on the structural and optical properties of Eu-implanted AlInN were reported by Roqan et al. [65]. Selectively excited PL and PLE spectra reveal the presence of a single dominant optical centre in AlInN, in contrast to GaN:Eu. In addition the Eu^{3+} emission from $In_{0.13}Al_{0.87}N$:Eu was shown to undergo significantly less thermal quenching than GaN:Eu, as the temperature is increased from cryogenic temperatures to room temperature.

7.8 Conclusion

This chapter has reviewed the luminescence of, mainly, Europium ions in a range of III-N hosts: namely GaN, AlGaN and AlInN. For GaN, Eu is shown to occupy at least two luminescent sites, labelled Eu1 and Eu2, which have been distinguished spectroscopically. For a GaN host, Eu1 luminescence can be excited by above or below band-gap light whilst Eu2 luminescence is excited only by above-gap light. Very recent work indicates that Eu2 is the pure Eu-on-Ga substitutional site, whilst the Eu1 site involves substitutional Eu in association with an additional defect. Examination of the luminescence of Eu in AlGaN as a function of AlN mole fraction showed increasing luminescence for the wider gap hosts, up to a point, and that the Eu1 centre dominates for AlN fractions in excess of 0.15. Analysis of the luminescence linewidth as a function of host composition and investigation of the excitation spectra reveal the core-exciton-like nature of Eu1. AlInN:Eu alloys are brighter than comparable GaN:Eu and have promising resistance to thermal quenching. Taken together the above results demonstrate the significant amount of interesting physics associated with the luminescence of RE ions in III-nitride hosts along with the range of potential light emitter applications.

Acknowledgements

The majority of the data and ideas presented here arise out of fruitful collaborations with a large group of excellent researchers, originating in the EU Network RENiBEl. I acknowledge the input of Kevin O'Donnell, leader of the semiconductor group at Strathclyde and also of the RENiBEl Consortium, and those of Eduardo Alves, Debbie Amabile, Alain Braud, Stephane Dalmasso, Paul Edwards, Sergi Hernandez, Ben Hourahine, Slava Kachkanov, Katharina Lorenz, Vasco Matias, Bert Pipeleers, Iman Roqan, Andre Vantomme, Bart De Vries, Akiro Wakahara, Ke Wang and Ian Watson. Support of the European Research Training Network Project RENiBEl (Contract No. HPRN-CT-2001-00297), EPSRC and the University of Strathclyde are gratefully acknowledged.

References

1 A. J. Steckl, J. C. Heikenfeld, D. S. Lee, M. J. Garter, C. C. Baker, Y.Q. Wang, and R. Jones, IEEE J. Selected Topics in Quant. Electronics **8**, 749 (2002)
2 P. N. Favennec, H. L'Haridon, M. Salvi, D. Moutonnet, and Y. Le Guillou, Electron. Lett. **25**, 718 (1989)
3 R.G. Wilson. R.N. Schwartz, C.R. Abernathy, S.J. Pearton, N. Newman, M. Rubin, T. Fu and J.M. Zavada, Appl. Phys. Lett. **65** (1994) 992
4 J.D. Mackenzie, C.R. Abernathy, S.J. Pearton, U. Hommerich, X. Wu, R.N. Schwartz, R.G. Wilson, J.M. Zavada, J. Cryst. Growth **175** 84 (1997)
5 A. J. Steckl and R. H. Birkhahn, *Appl. Phys. Lett.*, 73, 1700, 1998. *ibid.* 73 2450 (1998)
6 R. H. Birkhahn, M. J. Garter, and A. J. Steckl, *Appl. Phys. Lett.*, 74, 2161, 1999
7 J. Heikenfeld, M. J. Garter, D. S. Lee, R. H. Birkhahn, and A. J. Steckl, *Appl. Phys. Lett.*, 75, 1189, 1999
8 A. J. Steckl, M. J. Garter, D. S. Lee, J. Heikenfeld, and R. H. Birkhahn, *Appl. Phys. Lett.*, 75, 2184, 1999
9 H.J. Lozykowski *et al*. 1999, Appl. Phys. Lett., **74**, 1129
10 J.H. Park, A.J. Steckl, *Appl. Phys. Lett.* **85** 4588 (2004)
11 J.H. Park, A.J. Steckl, *Appl. Phys. Lett.* **88** 011111 (2006)
12 K. Gurumurugan, Hong Chen, G. R. Harp, W. M. Jadwisienczak and H. J. Lozykowski, Appl. Phys. Lett. **74** 3008 (1999)
13 H. J. Lozykowski, W. M. Jadwisienczak, J. Han, I. G. Brown, Appl. Phys. Lett. **77** 767 (2000)
14 A. Wakahara, Optical Materials **28**, 731 (2006)
15 E. Alves, K. Lorenz, R. Vianden, C. Boemare, M. J. Soares, and T. Monteiro, Mod. Phys. Lett. B **15**, 1281 (2001)
16 K. Lorenz, U. Wahl, E. Alves, T. Wojtowicz, P. Ruterana, S. Dalmasso, R.W. Martin, and K. P. O'Donnell, Mater. Res. Soc. Symp. Proc. **798**, Y5.5 (2004)
17 K. Lorenz, N. Franco, E. Alves, I.M. Watson, R.W. Martin, K.P. O'Donnell, Phys. Rev. Lett. **97** 085501 (2006)
18 R.W. Martin *et al*. 2002, Phys. Stat. Sol. (a) **192** 117

19 R.W. Martin, P.R. Edwards, K.P. O'Donnell, M.D. Dawson, C.-W. Jeon, C. Liu, G. R. Rice, and I. M. Watson, phys. stat. sol. (a) **201** 665 (2004)
20 P.R. Edwards, R.W. Martin, K.P. O'Donnell and I.M.Watson, phys. stat. sol. (c) **0** 2474 (2003)
21 P.R. Edwards, R.W. Martin, and M.R. Lee, American Mineralogist **92** 235 (2007)
22 S. Dalmasso, R.W. Martin, P.R. Edwards, K.P. O'Donnell, B. Pipeleers, B. de Vries, A. Vantomme, Y. Nakanishi, A. Wakahara, A. Yoshida & the RENiBEl Network, Inst. Phys. Conf. Series **180** 555 (2003)
23 J.F. Ziegler, J.P. Biersack and U. Littmark, The Stopping and Range of Ions in Solids (Pergamon Press, New York, 1985)
24 B. Pipeleers and A. Vantomme, unpublished results
25 E. Nogales, R. W. Martin, K. P. O'Donnell, K. Lorenz, E. Alves, S. Ruffenach and O. Briot, Appl. Phys. Lett. **88**, 031902 (2004)
26 S. J. Pearton, J. C. Zolper, R. J. Shul, and F. Ren, J. Appl. Phys. **86**, 1 (1999)
27 O. Kucheyev, J. S. Williams, and S. J. Pearton, Mater. Sci. Eng., R. **33**, 107 (2001)
28 J. C. Zolper, J. Han, R. M. Biefeld, S. B. van Deusen, W. R. Wampler, D. J. Reiger, S. J. Pearton, J. S. Williams, H. H. Tan, R. F. Karlicek, J. R. Stall, and R. A. Stall, J. Electron. Mater. **27**, 179 (1998)
29 K. Lorenz, U. Wahl, E. Alves, S. Dalmasso, R. W. Martin, K. P. O'Donnell, S. Ruffenach, and O. Briot, Appl. Phys. Lett. **85**, 2712 (2004)
30 K. Lorenz, E. Alves, U. Wahl, T. Monteiro, S. Dalmasso, R. W. Martin, K.P. O'Donnell, and R. Vianden, Mater. Sci. Eng., B **105**, 97 (2003)
31 E. Nogales, R. W. Martin, K. P. O'Donnell, K. Lorenz, E. Alves, S. Ruffenach and O. Briot, Appl. Phys. Lett. **88**, 031902 (2004)
32 E.E. Nyein, U. Hommerich, J. Heikenfeld, D.S. Lee, A.J. Steckl, J.M. Zavada, Appl. Phys. Lett. **82** (2003) 1655
33 U. Hommerich, E.E. Nyein, D.S. Lee, J. Heikenfeld, A.J. Steckl, J.M. Zavada, Mater. Sci. Eng. **B 105** (2003) 91
34 I.S. Rogan, K.P. O'Donnell et al., Phys. Rev. **B 81** 085209 (2010)
35 Chang-Won Lee, H.O. Everitt, D.S. Lee, A.J. Steckl, J.M. Zavada, J. Appl. Phys. **95** (2004) 7717
36 H.Y. Peng, Chang-Won Lee, H.O. Everitt, D.S. Lee, A.J. Steckl, J.M. Zavada, Appl. Phys. Lett. **86** (2005) 051110
37 V. Dierolf, C. Sandmann, J. Zavada, P. Chow, B. Hertog, Appl. Phys. Lett. **95** (2004) 5464
38 K.P. O'Donnell, V. Katchkanov, K. Wang, R.W. Martin, P.R. Edwards, B. Hourahine, E. Nogales, J.F.W. Mosselmans, B. De Vries, Mater. Res. Symp. Proc. 831 (2004) E9.6.1
39 K. Wang, R. W. Martin, K. P. O'Donnell, V. Katchkanov, E. Nogales, K. Lorenz, E. Alves, S. Ruffenach, and O. Briot, Appl. Phys. Lett. **87**, 112107 (2005)
40 K. Wang, R. W. Martin, E. Nogales, V. Katchkanov, K. P. O'Donnell, S. Hernandez, K. Lorenz, E. Alves, S. Ruffenach, and O. Briot, Opt. Mater. **28**, 797 (2006)
41 L. Bodiou, A. Oussif, A. Braud, J.-L. Doualan, R. Moncorgé, K. Lorenz, E. Alves, Opt. Mater. **28** 780 (2006)
42 K. Wang, K. P. O'Donnell, B. Hourahine, R. W. Martin, I. M. Watson, K. Lorenz, and E. Alves, Phys. Rev. **B 80** 125206(2009)
43 D.S. Lee and A.J. Steckl, Appl. Phys. Lett. **83** 2094 (2003)
44 U. Hommerich, E.E. Nyein, D.S. Lee, A.J. Steckl, and J.M. Zavada, Appl. Phys. Lett. **83** 4556 (2003)
45 K. P. O'Donnell and B. Hourahine, Euro. Phys. J. Appl. Phys. **36**, 91 (2006)
46 B. Judd, Phys. Rev. **127**, 750 (1962); G. Ofelt, J. Chem. Phys. **37**, 511 (1962)

47 P. Dorenbos and E. van der Kolk, Proc. of SPIE **6473**, 647313 (2007)
48 P. Dorenbos and E. van der Kolk, Optical Materials, **30** 1052 (2008)
49 H. J. Lozykowski, Phys. Rev. **B 48**, 17758 (1993)
50 H. J. Lozykowski, W. M. Jadwisienczak, A. Bensaoula, and O. Monteiro, Microelectronics J. **36**, 453 (2005)
51 S. Kim, S. J. Rhee, D. A. Turnbull, X. Li, J. J. Coleman, S. G. Bishop and P. B. Klein, Appl. Phys. Lett., **71**, 2662 (1997)
52 S. Petit, R. Jones, M. J. Shaw, P. R. Briddon, B. Hourahine, and T. Frauenheim, Phys. Rev. **B 72**, 073205 (2005)
53 I.M. Roqan, K.P. O'Donnell et al. to be published
54 M. Peres, S. Magalhaes, N. Franco, M.J. Soares, A.J. Neves, E. Alves, K. Lorenz, T. Monteiro, Microelectronics Journal **40** 377–380 (2009)
55 E. F. Schubert, E. O. Gobel, Y. Horikoshi, K. Ploog, and H. J. Queisser, Phys. Rev. **B 30**, 813 (1984)
56 A. N. Westmeyer, S. Mahajan, K. K. Bajaj, J. Y. Lin, H. X. Jiang, D. D. Koleske, and R. T. Senger, J. Appl. Phys. **99**, 013705 (2006)
57 N. Nepal, S.M. Bedair, N.A. El-Masry, D.S. Lee, A.J. Steckl, J.M. Zavada, Appl. Phys. Lett. **91**, 222503 (2007)
58 B. Henderson and G. F. Imbusch, *Optical Spectroscopy of Inorganic Solids*, Oxford: Clarendon Press (1989), p204
59 K. P. O'Donnell, K. M. Lee, and G. D. Watkins, J. Phys. C **16**, L723 (1983)
60 H. J. Lozykowski and W. M. Jadwisienczak, phys. status solidi (b) **244**, 2109 (2007)
61 L. Bodiou, A. Braud, C. Terpin, J. L. Doualan, R. Moncorge, K. Lorenz and E. Alves, Journal of Luminescence **122–123**, 131 (2007)
62 J. F. Carlin, C. Zellweger, J. Dorsaz, S. Nicolay, G. Christmann, E. Feltin, R. Butté, and N. Grandjean, phys. status solidi B **242**, 2326 (2005)
63 K. Wang, R.W. Martin, D. Amabile, P.R. Edwards, S. Hernandez, E. Nogales, K.P. O'Donnell, K. Lorenz, E. Alves, V. Matias, A. Vantomme, D. Wolverson and I.M. Watson, J.Appl. Phys. **103** 073510 (2008)
64 K. Wang, R.W. Martin, E. Nogales, P. R. Edwards, K. P. O'Donnell, K. Lorenz, E. Alves and I. M. Watson, Appl. Phys. Lett. **89**, 131902 (2006)
65 I.S. Roqan, K.P. O'Donnell, R.W. Martin, C. Trager-Cowan, V. Matias, A. Vantomme, K. Lorenz, E. Alves, and I. M. Watson, J. Appl. Phys. **106** 083508 (2009)

Chapter 8
Combined Excitation Emission Spectroscopy (CEES) of RE Ions in Gallium Nitride

Volkmar Dierolf

Abstract We review the results of site-selective spectroscopy studies of RE-doped III-nitrides performed using combined excitation emission spectroscopy (CEES). This systematic technique allows the identification of a large number of different incorporation sites for three RE dopants (Eu, Er, Nd) in GaN. The technique is ideally suited to distinguish different sites from additional lines that are caused by thermally activated levels or phonon-assisted transitions. In this way, we reassign spectra in a new consistent manner. Utilizing the spectral fingerprints of each different site, we show how the relative occupation of sites is influenced by the growth and doping conditions. For Er^{3+} we characterize how the sites participate in up-conversion excitation processes. For Eu^{3+} we are able to relate the sites to different excitation channels after above-bandgap excitation.

8.1 Introduction

RE ions in AlInGaN alloys have great potential as active ions in optical, electronic and magnetic application such as color displays, laser sources, optical amplifiers, and spintronics-type devices. It was realized early on that, depending on the growth conditions, RE ions may be incorporated into the GaN matrix with a range of environments, leading to different optical properties, excitation channels and emission efficiencies under electrical excitation. For this reason, it is crucial that the different incorporation environments (referred to as “sites” in

Physics Department, Lehigh University, 16 Memorial Drive East, Bethlehem, PA 18015, USA
Phone: USA-610-758-3915
Fax: USA-610-758-5730
vod2@lehigh.edu

the following) be characterized reliably. In this chapter, we will highlight the results obtained with the CEES technique, that is ideally suited for the required systematic studies [1].

We present in separate sections our results for Er, Nd, and Eu in GaN. For the latter ion, we also present some data on $Al_xGa_{1-x}N$ alloys. We will use the Erbium ion as the prime example to illustrate the power of our spectroscopic method. We performed the most extensive studies on Eu-doped materials, for which we will present many details such as electron-phonon coupling and the excitation channels for different sites, For all three ions, we will present fingerprints of their ground state and some excited states for a variety of sites, which will be useful to connect our work with that in other chapters of this book. Whenever possible we will also relate our results to results published in previous literature.

8.1.1 RE Ions in GaN: General Considerations

RE ions are characterized by a 4*f* shell that is sequentially filled as we go from La to Lu. The 4*f* electrons are well shielded from external fields by the completely filled $5s^2$ and $5p^6$ shells, which have a larger radial extension than the 4*f* shell. The neutral RE atoms have in addition to the filled shells and the 4*f* shell two or three electrons in the 5*d* and 6*s* shells. These electrons are removed to form ions. In the case of a trivalent ion, which is the most common valence state of RE ions, only the partially filled 4*f* shell and the [Xe] core remain. To calculate the energy levels of the ions, the Coulomb interaction between the 4*f* electrons and the spin-orbit interaction have to be taken into account. Both interactions are of about equal size such that neither the *LS* coupling nor the *jj* coupling scheme of atomic angular momenta is strictly applicable. Nevertheless, the *LS*-scheme (e.g.: $^{2S+1}L_J$) is used for naming the various levels. For example, for the 11 electrons of the Er ion the total orbital angular momentum can be L = 0...8 and for the total spin S = 1/2 and 3/2 are possible. This results in 41 $^{2S+1}L_J$ multiplets with $^4I_{15/2}$ being the ground state, as shown in the inset of Fig. 8.15 below. Similar level schemes can be obtained for the other ions (Nd, Eu) to be discussed in this chapter. They are shown in Fig. 8.18 and Fig. 8.26, respectively. For a discussion of the general properties of RE ions, see [2].

When an ion is introduced into a crystal lattice, it experiences the electric crystal field. However, due to the effective shielding of the outer shells the 4*f* electrons are only weakly influenced resulting in the sharp absorption and emission lines characteristic of trivalent RE ions in crystals. The crystal field interaction, however, is sufficient to allow these ions to probe the local environment and consequently, the excitation and emission transitions are modified. From an experimental point of view, the small interaction allows work in a narrow spectral range for which lasers and spectrometers can be optimized; due to the narrow linewidths, even small spectral changes can be resolved.

It has been established by Rutherford backscattering (e.g. [3, 4]), EPR ([5]) and EXAFS that the main RE incorporation site in GaN is substitutional for Ga. Since no charge compensation is required, little perturbation of the C_{3v} symmetry is expected. Nevertheless, we will demonstrate that in many samples multiple incorporation sites exist. Possible emitting centres are RE_{Ga} sites perturbed by neighbouring defects such as Ga- or N-vacancies.

8.1.2 CEES Experimental Setup

One aim of this chapter is to promote the experimental technique CEES for the detailed characterization of incorporation sites of dopants into a given host material. Excitation and emission spectroscopy are standard methods commonly used to study correlated absorption-emission transitions. However, sometimes several absorption and emission transitions are energetically very close, which makes it difficult to distinguish them. For this reason, it is important to systematically measure the emission spectra over a limited range of excitation energies. We employ array detectors for fast measurement of the individual spectra with high reproducibility, while we scan the excitation photon energy in small steps over the whole spectral range where photon absorption is expected. This is the basic idea behind CEES [6]. The experimental setup is sketched in Fig. 8.1. To encourage adoption of this technique and duplication of our set-up, we give here full details of our implementation. Readers familiar with the technique may choose to skip this description.

Measuring a large number of emission spectra while stepping the excitation photon energy leads to a two-dimensional data set of intensity as a function of both excitation photon energy and emission photon energy, which can be best visualized as a contour plot or as an image. In a contour plot, points of the same intensity are connected by a line similar to contour lines in a topographic map. The image plot assigns a color scale to the intensity. Intensity maxima correspond to excitation and emission maxima. The contour and image plots allow a relatively quick visual inspection of the spectral information, including identification of different defect sites which are only slightly separated in energy as well as the exact determination of excitation and emission lines. Image plots can be further treated with all the tools available in image processing software to mine information from a particular subset of data. For more rigorous analysis, we can extract excitation and emission spectra for any given energy in the region of our scan. Due to the limitation of the color scale this has to be done whenever relative intensities are to be compared quantitatively.

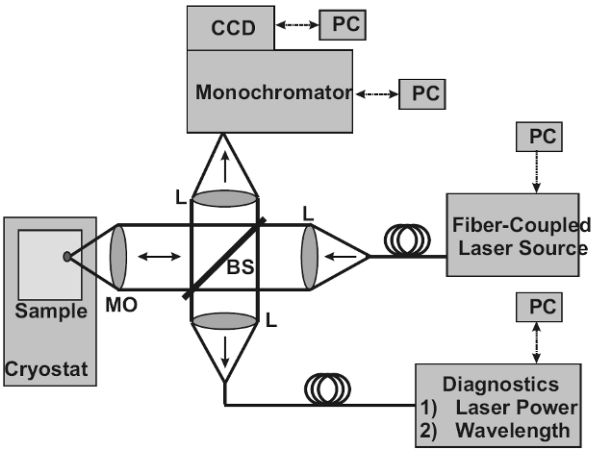

Fig. 8.1. Diagram of the basic setup for optical spectroscopy . BS: Beamsplitter, L: Lens, MO: Microscope objective.

The fiber-coupled laser in Fig. 8.1 was either an Argon Ion laser (manufacturer: Coherent, model: Innova 90 or Innova 200), an Argon Ion laser pumped dye laser (manufacturer: Coherent, model 590), external cavity diode laser (manufacturer: Sacher Lasertechnik, model Littman 500) or telecom-style tunable semiconductor laser for 1.5 μm (Photonetics Model: Tunics-Plus), which was amplified using an Er-doped fiber amplifier (IPG Photonics) The dye laser wavelength is tuned by turning a three-stage birefringent filter and the ECL wavelength is tuned by turning the grating of the external cavity. In practise, the wavelength tuning was performed by a personal computer controlled stepping motor. The stepping motor controller (manufacturer: Portescap, Inc., model:IM-483) received the step signal from the counter output of a multi-purpose digital analog PC interface card (manufacturer: National Instruments, model: DAQ 6025E). The linewidth of the dye-laser was about 500 MHz and of the ECL about 100 KHz. In all experiments, the linewidths of the lasers were smaller than the inhomogeneously broadened linewidths of the optical transitions of the ions under investigation. The laser light was coupled into a single mode fiber, which allows the use of lasers which are located in other rooms The other end of the fiber, which was brought to the experiment, acts as a well-defined point source. This allows easy interchange of the excitation sources.

The laser light diverging from the fiber was collimated and passed through a bandpass filter to suppress unwanted light from the argon plasma, spontaneous broadband emission of the dye solution or inelastic scattered light produced in the fiber. Part of the collimated laser beam was reflected by a beamsplitter or by an additionally introduced glass plate. This reflected light passed a second beamsplitter, which further separated the beam. One beam was directly imaged onto a photodiode connected to a Lock-In amplifier (manufacturer: Ithaco, model: 393)

while the second was coupled into a multimode fiber which was then plugged into a wavemeter (manufacturer: Coherent, model: Wavemaster) controlled through a general purpose interface bus (GPIB) interface by the PC. The output of the Lock-In amplifier was connected to the analog input of a multi-purpose digital analog PC interface card (manufacturer: National Instruments, model: DAQ 6025E). Combining these measurements yields a reliable diagnostic of the laser in terms of intensity and wavelength. The majority of the collimated laser beam is sent through a beamsplitter (prism cube or appropriately chosen dichroic mirror) and imaged onto the sample, mounted in a liquid-helium cooled cryostat (manufacturer: Oxford Instruments, model: Microstat) allowing continuous variation of the sample temperature between 4 K and 380 K. This microscope cryostat offers the possibility for sub-micron spatial resolution. On the other hand, by not using immersion for optimal heat contact with the sample, the local sample temperature might be higher than the temperature measured at the cold finger, in particular under intense laser excitation. All experiments that we report were performed at the lowest temperature achievable (nominally 4 K).

After 90º reflection by the beam splitter, luminescence from the sample was imaged on the entrance slit of the monochromator (manufacturer: Acton Research Corporation, model: SpectraPro 500i). Depending on the experimental conditions, suitable filters were used to suppress unwanted light. The slit width of the monochromator was always chosen according to the intensity of the emission light, desired spectral resolution, and chosen grating. The highest achievable resolution was ~ 0.1 meV in the green spectral region. The monochromator was controlled through a GPIB interface by the PC. A charge coupled device (CCD) (manufacturer: Princeton Instruments, model: LN/CCD/1340/100 E/1) cooled to –120 ºC with liquid nitrogen, and a thermoelectrically cooled InGaAs diode array (manufacturer: Hamamatsu, 49212-5125) were used as detectors. The CCD has an array size of 1340×100 pixels and was used primarily for visible light detection, while the InGaAs array, 512×64 pixels, was used primarily for near-IR light detection. Both detectors were permanently mounted on the monochromator and selected by movement of a mirror. For all measurements, and for both detectors, all rows that were exposed to emission light were binned together to increase the signal to noise ratio; all other rows were not considered. Usually all horizontal pixels were evaluated and no pixels were binned. The measurable spectral range varied with grating, grating position, and diffraction order. A shutter placed just in front of the CCD allowed precise timing of the exposure. An additional shutter positioned to switch on and off the excitation light allowed for the measurement of detector noise and any other background light. The background response of the array detector is often pixel-dependent and hence a background spectrum was subtracted from each measured spectrum. The GPIB interface, PCI interface, and the multi-purpose digital analog interface allowed computer control of the entire setup. Labview (manufacturer: National Instruments, version: 5.1) was used as the controlling software. This complete computer control is essential to expedite the measurement process and to obtain reliable reproducible data.

8.2 Application of CEES to Erbium in GaN

8.2.1 Introduction

We will use GaN:Er as the first example of the application of CEES. Due to its $^4I_{15/2}$ ground state, the spectra of Erbium are the most complicated that we investigated. In this section, we give a detailed review of the spectroscopic data obtained by CEES and illustrate the assignment of the spectral features to different sites, electron-phonon coupled transitions, and transitions from thermally activated sub-levels. We address the following issues:

- How many distinct Er sites can be identified in the various GaN samples? In this regard, we will clarify the apparent differences in the results published by us [7] and other groups [8, 9, 10, 11].
- How do the different sites participate in up-conversion processes?
- What is the excitation efficiency of the different sites under above-bandgap excitation?

Overall, we try to give a consistent picture of the optical transitions for a variety of excitation mechanisms.

Samples used in these studies were MOCVD-grown GaN:Er epilayers on sapphire substrates doped in situ with up to 10^{21} Er atoms cm^{-3}. Details of these samples are given in [12]. See also Chap. 5. Another set of GaN:Er epilayers, obtained from SVT Associates, were grown by solid source MBE either on a Si or sapphire (0001) substrate and also doped *in situ* [7]. The highly resistive layers had a thickness of 200 nm and an Er concentration of 10^{18} cm^{-3}. The data for the two sets of samples were obtained at different times when different spectroscopic capabilities were available to us. We will make connection between the results using a systematic approach of site assignment exploiting the strong consistency of the CEES technique and data for overlapping spectral regions.

8.2.2 Direct Excitation of 1.5 μm Emission

As a first step, we show in Fig. 8.2 the CEES data for the technologically important Erbium transition at around 1.54 μm (0.805 eV). We excite this transition using a tunable semiconductor laser at around 980 nm. A large number of peaks appear in the image plot even in the rather small energetic window (approx 8 meV by 5 meV) that is depicted. This may at first suggest a large number of sites. However, thermally activated levels, energy electron-phonon coupling, and energy transfer will increase the number of transitions expected in the ideal case of a single site at zero temperature. In the assignments, we adopt the following guidelines:

- The emission spectra of a single site must be identical in spectral position and relative heights for all of its excitation transitions.
- The excitation spectra (extracted by taking a vertical cross section of our data) of a single site must be identical in spectral position and relative heights for all its emission transitions.
- Excitation starting from thermally excited levels (such as A2) of the ground state must be reduced in energy by the same amount seen in the emission. In both emission and excitation we will hence see transitions with lower energy. The inverse is true when we consider emission starting from thermally excited states (such as B2).
- Phonon-assisted transitions also exhibit splittings of the same size (corresponding to the energy of the phonon) but we will find a shift to lower energies for emission while we see higher energies in excitation. Unless local modes are involved the shift should coincide in energy with the modes that are observed in Raman spectra (for GaN, see e.g.: [13, 14])
- We are dealing with different sites if both the excitation and emission spectra differ.
- In the case that only the emission spectra are different we may deal with a case in which one site or ion (A) is excited but transfers its energy to another site (B). In many cases of energy transfer, we see emission from both site A and B when we excite A.

Applying these rules to the Er:GaN spectra, it turns out that all transitions can be explained by considering thermal population of excited states. The measurement temperature is about 10 K and hence not only the lowest states (i.e.: A1, B1, as indicated in Fig. 8.2) of the ground and excited state multiplets are populated. We can explain all transition energies when we consider an excitation transition starting from the 2^{nd} level (A2) of the ground state multiplet as well as emission transitions from the 2^{nd} (B2) and 3^{rd} level (B3) of the $^4I_{13/2}$ excited state In both cases, this will lead to groups of transitions that are shifted relative to each other by an identical amount (viz. the energy of the thermally excited state). In Fig. 8.2, these groups are indicated by lines of the same shade, with black lines indicating transitions from the respective lowest level, the white and grey lines the groups from the 2^{nd} and 3^{rd} lowest levels. In the presented case, the original and final level is identical and we can test the assignments for consistency. The separation indicated as a and b both represent the splitting of the ground state and must be equal. This consistency condition is fulfilled with great accuracy, such that we are confident that the majority of lines can be assigned to a majority site. Using conventional excitation/emission spectroscopy, similar conclusions have been drawn independently for similar samples by Makarova et al. [8]. The state energies and splittings are listed in Table 8.1.

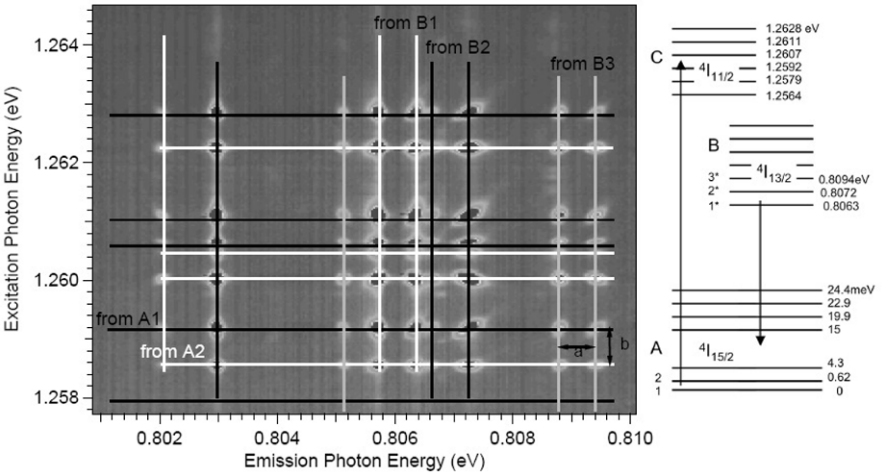

Fig. 8.2. Image plot of CEES data for Er-doped GaN epitaxial layers grown by MOCVD. Excitation is to the $^4I_{11/2}$ state while the emission is from $^4I_{13/2}$ to the $^4I_{15/2}$ ground state. The corresponding level scheme is shown on the left including the determined energy of the levels. The identification of the spectroscopic features is illustrated with black, gray and white lines for transitions from the first, second, or third level of the ground and excited state respectively.

Table 8.1. Energies of several levels of Er^{3+} in GaN and their Stark splittings (main site). For some splittings a range is given, determined from the inhomogeneous line broadening.

Energy level	$^4I_{15/2}$	$^4I_{13/2}$	$^4I_{11/2}$	$^4F_{9/2}$	$^4S_{3/2}$	$^2H_{11/2}$
Energy from ground state [eV]	0	0.80634	1.256361	1.8592	2.240	2.3271
	0.6	0.9	2.2	1.1	1.0	9.3
	4.7…3.6	3.1	2.8	4.3		16.1
Stark Splitting [meV]	14.0…15.5		4.3			
	19.8		4.6			
	22.9		6.4			
	24.5					

A particular strength of the CEES method is the ease with which inhomogeneous line broadening can be identified through the line narrowing effect. In inhomogeneously broadened emission or excitation lines, there are contributions from similar but not identical defect sites, which have slightly different excitation and/or emission energies, if both, then fluorescence line narrowing (FLN) can be observed since the precise choice of excitation energy will select a subset of the defects and lead to a narrowing of the emission line. In CEES measurements, FLN is revealed by emission features that have a tilted elliptical shape. If we inspect the data, we find that some features show this property and other do not. In Fig. 8.3, we show an enhanced subset of data, in which we highlight the features with FLN.

We find that certain energy level splittings are sensitive to these small changes in local environment while others are not. We depict the change in the splitting between level A1 and A3 and determine it as a function of excitation energy. Due to the presence of transitions from thermally excited levels, this splitting can be determined as the distance between several emission features. The differences taken from the pairs of transitions starting at B1 and B2 coincide very well; once again confirming our assignments.

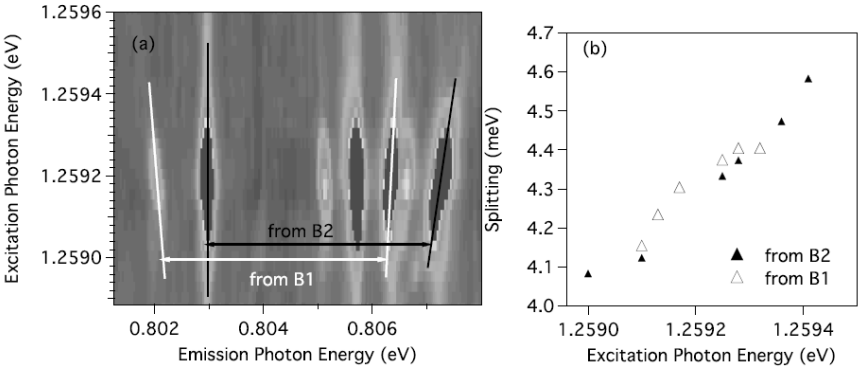

Fig. 8.3. (a) Illustration of the inhomogeneous broadening and the associate FLNeffect in our CEES data. The tilted features indicate transitions that show FLN. (b) Splittings between the levels A1 and A3 as a function of excitation energy indicated by arrows are depicted in (a).

A further strength of the CEES technique compared to traditional excitation/emission spectroscopy lies in the ability to identify weaker spectral features by exploiting the dynamic range by "over-exposing" the images either digitally after the measurements or in an analog way by increasing the exposure time of the CCD array. Using the first approach, we depict in Fig. 8.4 the same data as in Fig. 8.2 but with enhanced contrast. While the main site is overexposed in this way, a minority site becomes visible which exhibits an emission intensity weaker by a factor of about 40.

The identified transitions are indicated in our map by the black dotted lines. Once found in the CEES maps, the excitation and emission spectra of this minority site can also be obtained by evaluating vertical and horizontal cross sections of the data, as in Fig. 8.5. Even for the best spectral positions a strong overlap with the main site remains but several characteristic lines can be seen and are marked by arrows in the excitation and emission spectra shown in Fig. 8.5. While for the direct excitation at 980 nm this minority site does not play a major role, we will see that such minority sites become more important when we consider up-conversion excitation. Note that the absence of background in the excitation spectra around 980 nm indicates much smaller numbers of defects compared to Bishop et al. [10, 11]. We are thus dealing mainly with the site that has been labeled by these authors as "4*f*-pumped". We will try later on to correlate the other Er-sites seen by Bishop et al. with the minority sites that are revealed by up-conversion excitation.

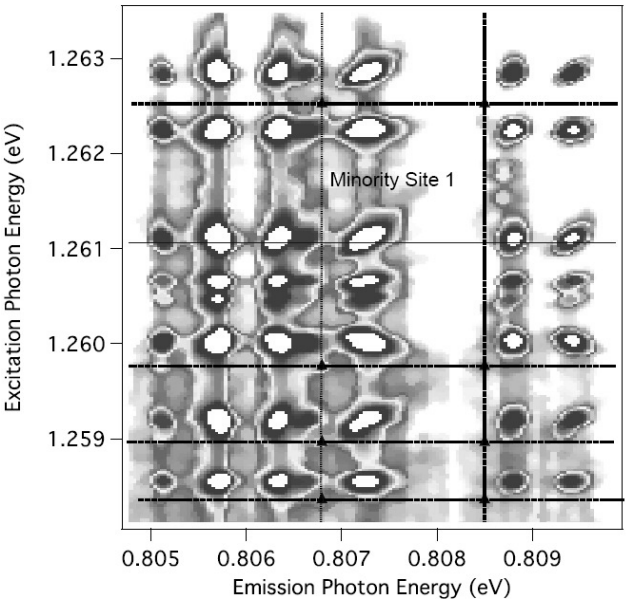

Fig. 8.4. Image plot of CEES data for Er-doped GaN epitaxial layers grown by MOCVD. Excitation is to the $^4I_{11/2}$ state while the emission is from $^4I_{13/2}$ to the $^4I_{15/2}$ ground-state for the same data as in Fig. 8.2 but with a 40 times enhanced contrast. Minority site MS 1 is indicated with dotted lines.

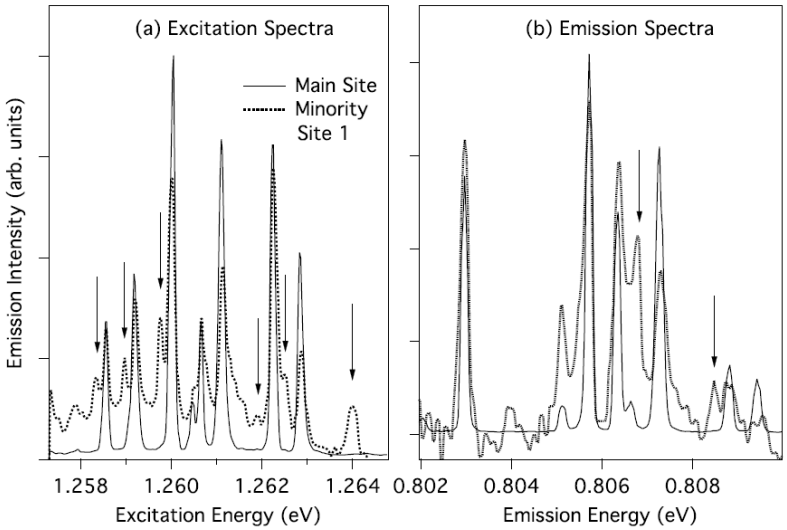

Fig. 8.5. (a) Photoluminescence excitation and (b) emission spectra of Er doped GaN of the main site (solid line) and the minority site 1 (dotted line).

8.2.3 Two-Step Excitation of 980 nm and 820 nm Emission

We start our consideration of the up-conversion processes with the case in which we excite at around 1.5 μm and detect emission near 980 nm and 800 nm. The first case is very interesting because the same transitions are involved as in the direct excitation case studied above. Therefore direct correlation between the two measurements can be obtained. In order to illustrate this we show in Fig. 8.6 the CEES data for both cases in a manner that the identical transitions can be compared directly. For that we exchanged the emission and excitation axis for the 1.5 μm emission data. This way we can easily correlate the emission peaks in the 1.5 μm emission with the excitation peaks of the 980 nm emission (compare the bottom left and bottom right images in Fig. 8.6). Similarly the emission peaks at 980 nm are compared with the excitation peaks of the 1.5 μm emission (see bottom left and top left image in Fig. 8.6). For clarity, we only chose those excerpts of our data for which we have both emission and excitation data.

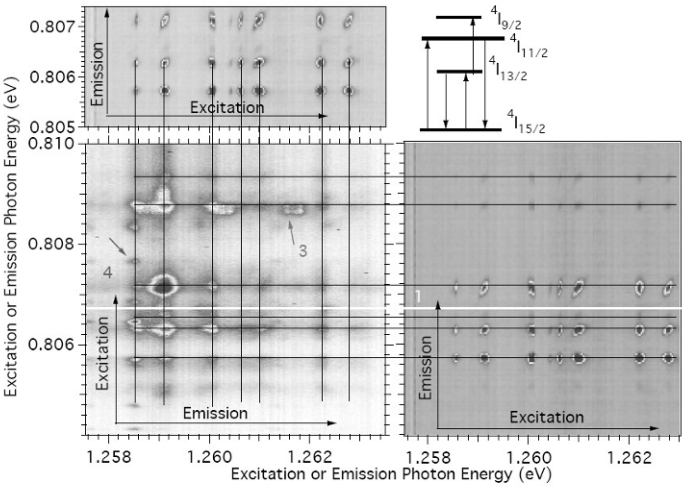

Fig. 8.6. Image plot of CEES data for Er-doped GaN epitaxial layers grown by MOCVD. On the bottom left excerpts of the data obtained for the 980 nm emission and 1.5 μm up-conversion excitation. The other two images are from the same data as in Fig. 8.2 and Fig. 8.4, but are rotated by 90º so that the identical transition energies can be compared. The inset on the top right indicates the two excitation schemes. The black lines indicate the transitions of the main site. Additional minority sites are depicted in white (Minority Site 1 and with arrows Minority site 3 and 4.)

We find that the main site is still dominating the emission such that many of the peaks can be accounted for but additional peaks become more prominent. A complete assignment of the 980 nm emission peaks observed for the main site is shown in Fig. 8.7, in which we use the energies and splittings of the $^4I_{11/2}$ and $^4I_{15/2}$

levels that we have worked out above to determine the transitions between them. We group these transitions according to the initial level and mark the transitions to the sublevels of the ground state. The splitting of the $^4I_{11/2}$ state is rather small and the power (1W) used in the up-conversion measurement leads to some local heating such that many thermally excited transitions come into play making the spectra very complex.

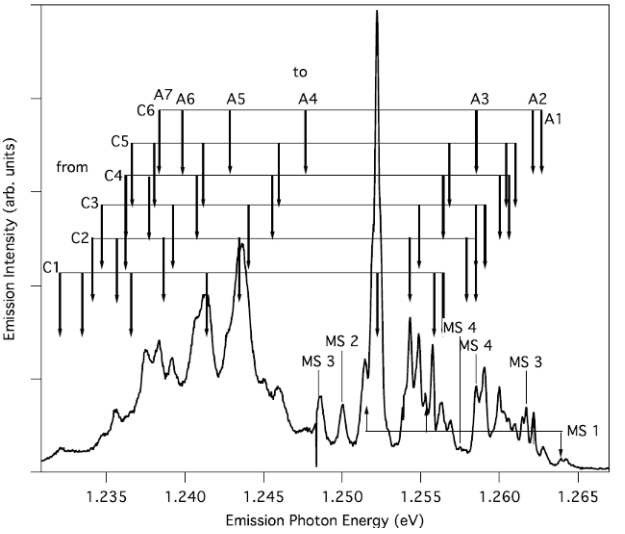

Fig. 8.7. Emission spectrum at around 980 nm obtained under resonant excitation at around 1.537 μm excitation of the main site. The transitions are identified using sets of lines that indicate different starting and ending levels of the same site. Several additional features are indicated with arrows.

Nevertheless, we find excellent agreement confirming the consistency of our assignment. As above, several peaks remain unassigned which belong to minority sites (MS) that we will explore in more detail in the following.

Exploiting again the dynamic range of the CEES method, we identify 4 minority sites and show in Fig. 8.8 the corresponding CEES data. We indicate by arrowed lines the spectral position in excitation and emission for which these sites appear. The corresponding excitation spectra are shown in Fig. 8.9. Despite considerable overlap, the excitation spectra enable us to clearly identify characteristic excitation energies for which a particular site is excited and which will be used in the following three-step excitation experiments in which the same excitation wavelength is used. These transitions are marked with arrows in Fig. 8.8. We include these transition energies in Table 8.2. The relative strength of the different emission features are seen by the multiplication factors in Fig. 8.9. Comparing the excitation energies in our case with the emission energies reported by Bishop et al. [10, 11], we find that our MS4 is a possible candidate for their “violet” center.

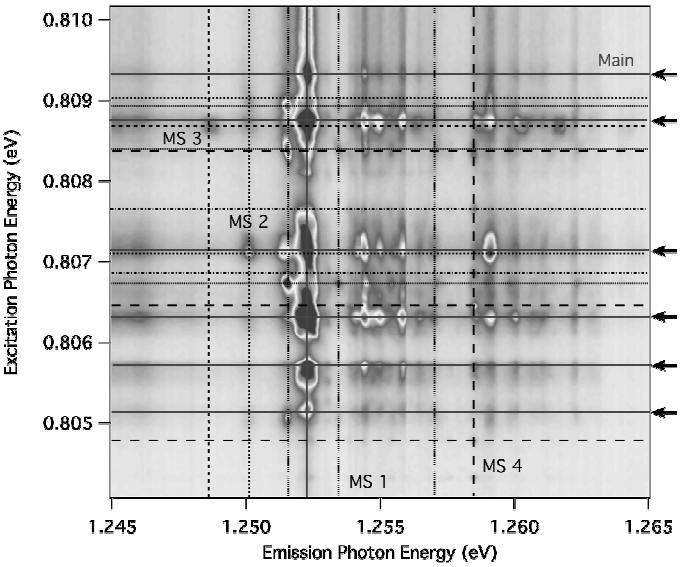

Fig. 8.8. Image plot of CEES data for Er-doped GaN epitaxial layers grown by MOCVD for the emission at around 980 nm and 1.5 µm up-conversion excitation. In comparison to Fig. 8.6, the contrast has been increased to make minority site more apparent. The different sites are identified by arrowheads.

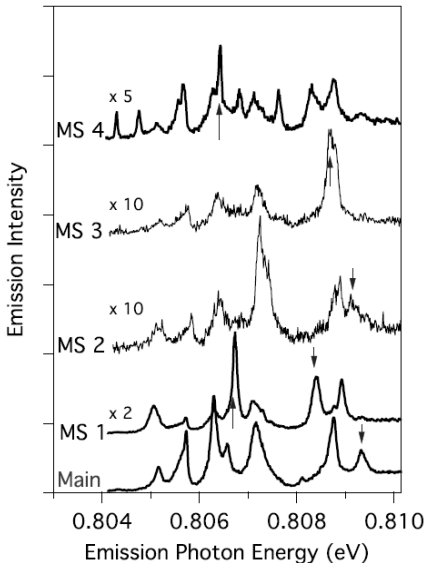

Fig. 8.9. Photoluminescence excitation spectra of the different incorporation sites or Er in Er-doped GaN epitaxial layers grown by MOCVD. The excitation spectra are taken at the lines that are indicated in Fig. 8.8.

Table 8.2. Characteristic transition energies of the observed minority sites of Er in GaN. Transition energies for which the sites are most distinct are chosen.

	MS 1	MS 2	MS 3	MS 4	MS 5	MS 6
$^4I_{15/2}\leftrightarrow{}^4I_{13/2}$	0.8040	0.8090	0.8087	0.8083	0.8066	
	0.8068	0.8071		0.8076		
	0.8085	0.8050		0.8068		
				0.8056		
				0.8042		
				0.8035		
$^4I_{15/2}\leftrightarrow{}^4I_{11/2}$	1.2640					
	1.2625					
	1.2619					
	1.2598					
	1.2590					
	1.2583					
$^4F_{9/2}\rightarrow{}^4I_{15/2}$		1.8524	1.8660	1.8146	1.8057	
			1.8495			
$^4S_{3/2}\rightarrow{}^4I_{15/2}$		2.2328		2.2436		
				2.2412		
				2.2360		
$^4I_{15/2}\rightarrow{}^2H_{11/2}$		2.3462	2.3308	2.3521	2.3545	2.3533
		2.3392		2.3503	2.3516	
		2.3345		2.3450	2.3462	
				2.3408		
				2.3378		
				2.3324		
				2.3286		

We use the characteristic excitation energies for the emission at around 800 nm obtained under the same 1.5 μm excitation. This is another two-step excitation and hence it is not surprising that all sites can be seen again with similar strength. We suspect that excitation occurs to the $^4I_{9/2}$ level from which either an emission transition back to the ground state occurs or a relaxation to the $^4I_{11/2}$ level. Hence the “800 nm” and “980 nm” up-conversion emission processes are governed by the same excitation mechanism. The relative differences in the emission strengths are governed by the branching ratio of “800 nm” emission and relaxation as well as the site-dependence of the transition probabilities. The corresponding data and resulting assignments are shown in Fig. 8.10. The assignment of the various transitions for the main site is done again in an individual emission spectrum as shown in Fig. 8.11. The agreement is again very good.

The dominant presence of the main site in the two-step up-conversion spectra suggests that excitation through excited state absorption of the same ion is the dominating process. As we will see in the following, this dominance of the main site vanishes when we consider three-step excitation processes to emission in the green and red spectral regions.

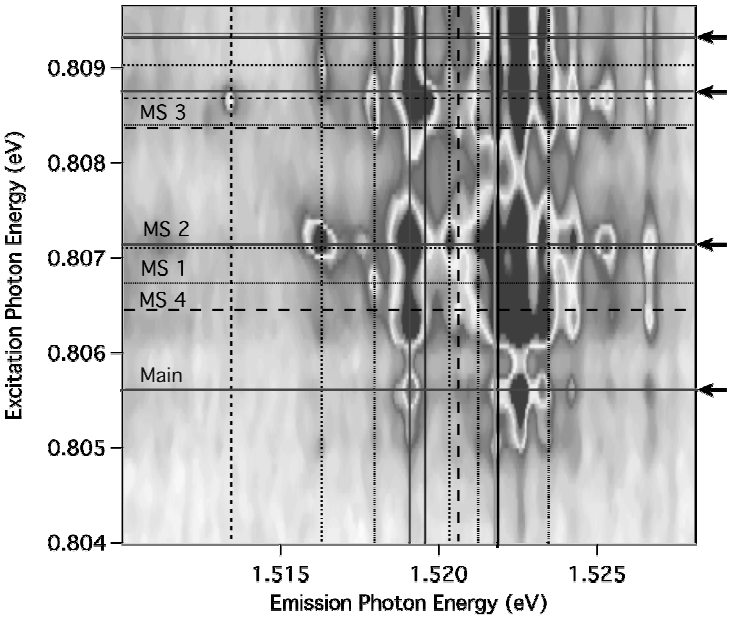

Fig. 8.10. Image plot of CEES data for Er-doped GaN epitaxial layers grown by MOCVD for the emission at around 800 nm and 1.5 µm up-conversion excitation. Using the excitation spectra from Fig. 8.9, the sites are identified and indicated with arrowed lines.

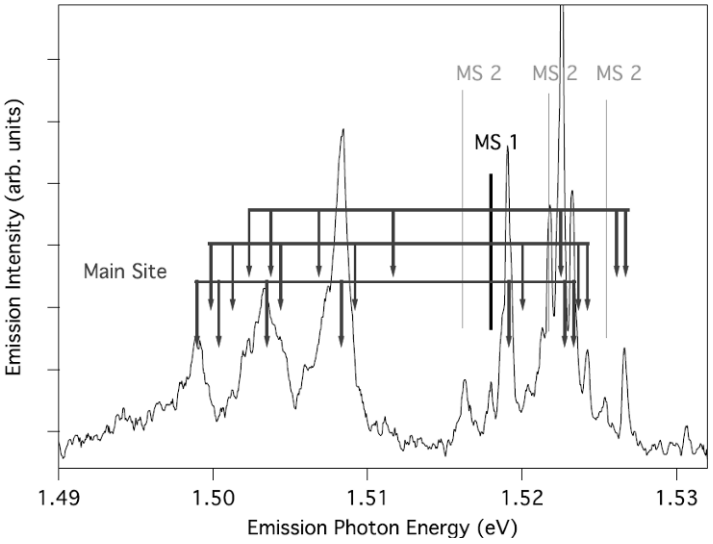

Fig. 8.11. Emission spectra at around 800 nm excited at about 1.537 µm. The different transitions for the mains site are indicated with groups of lines for the different starting and end levels Additional lines from Minority site MS 2 are indicated as well.

8.2.4 Three-Step Excitation of 670 nm and 550 nm Emission

The three-step excitation process is the critical link between our new data obtained on the MOCVD samples and earlier studies on the MBE samples. For this excitation process we have a direct comparison as well as the possibility to link the direct excitation processes studied in [7] to the up-conversion excitation data.

In Fig. 8.12, we show the CEES data for the red emission under excitation at 1.5 μm. By using the characteristic excitation energies of the main site, we notice that it is very weak. The up-conversion spectrum is clearly dominated by minority sites (MS 2 …MS 5) that we identify with color coded lines. These sites maintain their characteristic excitation pattern seen in two-step excitation, suggesting that energy transfer among them still does not play a major role and that the ions are quite isolated from each other but are selected in the three-step up-conversion process by the location of their energy levels and by a stronger coupling with the lattice which leads to sufficient spectral overlap for three consecutive absorption processes. The presence of low frequency local modes is the most likely origin for the excitation preference. Similar results are obtained for the green emission but fewer details can be extracted from these data due to the less defined emission spectra from the $^4S_{3/2}$ level and the data are hence not shown. For both emission regions, we can determine characteristic emission transitions that will be used for comparison with the direct excitation data that we will discuss in Sect.8.2.5. The data are included in Table 8.2. We will now consider the direct excitation of the red/green emission for which we only have data for MBE samples and will return to the comparison between MOCVD and MBE-grown samples in Sect. 8.2.6.

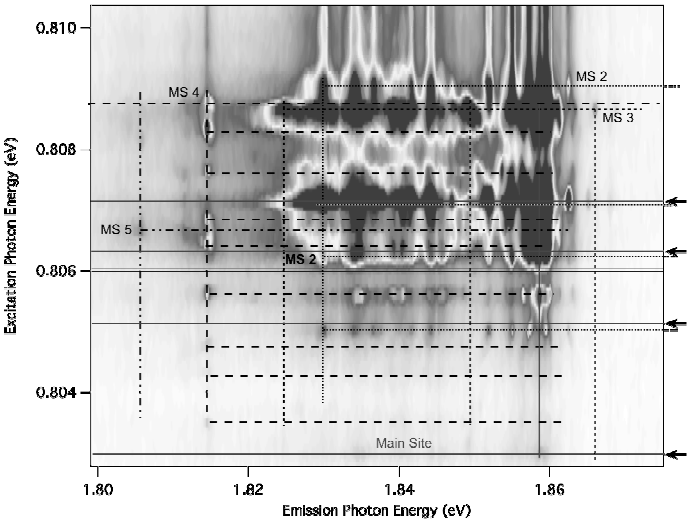

Fig. 8.12. Image plot of CEES data for Er-doped GaN epitaxial layers grown by MOCVD for the emission at around 670 nm and 1.5 μm 3-step up-conversion excitation. Using the excitation spectra from Fig. 8.9 the sites are identified and indicated with arrowed lines.

8.2.5 Direct Excitation of 670 nm and 550 nm Emission

The red and green emission provide a link between data that we obtained on the MOCVD samples with the earlier data measured on the MBE sample. The red region spectra are much better defined . Fig. 8.13 shows the emission at around 675 nm (1.84 eV) that were obtained by exciting the $^2H_{11/2}$ excited state at 530 nm. The image plot is again much better defined compared to the up-conversion CEES data and we are able to identify several sites. We find quite prominently the main site along with the minority sites MS 2...5. In Fig. 8.13, these sites are identified by arrowed lines and the characteristic excitation energies are included in Table 8.2. With these excitation energies it is now possible to assign the different sites found in the CEES data for the green emission ($^4S_{3/2}$ to $^4I_{15/2}$) under excitation at around 520 nm. These data are depicted along with the arrowed assignments in Fig. 8.14. We find again a dominant main site along with the minority sites MS 2, MS 4-MS 6. Despite careful evaluation, we were unable to find MS 3, which is quite apparent in the red emission. We suspect that this site may be related with a deep defect trap such that energy exchange occurs from the $^4S_{3/2}$ state to the trap and back to the $^4F_{9/2}$ state from which red emission occurs. Such traps have been observed by Bishop et al. [10, 11] and we suspect that our MS 3 is related to their "red center". Further evidence for this interpretation is given below when we discuss the efficiency of excitation through above band-gap excitation (Sect. 8.2.7).

Table 8.3. Energies of several levels of Er^{3+} in GaN and their Stark splittings (minority site MS 4).

Energy level	$^4I_{15/2}$	$^4I_{13/2}$	$^4F_{9/2}$	$^4S_{3/2}$	$^2H_{11/2}$
Energy from ground state [eV]	0	0.8056	1.8593	2.2414	2.33274
	4.1	0.8	2.2	2.4	5.2
	5.1	1.2	4.4.		10.4
Stark Splitting	12.8	2.0	8.7		12.4
[meV]	15.3	2.7			17.2
	19.5	3.1			19.7
	24.2				
	44.6				

In earlier work, we assigned several sites without input from the MOCVD data [7]. Furthermore, the presence of thermally excited levels was omitted from that work. The assignments can be correlated as follows: Site 1 = Main Site, Site 2/Site6 = MS 4, Site 3 = MS 7, Site 4 = MS 2, Site 5 = MS 4. It should be noted that with additional data a much more consistent assignment could be achieved. We summarize our assignments by listing all observed characteristic transitions of the minority sites in Table 8.2. In Table 8.3, we summarize the Stark splittings for the most distinct minority site (MS 4), although the assignment is less certain because some data was obtained using up-conversion excitation ($^4I_{13/2}$ level) in which energy transfer and the influence of the upper levels have been neglected. Moreover, fewer tests of consistency of the assignment could be done for this site.

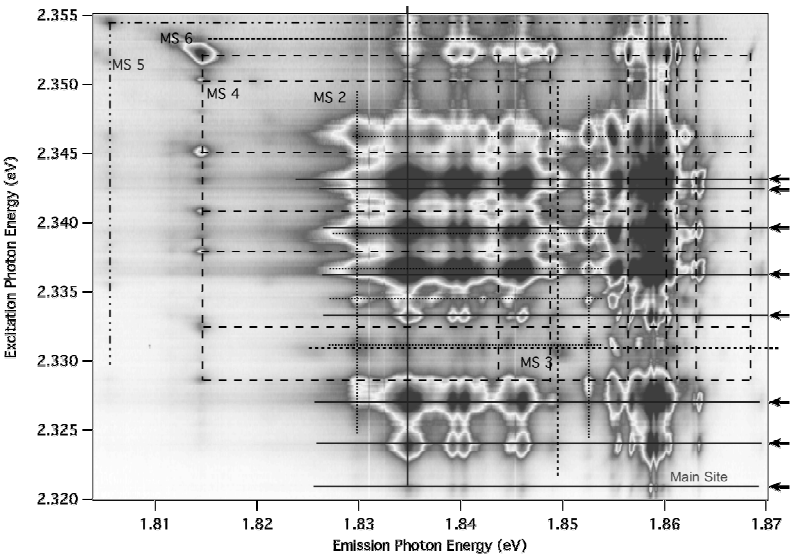

Fig. 8.13. Image plot of CEES data for Er-doped GaN epitaxial layers grown by MBE for the emission at around 670 nm ("red emission") and direct excitation. The sites are identified by the arrowed lines.

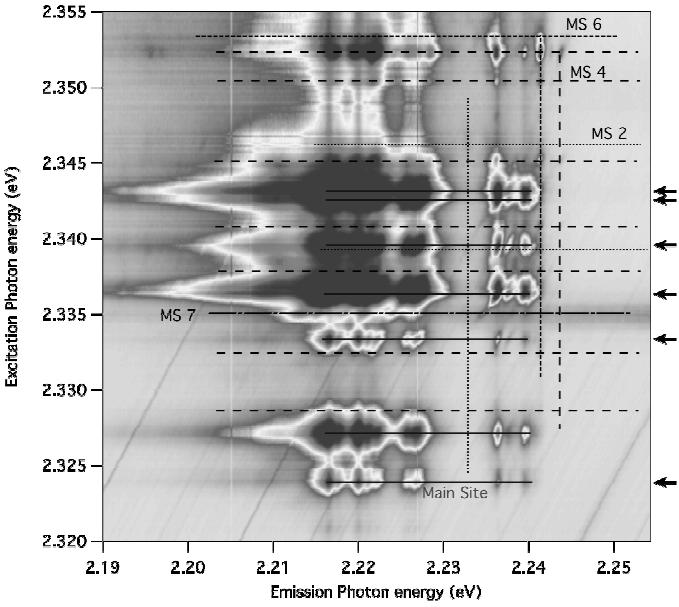

Fig. 8.14. Image plot of CEES data for Er-doped GaN epitaxial layers grown by MBE for the emission at around 550 nm ("green emission") and direct excitation. The sites are identified by the arrowed lines.

8.2.6 Comparison of in situ Doped MBE and MOCVD Grown GaN:Er Samples

We have now successfully linked the two measurement sets available for the two sample types that we have investigated. We found a main site in both cases, which is identical within the accuracy obtained by the tracking of the transitions. For closer inspection, we select in Fig. 8.15 emission spectra which preferentially reveal the main site. For comparison we shifted the red emission in energy to lie above the green emission.

We are able to assign all peaks if we assume that splittings of the ground state and thermally excited states lead to satellite peaks at higher energies but with different shifts for red and green. As a nice confirmation of this assignment, we find that the green emission from the $^4S_{3/2}$ state only shows one satellite (shifted by 1 meV) as expected, while the red emission shows two (shifted by 1.1 and 4.3 meV). If we inspect the emission and excitation spectra even more closely we find very good agreement in the total crystal field splitting but small discrepancies in the individual splittings. (see peaks labeled with * in Fig. 8.15). In particular, for the ground state splitting between level A1 and A3 as well as between A1 and A4 we find a reduced value in the MBE-grown samples (4.2 vs. 3.5 meV and 14 vs. 15 meV, respectively). The particular sensitivity of these levels to the environment is consistent with our observation of strong inhomogeneous broadening of these levels (see Fig. 8.3). From this we conclude, that while the main incorporation site in the two types of samples is essentially the same (most likely Er on a Ga-site with no disturbance in the close neighborhood) they differ in the more long range environment (e.g.: strain, overall defect density, lattice constant,..).

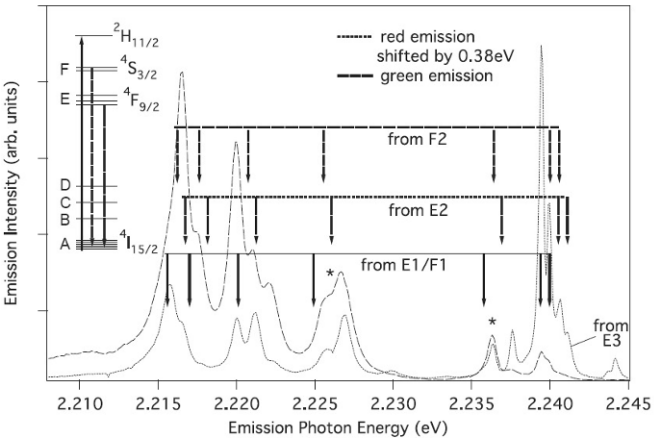

Fig. 8.15. Emission spectra of the red and green emission. The red emission is shifted by approx. 0.38 eV such that corresponding peaks are overlapped. Using the splitting data of the $^4I_{15/2}$ ground state obtained for the 1.5 μm emission, the different transitions are assigned. The groups of arrows indicate the respective starting levels. D=$^4F_{9/2}$, E=$^4S_{3/2}$.

This becomes more evident when we compare the CEES data for the up-converted red emission (for which we have data for both sets of samples). The CEES data for both sample types, shown in Fig. 8.12, reveal similar features in both, but also a clear broadening effect for the MBE sample.

To make the comparison more quantitatively, we display in Fig. 8.16 the red emission spectra that are observed under 1.5 μm excitation. The broadening of lines is very apparent for all sites. The width of the lines is increased by at least a factor of two even in the presence of fluorescence line narrowing effects. This suggests that the homogeneous line width is also increased possibly due to dynamic coupling effects with the disturbed lattice. Moreover, the strengths of the minority sites are similar to each other, but the main site is much stronger in the MBE samples. The increased spectral width will give better spectral overlap allowing for a more efficient multi-step excited state absorption process.

Considering that spectral lines are narrower in the MOCVD samples despite its higher RE incorporation, we conclude that the environmental disorder and the resulting broadening of spectral lines is not due to the interaction between the RE ions but the presence of defects that are more numerous in the MBE samples. Consequently, we also see in direct excitation for the MBE-grown samples several minority sites (see Fig. 8.13 and Fig. 8.14) that are related to perturbation of the nearest neighborhood by defects while for the MOCVD-grown samples essentially only the main site is observed. (see Fig. 8.2). We will see later a case in which RE ion interactions broaden the spectral lines.

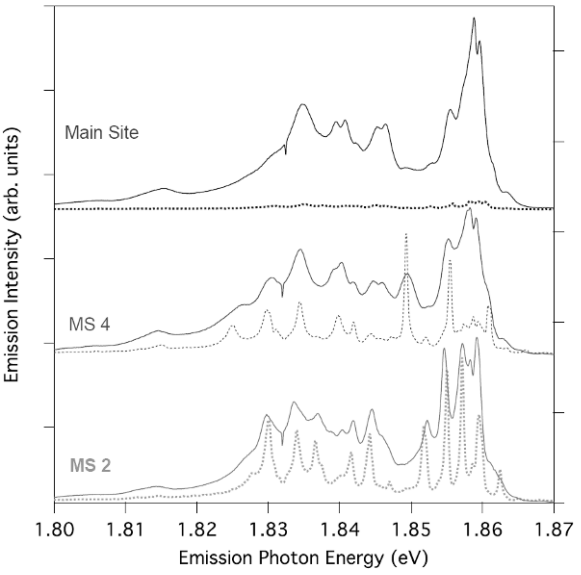

Fig. 8.16. Emission spectra in the red spectral region for different sites as seen under up-conversion excitation. The spectra are scaled such that relative intensities between the MBE-grown sample (solid lines) and the MOCVD-grown sample can be compared.

At this point, we have a good characterization of the different incorporation sites of Er for the two sets of GaN samples. This will enable us in the following to identify the nature of the emission that is induced by above-bandgap excitation through the creation of electron-hole pairs and excitons.

8.2.7 Above Bandgap Excitation of 1.5 µm Emission

Above bandgap excitation is essential for the application of RE-doped GaN in electroluminescent devices in which excitation is achieved through electron-hole pairs or possibly by direct impact with fast charge carriers [15]. We use the 325 nm line of a HeCd laser for this excitation and observe the emission at 1.5 µm (see Fig. 8.17). This laser is not tunable such that we obtain only a single spectrum. For the two sets of samples, we see spectra that are quite different from each other. Despite the much higher Er-concentration in the MOCVD samples, the relative intensities are quite similar suggesting a more efficient excitation process for the MBE samples which has a higher degree of disorder and hence a higher concentration of defects. Comparing the spectral features with the spectra obtained under resonant excitation, we find for the MOCVD samples mainly the main center while for the MBE sample there is a strong contribution from MS 3. In order to make this assignment, we compare the emission spectra with those obtained under 980 nm excitation and with the excitation spectrum for the MS 3 site. It appears that this site is particularly efficient in capturing the energy from electron-hole pairs. This is consistent with the hypothesis that this site is related to a deep defect trap as well as the observations by Bishop et al. [10]. The role of such deep defects becomes clearer in our studies of Eu-doped GaN that will be presented in Sect. 8.3.

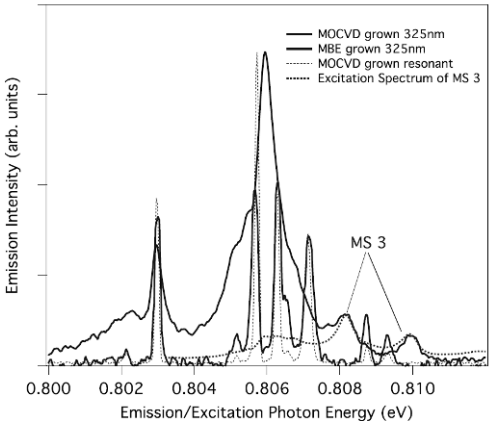

Fig. 8.17. Emission at 1.5 µm excited using the 325 nm line of a HeCd laser for the MOCVD sample (blue line) and MBE-grown sample (black line). To aid identification dotted lines are added: (blue) spectrum obtained in MOCVD grown sample under resonant excitation (purple) excitation spectrum for MS 3.

8.2.8 Summary of CEES Spectroscopy of GaN:Er

In Sect. 8.2, we have reviewed work on Er-doped GaN for two different sets of samples. We were able through systematic evaluation of the respective experimental data set to identify a main site that is somewhat perturbed in the MBE-grown samples as well as several minority sites that are however quite abundant in the MBE-grown samples. As a result we were able to combine existing published data in a unified picture of the incorporation sites of Er in GaN. Minority sites are more efficient in the up-conversion processes, in particular MS 3, which we assign to a defect-trap related site, that can be efficiently excited through electron-hole pairs.

8.3 Application of CEES to Neodymium in GaN

8.3.1 Introduction and Experimental Background

As a second example of a RE ion in GaN, we consider Nd, which has excellent prospects for obtaining optical gain. Combined with the favorable thermal properties of GaN, the GaN:Nd system may be a good candidate for high power lasers. Although photoluminescence (PL) [16, 17] and electroluminescence (EL) [18] from Nd-doped GaN have been observed, the Stark levels of the 4*f* states have never been resolved, partly due to implantation-related damage of the host material and partly to Nd^{3+} ions occupying multiple sites. Again the CEES technique is ideally suited to identify sites and transition energies. This section will be much shorter than the previous one because no up-conversion excitation has been observed for GaN:Nd and hence the number of sites that we are able to identify is much lower.

The samples used for these studies were obtained from E. Readinger at the Army Research Lab, Adelphi Md, The GaN layers were grown on single side polished c-plane sapphire by plasma assisted-MBE and consist of a 200 nm undoped GaN base layer followed by a Nd-doped ~ 1 micron GaN layer with a Nd concentration of up to ~ 5 at%. Quantitative analysis of the Nd concentration was attained by Rutherford backscattering spectroscopy (RBS) and secondary ion mass spectrometry (SIMS). A detailed sample description can be found in Readinger et al. [19].

We performed spectroscopic studies with excitation wavelengths that sponsor transitions from the $^4I_{9/2}$ ground state to the overlapping $^4G_{5/2}$ and $^2G_{7/2}$ excited states. (Studies of a wider range of excitation energies using conventional spectroscopy are reported in [20]). Excitation uses a cw-tunable dye laser system (manufacturer: Coherent, model: 590). We observe emission from the $^4F_{3/2}$ state to the ground state (see Fig. 8.18). For the C_{3v} symmetry experienced by a Nd ion on a Ga site, the ground state ($^4I_{9/2}$) is split into five crystal field levels, while the

excited states, $^4G_{5/2}$, $^2G_{7/2}$, and $^4F_{3/2}$ are split into 3, 4, and 2 levels respectively. In the absence of thermal activation, we expect to observe $(3 + 4) \times 5 = 35$ combinations of transitions for a single site. This number is increased if thermal activation, other defect sites, and phonon-assisted transitions are taken into account. Hence even for a single site we expect a large number of peaks as seen above for the direct excitation of Erbium ions (see Fig. 8.2).

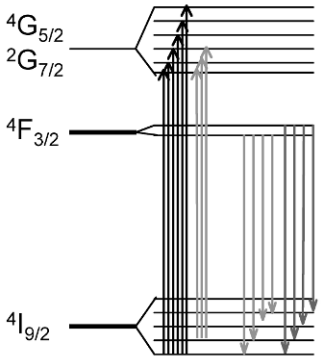

Fig. 8.18. Schematic of energy levels of Nd ions in GaN and transitions relevant for site selective spectroscopy studies

The key experimental findings are summarized in Fig. 8.19 for a sample doped with about 0.2 at% of Nd. The data are rich in spectral features. We will use the same strategy for the assignment of peaks, as stated above for the Er case.

8.3.2 Assignment of Excitation and Emission Peaks

Overall, we find in Fig. 8.19 more than 100 excitation/emission peaks. These appear in the images as "mountains". Although this number is much higher than the 35 estimated for the spectral region, this is not an immediate evidence for multiple sites because thermally excited level and phonon-assisted transitions have been neglected in the determination of this number. In order to distinguish between transitions originating from different sites, we carefully examine individual excitation and emission spectra. Critical for distinction between transitions of different origins is the property that in order to belong to the same site these spectra need to be identical both in spectral position and relative intensities of individual emission and excitation peaks. Applying this principle in the evaluation of our data reveals that the majority of the observed peaks are related to a single site. The black lines in Fig. 8.19 indicate the 7×5 combinations of excitation and emission energies for the transitions from the respective lowest levels within the excited and ground state multiplets.

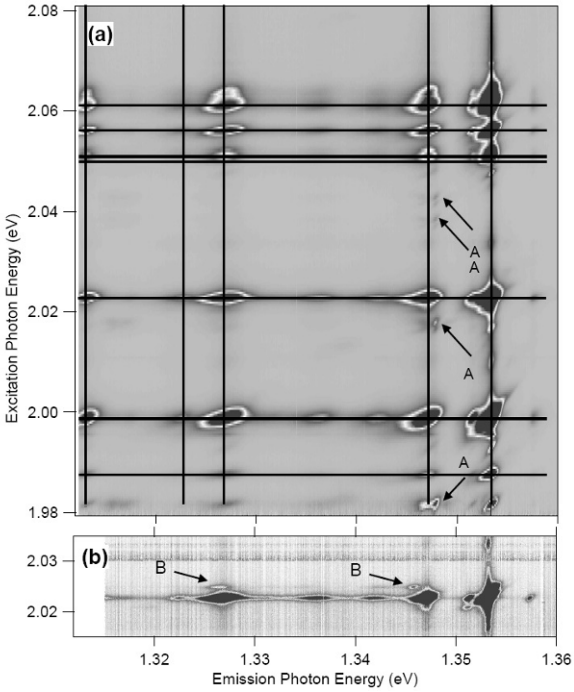

Fig. 8.19. Image plot of emission intensity as a function of excitation and emission energies for GaN doped with approx 0.2%at Nd. Crossing of the solid lines indicates, the identified 35 transitions expected in the absence of thermal activation and electron-phonon coupling.

Additionally, we find in the emission spectra transitions that appear as satellites of the main peaks. All these satellite peaks are shifted by 4.1 meV to higher energy. This is clear evidence that these peaks belong to transitions from the upper state of the $^4F_{3/2}$ multiplet. Similarly, we find excitation peaks with energies 6.1 meV lower than the corresponding main peaks. We assign these to excitations from the first thermally excited level within the $^4I_{9/2}$ ground state multiplet. The latter assignment can easily be checked for consistency since the splitting of the $^4I_{9/2}$ ground state is also measured in the emission spectrum.

In order to illustrate the assignment that has been obtained so far, we show in Fig. 8.20 and 21 individual excitation and emission spectra. The energies of the various levels for this dominant site are summarized in Table 8.4.

While this main site clearly dominates the emission under resonant excitation, other defect sites can be identified through their characteristically different spectra. In Fig. 8.19 (a), peaks associated with one of the minority sites (labeled A in Table 8.4) are indicated by an arrow. Another site can be identified by closer inspection utilizing the 'over-exposure' technique as shown in Fig. 8.19 (b). The energies of the identified transitions of the minority sites are included in Table 8.4. Both sites become apparent only through the sensitivity of our technique, being

two orders of magnitude weaker in emission under resonant excitation conditions. To what extent these additional sites contribute to the emission under electrical and/or above bandgap excitation is currently under investigation. Based on our experience with Er (see above) and Eu (see below), we suspect that the minority site may contribute disproportionately under electrical excitation.

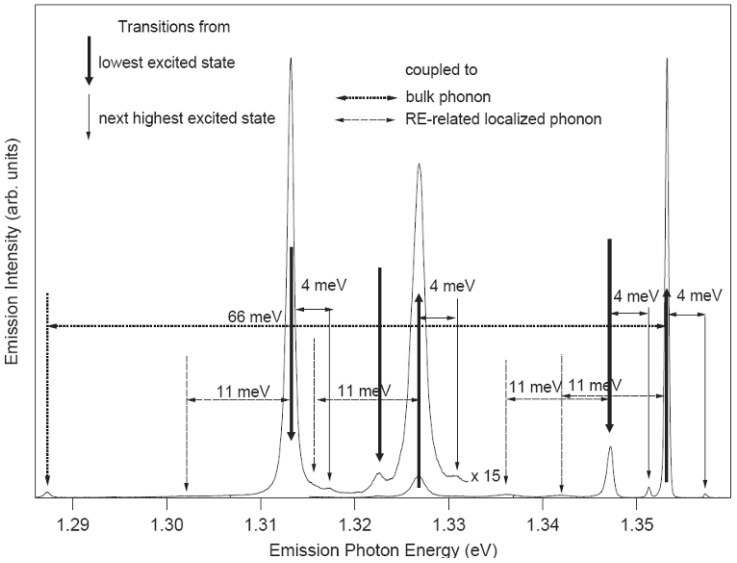

Fig. 8.20. Emission spectrum for a single Nd site in GaN:Nd obtained under excitation at 2.023 eV. The assignments to transitions of different nature are indicated.

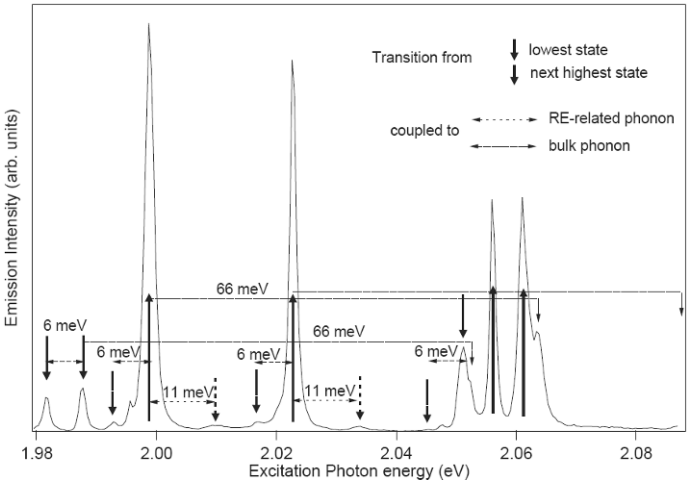

Fig. 8.21. Excitation spectrum for the emission at 1.328 eV. The assignments to transitions of different nature are indicated.

Table 8.4. Energy levels of GaN:Nd for the main incorporation site and two minority sites A and B.

Level	Main Site	Minority Site A	Minority Site B
	2.0615		2.063
$^2G_{7/2}$	2.0563		2.0589
	2.0511	2.0426	2.0551
	2.0504	2.0383	2.05374
	2.0228	2.0179	-
$^4G_{5/2}$	1.9985		2.0249
	1.9877	1.9818	2.0012
	1.3575		
$^4F_{3/2}$	1.3534	1.3478	1.35385
	40.1	32.2	46
$^4I_{9/2}$	30.6	30.7	32
	26		
	6.2	13.2	12
	0	0	0

8.3.3 Electron-Phonon Coupling

Even after assigning transitions between multiplets for the main site several peaks remain unassigned although they are unambiguously related to the same site. Their characteristic identifier is that the same energy separations from the main transitions occur in both excitation and emission. The characteristic energy shifts are 11 meV and 66 meV, to higher and lower energy for excitation and emission respectively. The corresponding lines are indicated in Fig. 8.20 and 21. The value of 66 meV corresponds well with the TO-type mode of bulk GaN [13, 14] and has been observed in Er-doped samples also [7]. We show below that it occurs for Eu as well. On the other hand, the 11 meV-mode is not observed in Raman measurements of bulk GaN and is hence assigned to a local mode that involves the Nd-ion. A mode of similar energy (12 meV) has recently been found in the excitation-emission spectra of Eu-doped samples [21]. From the intensity ratio, we can estimate the electron phonon coupling strength: the Huang-Rhys factor is less than ~ 0.1. Even weak phonon coupling can play a prominent role when a no-phonon transition is forbidden, as in GaN:Eu, below.

8.3.4 Inhomogeneous Broadening: Spectral and Spatial Aspects

Now that all CEES lines are assigned for GaN:Nd, we turn our attention to the 2D profile of the excitation emission peaks in Fig. 8.19, which are related, as we have discussed above (Sect. 8.2.2) to fluorescence line narrowing (FLN). To make this

analysis more clear, we depict in Fig. 8.22(a) a small excerpt of our data that includes only two transition pairs. For the depicted region, we see one emission and two excitation transitions that show quite different shapes.

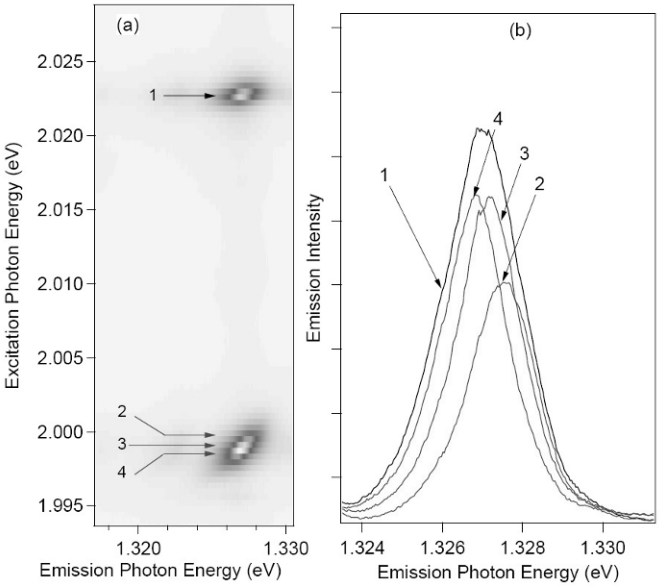

Fig. 8.22. (a) Excerpt of our CEES data for two transition pairs that show different behavior in terms of FLN of the inhomogenously broadened emission line. (b) Emission spectra obtained for the excitation energies indicate by arrows in (a).

The peak at higher transition energy is an ellipse with its axis parallel to the emission energy axis. This indicates that tuning the excitation through this peak will always yield the same emission spectrum. The peak at lower transition energy on the other hand has the shape of a tilted line, which indicates that the emission peak changes as we change the excitation energy. Since the overall width of the total feature is the same as for the other transitions, the emission lines are narrower. This is a characteristic feature of an inhomogenously broadened emission line with an FLN effect. The corresponding emission lines at various excitation energies are shown in Fig. 8.22(b). Exciting at the higher spectral position does not lead to the same narrowing since apparently the excitation transition is not sensitive to the perturbations that cause the broadening in emission. Consequently, the spectral width in excitation is smaller than in emission. We have picked two extreme cases. For other excitation emission energy pairs the situation falls between the extremes and may also reverse compared to the depicted cases (viz. show broad excitation and sharp emission).

To further explore this spectral broadening effect as a function of concentration, we choose a transition that does not exhibit FLN and hence represents the

total inhomogenously broadened line width. The results are shown in Fig. 8.23. We find that (1) the emission is shifted as a whole, (2) the emission line is significantly broadened, and (3) beyond 1% Nd ion concentration the emission intensity no longer increases. The first two observations lead to the conclusion that the inhomogeneous broadening in this case is due to interaction with other Nd ions, which shifts the emission to higher energies for the considered transitions. This is in contrast to our observation for the MBE-grown Er-doped sample, which showed a much more pronounced broadening at low concentrations. For higher Nd concentration, the fluctuation of Nd-Nd interactions leads to a broader distribution. Above 1% the probability to have Nd pairs or higher aggregates increases strongly. However, no emission from these could be identified.

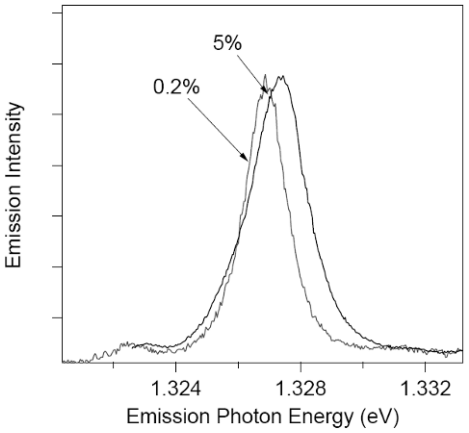

Fig. 8.23. Emission spectra of a peak without FLN for different concentrations of Nd ions. Reprinted with permission from [33]

Inhomogeneous broadening is caused by the existence of slightly different environments for otherwise identical defects. In order to evaluate to what extent spatial variation across the sample contributes to line broadening, we employed spatially resolved spectroscopy in which, as a first step, we record the emission for a fixed excitation wavelength using a confocal scanning microscope. We evaluate the resulting 2D emission map in terms of the emission position of a given peak (see Fig. 8.24(a)). We find that the emission peaks narrow as we restrict the addressed sample area, giving evidence of spatial inhomogeneities, which is further supported by the observed changes of the emission peak energies across the scanned region. This point can be made even more convincingly when we look at the CEES data obtained for two distinctly different regions A and B and subtract the data from each other see (Fig. 8.24(b)). We find that the shifts are present consistently for all transitions that exhibited fluorescence line narrowing. The 2D shift in the excitation/emission energy coordinate is reflected in the subtracted data image as positive and negative peaks.

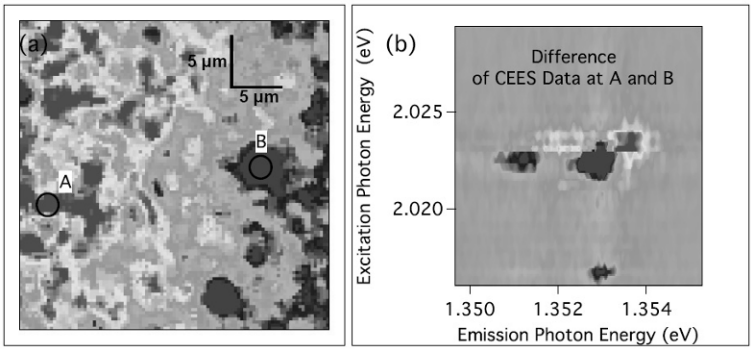

Fig. 8.24. (a) Spatial dependence of the emission peak position (b) Difference in the CEES spectrum taken at position A and B. Reprinted with permission from [33]

The extent of spatial narrowing and spectral shift is much smaller than observed in spectral line narrowing experiments. This suggests that lateral variations play only a minor role in the broadening. We suspect that a variation in depth (not accessible in our measurements) may have a more significant influence. The concentration variation gives an important clue about the origin of the spatial inhomogeneities. Fluctuation of RE concentration and the corresponding shifts in emission energy across the sample will result in the observed broadening. However, the fluctuation for the length scale that we resolved are small and rather negligible compared to the statistical variation of the local environment on a sub-micron and possibly smaller length scale.

8.3.5 Summary of CEES of GaN:Nd

Utilizing a combination of excitation emission spectroscopy and confocal microscopy with high spatial resolution, we assigned the transition of *in situ* doped Nd-ions in GaN by PA-MBE to essentially a single site. The large number of transitions that is observed is the combined result of the small splitting of the multiplets (leading to thermal activation even at low temperature) and electron-phonon coupling to a vibrational mode of the bulk material and to a localized Nd-related mode. The presence of a single site suggests that we are dealing with a locally unperturbed Nd ion that replaces a Ga ion. This assumption is based on the observation that in GaN the RE ions generally occupy the Ga site (see e.g.: results by RBS [4]) and that in samples where the RE ions experience perturbation by other defects, we always find multiple variation of this perturbation resulting in multi-site spectra as seen above for GaN:Er. While the local environment of the ions is unique, the presence of inhomogeneous broadening indicates that variations beyond the nearest neighbor environment exist. Based on our results for different concentrations, we deduce that this broadening is mainly due to perturbation by other Nd ions. However, a quenching of the emission due to interaction between the Nd ions occurs only at concentrations above 1 at%.

8.4 Application of CEES to Europium in GaN and AlGaN

8.4.1 Introduction

Europium ions in GaN have attracted considerable attention in the semiconductor laser community due to the recent success by Steckl et al. [22, 23, 24, 25, 26] in realizing both efficient electroluminescence devices and laser action under optical excitation. However, lasing under electrical excitation has not been obtained so far. In the laser experiments, an interesting change of laser wavelength has been observed with the length of the excitation channel indicating a critical role of different incorporation sites [26]. After growth, the first evaluation of the material quality as an EL phosphor is usually done by measuring the photoluminescence (PL) spectrum using above-bandgap excitation. Such measurements, however, are not site-selective and the spectra show overlapping contributions that are hard to analyze. To make this point, we show in Fig. 8.25 spectra taken from 3 samples produced with different growth conditions. For the depicted ^5D_o to $^7F_2$ transition, a maximum of three peaks is expected for a site of C_{3v} symmetry. As we have seen before, additional peaks can be caused by various mechanisms and in order to conclusively determine the origin of each of these peaks, site selective PL measurements must be carried out. Excitation spectra observed by Hömmerich et al. [27] added to the puzzle: In the spectral region of the ^7F_o to ^5D_o transition five peaks were observed in place of the one expected. The large shifts amongst peaks makes it unlikely that we are dealing with different sites alone. Detailed studies by Peng et al. [28], clearly revealed different sites and excitation pathways but still some peak assignments remained tentative. Most recently, Bodiou et al. [29] delivered direct evidence that defect-traps are involved in the excitation of some of the ions. In this section, we will make an attempt to clarify some of the peak assignments as well as correlate the identified sites with a particular excitation pathway.

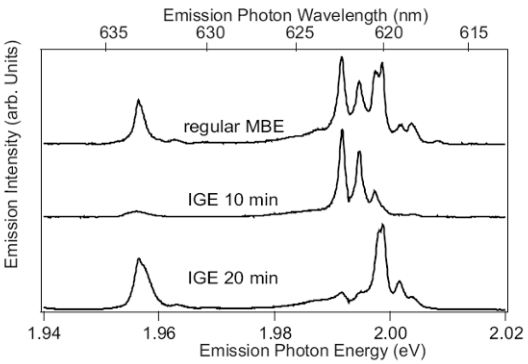

Fig. 8.25. Emission spectra due to the $^5D_0$ to $^7F_2$ transition obtained under above bandgap 351 nm excitation for samples grown under different conditions. Reprinted with permission from [33]

The site-selective PL characterization of the Eu-doped GaN samples that we will present here was carried out under several different excitation-emission schemes, illustrated in Fig. 8.26.

Using CEES we will address in this section the following tasks:

- Identify sites and fingerprint their energy levels.
- Identify and determine the relative strength of phonon-assisted transitions
- Assess the influence of the growth conditions on the site distribution
- Relate non-resonant and resonant excitation schemes.

We will start with samples that were produced by the group of Andrew Steckl in the Nanoelectronics Laboratory at the University of Cincinnati. The thin layers were grown by PA-MBE on sapphire substrates and were *in situ* doped with Eu to a concentration of about 0.5 at%, which is below the threshold of luminescence concentration quenching in GaN [30]. These samples have been studied by other groups hence allowing us to link our measurements to published data [28, 31, 32]. For comparison, we also studied samples from Prof. Wakahara's laboratory that were grown by MOCVD and ion-implanted with Eu [21].

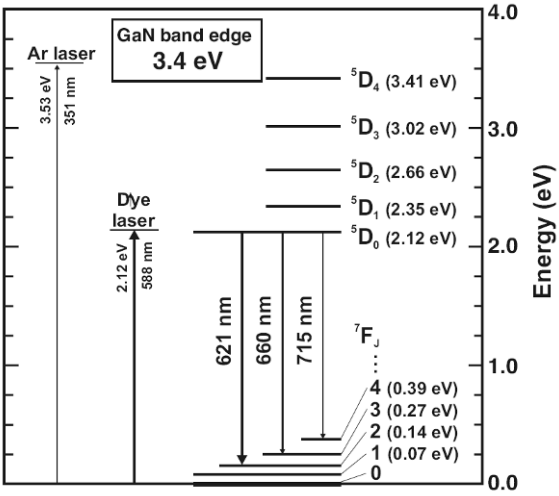

Fig. 8.26. Schematic of energy levels of Eu ions in GaN and transitions relevant for site selective spectroscopy studies. Reprinted with permission from [33]

8.4.2 Energetic Fingerprints of Different Sites

For our CEES measurements [33], we chose the $^7F_0$ to $^5D_0$ transition for excitation due to its simplicity. Since both levels have J=0, no crystal field splittings will exist in any symmetry, and each distinct site should demonstrate only one excitation peak. Resonant excitation was performed for this transition using a tunable dye laser

operating in the region of 2.095 - 2.183 eV (568-592 nm). For emission, we focused mainly on the $^5D_0$ to $^7F_2$ transition which has been shown to have the highest emission intensity and which is also very important technologically as a source of red emission. Measurements of the $^5D_0$ to $^7F_3$ transition were made for comparison. In Fig. 8.27, the CEES data for an MBE sample are presented for the ^5D_o to $^7F_2$ transition. Immediately apparent is the richness of the data image, which evidences the variety of different emission structures present in this region. There are four emission peaks that show up as vertical bands, indicating that they can be excited over the entire range of energies presented in the image. Two fairly strong bands appear at 1.956 eV (634 nm) and 1.997 eV (621 nm), and two weaker ones at 2.0018 eV (620 nm) and 2.0039 eV (619 nm). These will be discussed further in Sect. 8.4.5, when we deal with non-resonant excitation channels. In addition, a number of different emission peaks occur at discrete excitation energies. The changes in emission peak structure with excitation energy in this image clearly show the multisite nature of the Eu ions in this sample. Assigning the peaks to different sites and/or transitions is a challenging task. We make use of the fact that a particular site will yield its own unique emission spectra in terms of both line position and relative intensity. In this way, we are able to identify a total of eight different europium incorporation sites whose excitation energies are indicated by dotted lines in Fig. 8.27. The sites are labeled one to eight in order of ascending excitation energy. For further reference, we highlight the main site in blue and the minority site MS 3 in red.

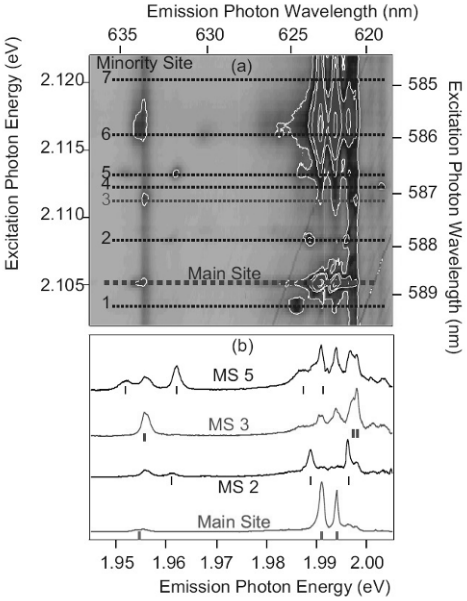

Fig. 8.27. (a) Image plot CEES data for $^5D_0$ to $^7F_2$ emission and $^5D_0$ to ^7F_o excitation obtained for an MBE grown sample that has been *in situ* doped with Eu ions. Different sites are indicated with dashed lines. Selected emission spectra under resonant excitation are shown in (b). Reprinted with permission from [33]

Fig. 8.27(b) shows several unique emission spectra for a few of the europium sites. The most dominant excitation peaks occur at 2.105 eV and 2.117 eV. For both we obtain identical emission spectra. We assign the lower energy transition to the main site and the higher to electron-phonon coupling, which we will discuss in more detail in Sect. 8.4.3. The other sites fall under the classification of minority sites whose emission intensities are typically much lower than that of the majority site. The identified peak positions for all eight sites are given in Table 8.5, which also includes the peak positions obtained from CEES measurements of the ^5D_o to $^7F_3$ transition.

Table 8.5. Peak positions determined for 10 sites of Eu in GaN. All values are given in eV

Transition	Main Site	MS 1	MS 2	MS 3	MS 4	MS 5	MS 6	MS 7	MS 8	MS 9
$^7F_0$ to ^5D_o	2.1059	2.1042	2.1091	2.1124	2.1131	2.1142	2.1171	2.1211		2.1091
^5D_o to $^7F_3$	1.8735	1.8574	1.8715	1.8700	1.8719	1.8832	1.8845	1.8939		
	1.8678		1.8687	1.8691	1.8645	1.8816				
	1.8641		1.8648			1.8672				
			1.8624			1.8557				
^5D_o to $^7F_2$	1.9947	1.9868	1.9968	1.9986	2.0036	1.9966	1.9684	2.0092	1.9969	1.9685
	1.9917		1.9894	1.9976	2.0014	1.9899		1.9880	1.9940	
	1.9550		1.9679	1.956	1.9599	1.9627		1.9716		
						1.9528				

The main site produces the most intense emission and it is reasonable to assume that it originates on Eu ions that occupy a substitutional Ga lattice site, with the dopant in C_{3v} symmetry. In this case we expect three emission lines for the ^5D_o to $^7F_2$ transition, two at higher transition energy corresponding to the two lower crystal field levels and one at lower transition energy corresponding to the one higher crystal field level. This expectation matches very well with the emission spectra. It should be noted that the peak at 1.9550 eV (634.27 nm) has been assigned to the $^5D_1$ to $^7F_4$ transition [3, 28, 34]. We can exclude the latter assignment in our measurements since the peak appears already under excitation of the ^5D_o state at low excitation intensities such that the $5D_1$ level won't be excited at all.

As shown in Table 8.5, the minority sites produce from one to four emission peaks for the ^5D_o to $^7F_2$ transition. (It should be noted that these are "identified" emission peaks; there could be more peaks associated with a particular site hidden under the peaks of other sites.) The unique spectral signatures of the different incorporation sites indicate an unique local environment for the emitting Eu ion. These environments could involve ions in the proximity of lattice vacancies, interstitials, or other intrinsic defects in the host lattice. It is also extremely likely that some of these different sites could represent Eu on the Ga substitutional lattice location that is being perturbed by a nearby impurity.

Also worth mentioning is that the main site and minority sites 1,2 correspond very nicely to the three lowest energy excitation peaks identified by Hommerich et al. in their studies of this transition region [27]. The integrated PL intensity for each site is shown in Fig. 8.28. The main site contributes about 75% of the total emission while 2 minority sites produce emission on the order of one-tenth that of the main site. Most of the minority sites contribute even lower intensity. It should be noted that these intensities only provide a rough indication of the relative abundance of the different sites since we lack information on the transition probabilities and branching ratios. Due to the forbidden character of the ^7F_o to ^5D_o transition, we suspect that the least perturbed (main site) has the lowest transition probability and may hence be underestimated by Fig. 8.28. The ratio between main and minority site may well be similar to the one observed for Nd-doped samples that have been grown under similar conditions.

Comparing our results with those on optical gain in GaN:Eu [26], we find that the main site and MS 3 are the principal components with the site labeled Eu_x corresponding to the main site while Eu_y corresponds to MS 3.

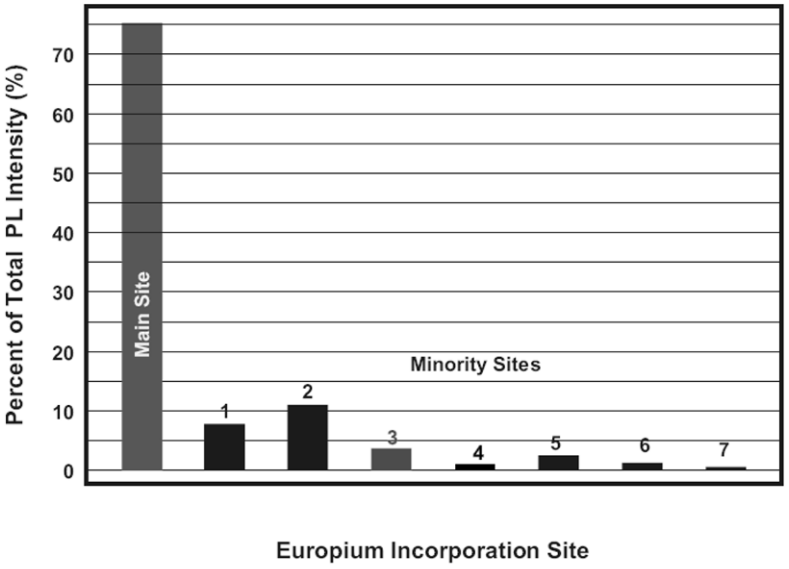

Fig. 8.28. Photoluminescence intensity of the various identified europium incorporation sites integrated over the region of the $^5D_0$ to $^7F_2$ transition. Reprinted with permission from [33]

In assigning the excitation peaks we have left out the higher energy peaks that are not expected for the single transition that we considered. We will deal with these in the following and show that they are related to electron-phonon coupling.

8.4.3 Electron Phonon Coupling

In the spectral range of the ^7F_o to $^5D_0$ transition above 2.1 eV (590-570 nm), we find three distinct excitation peaks, shown in Fig. 8.29, which exhibit exactly the same spectral pattern as the main site. The excitation peaks are quite different in width (0.7, 3.1, 0.4 meV for the peaks at 2.105, 2.117, and 2.171 eV respectively).

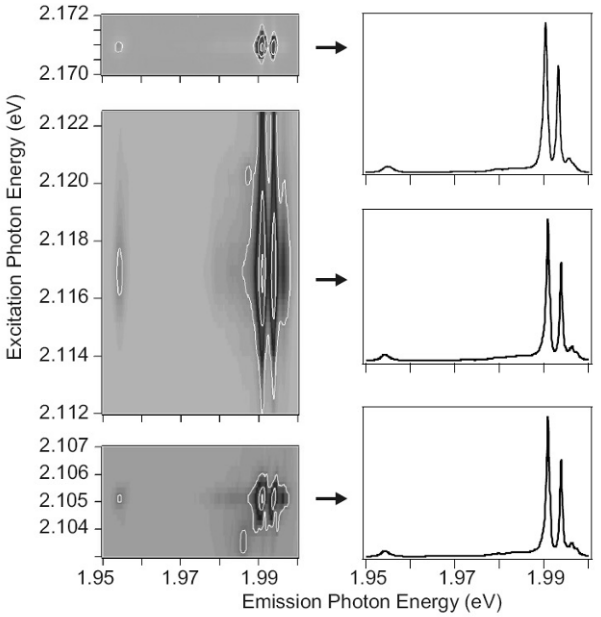

Fig. 8.29. (left) CEES image/contour plots of the $^5D_0$ to $^7F_2$ transition region for three different excitation energies associated with the $^5D_0$ to $^7F_0$ transition. (right) are the emission spectra associated with each of these excitation peaks. Reprinted with permission from [33].

We need to consider electron-phonon coupling here. Due to the forbidden character of the transition this could lead to relatively more pronounced features if the vibration leads to dynamic admixing of states for which transitions are allowed. In order to confirm the corresponding energy shifts, we need to look for the phonon replica in the emission spectrum as well. By closer inspection of the data presented in Fig. 8.27, we can find such features shifted by 66 meV and 12 meV, which is exactly the same as in the excitation spectrum. We show the shifted spectra in Fig. 8.30. The shift of 66 meV corresponds closely to the GaN TO phonon energy. The replica that is shifted by 12 meV has not been reported before and most likely originates from a phonon that is local to the Eu site. This would account for the homogeneous broadening of the excitation peak associated with this phonon mode. We have found a mode of similar energy for Nd already. The

coupling as shown for the allowed emission transitions is rather weak (S approx. 0.01) for both modes.

Despite such weak electron-phonon coupling, the data show very efficient phonon-assisted excitation for both types of phonon as seen in the excitation spectrum of Fig. 8.31. We find that the total emission intensity of the localized phonon-assisted excitation is 7 times larger than that of the zero-phonon excitation, while the total emission intensity of the GaN LO phonon-assisted excitation is 3 times larger than that of the zero-phonon excitation.

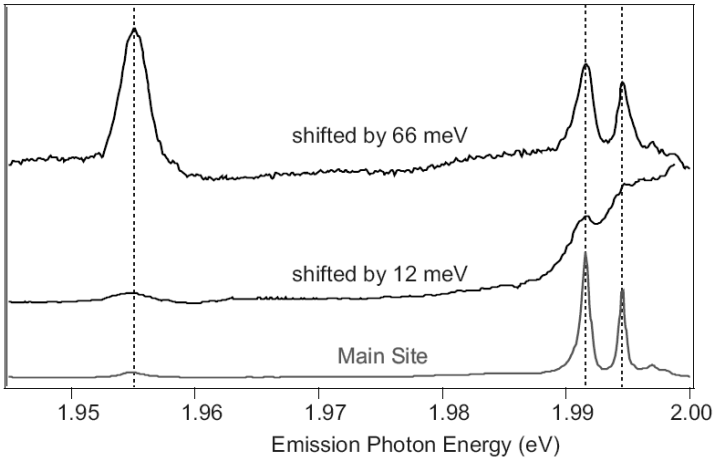

Fig. 8.30. Two phonon replicas of the red emission from the main site. The replicas are shifted by 12 meV and 66 meV from the zero-phonon emission. Reprinted with permission from [33]

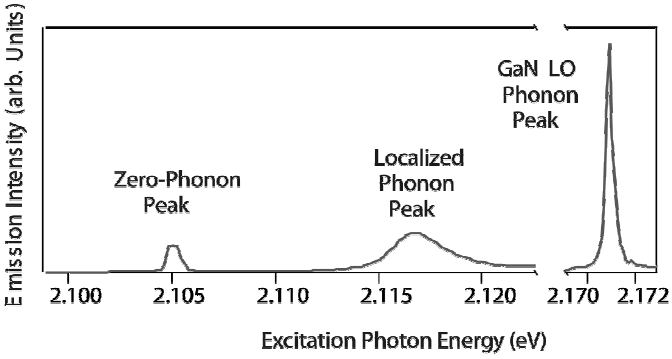

Fig. 8.31. Integrated excitation spectrum of the ^5D_o to $^7F_2$ emission transition showing the zero-phonon excitation line at 2.105 eV as well as the localized-phonon-assisted excitation peak at 2.112 eV and the GaN LO phonon-assisted peak at 2.171 eV. Reprinted with permission from [33].

To confirm our assignment, we studied the evolution of these excitation peaks as a function of the Al/Ga ratio. A series of $Al_xGa_{1-x}N$ alloy samples with different AlN content ($0<x<1$) was produced for that purpose by A. Wakahara group at the Toyohashi University of Technology in Japan [35].

In Fig. 8.32, we show CEES images for this set of samples. The zero phonon line as well as the sidebands associated with the localized phonon and the GaN LO phonon can be found for all compositions. The phonon-coupled transitions become relatively weaker at first but increase again as we approach AlN. This may be explained by the degree of order in the samples due to the alloying. In the case of GaN and AlN the zero-phonon line is forbidden such that the phonon-coupled transitions start to dominate. In the disordered alloys, the zero-phonon lines are stronger by themselves. The energy shift relative to the zero-phonon lines increase for both modes as shown in Fig. 8.33. This is, for the TO-mode, consistent with what is found in Raman spectroscopy, providing us with solid confirmation of the assignment. It should be noted that Peng et al. [28] also observed shifts of about 12 meV, which they however assigned to additional sites. In view of our assignment, their result may have to be revisited and reinterpretation might be necessary to take the electron phonon coupling into consideration. With the fingerprints of our sites at hand we can turn our attention to the variation in site incorporation as growth parameters are varied.

8.4.4 Effect of Growth Conditions

In this section, we will look at a series of samples produced by an innovative growth technique called Interrupted Growth Epitaxy (IGE), which was designed by A. Steckl's group at the University of Cincinnati to optimize the GaN growth conditions for efficient RE luminescence. Originally designed to limit the formation of GaN surface islands, the film is exposed for 5 minutes to flowing nitrogen while the gallium beam is interrupted. The total time that the gallium beam is on is kept constant but the on/off period is varied while the time it is interrupted is varied. Consequently, more on/off cycles are performed for shorter on-times. The samples are labeled according to the time the Ga beam is open during each cycle.

We find strong variation of the relative abundance of the various sites. Since we expect that the total number of the main sites is not changing drastically, we use it as a reference and depict in Fig. 8.34 the relative PL intensities of the other sites as a function of time that the Ga beam is open during each cycle.

No systematic behavior appears at first sight. While MS 1,3,4,5,6 show fairly similar dependences, MS 2 exhibits a different behavior. The first group has a maximum for a shutter-open-time of about 20 minutes, while MS 2 increases continuously up to a shutter-open-time of 60 minutes.

We also investigated samples that have been ion-implanted as described in Sect. 8.4.3 and in [34]. In Fig. 8.35, we show the CEES data in the energy range of the ^5D_o to $^7F_2$ transition. It is immediately apparent that the number of sites is reduced. We see three main features: (1) the main site with its phonon-assisted excitation band, (2) the minority site 2, which is however much stronger, and may hence be connected with the defects that are introduced by implantation, and (3) a vertical stripe at 1.997 eV that will be discussed in the next section.

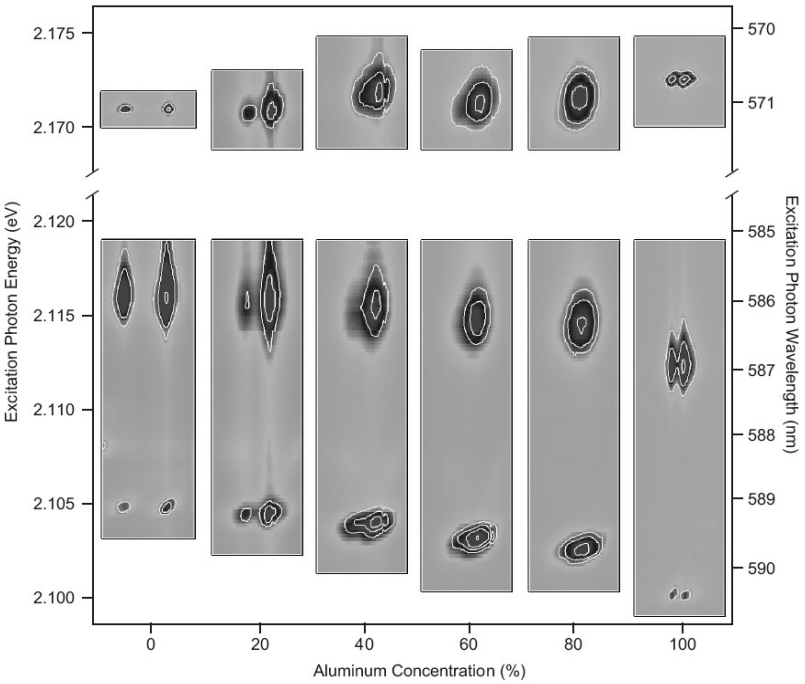

Fig. 8.32. Site-selective CEES images obtained from resonant excitation of the $^5D_0$ to $^7F_0$ Eu transition while looking at the $^5D_0$ to $^7F_2$ emission of a series of Eu-doped $Al_xGa_{1-x}N$ samples with varying AlN content The peaks occurring at lowest excitation energy correspond to zero phonon emission, those occurring at the middle excitation energy correspond to the localized phonon sideband emission, and the peaks occurring at highest excitation energy correspond to the GaN LO phonon sideband emission. Reprinted with permission from [33]

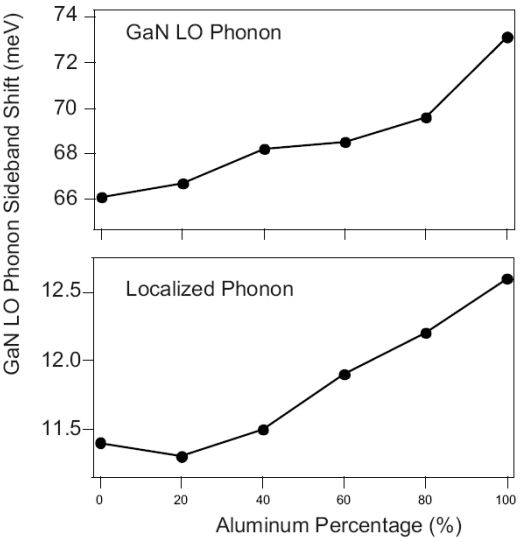

Fig. 8.33. LO phonon sideband and localized phonon sideband energy shifts as a function of aluminum concentration in $Al_xGa_{1-x}N$. Reprinted with permission from [33]

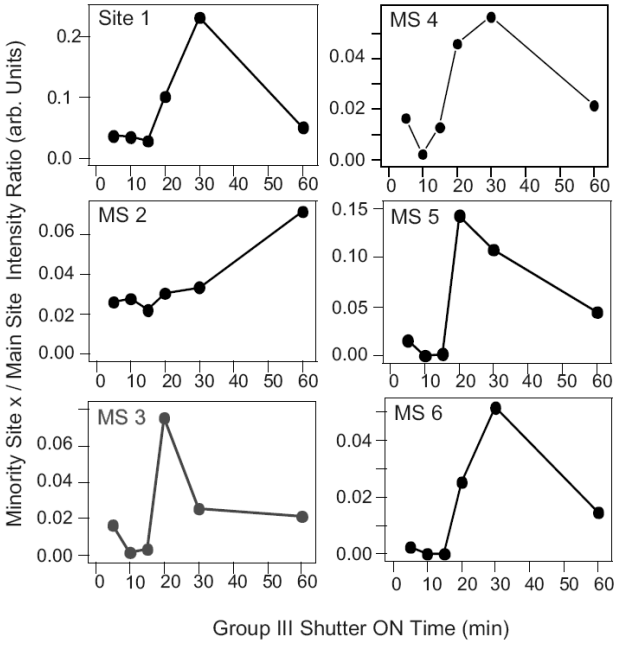

Fig. 8.34. Relative numbers of sites obtained for different Ga shutter open times in the IGE growth method for Eu-doped GaN. Reprinted with permission from [33]

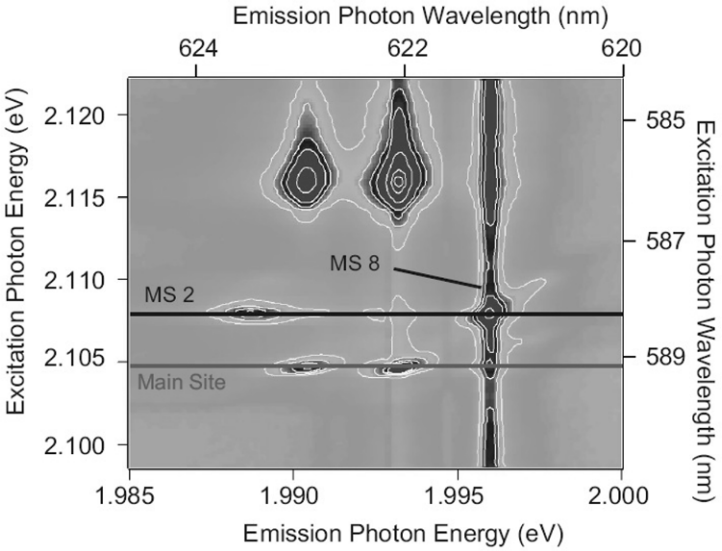

Fig. 8.35. Image plot CEES data obtained for an MOCVD sample that has been ion implanted with Eu.

8.4.5 Excitation under Non-Resonant Conditions

After obtaining a detailed fingerprint of the different incorporation sites, we will explore in this section how these sites may be excited non-resonantly. For this purpose we use four different excitation modes:

1. Excitation far below the bandgap of GaN in the visible spectral region
2. Excitation below but fairly close to the bandgap
3. Above-bandgap excitation
4. Excitation by energetic electrons in a scanning electron microscope SEM

Through the site specificity of our studies, we will be able to relate the excitation channels and determine relative excitation efficiencies.

8.4.5.1 Non-Resonant Excitation in the Visible

Besides the abundance of different incorporation sites seen in Sect. 8.4.2 and the phonon assisted excitation peaks identified in Sect. 8.4.3, there is a third type of emission feature: vertical stripes occur at 1.956 eV, 1.9627 eV, 1.9970

eV, 2.0018 eV, and 2.0039 eV. Careful inspection of the 1.9970 eV stripe shows that two different peaks are associated with this emission: one at 1.9976 eV and the other at 1.9986 eV. Referring back to Table 8.5, we see three of the emission energy peaks corresponding to these excitation stripes match up exactly with the peaks defining MS 3. This becomes even more apparent when we compare in Fig. 8.36 the emission spectra of MS 3 with the spectra that are obtained non-resonantly in the visible red region. Within our uncertainty due to the spectral overlap of different sites, the two spectra are identical.

We further find that the emission energy of the other stripes match up with the emission energy peak associated with Minority Sites 4 and 5. Apparently, MS 3,4, and 5 can be excited non-resonantly in the visible while the other sites cannot or only with very low efficiency. We suspect that deep traps are excited with visible light, which can then transfer their energy to the Europium ions. The efficiency of the process suggests that the ions and the traps form complexes or are at least in close vicinity to one another. In fact the presence of a trap in the close vicinity of an ion will change the resonant properties of the RE ion such that we could identify them as individual different sites.

Looking more closely at the CEES data for the ion-implanted sample shown in Fig. 8.35, we see a very pronounced vertical stripe at a position that overlaps with the higher energy emission line of MS 2. There is also an apparent resonance at the excitation energy of MS 2 but only for the higher energy emission line. Decomposing the emission spectra on-resonance and off-resonance reveals a new site (MS 8) with a high-energy emission peak that strongly overlaps but is not identical to MS 2. Both MS 2 and MS 8 are dominantly present in ion-implanted samples. This has to be kept in mind when *in situ* doped samples and ion-implanted samples are compared.

Broad below-gap excitation bands in the visible were also observed for Er-doped GaN [10, 11] and were attributed to excitation mediated through deep impurity- or defect-related traps. In our studies of the emission of Er-doped GaN, we noted the absence of the green emission for one of the sites and suspected a role of the defect-traps (see Sect. 8.2.5). This shows that a non-resonant visible excitation channel is not unique to Eu. The spectral position of the non-resonant excitation bands raises the suspicion that the defect-traps may be related to the defects that cause the yellow emission in GaN (see e.g.: [36 37 38] which has been associated with intrinsic nitrogen vacancies [39, 40] or may be related to Eu ions in the vicinity of nitrogen vacancies. It is well known that shallow traps with emission features close to the bandedge exist in GaN as well. Hence we also explore the possibility of exciting the RE sites close to the band gap.

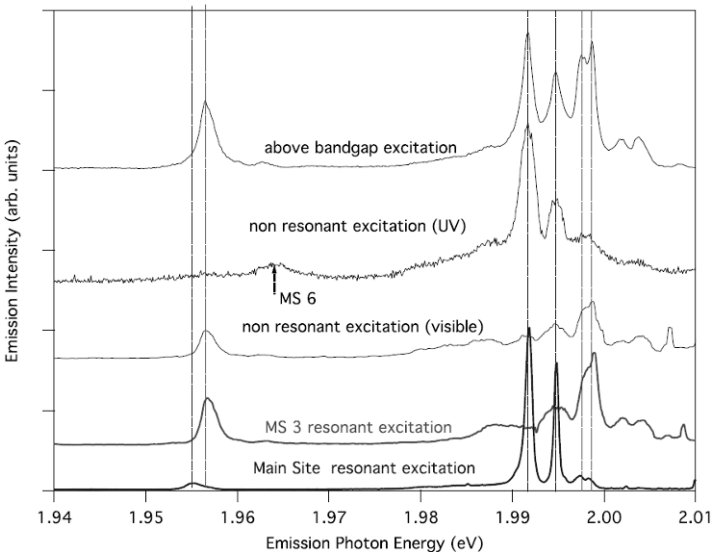

Fig. 8.36. Comparison of emission spectra obtained under different resonant and non resonant excitation energies: MS 1 resonant to excited at 2.1059 eV, MS 3 resonant at 2.1124 eV, non-resonant visible excitation at 2.1024 eV, non resonant UV excitation at 3.06 eV and above bandgap excitation at 3.53 eV. Reprinted with permission from [33]

8.4.5.2 Excitation Close to the Bandgap

Wang et al. performed PLE measurements in the band edge region on peaks associated with both the main site and the site identified here as MS 3 [41]. Their PLE spectra illustrated how the emission of the MS 3 site drops sharply for excitation energies just below the band edge at 3.4 eV, whereas the main site continues to emit with excitation in the region between 3.0 eV and 3.4 eV. Similar results were reported by Peng et al. [28]. This observation provides clear evidence that different excitation pathways are at play for these two sites.

In order to relate these observations more closely with our site-selective measurements, we measured an emission spectrum with below-bandgap excitation, using an InGaN LED emitting at 3.06 eV (405 nm). This spectrum is included in Fig. 8.36 to allow comparison of the emission produced by the two non-resonant excitation pathways. The differences are drastic and it appears that those sites that are excited through the one channel are not excited through the other. We find that the main site and MS 1 are excited efficiently with sub-bandgap light while MS 3,4,5 are excited through visible light. Another weak feature near 1.968 eV becomes apparent that does not match any of the sites that have been identified so far. Inspecting again the CEES data we find a very weak feature that we label MS 9. It is most apparent

in IGE samples with Ga-Shutter-open times larger than 20 minutes and can be observed in the MBE-grown sample. The enhancement of emission through near band edge excitation is very strong such that we suspect that it is directly connected with the shallow trap just as MS 3 is related to the deep trap.

Based on these observations, the relative strength for different growth conditions and the spectral positions allows us to correlate the sites from Peng's study [28] with ours. Site 1 corresponds to our main site, while Site 2 corresponds to MS 3. More tentatively, we identify Site 3 with our MS 9. Site 4 may include some contributions from phonon-assisted transitions of the main site and may hence not be an independent site.

8.4.5.3 Above-Bandgap Excitation

We finally turn to the excitation of GaN:Eu with light above the bandgap, which is crucial to understanding the performance of electroluminescent devices. A spectrum of an MBE sample was obtained with above-bandgap excitation (3.53 eV, 351 nm). By comparison with the emission spectra under direct resonant excitation, we find that, beside the main site, the minority sites MS 3, 4, and 5, which are related to deep defect traps, dominate the emission spectra. Closer inspection reveals contributions from the other minority sites that are related to more shallow traps. In any case, the main site is much less dominant with above-bandgap excitation, suggesting that the excitation efficiency of the minority sites is enhanced compared to the main site. We quantify this enhancement in Table 8.6, which lists the relative emission strengths of each minority site in comparison to the main site for both resonant and above- bandgap excitations.

Table 8.6. Relative percentage of the indicated minority site emission with respect to majority site emission for resonant and above-bandgap excitation. Error estimates for these values are +/- 0.5 percent. The enhancement factor is calculated as the ratio of the two numbers above.

	MS 1	MS 3	MS 4	MS 5	MS 6	MS 7
Above-bandgap	18.2	103.7	11.1	6.4	1.8	1.6
Resonant excitation	9.3	5.3	2.6	4.0	1.4	1.3
Enhancement factor	2	19.5	4.2	1.6	1.3	1.2

MS3 has a significantly higher excitation efficiency compared to the main site, quantified by the enhancement factor in Table 8.6. This factor becomes even higher (up to 60) for some samples that we studied. Being just a relative measure, it is unclear if this sample dependence is due to a change in efficiency of MS 3 or of the main site.

We also note that we cannot find the feature associated with MS 2 and suspect that this site can only be excited resonantly. It appeared quite strongly

in our ion-implanted sample but even there it was absent from the spectra excited above the bandgap. This gives first evidence that some RE sites in GaN can not be excited through the creation of electron-hole pairs. In particular, MS 2 has to be avoided in the ion-implanted samples.

8.4.5.4 Excitation through Energetic Electrons

As a final way of exciting RE ions in GaN, we use the electron beam in a SEM and measure the resulting cathodoluminescence (CL). For weak excitation density the emission spectra resemble most those obtained using above-bandgap optical excitation, suggesting that excitation through the creation of electron-hole pairs by the impinging electron beam is the main excitation pathway. In the SEM, however, we have the opportunity to increase the excitation density to saturate the long-lived transitions. Under such conditions, we would expect that all possible ions are excited and hence the emission should come dominantly from the main site. However, we find in our measurements that the emission intensity from site MS 3 and the main site are still almost equal in intensity [42]. From this we have to conclude that not all ions that we see as the main site can be excited by energetic electrons.

8.4.5.5 Excitation Model for Non Resonant Excitation

Based on the data observed so far, it is apparent that there are two dominant excitation pathways that account for the majority of above-bandgap excited Eu emission. Both of these pathways involve excitation of the Eu by a trap mediated energy transfer process. Shown in Fig. 8.37 is a schematic representation of the two dominant excitation pathways: here labeled Shallow Trap Excitation Pathway (corresponding to the MS 1 and Main Site excitation) and the Deep Trap Excitation Pathway (corresponding to excitation of MS 3, 4, and 5)). In both pathways, we assume that above-bandgap excitation first creates an electron-hole pair which then transfers the energy to the respective defect-trap. Energy can be transferred on, most likely via an Auger process [43, 44]. There may be several kinds of each type of defect trap and some of them may be directly related to the Eu ions. In particular, we assume this to be the case for MS 3 and MS 9 for which a very efficient excitation is possible after excitation of the traps. On the other hand, it is also possible that some Eu incorporation sites that do not act as traps themselves can be excited through a defect-trap in their vicinity. The distance to such defect–traps will then govern the excitation efficiency and some ions may be too far away to be excited at all. This interpretation explains the observations that not all main sites and essentially none of MS 2 can be excited through electron-hole pairs.

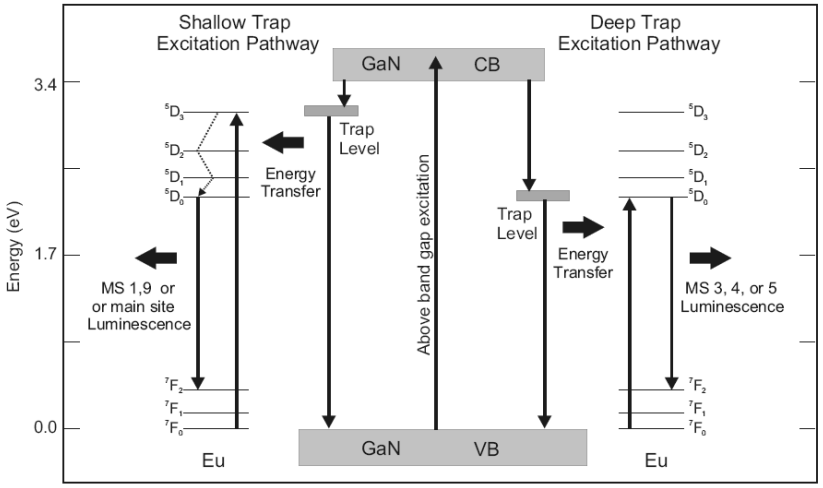

Fig. 8.37. Simple Excitation model for RE ions after excitation of electron-hole pairs. Reprinted with permission from [33]

8.4.6 Summary

We have identified through the use of resonant excitation at least 10 different incorporation sites involving Eu ions in GaN and studied how these sites behave under different excitation conditions and how their relative number depends on growth and doping conditions. For the latter, we find that a main site, most likely a fairly unperturbed Eu ion on a Ga site, is always dominant while the minority sites change substantially in relative numbers and can become competitive with the main site for the case of MS 2 in ion-implanted samples.

In terms of the excitation pathway after the creation of electron-hole pairs, we found three types of processes associated with different sites: (1) MS 1, MS 9, and the main site are excited through shallow traps, (2) MS 3, 4, and 5 are excited through deep traps, and (3) some sites like MS 2 and a large fraction of the main site cannot be excited at all or very inefficiently. The relative number for the remaining sites is too small to decide on their excitation pathway. The efficiency of excitation is highest for excitation involving the deep traps such that it would be desirable to enrich MS3 as done to some extent in the IGE samples with 15-20 minutes shutter-closed times.

8.5 Conclusion

We have reviewed results on site-selective spectroscopy obtained by using combined excitation emission spectroscopy for three different dopant ions and a variety of sample preparations. Utilizing the unique strength of this technique, we obtained a reliable assignment of peaks to different sites, transitions from thermally excited states and electron-phonon coupled transitions and in some cases, we reassigned previously assigned transitions in a more consistent way. We also found a rather large number of minority sites for all dopants with abundances below 10% of the total in terms of emission intensity. With the spectral fingerprints of different sites, we showed how the site distribution is influenced by variation of growth conditions, and for Er and Eu we are able to relate the sites to different excitation channels following above-bandgap excitation. For Er in GaN, we also characterize how the sites participate in up-conversion excitation processes.

While some of the properties are found to be dopant-specific, we found some more general principles that are related with the excitation channel for above-bandgap optical excitation and non-resonant excitation below the bandgap: The excitation efficiency of the main site is considerably lower than that of some of the minority sites. We interpret this to mean that the ion itself is not very efficient in trapping excitation and that its excitation involving other traps depends on the ion-trap distance. Many of the main sites are far away from these traps and cannot be excited through this channel at all. The most efficient excitation channel involves deep-trap states. Unfortunately, the corresponding RE ions are not very abundant. The deep trap states are not uniquely defined since, at least for Eu, several sites are observed that are excited in this way. In particular, in ion implanted and *in situ* doped samples the dominant defect related sites are quite distinct from each other (MS 3 vs. MS 8) The presence of RE ions that cannot be excited efficiently through electron-hole pairs poses a significant hurdle for the realization of electrically pumped RE-based GaN lasers due to the added loss that they will represent. In maximising the defect-related incorporation sites for improved performance of light emitting devices, one is faced with the limitation of growth parameters and the requirement that the active layers are still viable to be used in an injection or p-n junction device.

Acknowledgements

A number of graduate students strongly contributed to this work through careful measurements and interpretations: C. Sandmann, S. Penn Tafon, Z. Fleischman and N. Woodward. The work would have been impossible without the generous supply of samples from A. Steckl, A. Wakahara, H. X. Jiang, E. Readinger, K. Akimoto, P. Chow and B. Hertog. The author further acknowledges numerous discussions with J. Zavada, A. Kozanecki and K. P. O'Donnell.

References

1. V. Dierolf and C. Sandmann, Journal Of Luminescence 125, 67-79 (2007).
2. S. Hüfner, Optical spectra of transparent RE compounds (Academic Press, New York, 1978).
3. T. Monteiro, C. Boemare, M. J. Soares, R. A. S. Ferreira, L. D. Carlos, K. Lorenz, R. Vianden, and E. Alves, Physica B 308, 22-25 (2001).
4. U. Wahl, E. Alves, K. Lorenz, J. G. Correia, T. Monteiro, B. De Vries, A. Vantomme, and R. Vianden, Mat. Science Eng. B 105, 132-140 (2003).
5. R. Maclej, S. Kammoun, M. Dammak, and M. Kammoun, Materials Science & Engineering B 146, 183-185 (2008).
6. V. Dierolf and M. Koerdt, Physical Review B61, 8043 (2000).
7. V. Dierolf, C. Sandmann, J. Zavada, P. Chow, and B. Hertog, Journal Appl. Physi. 95, 5464-5470 (2004).
8. K. Makarova, M. Stachowicz, V. Glukhanyuk, A. Kozanecki, C. Ugolini, J. Y. Lin, H. X. Jiang, and J. Zavada, Mat. Science Eng. B 146, 193-195 (2008).
9. V. Glukhanyuk, H. Przybylinska, A. Kozanecki, and W. Jantsch, Physica Status Solidi A 201, 195-198 (2004).
10. S. Kim, S. J. Rhee, D. A. Turnbull, E. E. Reuter, X. Li, J. J. Coleman, and S. G. Bishop, Applied Physics Letters 71, 231-233 (1997).
11. S. Kim, S. J. Rhee, X. Li, J. J. Coleman, S. G. Bishop, and P. B. Klein, Journal Electronic Materials 27, 246-254 (1998).
12. C. Ugolini, N. Nepal, J. Y. Lin, H. X. Jiang, and J. Zavada, Applied Physics Letters 89, 151903 (2006).
13. P. Verma and A. Yamada, Materials Science Forum 389-3, 1501-1504 (2002).
14. S. Tripathy, S. J. Chua, P. Chen, and Z. L. Miao, Journal Of Applied Physics 92, 3503-3510 (2002).
15. A. J. Steckl, J. H. Park, and J. M. Zavada, Materials Today 10, 20-27 (2007).
16. E. Silkowski, Y. K. Yeo, R. L. Hengehold, B. Goldenberg, and G. S. Pomrenke, RE Doped Semiconductors II Symposium 69 (1996).
17. S. Kim, S. J. Rhee, X. Li, J. J. Coleman, and S. G. Bishop, Physical Review B 57, 14588-14591 (1998).
18. J. H. Kim and P. H. Holloway, Appl. Phys. Lett. 85, 1689 (2004).
19. E. D. Readinger, G. D. Metcalfe, H. Shen, and M. Wraback, Applied Physics Letters 92, 061108 (2008).
20. G. Metcalfe, E. Readinger, P. Shen, N. Woodward, V. Dierolf, and M. Wraback, Journal Of Applied Physics 105, 053101 (2009).
21. V. Dierolf, Z. Fleischman, C. Sandmann, A. Wakahara, T. Fujiwara, C. Munasinghe, and A. Steckl, Mater. Res. Soc. Symp. Proc 866, V3.6.1 (2005).
22. A. J. Steckl, J. C. Heikenfeld, D. S. Lee, M. J. Garter, C. C. Baker, Y. Q. Wang, and R. Jones, IEEE Journal Of Selected Topics In Quantum Electronics 8, 749-766 (2002).
23. J. H. Park and A. J. Steckl, Applied Physics Letters 85, 4588-4590 (2004).
24. C. Munasinghe and A. J. Steckl, Thin Solid Films 496, 636-642 (2006).
25. J. H. Park and A. J. Steckl, Optical Materials 28, 859-863 (2006).
26. J. H. Park and A. J. Steckl, "Site specific Eu^{3+} stimulated emission in GaN host", Applied Physics Letters 88, 011111 (2006).
27. U. Hommerich, E. E. Nyein, D. S. Lee, J. Heikenfeld, A. J. Steckl, and J. M. Zavada, Mat.Science Eng. B- 105, 91-96 (2003).
28. H. Peng, C. Lee, H. O. Everitt, C. Munasinghe, D. S. Lee, and A. J. Steckl, J. Appl. Phys. 102, 073520 (2007).

29. L. Bodiou, A. Braud, J. L. Doualan, R. Moncorge, K. Lorenz, and E. Alves, Journal Of Alloys And Compounds 451, 140-142 (2008).
30. H. J. Bang, S. Morishima, J. Sawahata, J. Seo, M. Takiguchi, M. Tsunemi, K. Akimoto, and M. Nomura, Applied Physics Letters 85, 227-229 (2004).
31. E. E. Nyein, U. Hommerich, J. Heikenfeld, D. S. Lee, A. J. Steckl, and J. M. Zavada, Applied Physics Letters 82, 1655-1657 (2003).
32. H. Y. Peng, C. W. Lee, H. O. Everitt, D. S. Lee, A. J. Steckl, and J. M. Zavada, Applied Physics Letters 86, 051110 (2005).
33. Z. Fleischman, C. Munasinghe, A.J. Steckl, A. Wakahara, J. Zavada, V. Dierolf, Appl Phys B 97, 607–618 (2009).
34. M. Pan and A. J. Steckl, Applied Physics Letters 83, 9-11 (2003).
35. T. Fujiwara, A. Wakahara, Y. Nakanishi, and A. Yoshida, phys. stat. sol.(c) **2,** 2805-2808 (2005).
36. R. Singh, R. J. Molnar, M. S. Unlu, and T. D. Moustakas, Applied Physics Letters 64, 336-338(1994).
37. C. H. Chiu, F. Omnes, C. Gaquiere, P. Gibart, and J. G. Swanson, Journal of Physics D: Applied Physics 35, 609-614(2002).
38. M. H. Zaldivar, P. Fernandez, and J. Piqueras, Semicond. Sci. Technol 13, 900-905(1998).
39. H. M. Chen, Y. F. Chen, M. C. Lee, and M. S. Feng, Physical Review B 56, 6942-6946(1997).
40. J. Bernholc, J. C. Chervin, A. Polian, and T. D. Moustakas, Physical Review Letters 75, 296-299(1995).
41. K. Wang, R. W. Martin, K. P. O'Donnell, and V. Katchkanov, Applied Physics Letters 87, 1121072 (2005).
42. S. Tafon Penn, Z. Fleischman, V. Dierolf,phys. stat. sol. (a) 205, No. 1, 30–33 (2008).
43. W. Fuhs, I. Ulber, G. Weiser, M. S. Bresler, and O. B. Gusev, Physical Review B 56 9545-9551 (1997).
44. N. Yassievich, M. S. Bresler, and O. B. Gusev, J. Phys. Cond. Mat.9, 9415 (1997).

Chapter 9
Excitation Mechanisms of RE Ions in Semiconductors

Alain Braud

Abstract This chapter presents an overview of the mechanisms responsible for the excitation of optically active rare-earth (RE) ions in semiconductors. Besides resonant excitation of the RE 4*f* shell, several non-resonant processes can take place in which the host is excited first. These indirect mechanisms involve non-radiative transfer of the recombination energy of electrons and holes to nearby RE ions. Distinct excitation processes arise because of the various conditions under which the electron may recombine with a hole. The different possibilities are presented and discussed in the first part of this chapter. Carriers of opposite charge bind to each other to form either a free exciton or a trapped (bound) exciton. In the latter case, the trapping can arise from the incorporation of RE ions which induces distortions of the host lattice. The exciton trapping can also be due to an impurity, a local defect or even an extended defect. Other possible mechanisms involve the capture of an electron by the 5*d* shell changing the valence state from trivalent to divalent with the subsequent capture of a hole. Finally, the role of impurities associated with donor-acceptor pairs in the recombination of electrons and holes with energy transfer to RE ions is discussed. In the second part of this chapter the specific case of RE-doped GaN is considered. Results are presented to show that local defects play a major role in the excitation process by binding excitons with a subsequent energy transfer to RE ions. A general modelling of the RE excitation mechanism mediated by bound excitons (BE) is presented and discussed. Finally, experiments using two excitation sources are shown to give valuable information concerning the RE-related defects.

Centre de Recherche sur les Ions, les Matériaux et la Photonique (CIMAP)
UMR 6252 CNRS-CEA-ENSICAEN, Université de Caen, 14050 Caen, France
alain.braud@ensicaen.fr

9.1 Introduction

Rare-earth (RE) doped semiconductors, starting with II-VI compounds, have been studied for a long time for the development of thin-film electroluminescent color displays [1]. This research led to the development of efficient electroluminescent materials such as terbium-doped zinc sulphide [2] (ZnS:Tb) and cerium-doped strontium sulphide [3] (SrS:Ce). Later on, the luminescence from erbium-doped III-V semiconductors received considerable attention with the goal of developing electrically pumped optical sources and amplifiers for use in optical communications [4]. RE emission in doped small-bandgap semiconductors such as InP, GaAs or Si is unfortunately limited by strong thermal quenching [5]. In contrast, wide-bandgap (Al, Ga)-N semiconductors feature a reduced RE emission quenching. Therefore, they are being widely studied for various applications in optoelectronics [6, 7, 8, 9]. Another very active field deals with Er ions coupled to Si nanocrystals in a SiO_2 matrix with the goal of developing an erbium-doped silicon amplifier [10].

The overall interest in RE-doped semiconductors is motivated by the unique optical properties of RE-doped materials. Optically active 4*f* electrons of RE ions are shielded from the influence of the local crystal field by outer 5*s* and 5*p* electron shells. Therefore, energy levels of the $4f^n$ configurations are only slightly different from free ion energy levels. When these ions are incorporated in semiconductors the fundamental understanding of the mechanisms underlying the excitation of RE ions is still under scrutiny. The first part of this chapter will be devoted to the description of the main mechanisms which are responsible for the RE excitation in various semiconductors.

The simplest way of exciting RE ions, as is done for instance in most RE-based lasers, is to use an optical pumping source with a photon energy that matches a higher-lying inner 4*f* shell transition. This type of excitation scheme is therefore called resonant or direct excitation. Other types of excitation mechanism involve exciting the host first and then the RE ions; these are called non-resonant or indirect excitation processes.

The excitation can take several steps before reaching the luminescent ion. The impact excitation of RE ions by hot electrons is one possible indirect RE excitation mechanism. This inelastic scattering of hot electrons by RE ions leads to the excitation of 4*f* electrons and takes place in both cathodoluminescence (CL) and electroluminescence (EL) processes [11]. Besides this well-known excitation mechanism, one can find other processes involving free or trapped carriers, donor-acceptor pairs or even RE ion valence change.

The common feature to all these excitation mechanisms is that they involve the recombination of electrons and holes with non-radiative energy transfer of the recombination energy to nearby RE ions. However, distinctions arise between excitation processes because of the various conditions under which the electron recombines with a hole in the vicinity of an RE ion. Both carriers can be bound to each other forming either a free exciton or a trapped (bound) exciton. In the last

case, the trapping of the exciton can be due to the incorporation of RE ions which induces distortions within the host lattice. The exciton trapping can also be due to an impurity, a local defect or an extended defect. The impurity or the defect has to be close to an RE ion in order for the energy transfer to be efficient. Another possible mechanism involves the capture of an electron changing the RE ion valence state from trivalent to divalent with a subsequent capture of a hole. Finally, impurities associated with donor-acceptor pairs can induce the recombination of electrons and holes with energy transfer to RE ions.

The specific case of RE-doped GaN will be discussed in Part II of this chapter. RE ions in III-V compounds mainly substitute for the III elements and can therefore be considered as isoelectronic impurities. Because of the change in electronegativity and size, RE ions can be electrically active and trap carriers. In that case, the RE excitation involves first the binding of an exciton by RE ions and then the excitation of RE ions by energy transfer. However, the situation appears to be different for RE ions in GaN since only some of the RE incorporation sites can be excited indirectly. Results to be presented later indicate that local defects play a major role in the excitation process by binding excitons with a subsequent energy transfer towards RE ions. A general modelling of the RE excitation mechanism mediated by bound excitons (BE) is presented and discussed in the case of RE ions in GaN. It shows the different steps of the RE excitation process and the importance of unwanted de-excitation pathways competing with the RE excitation process. Finally, the parameters that govern the excitation process, i.e. the trap capture coefficient and the BE-RE ion energy transfer rate, are discussed in the specific case of RE-doped GaN.

9.2 Excitation Mechanisms

9.2.1 Excitation Paths Involving Electron-Hole Pairs

Electron-hole pairs, whether they are free particles or bound as excitons, can be generated under optical excitation (yielding photoluminescence, PL) or impact ionization of the host lattice atoms by hot electrons in the case of CL and EL. These electron-hole pairs can then transfer their energy to a nearby RE ion.

9.2.1.1 RE Excitation Mediated by Free Excitons

Following a band-to-band electronic transition, free carriers are created in the conduction and valence bands of a semiconductor. Free excitons can then form and interact with an RE ion through non-radiative energy transfer. This type of energy transfer can be evidenced when observing strong correlations between the

excitonic spectral features such as luminescence intensity and dynamics and the RE emission intensity or concentration. Several correlations can be shown, for instance the decrease of the excitonic luminescence intensity as the RE concentration increases. An even more convincing correlation can be seen when investigating the excitonic PL dynamics. Indeed, the energy transfer towards the RE ion represents one of the deactivation channels for the free exciton population. Therefore, it becomes possible to observe an increase of the excitonic lifetime when the RE luminescence intensity starts to saturate. Such a result shows that when most of the RE ions are excited, energy transfer from free excitons to RE ions is no longer possible. The slowdown of the free exciton deactivation rate upon losing one of its most efficient recombination channels is shown in erbium-doped silicon [12].

9.2.1.2 RE Excitation Mediated by BEs

The most prominent excitation mechanism in several RE-doped semiconductors involves the coupling between BEs and RE ions [13]. BEs can be created following a band-to-band transition or even by below-bandgap excitation. The carriers can be trapped by impurities (rare-earth ions or other impurities), local or extended defects.

An electron (hole) from the conduction (valence) band can be captured by an acceptor- (donor-) like trap within the bandgap. By Coulomb attraction, the trapped electron (hole) will then attract a free hole (electron) from the valence (conduction) band, thus forming a BE. In Fig. 9.1, two important types of RE-related BEs are depicted. Fig. 9.1a shows an RE ion acting as an acceptor-like trap by trapping first an electron and then a hole (RE^{3+}, e)h. Fig. 9.1b shows an electrically active local defect (for instance a vacancy) behaving as an acceptor-like trap capturing first an electron and then a hole.

Fig. 9.1. Schematic illustration of two different types of RE-related BEs: (a) RE ion as an acceptor-like electron trap attracting an electron first and then a hole (RE^{3+}, eh. (b) Acceptor type local defect binding an exciton near an RE ion.

Fig. 9.2 illustrates the different steps of the RE excitation process with a band-to-band transition producing a free electron (step 1) which is captured (step 2) with a subsequent binding of a hole from the valence band (step 3). In a final step, the BE recombination energy transfers non-radiatively to the RE ion (step 4). The excited RE ion will then relax by emitting light (step 5).

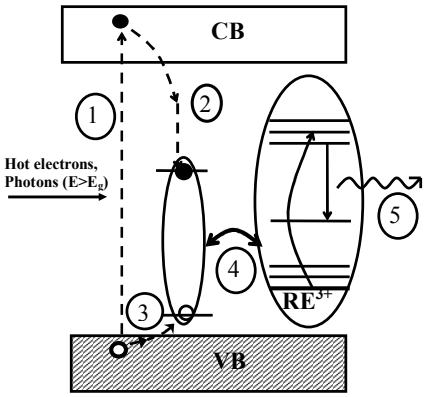

Fig. 9.2. RE excitation scheme following a band-to-band transition. Step 2: Electron capture. Step 3: BE formation. Step 4: Non-radiative energy transfer. Step 5: RE emission.

Fig. 9.3 shows how a below-bandgap excitation can also induce the formation of BEs. In this case, an electron is directly promoted from the valence band to an acceptor-like trap (step 1). The electron once again attracts a carrier of opposite charge creating a BE (step 2). The energy transfer and RE emission are then similar to the band-to-band excitation mechanism depicted in Fig. 9.2.

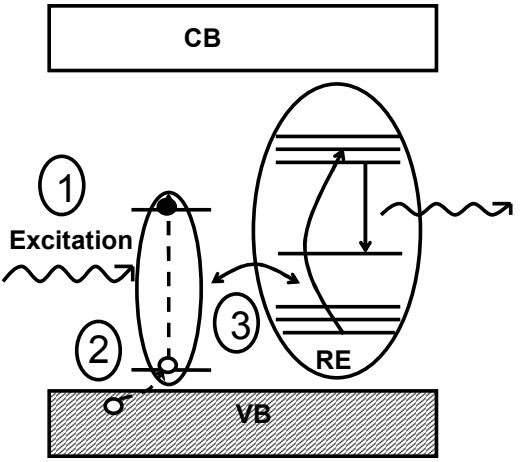

Fig. 9.3. RE excitation scheme following below-bandgap excitation.

The excitation of RE ions by energy transfer from BEs can be clearly demonstrated if, as in the case of free exciton mediated excitation (Section 9.2.1.1), strong correlations can be identified between RE luminescence and BE related luminescence. The problem often encountered is the absence of efficient radiative recombination of RE-related BEs.

In some RE-doped III-V semiconductors (InP [14] ,GaAs [15], GaP [16] and alloys), RE ions, which are isoelectronic impurities, are believed to act as carrier traps, capturing either a hole (RE^{3+},h) or an electron (RE^{3+},e) (see Fig. 9.1a). After capture of the opposite carrier, the corresponding BEs (RE^{3+},h)-e or (RE^{3+},e)-h mainly recombine through non-radiative channels (energy transfer to RE ions, other impurities, defects or carriers), impairing the possibility to obtain direct information from the BE luminescence. In the case of erbium-doped Si-rich SiO_2 (SRSO) samples, Er ions are excited by excitons recombining within Si nanocrystals. In this particular case, luminescence from silicon nanocrystals shows strong correlations with the Er luminescence [17]. The rate equations governing the different steps of this excitation mechanism are detailed later.

9.2.1.3 RE Excitation Mediated by a Trapped Electron (Hole) and Free Hole (Electron) Pair

Like the mechanisms described in the previous section, free carriers can be captured by impurities or defects. However, instead of attracting a carrier of opposite charge and forming a BE, the trapped electron (hole) can recombine with a free hole (electron) in the valence (conduction) band. This recombination can also lead to RE excitation via energy transfer.

9.2.2 Excitation Paths Involving Change of RE Ion Charge

Excitation mechanisms involving a change of the RE ion charge have also been proposed as indirect excitation mechanisms [18]. In this case, the exact position of the 4*f* levels of divalent and trivalent RE impurities relative to the conduction and valence band is crucial.

9.2.2.1 Divalent RE Ground State Relative to the Valence Band

To locate the 4*f* levels relative to the host bands is not an easy task. It is possible to use for that purpose the value of the energy required for a ligand to transfer an electron to the RE ion which is called a ligand-to-metal charge transfer (LMCT) transition [18]. This process is often described as the transfer of an electron from the valence band to a trivalent lanthanide impurity. The energy needed for this charge transfer is a measure of the separation of the ground state of the divalent

RE and the top of the valence band. This energy can in principle be simply measured by means of optical absorption experiments. An estimate of this LMCT energy can also be derived from a very simple equation. According to C.K. Jörgensen, the charge transfer energy σ is approximately the difference between the electronegativity of the anion $\chi(X)$ and the electronegativity of the central metal ion $\chi(M)$, (expressed in eV) [19]:

$$\sigma^{CT}(cm^{-1}) = 30000 \cdot [\chi(X) - \chi(M)] \ . \tag{1}$$

However, this empirical equation is rather crude since it cannot explain the variation of charge transfer energies measured in different compounds with the same anion and the same metal ion. A more detailed description should account for the dependence of the charge transfer band on the nature of the ligand (anion or even cation) and the metal (RE) ion as well as the coordination and the size of the metal site. Nevertheless, Eq. (1) can give some insight on the effect of a given anion on the charge transfer energy and hence on the position of the divalent RE ground state relative to the top of the valence band.

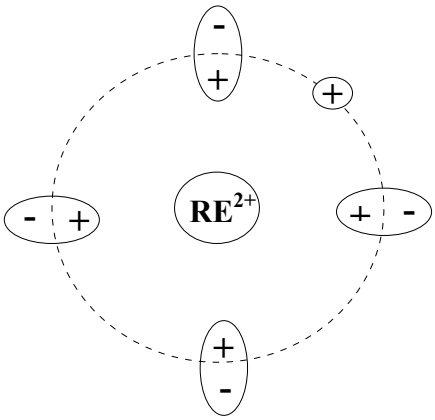

Fig. 9.4. Schematic representation of the charge transfer state (CTS) with a hole bound to the RE^{2+} ion.

A more accurate description of the charge transfer transition entails a major reorganization of the charge density distribution around the metal ion [20]. This reorganization leads to an expansion of the metal-ligand bonds in the excited state. The corresponding charge transfer state can be described as a hole transferred from RE^{3+} to the ligands moving around the RE^{2+} core in a potential field due to the effective negative charge with respect to the lattice [21] as illustrated in Fig. 9.4. Because of the complex nature of the LMCT transition, the LMCT energy has to be used carefully.

9.2.2.2 Trivalent RE Ground State Relative to the Valence Band

The position of the RE ground state relative to the host valence band can be measured by photoemission spectroscopy [22]. Optical methods such as excited state absorption spectroscopy or photoconductivity thresholds can on the other hand give the position of the metal electronic states (trivalent or divalent) relative to the conduction band [23, 24, 25].

In the case of ionic host lattices the trivalent RE binding energies can be derived from an electrostatic point charge-model based on the RE free-ion ionization potentials which correspond to the 4*f* electron binding energies in the free ions. Within this model the free-ion binding energy is viewed as being shifted by the Madelung potential of the lattice site that the ion occupies. This energy shift is considered to be the same for all RE ions in the same host. Therefore, the differences in binding energies for different ions appear to be equal regardless of the host material because of the shielded nature of 4*f* electrons. Thus, the measurement of one RE ion in a given material allows the prediction of the binding energies of all the other RE ions in this same compound by taking into account the differences in the free-ion ionization potentials [22].

This convenient result must be handled with care since its validity relies first on the ionic character of the host and secondly on the assumption that the RE ion substitutes for one with a similar ionic radius. More accurate calculations must take into account not only the distortion of the lattice induced by the substituting impurity, but also the polarizability of the lattice, interatomic Born repulsive energies and van der Waal's forces.

9.2.2.3 RE^{2+} and RE^{3+} Levels Relative to the Host Bands

Once the positions of the RE divalent and trivalent ground states relative to the valence band or conduction band are known, the whole picture can be completed in a straightforward way. A typical energy diagram with all trivalent RE ions in a fluoride host is given in Fig. 9.5. The RE binding energy is largest when the 4*f* shell is half (Gd^{3+}) or completely filled (Lu^{3+}) and it is smallest when the shell is occupied by one (Ce^{3+}) or eight electrons (Tb^{3+}). This characteristic pattern is found for all hosts. The only difference lies in the separation in energy between the divalent and the trivalent ground states, which increases as the bandgap gets larger.

With this type of picture it is possible to locate the divalent ground states relative to the conduction band and hence to know the stability of the 2+ charge state. If the divalent ground state lies in the conduction band, it will not be stable as the electron will rapidly autoionize in the conduction band.

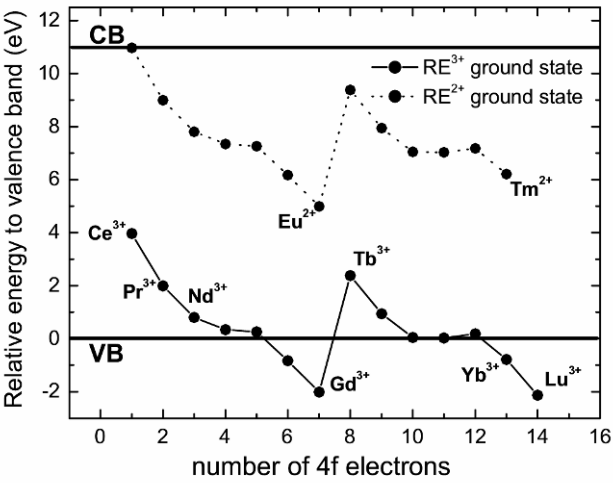

Fig. 9.5. Energy levels scheme of divalent and trivalent RE ion ground states in $LiYF_4$. (Courtesy of R.Moncorgé [26])

9.2.2.4 Excitation Mechanism with RE Ion Valence Change

The excitation mechanism involving a change in the RE charge state comprises two steps. The first step consists of an LMCT transition following an optical excitation. As described earlier, the LMCT transition can be described in a simple way as the promotion of an electron from the valence band to an RE ion that changes the RE valence state: $RE^{3+} \rightarrow RE^{2+} + h$. The hole, although delocalized over the ligands, is bound to the RE^{2+} core forming an $RE^{2+}+h$ charge transfer state (Fig. 9.4). The second step of the excitation process takes place if the CTS is close in energy to $4f$ (RE^{3+}) energy levels. In that case, a fast intersystem crossing to $4f$ states will occur and be followed by $4f \rightarrow 4f$ emission [27] as illustrated in the configuration coordinate diagram, Fig. 9.6. In order for this process to be efficient the excited state of the RE^{3+} ion has to lie below the $RE^{2+}+h$ CTS.

Dorenbos and Van der Kolk [28] suggest that Eu^{2+} and Yb^{2+} ions are stable in GaN as the 2+ ground state lies below the conduction band and that Eu^{3+} and Yb^{3+} ions are excited following a ligand-to-metal charge transfer (LMCT) process (Fig. 9.6). This suggestion was proposed earlier on the basis of PLE studies of GaN [29]. Although this explanation could be valid for Eu^{3+} under below-bandgap excitation, it seems inappropriate for above-bandgap excitation, which creates free carriers in the conduction and valence bands. More importantly, this mechanism can hardly explain excitation features similar to Eu-doped GaN observed with other RE ions (Er, Tm) for which divalent ground states lie in the conduction band and thus are not stable.

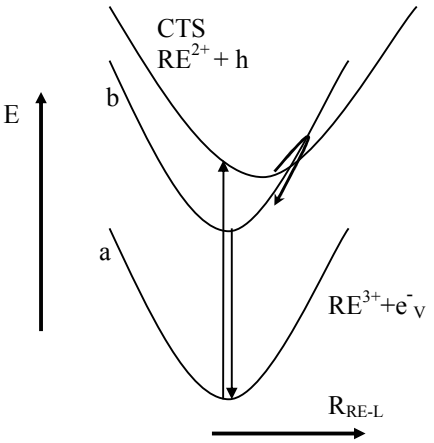

Fig. 9.6. Configuration coordinate diagram. Initially, the system consists of an RE^{3+} ion in its ground state with an electron in the valence band (parabola **a**). After excitation into the CTS (RE^{2+}+h), a crossover to an excited state of RE^{3+} (parabola **b**) takes place which leads to *4f→4f* emission.

In Section 9.2.1.2, RE excitation mechanisms involving BEs were discussed. In some cases, the exciton might be bound to the RE itself. This trapping is due to a short-range binding potential arising from the substitution of cations by RE ions inducing trap levels within the host bandgap, but does not imply a change in the RE ion valence state. There is a difference between excitons bound to RE ions (RE^{3+},e)-h described in Fig. 9.1a and ligand-to-metal charge transfer (LMCT) transitions followed by the formation of RE^{2+}+*h* charge transfer states (Fig. 9.4). First of all, the electron binding is much stronger in the case of RE^{2+}+*h* charge transfer states than for (RE^{3+},e)-h BEs. Also, the hole binding might be different since the attractive potential of (RE^{3+},e) is different from the RE^{2+} ion potential.

9.2.3 Excitation Paths Involving Donor-Acceptor Pairs

RE excitation involving donor-acceptor pairs (DAP) is the most efficient indirect excitation scheme for RE-doped II-VI semiconductors [30]. The incorporation of RE ions in II-VI semiconductors necessitates charge compensation since most RE ions in these compounds are in a trivalent state. The only noticeable exception is europium for which the 2+ charge state has been detected by EPR (Electron paramagnetic resonance) in several cases [30]. This means that the Eu^{2+} ground state is located in the bandgap or valence band. On the contrary, for all the other RE ions only the 3+ charge state has been detected

implying that their 3+ ground levels lie most probably within the valence band. In order to facilitate the incorporation of RE ions through charge compensation, acceptor-like co-dopants, especially alkali metals, have been used in RE-doped II-VI semiconductors. In general, because of the excess positive charge, trivalent RE ions have a natural tendency to associate with acceptors (introduced intentionally or not) to form DAP or more general complexes. Under optical pumping, an electron is transferred from an orbital localized on the acceptor to an orbital on the RE ion, substitutional on the metal site, which acts as a donor [30] as depicted in Fig. 9.7. In a subsequent step, the donor-acceptor pair recombines, transferring its energy to the RE ion. The DAP recombination rate and the energy transfer efficiency therefore depend on the spatial proximity of the acceptor to the RE ion and on the spectral overlap between the DAP emission and the RE absorption spectra (Section 9.2.4).

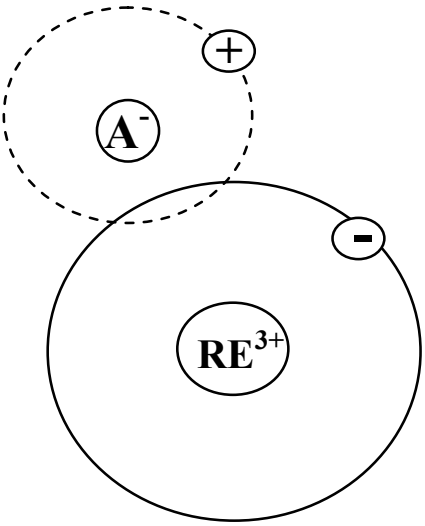

Fig. 9.7. Schematic illustration of a donor-acceptor pair involving an RE ion as the donor capturing an electron and the acceptor with a hole localized around it.

Another possible situation is that the RE ion is not a component of the DAP, but located in the vicinity of a DAP. In this case, the recombination energy of the DAP is again transferred to the RE ion within the excitation process [31, 32]. The energy transfer appears to be efficient only for RE ions that are closely associated with one of the components of the DA pair [33].

The excitation schemes involving DAP which are important in RE-doped II-VI semiconductors have not been observed in III-V compounds.

9.2.4 Energy Transfer Processes

Most of the excitation mechanisms previously described involve a non-radiative energy transfer from electron-hole pairs, excitons or DAP to trivalent RE ions. The most well-known mechanism for the transfer of energy from one site to another in crystals, amorphous materials, solutions and biological systems is Förster Resonant Energy Transfer (FRET). This mechanism was first invoked for transfer between organic molecules in the dipole approximation [34]. Dexter generalized the theory to higher-order interactions, including the exchange interaction, and applied it to energy transfer between dopant ions in inorganic solids [35].

9.2.4.1 Microscopic Description

Energy transfer takes place between an energy donor (also called a sensitizer) and an energy acceptor (also called an activator). These are not to be confused with donors and acceptors of charge carriers in semiconductors. They only undergo changes in their state of excitation, not in their state of ionization. Let us consider that the radiative emission transition $D^* \rightarrow D$ and the radiative absorption transition $A \rightarrow A^*$ have normalized lineshape functions $g_D(E)$ and $g_A(E)$ respectively. Initially, the donor and acceptor are in the state $|D^*, A\rangle$. An interaction H' between the donor and the acceptor causes a transition from $|D^*, A\rangle$ to $|D, A^*\rangle$. The transfer probability W_{DA} depends on the spectral overlap between the emission spectrum of the energy donor and the absorption spectrum of the energy acceptor:

$$W_{DA} = \frac{2\pi}{\hbar} \left| < D, A^* \left| H' \right| D^*, A > \right|^2 \int g_D(E) \cdot g_A(E) \cdot dE \quad . \tag{2}$$

This process is non-radiative; it does not involve the emission of photons by D and the subsequent absorption by A. It is a simultaneous deactivation of D and activation of A. The basic interaction which drives the transfer, the coupling between the donor and the acceptor, can be an electrostatic, magnetic and/or exchange coupling.

In the case of electrostatic coupling, which is the predominant mechanism in RE-doped materials, the transfer probability W_{DA} on a microscopic scale can be written:

$$W_{DA} = \frac{1}{\tau_0} \cdot \left(\frac{R_0}{R} \right)^n \tag{3}$$

where n=6, 8 or 10 in the case of dipole-dipole, quadrupole-dipole or quadrupole-quadrupole coupling, respectively and R_0 is the distance between the donor and acceptor at which the transfer rate is equal to the donor decay rate (τ_0^{-1}).

Non-resonant energy transfer takes place when there is a mismatch in energy between the transitions of the donor and acceptor. Such an energy mismatch may be bridged by lattice vibrations, in which case the electron-phonon coupling must be taken into account together with the electromagnetic coupling between *D* and *A*. Miyakawa and Dexter have shown that one can still use Eq. (2), but taking into account vibronic components [36] :

$$W_{DA} = \frac{2\pi}{\hbar} \left| < D, A^* \left| H' \right| D^*, A > \right|^2 \cdot S_{DA} \tag{4}$$

where S_{DA} is the spectral overlap between the donor and acceptor normalized lineshapes including vibronic sidebands.

If acceptor and donor are close enough for direct overlap of the electron clouds to occur, there can be a direct exchange interaction between donors and acceptors. Exchange interactions, H'_{EX}, are very short range and the transfer matrix element $< D, A^* \left| H'_{EX} \right| D^*, A >$ may reasonably be written as $J_0.exp(-2R/L)$, where J_0 is approximated by the diagonal exchange terms between *D* and *A* in nearest-neighbour positions [37] and *L* is the nearest-neighbour distance (typically ~10^{-10}m).

In summary, the main parameters governing the rate of any type of non-radiative energy transfer on a microscopic scale are on the one hand the donor/acceptor distance and on the other hand the spectral overlap between the donor emission spectrum and the acceptor absorption spectrum.

9.2.4.2 Macroscopic Description

Once the type of interaction mediating the transfer of energy is identified and the spectral overlap between the donor emission and acceptor absorption is calculated, the accurate description of the distribution of ions throughout the host lattice remains a difficult task. The pioneering work of Förster and Dexter assumed a random distribution of dopants in the host matrix which in some cases might be an invalid approximation. More sophisticated approaches tend to take into account non-random distributions of ions using either specific dopant distribution functions [38] or Monte Carlo methods [39].

9.3 RE Excitation Processes in GaN

9.3.1 RE Excitation Schemes

9.3.1.1 Free Exciton Mediated Excitation

Earlier in this chapter a number of indirect excitation paths have been described. RE excitation through free excitons, as presented in Section 9.2.1.1, is unlikely to take place in GaN as no correlation between the excitonic luminescence and the RE luminescence has been made clear. The mere observation of below-bandgap excitation in RE PLE experiments indicate that trapped carriers rather than free excitons contribute to the excitation pathway.

A type of correlation between excitonic and RE luminescence was shown for samples grown by molecular beam epitaxy (MBE). By changing the growth conditions, either the Ga flux [40] or the Eu cell temperature [41], the 365 nm band-edge luminescence is seen to decrease as the RE luminescence increases. These correlations do not bring strong evidence for a coupling between free excitons and RE ions, but show the importance of the growth conditions on the optimization of RE ion luminescence in MBE GaN. In fact, the growth conditions affect the samples' crystalline quality, which appears to play an important role in the excitation and emission efficiency of RE ions in GaN.

It is well known that the deterioration of the sample crystallinity impairs excitonic luminescence as new non-radiative de-excitation pathways emerge. But a very important result is that at the same time the deterioration of the crystallinity takes place, the RE luminescence intensity is enhanced to some extent. The increase of the RE luminescence stops if the sample crystallinity is degraded beyond a certain point. From this result, we can reasonably assume that the formation of defects can efficiently mediate the excitation from the host to the RE ions, but that an extensive number of defects will prevent the RE ions from emitting.

9.3.1.2 Donor-Acceptor Pair Mediated Mechanism

In the specific case of RE ions in GaN an excitation mechanism mediated by DAP, as described in Section 9.2.3, has not been yet clearly evidenced. Kim et al. show an enhancement of the luminescence of one Er site in Er-implanted GaN upon codoping the samples with Mg [42]. It is not yet possible to conclude, on the basis of the PL and PLE data alone, whether this effect can be assigned to an increase in the concentration of the Mg-related Er centres or to an enhancement in the efficiency of the optical excitation mechanisms. Moreover, the exact nature of the defect levels introduced in the GaN forbidden gap as a result of Mg

doping is not well understood. The only firmly established fact is that Mg doping efficiently introduces a relatively shallow acceptor trap Mg_{Ga} with an ionization energy of 200 meV [43]. Therefore, it is very difficult to connect the Mg-related excitation scheme observed by Kim et al. with a donor-acceptor pair mediated process.

9.3.2 Isolated RE Ions Versus RE Ions Coupled to Carrier Traps

The vast majority of RE ions in GaN are most likely to occupy Ga substitutional sites, as revealed by Rutherford Backscattering Spectroscopy (RBS) experiments [44] and confirmed by ab-initio calculations [45]; RE ions in III-V semiconductors can be considered as isoelectronic impurities. Such impurities can induce trap states in the forbidden gap binding either a hole or an electron (Fig. 9.1a). The occurrence of a carrier trap is primarily related to differences in electronegativity and size between the RE ion and the ion it replaces [46]. The trivalent RE ion being bigger than the Ga ion for which it substitutes, one could expect the RE ions to act as isoelectronic traps due to the large lattice distortion induced by the substitution.

Density Functional Theory calculations show that the situation is different for RE ions in GaN [47]. The experimental results presented in this chapter also support the conclusion that RE ions in GaN do not induce trap levels in the forbidden gap. The indirect excitation of RE ions appears to be possible only if a nearby impurity or defect efficiently traps carriers.

A first evidence that RE ions in Ga substitutional sites do not trap carriers lies in the comparison between the resonant intra 4*f* shell excitation and the non-resonant RE excitation. In Fig. 9.8 we show PL excited resonantly at 809 nm within the Er^{3+} $^4I_{15/2} \rightarrow ^4I_{9/2}$ transition in Er-implanted GaN [48]. The PL spectrum recorded around 1.54 μm $^4I_{13/2} \rightarrow ^4I_{15/2}$ at 10 K is the same for all Er-implanted GaN samples and for any excitation wavelength within the $^4I_{15/2} \rightarrow ^4I_{9/2}$ transition. The structure composed of sharp lines is characteristic of intra-4*f* shell transitions. Each line corresponds to a transition between Stark sublevels. The typical linewidth of these lines which is about 0.3 nm indicates that the Er local site symmetry is not distorted. Excitation of Er-implanted GaN at a non-resonant wavelength of 800 nm leads to a different PL spectrum, presented in Fig. 9.8b. The large number of lines indicates that different subsets of Er centres with various local site symmetries contribute to this spectrum.

RE PL in the case of non-resonant excitation, whether the excitation is above or below the bandgap, has been observed for numerous RE ions in GaN [49, 50]. As depicted in Fig. 9.2, under non-resonant below-bandgap excitation, the excitation of Er centres is commonly described as involving BEs with subsequent non-radiative transfer of the BE energy to nearby Er ions. The exact nature of the carrier trap is still under discussion, but is believed to

be related to defects, impurities or defect–impurity complexes, rather than to RE ions acting as traps. The fact that the resonant and non-resonant spectra (Fig. 9.7(a) and (b)) are different enables us to identify two types of Er centres: Er ions in a site with a well-defined symmetry which will be referred to as "isolated" Er ions and Er ions in a distorted site associated with local defects or impurities which can be excited indirectly *via* the host and will be referred to as Er-trap complexes. The most striking feature of the resonant PL spectrum is that it intrinsically shows the PL signal from all Er ions whether they are isolated or not. The PL spectrum in Fig. 9.8(a) does not exhibit any significant contribution from the non-resonant Er spectrum (Fig. 9.8(b)) which corresponds to Er ions in complexes. This result by itself is an indication that the number of Er ions in complexes is smaller than the number of isolated Er ions.

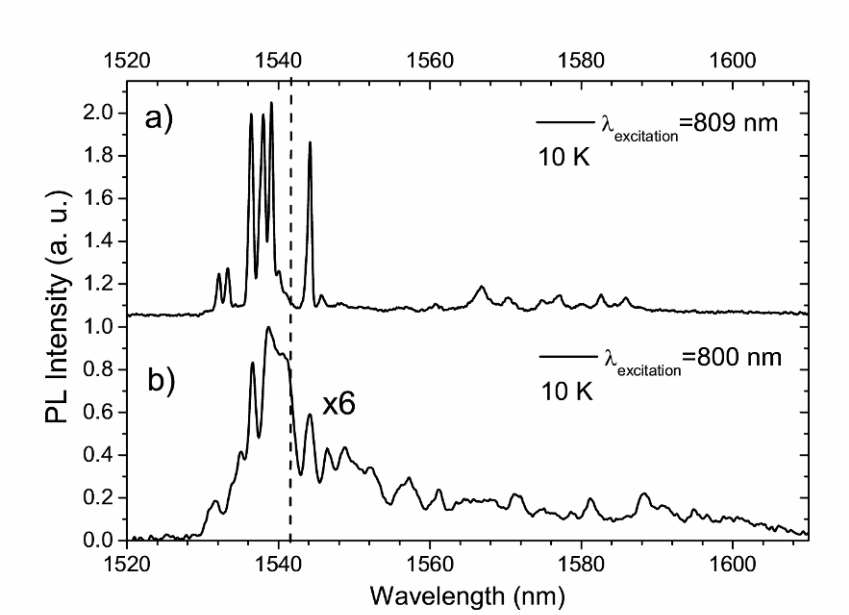

Fig. 9.8. 1.5 μm PL spectra at 10 K for two excitation wavelengths in GaN:Er^{3+}: (a) resonant excitation and (b) non-resonant excitation (×6 for normalization). The PL spectra resolution is 0.1 nm. The integrated intensity (without normalization) is 3 times larger for resonant excitation (a) than for the non-resonant excitation (b).

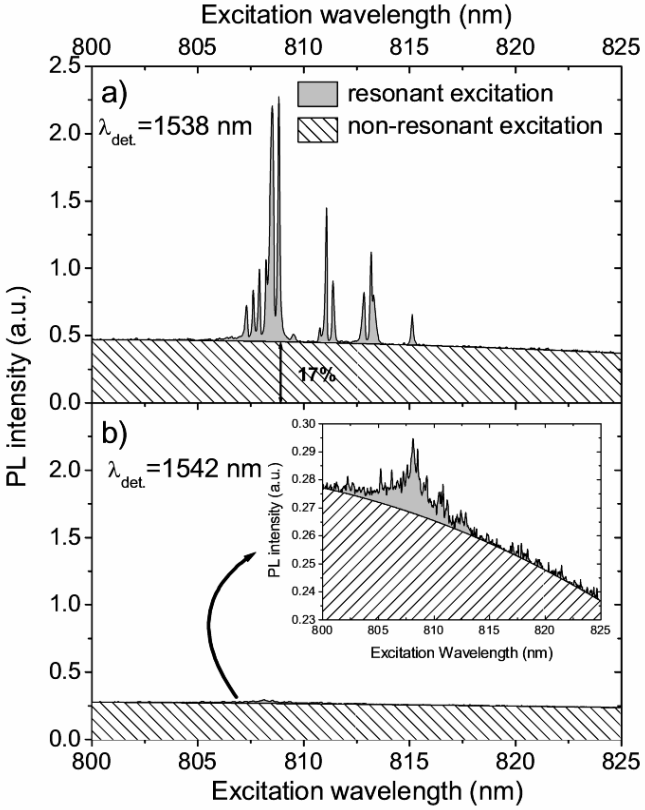

Fig. 9.9. PLE spectra in GaN:Er recorded at 1538 nm (a) and at 1542 nm (b). Inset: Zoom on the resonant part of the PLE spectrum.

In order to verify this deduction, photoluminescence excitation (PLE) spectra around 800 nm are recorded and presented in Fig. 9.9. For detection at 1538 nm, the PLE spectrum exhibits two components (Fig. 9.9(a)). The first component consists in sharp lines corresponding to inter Stark sublevel transitions within the $^4I_{15/2} \rightarrow {}^4I_{9/2}$ transition. The second component of this PLE spectrum is a broad absorption band which is part of the absorption spectrum of the above-mentioned local defect or impurity [48].

It is possible with this PLE spectrum to separate the luminescence contributions of "isolated" Er and Er-trap complexes. For instance, with a resonant excitation wavelength of 809 nm, for which the luminescence contribution of "isolated" Er is the strongest, the PLE spectrum shows that only 17% of the

luminescence at 1538 nm comes from Er-trap complexes. This result explains why the resonant spectrum of Fig. 9.8(a) is dominated by the PL signal from isolated Er ions. More generally, the PL spectrum changes with the excitation wavelength since the luminescence contribution from both types of Er centre depends on the excitation wavelength. A second PLE spectrum is displayed in Fig. 9.9(b) for the different detection wavelength of 1542 nm. This emission wavelength is particularly interesting because there is no luminescence from isolated Er ions at this wavelength (see Fig. 9.9(a)). As expected, the PLE spectrum exhibits a broad absorption band related to traps coupled to Er ions within Er-trap complexes. However, small lines associated with the resonant excitation of Er ions within complexes can be observed when magnifying the appropriate spectral region as illustrated in the inset of Fig. 9.9(b). The PLE integrated intensity from Er ions in complexes under resonant excitation (insert Fig. 9.9(b)) is 15 times smaller than the resonant PLE intensity from isolated Er ions (Fig. 9.9a). This result is consistent with the fact that very few Er ions are part of complexes and can thus be excited indirectly. As mentioned earlier, RBS measurements performed on various RE-doped GaN samples show that a large percentage (from 92 to 70% depending on the sample) of Er ions occupies a Ga substitutional site [44]. Therefore, "isolated" Er ions, which represent the main type of Er centre, most likely occupy Ga substitutional sites whereas Er ions within complexes occupy distorted sites with a local symmetry which might be strongly influenced by the proximity of a local defect such as an N vacancy.

Despite the small number of Er-trap complexes (factor 15 under resonant excitation between the PLE intensity of isolated Er ions and Er in complexes), the luminescence from these Er ions is not negligible (factor 3 between the PL integrated intensities in Fig. 9.8). This could imply that the effective excitation cross-section associated with the excitation of Er ions through local defects is larger than intra-4*f*-shell absorption cross-sections. It is possible to assess the value of this effective excitation cross-section by considering the evolution of the Er PL intensity as a function of the excitation photon flux. Fig. 9.10 shows the saturation of the Er PL intensity for a below-bandgap non-resonant excitation at 800 nm and an above-bandgap excitation at 325 nm. It is possible to describe the data in Fig. 9.10 by a rather simple equation [51]:

$$I_{Er} \propto N_{Er}^{*} = \frac{N_{Er}}{1 + \dfrac{1}{\sigma_{exc}^{eff} \cdot \tau_{Er} \cdot \phi}} \tag{5}$$

where σ_{exc}^{eff} is the effective excitation cross-section and ϕ the excitation photon flux. N_{Er} is the total concentration of erbium ions and τ_{Er} the $^4I_{13/2}$ emitting level lifetime. From the fitting displayed in Fig. 9.10, we can derive a value of the effective excitation cross-section equal to 1×10^{-19} cm^2 at 800 nm. The typical intra-4*f*-shell absorption cross-section is typically 10 times smaller [52].

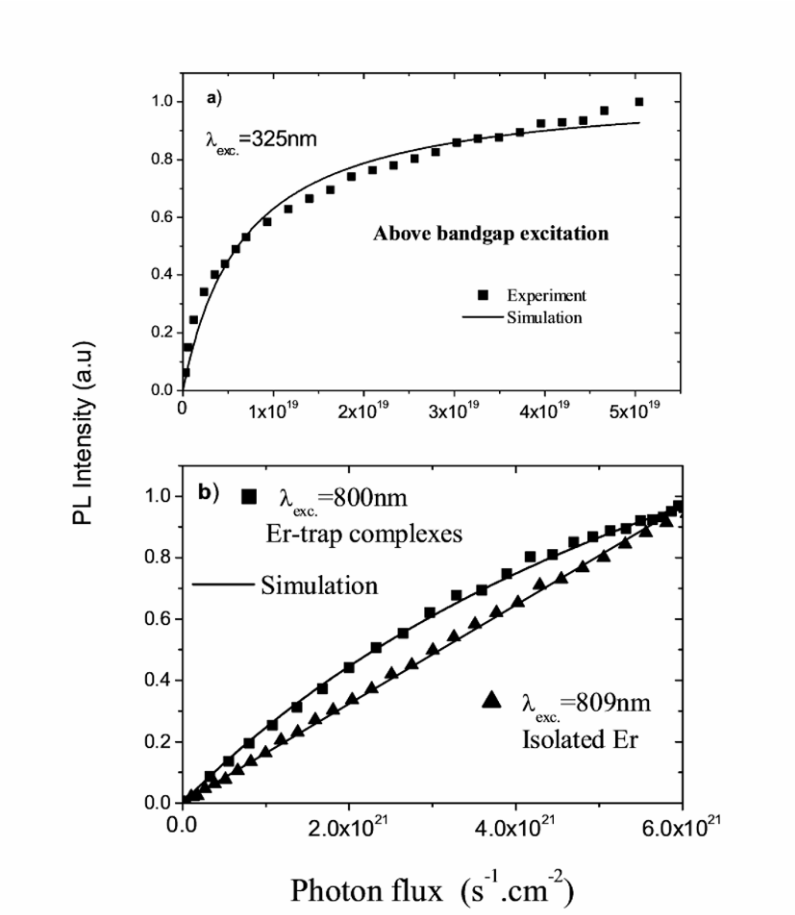

Fig. 9.10. PL intensity at 1.5 μm in GaN:Er versus the excitation photon flux for (a) above-bandgap excitation (λ=325 nm), (b) non-resonant below-bandgap excitation (λ=800 nm) and resonant below-bandgap excitation (λ=809 nm).

The same type of Er non-resonant excitation was performed throughout the GaN gap and the Er PL signal appears to saturate for lower photon flux values when the excitation wavelength is decreased. Fits to data using Eq. (1) allow the determination of several effective excitation cross-sections which are summarized in Table 9.1. The effective excitation cross-section increases as the excitation photon energy approaches the bandgap value and reaches 1×10^{-15} cm^2 for band-to-band excitation.

A clear understanding of the increase of the effective excitation cross-section with photon energy necessitates clarifying the nature of the different steps of the RE excitation pathway.

Table 9.1. Erbium effective excitation cross-sections for different non-resonant excitation wavelengths.

$\lambda_{exc.}$ (nm)	$\sigma_{exc.}^{eff.}$ (cm^2)	
325	1×10^{-15}	$E>E_{Gap}$
488	1×10^{-17}	$E<E_{Gap}$
647	4×10^{-18}	$E<E_{Gap}$
800	1×10^{-19}	$E<E_{Gap}$
Resonant excitation	$\sim 1 \times 10^{-20}$	

9.3.3 Effective Excitation Cross-Section

Besides the case of RE-doped GaN, RE luminescence in numerous RE-doped semiconductors is also explained by the coupling between BEs and RE ions and the effective excitation cross-section is extensively used to quantify the efficiency of non-resonant excitation. Examples of effective excitation cross-section values range from 7.3×10^{-17} cm^2 in erbium-doped silicon nanocrystals in silica [53] to 3×10^{-15} cm^2 in erbium-doped crystalline Si [51]. The following description of the physical meaning of the effective excitation cross-section goes beyond the case of RE-doped GaN samples and can be used in other systems in which the excitation is mediated by BEs.

9.3.3.1 Low Pumping Regime

Following a band-to-band transition (Fig. 9.2) free electrons and holes are created and subsequently form electron-hole pairs (free excitons). Several mechanisms, both radiative and non-radiative, can then lead to the recombination of these free excitons. The simplest mechanism is the radiative recombination with a specific radiative rate (τ_{rad}^{-1}). Among non-radiative recombination processes is the trapping of the electron-hole pairs by RE-related traps with an associated capture coefficient C_T and a concentration N_T. Other electrically active centres (defect, impurity…) can

also compete for the exciton capture with effective capture coefficient C_i and concentration N_i. The rate equations describing the concentration of free excitons N_x under above-bandgap excitation are then:

$$\frac{dn}{dt} = \frac{dp}{dt} = \alpha \cdot \phi - \gamma \cdot n \cdot p \tag{6}$$

and

$$\frac{dN_X}{dt} = \gamma \cdot n \cdot p - \frac{N_X}{\tau_X} \tag{7}$$

with

$$\frac{1}{\tau_X} = C_i \cdot N_i + C_T \cdot N_T + \frac{1}{\tau_{rad.}} \tag{8}$$

where α is the GaN absorption coefficient, ϕ the excitation photon flux, γ the exciton binding coefficient, n and p are the concentrations of free electrons and holes, respectively. In the low pumping regime, the rate equation governing the concentration of excitons which are trapped, for instance by local defects, in the vicinity of RE ions (N^*_T) can be written as:

$$\frac{dN_T^*}{dt} = C_T \cdot N_T \cdot N_X - \frac{N_T^*}{\tau_T} - W \cdot N_T^* \cdot N_{RE} \tag{9}$$

where W is the energy transfer parameter (in $s^{-1}.cm^{-3}$) for the energy transfer between BEs and RE ions and N_{RE} the total concentration of RE ions coupled to carrier traps. Different de-excitation processes can affect the BEs and compete with the transfer of energy to the RE ions. The BE dissociation can, for instance, be induced by thermally activated processes while the BE recombination can occur through radiative recombination or non-radiative energy transfer to free or trapped carriers (Auger type process) or to other defect centres than the RE ions. All these de-excitation mechanisms (except the transfer to RE ions) are included in the RE-related BE lifetime (τ_T in Eq. (9)).

Finally, the rate equation describing the number of excited RE ions (N^*_{RE}) is the following:

$$\frac{dN_{RE}^*}{dt} = W \cdot N_T^* \cdot N_{RE} - \frac{N_{RE}^*}{\tau_{RE}} \tag{10}$$

where τ_{RE} is the RE emitting level lifetime. The RE lifetime τ_{RE} encompasses the radiative deexcitation and all possible non-radiative mechanisms which can affect the RE luminescence (multi-phonon processes, back-transfer to the carrier trap with

subsequent formation of a new BE, energy transfer to defects or impurities, Auger effect with trapped or free carriers). Models developed in the case of erbium-doped silicon [12, 54] describe the trapping of free excitons by the RE ions, but do not detail the fact that different BE deexcitation pathways compete with the energy transfer to RE ions Eq. (9). On the other hand, models used for small band-gap III-V semiconductors such as InP [55] take into account the fact that different trapped exciton recombination processes coexist, but do not describe the trapping of the carriers (see Eqs (6), (7), (8)). In the case of erbium ions coupled to Si nanocrystals in silica [56], the situation is simpler since the excitons are readily created within Si nanocrystals and therefore no mechanism of carrier trapping is involved.

Solving Eqs (6), (7), (8), (9), (10) in a steady-state regime, one can obtain:

$$N_X = \alpha \cdot \phi \cdot \tau_X \tag{11}$$

$$N_T^* = \frac{C_T \cdot N_T \cdot N_X \cdot \tau_T}{1 + W \cdot N_{RE} \cdot \tau_T} = \frac{C_T \cdot N_T \cdot \alpha \cdot \phi \cdot \tau_X \cdot \tau_T}{1 + W \cdot N_{RE} \cdot \tau_T} \tag{12}$$

$$\begin{aligned} N_{RE}^* &= W \cdot N_{RE} \cdot N_T^* \cdot \tau_{RE} \\ &= W \cdot N_{RE} \cdot \tau_{RE} \cdot \frac{C_T \cdot N_T \cdot \alpha \cdot \phi \cdot \tau_X \cdot \tau_T}{1 + W \cdot N_{RE} \cdot \tau_T} \quad . \end{aligned} \tag{13}$$

On the other hand, when using the effective excitation cross-section, under low excitation density the concentration of RE ions in the excited state is simply given by:

$$N_{RE}^* = \sigma_{exc}^{eff} \cdot \tau_{RE} \cdot \phi \cdot N_{RE} \tag{14}$$

By comparing Eqs (13) and (14), one can easily derive an expression for the effective excitation cross-section assuming that each RE-related trap is only coupled to one RE ion ($N_T = N_{RE}$) :

$$\sigma_{exc}^{eff} = \frac{\alpha \cdot C_T \cdot \tau_X}{1 + \beta} \tag{15}$$

with

$$\beta = \frac{{\tau_T}^{-1}}{W \cdot N_{RE}} \quad .$$

Eq. (15) is particularly interesting because it emphasizes the key parameters at the centre of the RE excitation process. One can observe that the effective excitation cross-section has a linear dependence on the GaN absorption coefficient α and with the product $C_T.\tau_x$ which shows that efficient RE excitation implies the formation of traps with high capture coefficient and limited trapping or deexcitation channels

competing with the trapping of excitons in the vicinity of RE ions. Eq. (15) also underlines the importance of a large energy transfer parameter W to RE ions and reduced competing deexcitation channels (small τ_T^{-1}). More precisely, the ratio β represents the branching ratio between the energy transfer rate from the BEs to the RE ions ($W.N_{RE}$) and all the other BE deexcitation pathways (τ_T^{-1}).

If the energy transfer to RE ions is the only deexcitation mechanism available to RE-related BEs, then β equals 0 and the effective excitation cross-section becomes simply:

$$\sigma_{exc}^{eff} = \alpha \cdot C_T \cdot \tau_X \ . \tag{16}$$

When comparing above- and below-bandgap excitations, Eq. (15) suggests that the very high effective excitation cross-section of the above-bandgap excitation (Table 9.1) is mainly due to the high value of the absorption coefficient for a band-to-band transition in comparison to the excitation of carriers from a band to a carrier trap.

9.3.3.2 High Pumping Regime

Eq. (15) holds under low pumping conditions while the effective excitation cross-section values presented in Table 9.1 are derived from RE PL saturation curves, that is to say, under high pumping conditions. In order to verify the validity of Eq. (15) in the description of the PL intensity saturation, it is necessary to determine which step of the excitation pathway is responsible for the RE PL saturation.

The first step to consider is a saturation of the number of filled traps coupled to RE ions. Eq. (9) describing the number of filled traps can be rewritten taking into account this possible saturation:

$$\frac{dN_T^*}{dt} = C_T \cdot (N_T - N_T^*) \cdot N_X - \frac{N_T^*}{\tau_{Ttot.}} \ . \tag{17}$$

For the sake of clarity, we introduce a total deexcitation rate ($\tau_{Ttot.}^{-1}$) for the RE-related BEs which encompasses all the possible deexcitation channels including the energy transfer to RE ions. Keeping in mind that $N_X = \alpha \cdot \phi \cdot \tau_X$ Eq. (11) and solving Eq. (17) in steady-state leads to:

$$N_T^* = \frac{N_T}{1 + \dfrac{1}{C_T \cdot \tau_{Ttot.} \cdot N_X}} = \frac{N_T}{1 + \dfrac{1}{C_T \cdot \tau_{Ttot.} \cdot \alpha \cdot \phi \cdot \tau_X}} \ . \tag{18}$$

Considering for GaN the typical values of the parameters used in Eq. (18), it becomes possible to verify whether or not the PL intensity saturation observed in Fig. 9.10 can be due to the saturation of the number of filled traps.

The absorption coefficient α for band-to-band transitions in GaN [57] is ~10^5 cm^{-1} and the free exciton lifetime [58, 59] is about 100 ps. Despite the fact that there is no exact value yet for the RE-related BE lifetime τ_{Ttot}, Peng et al. show that it is shorter than 25 ps [60]; we consider 10 ps to be a reasonable estimate. In order to maximize in the calculation the possibility of saturation of the number of filled traps, we will consider the capture coefficient C_T to be equal to 10^{-6} $cm^3.s^{-1}$ which is a very high value in GaN [61]. Finally, we can use a photon flux value of $10^{19}cm^{-2}.s^{-1}$, for which the saturation of the RE PL intensity is well pronounced for a band-to-band transition (Fig. 9.10). Using these values in Eq. (18), we can see that the number of filled traps N^*_T only represents 10^{-3} of the total concentration of RE-related traps N_T. This value is in fact an overestimate of the real fraction of filled traps since the capture coefficient is likely to be overestimated. Therefore, we can conclude that the RE PL intensity saturation can not be explained by a saturation of the number of filled traps.

The saturation must in fact be due to a saturation of the actual number of RE ions in the excited state. We can now rewrite Eq. (10) taking into account the depletion of the RE ground state:

$$\frac{dN^*_{RE}}{dt} = W \cdot N^*_T \cdot (N_{RE} - N^*_{RE}) - \frac{N^*_{RE}}{\tau_{RE}} . \tag{19}$$

As shown previously, the number of filled traps does not saturate within the photon flux range used in Fig. 9.10. However, Eq. (9), which describes the evolution of the number of filled traps, needs to be rewritten to take into account the RE ground state depletion:

$$\frac{dN^*_T}{dt} = g_T - \frac{N^*_T}{\tau_T} - W \cdot N^*_T \cdot (N_{RE} - N^*_{RE}) \tag{20}$$

where

$$\mathbf{g_T = C_T \cdot N_T \cdot N_X = C_T \cdot N_T \cdot \alpha \cdot \tau_X \cdot \varphi}$$

represents the generation rate of BEs related to RE ions.

Solving Eqs (19) and (20) in steady state leads to a quadratic equation:

$$N^{*2}_{RE} - N^*_{RE} \cdot \left(g_T \cdot \tau_{RE} + \frac{\tau_T^{-1}}{W} + N_{RE} \right) + g_T \cdot \tau_{RE} \cdot N_{RE} = 0 . \tag{21}$$

Only one of the two possible solutions can describe the excited RE population saturation with the excitation photon flux ϕ:

$$N_{RE}^{*} = \frac{1}{2} \cdot \left(B \cdot \phi + C - \sqrt{(B \cdot \phi + C)^2 - 4 \cdot N_{RE} \cdot B \cdot \phi} \right) \tag{22}$$

with $\mathbf{B} = \boldsymbol{\tau}_{\mathbf{RE}} \cdot \mathbf{C}_{\mathbf{T}} \cdot \mathbf{N}_{\mathbf{T}} \cdot \boldsymbol{\alpha} \cdot \boldsymbol{\tau}_{\mathbf{X}}$ and $C = \frac{\tau_T^{-1}}{W} + N_{RE}$.

Using the values previously mentioned (C_T =10^{-6} cm^3.s^{-1}, α=10^5 cm^{-1}, τ_X=100ps, ϕ=10^{19}cm^{-2}.s^{-1}, N_T = N_{RE}) and for erbium τ_{RE}= 1ms, we find that $B.\phi = 10^5 . N_{RE}$. Consequently, in Eq. (22), we can conclude that $(B \cdot \phi + C)^2 >> 4 \cdot N_{RE} \cdot B \cdot \phi$. Following this condition, Eq. (22) can be approximated by its Taylor polynomial expression:

$$N_{RE}^{*} \approx \frac{1}{2} \cdot \left(B \cdot \phi + C - \left(B \cdot \phi + C \right) \cdot \left(1 - \frac{1}{2} \cdot \frac{4 \cdot N_{RE} \cdot B \cdot \phi}{\left(B \cdot \phi + C \right)^2} \right) \right) = \frac{N_{RE} \cdot B \cdot \phi}{B \cdot \phi + C} \tag{23}$$

$$\mathbf{N}_{\mathbf{RE}}^{*} = \frac{N_{RE}}{1 + \frac{1}{(B/C) \cdot \varphi}} \tag{24}$$

with $$\frac{B}{C} = \frac{\tau_{RE} \cdot C_T \cdot \alpha \cdot \tau_X}{1 + \frac{\tau_T^{-1}}{W \cdot N_{RE}}} = \tau_{RE} \cdot \sigma_{exc}^{eff} .$$

We see that the expression of the effective excitation cross-section is the same as in Eq. (15) which confirms its validity for low and high pumping regimes.

9.3.3.3 Trap Capture Coefficient Versus BE Branching Ratio β

Eq. (15) can be used along with the effective excitation cross-section value to obtain some information concerning the trap capture coefficient (C_T). Substituting in Eq. (15) the absorption coefficient (α = 10^5 cm^{-1}), the free exciton lifetime (τ_X = 100ps) and the effective excitation cross-section (σ_{exc}^{eff} =10^{-15} cm^2) value obtained in GaN:Er under above-bandgap excitation, one can obtain a relationship between the capture coefficient and the branching ratio β in GaN:Er:

$$C_T = 10^{-10} \left(1 + \beta \right) . \tag{25}$$

From Eq. (25), it is possible to draw some conclusions concerning the capture coefficient of the erbium-related traps. If the capture coefficient is equal to 10^{-6} cm^3.s^{-1} which can be considered as a high value, the branching ratio β is then equal

to 10^4 meaning that almost all the BEs close to Er ions deexcite through other channels than by transferring energy to Er ions. In contrast, the minimum value for the capture coefficient according to Eq. (25) is 10^{-10} $cm^3.s^{-1}$ which would imply that the branching ratio β is zero suggesting that the energy transfer towards Er ions is the only BE deexcitation channel. In conclusion, Eq. (25) shows that a possible way to get an estimate of the capture coefficient is to determine the BE branching ratio β and vice-versa.

Interestingly, in the case of Eu-doped GaN, two incorporation sites coexist with different effective excitation cross-sections [62]. Under band-to-band excitation, one of the Eu sites (Eu_1) has a low excitation cross-section of 10^{-17} cm^2 which would imply $C_{T1} = 10^{-12}(1+\beta_1)$ while the other Eu centre (Eu_2) exhibits a 10 times higher excitation cross-section ($C_{T2} = 10^{-11}(1+\beta_2)$). PL and decay dynamics studies [63] suggest that the spatial proximity of Eu_2 ions with local defects acting as carrier traps is responsible for the higher excitation cross-section. Eu_2 ions being strongly coupled to local defects are thus located in distorted incorporation sites whereas Eu_1 ions occupy Ga substitutional sites with a rather weak coupling to remote local defects. The reduced distance between carrier traps and Eu_2 ions leads to a higher energy transfer rate (see Section 9.2.4) and thus to a smaller branching ratio β. If the carrier trap is of the same nature for both centres (for instance a N vacancy), the capture coefficients could be considered equal ($C_{T2} = C_{T1}$) which would lead to $\beta_1 = 9+10.\beta_2$.

9.3.4 RE-Related Carrier Trap

Different techniques can be used to assess the properties of RE-related carrier traps. One can divide these techniques into two categories, i.e. PL and non-PL techniques. Classical optical techniques (PL, PLE, time-resolved optical spectroscopy) give interesting but limited results in the case of RE-doped GaN since no clear correlation has been evidenced between the RE luminescence and BE luminescence. Non-PL techniques such as Deep Level Transient Spectroscopy (DLTS) or Positron Annihilation Spectroscopy (PAS) can also provide valuable information, but yet incomplete since they can hardly show a direct link between the local defects observed with these techniques and RE optically active centres. In this section, we will present an original optical spectroscopy experiment using two lasers which can potentially overcome the limitations of classical PL and non-PL techniques.

9.3.4.1 Non-PL Techniques

Deep Level Transient Spectroscopy (DLTS)

DLTS is a useful tool when attempting to identify defect levels. DLTS experiments performed on Er- and Pr-implanted GaN samples show four defect levels located at 0.3 (E_1), 0.2 (E_2), 0.6 (E_3), and 0.4 (E_4) eV below the conduction band [64]. Trap E_1 is believed to be related to N-vacancy defects (V_N). Trap E_2 might be associated with RE_{Ga}–V_N complexes. Trap E_3 may originate from a nitrogen antisite point defect, N_{Ga}. Trap E_4 is believed to be related to RE dopants, but the origin of this deep trap is not yet clear. However, a real correlation between these electrically active defects and the actual RE luminescence remains to be shown. It is crucial to provide evidence that these carrier traps are part of the RE excitation scheme. Another limitation with classical DLTS measurements worth mentioning is that they can only probe defect levels up to 1 eV below the conduction band.

Positron Annihilation Spectroscopy (PAS)

PAS, also called positron lifetime spectroscopy, is a non-destructive technique used to study defects in solids, in particular vacancy-type defects. A recent study shows a correlation between the Er concentration in MBE-grown GaN samples and the Ga vacancy concentration [65]. However, the Ga vacancy is known to introduce a deep triple acceptor level located about 1 eV above the valence-band maximum. Therefore, as mentioned by the authors, such a correlation cannot be considered as direct evidence of a role played by the Ga vacancy within the Er excitation pathway. Nevertheless, this result is very interesting since it might show that the Ga vacancy indirectly influences the trapping of carriers and the subsequent RE excitation. It is not clear how this could happen. A possible explanation would be that the occurrence of a Ga vacancy perturbs the RE incorporation site in a manner that the RE becomes an isoelectronic trap able to capture carriers and thus be excited. For instance, RE ions occupying interstitial positions in GaN seem to introduce a mid-gap level according to DFT calculations [47], but appear not to be stable.

9.3.4.2 Two-Colour Experiment

Photoluminescence excitation (PLE) experiments that monitor the excitation wavelength dependence of RE emission in RE-implanted and *in situ* doped GaN samples show, in many cases, prominent broad below-bandgap bands [48, 50, 66]. However, the exact nature of these broad bands is still in question.

In MBE-grown GaN:Eu samples, Peng et al. reported the signature of the I_2 BE peak at 3.473 eV at 86 K in the PLE spectrum of the Eu $^5D_0 \rightarrow {}^7F_2$ transition superimposed on a broad PLE band [67]. The I_2 BE peak corresponds to excitons bound to

neutral donors D^0X_A which are commonly responsible for the dominant PL line in *n*-type GaN grown by any technique on any substrate [43]. The neutral donors in question for the I_2 BEs are Si_{Ga} and O_N [43]. However, the I_2 BE peak was not reported in band-edge PLE spectra of other samples, whether implanted [66] or grown by gas-source molecular beam epitaxy [68]. Recently, Ishizumi et al. [69] reported in MBE grown GaN:Eu samples an anti-correlation at 20 K between the Eu luminescence and the luminescence at 356 nm and 377 nm from excitons bound at C impurities on Ga sites and on N sites, respectively. A possible explanation of this type of anti-correlation is that the incorporation of RE ions impairs the formation of BEs which otherwise emit in the 350 to 400 nm spectral region. In conclusion, even though all these results are interesting, they do not give conclusive results concerning the exact nature of the carrier traps coupled to the RE ions.

In addition to classical optical techniques such as PL and PLE, we introduced a specific two-laser experiment which can potentially probe RE-related defect levels almost throughout the full extent of the GaN forbidden gap. The main benefit of this technique is to show the involvement of a given defect level in the RE excitation mechanism by monitoring the RE luminescence. By this means, in contrast to non-optical techniques, one can determine whether the defect level of interest acts as a mediator in the excitation path.

In the two-beam experiment, a first excitation leads to a specific RE luminescence while the second excitation acts as a perturbation to reduce the PL signal. This type of technique offers the benefit of selectively affecting the RE luminescence either before or after the RE-related BE transfers its energy to a nearby RE ion. One possible experimental arrangement uses a pulsed below-bandgap laser as the primary excitation source and a CW laser as the secondary source. Following pulsed excitation, RE ions exhibit a characteristic decay which can be affected by the additional CW excitation [70, 71].

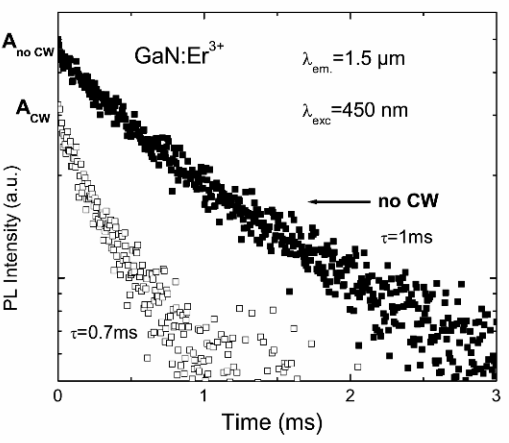

Fig. 9.11. Er decay at 1.5 μm under pulsed excitation at 450 nm without (■) and with (□) an extra cw laser at 325 nm (above-bandgap excitation, $\phi=4\times10^{17}$ s^{-1} cm^{-2}).

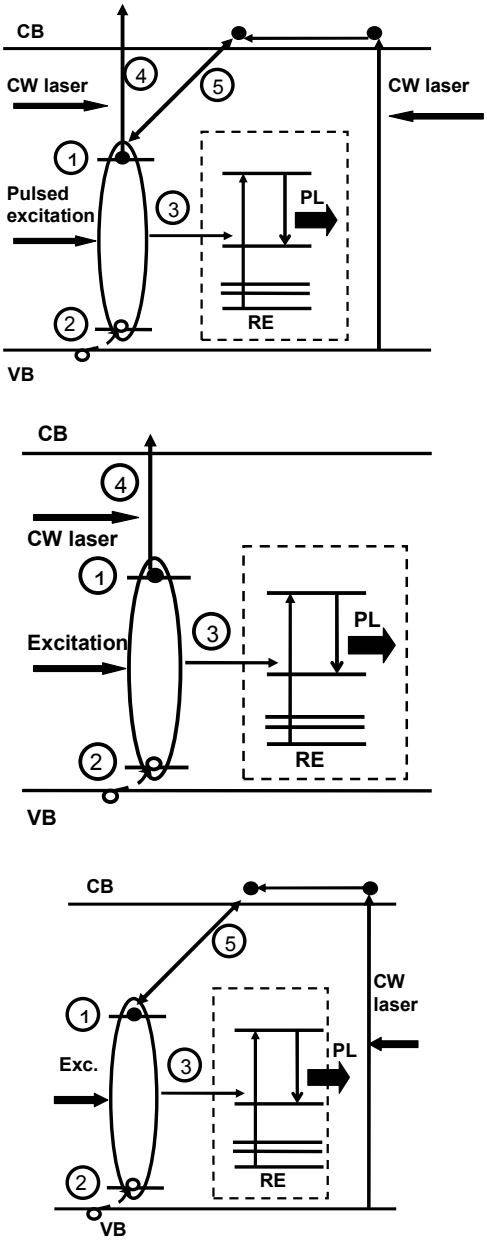

Fig. 9.12. After below-bandgap excitation, a carrier (here an electron) is trapped **1**. A hole is then attracted by the electron forming a BE **2**. The BE transfers its energy to the RE ion **3** which then emits light. Two processes induced by an additional CW beam can dissociate the electron-hole pair: photo-ionization of the trap **4** or an Auger effect between the trapped carrier and free carriers **5**.

Fig. 9.11 presents the example of the Er^{3+} PL decay at 1.5 μm ($^4I_{13/2}$ to $^4I_{15/2}$ transition) recorded under pulsed below-bandgap excitation ($\lambda_{exc.}$= 450 nm) with and without additional above-bandgap (CW, 325 nm) illumination. Two parameters can be extracted from these decays, namely their amplitude and decay constant. The term "amplitude" refers to the PL intensity detected at the end of the 6 ns excitation pulse. A significant quenching of both amplitude and lifetime is observed when applying the CW laser at 325 nm. Low excitation densities for both lasers ($\phi=10^{17}$ s^{-1} cm^{-2}) were used so as to avoid "parasitic" effects such as PL intensity saturation or upconversion among excited RE ions. Unwanted heating effects are also very unlikely to occur due to the association of very low excitation densities and the excellent thermal properties of GaN. Finally, it is worth mentioning that excited state absorption (ESA) cannot contribute to the PL quenching observed in Fig. 9.11 since the CW laser wavelength does not match any ESA line within the Er 4*f* configuration.

In order to have a clear understanding of the role played by the CW optical excitation in the Er decay it is necessary to consider individually the quenching of the amplitude and that of the decay constant, as they correspond to different stages of the Er luminescence process. The decay constant quenching is related to quenching mechanisms affecting Er ions once they are excited. On the other hand, the decay amplitude is proportional to the number of excited Er ions at the end of the 6 ns excitation pulse. Therefore, any perturbation which prevents Er ions from being excited directly affects the decay amplitude.

In fact, following the generally accepted excitation model (Fig. 9.12), after the pulsed excitation and the subsequent trapping of carriers, the CW optical excitation can hinder the Er excitation in two different ways. It can photo-ionize the trapped carriers by promoting them into the conduction band (Fig. 9.12, (4)) or into the valence band depending on the nature of the trapped carrier (electron or hole). The second possible effect is an Auger effect between the trapped carriers and free carriers created by the CW beam (Fig. 9.12, (5)). In both trap photo-ionization and Auger effects, BEs are dissociated and can no longer excite nearby RE ions leading to a decrease in the RE PL intensity.

In order to assess whether the trap photo-ionization mechanism or the Auger effect can explain the Er decay amplitude quenching observed in Fig. 9.11, one can use a set of rate equations governing the evolution of BEs and excited RE ions with and without the additional CW laser. Simplifications can be made in the rate equations when considering the first 6 ns. As mentioned earlier, the RE-related BE lifetime was reported to be shorter than 25ps in GaN:Eu[43]. Thus, the BE population can reasonably be treated as steady-state during the 6ns of the pulsed excitation. Taking into account these considerations and the fact that low excitation densities are used, the rate equation describing the number of filled traps (BEs) during the laser pulse can be written as follows:

$$\frac{dN_T^*}{dt} = \sigma_{trap}^{eff} \cdot \phi_{pulse} \cdot N_T - \frac{N_T^*}{\tau_T} - W \cdot N_T^* \cdot N_{RE} = 0 \qquad (26)$$

where, as before, τ_T is the BE lifetime without energy transfer to RE ions, N_T corresponds to the total concentration of RE-related carrier traps and N_T^* to the concentration of traps with a BE. The parameter ϕ_{pulse} is the pulsed laser photon flux and σ_{trap}^{eff} is the effective trap excitation cross-section associated with the pulsed laser. Using the rate (6) to (9) presented earlier, we see that under band-to-band excitation, σ_{trap}^{eff} can be expressed as:

$$\sigma_{trap}^{eff} = \alpha \cdot C_T \cdot \tau_X \ . \tag{27}$$

Simplifications can also be made concerning the RE population in the excited state. The excited RE ions do not relax during the first 6 ns since RE excited state lifetimes are usually of the order of several microseconds or even milliseconds. Therefore, the rate equation describing the number of excited RE ions (N^*_{RE}) can be written as:

$$\frac{dN_{RE}^*}{dt} = W \cdot N_T^* \cdot N_{RE} \ . \tag{28}$$

N_T^* being constant during the laser pulse, the number of excited RE ions N^*_{RE} can be considered as proportional to the number of BEs N_T^*:

$$N_{RE}^* = W \cdot N_T^* \cdot N_{RE} \cdot \Delta t_{pulse} \tag{29}$$

where Δt_{pulse} is the laser pulse duration.

By solving Eq. (26) and using Eq. (29), one can show that without an additional CW laser the excited RE population at the end of the Δt_{pulse} laser pulse is:

$$N_{RE}^*(noCW) = \frac{\phi_{pulse} \cdot W \cdot \sigma_{trap}^{eff} \cdot N_{RE} \cdot N_T \cdot \tau_T \cdot \Delta t_{pulse}}{1 + W \cdot N_{RE} \cdot \tau_T} \ . \tag{30}$$

Introducing an additional CW laser adds a new term in Eq. (26) to describe either the trap photo-ionization:

$$\frac{dN_T^*}{dt} = \sigma_{trap}^{eff} \cdot \phi_{pulse} \cdot N_T - \frac{N_T^*}{\tau_T} - W \cdot N_T^* \cdot N_{RE} - \sigma_{PI}^{CW} \cdot \phi_{CW} \cdot N_T^* = 0 \tag{31}$$

or an Auger effect between the trapped carriers and free carriers:

$$\frac{dN_T^*}{dt} = \sigma_{trap}^{eff} \cdot \phi_{pulse} \cdot N_T - \frac{N_T^*}{\tau_T} - W \cdot N_T^* \cdot N_{RE} - C_A \cdot n \cdot N_T^* = 0 \ . \tag{32}$$

In Eq. (31), the parameter σ_{PI}^{CW} is the cross-section related to the carrier trap photo-ionization process induced by the CW laser and Φ_{CW} is the CW laser photon flux. In Eq. (32) C_A is the Auger coefficient and n the free carrier concentration.

The excited RE population in the presence of a CW laser can then be written:

$$N_{RE}^{*}(CW) = \frac{\phi_{pulse} \cdot W \cdot \sigma_{trap}^{eff} \cdot N_{RE} \cdot N_T \cdot \tau_T \cdot \Delta t_{pulse}}{1 + W \cdot N_{RE} \cdot \tau_T + \left| \begin{matrix} \sigma_{PI}^{CW} \cdot \phi_{CW} \cdot \tau_T \\ C_A \cdot n \cdot \tau_T \end{matrix} \right.} \tag{33}$$

where the additional term in comparison to Eq. (30) describes either the trap photo-ionization or the Auger effect.

In the case of the Auger effect, if the CW laser induces a band-to-band transition, it continuously creates free carriers at a rate:

$$\frac{dn}{dt} = \frac{dp}{dt} = \alpha \cdot \phi_{CW} - \gamma \cdot n \cdot p = 0 \tag{34}$$

with $n = p$, where α is the absorption coefficient at the CW laser wavelength. From Eq. (34), the free carrier concentration is:

$$n = \sqrt{\frac{\alpha \cdot \phi_{CW}}{\gamma}} . \tag{35}$$

From this result, we see that it is possible to discriminate between the Auger process and the trap photo-ionization mechanism since they each exhibit a characteristic dependence on the CW excitation photon flux. The Auger effect probability has a linear dependence with the free carrier concentration n created by the CW excitation. However, the free carrier concentration n is governed by bimolecular recombination processes and consequently the Auger effect exhibits a square-root dependence on the excitation photon flux Eq. ((35)). In contrast, the trap photo-ionization probability depends linearly on the excitation photon flux.

These different dependencies on the excitation photon flux are clearly illustrated when considering the ratio between the RE decay amplitudes at the end of the laser pulse without (A_{noCW}) and with the CW laser (A_{CW}). Using Eqs (30) and (33) and keeping in mind that the decay amplitude is proportional to the number of excited RE ions, one can derive for the trap photo-ionization process:

$$\frac{A_{noCW}}{A_{CW}} \propto \frac{N_{RE}^{*}(noCW)}{N_{RE}^{*}(CW)} = 1 + A \cdot \phi_{CW} \tag{36}$$

with

$$A = \frac{\sigma_{PI}^{CW}}{\tau_T^{-1} + W.N_{RE}}$$

and for the Auger effect :

$$\frac{A_{noCW}}{A_{CW}} \propto 1 + B \cdot \sqrt{\phi_{CW}} \tag{37}$$

with $$B = \frac{C_A}{\tau_T^{-1} + W.N_{RE}} \cdot \sqrt{\frac{\alpha}{\gamma}} \quad .$$

In the case of the results displayed in Fig. 9.11, we plotted the ratio between A_{noCW} and A_{CW} in Fig. 9.13a as a function of the square-root of the above-bandgap CW photon flux.

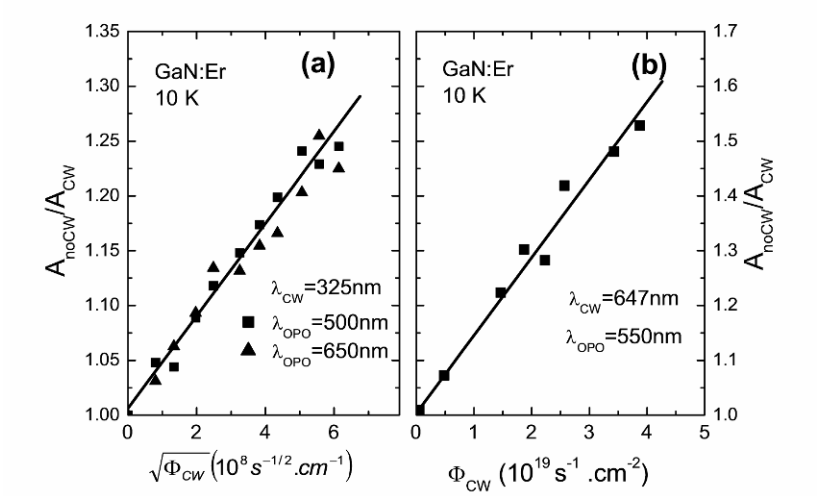

Fig. 9.13. Ratio between the Er decay amplitude at 1.5 µm without (A_{noCW}) and with an additional CW laser (A_{CW}): (a) versus the square-root of a CW photon flux at 325 nm (above-bandgap excitation) for a pulsed excitation (OPO) at 500 and 650 nm, (b) versus a CW photon flux at 647 nm (below-bandgap excitation) for a pulsed excitation (OPO) at 550 nm.

The Er decay amplitude quenching clearly exhibits a square-root dependence on the CW photon flux (Fig. 9.13(a)) showing that an Auger effect takes place. This result is not surprising since the CW band-to-band excitation continuously creates free carriers which can interact through an Auger effect with trapped carriers before they excite Er ions. Interestingly, the Auger effect does not seem to depend on the below-bandgap pulsed excitation (Optical Parametric Oscillator, OPO) wavelength within the studied spectral range (400 to 650 nm) as illustrated in Fig. 9.13(a) for 500 nm and 650 nm. This result can be interpreted in two ways. Different below-bandgap excitation wavelengths within the 400 nm to 650 nm range might lead to the trapping of carriers by the same Er-related traps. This could either imply that the Er-related traps are characterized by broad absorption bands or the occurrence of excitation hopping mechanisms between traps particularly when exciting at shorter wavelengths. Another possible explanation is that

different types of traps coupled to Er ions are populated depending on the excitation wavelength, but that they are all affected in the same way by the Auger effect with free carriers.

When using a below-bandgap instead of an above-bandgap CW excitation, in addition to the pulsed below-bandgap excitation, a quenching of the Er decay amplitude is also observed. Fig. 9.13(b) shows the ratio A_{noCW}/A_{CW} as a function of CW photon flux at 647 nm. In contrast with the case of above-bandgap excitation, the quenching effect with a below-bandgap laser (Fig. 9.13(b)) is linear in photon flux suggesting that a photo-ionization of Er-related traps takes place rather than an Auger effect. Unsurprisingly, an Auger effect with free carriers is very unlikely to happen when using a below-bandgap CW excitation since it can hardly create free carriers. This specific experiment showing a photo-ionization of Er-related traps is particularly promising since the trap depth in relation to the valence and conduction bands can be determined by tuning the CW below-bandgap wavelength. When the CW photon energy becomes too small to enable the photo-ionization of a trapped carrier to the conduction band, the Er amplitude quenching ceases to exist and the trap depth can then be assessed.

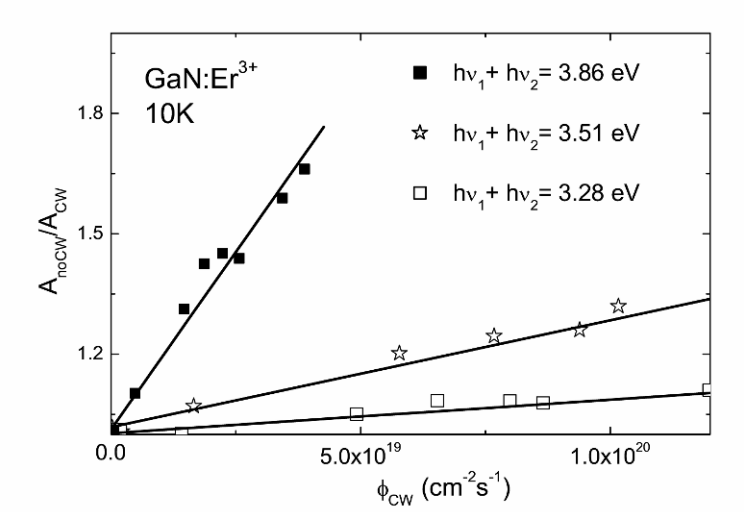

Fig. 9.14. Ratio between the Er decay amplitude at 1.5 μm without (A_{noCW}) and with an additional CW laser (A_{CW}) versus the CW photon flux for a pulsed excitation at 640 nm and different CW excitation wavelengths at 647 nm, 790 nm and 925 nm.

The decrease in quenching with decreasing photon energy is illustrated in Fig. 9.14 with a pulsed laser at 640 nm along with a CW laser tuned between 647 and 920 nm. We clearly observe in the A_{noCW}/A_{CW} ratio in Fig. 9.14 that the photo-ionization process is efficient when the summation of the two photon energies ($h\nu_{640\,nm} + h\nu_{647\,nm} = 3.86$ eV) is larger than the GaN bandgap (3.46 eV). When the

energy sum becomes about equal to the bandgap ($h\nu_1 + h\nu_2 = 3.51$ eV), one can observe a drastic decrease in the photo-ionization process. As expected, the trap photo-ionization process disappears almost completely when the CW laser photon energy is no longer large enough to promote the trapped electron (hole) to the conduction (valence) band ($h\nu_1 + h\nu_2 = 3.28$ eV).

As shown in (36), the slope of the A_{noCW}/A_{CW} ratio is proportional to the photo-ionization cross-section σ_{PI}^{CW} which itself depends on the trap depth E_T [72]:

$$\sigma_{PI}(E) \propto \frac{(E - E_T)^{3/2}}{E^{3+2\cdot\gamma}} \tag{38}$$

where E is the energy of the photo-ionizing light and γ a parameter depending on the specific type of potential binding the carrier to the trap ($0<\gamma<1$). It should be possible to precisely assess the trap depth using the A_{noCW}/A_{CW} ratios depicted in Fig. 9.14 along with Eq. (38). But, the fact that in Fig. 9.14 some small RE decay amplitude quenching can still be observed at low energy ($h\nu_1 + h\nu_2 = 3.28$ eV) makes difficult the precise determination of the trap depth and might be due to the photo-ionization of a possible shallow additional trap by the CW laser. Nonetheless, results in Fig. 9.14 give a rough estimate of the trap depth around 1.6 eV.

In summary, the two-beam experiment directly shows evidence of the intermediate step in Er excitation in GaN by photo-dissociation of the intermediate Er-related BEs and by Auger effect between Er-related trapped carriers and free carriers. This technique not only gives information concerning the depth of RE-related traps, but also concerning quenching mechanisms which are crucial in the development of efficient electroluminescent devices or even lasers. Under a strong electrical or optical pumping, a large number of free carriers are created in RE-doped GaN samples which can interact through the Auger effect either with RE-related excitons or even excited RE ions thus limiting the device efficiency or increasing the laser threshold in the case of laser development. In this latter case, even once laser action is achieved, the large density of photons within the device can lead to the photo-ionization of RE-related traps, consequently reducing the number of excited RE ions. Therefore, it is essential to have a clear understanding of both Auger and trap photo-ionization processes.

9.4 Conclusion

Besides the well-known impact excitation mechanism, which is often responsible for the electroluminescence of RE ions in EL devices, other indirect excitation mechanisms can take place under optical or electrical pumping. These excitation processes are based on the coupling between RE ions and free or trapped carriers, impurities (D-A pairs for instance), local or extended defects or even ligands and might even involve a change of the RE charge state. Among all these mechanisms

the most prominent is the energy transfer between BEs and RE ions. The nature of the potential binding the excitons can be different depending on the system under consideration. For instance, excitons are confined within nanocrystals in Er-doped Si-rich SiO_2. In the case of some II-VI and III-V semiconductors (InP, GaAs and GaP), the excitons are bound to the RE ions which act as carrier traps.

In the specific case of GaN, the excitons mediating the excitation appear to be bound to local defects close to RE ions. The distance between the RE ions and the local carrier trap is then the key parameter in determining an efficient coupling between the RE ions and the BEs. One can observe in a given RE-doped GaN sample, RE ions with very different excitation efficiencies because of the distance (and hence the coupling) between the traps and the RE ions. The optimization of the excitation mechanism requires defect engineering procedures in order to create defects close to RE ions exhibiting high capture coefficients. This "defect engineering" has also to take into account the reduction of parasitic mechanisms which might compete with the RE excitation mechanisms and/or quench the RE luminescence.

The exact nature of the RE-related carrier traps in GaN is still under debate and could be assigned to N vacancies [47]. The main problem is the absence of luminescence from the RE-related BEs. This only leaves the possibility of getting indirect information concerning the carrier traps using conventional techniques. An interesting parameter is the effective excitation cross-section which can be derived from the dependence of the RE intensity on the excitation photon flux. Using an adequate modelling of the excitation mechanism, it is possible to use the effective excitation cross-section to determine the trap capture coefficient provided that the ratio between the exciton-RE energy transfer rate and all the other exciton recombination pathways is known and vice-versa. More original optical experiments, using for instance two light sources, can give more direct information about the carrier trap such as the trap depth or its photo-ionization cross-section. On the other hand, defect characterization techniques such as DLTS or PAS may provide detailed information about point defects or even extended defects, but can hardly confirm the role played by these defects in the RE excitation process.

A technique which would show, without ambiguity, correlations between electrically active defects and RE luminescence in semiconductor hosts would be extremely useful in order to clarify the exact RE excitation mechanism. Because of these unanswered questions and the potential applications in optoelectronics, the research concerning RE-doped semiconductors remains very active. It is more than ever crucial to deepen our understanding of the excitation processes of the 4*f*-shell ions as well as the quenching mechanisms impairing the RE luminescence in order to improve the performance of RE-doped semiconductor devices whether they are optically or electrically pumped.

Acknowledgements

The author would like to thank L. Bodiou for his contribution to the results presented in this chapter.

References

1. V.E. Oranovsky, Z.A. Trapeznikova , Opt. Spect. **5,** 302 (1958).
2. E.W. Chase, R.T Hepplewh., D.C. Krupka, D. Kahng, J. Appl. Phys. **40,** 2512 (1969).
3. M. Leskela, J. All. Comp. **275,** 702 (1998).
4. J.M. Zavada, D.H. Zhang, Sol.St. Electr.. **38**, 1285 (1995).
5. P.N. Favennec, H. L'Haridon, M. Salvi, D. Moutonnet, Y. Le Guillou, Electron. Lett. **25**, 718 (1989).
6. A.J. Steckl, J.M. Zavada, MRS Bull. **24**, 33 (1999).
7. A.J. Steckl, J.H. Park, J.M. Zavada, Mat. Today **10**, 20 (2007).
8. H.J. Lozykowski, W.M. Jadwisienczak, I.G. Brown, App. Phys. Lett. **74,** 1129 (1999).
9. H. Bang, S. Morishima, Z. Li, K. Akimoto, M. Nomura, E. Yagi, J. Cryst. Growth, **237–239**, 1027 (2002).
10. M. Fujii, M. Yoshida, S. Hayashi, K. Yamamoto, J. Appl. Phys. **84,** 4525 (1998)
11. Y.A. Ono, Electroluminescent Displays, World Scientific Press (1995)
12. O.B. Gusev, M.S. Bresler, P.E. Pak, I.N. Yassievich, M. Forcales, N.Q. Vinh, T. Gregorkiewicz, Phys. Rev. B **64**, 075302 (2001)
13. A.J. Kenyon, Prog. Quant. Elect. **26,** 225(2002)
14. K. Takahei, A. Taguchi, H. Nakagome, K. Uwai, P.S. Whitney, J. Appl. Phys. **66**, 4941 (1989)
15. G.S. Pomrenke, H. Ennen, W. Haydl, J. Appl. Phys. **59,** 601 (1986)
16. A.J. Neuhalfen, B.W. Wessels, Appl. Phys. Lett. **60,** 2657 (1992)
17. P.G. Kik, A. Polman, J. Appl. Phys. **88**, 1992 (2000)
18. P. Dorenbos, J. Phys. Cond. Mat. 15, 8417 (2003)
19. C.K. Jörgensen, Progr. Inorg. Chem. **12** (1970) 101
20. L. van Pieterson, M. Heeroma, E . de Heer, A. Meijerink, J. Lumin. **91** 177 (2000)
21. T. Hoshina, S. Imanaga, S. Yokono, J. Lumin. **15,** 455 (1977)
22. C.W. Thiel, H. Cruguel, H. Wu, Y. Sun, G.J. Lapeyre, R.L. Cone, R.W. Equall, R.M. Macfarlane, Phys. Rev. B **64**, 085107 (2001)
23. J.F. Owen, P.B. Dorain, T. Kobayasi, J. Appl. Phys. **52**, 1216 (1981)
24. C. Pedrini, F. Rogemond, D.S. Mcclure, J. Appl. Phys. **59** 1196 (1986)
25. D.S. Hamilton, S.K. Gayen, G.J. Pogatshnik, R.D. Ghen, W.J. Miniscalco, Phys. Rev. B **39**, 8807 (1989)
26. R. Moncorgé, J. Phys. IV (France) **138**, 171 (2006)
27. C.W. Struck, W.H. Fonger, J. Lumin. **1-2,** 456 (1970)
28. P. Dorenbos, E. Van der Kolk, Appl. Phys. Lett. **89**, 061122 (2006)
29. S. Morishima, T. Maruyama, M. Tanaka, Y. Masumoto, K. Akimoto, Phys. Stat. Sol. A **176**, 113 (1999)
30. R. Boyn, Phys. Stat. Sol. (b) **148**, 11 (1988)
31. J. Schaffer, F.williams, Phys. Stat. Sol. **38** (1970) 657
32. M. Godlewski, A.J. Zakrzewski, V.Y. Ivanov, J. All. Comp., **300-301**, 23 (2000)

33. K. Swiatek, A. Suchocki, A. Stapor, L. Niinisto, M. Leskela, J. Appl. Phys. **66**, 6048 (1989)
34. T.Förster, Ann. Phys. **2** , 55 (1948)
35. D.L. Dexter, J. Phys. Chem. **21** , 836 (1953)
36. T. Miyakawa, Dexter D.L., Phys. Rev. B **1** , 70 (1971)
37. M. Inokuti, F. Hirayama, J. Chem. Phys. **43**, 1978 (1965)
38. S.R Rotman, F.X. Hartmann, Chem. Phys. Lett. **152,** 311 (1988)
39. O. Barbosa-Garcia, C.W. Struck, J. Chem. Phys. **100,** 4554 (1994)
40. D.S. Lee, A.J. Steckl, Appl. Phys. Lett. **80**, 728 (2002)
41. Z. Li, H. Bang, G. Piao, J. Sawahata, K. Akimoto, J. Cryst. Growth **240**, 382 (2002)
42. S. Kim, R.L. Henry, A.E. Wickenden, D.D. Koleske, S. J. Rhee, J.O. White, J.M. Myoung, K. Kim, X. Li, J.J. Coleman, S.G. Bishop, J. Appl. Phys. **90**, 252 (2001)
43. M.A. Reshchikov, H. Morkoç, J. Appl. Phys. **97**, 061301 (2005)
44. U. Wahl, E. Alves, K. Lorenz, J.G. Correia, T. Monteiro, B. De Vries, A. Vantomme, R. Vianden, Mat. Sc. Eng. B **105**, 132–140 (2003)
45. K.C. Mishra, V. Eyert, P.C. Schmidt, Zeit. fur Phys. Chem. **221** (11-12) 1663 (2007)
46. D.G. Thomas, J.J. Hopfield, C.J. Frosch, Phys. Rev. Lett. **15**, 857 (1965)
47. J-S Filhol, R. Jones, M.J. Shaw, P.R. Briddon, App. Phys. Lett. **84**, 2841 (2004)
48. A. Braud, J.L. Doualan, R. Moncorgé, B. Pipeleers, A. Vantomme, Mat. Sc. Eng. B **105**, 100 (2003)
49. S. Kim, S.J. Rhee, D.A. Turnbull, E.E. Reuter, X. Li, J.J. Coleman, S.G. Bishop, Appl. Phys. Lett. **71**, 231 (1997)
50. Ei Ei Nyein, U. Hommerich, J. Heikenfeld, D.S. Lee, A.J. Steckl, J.M. Zavada, Appl. Phys. Lett. **82**, 1655 (2003)
51. F. Priolo, G. Franzo, S. Coffa, and A. Carnera, Phys. Rev. B, **57**, 4443 (1998)
52. S.A. Payne, L.L. Chase, L.K. Smith, W.L. Kway et F.W. Krupke, IEEE J. of Quant. Elect., **28** (11) 2619 (1992)
53. A.J. Kenyon, C.E. Chryssou, C.W. Pitt, T. Shimizu-Iwayama, D.E. Hole, N. Sharma, C.J. Humphreys, J. Appl. Phys. **91,** 367 (2002)
54. M. Forcales, T. Gregorkiewicz, M.S. Bresler, O.B. Gusev, I.V. Bradley, J.P.R. Wells, Phys. Rev. B **67**, 085303 (2003)
55. A. Taguchi, K. Takahei, Y. Horikoshi, J. Appl. Phys.**76**, 7288 (1994)
56. D. Pacifici, G Franzo, F. Priolo, F. Iacona, L. Dal Negro, Phys. Rev. B **67,** 245301 (2003)
57. J.F. Muth, J.H. Lee, I.K. Shmagin, R.M. Kolbas, H.C. Casey, Jr., B.P. Keller, U.K. Mishra, S.P. DenBaars, Appl. Phys. Lett. **71,** 18, (1997)
58. B. Monemar, P.P. Paskov, J.P. Bergman, T. Paskova, C. Hemmingsson, T. Malinauskas, K. Jarasiunas, P. Gibart, B. Beaumont, Physica B: Cond. Mat. **376**, 482 (2006)
59. Y. Yamada, Y. Yoshida, T. Taguchi, H. Miyake, K.Iyechika, T. Maeda, J. Appl. Phys. **96,** 138 (2004)
60. H. Peng, C.W. Lee, and H.O. Everitt, C. Munasinghe, D.S. Lee, A.J. Steckl, J. Appl. Phys. **102**, 073520, (2007)
61. M.A. Reshchikov and R.Y. Korotkov, Phys. Rev. B **64**, 115205 (2001)
62. L. Bodiou, A. Oussif, A. Braud, J.-L. Doualan, R. Moncorgé, K. Lorenz, E. Alves, Opt. Mat., **28**, 780 (2006)
63. L. Bodiou, A. Braud, J.-L. Doualan, R. Moncorgé, J.H. Park, C. Munasinghe, A.J. Steckl, K. Lorenz, E. Alves, B. Daudin, J. Appl. Phys. **105**, 043104 (2009)
64. S.F. Song, W.D. Chen, C. Zhang, L. Bian, and C.C. Hsu, L.W. Lu and Y.H. Zhang, J. Zhu, Appl. Phys. Lett. **86**, 152111 (2005)
65. A. Uedono, C. Shaoqiang, S. Jongwon, K. Ito, H. Nakamori, N. Honda, S. Tomita, K. Akimoto, H. Kudo, S. Ishibashi, J. Appl. Phys. **103**, 104505, (2008)

66. K. Wang, R.W. Martin, K.P. O'Donnell, V. Katchkanov, E. Nogales, K. Lorenz, E. Alves, S. Ruffenach, O. Briot, Appl. Phys. Lett. **87**, 112107 (2005)
67. H.Y. Peng, C.W. Lee, H.O. Everitt, D.S. Lee, A.J. Steckl, J.M. Zavada, Appl. Phys. Lett. **86**, 051110 (2005)
68. J. Sawahata, H. Bang, J. Seo, K. Akimoto, Sc. Tech. Adv. Mat. **6**, 644 (2005)
69. A. Ishizumi, J. Sawahata, K. Akimoto, Y. Kanemitsu, Mat. Sc. Eng. B **146** , 186 (2008)
70. L. Bodiou, A. Braud, Appl. Phys. Lett. **93** (2008) 151107
71. L. Bodiou, A. Braud, J.L. Doualan, R. Moncorgé, K. Lorenz, E. Alves, J. All. Comp. **451,** 140 (2008)
72. G. Lucovsky, Sol. State Comm. **3**, 299 (1965)

Chapter 10
High-Temperature Ferromagnetism in the Super-Dilute Magnetic Semiconductor GaN:Gd

O. Brandt, S. Dhar, L. Pérez, V. Sapega

Abstract We present a systematic study of the growth, structural, magnetic and magneto-optical properties of GaN:Gd layers grown directly on 6H-SiC(0001) substrates by reactive molecular-beam epitaxy with a Gd concentration ranging from 7×10^{15} to 2×10^{19} cm^{-3}. The structural properties of these layers are found to be identical to those of undoped GaN layers. However, the magnetic characterization reveals an unprecedented effect. The average value of the magnetic moment per Gd atom is found to be as high as 4000 μ_B as compared to its atomic moment of 8 μ_B. This colossal magnetic moment can be explained in terms of a long-range spin polarization of the GaN matrix by the Gd atoms which is also reflected by the circular polarization of the excitonic emission in magneto-photoluminescence measurements. Moreover, the material system is found to exhibit ferromagnetism well above room temperature in the entire concentration range under investigation. We propose a phenomenological model to understand the macroscopic behavior of the system. Our study reveals a close connection between the observed ferromagnetism and the colossal magnetic moment

Oliver Brandt, Subhabrata Dhar, Lucas Pérez, Victor Sapega
Paul-Drude-Institut für Festkörperelektronik, Hausvogteiplatz 5–7, 10117 Berlin, Germany, brandt@pdi-berlin.de

Subhabrata Dhar
Present address: Department of Physics, Indian Institute of Technology Bombay, Powai, Mumbai 400076, India, dhar@phy.iitb.ac.in

Lucas Pérez
Present address: Departmento de Física de Materiales, Universidad Complutense, 28040 Madrid, Spain, lucas.perez@fis.ucm.es

Victor Sapega
Permanent address: Ioffe Physico-Technical Institute, Russian Academy of Sciences, 194021 St. Petersburg, Russia, sapega@dnm.ioffe.rssi.ru

of Gd. This model also provides a natural explanation for the coexistence of two ferromagnetic phases observed in this material. The microscopic origin for the long-range spin polarization remains unclear at the moment, but recent studies in the literature strongly suggest that native point defects play a crucial role for this phenomenon.

10.1 Introduction

Rare-earth (RE) doping of the wide band gap semiconductor GaN has recently attracted great attention, as light emission extending from the infrared to the blue arising from sharp intra-*f*-shell optical transitions has been observed [1, 2]. Assuming that the RE exists in the RE^{3+} oxidation state in GaN, it was found that the RE readily substitutes Ga leading to electrically inert centers [3, 4]. The substitutional RE impurity does not possess any deep gap state. In the current search for ferromagnetic wide band gap semiconductors with a Curie temperature above 300 K, doping with RE elements could be a promising alternative to transition metals (TM). RE atoms have partially filled *f*-orbitals which carry magnetic moments and may take part in magnetic coupling like in the case of transition metals with partially filled *d*-orbitals. While it is expected that the magnetic coupling strength of *f*-orbitals is much weaker than that of *d*-orbitals due to the stronger localization of *f*-electrons, Gd has both partially filled 4*f* and 5*d* orbitals. Both the 5*d* and 4*f* orbitals can take part in a new coupling mechanism proceeding via intra-ion 4*f*-5*d* exchange interaction followed by inter-ion 5*d*-5*d* coupling mediated by charge carriers [5, 6]. Teraguchi et al. [7] have recently observed ferromagnetism in ternary alloy $Ga_{0.94}Gd_{0.06}N$ films with a Curie temperature of 400 K. Moreover, even at this high concentration, Gd was shown to occupy predominantly Ga sites in the hexagonal GaN lattice.

In this chapter we review the results of our systematic study of growth and magnetic properties of Gd-doped wurtzite GaN layers with a concentration of Gd ranging from 7×10^{15} to 2×10^{19} cm^{-3}. In the entire concentration range studied here the Gd-doped GaN layers are found to be ferromagnetic with Curie temperatures far above room temperature. Moreover, our magnetization measurements reveal an extremely high magnetic moment of up to 4×10^3 μ_B per Gd atom [8]. This colossal magnetic moment can be understood in terms of a long-range spin polarization of the GaN matrix by Gd. A phenomenological model is developed to explain the macroscopic magnetic behavior of the system, demonstrating a close connection between the observed ferromagnetism and the colossal magnetic moment of Gd. This interpretation is supported by the pronounced change of the circular polarization in magneto-photoluminescence measurements upon light Gd-doping [9]. Furthermore, the experimentally observed coexistence of two distinct ferromagnetic phases is consistent with our model [10].

The chapter is organized as follows: in Sect. 10.2, we provide details on the experimental techniques utilized in this work. Sect. 10.3 presents the basic structural and magnetic properties of GaN:Gd, and Sect. 10.4 discusses the phenomenological model

for interpreting the experimentally observed collosal magnetic moment and the high-temperature ferromagnetism. Sect. 10.5 discusses the circular polarization of the excitonic luminescence in an external magnetic field, and demonstrates how these results can be explained in the framework of our model. Sect. 10.6 is devoted to the coexistence of distinct magnetic phases evident from our experimental results, as well as to the pronounced magnetic anisotropy observed in this material system. It will be shown that this coexistence is a natural consequence of the occurence of ferromagnetism in GaN:Gd as predicted by our model. Finally, Sect. 10.7 briefly reviews recent work of other groups relevant in the present context.

10.2 Experimental

10.2.1 Sample Growth and Structural Characterization

The hexagonal GaN layers of thickness 400–700 nm, and with a Gd concentration ranging from 7×10^{15} to 2×10^{19} cm^{-3} were grown by reactive molecular beam epitaxy (MBE) directly (i.e., without any buffer layer) on 6H-SiC(0001) substrates. The MBE system is equipped with conventional effusion cells for Ga (7 N purity) and Gd (4 N purity) and an unheated gas injector for NH_3 (6 N before, and 9 N purity after the filter). The base pressure of the chamber reaches 2×10^{-10} Torr with cryoshrouds only around the effusion cells.

The Gd ingot was produced by Stanford Materials Corporation and has a purity of 4 N (99.99%) as certified by a chemical analysis (inductively-coupled plasma mass spectroscopy) performed by the manufacturer. The data sheet of our ingot certifies that the ferromagnetic elements Fe and Ni are present in residual traces of $\ll$100 ppm, $\ll$50 ppm, respectively, while the concentrations of other TMs such as Cr and Co are found to be below the detection limit (0.5 ppm). As we remained below the melting point of Gd (1312 ºC) during growth, the evaporation occurs by sublimation and the given values correspond to the ratio of the trace elements to Gd in the GaN layer. In addition, the vapour pressures of Gd, Fe, Ni, Cr and Co are quite close in the temperature range 1100 to 1500 K. The maximum concentration of ferromagnetic contaminants might thus be in the range of 1×10^{12} to 3×10^{15} cm^{-3} in these samples.

The substrate temperature was kept at 810 ºC , which is our standard growth temperature for GaN in this system. The growth rate was set to our standard value of 0.6 μm/hr. The NH_3 flux was regulated to keep the chamber pressure at $4–5 \times 10^{-6}$ Torr and the Ga cell temperature was kept at 1000 ºC during growth. To control the Gd incorporation into the GaN layers, the Gd/Ga flux ratio was adjusted by varying the Gd cell temperature in the range of 950 to 1300 ºC . Nucleation and growth of GaN on SiC was monitored *in situ* by reflection high-energy electron diffraction (RHEED). A spotty (1×1) RHEED pattern, reflecting a purely three-dimensional growth mode, was observed during nucleation of the layers. The pattern

quickly became streaky, reflecting two-dimensional growth. At this stage, a (2×2) surface reconstruction appears. It is noteworthy that all these features in RHEED are also observed when pure GaN layers are grown [11]. An undoped GaN sample for reference purpose was also grown under similar growth conditions in the sequence of the GaN:Gd samples.

The Gd concentration of the layers was determined by secondary ion mass spectrometry (SIMS) using a CAMECA IMS 4F system, employing 0_2^+ primary ions with an impact energy of 7 keV. Mass interference due to parasitic molecular ions was avoided by selecting precisely the masses of two Gd isotopes (155.922 and 157.924). The resulting ion rates were identical to within 1%. Measurements at different locations of the GaN:Gd samples, each of which involved an area of $50 \times 50\ \mu m^2$, deviated by no more than 5%. The concentration was calculated according to measurements of an ion-implanted GaN standard (sample I), which was implanted with a Gd dose of 10^{15} cm^{-2}. The detection limit of SIMS was found to be 2×10^{15} cm^{-3} for Gd. In order to get an estimate of the concentration of the residual magnetic impurities, one GaN:Gd layer with a high Gd concentration of 1×10^{19} cm^{-3} was scanned in the entire TM and RE series of the periodic table by SIMS. A very low concentration of Cr in the range of 10^{13} cm^{-3} was found in this layer. None of the other TM or RE elements was detected. It has to be noted that the detection limit for Cr in SIMS is low (10^{12} cm^{-3}). For the rest of the TM and RE elements the detection limit is around 10^{15} cm^{-3}. This finding is in accordance with our upper-bound estimate of these impurities from the purity chart of the Gd ingot provided by the manufacturer as stated above.

The structural properties of the layers were investigated by x-ray diffraction (XRD) and transmission electron microscopy (TEM). For TEM, a JEOL3010 microscope operating at 300 kV was used. Symmetric high-resolution triple-axis x-ray $\omega - 2\theta$ scans were taken with a Phillips X-pert diffractometer equipped with a Cu $K\alpha_1$ source, a Bartels-type Ge(002) monochromator and an Si(111) analyzer. The dynamic range of these measurements is larger than 6 orders of magnitude. The surface morphology of the films was examined by atomic force microscopy (AFM) and scanning electron microscopy (SEM).

10.2.2 Assessment of Electrical and Magnetic Properties

Magnetization measurements up to 360 K were done in a Quantum Design superconducting quantum interference device (SQUID) magnetometer. The sample holder (a 20 cm long plastic straw provided by Quantum Design) was found to yield no magnetic signal at all. This finding is in accordance with the statement of Quantum Design that the MPMS magnetometer pick-up coil (which takes the form of a second-order gradiometer) detects changes of the magnetization induced by a sample, but not the spatially homogeneous diamagnetic signal of the straw itself. The response of the magnetometer was calibrated with thin epitaxial Fe and MnAs layers on GaAs(001) whose magnetization is accurately known. The typical surface area of the samples for the magnetization measurements is 35–40 mm^2. The magnetization of undoped GaN

layers was found to be indistinguishable from the diamagnetic response of bare SiC substrates.

Magnetization loops were recorded at various temperatures for magnetic fields between ± 50 kOe. The magnetic properties of several samples were investigated up to 800 K using a separate Quantum Design SQUID magnetometer equipped with an oven which is specially designed for high temperature measurements. Unless stated otherwise, the magnetic field was applied parallel to the sample surface, i.e., perpendicular to the *c*-axis. Prior to measuring the temperature dependence of the magnetization, the sample was first cooled from room temperature to 2 K either under a saturation field of 20 kOe (Field cooled: FC) or at zero field (zero field cooled: ZFC). In case of ZFC measurements the sample is demagnetized under an oscillatory magnetic field at room temperature before cooling it down to 2 K. Since the magnetization was measured at a very low magnetic field of 100 Oe, the FC curves are expected to qualitatively represent the temperature dependence of the remanence while the ZFC curves should reflect the temperature dependence of the susceptibility. For the measurement of the magnetic anisotropy, the first magnetization curves (FMC) were recorded after demagnetizing the sample in an alternating magnetic field and scanning the field from zero to 50 kOe. The magnetic field was applied along different crystallographic directions of GaN. All data presented here were corrected for the diamagnetic background of the substrate according to the following procedure: We measured the magnetization of the respective sample up to the highest magnetic field available (± 50 kOe). At this high field, the diamagnetic contribution from SiC is dominating the signal. A linear fit yields the slope of the signal at high fields, which in all cases was virtually identical to that of bare SiC substrates. A straight line with the slope determined from the fit was then subtracted from the raw data.

Conductivity measurements revealed all samples (including the reference sample) to be electrically highly resistive ($\rho \approx 1$ MΩ cm) even at room temperature. Note that the level of O, which acts as an unintentional donor in GaN, was found by SIMS to be 1×10^{18} cm^{-3} in these samples including the reference sample.

10.2.3 Assessment of Optical Properties

For magneto-photoluminescence (MPL) spectroscopy, the samples were excited by the linearly polarized emission of a He-Cd ion laser at a wavelength of 325 nm. The laser power densities focused on the sample varied between 200 and 250 Wcm^{-2}. The PL light was dispersed in a single-path spectrograph and detected by a charge-coupled device (CCD) array. The experiments were carried out in the temperature range 5–100 K in a continuous He-flow cryostat and in magnetic fields up to 12 T using the backscattering Faraday geometry. In all measurements, the magnetic field was oriented parallel to the *c*-axis of the samples. The magnetic field-induced circular polarization of the PL light was analyzed by passing it through a photoelastic modulator (PEM), a quarter-wave plate, and a linear polarizer.

10.3 Basic Structural and Magnetic Properties

10.3.1 Gd Incorporation in GaN

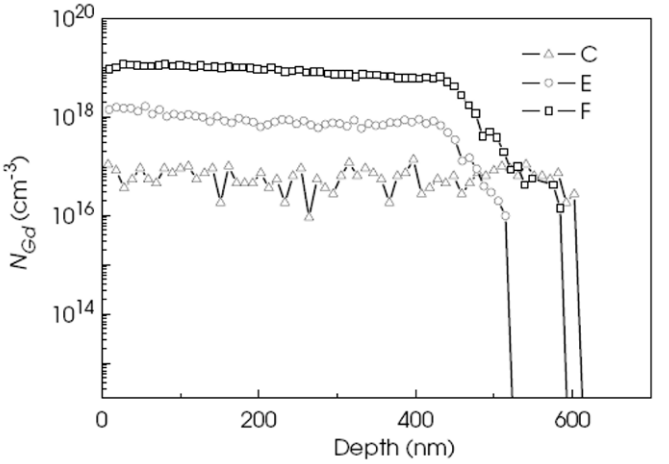

Fig. 10.1. SIMS depth profiles for samples C, E, and F. Reprinted from [9]. Copyright (2005) The American Physical Society.

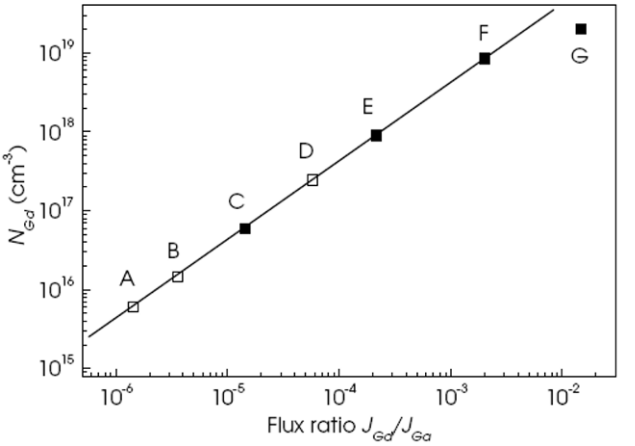

Fig. 10.2. Gd concentration as measured by SIMS as a function of Gd/Ga flux ratio (solid squares). The solid line is a linear fit to the data representing samples C, E, and F. The Gd concentration for samples A, B and D (open squares) is obtained from the corresponding Gd/Ga flux ratio by extrapolation. Reprinted from [9]. Copyright (2005) The American Physical Society.

Fig. 10.1 shows the SIMS depth profiles obtained for three Gd-doped GaN layers C, E, and F. Clearly, the concentration of Gd remains constant over the entire depth. In Fig. 10.2, the Gd concentration N_{Gd} as measured by SIMS is plotted as a function of the Gd/Ga flux ratio ϕ. Samples C, E, and F (solid squares) are lying on a straight line with a slope of unity indicating that the Gd incorporation depends linearly on ϕ up to a Gd concentration of 1×10^{19} cm^{-3}. The Gd concentration of sample G as measured by SIMS (2×10^{19} cm^{-3}) is found to be smaller than what is expected from this linear dependence. In fact, we have observed a strongly faceted surface for sample G, indicating that Gd is affecting the growth mode at these high concentrations. N_{Gd} for sample A, B, and D (open squares) is obtained by linearly extrapolating the curve passing through samples C, E, and F.

Fig. 10.3 shows the AFM surface image of a GaN:Gd layer with a Gd concentration of 1×10^{19} cm^{-3}. The peak-to-valley and the rms roughness for the 1 mm × 1 mm scan are found to be 3 and 0.14 nm, respectively. Monolayer steps (about 0.3 nm high) are clearly visible on the surface, representing an atomically flat surface morphology. It is clear from this figure and the RHEED patterns that the incorporation of Gd in GaN up to a concentration of 10^{19} cm^{-3} does neither modify the surface reconstruction of the growing GaN layer nor degrade the surface morphology of the 0.5 μm thick film. The surfaces of these films were additionally investigated by SEM (images not shown here) both in topographic and material contrast mode. No contaminating material is found on the surface.

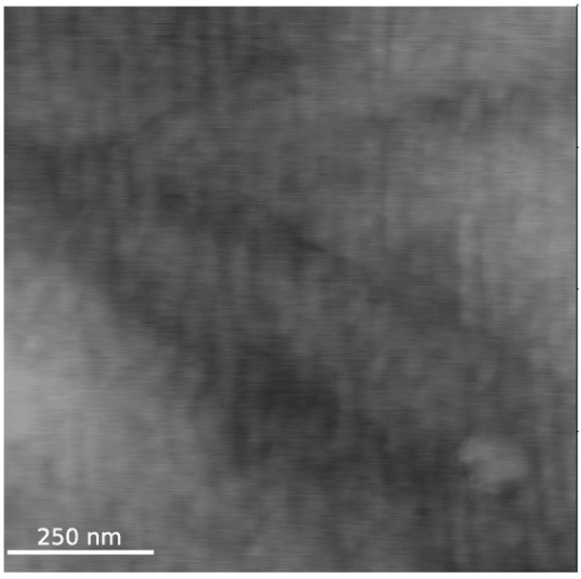

Fig. 10.3. AFM surface image of a GaN:Gd film with a Gd concentration of 1×10^{19} cm^{-3}. Reprinted from [9]. Copyright (2005) The American Physical Society.

The crystal quality of the samples was investigated by XRD. Symmetric (0002) and asymmetric skew-geometry $(1\bar{1}02)$ X-ray rocking curves for these samples exhibit a width of 300″ and 900″, respectively, similar to the values observed for equally thin pure GaN layers grown under the same conditions, and comparable to the values reported for high-quality GaN grown by MBE in general. Fig. 10.4 compares high-resolution triple-axis $\omega - 2\theta$ symmetric scans of sample C and the reference sample. Clearly, for both the samples the GaN reflection occurs at the same angular distance from the substrate peak, indicating that the c-lattice constant is not changed by Gd-doping. In fact, it is found that both the in and out of plane lattice constants (measured from asymmetric $[1\bar{1}05]$ scans) remain practically unchanged in all samples from A to F. The incorporation of Gd within that range thus does not influence the crystal quality. However, it is important to note that the c-lattice constant in sample G (which is the highest Gd doped sample in this batch) was found to be less than that of GaN, while the a-lattice constant was found to be practically unchanged.

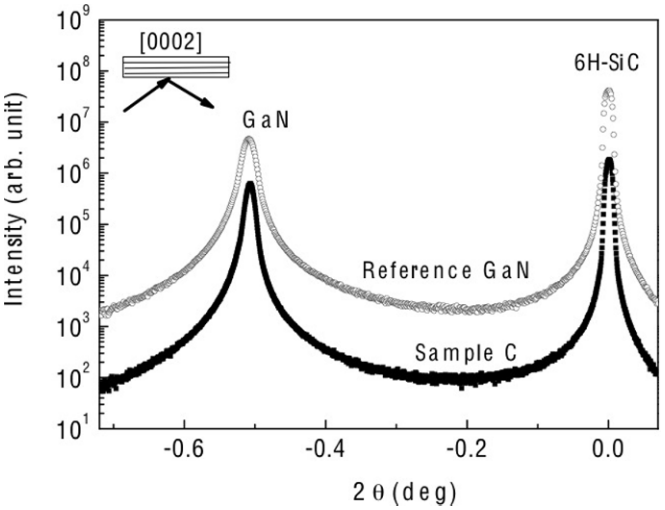

Fig. 10.4. Symmetric triple-axis $\omega - 2\theta$ XRD scans of the reference sample (empty circles) and sample C (solid squares). Reprinted from [9]. Copyright (2005) The American Physical Society.

All samples were subject to an extensive investigation by high-resolution XRD in a wide angular range. Fig. 10.5 shows a symmetric X-ray $\omega - 2\theta$ scan taken within a wide angular range of ω from 5° to 55° with a 1 mm slit in front of the detector for sample F. Apart from the reflections of the substrate and the layer, no additional reflections related to a secondary phase were detected. Moreover, we have investigated sample C and F by cross-sectional transmission electron microscopy. Both dark and bright-field micrographs are taken with different diffraction vectors. No evidence for a secondary phase was found in either of these samples. Fig. 10.6 shows a bright-field TEM micrograph of sample F taken with a

diffraction vector **g** = [0002]. Clearly, the sample consists of a homogeneous layer without any evidence for a secondary phase. Note that nm-scale Mn-rich clusters were clearly resolved in (Ga,Mn)N layers by cross-sectional TEM [12].

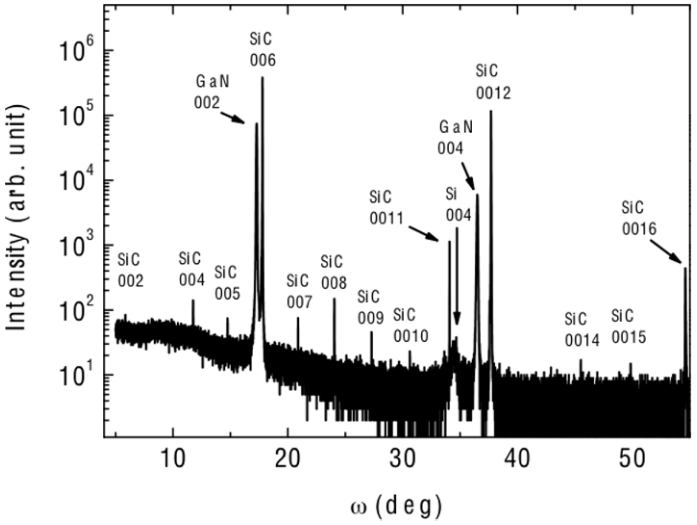

Fig. 10.5. Symmetric $\omega - 2\theta$ XRD scan taken with a 1 mm slit in front of the detector for sample F. Note that the Si(004) reflection originates from the sample holder. Reprinted from [9]. Copyright (2005) The American Physical Society.

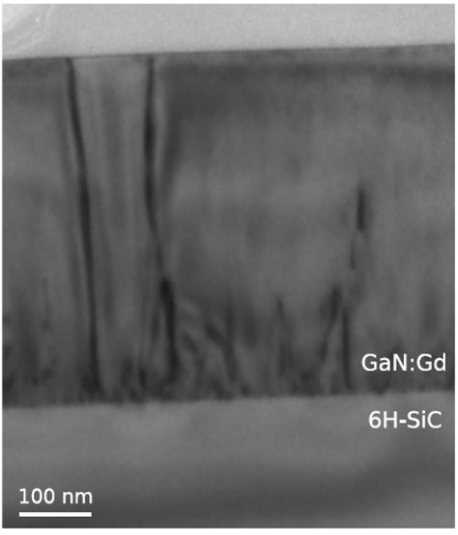

Fig. 10.6. Bright-field TEM micrograph of sample F. The contrast close to the GaN/SiC interface stems from dislocation loops. The dark lines intersecting the micrographs originate from screw dislocations. Reprinted from [9]. Copyright (2005) The American Physical Society.

10.3.2 Magnetic Characteristics

Fig. 10.7 shows the magnetization loops obtained for sample C at different temperatures. At all temperatures, the magnetization saturates at high magnetic fields and exhibits a hysteresis at lower fields, consistent with a ferromagnetic response. The inset of Fig. 10.7 shows the saturation magnetization (M_s) as a function of temperature. M_s drops to zero at a temperature of 780 K marking the Curie point for sample C. An unusual behavor is the sharp fall of M_s between 2 to 10 K, suggesting the coexistence of two phases of different magnetic nature at low temperatures. The presence of a secondary phase is also evident from the different shape of the magnetization loops at low and elevated temperature. Fig. 10.8 compares the hysteresis loop obtained at 2 K to the one observed at 300 K. The loop obtained at 2 K appears indeed to be a superposition of two loops with apparently different coercive fields (H_c) and remanent magnetizations (M_r). At temperatures higher than 10 K, the component with apparently larger H_c and M_r ceases to exist. We will examine this coexistence of different magnetic phases in more detail in Sect. 10.6.

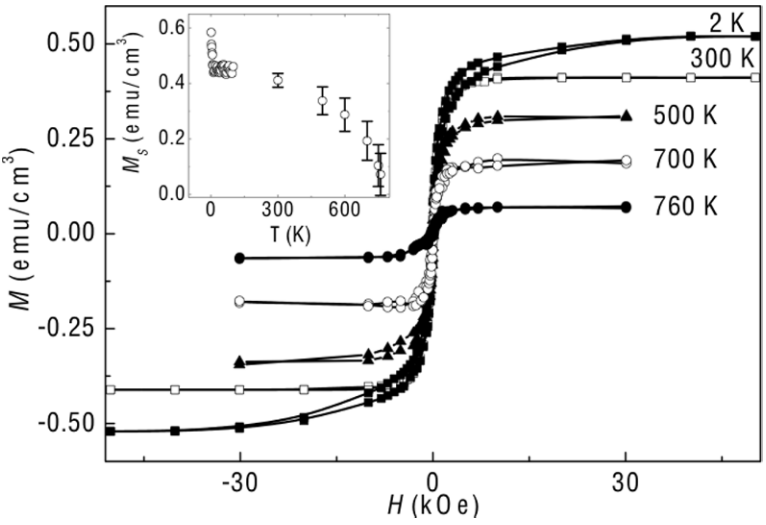

Fig. 10.7. Magnetization loops obtained for sample C at different temperatures. The inset shows the temperature dependence of the saturation magnetization. Reprinted from [9]. Copyright (2005) The American Physical Society.

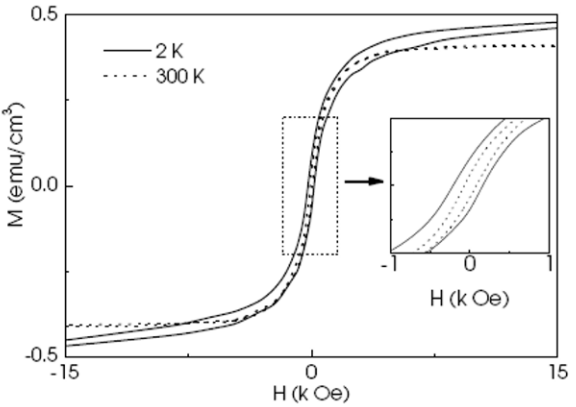

Fig. 10.8. Comparison of the magnetization loops obtained for sample C at 2 K (solid line) and 300 K (dashed line). The inset shows an expanded region of the loops where the hysteresis is clearly visible. Reprinted from [9]. Copyright (2005) The American Physical Society.

Fig. 10.9 compares the field dependence of the magnetization for samples A, C, G and I at 300 K. In this figure, only a part of the full loops which is obtained when the field decreases from + 50 kOe to zero is shown for clarity. Clearly, both M_s and M_r (indicated by arrows) increase as the concentration of Gd increases in these samples. It is noteworthy that the Gd-implanted GaN sample (sample I) which is estimated to have a Gd concentration of 1×10^{20} cm^{-3} (more than what we could reach by incorporation during growth) also exhibits ferromagnetism at and well above room temperature.

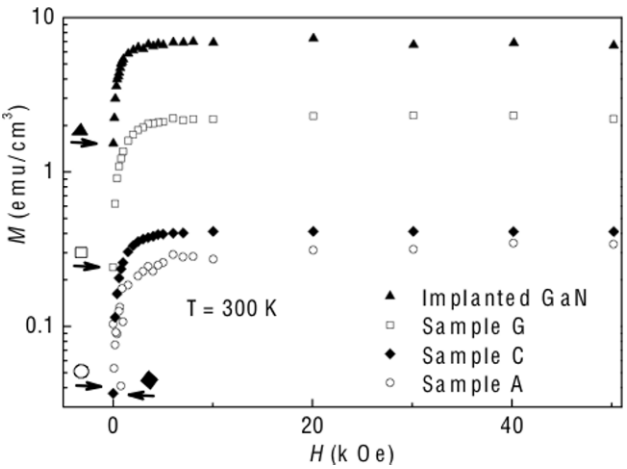

Fig. 10.9. Part of the full hysteresis loops for sample A, C, G and I which are obtained when the field decreases from 50 kOe to zero. The positions of M_r are indicated by arrows attached with the respective sample labels. Reprinted from [9]. Copyright (2005) The American Physical Society.

Fig. 10.10 shows the temperature dependence of the FC and ZFC magnetization under a magnetic field of 100 Oe for samples A, C, G and I. It is clear from this figure that the FC and ZFC curves are qualitatively similar for all samples, featuring a double step-like structure below 70 K in the FC curves for samples A, C and G. In the case of samples C, G and I the two curves remain separated throughout the entire temperature range 2 to 360 K, while they coincide at around 360 K for sample A. The separation between the FC and ZFC curves indicates a hysteretic behavior which is consistent with our observation shown in Fig. 10.7. The two curves coincide at the Curie temperature T_c, when the hysteresis disappears. Clearly, T_c is around 360 K for sample A while it is much higher for samples C, G and I. Since the applied field was only 100 Oe for the measurement of the magnetization, the FC curve is expected to qualitatively represent the temperature dependence of M_r. We have also measured M_r directly from the loops obtained at different temperatures which is found to exhibit a similar temperature dependence (see Sect. 10.6). The origin of the step appearing at 70 K will be discussed in detail in Sect. 10.6.

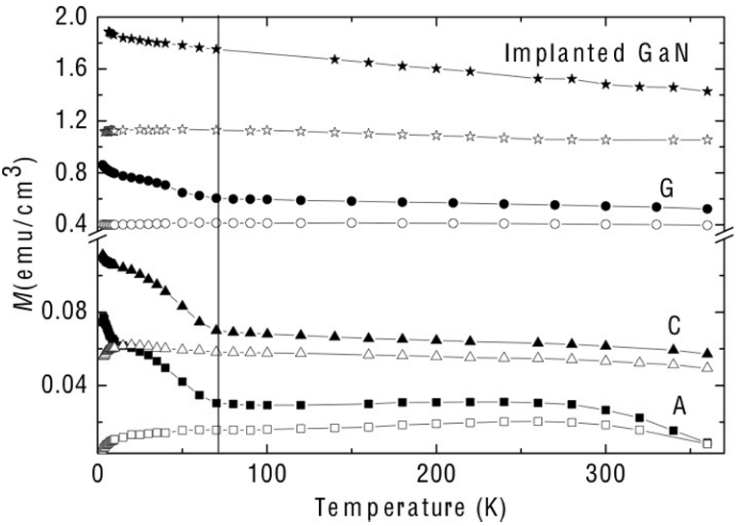

Fig. 10.10. Temperature dependence of magnetization under field-cooled (solid symbols) and zero-field-cooled (open symbols) conditions at a magnetic field of 100 Oe for samples A, C, G and I. The vertical line indicates the change of slope observed for samples A, C, and G. Reprinted from [9]. Copyright (2005) The American Physical Society.

The separation between the FC and ZFC curves obtained at 360 K is plotted as a function of Gd concentration in Fig. 10.11. It clearly increases with increasing Gd concentration, revealing a shift of T_c toward higher temperatures. The magnetization as a function of temperature under a magnetic field of 100 Oe for sample A and C are compared in the inset of the figure. The magnetization suddenly drops to zero around T_c indicating a ferro-to-paramagnetic phase

transition. This behavior of the temperature dependence of the magnetization is archetypical for a ferromagnet and present in all samples under investigation. T_c is 780 K for sample C, which is much larger than T_c (360 K) for sample A. This finding is consistent with the data of Fig. 10.10. In fact, T_c for samples F and G is found to be also around 780 K.

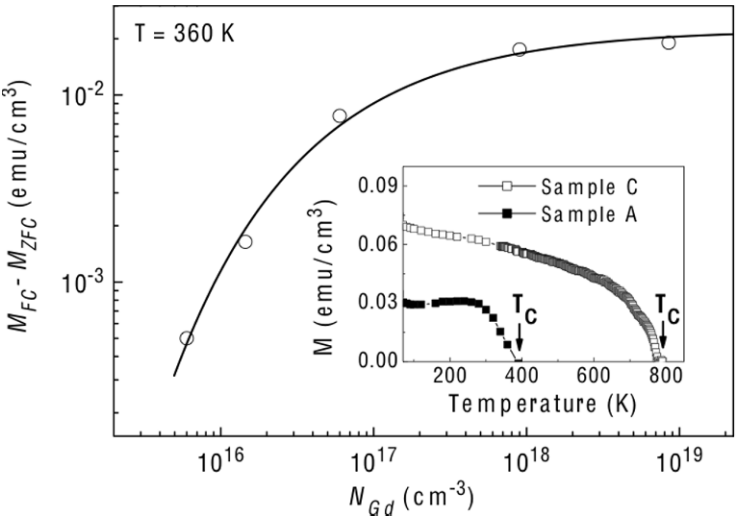

Fig. 10.11. Difference between FC and ZFC magnetization measured at 360 K plotted as a function of N_{Gd}. The solid curve through the data is a guide to the eye. Inset compares the magnetization as a function of temperature under a magnetic field of 100 Oe for samples A and C. Reprinted from [9]. Copyright (2005) The American Physical Society.

Fig. 10.12 shows the observed values of M_s at 2 K as a function of Gd concentration. The data obtained from sample I are also included in this figure (solid squares). At high Gd concentrations, M_s decreases with the decrease of N_{Gd}. However, below a Gd concentration of about 1×10^{18} cm^{-3}, M_s becomes independent of N_{Gd}. At 300 K a qualitatively similar behavior is observed [8]. The effective magnetic moment per Gd atom p_{eff} obtained from M_s ($p_{eff} = M_s/N_{Gd}$) for sample C is found to be 935 and 737 μ_B at 2 K and 300 K, respectively. These values are about two orders of magnitude larger than the pure moment of Gd. In the inset of Fig. 10.12, p_{eff} obtained at 2 K is plotted as a function of N_{Gd} and is found to be extraordinarily large, particularly for low Gd concentrations, when M_s becomes independent of N_{Gd}. p_{eff} is seen to saturate at high Gd concentrations. It is interesting to note that at 300 K, the saturation value in these heavily Gd-doped GaN samples is close to that of the atomic moment of Gd (8 μ_B), while at 2 K, it is clearly higher. This is true even for sample I. This colossal magnetic moment can be explained in terms of a very effective spin polarization of the GaN matrix by the Gd atoms. Gd atoms are inducing magnetic moments in a large number of Ga and/or N atoms. In fact, in certain dilute metallic alloys, the solute atoms exhibit

an average magnetic moment larger than their atomic value. This effect is called giant magnetic moment. There are several reports on a giant magnetic moment of Fe, Mn, and Co, when they are either dissolved in or residing on the surface of Pd [13, 14, 15]. This effect is explained in terms of a spin polarization of the surrounding Pd atoms. Very recently, a giant moment was observed in Co-doped $SnO_{2-\delta}$ [16], a dilute magnetic semiconductor. High-temperature ferromagnetism and an unusually large magnetic moment were observed also in Fe-doped SnO_2, which was argued to originate from a ferrimagnetic coupling mediated by electrons trapped on bridging F-centers [17]. In the band-structure terminology, the spin polarization of the matrix can be understood as a spin splitting in the conduction and/or valence band. Since our samples are highly resistive which most likely means that there are no electrons (holes) in the conduction (valence) band, a flat band picture can not explain the spin polarization even if the band structure is spin-split by Gd. Since Gd has a larger atomic size than Ga, it is possible that the substitution of Ga by Gd in GaN produces a large strain field. Keeping in mind the large piezoelectric coefficient of GaN along the *c*-axis, it is quite plausible that the strain field generates a potential dip around each Gd atom. These potential minima can trap carriers locally. If there is a spin splitting in the band structure, these localized carriers will be spin-polarized.

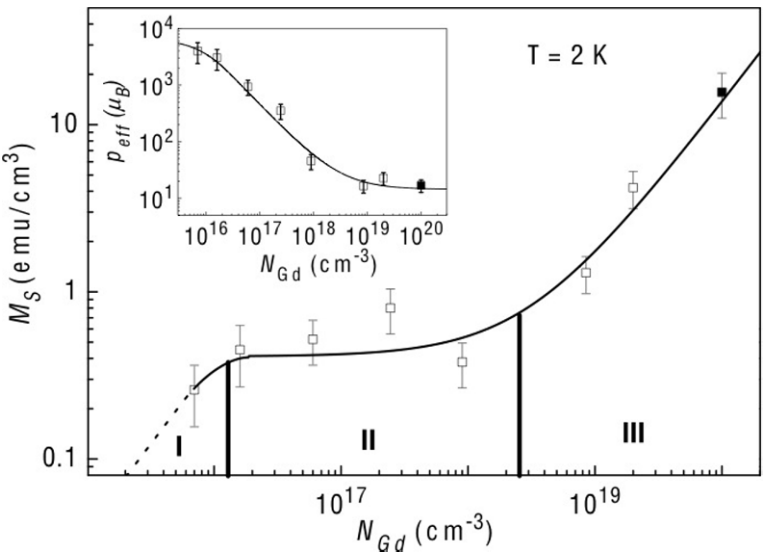

Fig. 10.12. Saturation magnetization M_s as a function of Gd concentration at 2 K. The magnetic moment per Gd atom (p_{eff}) as a function of Gd concentration at 2 K is shown in the inset. Open squares represent the experimental data for samples A to G and solid squares for sample I. The solid lines are the fits obtained from our model (discussed in the text). Note that the magnetic moment reaches values up to 4000 μ_B for the lowest Gd concentration. Reprinted from [9]. Copyright (2005) The American Physical Society.

Because of the unexpected nature of our observation, we have in fact proceeded with particular care in all experiments as described in the following.

1. We have grown more than 40 samples with different Gd concentrations and thicknesses. We also grew many undoped GaN reference samples in between these growth runs. The ferromagnetic signal is found only in Gd-doped samples. It is also observed that the magnetization per unit area for a given concentration of Gd scales with the sample thickness.
2. We etched the top 120 nm of sample C and find similar ferromagnetic behavior for the remaining material. The magnitude of the signal scales with the thickness.
3. The surface of these layers was analyzed using three different techniques, RHEED (during growth), AFM and SEM as mentioned before. Neither Gd nor any other material was found on the surface.

It is clear from the above mentioned observations that the magnetic signal is stemming from the bulk, not from the surface. On the other hand the maximum concentration of ferromagnetic contaminants in these samples is estimated to be on the order of 3×10^{15} cm^{-3} as has been described earlier, which obviously cannot explain the observed magnetization. Note that the magnetization observed in this work for, e.g., samples A and C would require an Fe (Ni, Co) concentration of 10^{19} cm^{-3} and above, three orders of magnitude higher than the Gd concentration.

10.4 Phenomenological Model

In order to get a quantitative understanding of the range of the spin polarization, we have developed a phenomenological model as explained in the following. The polarization of the GaN matrix by the randomly positioned Gd atoms is described as a rigid sphere of influence around each Gd atom, meaning that all the matrix atoms (or, alternatively, point defects) within the sphere are polarized by an equal amount whereas matrix atoms falling outside of this sphere are not affected. Let us associate an induced moment of p_0 with each of the matrix atoms lying in the region occupied by one sphere. As one should expect an increase of the polarization of matrix atoms if they belong to a region where two (or more) spheres of influence overlap, we attribute an additional moment np_1 to matrix atoms occupying sites in regions where n ($n = 2, \ldots N_{Gd}$) spheres overlap. Since their radius r is presumably much larger than the lattice spacing in GaN, we further assume that the spheres are randomly arranged in a three-dimensional continuum (continuum percolation). Within this framework, the saturation magnetization can be expressed as

$$M_s = p_{Gd} N_{Gd} + p_0 v N_0 + p_1 N_0 \sum_{n=2}^{N_{Gd}} n v_n \tag{1}$$

where N_0 is the concentration of matrix atoms (point defects) per unit volume, v is the volume of each sphere, $\tilde{v} = 1 - \exp(-vN_{Gd})$ is the volume fraction occupied by the spheres, and

$$\tilde{v}_n = \frac{(vN_{Gd})^n}{n!} e^{-vN_{Gd}} \tag{2}$$

is the volume fraction of the regions contained within n spheres. The average magnetic moment per Gd atom p_{eff} is then obtained as

$$p_{eff} = p_{Gd} + p_1 N_0 v + \left[p_0 - (p_0 + p_1 N_{Gd} v) e^{-vN_{Gd}} \right] \frac{N_0}{N_{Gd}} \tag{3}$$

On the basis of the behavior of M_s as a function of N_{Gd}, three regimes can be distinguished. At low Gd concentrations (regime I), most of the spheres are well separated as shown schematically in Fig. 10.13 (i) and p_{eff} has its maximum value. However, in this regime M_s increases with N_{Gd} since $\tilde{v}$ is an increasing function of N_{Gd}. At one point N_{Gd} crosses the percolation threshold and $\tilde{v}$ becomes very close to unity. This point marks the beginning of regime II [Fig. 10.13 (ii)]. In this regime M_s remains independent of N_{Gd} and p_{eff} decreases as N_{Gd} increases. Finally, at very high Gd concentrations the entire matrix becomes polarized [Fig. 10.13 (iii)] and M_s enters into regime III. In this regime, as the first term in (1) starts to dominate over the rest of the other terms, M_s increases again with N_{Gd} and p_{eff} approaches a saturation. The three regimes are indicated in Fig. 10.12. Note that in regime III, the value of saturation is larger than the magnetic moment of bare Gd atoms by an amount of $p_1 N_0 v$ (3). We use Eq. (1) to fit our experimental data with $p_{Gd} = 8\ \mu_B$ and p_0, p_1 and r as free parameters. The agreement is quite satisfactory as shown in Fig. 10.12. The fit yields $p_0 = 1.1 \times 10^{-3}\ \mu_B$, $p_1 = 1.0 \times 10^{-6}\ \mu_B$, and $r = 33$ nm at 2 K and $p_0 = 8.4 \times 10^{-4}\ \mu_B$, $p_1 \approx 0$, and $r = 28$ nm at 300 K [8]. The finite value of p_1 at 2 K explains why p_{eff} saturates at a value which is still higher than the atomic moment of Gd. Note that the values obtained for p_0 and p_1 will change if N_0 denotes the concentration of point defects per unit volume instead of representing that of matrix atoms as assumed here.

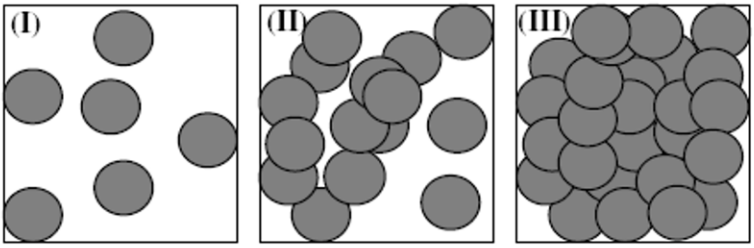

Fig. 10.13. The panels I – III represents schematically how the overlap changes as the concentration of Gd increases. Reprinted from [9]. Copyright (2005) The American Physical Society.

The second remarkable property of our GaN:Gd layers is the high-temperature ferromagnetism observed in all samples (well above room temperature, compared to a T_c of 289 K for bulk Gd). It is clear that the coupling cannot be explained simply in terms of direct, double or superexchange interaction between Gd atoms since the average Gd-Gd distance is too large for such a coupling to exist. Furthermore, all samples are found to be electrically highly resistive, ruling out free-carrier mediated RKKY (Rudermann–Kittel–Kasuya–Yosida) type long-range coupling. The possibility that the ferromagnetism originates from a Gd-related secondary phase formed by precipitation during growth can also be disregarded for several reasons. First, neither XRD (Fig. 10.5) nor TEM (Fig. 10.6) show any evidence for a secondary phase. Second, the Gd concentration in our samples is low, making precipitation extremely unlikely. Third, no (Gd,Ga) or (Gd,N) phases with a T_c as high as observed here are known to exist. We believe that the ferromagnetism and the colossal moment of Gd observed in these samples are in fact closely related. An overlap of the spheres of influence establishes a (long-range) coupling between the individual spheres. Within the framework of percolation theory, ferromagnetism is expected to occur at the percolation threshold, when an "infinite cluster" spanning macroscopic regions of the sample is formed. The percolation threshold is reached for our model at $\tilde{\nu}$ = 0.28955 [18, 19]. With increasing Gd concentration, we would thus expect a phase transition from paramagnetic to ferromagnetic behavior. Furthermore, T_c, which depends upon the strength of the overlap, is expected to increase with the Gd concentration. This is clearly consistent with the results shown in Fig. 10.11.

The well-established percolation formalism as described above cannot be straightforwardly adopted to quantitatively explain the current problem. It is intuitively clear that the spheres of influence are not hard but soft, i.e., the polarization of the matrix induced by the Gd atoms must decay with increasing distance. The onset of ferromagnetic order now depends upon the precise shape of this polarization cloud as well as on the overlap of two or more of these clouds. A quantitative prediction of the onset of ferromagnetism in this situation thus requires a detailed understanding of the nature of the ferromagnetic coupling in this material.

Finally, also very recent proposals aimed at explaining a giant magnetic moment and/or high-temperature ferromagnetism in various material systems [13, 14, 15, 16, 17] do not apply to the current requirement of a long-range coupling. An actual understanding of the phenomenon observed in the present paper will require detailed *ab initio* studies, particularly of the $f - d$ coupling between Gd and Ga. Considering the long spatial range of the coupling evident from our experiments, such calculations are computationally very demanding and are therefore beyond the scope of the present work. It is also possible and even likely (cf. Sect. 7) that the polarization is created not in the matrix atoms but in certain lattice defects generated during growth, such as point defects or complexes. A large density of such defects may form a narrow impurity band in the gap. If the Gd *f* or *d* orbital is allowed to mix with the band, it could in principal generate a spin-splitting there. A large spin polarization could be realized provided that the splitting is more than the width of the band. As has been stated earlier all of our samples, even the undoped GaN layers, are found to be electrically highly resistive, even though a large concentration (more than 10^{18} cm^{-3}) of O (an unintentional donor) is found by SIMS. This finding in fact indicates that a large density of defect states is present in the gap. Here, it is worth to mention that Venkatesan et al. [20] have recently reported an unexpected ferromagnetic behavior in HfO_2, where neither Hf^{4+} nor O^{2+} are magnetic ions, meaning the *d* and *f* shells of Hf^{4+} ions are either empty or full. A similar proposal was introduced in order to explain this unprecedented result.

10.5 Optical Properties

The above conclusion of a long-range spin polarization of the GaN matrix by the Gd atoms is independently supported by magneto-photoluminescence (PL) measurements. In the absence of an external magnetic field, the PL spectra of all samples are characteristic for undoped epitaxial GaN layers in that they are dominated by the (D^0, X) transition at a photon energy of about 3.458 eV. The lower energy of this transition, when compared to homoepitaxial GaN, is consistent with the tensile in-plane strain in these layers of 0.15% [21]. In all cases, the donor responsible for this transition is oxygen with a concentration of about 10^{15} cm^{-3} as measured by SIMS. Since these donors are distributed homogeneously over the entire GaN matrix, the (D^0, X) emission can be utilized as a probe for the properties of the electronic band structure. Fig. 10.14 shows the PL spectra for an undoped GaN reference sample and sample B under an external magnetic field of B = 10 T. The observed (D^0, X) emission is polarized in both samples, which is evident from the difference in intensities of the two circularly polarized σ^+ (full squares) and σ^- (open squares) components. Most importantly, the polarization for sample B has the opposite sign of the one in the reference sample. This finding is remarkable since it implies that a relatively small amount of Gd is able to reverse the sequence of Zeeman split states in a large volume fraction of the GaN matrix.

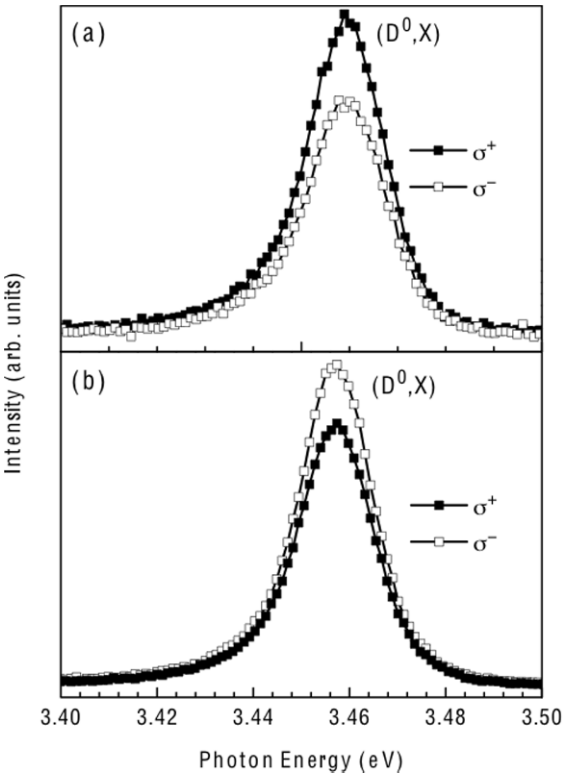

Fig. 10.14. Circularly polarized PL spectra for (a) the reference sample and (b) sample B measured at 7 K under a magnetic field of $B = 10$ T in the Faraday configuration $B \parallel c$.

The (D^0, X) complex consists of three particles, two electrons (one each in the donor and exciton) and one valence band hole (in the exciton). In the ground state, two electrons are in antiparallel spin orientation (singlet state), while the spin of the valence band hole is uncompensated. The uncompensated hole spin has a non-zero projection only along the c-axis because the ground state of (D^0, X) in GaN is associated with the A exciton. An external magnetic field along the c-axis thus splits the (D^0, X) ground state into two Zeeman sublevels with up and down projection of the hole spin. Here we assume that the Zeeman splitting (due to an external magnetic field) is much smaller than the singlet-triplet energy splitting of the electron pair in the complex. Hence, the (D^0, X) emission is expected to be composed of two types of circularly polarized light (σ^+ and σ^-). The relative population of the two Zeeman sublevels determines the circular polarization degree of the emitted light, which is defined as

$$\rho(B) = \frac{I^{\sigma^+} - I^{\sigma^-}}{I^{\sigma^+} + I^{\sigma^-}} = \frac{\tau_0}{\tau_0 + \tau_s} \tanh\left[\frac{\Delta E(B)}{2k_B T}\right] \tag{4}$$

where $I^{\sigma\pm}$ denotes the intensity of the $\sigma^{\pm}$ polarized light, k_B the Boltzmann constant and T the temperature. τ_0 and τ_s are the lifetime of the (D^0, X) transition and the spin-relaxation time of the holes, respectively. To account for the variation of the spin-relaxation time with the magnetic field observed in [22], we assume

$$\frac{\tau_s}{\tau_0} = \alpha \left(\frac{B}{B_0} \right)^{-\gamma} \tag{5}$$

where α and γ are constants and B_0 = 12 T the maximum magnetic field. $\Delta E(B) = g_h \mu_B B$ is the energy separation between the Zeeman sublevels of holes at an external magnetic field B. Since the g-factors for electrons g_e (= 1.95 [23]) and A-valence band holes g_h (= 2.25 [24]) are quite close to each other in GaN, the energy splitting of the (D^0, X) transition in a magnetic field

$$\Delta E_{(D^0,X)} = (g_e - g_h)\mu_B B$$

is thus expected to be ≈ 0.1 meV at B = 10 T, which is too small to be resolved. However, the same magnetic field can produce a noticeable polarization of the PL emission as apparent from Fig. 10.14. The sign reversal of the polarization in sample B with respect to the reference sample (Fig. 10.14) implies that $\Delta E(B)$ has changed its sign. For a magnetic semiconductor, $\Delta E(B) = g_h \mu_B B + \Delta E_{\text{int}}$, where ΔE_{int} is the additional splitting generated by the internal field produced by the magnetic atoms. In our case, ΔE_{int} is evidently negative and stronger than the Zeeman term, which is possible only when the excitonic ground state is subject to a strong influence of the Gd ions.

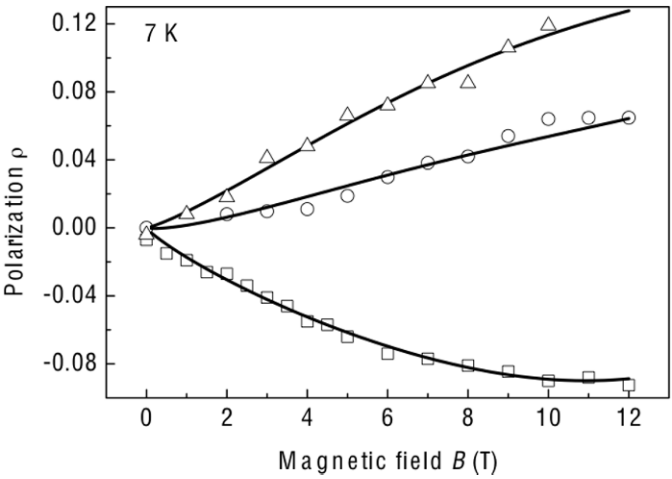

Fig. 10.15. Circular polarization ρ of the D^0, X emission as a function of the external magnetic field B measured at 7 K for the reference sample (triangles) as well as samples A (circles) and B (squares). Solid lines are the theoretical fit obtained from our model (discussed in the text).

Fig. 10.15 displays the (D^0,X) polarization ρ as a function of magnetic field for sample *A* (circles), *B* (squares) and the reference sample (triangles). Clearly, the magnetic field dependence of the polarization for the Gd-doped samples is different from that of the reference sample. While the reference sample exhibits, as expected, a nearly linear magnetic-field dependence, a tendency toward saturation is observed in particular for the Gd-doped sample B. It is also evident from Fig. 10.15 that the relative change of the polarization with respect to the reference sample increases with the concentration of Gd. All these findings confirm that a large fraction of excitons is influenced by the presence of Gd.

A sign reversal and a qualitatively similar magnetic-field dependence of the polarization of the PL emission due to the recombination of neutral Mn-acceptor-bound excitons (A^0,X) has been observed in (Ga,Mn)As which is a III-V dilute magnetic semiconductor (DMS). The observed behavior of the PL polarization has been explained in terms of an antiferromagnetic coupling between the valence band hole and the Mn *d*-orbital [25]. In this case, however, the excitons are bound to the magnetic dopant itself and are, consequently, easily influenced by the Mn *d*-orbitals. On the contrary, the excitons in our Gd-doped GaN layers are bound to O donors, which are homogeneously distributed within the matrix. The mean Gd-Gd separation in sample B is 25 nm resulting in an average distance between a (D^0,X) site and a Gd ion as large as 12 nm [26]. As mentioned before, none of the existing theories can explain a magnetic coupling across such a large distance [27].

The extraordinary situation encountered here becomes obvious when we attempt to analyze our data in the conventional framework valid for DMS such as (Ga,Mn)As, i.e., under the assumption of a direct interaction between Gd ions and (D^0,X). It is then expected that the additional splitting ΔE_{int} follows the external-field dependence of the macroscopic magnetization. SQUID measurements reveal a ferromagnetic behavior in these samples with a saturation of the magnetization above $B = 2$ T in both samples A and B. For the sake of simplicity, let us consider sample B in the following example. A fit of the experimental results to ρ in the magnetization-saturation range (cf. Fig. 10.15) yields $\Delta E_{\text{int}} = -2.5$ meV. However, $\Delta E_{\text{int}} = N_0\beta x\mu_{Gd}$, where $\mu_{Gd} = 8\ \mu_R$ is the bare atomic moment of Gd, N_0 is the number of Ga or N atoms per unit volume, $x = N_{Gd}/N_0$, and $N_0\beta$ is a constant which defines the strength of the exchange coupling between the Gd ions and the valence band holes. The corresponding value of $N_0\beta \approx -200$ eV is two orders of magnitude larger than the ones obtained in II-VI and III-V DMS and thus much too large to be physically meaningful. A reasonable value of $N_0\beta$ is only obtained when the effective magnetic moment per Gd atom is two orders of magnitude larger than its atomic moment of 8 μ_B, which is consistent with the colossal magnetic moment of 1000 μ_B obtained from the magnetization measurements in sample B. Repeating this analyis for sample A, we obtain an even larger value for $N_0\beta$, in agreement with the fact that the measured magnetic moment per Gd atom is as high as 3000 μ_B in this sample. In agreement with our previous conclusion, we thus have to consider that the Gd ions induce a magnetic moment in a large number of matrix atoms (Ga and/or N) in order to understand the efficient spin-polarization of a large fraction of excitons by the Gd doping.

To account for this polarization of the matrix, we associate as before a sphere of influence with each of the randomly positioned Gd ions. Since the radius r of these spheres is presumably much larger than the lattice spacing in GaN, we further assume that the spheres are randomly arranged in a three-dimensional continuum (continuum percolation). The polarization ρ of the (D^0,X) emission can now be expressed as

$$\rho = (1-y)\rho_{\text{out}} + y\rho_{\text{in}} \tag{6}$$

where y is the volume fraction of the regions occupied by the spheres of influence, and "in" and "out" denote the contributions to the polarization by excitons bound to donors inside and outside the regions spanned by the spheres, respectively. Within the framework of continuum percolation, y can be expressed as

$$y = 1 - e^{-\upsilon N_{\text{Gd}}} \tag{7}$$

where $\nu = 4\pi r^3/3$ is the volume of the sphere of influence. Both ρ_{in} and ρ_{out} can be expressed by (4), whereas $\Delta E(B)$ is given by:

$$\Delta E_{\text{out}}(B) = g_h \mu_B B$$

$$\Delta E_{\text{in}}(B) = g_h \mu_B B + \Delta E_{\text{int}}. \tag{8}$$

The values of α and γ [cf. (5)] are expected to be different inside and outside the regions occupied by the spheres of influence. $\tau_s(B)$ for regions not occupied by a sphere of influence is required to be identical to that in undoped GaN, which can be obtained from a fit to the data for the reference sample by using Eq. (4).

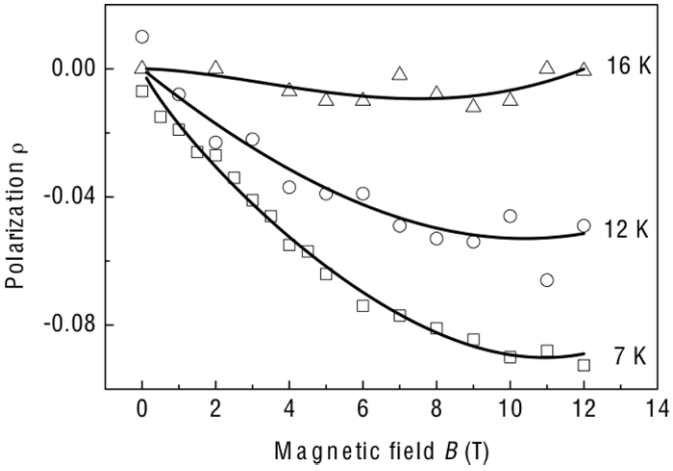

Fig. 10.16. Circular polarization of the (D^0, X) emission as a function of the external magnetic field B measured at different temperatures for sample B. Solid lines are theoretical fits obtained from our model (discussed in the text).

Next, we use this model to fit the experimental field dependence of the polarization at 7 K (Fig. 10.15) using a constant ΔE_{int} in the magnetization-saturation range, and α, γ and y as fit parameters. The central result of this approach is that satisfactory fits are obtained *only* with finite values for y, particularly so for sample B, for which y has to be very close to unity. A volume fraction of $y = 1$ means that the entire matrix is under the influence of the Gd ions, i.e., the radius of the sphere of influence is close to the average Gd-Gd spacing (25 nm) in this sample. Consequently, the fitting procedure was first applied to the reference sample and to sample B, representing the cases of y = 0 and y = 1, respectively. The obtained values of α and γ were subsequently taken into account to calculate the polarization curve of sample A using only ΔE_{int} and y as fit parameters. This fit yields r = 17.2 nm, which is close to the value obtained for sample B, demonstrating the consistency of this approach.

A further test of our model is given by the temperature dependence obtained for sample B. As shown in Fig. 10.16, our model is able to reproduce the data with reasonable values for all fit parameters (Table 10.1). Furthermore, the temperature dependence of ΔE_{int} is in excellent agreement with the decrease in saturation magnetization observed in the SQUID measurements. Finally, we point out that our findings are consistent with the size of the Gd sphere ($r \approx 30$ nm) estimated in Sect. 10.4 to account for the colossal magnetic moment per Gd ion observed in these samples, thus providing independent quantitative support in favor of a long-range interaction of Gd with the GaN matrix.

Table 10.1. Parameters obtained from the fits for different GaN:Gd samples used in this study: Gd concentration N_{Gd} (10^{16} cm^{-3}), sample temperature T (K), additional splitting ΔE_{int} (meV) generated by the Gd ions, parameters α and γ for the magnetic-field dependence of the hole spin relaxation time, volume fraction y ocuupied by the Gd-spheres of influence, and corresponding radius r (nm) of the spheres [cf.Eq. (7)].

Sample	N_{Gd}	T	ΔE_{int}	α	γ	y	r
Ref.	0	7	0	5.74	0.234	0	0
A	1.6	7	– 2.5	6.16	0.86	0.29	17.22
B	6	7	– 2.57	6.16	0.86	1	> 25
B	6	12	– 2.61	6.99	1.02	1	> 25
B	6	16	– 1.63	9.11	1.678	1	> 25

10.6 Magnetic Phases and Anisotropy

In addition to the colossal magnetic moment, GaN:Gd exhibits a magnetic behavior very different from that of classical ferromagnets. In particular, the layers show low coercivity and remanence in all directions. This magnetic behavior is also found in other magnetic nitrides [7, 28, 29, 30, 31, 32] and in dilute magnetic oxides [33, 34, 35, 36]. Dilute magnetic oxides also show different values of saturation magnetiza-

tion along different crystallographic directions, an effect that has never been observed in classical ferromagnets. Therefore, new efforts are needed to understand the mechanisms inducing ferromagnetism in these wide bandgap ferromagnetic materials. Note that all of the results presented in this section are obtained from samples different from those of Sect. 10.3. The similarity of the FC and ZFC curves shown below manifest the reproducibility of the phenomena under investigation.

10.6.1 Magnetic Phases

Fig. 10.17 shows the FC and ZFC curves for a GaN:Gd sample with a Gd-concentration of 6×10^{16} cm^{-3} (cf. Fig. 10.10). The shape of these curves is very similar for all the studied samples, with a clear increase of magnetic moment in the FC curve below 10 K and a separation between both curves reflecting a hysteretic behavior. For most of the samples, except the most highly doped ones, an additional kink at 70 K can be seen in the FC curve, but not in the ZFC curve. Therefore, the temperature dependence of magnetization in this system can be split into three contributions or phases. One contribution (1) at low temperature, a second one (2) which vanishes at the same temperature (70 K) for all the measured samples and a third one (3) which remains ferromagnetic above room temperature. The Curie temperature of the sample is determined by contribution 3 and depends on the Gd content as shown in Sect. 10.3.

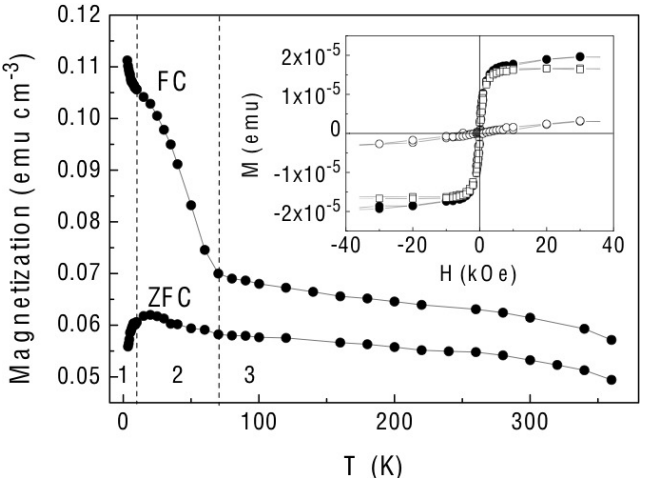

Fig. 10.17. FC and ZFC curves for a GaN:Gd sample with $N_{Gd} = 6{\times}10^{16}$ cm^{-3}. The temperature ranges 1, 2, and 3 refer to the three distinct magnetic contributions as discussed in the text. The inset shows the magnetization loops measured at 2 (solid circles) and 10 K (open squares), and the difference between both curves (open circles). It is important to note that the difference was calculated before correcting the diamagnetic background. Reprinted from [10]. Copyright (2006) The American Physical Society.

Magnetization loops measured in the temperature ranges 1 and 2 are clearly different at high field. In the inset of Fig. 10.17, loops measured at 2 and 10 K are shown. Whereas the latter loop clearly saturates at 0.6 T, the saturation field at 2 K is much higher. In the inset of Fig. 10.17, the difference between both curves is shown, calculated as $M_{2K} - M_{10K}$ before correcting for the diamagnetic background from the substrate. The shape of this difference suggests that contribution 1 is paramagnetic. The hysteresis loops measured at 50 K and 100 K (not shown) are qualitatively similar to the one measured at 10 K, except for smaller values of remanence and coercivity. It is important to remark that we have not found any significant change in saturation magnetization from 10 to 100 K within the resolution of the measurement.

Fig. 10.18 compares the FC curves recorded for samples with different Gd concentrations. The curves are normalized to their values at 100 K. It can be seen that the relative contribution of the transition at 70 K is enhanced when the Gd content in the sample is reduced. The ratio between both components of the magnetic moment can be estimated as

$$\frac{\Delta M}{M} = \frac{(M_{80K} - M_{10K})}{M_{80K}}. \tag{9}$$

In the inset of Fig. 10.18, this ratio is plotted as a function of the Gd concentration. It is clear that, on average, this ratio is higher for lower Gd doping in GaN.

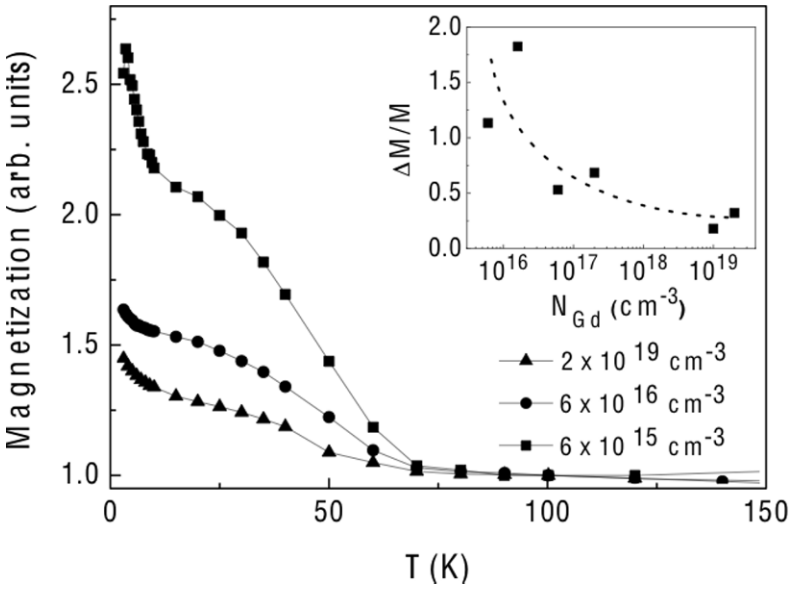

Fig. 10.18. FC curves for samples with different Gd content. The inset shows an estimation of the change in the magnetic moment at 70 K as a function of the doping. The dotted line is a guide to the eye. Reprinted from [10]. Copyright (2006) The American Physical Society.

The presence of contribution 2 has also been checked by measuring the temperature dependence of the saturation magnetization M_s and the remanence M_r, calculated from the hysteresis loops measured at different temperatures for a sample with $N_{Gd} = 6\times 10^{16}$ cm^{-3} (Fig. 10.19). The temperature dependence of the remanence shows the same two steps at 10 and 70 K as the FC curves. In contrast, the thermal dependence of the saturation magnetization shows one step at about 10 K, whereas the transition at 70 K is absent.

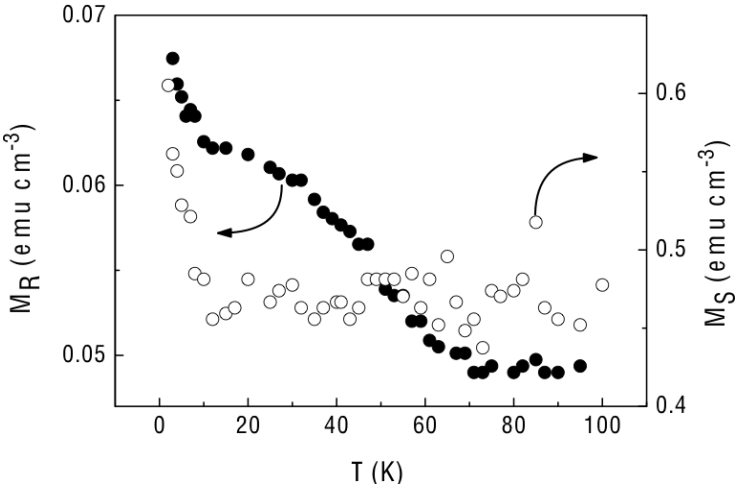

Fig. 10.19. Temperature dependence of the remanence (solid circles) and the saturation magnetization (open circles) for a GaN:Gd layer with $N_{Gd} = 6 \times 10^{16}$ cm^{-3}. Reprinted from [10]. Copyright (2006) The American Physical Society.

It is worth mentioning that the magnetic viscosity effect gives rise to hysteretic behavior in spin-glasses and superparamagnetic materials below the transition and the blocking temperature, respectively. However, the isothermal remanent magnetization in these systems decays on a timescale of minutes to hours. We have carried out isothermal magnetization measurements at 10 and 100 K in different magnetic fields (at remanence, 100 Oe and 10 kOe) after saturating the sample in a field of 50 kOe. No changes in the magnetic moment within the resolution of our SQUID setup were observed even after 10 hours.

10.6.2 Magnetic Anisotropy

Fig. 10.20 shows the first magnetization curves of a sample with $N_{Gd} = = 3 \times 10^{15}$ cm^{-3} for the $[1\bar{1}00]$ (in plane) and $[0001]$ (out of plane) directions. The first magnetization curve along the perpendicular in-plane direction $[11\bar{2}0]$ is very similar to that obtained along $[1\bar{1}00]$ and is not shown for sake of clarity. The

magnetization has been normalized to the value of the saturation magnetization to allow a better comparison between the different directions. Two different effects related to anisotropy can be observed.

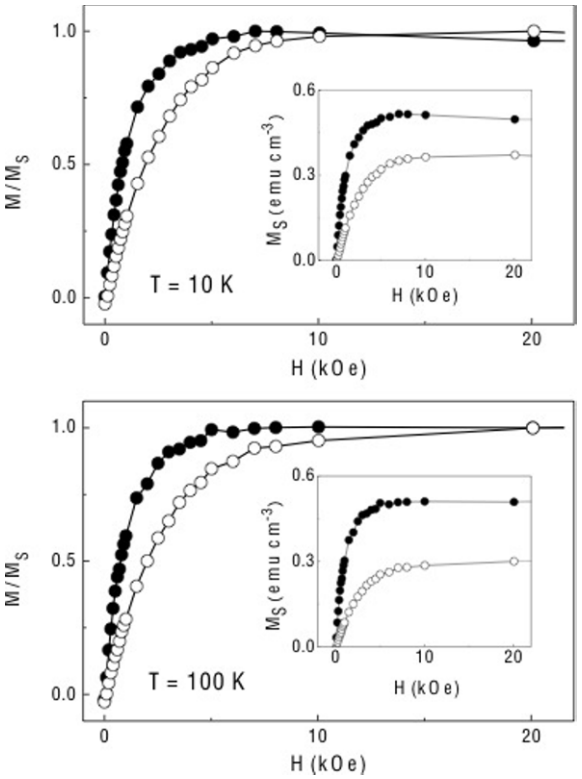

Fig. 10.20. First magnetization curves measured in two perpendicular directions (open circles: [0001], solid circles: [$1\bar{1}00$]) for $N_{Gd} \times 10^{15}$ cm^{-3}. The curves have been normalized to the values of the saturation magnetization. The inset shows the same curves, but not normalized. Reprinted from [10]. Copyright (2006) The American Physical Society.

First, there is a soft plane of magnetization perpendicular to the [0001] direction, i.e., [0001] is the hard axis for magnetization. Nevertheless, although it is easier to saturate the sample with a field applied parallel to the surface, it should be noted that also in this case it is necessary to apply a high field ($\simeq 10^4$ Oe) to saturate the sample. The energy needed to reach saturation – the so called anisotropy energy in classical ferromagnets – can be calculated by numerical integration of the first magnetization curve. At 100 K, for example, the value of this energy amounts to $\simeq 1500$ erg cm^{-3} for the in-plane compared to $\simeq 3000$ erg cm^{-3} for out-of-plane measurements.

The second effect related to anisotropy can be observed in the insets of the figures, where the non-normalized magnetization has been plotted as a function of

the applied magnetic field: the saturation magnetization is smaller along the hard axis at all temperatures. This anisotropy in the magnetic moment has been observed in samples with different Gd content and also in samples containing undoped GaN buffer and cap layers.

10.6.3 Discussion

Several magnetic phases have been observed in the temperature dependence of the magnetic moment. An increase in the FC curves at low temperature has also been observed in bare SiC substrates, undoped GaN layers and also in other GaN-based magnetic semiconductors [7, 28, 30, 37]. From the measurements of the hysteresis loops at different temperatures, it seems clear that phase 1 is not ferromagnetic. Therefore, this phase might stem from a change in susceptibility of GaN or to a small paramagnetic contribution of some dopants in the SiC substrates, not related to the presence of Gd in the layers. However, there is a small increase in the remanence at low temperature and, therefore, the presence of a ferromagnetic phase with Curie temperature around 10 K cannot be completely excluded.

The transition at 70 K has not been observed in undoped samples and is thus related to the presence of Gd in the layer. The Curie temperature for GdN is close to 70 K. However, the structural characterization of these layers by RHEED, XRD, and TEM has not revealed the presence of any cluster or secondary phases in these layers [9]. In order to exclude the possibility of the formation of GdN in the first stages of the growth or after closing the shutters of the effusion cells of the MBE system, we have grown layers with and without buffer and/or capping layers. Furthermore, we have etched a few hundred nanometers from the top of some layers by reactive ion etching. The FC curves of all these layers show the transition at 70 K. Therefore, we believe that this step stems from the bulk and not from the surface or interface.

In addition to the above considerations, we have not observed any relaxation phenomena in the isothermal behavior of magnetization above and below 70 K. This fact, together with the absence of any transition in the ZFC curve at 70 K, suggests that contribution 2 is not a superparamagnetic or spin-glass contribution arising from GdN clusters but a ferromagnetic one.

In Sects 10.3 and 10.5, we have explained the colossal magnetic moment of Gd observed in this system in terms of a Gd-induced spin polarization either of the GaN matrix atoms (Ga and/or N) or of a certain type of defect residing in the matrix. We have proposed a phenomenological model associating a sphere of influence with every Gd atom. We believe that an overlap of these spheres of influence establishes a long-range magnetic order, which could explain the ferromagnetic behavior observed in these samples. In order to achieve such a long-range order, it is not necessary that *all* spheres are interconnected. Within the framework of percolation theory, a long-range order is expected to occur at the percolation threshold, which is equivalent to the formation of an “infinite cluster”

spanning macroscopic regions of the sample. The percolation threshold is reached at a much lower Gd concentration than that necessary to achieve the situation when all spheres are interconnected. In other words, a large fraction of these spheres will still be isolated or form part of small isolated clusters even if the percolation threshold is reached.

It is plausible that the magnetic behavior attributed to phase 2 is in fact resulting from isolated spheres and small isolated clusters, while the ferromagnetic behavior with an order temperature above 300 K (phase 3) is likely to stem from connected spheres, forming clusters comparable in size to the size of the sample. According to this model, the relative magnetic contribution of phase 2 with respect to that of phase 3 should decrease with increasing Gd concentration since the ratio between the volumes occupied by the isolated and connected spheres is expected to decrease as the concentration of Gd is increased. In fact, this trend is seen in the experiments depicted in Fig. 10.18. The nature of the isolated spheres is expected to be independent of the Gd content of the layer and therefore the same transition temperature for phase 2 is expected in all layers, as is indeed observed in the experiments.

We have found a magnetic anisotropy with a hard axis along the direction perpendicular to the surface and a soft plane parallel to the surface in these samples. The presence of magnetic anisotropy in the samples is also a clear indication that the magnetic properties are related to the material itself. The hard axis along the direction perpendicular to the surface cannot be due to the demagnetizing field. Taking into account that the lateral dimensions of the samples are orders of magnitude larger than the thickness, we can assume a demagnetizing factor of 4π along the [0001] direction [38]. The saturation magnetization M_s for the sample investigated here is $\approx$ 1.8 emu cm^{-3} which results in a demagnetizing field of only 22 Oe at saturation, clearly too small to explain the observed result.

We have observed that the saturation magnetization measured in these samples with an in-plane orientation of the magnetic field is larger than that obtained with the field applied along the out-of-plane direction. The anisotropy in the saturation magnetization, never observed in magnetic nitrides but only recently in some dilute magnetic oxides [34], leads to a new concept of magnetic anisotropy. These systems are expected to have two contributions to the total magnetic moment: the permanent moment of the magnetic atoms introduced as dopants and the polarization induced in the matrix or in some other dopants or defects by the internal and the external magnetic field [39]. When the external field is high enough to saturate the system, the value of the permanent magnetic moment should be constant and independent of the direction of the measurement. However, the polarization of the matrix may be anisotropic, giving rise to the observed effect. Therefore, a new concept of anisotropy arises, related not only to the difference in energy necessary to align permanent magnetic moments along different directions, but also related to the anisotropic polarization of the matrix by the internal and external magnetic field.

10.7 Recent Studies in the Literature

After our initial discovery of room temperature ferromagnetism and colossal magnetic moment in GaN:Gd [8, 9], several other researchers have initiated studies of GaN:Gd in an attempt to shed light upon the origin of these two phenomena.

Hite et al. have reported ferromagnetism above room-temperature for epitaxial GaN:Gd layers grown by plasma-assisted MBE [40]. The Gd concentration in their layers was below 1×10^{17} cm^{-3}, and the O concentration 1×10^{19} cm^{-3}. Although not stated explicitly by these authors, the magnetization observed implies a magnetic moment per Gd atom comparable to the highest values observed in our work. Codoping the layers with Si resulted in conducting films and an even higher magnetization.

Dhar et al. have employed focused ion-beam (FIB) implantation of Gd in GaN layers grown by MBE with a concentration from 2.4×10^{16} to 1×10^{20} cm^{-3} [41]. As grown, the implanted samples were ferromagnetic above room temperature and exhibited a magnetic moment even larger than the one observed in our samples doped during epitaxy. As implantation induces an abundance of native point defects, this finding provides direct evidence for the participation of defects in the formation of the colossal magnetic moment.

Khaderbad et al. investigated the effect of annealing on these ion-implanted samples in detail [42]. In samples with a low Gd concentration, the magnetic moment was found to be reduced by a factor of 2 after annealing at 800°C. Based on XRD measurements, the authors proposed that the implantation induces a high density of Ga and N interstitials, the density of which is reduced by annealing. It thus seems that these interstitials are directly responsible for the colossal magnetic moment of GaN:Gd.

Ney et al. have performed measurements using X-ray absorption near-edge spectroscopy (XANES), X-ray linear dichroism (XLD) and X-ray magnetic circular dichroism (XMCD) on a GaN:Gd sample with $N_{Gd} = 2\times 10^{19}$ cm^{-3} [43]. From the XANES and XLD measurements, they confirmed that at least 85% of the Gd atoms are incorporated subsitutionally on Ga sites without any detectable clustering. A clear XMCD signal was measured at the Gd L_3 edge. The authors compared the dependence of the XMCD signal on magnetic field with the hysteresis loops measured by a SQUID magnetometer, and showed that the signal corresponding to Gd (from the XMCD data) is considerably lower than the total magnetic signal (from SQUID), particularly at low temperatures. Therefore, the ferromagnetic behavior and the magnetic moment of GaN:Gd cannot be explained by taking into account the contribution of the Gd atoms alone. This finding is thus a direct confirmation of our phenomenological concept of the sphere of influence.

Roever et al. grew GaN:Gd layers by plasma-assisted MBE and codoped these layers with Si or H [44]. They obtained ferromagnetism at room temperature and magnetic moments of a magnitude comparable to those observed in our work. The fact that they observe an increase of the magnetic moment upon codoping with Si

led them to conclude that the ferromagnetism is stabilized by electrons. In a subsequent work, Martínez-Criado et al. furthermore showed that Gd occupies predominantly Ga sites [45].

From the theoretical point of view, Dalpian and Wei conducted an *ab initio* study of the zincblende (Ga,Gd)N alloy [46]. They found that the coupling between Gd atoms is antiferromagnetic, while ferromagnetism can be stabilized by the introduction of donors. They proposed a model for the experimentally observed colossal magnetic moment based on the coupling of the unoccupied *f* states of Gd with the occupied *s* states of donor levels.

In contrast, both Gohda and Oshiyama [47] and Dev et al. [48] attribute the observed ferromagnetism to defects and particularly, Ga vacancies. The former authors report that Ga vacancies with the magnetic moment of 3 μ_B formed upon Gd doping interact ferromagnetically with each other and thus cause gigantic magnetic moments per Gd atom. The latter authors found that a neutral Ga vacancy leads to the formation of a net moment of 3 μ_B in exact agreement with the above work. The extended tails of defect wave functions were found to mediate surprisingly long-range magnetic interactions between the defect-induced moments.

Lo et al. reported the first study of the magnetic properties of zincblende GaN:Gd [49]. The GaN layers were implanted with Gd using FIB, analogously to the approach of the authors in [41]. Contrary to implanted wurtzite GaN:Gd, the zincblende samples exhibited ferromagnetism only in the highest doped sample ($N_{Gd} = 1 \times 10^{20}$ cm^{-3}) and with a Curie temperature below 60 K. From this result, the authors concluded that the spontaneous polarization of the wurtzite phase is crucial for determining the magnetic properties of GaN:Gd.

10.8 Conclusions

Our study has revealed an extraordinarily large magnetic moment of Gd in GaN. This colossal moment of Gd arises from a long-range spin polarization of the GaN matrix by the Gd atoms. In particular, the results from other researchers using implanted samples imply that point defects or defect complexes are responsible for this efficient spin polarization, which is also supported by first principles calculations. As a direct result of this peculiar effect, the material is ferromagnetic above room temperature even with a Gd concentration less than 10^{16} cm^{-3}. This finding offers an exciting opportunity, since GaN:Gd may be easily doped with donors (acceptors) with a concentration exceeding that of Gd to generate spin polarized electrons (holes) in the conduction band (valence band). Gd-doped GaN with its T_c above room temperature might thus be a very attractive candidate as a source of spin-polarized carriers for future semiconductor-based spintronics [50].

Acknowledgements

We are indebted to K.H. Ploog for sparking our interest in Gd doping of GaN. Furthermore, we are grateful to G.S. Lau, M. Ramsteiner, U. Jahn and K.J. Friedland for important contributions to this work, J. Herfort, M. Bowen and R. Koch for valuable discussions and suggestions, and J. Keller and B. Beschoten for the high-temperature SQUID measurements. We also acknowledge partial financial support of this work by the Bundesministerium für Bildung und Forschung of the Federal Republic of Germany. One of us (L. Pérez) thanks the Alexander von Humboldt Foundation, Germany, for financial support.

References

1. P.N. Favennec, H. Lharidon, M. Salvi, M., D. Moutonnet, Y. Leguillou.. *el*, 25(11):718-719, 1989.
2. Y.Q. Wang and A.J. Steckl. *App. Phys. Lett.*, 82(4):502-504, 2003.
3. J.S. Filhol, r. Jones, M.J. Shaw, P.R. Briddon. *Appl. Phys. Lett.*, 84(15):2841-2843, 2004.
4. M. Hashimoto, S. Emura, R. Asano, H. Tanaka, Y.K. Zhou, N. Teraguchi, A. Suzuki, Y. Nanishi, T. Honma, N. Umesaki, H. Asahi. *Phys. Status Solidi C*, 7:2650, 2003.
5. t. Story, M. Gorska, A. Lusakowski, M. Arciszewska, W. Dobrowolski, E. Grodzicka, Z. Golacki, R.R. Galazka.. *Phys. Rev. Lett.*, 77(16):3447-3450, 1996.
6. H.S. Li, Y.P. Li, J.M.D. Coey. *J. Phys.: Condens. Matter)*, 3(38):7277-7290, 1991.
7. N. Teraguchi, A. Suzuki, Y, Nanishi, Y.K. Zhou, M. Hashimoto, H. Asahi. *Sol. State Commun.*, 122(12):651-653, 2002.
8. S. Dhar, O. Brandt, M. Ramsteiner, V.F. Sapega, K.H. Ploog. *Phys. Rev. Lett.*, 94(3):037205, 2005.
9. S. Dhar, L. Pérez, O. Brandt, A. Trampert, K.H. Ploog, J. Keller, B. Beschoten.. *Phys. Rev. B.*, 72:245203, 2005.
10. L. Perez, G.S. Lau, S. Dhar, O. Brandt, K.H. Ploog. *Phys. Rev. B*, 74:195207, 2006.
11. A. Thamm, O. Brandt, Y. Takemura, A. Trampert, K.H. Ploog.. *Appl. Phys. Lett.*, 75(7):944-946, 1999.
12. S. Dhar, O Brandt, A. Trampert, L. Däweritz, K.J. Friedland, K.H. Ploog, J. Keller, B. Beschoten, G. Güntherodt.. *Appl. Phys. Lett.*, 82(13):2077-2079, 2003.
13. G. Bergmann. *Phys. Rev. B*, 23(8):3805-3815, 1981.
14. J. Flouquet, O. Taurian, J. Sancheza, M. Chapellier, J.L. Tholence. *Phys. Rev. Lett.*, 38:81-84, 1977.
15. J. Crangle and W.R. Scott. *J. App. Phys.*, 36(3):921-928, 1965.
16. S.B. Ogale, R.J. Choudhary, J.P. Buban, S.E. Lofland, S.R. Shinde, S.N. Kale, V.N. Kulkarni, J. Higgins, C. Lanci, J.R. Simpson, N.D. Browning, S. Das Sarma, H.D. Drew, R.L. Greene, T. Venkatesan.. *Phys. Rev. Lett.*, 91(7):4, 2003.
17. J.M.D. Coey, A.P. Douvalis, C.B. Fitzgerald, M. Venkatesan.. *Appl. Phys. Lett.*, 84(8):1332-1334, 2004.
18. R. Consiglio, D.R. Baker, G. Paul, H.E. Stanley.. *Physica A*, 319:49-55, 2003.

19. D.R. Baker, G. Paul, S. Sreenivasan, H.E. Stanley. *Phys. Rev. E*, 66(4):5, 2002.
20. M. Venkatesan, C.B. Fitzgerald, J.M.D. Coey. *Nature*, 430(7000):630-630, 2004.
21. P. Waltereit, O. Brandt, A. Trampert, M. Ramsteiner, M. Reiche, M. Qi, K.H. Ploog. *Appl. Phys. Lett.*, 74(24):3660-3662, 1999.
22. B. Beschoten, E. Johnston-Halperin, D.K. Young, M. Poggio, J.E. Grimaldi, S. Keller, S.P. DenBaars, U.K. Mishra, E.L. Hu, D.D. Awschalom. *Phys. Rev. B*, 63:121202, 2001.
23. A.V. Rodina and B.K. Meyer. *Phys. Rev. B*, 64:245209, 2001.
24. A.V. Rodina, M. Dietrich, A. Göldner, L. Eckey, A. Hoffman, A.L. Efros, M. Rosen, B.K. Meyer. *Phys. Rev. B*, 64:115204, 2001.
25. I.Ya. Karlik, I.A. Merkulov, D.N. Mirlin, L.P. Nikitin, V. I. Perel, V.F. Sapega. *Sov. Phys. Solid State*, 24:2022, 1982.
26. It can be easily shown that the average distance of an exciton binding site from its nearest Gd ion is = 0.480296 a , where a is the average Gd-Gd separation.
27. It is clear that the average distance of an exciton formation site from a Gd ion is too large for a direct exchange coupling between them to exist. Furthermore, all samples are found to be electrically highly resistive, ruling out free-carrier mediated RKKY (Rudermann-Kittel-Kasuya-Yosida) type long-range coupling.
28. M. Hashimoto, A. Yanase, R. Asano, H. Tanaka, Y. Bang, K. Akimoto, H. Asahi. *Jpn. J. Appl. Phys.*, 42:L1112-L1115, 2003.
29. H. Asahi, Y.K. Zhou, M. Hashimoto, M. S. Kim, X. J. Li, S. Emura, S. Hasegawa. *J. Phys.: Condens. Matter*, 16:S5555, 2004.
30. S. J. Pearton, C.R. Abernathy, G.T. Thaler, R.M. Frazier, D.P. Norton, F. Ren, Y.D. Park, J.M. Zavada, I.A. Buyanova, W.M. Chen,A.F. Hebard. *J. Phys.: Condens. Matter*, 16:R209, 2004.
31. Y. Shon, Y.H. Kwon, Y.S. Park, Sh.U. Yuldashev, S.J. Lee, C.S. Park, K.J. Chung, S.J. Yoon, H.J. Kim, W.C. Lee, D.J. Fu, T.W. Kang, X.J. Fen, Y.J. Park, H.T. Oh. *J. Appl. Phys.*, 95(2):761, 2004.
32. H.X. Liu, Stephen Y. Wu, R.K. Singh, Lin Gu, David J. Smith, N. Newman, N.R. Dilley, L. Montes, M. B. Simmonds. *Appl. Phys. Lett.*, 85(18):4076-4078, 2004.
33. J.M.D. Coey. *J. Appl. Phys.*, 97:10D313, 2005.
34. M. Venkatesan, C.B. Fitzgerald, J.M.D. Coey. *Nature*, 430(7000):630, 2004.
35. H. Saeki, H. Matsui, T. Kawai, H. Tabata. *J. Phys.: Condens. Matter 16*, 16:S5533, 2004.
36. M. Venkatesan, C.B. Fitzgerald, J.G. Lunney, J.M.D. Coey. *Phys. Rev. Lett.*, 93(17):177206, 2004.
37. S.Y. Han, J. Hite, G.T. Thaler, R.M. Frazier, C.R. Abernathy, S.J. Pearton, H.K. Choi, W.O. Lee, Y.D. Park, J.M. Zavada, R. Gwilliam. *Appl. Phys. Lett.*, 88:042102, 2006.
38. S. Chikazumi. *Physics of Ferromagnetism*. Oxford University Press, 1997.
39. A.C. Durst, R.N. Bhatt, P.A. Wolff. *Phys. Rev. B.*, 65:235205, 2002.
40. J.K. Hite, R.M. Frazier, R. Davies, G.T. Thaler, C.R. Abernathy, S.J. Pearton, J. M. Zavada. *App. Phys. Lett.*, 89:092119, 2006.
41. S. Dhar, T. Kammermeier, A. Ney, L. Pérez, K.H. Ploog, A. Melnikov, A.D. Wieck. *Appl. Phys. Lett.*, 89:062503, 2006.
42. M.A. Khaderbad, S. Dhar, L. Pérez, K.H. Ploog, A. Melnikov, A.D. Wieck. *Appl. Phys. Lett.*, 91:072514, 2007.
43. A. Ney, T. Kammermeier, E. Manuel, V. Ney, S. Dhar, K.H. Ploog, F. Wilheim, A. Rogalev. *Appl. Phys. Lett.*, 90:252515, 2007.
44. M. Roever, D.-D. Mai, A. Bedoya-Pinto, J. Malindretos, A. Rizzi. *phys. stat. sol (c)*, 5(6):2352, 2008.

45. G. Martínez-Criado, O. Sancho-Juan, N. Garro, J.A. Sans, J. A., A. Cantarero, J. Susini, M. Roever, D.-D. Mai, A. Bedoya-Pinto, J. Malindretos, A. Rizzi. *Appl. Phys. Lett.*, 93(2):021916, 2008.
46. Gustavo M. Dalpian and Su-Huai Wei. *Phys. Rev. B*, 72:115201, 2005.
47. Y. Gohda and Atsushi Oshiyama. *Phys. Rev. B*, 78(16):161201, 2008.
48. Pratibha Dev, Yu Xue, Peihong Zhang. *Phys. Rev. Lett.*, 100(11):117204, 2008.
49. F. Lo, A. Melnikov, D. Reuter, A.D. Wieck, V. Ney, T. Kammermeier, A. Ney, J. Schormann, S. Potthast, D.J. As, K. Lischka. *Appl. Phys. Lett.*, 90:262505, 2007.
50. S.A. Wolf, D.D. Awschalom, R.A. Buhrman, J.M. Daughton, S. von Molnar, M.L. Roukes, A.Y. Chtchelkanova, D.M. Treger. *Science*, 294(5546):1488-1495, 2001.

Summary and Prospects for Future Work

The various chapters of this book, dealing with several aspects of the science and technology of RE ions embedded in group-III nitride semiconductors, have been written independently by different authors, who mainly report results obtained within their own laboratories and those of their collaborators. As a consequence, some duplications and contradictions will be apparent to the careful reader of these pages. It is the purpose of this summary to highlight certain areas for which general agreement has been reached and others where controversy still exists. Open questions, which offer opportunities for future research efforts, will also be summarized here.

The recent successes of Jiang et al (for GaN:Er, Chapter 5) and Nishikawa et al [1]. (for GaN:Eu) suggest that in-situ doping during MOCVD growth offers the best potential for producing working optical devices, due to the superior crystalline quality of active layers produced by this technique, resulting in sharp, intense spectral transitions.

The wide variety of growth and doping methods employed over the years, including ion implantation (Chapter 2) and in-situ doping of samples grown by sputtering, MBE, MOMBE, and MOCVD have in fact contributed to some confusion in the literature; samples from different sources cannot be compared readily to each other. This is particularly true in terms of the related problems of site multiplicity and excitation mechanism (Chapters 6-9). For example, it is shown in Chapter 8 that quite different centres are produced in samples doped *in situ* compared to those doped by ion implantation. Although the process conditions for the latter doping method have been optimized to some extent, its application in device production, with the attendant benefits of lateral patterning, has not been investigated in detail (Chapters 2 and 4).

The lattice location of RE ions in wurtzite GaN has been identified by ion channelling, RBS and EXAFS techniques; it is widely accepted that RE ions substitute for Ga but tend to be randomly displaced from the site centre by an amount that depends on the ion (Chapter 3). However, through site selective spectroscopy, it becomes clear that multiple variants of the primary site exist which are most likely to be identified as different centers in which an apparent off-centre displacement arises due to the presence of lattice relaxation associated with

neighbouring defects. The precise microscopic structure of the various light-emitting centers still needs to be pinned down experimentally [2].

The theoretical modeling of RE centers in group-III nitride semiconductors (Chapter 1) is still in its infancy but has already delivered significant insights. LDA+U computer modelling of the stability and electronic structure of RE-defect complexes confirms experimental lattice locations and suggests that isolated RE ions are optically and electrically inert in GaN while they form deep traps in AlN. This change in behaviour may explain some aspects of the excitation spectra recently obtained for the entire $Al_xGa_{1-x}N$ alloy composition range by Wang et al. [3] It has also been established that several defect complexes, such as RE pairs [4] and RE ions bound to nitrogen vacancies, are sufficiently stable to play an important role and may be responsible for the formation of shallow traps.

Throughout the book it becomes clear that the excitation mechanism of the RE ion by means of photogenerated electron-hole pairs is still a matter for debate and some controversy. This mechanism should dominate in injection-pumped, as opposed to (high-field) electroluminescent devices. Most of the relevant studies have been performed on GaN doped with Eu or Er. For this wide-gap host, it is generally assumed that direct transfer of excitation to the RE ions is rather inefficient and that energy mediation by defects must play a significant role. Both shallow and deep traps seem to be involved, with the latter offering higher efficiency. Although theory supports this conclusion to some extent, the possible role of the RE ion itself in the formation of the mediating trap is not yet clarified, in particular with $Al_xGa_{1-x}N$ alloys for which the excitation path depends on the type of center that is considered[3].

One possibility to improve the excitation efficiency for direct energy transfer is to tune the band-gap into resonance with transitions of the respective RE ions. However, attempts to alloy GaN with AlN or InN suffer from a deterioration of crystal quality and increased number of (unhelpful) defects. As with commercial InGaN blue diodes, exciton localization plays a critical role. This is highlighted by the improvement of performance that can be achieved by confining RE ions in quantum dots (Chapter 6).

Most of this book focuses on the optical properties and their optimization for light emitting devices (Chapters 4 and 5) but the observation of significant ferromagnetic spin polarization in Eu- and Gd-doped III-nitrides opens the door to their application in spintronics (Chapter 10). A combination of optical and magnetic functionalities may allow the control and detection of spin by optical means. It is found that the RE ions couple to each other and to the host electrons ferromagnetically but the detailed mechanism and the role of defects and dopants remains unclear. Experiments by Zavada et al. revealed no correlation between emission efficiency and magnetization for the Eu ion [5].

Three obvious open questions that need further investigations include the following:

- Which are the defects that can act most efficiently as mediators of the energy transfer between electron-hole pairs and RE ions in III-N? Can these defects be enriched without sacrificing the film quality and the electrical properties?
- What is the mechanism of enhanced ferromagnetism for Gd and Eu-doped GaN?
- Given the 'green droop' that compromises InGaN-based optical devices, is there a realistic prospect of commercialization of III-N:RE technology?

It is a fervent wish of the book's authors that continuing time and effort will bring positive answers to these questions. If any of the book's readers wish to join this quest, we surely welcome you!

Kevin O'Donnell
Volkmar Dierolf
April 2010

References

1 A. Nishikawa, T. Kawasaki, N. Furukawa, Y. Terai and Y. Fujiwara, Appl. Phys. Express 2, 071004(2009).
2 I. S. Roqan, K. P. O'Donnell, R. W. Martin, P. R. Edwards, S. F. Song, A. Vantomme, K. Lorenz, E. Alves, and M. Boćkowski, Phys. Rev. B 81, 085209 (2010)
3 K. Wang, K. P. O'Donnell, B. Hourahine, R. W. Martin, I. M. Watson, K. Lorenz, and E. Alves, Phys. Rev. B 80, 125206 (2009),
4 Simone Sanna, W. G. Schmidt, Th. Frauenheim, and U. Gerstmann, Phys. Rev. B 80, 104120 (2009).
5 J. M. Zavada, N. Nepal, C. Ugolini, J. Y. Lin, H. X. Jiang, R. Davies, J. Hite, C. R. Abernathy, S. J. Pearton, E. E. Brown, and U. Hommerich, Appl. Phys. Lett. 91, 054106 (2007).

Index

ω – 2θ scans, 312, 316
II–VI semiconductor, 278–9
2D/3D transition, 161, 163
5*d*-shell, 212

ab initio, 58, 326, 339
above-bandgap excitation, 118, 120, 124–5, 133–4, 139, 170, 221, 226, 241, 250, 263–4, 266–7, 286, 289, 291, 293, 296, 302
above-gap excitation, 14, 203
absorption cross-section, 286
acceptor, 2, 12–13, 17–19, 269–73, 278–81, 283, 295, 329, 339
acceptor-like trap, 272–3
activation energy, 140, 148–9
activator, 280
aimpro, 7
AlGaN, 18, 25, 48, 51, 102–3, 108, 132–4, 152, 162, 173, 182–5, 189–93, 195–219, 250
AlInN, 25, 51, 189–99, 201–19
AlN, 1–2, 10, 18–20, 23, 25, 34, 39, 42–48, 50–52, 56, 58, 67, 70, 77, 90–6, 102, 160–2, 164–79, 183–9, 192, 196–213, 216, 257–58, 344
  capping, 25, 47
$Al_xGa_{1-x}N$, 48, 70–1, 90, 187–8, 203, 205, 206–8, 210–213, 222, 257–9, 344
amorphization, 27, 30, 61, 67
amorphous layer, 50–1, 199
annealing, 14, 25–7, 30–48, 52, 55, 62, 65–78, 82–94, 117, 120, 124, 127–9, 171, 185–7, 192–4, 197–209, 214–16, 338
  atmosphere, 39
  temperature, 14, 37–40, 44–47, 72–8, 82–93, 120, 124, 187, 198–202, 214–16
array detector, 223, 225
Arrhenius plot, 123, 139, 141, 148–9
as-implanted, 43, 75, 87, 215
aspect ratio, 162, 185
atomic concentration, 196
atomic force microscopy (AFM), 9–10, 15, 136, 142–3, 162–3, 166, 168, 312, 315, 323
atomic moment of Gd, 321, 324, 329
atomic properties, 206
auger, 2, 17, 139, 178, 264, 289–90, 297–303
avalanche, 103

backtransfer, 178, 179, 182, 188, 289
band offset, 133
band-gap, 6, 148, 149, 171, 173, 178, 189, 190, 192, 202, 205, 208, 210, 211, 212, 216, 237, 290, 344
BE lifetime, 289, 292, 298–9
below-bandgap excitation, 117, 120, 122, 124, 127, 129, 133, 139, 161, 262, 272–3, 277, 282–3, 287, 291, 297–8, 301–2
below-gap excitation, 261
beta decay, 72
bimodality, 162, 185

bond length, 5, 15–16, 175
bound exciton (BE), 17–18, 26, 55, 69, 79, 82–3, 86, 94–5, 97, 106, 117, 120, 124, 129–36, 139, 160–3, 170–1, 186, 190, 192, 209, 217–8, 226, 236–42, 248–9, 251–2, 263, 269, 271–4, 278, 282–3, 288–99, 303–4, 311, 316, 329-30, 336, 338, 343
bowing parameter, 210
branching ratio, 234, 254, 291, 293–4
bridging F-center, 322

c-band, 139, 152, 155
C_{3v} symmetry, 15, 182, 223, 242, 250, 253
capping, 25, 34, 37, 42–4, 47, 52, 198, 206, 336
capping layer, 34, 37, 43–4, 52, 198, 206, 336
capture coefficient, 271, 288–94, 304
carrier confinement, 159, 173, 185
carrier trap, 14, 170–1, 290–1
carrier-mediated energy transfer, 169
cathodoluminescence (CL), 38, 118, 186–8, 192, 197, 264, 270
  intensity, 18–19, 38–9, 41, 44, 47–8, 51, 196, 199–200, 215–6
channelled implantation, 29, 48, 50, 83–5, 194
  and random implantation, 29, 48, 50
channelling, 13, 27, 30, 35, 40–2, 46–8, 55–6, 59, 60–95, 127, 214, 343
  pattern, 63–4, 73–6, 81, 88, 91
charge transfer, 206, 212, 274, 275, 277, 278
chemical potential, 11, 12
chromaticity, 100, 160, 183, 193
  diagram, 100
CIE, 100, 107
cluster, 2, 10, 22, 26, 30, 33–4, 43, 52, 83, 88, 94, 168, 177, 213, 317, 325, 336–8
clustering, 88, 94, 168, 177, 213, 338
co-doped SnO2–δ, 322
co-doping, 56, 86–7, 95, 132
co-implantation, 86
codoping, 117, 122, 282, 338
coercive field, 318
colossal magnetic moment, 56, 309–10, 321, 329–31, 336–9
combined excitation emission spectroscopy (CEES), 57, 201, 221–66
configuration interaction, 4
confocal scanning microscope, 248
conversion electron, 61, 70–4, 88
core exciton, 212
Coulomb interaction, 8, 178, 222
crack, 44, 196
cross-relaxation, 179
crystal field, 2, 56–7, 86, 94, 173, 206, 212–13, 222, 239, 242, 251–3, 270
Curie temperature, 310, 320, 332, 336, 339
current injection, 109–11, 171

D^0, X emission, 328
D^0X_A, 296
damage, 16, 25–52, 56, 69–70, 77–8, 82, 84–6, 90, 117, 124, 127, 129, 185, 192, 195–9, 202, 204, 214, 242
DC bias, 107
dechannelling, 30, 76–7, 85
deep defect, 237, 241, 263
deep gap state, 310
deep level emission, 147
deep level transition spectroscopy (DLTS), 16–17, 78, 140, 294–5, 304
defect
  engineering, 171, 304
  level, 85, 282, 295–6
  physics, 206
density functional based tight binding (DFTB), 7–8, 15–16
density functional theory (DFT), 2, 4, 6–10, 15–16, 18, 295
dilute magnetic oxide, 331, 337
dilute magnetic semiconductor (DMS), 56, 322, 329
dipole-dipole, 281
direct excitation, 229, 231, 236, 238, 240, 243, 270, 274, 278, 282–3, 303
dislocation, 30, 117, 145, 148, 160–1, 317
dislocation loop, 30, 317

disorder, 30, 43, 52, 64–5, 67, 82–3, 87, 90, 210, 214, 240–1, 257
displacement, 12, 18, 30, 33–5, 55, 59, 60–95, 126–7, 192, 200, 343
displacements per atom, 79
dissociation, 26, 37, 41, 52, 196, 289, 303
donor, 1–2, 12–13, 17–20, 139, 269–72, 278–83, 296, 313, 326–30, 339
donor acceptor pair (DAP), 270, 278–80, 282
doping profile, 30, 117, 129
double heterostructure (DH), 109, 132–4
DXcenter, 18
dynamic annealing, 26–7, 30, 32, 35, 43, 52, 67, 70, 77, 86
dynamic coupling, 240

EL device, 101–8, 303
EL spectrum, 133–4, 150, 154
elastic strain, 82, 95, 162, 184
electric field gradient, 70
electrical activity, 1, 96, 129
electrical breakdown, 102
electrical excitation, 101
electrical properties, 20, 128, 136, 140, 142, 345
electroluminescent (EL) device, 99, 111, 159, 171, 186, 241, 263, 303, 344
electron
  energy distribution, 105
  mobility, 108, 118, 140
electron emission channelling, 55, 56
electron probe micro-analyser (EPMA), 40, 192–5
electron trap, 14, 16, 128, 272
electron-hole pair, 101, 149, 168, 173, 178, 241–2, 264–6, 271, 280, 288, 344, 345
electron-phonon coupling, 222, 226, 244, 249, 253–6, 281
electronegativity, 2, 271, 275, 283
energy levels of defects, 13
energy transfer, 57, 101, 110, 124, 129–30, 139, 148, 159, 162, 169, 176–9, 182–3, 188, 201, 206, 226–7, 236–7, 264, 269–74, 279–81, 289–91, 294, 299, 304, 344–5
energy transfer parameter, 289, 291
energy transfer rate, 271, 291, 294, 304
EPR, 223, 278
EPSRC, 217
Er, 1, 2, 6–7, 13–20, 26–33, 40–4, 48–51, 57, 68–71, 77–94, 100–10, 115–61, 173, 186–96, 201, 213–15, 221–49, 261, 263, 266, 270, 272, 274, 277, 282–98, 301–4, 343–4
Er precursors, 136
Er site, 57, 226, 282
Er-C complex, 132
Er-doped nitride amplifier (EDNA), 152–4
Er_{Ga}-V_N complex, 140
Eu, 2, 13–14, 17–19, 24, 26–31, 33, 35, 36–9, 41, 43–52, 55, 57, 68–70, 76–9, 83, 86, 94–6, 100, 102, 105, 107–8, 110–11, 156, 159–66, 168–72, 178–80, 183–218, 221–2, 241, 245–6, 250–5, 258–68, 277–8, 282, 294–6, 298, 343–5
Eu_1, 171, 196, 203, 205, 208, 211–12, 216, 294
Eu_2, 171, 196, 203–5, 208, 213, 216, 277–78, 294
Eu_x, 170, 254
Eu_y, 170, 254
exchange correlation, 5, 11
exchange interaction, 28–1, 310, 325
excitation
  channel, 57, 221–2, 250, 252, 260–1, 266, 290–1, 294
  cross-section, 118, 286–94, 299, 304
  mechanism, 17, 99, 103–4, 109, 117, 129, 132, 140, 149, 160, 177, 226, 234, 269–82, 289, 291, 296, 303–4, 343–4
  model, 206, 265
  path, 38, 205, 213, 250, 262, 264–5, 271, 282, 288, 290–1, 295–6, 344
excitation/emission spectroscopy, 227, 229
excited state absorption (ESA), 234, 240, 276, 298

exciton, 1–2, 14, 17–18, 20, 120, 133, 139, 200, 203, 206, 209–13, 216, 241, 269–74, 278–82, 288–96, 303–4, 309–11, 327–30, 341, 344
  binding coefficient,, 289
  exciton radius, 210
  exciton trap, 14
  exciton trapping, 269, 271
  lifetime, 272
exponential decay, 179–81
extended X-ray absorption fine structure (EXAFS), 14, 164–5, 167, 213, 223, 343

Faraday geometry, 313
Favennec rule, 190, 212
f – d coupling, 326
Fe-doped SnO_2, 322
ferromagnetism, 309–41
ferro-to-paramagnetic phase transition, 320-1
field effect transistor, 108
fine structure, 59, 65–6, 91, 94, 164, 199, 201, 205
flat panel display, 100–11
fluence, 1, 15–16, 25–55, 61–2, 67–8, 70–1, 77–95, 102, 117, 120–4, 127–33, 159–63, 168, 194–6, 201, 206–10, 221–2, 237, 249, 251, 266, 270, 286, 295, 316, 323, 325, 328–31, 336–8
fluorescence line narrowing (FLN), 228–9, 240, 246–8
FLUX, 61, 68, 70, 79
focused ion-beam (FIB) implantation, 338–9
formalism, 4, 10, 71, 325
Förster resonant energy transfer, 280
Frank-Condon, 18–19
free electron concentration, 128, 140
FRET, 280
FWHM, 93, 136, 173, 202, 209, 210–11, 214

Ga vacancy (V_{Ga}), 136, 295, 339
$Ga_{0.94}Gd_{0.06}N$, 310
(Ga,Mn)As, 329
GaN
  :Er, 16, 57, 86, 100–9, 115–17, 120–53, 187, 190, 201, 214–15, 226, 239, 242, 249, 284–5, 287, 293, 343
  :Eu, 17, 69, 102, 111, 170–2, 179–80, 184, 191–2, 199–16, 246, 254, 263, 295–96, 298, 343
  :Gd, 56, 309, 310–41
  :Nd, 102, 242, 245–6, 249
  :Tb, 175, 184
gap level, 2
GdN, 324, 331, 334–6
giant magnetic moment, 322, 326
gradient corrected formalism, 4
GW approximation, 5

hard axis, 335–7
harmonic approximation,, 12
Hartree energy, 11
Hartree-Fock, 4
HEMT, 108
Henry's law, 145
HfO_2, 326
high pressure/high temperature annealing, 78
high resolution Xray diffraction, 29
high pressure annealed, 204
high temperature implantation, 67, 80, 86
hot carrier, 102, 103, 110
hot electron, 103, 109, 270–3
Huang-Rhys factor, 246
Hubbard Hamiltonian, 5, 9
HVPE, 118, 129, 131, 136, 206
hydride vapor phase epitaxy, 129
hyperfine interaction, 56, 66, 70, 95
hyperfine structure, 66
hysteresis, 318–20, 333–4, 336, 338

I2 BE, 295, 296
II-VI semiconductor, 278, 279
image plot, 223, 228, 230–38, 244, 252, 260
impact excitation, 101–4, 108, 110, 118, 270, 303
implantation, 31, 33, 41, 43, 45, 47, 49, 53, 71, 83, 126, 192

damage, 16, 25–7, 32–4, 37, 40, 48, 52, 70, 90, 117, 129, 185, 197
fluence, 29, 32, 35, 38–9, 51, 80, 82, 128
geometry, 56, 78, 83–5
temperature, 35, 86
indirect excitation, 270, 274, 278, 282–3, 303
indium-tin-oxide (ITO), 102
InGaN, 115, 117, 123, 136, 142, 145–6, 148–50, 152, 155, 160, 165, 168, 171–2, 185–90, 197, 221, 262, 344, 345
inhomogenously broadened emission line, 247
intensity map, 193, 196
interface energy, 162
internal electric field, 173, 176, 179
interrupted growth epitaxy (IGE), 188, 257
interstitial, 14, 26, 30, 59, 60–3, 68, 78, 253, 295, 338
interstitial site, 59, 62–3, 68
intrinsic defect, 2, 59, 253
inversion symmetry, 56
ion beam channelling, 55–6, 59–62
ion implantation, 25–6, 52, 92, 117, 197
islanding, 160, 162–3
isoelectronic, 140, 182, 188, 206, 213, 271, 274, 283, 295
centre, 213
doping, 140, 206, 283, 295
ISOLDE, 23, 61, 96–8
isotope, 61, 70–8, 81, 312

Janak's theorem, 11
jj coupling, 222

k-point sampling, 15
Kohn-Sham, 7, 9–11, 13

laser, 99, 116–9, 129, 131, 152–5, 159, 168, 174, 186, 189–90, 193, 201–2, 207, 221–6, 241–2, 250–1, 266, 270, 294, 296–303, 313
laser diode, 129, 155
lattice
defect, 43, 83, 94, 326
distortion, 15, 171, 283
match, 213
site location, 55–95
LDA+U, 5, 8–10, 15–16, 344
leakage current, 110
lifetime, 17, 61, 103, 118, 132, 140, 272, 286, 289, 292–5, 298–9, 328
ligand-to-metal charge transfer (LMCT), 274–5, 277–8
light emitting diode (LED), 109–11, 129, 133–34, 142, 148, 150–5, 159–62, 185, 190, 262
line narrowing, 228, 240, 246–9
linewidth, 200, 204, 209–12, 216, 222, 224, 283
local density functional approximation, 4
local mode, 227, 236, 246
local structure, 15, 66, 85
localization center, 160
localized state, 16, 206
long-range order,, 336
LS coupling, 222
luminescence, 1–2, 12, 14, 17–19, 38–9, 44, 47–8, 51–7, 69, 78, 83, 86–7, 94, 99–102, 108–12, 115–8, 159–61, 168–72, 175–83, 185–93, 196–200, 204–16, 225, 230, 233, 242, 250–51, 254, 257, 264, 270–4, 282, 285–9, 294–8, 303–4, 309–13, 326
luminescence intensity, 38–9, 44, 48, 51, 86, 108, 182, 198–200, 254, 272, 282
luminescence mechanism, 17, 19, 57

magnetic
anisotropy, 311, 313, 337
moment, 16, 56, 210, 309–11, 321–6, 329–39
nitride, 331, 337
viscosity, 334
magnetization, 310–13, 318–23, 329, 331–38, 344
magneto-photoluminescence (MPL), 309, 326

spectroscopy, 313
majority site, 57, 227, 253, 263
map, 33, 65–6, 192–3, 223, 229, 248
mapping, 46, 192, 196–7
material composition, 194, 196
mean field theory, 9
metal organic chemical vapor deposition (MOCVD), 26, 39, 42, 87, 115, 117, 120, 122, 124, 127–9, 132–50, 155, 191, 198, 226, 228, 230–41, 251, 260, 343
metal organic molecular beam epitaxy (MOMBE), 129, 161, 343
metal organic vapor phase epitaxy (MOVPE), 184, 186, 192, 194, 206
minimum (channelling) yield, 67
minority site (MS), 57, 129, 131, 136–7, 142, 229-237, 240–6, 252–4, 257–8, 261–6, 312–15, 326, 329
misfit dislocation, 161
molecular beam epitaxy (MBE), 26, 55, 69, 79, 82–3, 86, 94–5, 106, 117, 120, 124, 129–36, 139, 160–3, 170–1, 186–7, 190, 192, 226, 236–42, 248–52, 263, 282, 295–6, 311, 316, 336, 338, 343
growth, 26, 82, 95, 106, 132, 186
Monte-Carlo simulations, 77
mosaic spread, 77, 92–3
mosaic tilt and twist, 92
mosaicity, 56, 70, 77, 91–3
Mössbauer spectroscopy, 66, 70
multiple Lorentzian curve fit, 181
multiple site, 2, 57, 60, 161, 242–3
multiplet, 2, 17, 201, 203–5, 209, 222, 227, 243–4, 246, 249
^{2}G7/2, 242–3, 246
$^2H_{11/2}$, 41, 103, 106, 139, 194, 228, 234, 237
$^{2S+1}L_J$, 222
$^4F_{3/2}$, 242–4, 246
$^4F_{9/2}$, 173, 228, 234, 237, 239
$^4G_{5/2}$, 242–3, 246
$^4I_{11/2}$, 138, 228, 230–2, 234
$^4I_{13/2}$, 116, 138, 190, 227–8, 230, 234, 237, 283, 286, 298
$^4I_{15/2}$, 41, 103, 116, 133, 138–9, 173, 190, 194, 222, 226, 228, 230–1, 234, 237, 239, 283, 285, 298
$^4I_{9/2}$, 234, 242, 244, 246, 285
$^4S_{3/2}$, 41, 133, 139, 194, 228, 234, 236–7, 239
$^5D_0$-$^7F_1$, 202
$^5D_0$-$^7F_2$, 194, 205–11, 213
$^5D_1$, 253
^5D_o, 250, 252–4, 256, 258
$^7F_2$, 17, 38, 110, 171, 179–80, 194, 196–7, 201–2, 205–11, 213, 250, 252–6, 258, 295
$^7F_3$, 17, 204, 252–3
^7F_o, 250, 252, 254–5
multiplicity, 13, 57, 343

nanocrystalline surface layer (NCSL), 30, 32, 34–5, 42
nanocrystallization, 32, 34, 48, 52
narrow bandgap semiconductor (NBGS), 116, 139, 155
negative-U, 19
nitrogen vacancies, 14, 20, 78, 140, 148, 261, 344
non-linear core correction, 5–6
non-radiative recombination, 129, 132, 145, 148, 160, 170, 182, 288
non-resonant excitation, 252, 261–2, 266, 283–8
nonlinear Stark effect, 173
nonradiative transfer, 269
nucleation, 34, 163, 166–8, 311

optical
activation, 25–6, 38, 51, 52, 86, 117, 198
amplifier, 139, 154–5, 221
communication, 115–6, 136, 152, 270
gain, 154, 242, 254
transition, 1, 18, 19, 56, 224, 226, 310
waveguide amplifier, 115, 154–5
over-exposure technique, 244
oxygen, 12, 14, 19–20, 59, 78, 86–90, 326

p-n junction, 101, 109, 266
PA-MBE, 249, 251
percolation, 323–5, 330, 336–7
  threshold, 324–5, 336–7
perturbed angular correlation (PAC), 55, 66, 70, 95
phenomenological model, 92, 309–10, 323, 336
phonon-assisted
  excitation, 256
  transition, 221, 243, 251, 263
photoemission spectroscopy, 276
photoionization
  cross-section, 303
  mechanism, 298, 300
photoluminescent (PL)
  decay, 141, 170, 181, 200, 201, 298
  decay dynamics, 200
  dynamics, 159, 180
  excitation (PLE), 2, 13–14, 18, 57, 78, 115, 117, 120, 122, 133, 149–50, 161, 172, 187, 200–16, 262, 277, 282, 285–6, 294–6
photon escape probability,, 102
photonic
  crystal, 154
  integrated circuit, 152
PIC, 152, 154, 155
piezoelectric coefficient, 322
planar waveguide amplifier, 129, 155
plasma-assisted MBE, 162, 163, 338
point defect, 22, 26, 30, 33–4, 52, 62, 77–8, 199, 212, 295, 304, 310, 323–6, 338–9
  cluster, 30, 33–4, 52
polycrystalline growth, 133
positron annihilation, 136
positron annihilation spectroscopy (PAS), 294–5, 304
propagation loss, 152
proximity cap, 37–8, 44, 198, 206
pseudopotential, 5–7, 15–6

quadrupole splitting, 70
quadrupole-dipole, 281
quadrupole-quadrupole coupling, 281
quantum confined Stark effect, 173
quantum dot (QD), 129, 159–85, 171, 186–8, 344
quantum well, 129, 152, 160
quenching, 2, 47–8, 99, 102, 116, 121, 129–30, 139–40, 151, 170, 185, 188–9, 200, 204–5, 216, 249, 251, 270, 298, 301–4

R-plane sapphire, 117–8
radiative rate, 288
radioactive probe, 59, 62–3, 66
random (R) site, 64
random implantation, 28–9, 48, 50, 85–6
random site, 55, 71–6, 79, 88, 91, 94–5
rate equation, 274, 289, 298, 299
rare earth (RE)
  concentration, 16, 56, 61, 82–3, 95, 179, 195–6, 249, 272
  nitride, 83, 94
  related trap, 2, 177
RE-VN, 14, 19
RE_{Al}-O_N, 19
  complex, 19
reflection high-energy electron diffraction (RHEED), 133, 135, 311–2, 315, 323, 336
RE_{Ga}, 15, 76–8, 83, 223, 295
RE_{Ga}-V_N
  pair, 78
  complexes, 259
RE_{III}, 94–5
relaxation energy, 18–9
remanence, 313, 331–6
remanent magnetization, 318, 334
RENiBEl, 95, 97, 217–8
resonant excitation, 118–9, 161, 232, 241, 244–5, 251–2, 258, 261–3, 265–6, 269, 283–8
RE-VN, 2
ridge waveguide, 153
rise time, 17, 178–9
RKKY, 325, 341

rms displacement, 64, 68–78, 82, 85, 88–90, 95
Rutherford backscattering, 13, 60, 66, 163, 223, 242
  spectrometry, 60, 163
  and chanelling spectrometry (RBS/C), 27, 28, 30–1, 34–50, 66, 70–1, 78–9, 82–3, 87, 90, 198, 199

satellite peak, 239, 244
saturation, 34, 50, 103, 182, 286, 291–2, 298, 313, 318, 321, 323–4, 329–37
scanning electron microscope (SEM), 43, 45–6, 215–6, 260, 264, 312, 315, 323
secondary ion mass spectrometry (SIMS), 129, 131, 136–7, 242, 312–5, 326
secondary phase, 316–8, 325, 336
selection rules, 2, 206
self-interaction, 10
sensitizer, 212, 280
sensitizing defect, 206, 211–2
S_{Ga}
  fraction, 71, 76–7, 84–5, 89
  site, 55, 64–5, 69, 78–9, 86, 89–90
shallow trap, 261–5, 344
shielding, 222
Si nanocrystal, 1, 270, 274, 290
Si photonics, 155
simulation, 195
single heterostructure (SH), 132–4
site-selective spectroscopy, 221, 266
Slater determinant, 3–4
solid-source molecular beam epitaxy, 161
spatial resolution, 192
spatially resolved spectroscopy, 248
spectral overlap, 236, 240, 261, 279–81
spectral resolution, 201, 225
spin polarization, 309, 310, 321–3, 326, 336, 339, 344
spin-LED, 111
spin-on-glass (SOG), 106–7
spin-orbit interaction, 222
spin-relaxation time, 328
spintronics, 221, 339, 344
splitting of lines, 202
spontaneous emission lifetime, 103
sputtering, 34, 111, 117, 192, 198–9, 343
SrS:Ce, 270
SSMBE, 161
stacking fault, 26, 30, 33–5, 42–3, 45, 52, 92
Stark splitting, 56, 94, 188, 228, 237
Stark-splitting, 182
sticking coefficient, 145
strain relaxation, 161, 184
Stranski-Krastanow (SK), 160–2, 166, 168, 183, 185–6
structural energy, 3, 10–12
substitutional
  fraction, 35, 55–6, 65, 70, 73–86, 89, 94–5, 126, 200
  site, 13, 43, 46, 58, 70–1, 79, 81–3, 88, 94, 167, 171, 200, 204–5, 216, 283, 286, 294
supercell, 2, 10, 13
superconducting quantum interference device (SQUID) magnetometer, 312–3, 329, 331, 334, 338, 340
superexchange, 325
surface kinetic, 161, 163
surface reconstruction, 163, 312, 315
susceptibility, 313, 336
symmetry, 203
synchrotron, 65

TEM, 27, 30–6, 42–3, 45, 50–2, 199, 312, 316–7, 325, 336
temperature quenching, 99
ternary alloy, 48
thermal quenching, 48, 116, 129–30, 139–40, 151, 190, 200, 204–5, 216, 270
thermal vibration, 55, 65, 68, 75–6, 78, 85, 90, 94
thermally activated level, 221, 226
thin layer, 196, 251
three-step excitation, 232–6
tight binding, 3
tilt, 27, 28, 71, 92, 214, 228–9, 247
time-resolved PL, 140, 182
Tm-doped
  AlN, 172

GaN, 172–3, 180, 186
TmN, 83
transfer probability, 280
transition metal (TM), 5, 8, 213, 310–2
transmission electron microscopy, 30, 312, 316
trap capture coefficient, 271, 293, 304
travelling wave optical amplifier, 154
twist, 92
two-beam experiment, 296, 303
two-step excitation, 231

u-parameter, 57
ultra-high pressure annealing, 47
ultra-high temperature annealing, 200
up-conversion, 221, 226, 229, 231–7, 242, 266

valence state, 15, 222, 269, 271, 277–8
Vegard's law, 184
visible emission, 26, 103, 138, 183, 190
V_N, 2, 14, 17, 19, 78, 140, 295

waveguide, 115, 129, 152–5
wavelength dispersive X-ray, 192
wavelength division multiplexing (WDM), 154–5
Wien2K code, 16
wurtzite, 15, 35, 55, 57–9, 61, 64, 209, 310, 339, 343

X-ray
linear dichroism (XLD), 338
magnetic circular dichroism (XMCD), 338
rocking curve, 92–3, 136, 143–4, 316
X-ray absorption
diffraction (XRD), 29, 92, 136, 142–5, 184, 312, 316–7, 325, 336, 338
fine structure (XAFS), 14, 56, 59, 65–6, 79, 83, 94, 164–5, 167, 213, 223, 343
near-edge spectroscopy (XANES), 338

yellow band, 127, 146, 173

Zeeman splitting, 327
Zener mechanisms, 103
zero phonon line, 257
zincblende, 57, 339
GaN:Gd, 339
ZnS:Tb, 270